

**SYNTHESIS AND CHARACTERIZATION OF SOME  
TRANSITION METAL COMPLEXES AND THEIR  
REACTIVITY STUDIES**

**Ph.D. THESIS**

*by*

**OVENDER SINGH**



**DEPARTMENT OF CHEMISTRY  
INDIAN INSTITUTE OF TECHNOLOGY ROORKEE  
ROORKEE - 247 667 (INDIA)  
NOVEMBER, 2017**



# INDIAN INSTITUTE OF TECHNOLOGY ROORKEE ROORKEE

## CANDIDATE'S DECLARATION

I hereby certify that the work which is being presented in the thesis, entitled “**SYNTHESIS AND CHARACTERIZATION OF SOME TRANSITION METAL COMPLEXES AND THEIR REACTIVITY STUDIES**” in partial fulfilment of the requirements for the award of the Degree of Doctor of Philosophy and submitted in the Department of Chemistry of the Indian Institute of Technology Roorkee, Roorkee is an authentic record of my own work carried out during a period from December, 2011 to November, 2017 under the supervision of Dr. Kaushik Ghosh, Associate Professor, Department of Chemistry, Indian Institute of Technology Roorkee, Roorkee.

The matter presented in the thesis has not been submitted by me for the award of any other degree of this or any other Institute.

**(OVENDER SINGH)**

This is to certify that the above statement made by the candidate is correct to the best of my knowledge.

**(Kaushik Ghosh)**  
Supervisor

Date: November, 2017

## ACKNOWLEDGEMENT

---

Foremost, I humbly and politely bow my head in front of, the *Lord Shiva* and *Goddess Saraswati* “*The Goddess of Wisdom*” who bestowed upon me an opportunity to do this work and gave me ample vision and strength to accomplish this work successfully. .

I would like to convey my deepest gratitude and reverence to my supervisor **Dr. Kaushik Ghosh** for his helpful counsel, management, and professionalism. I am highly thankful for his time, attempt and editing skills. His constant support, the trust he placed in my abilities, encouragement and judicious interventions made this thesis to come into picture. I humbly acknowledge a life time’s gratitude to him. No words articulate to acknowledge the didactic guidance rendered by him. I pay my heartily gratitude to his wife **Rupa Ghosh** who supported and motivated me all the time from the joining of research programme till today in every aspect of life. She virtuously encouraged me every time with her motherly support, love and care. It is very pleasant to have some joyful moments with Raunak and Rahi.

I am thankful to Prof. Mannar Ram Maurya and Prof. Anil Kumar, the present and the former Heads, Department of Chemistry, IIT Roorkee, for providing me all the instrumental and necessary facilities and support to carry out these investigations.

The financial support from Ministry of Human Resource Development (MHRD) to complete the present investigations is highly acknowledged.

My thanks are due for the Institute Instrumentation Centre, IIT Roorkee. I am thankful to Prof. U. P. Singh, Dr. Kapil Tomar, Dr. Shikha Narang and Dr. Neetu Singh, Dr. Sujata for the help in XRD analysis. Mr. Charan Singh for NMR analysis.

I wish to thank all the faculty members and non-teaching staff of the Department of Chemistry, IIT Roorkee. I would also like to thank Mr. S.P. Singh, Mr. Madan Pal, Mr. Duli Chand Meena, Mr. Ramesh ji, Mr Aashu, Mr. Ankur, Mr. deepak, Mr. Rohit, Mr. Pankaj for all the technical assistance in the Department of Chemistry.

In my lab, I express my special thanks to Dr. Nidhi Tyagi, Dr. Pramod Kumar, Dr. Sushil Kumar, for all the scientific discussions and his invaluable help to make my work more precious. Without his help it was not possible to produce so many results. My sincere appreciation goes to Mr. Ankur Maji, Ms. Anshu Singh for their timely help during the execution of this work and moral support. Their valuable suggestions were always helpful for improving the quality of the work.

I wish to thank my other members Dr. Rajan Kumar, Dr. Varun Mohan, Dr. Sweety Rathi, Anand, Manju, Kiran, Kapil, Sheela, Atul Choudhary, Priyanka, Prasoon Raj Singh Thakur for their support valuable suggestions.

I express my special thanks to my lovely friend Dr. Manoj Kumar who always stayed with me during all the ups and downs of my life. My sincere appreciation goes to my friends Dr. Ram Jiwari, Dr. Arun Choudhary, Dr. Inam, Dr. Tejveer Singh, Mr. Paritosh Kumar, Ms. Bhawana Singh, Ms. Priyanka Singh, Mr. M. Venkatesan. Dr. Lovely Mallick, Mr. Harshit Mahendra, Ms. Moupia Mondal,

I wish to thank my younger brothers and sister Mr. Adesh kumar, Mr. Praveen kumar, Mr. Alil kumar, Mr. Sonu, Mr. Monu, Mr. Gaurve, Mr. Pravesh, Mr. Shubham, Mrs. kavita, Mrs. Neelam, Mrs. Sabnam, Mr. Joni, Ms. Shivani for their support and encouragement.

Finally, I express my heartfelt gratitude to my highly respectable and adorable father, Sh. Tejpal Singh and mother, Smt. Premvati, my elder brother Mr. Balender Singh for their unconditional love, encouragement and blessings. I also wish to express my feelings from the bottom of my heart for my bhabhi ji Mrs Pinki Rathi for encouragement and blessings. I would like to thank to my wife Mrs. Munesh Singh for timely support. It is very pleasant to have some wonderful moments with Sachin and Suraj.

At last, I am extremely grateful to the people whose names have been unknowingly left. I apologize and believe that their wishes will always be with me as they were during the times of need.

**Ovender Singh**

## ABSTRACT

---

Inorganic chemistry is the deep understanding of the synthesis, reactions, structures and properties of compounds of the elements. Inorganic chemistry has several branches and bioinorganic chemistry is one of them. Bioinorganic chemistry describes the mutual relationship between inorganic chemistry and biochemistry. This basically deals with the role of inorganic substances such as metal ions, composite ions, coordination compounds or inorganic molecules inside the living organism. Role of bioinorganic chemistry is to understand all the possible interactions between these inorganic substances and the biological tissues. These interactions can only be studied with the knowledge of coordination chemistry where metal ions bind with the ligands which could be the side chain of amino acid or any other biomolecule. Hence bioinorganic chemistry goes hand in hand with the coordination chemistry.

In present study, the designing of few new ligands, their synthesis and characterization will be described. Manganese, iron, cobalt, nickel and copper complexes derived from those ligands and their spectroscopic studies will be described. Molecular structures of the few ligands and representative metal complexes were determined by X-ray crystallography. The results of reactivity studies on above mention metal complexes will be scrutinized in this thesis. The Thesis is divided into the following chapters.

**First chapter** presents an introduction to coordination chemistry and several reactivity studies. The various chemical methods and spectroscopic techniques used were comprehensively summarized in this chapter.

In **chapter two**, we have described Complexes  $[\text{Cu}(\text{PyPhime-sali})\text{ClO}_4]$  (**1**) and  $[\text{Cu}(\text{PyPhime-}^t\text{Bu-sali}(\text{CH}_3\text{OH}))\text{NO}_3].2\text{CH}_3\text{OH}$  (**2**) ( $\text{L}^1\text{H}_2$  and  $\text{L}^2\text{H}_2$  (PyPhime-sali = 2,2'-

((1E,1'E)(2,2'-(pyridine-2,6-diyl)bis(2-phenylhydrazin-2-yl)ylidene))bis(methanylylidene))diphenol, PyPhime-<sup>t</sup>Bu-sali = 6,6'-((1E,1'E)-(2,2'-(pyridine-2,6-diyl)bis(2-phenylhydrazin-2-yl)ylidene))bis(methanylylidene))bis(2,4-di-tert-butylphenol) and H is dissociable proton) were synthesized and characterized by different spectroscopic methods. Molecular structures of the complexes were determined by X-ray crystallography and redox properties were investigated. Complex **1** was found to be a phenolato complex whereas complex **2** was a phenoxyl radical complex.

**Chapter three**, describes hexacoordinated non-heme iron complexes [Fe<sup>II</sup>(Cl-pyhyd-Pycarbo)<sub>2</sub>](ClO<sub>4</sub>)<sub>2</sub> (**3**) and [Fe<sup>II</sup>(Cl-pyhyd-methyl-Pycarbo)<sub>2</sub>](PF<sub>6</sub>)<sub>2</sub> (**4**) have been synthesized using ligands [Cl-pyhyd-Pycarbo = (E)-2-chloro-6-(2-(pyridin-2-ylmethylene)hydrazinyl)pyridine and Cl-pyhyd-methyl-Pycarbo = (E)-2-chloro-6-(2-(1-(pyridin-2-yl)ethylidene)hydrazinyl)pyridine]. These complexes are highly active non-heme iron catalysts to catalyse the C(sp<sup>3</sup>)-H bonds of alkanes. These iron complexes have been characterized using ESI-MS analysis and molecular structures were determined by X-ray crystallography. ESI-MS analysis also helped to understand the generation of intermediate species like Fe<sup>III</sup>-OOH and Fe<sup>IV</sup>=O. These complexes have also been utilized in degradation of organic dyes. DFT and TD-DFT calculations revealed that the oxidation reactions were performed through high-valent iron centre and a probable reaction mechanism was proposed. These complexes were also utilized for the degradation of orange II and methylene blue dyes. In **chapter four**, copper complex [Cu(TETA<sup>TA</sup>)(Cl<sub>2</sub>)] (**5**) derived from tridentate ligand (TETA<sup>TA</sup>) (L=2-(2-((2-(2-aminoethyl)amino)ethyl)-amino)ethyl)isoindoline-1,3-dione) having NNN donor, was synthesized, characterized and molecular structure was determined using X-ray crystallography. This was found a robust

catalyst for the degradation the organic dyes such as Orange II dye, Rhodamine B and Methylene blue. This catalyst was also utilised for the oxidation of catechol and 2-aminophenol. The catecholase and phenoxazinone synthase activity were determine using UV-visible spectroscopic studies. Theoretical calculations were performed to understand the electronic properties of this molecule.

In **chapter five**, Bio-inspired  $[\text{Mn}(\text{PyPhime-Pycarbo})(\text{H}_2\text{O})(\text{CH}_3\text{OH})](\text{ClO}_4)_2$  (**6**) and  $[\text{Fe}(\text{PyPhime-Pycarbo})(\text{H}_2\text{O})(\text{ClO}_4)]\text{ClO}_4$  (**7**). Complexes with a pentadentate ligand (PyPhime-Pycarbo = 2,6-bis((E)-1-phenyl-2-(pyridin-2-ylmethylene)hydrazinyl)pyridine) framework containing  $\text{N}_5$  binding motif displayed excellent superoxide dismutase activity (SOD), with high stability in physiological conditions.

In **chapter six**, Complexes  $[\text{Mn}(\text{PyPhime-Cina})\text{Cl}_2]$ , (**8**)  $[\text{Fe}(\text{PyPhime-Cina})\text{Cl}_2]$  (**9**)  $[\text{Co}(\text{PyPhime-Cina})\text{Cl}_2]$  (**10**),  $[\text{Ni}(\text{PyPhime-Cina})\text{Cl}_2]$  (**11**)  $[\text{Cu}(\text{PyPhime-Cina})\text{Cl}_2]$  (**12**) have been synthesized using ligand (PyPhime-Cina=2,6-bis((E)-1-phenyl-2-((E)-3-phenylallylidene)hydrazinyl)pyridine) with NNN type moiety. The complexes have been used to studies the DNA interaction studies.

**Chapter seven** presents the synthesis of complexes  $[\text{Cu}(\text{PyPhime-Ben})_2](\text{NO}_3)_2$  (**13**),  $[\text{Cu}(\text{PyPhime-Ben})_2](\text{ClO}_4)_2$  (**14**) using ligand PyPhime-Ben = 2,6-bis((E)-2-benzylidene-1-phenylhydrazinyl)pyridine and complexes of  $[\text{Cu}(\text{PyPhime-p-methoxyBen})(\text{PF})_2]$  (**15**) and  $[\text{Co}(\text{PyPhime-p-methoxyBen})\text{Cl}_2]$  (**16**) using ligand PyPhime-p-methoxyBen = 2,6-bis((E)-2-(4-methoxybenzylidene)-1-phenylhydrazinyl)pyridine these complexes were utilized for DNA interaction studies. Using tetradentate ligand (Gimpy = (1E,2E)-1,2-bis(2-phenyl-2-(pyridin-2-yl)hydrazono)ethane) we have synthesized eight coordinated  $[\text{Mn}(\text{Gimpy})_2](\text{ClO}_4)_2$ (**17**) and  $[\text{Mn}(\text{Gimpy})(\text{NO}_3)_2]$ (**18**) complexes. In this chapter we

have utilised pentadentate ligand  $L^6$  for  $[\text{Co}(\text{PyPhime-Pycarbo})(\text{H}_2\text{O})(\text{ClO}_4)](\text{ClO}_4)$ , (**19**),  $[\text{Mn}(\text{PyPhime-Pycarbo})(\text{H}_2\text{O})_2] (\text{Fe}(\text{CN})_5\text{NO})$  (**20**) and  $[\text{Ni}_2(\text{PyPhime-Pycarbo})_2\text{Cl}_2](\text{ClO}_4)_2$ , (**21**) complexes. These complexes have been synthesized and their molecular structure characterized with single crystal X- ray diffraction analysis. These complexes utilised for the in- vitro inhibition of superoxide anion i.e superoxide dismutase activity (SOD) studies. We have also synthesized complexes  $[\text{Fe}_2(\text{PyPhime-sali})_2](\text{Fe}(\text{CN})_5\text{NO})$  (**22**) and  $[\text{Fe}_2(\text{PyPhime-sali})_2](\text{ClO}_4)_2$  (**23**) using pentadentate ligand  $L^1$  for in- vitro superoxide dismutase activity (SOD) studies.





## **1.1 Introduction**

Coordination chemistry is the chemistry of transition metal ions with different type of ligands. This is an important branch of chemistry and chemical research where design, synthesis, characterization and applications of coordination complexes derived from metal ions and ligands are generally discussed.<sup>1</sup> It is well known in the literature that the ligands having pyridine nitrogen,<sup>2</sup> imidazole nitrogen and thioether donors<sup>3</sup> stabilize the lower oxidation state of the metals. On the other hand, carboxylic acid, carboxamido nitrogen,<sup>4-5</sup> phenolato<sup>6-7</sup> oxygen stabilize the metal ions in higher oxidation state. In a particular oxidation state, ligands could also stabilize the metal ion in low spin or high spin or in spin-state equilibrium states.<sup>8</sup> Hence, a ligand impart attractive properties to a metal ion by stabilizing the specific oxidation state and in a particular spin-state.

## **1.2 Ligand**

A ligand may be defined as a molecule or ion containing at least a pair of electrons which could be donated to the metal ion so that complexes are formed. The ligands serve as electron donors acting as a Lewis base and metals as electron acceptor acting as Lewis acid. Generally, any part in a molecule that happens to be more basic than the C-H portion may act as a ligand.<sup>1</sup>

### **1.2.1 Classification of ligands**

There may be several ways of classifying the ligands. Based on donor and acceptor properties, ligands may be of following types:<sup>1</sup>

**(a) Classical ligands:** These ligands donate the electron pair to all sorts of Lewis acids including metal ions to form the complexes e.g.  $\text{NH}_3$  and  $\text{H}_2\text{O}$ .

**(b) Nonclassical ligands:** These ligands are also called  $\pi$ -acid ligands. These can donate the electrons to the metal in the empty d-orbitals as well as accept the electrons from the metal through  $\pi$ -bonding e.g.  $\text{PPh}_3$  and  $\text{CO}$ .<sup>1</sup>

Alternatively, ligands may be also classified as:

- (1) **Ligands with lone pairs of electrons:** These may further be of two types.
- (a) Ligands with no vacant orbitals to receive back donated electrons from metal e.g. H<sub>2</sub>O.
- (b) Ligands with vacant orbitals to receive back donated  $\pi$  electrons from the low oxidation state metal e.g. CO.
- (2) **Ligands without lone pair of electrons:** These ligands do not have lone pairs of electrons but have  $\pi$ - bonding electrons e.g. ethylene.

Ligands may also be categorised electronically i.e. according to the number of electrons donated to the central metal atom (when those are considered as neutral species).<sup>1</sup>

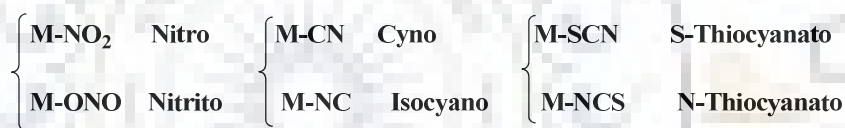
- (i) One electron donors: This type of ligands form a single covalent bond e.g. F and SH.
- (ii) Two electron donors: This type of ligands donate a pair of electrons to form the complexes e.g. NH<sub>3</sub> and H<sub>2</sub>O.
- (iii) Three electron donors: This type of ligands form a covalent bond besides the donation of an electron pair e.g. an acetate ion coordinated to a metal ion by both oxygen atoms.
- (iv) Four electron donors: These ligands donate two pair of electrons hence regarded as four electron donors e.g. *N,N'*-ethylenediamine.

Alternatively, ligands may also be classified structurally. Depending upon the number of donor atoms available for coordination site. There may be several types of ligands in coordination chemistry like uni-, bi-, tri-, tetra-, penta-, hexadentate ligands and so on.<sup>3</sup> Some examples of uni- (or mono-) and multidentate (polydentate) ligands are illustrated in Table 1.1.

**Table 1.1** Representative examples of some unidentate and polydentate ligands

Denticity	Example
Unidentate	Ammonia, water
Bidentate	<i>N,N'</i> -ethylenediamine, 1,10-phenanthroline
Tridentate	Terpyridine ligands
Tetradentate	Salen ligands
Pentadentate	Tetraethylenepentamine
Hexadentate	Ethylenediaminetetraacetate (EDTA <sup>4-</sup> )

Some unidentate ligands have two or more different donor sites and may coordinate to metal ion using either of them. These type of ligands are called ambidentate ligands. These ligands give rise to the possibility of linkage isomerism (Scheme 1.1).<sup>1</sup>



**Scheme 1.1** Ambidentate ligands and their coordination sites

Furthermore, the ligands may also be classified on the basis of the nature of donor atoms like oxygen donor ligands (e.g. H<sub>2</sub>O, Ph<sub>3</sub>PO and SO<sub>4</sub><sup>3-</sup>), nitrogen donor ligands (CO, η-C<sub>5</sub>H<sub>5</sub>, CH<sub>3</sub>CH=CH<sub>2</sub>) and nitrogen donor ligands (NO and NO<sub>2</sub><sup>-</sup>).<sup>3</sup>

## 1.2.2 Special types of ligands

### 1.2.2.1 Macrocyclic ligands

Polydentate ligands in which the donor atoms are constrained in a large ring encompassing the metal atom.<sup>9</sup> A well known example of macrocyclic ligands is polyether in which the ether oxygen atoms bind to the central metal atom in a nearly planar arrangement with the separating methylene moieties forming a crown above the ligand binding plane. A wide range of macrocyclic ligands having a conjugated π-system is also known. Phthalocyanines,

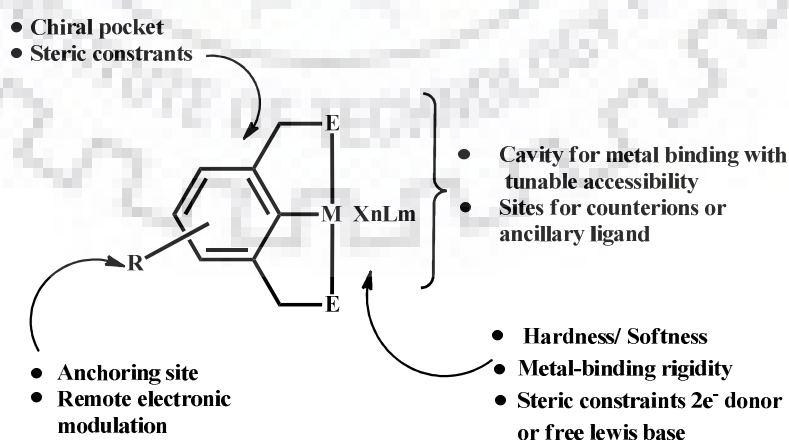
porphyrins, corrins and corroles are the well known examples of such type of macrocycles. Macrocyclic ligands exhibit greater thermodynamic and kinetic stability in their complexes than the corresponding open-chain chelating ligands.<sup>1</sup> These ligands also exhibit the unique property of stabilizing higher oxidation states of metals such as Cu<sup>III</sup> and Ni<sup>III</sup> which are difficult to attain under normal conditions.<sup>1</sup> The properties of the complexes derived from these ligands greatly depends upon the size of the cavity within the macrocycle. Among various approaches adopted for the synthesis of macrocyclic ligands, template directed synthesis and high dilution technique are the most common.<sup>10</sup>

### **1.2.2.2 Clathrochelate, sepulchrates, sphere and hemisphere**

Clathrochelate or cryptands are bicyclic or polycyclic multidentate macromolecules, generally containing bridgehead nitrogen atoms which form a three-dimensional cage around the metal ion.<sup>9</sup> These ligands exhibit selectivity for complexation of alkali and alkaline earth metal ions. Apart from the cryptands which are first synthesized and then utilized for complexation, there are other types of multicyclic ligands also, known as encapsulating ligands, which are synthesized around the metal ions and cannot release it.<sup>1</sup> A very well known example of such ligands is nitrogen analogs of the cryptands, known as *sepulchrates*. These are basically polyaza cage macrocycles which exhibit exceptionally strong hold on the encapsulated metal ions. These ligands bind the metal ion by six N-donors which do not leave the coordination sphere even under extremely acidic or basic conditions or with the changes of the oxidation state of the metal atom thereby permitting the study of their complexes in various oxidation states while keeping their constitution and stereochemistry unchanged.<sup>1</sup> There is another type of macrocyclic ligands known as *spherands/hemispherands*. These ligands consist of macrocycles derived from phenyl groups arranged in a specific way to provide a preorganized cavity for complexation.

### 1.2.2.3 Pincer ligands

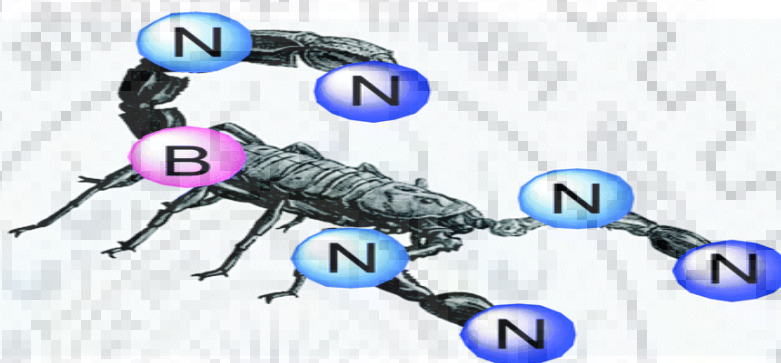
Pincer ligands are tridentate ligands which are connected to the metal *via* at least one metal–carbon  $\sigma$  bond. The most common pincer scaffold is composed of an anionic aryl ring which is *ortho*, *ortho*-disubstituted with heteroatom substituents like  $\text{CH}_2\text{NR}_2$ ,  $\text{CH}_2\text{PR}_2$  or  $\text{CH}_2\text{SR}$ . These ligands coordinate with the metal centre in a  $\eta^3$ -*mer* fashion constructing one M–C  $\sigma$  bond along with the formation of two thermodynamically stable five-membered metallacycles sharing together the M–C bond. These are named as “pincer” owing to their specific binding mode. These may be represented by the general formula  $[2,6-(\text{ECH}_2)_2\text{C}_6\text{H}_3]^-$  or (ECE) where E denotes a neutral two electron donor like  $\text{NR}_2$ ,  $\text{PR}_2$ ,  $\text{AsR}_2$ , OR or SR and C is the anionic aryl carbon atom of the 2,6-disubstituted phenyl ring. These ligands coordinate to metals affording the complexes of general formula  $[\text{MX}_n(\text{ECE})\text{L}_m]$  which generally exhibit exceptional thermal stability along with high reactivity.<sup>11</sup> In these systems, the steric and electronic properties of the complexes can be efficiently tailored without any significant changes in their coordination pattern (Scheme 1.2). Organometallic complexes derived from pincer type ligands are used as catalyst in a wide variety of organic transformations and in light emitting materials.



**Scheme 1.2** Pincer ligands modification sites and their effects on properties of complexes<sup>11</sup>

### 1.2.2.4 Scorpionate or tripodal ligands

These are tridentate ligands in which two of the donor sites bind with metal occupying adjacent coordination sites (pincers) while the third donor coordinates to metal reaching over the plane containing other two donor atoms along with the metal ion (stinger). The overall binding mode of the ligand remains facial and the molecule may be visualized as being like a scorpion (ligand) grabbing the prey (metal) with its pincers before stinging it (Scheme 1.3).



**Scheme 1.3** Binding mode of scorpionate or tripodal ligands

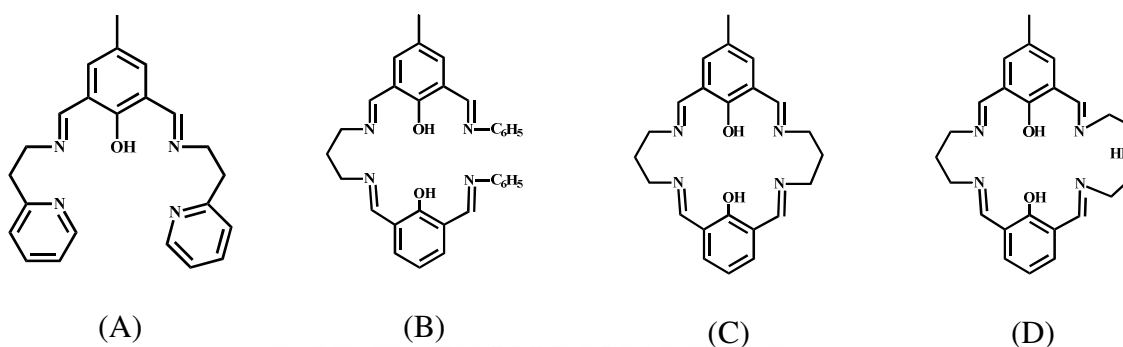
In fact, the term “scorpionate” describes the interchange of bidentate and tridentate coordination modes of such ligands. These ligands may be boro-centric or carbo-centric depending on the nature of the central atom. The most familiar class of scorpionate ligands is Trofimenko’s tris(pyrazolyl)borate or “Tp” ligands. It is important to note that variation in the steric requirements of the substituents present on 3-position of pyrazolyl ring, nearest to the metal centre, may give rise to remarkable changes in the reactivity of the ligand scaffold and properties of the resulting metal complex. However, the ligands are termed as second-generation scorpionate ligands when such steric changes at 3-position of the pyrazolyl ring lead to drastic changes in the coordination chemistry of the ligand or the metal complex.<sup>12</sup> Scorpionate ligands may further be classified as homoscorpionates or heteroscorpionates. Homoscorpionates contain three identical pyrazolyl based donor groups e.g.

$(1\text{-pyrazolyl})_3\text{BH}^-$  and  $(1\text{-pyrazolyl})_3\text{CH}$ . Heteroscorpionates possess two identical pyrazolyl groups (pincers) along with a different donor group (stinger) which can bind with the metal centre.<sup>13</sup>

#### **1.2.2.5 Compartmental ligands**

These are acyclic or cyclic, dinucleating or polynucleating ligands which exhibit the ability to selectively recognize and bind two or more metal ions in close proximity through their in-built two or more, identical or different, adjacent or non-adjacent compartments having appropriate donor sets. In compartmental ligands with adjacent chambers, the metal ions held in close vicinity may generally communicate with each other through endogenous bridging atoms. Conversely, in the ligands composed of non-adjacent chambers, such communication between the metal centers is not possible through endogenous bridging groups and takes place through exogenous bridging groups and/or through the shape and connectivity of the entire coordination moiety.<sup>14-15</sup> Such ligands are widely used to synthesize dinuclear metal complexes of potential catalytic and biological interest. These ligands encompass a large variety of molecules e.g.

- (a) End-off acyclic ligands: These are obtained by [1+2] condensation between a keto precursor and diamine (Scheme 1.4, A).
- (b) Side-off acyclic ligands: These are prepared by [2+1] condensation between a keto-precursor and diamine followed by condensation of remaining keto groups with a primary amine (Scheme 1.4, B).
- (c) Symmetric dinucleating ligands: Cyclic or acyclic molecules with similar compartments (Scheme 1.4, C).
- (d) Dissymmetric dinucleating ligands: Cyclic or acyclic molecules with different compartments. These ligands are especially suited for synthesis of heterobimetallic complexes (Scheme 1.4, D).



Scheme 1.4 Representation of compartmental ligands

### 1.2.2.6 Hemilabile ligands

The term “Hemilabile” was first introduced by Jeffrey and Rauchfuss in 1979.<sup>16</sup> Many polydentate ligands are known to possess a Lewis basic moiety which can dissociate from the metal reversibly leading to the generation of a transient coordinative unsaturation over the metal ion. Such types of ligands are known as hemilabile ligands. These ligands are generally composed of the coordinating atoms which differ in their electronic nature like hard and soft donors or substitutionally inert and substitutionally labile groups. This unique feature of hemilabile ligands allows the temporary dissociation of one of the coordinating groups (substitutionally labile) from the metal making the room for substrate binding while the other group (substitutionally inert) remains firmly anchored to the metal ion. The bifunctional character of hemilabile ligands has been successfully exploited for chemical sensing as well as to stabilize some reactive unsaturated transition metal species. Complexes derived from such type of ligands are widely used for metal complex small molecule bond activation reactions and transition metal catalysis.<sup>17</sup>

### 1.2.2.7 Non-innocent ligands

The general behaviour of transition metal complexes during the course of a redox process involves oxidation or reduction of the metal centre, leaving the ligand part unaffected. However, in some cases, ligands can also participate in the redox processes acting as a source or sink of electrons with the metal retaining its original oxidation state. Such ligands



are termed as “non-innocent” or “suspect” ligands. The terms “redox-active ligands” or “redox ambi-valent ligands” have also been used as their synonyms<sup>18</sup> though distinctions have been made in some cases.<sup>19</sup> According to Jorgenson, a ligand is considered as innocent if the oxidation states in its complexes can be strictly assigned however in case of non-innocent ligands the assignment of oxidation states is ambiguous.<sup>20</sup> However, Chirik pointed out that appropriate assignment of the oxidation states of metals in such cases is often possible by means of modern experimental and computational methods.<sup>19</sup> Two types of terms are generally used to explain the oxidation state of metals in mononuclear metal complexes.<sup>21-22</sup>

**(a) Formal oxidation state:** It can be defined as “the charge remaining on the metal ion when all the ligands attached with the metal are removed in their normal, closed-shell configuration – that is with their electron pair”.

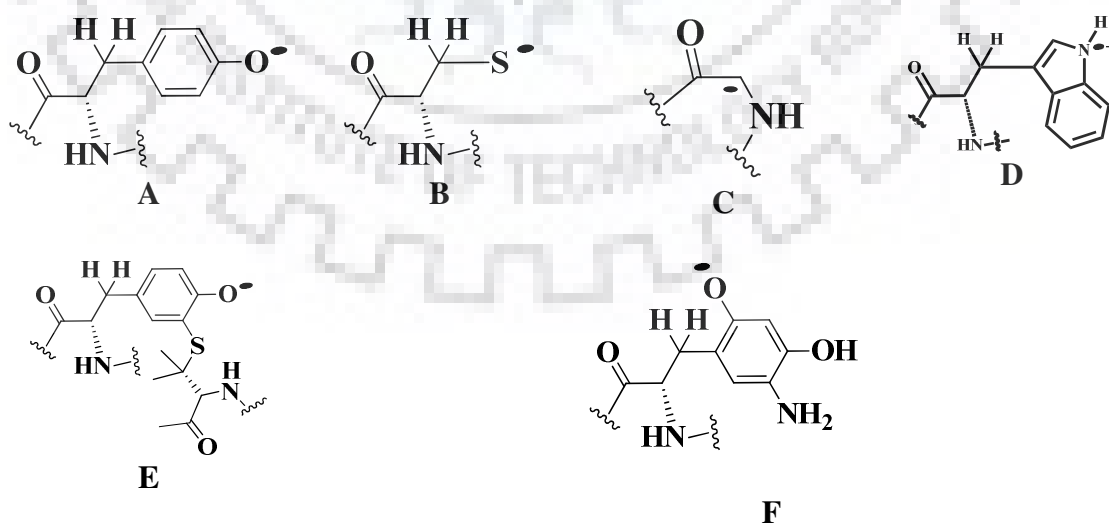
**(b) Spectroscopic or physical oxidation state:** It is described as “the oxidation state of the metal ion which is directly deduced with the help of various spectroscopic techniques by ascertaining its electronic configuration”.

Both formal and physical oxidation states are often used interchangeably but such practice may lead to absurd or erroneous description of oxidation states in certain areas of coordination chemistry, especially in those cases where the ligands can exist in several or at least two different oxidation states available at common redox potentials. To avoid misleading descriptions, it is desirable to switch from the formal oxidation state to physical oxidation state in such cases.

The phenomenon of non-innocence is exemplified by ligands when there is very small energy difference between metal-centered and ligand-centered frontier orbitals thus enabling a ready electron transfer.<sup>23</sup> It is worthnoting that the innocence or non-innocence is

not a permanent attribute of a ligand but a function of specific circumstances in certain situations.<sup>18</sup> Furthermore, the redox-active ligands can behave both, in an innocent or in a non-innocent way.<sup>20</sup> The category of non-innocent ligands encompasses a large array of molecules including bio-relevant as well as non-bio-relevant ones. Among biologically relevant redox non-innocent ligands, the prominent examples are  $\text{NO}^{+/-}$ ,  $\text{O}_2^{0/-/2-}$ , tetrapyrrole ligands such as porphyrins, chlorins and corroles, pterins, flavins and 4-centered chelate redox systems with *o*-quinone/*o*-semiquinone/catecholate,<sup>25,26</sup>  $\alpha$ -iminocarbonyls or  $\alpha$ -dithiolene/ene-1,2-dithiolate functions.<sup>18,21</sup> Cyanides (as in iron hydrogenases), oxo ligands (as in P-450 dependent enzymes and copper containing monooxygenases), hydrides and alkyl ligands (as in B<sub>12</sub> coenzymes and methane producing nickel dependent coenzymes) are among those biologically relevant ligands which possess “hidden” non-innocence essential for their biochemical functioning. Several stable and transient amino acids radicals have also been identified as localized to glycines, cysteines, tryptophans, tyrosines as well as a variety of modified tryptophan and tyrosine residues within proteins<sup>27</sup> which are illustrated in Scheme 1.5 along with their protein source

(Table 1.2)



Scheme 1.5 Ligands with radicals in various amino acids<sup>27</sup>

**Table 1.2** Protein sources of amino acid radicals<sup>27</sup>

Radical	Protein Source
A	Class I ribonucleotide reductase (RNR), photosystem II, prostaglandin H synthase
B	Class II RNR
C	Class III RNR, pyruvate formate lyase
D	Cytochrome peroxidase
E	Galactose oxidase
F	Plasma amine oxidases
G	Methylamine dehydrogenases

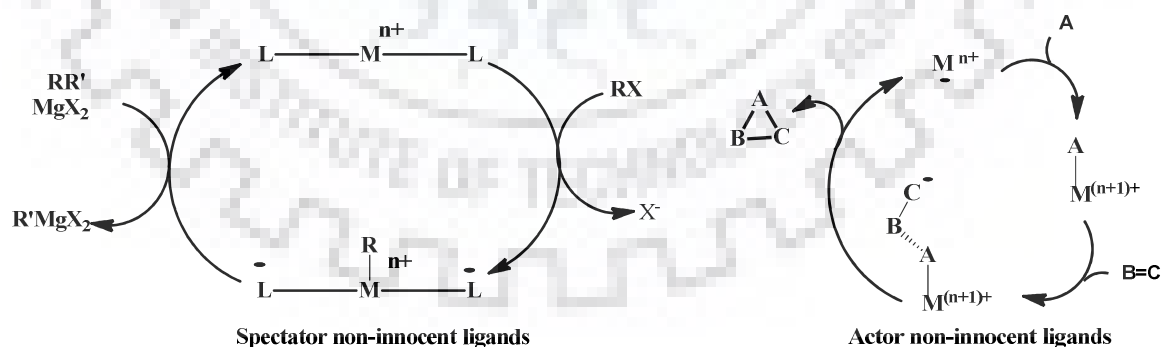
Non-bio-relevant redox non-innocent ligands include  $\alpha$ -diimine,  $\alpha$ -dicarbonyl and  $\alpha$ -azo functional 4-centered system,<sup>18</sup> iminepyridines,<sup>28</sup> bipyridines,<sup>28</sup> terpyridines,<sup>28</sup> Fischer type carbene ligands,<sup>29</sup> N=N containing tetrazine ligands and acceptor substituted olefins.<sup>18,21</sup> The redox-active ligands may serve in several aspects:<sup>18</sup>

- (i) As substrate of reactions (examples include O<sub>2</sub> or quinones/catechols in oxygenation reactions).
- (ii) As reactive intermediates (like H-abstracting oxyl or oxidizing phenoxyl radical).
- (iii) As controlling electron reservoirs (examples include dithiolene or porphyrin  $\pi$ -systems).

These ligands find their potential application in developing molecular conductors and switches,<sup>18</sup> molecular magnets,<sup>18</sup> photoactive components such as emitters and sensitizers,<sup>18</sup> synthetic models for metalloenzymes (vide infra) and in the synthetic conversions also. Ligand redox non-innocence has been proven to be a great synthetic tool offering unique

opportunities to enhance reactivity and steer selectivity by modifying the properties of transition metal catalysts. A number of organometallic transformations are generally catalysed by noble and expensive transition metals like Pd, Rh and Pt which undergo oxidative addition and/or reductive elimination processes involving two-electron transfer. On the contrary, most of the inexpensive metals, mainly from the first row transition series, exhibit one electron transformations and hence are more suitable for catalyzing the radical type reactions. Utilizing redox non-innocent ligands has opened a new window in the realm of catalytic processes where low-cost transition metals can be used as surrogates for expensive metals. Now-a-days, the non-innocence of ligands is being successfully exploited for organometallic catalysis and two complementary strategies are generally adopted for this purpose (Scheme 1.6):<sup>29,30</sup>

- (a) Through the use of non-reactive redox-active ligands which behave as electron reservoirs inducing noble metal character (two-electron reactivity) (spectator ligand);
- (b) Through the generation of reactive ligand radicals and their utilization in catalysis to impose controlled ligand-centered radical-type reactivity (actor ligand).



**Scheme 1.6** Organometallic ligand as redox-noninnocence in catalysis application

A number of classifications have been proposed to categorize the redox-active ligands employed in catalysis and a few of them are as follows:<sup>19</sup>

- (a) Actor versus spectator ligands: Actor ligands are those which engage directly with the substrate molecule during the catalytic process whereas spectator ligands exert their effect on the metal center which forms the site of reactivity.
- (b) Closed shell *versus* open shell redox active ligands: In closed shell redox activity, the ligand exhibits redox changes in such a way that the system remains spin-paired whereas in case of open shell redox active ligands, some unpaired electron density may be present at some stage.
- (c) Covert radical *versus* overt radical ligands: Covert ligand radical describes those cases where the ligand in the reactant complex is essentially spin-paired but attains radical character as the transition state of the reaction is approached. The overt ligand radical refers to those systems where the ligand possesses significant unpaired spin density even in the reactant

### **1.3 Metal ions**

Metal ions are another main constituent of coordination complexes which are generally responsible for substrate binding and forming the site of reactivity. The present work deals with five metals: Manganese, iron, cobalt, nickel, copper.

#### **1.3.1 Manganese (*symbol*: Mn; *electronic configuration*: [Ar] 3d<sup>5</sup>, 4s<sup>2</sup>)**

Manganese is produced in very large amounts, most of which is used in the steel industry. Large amount of MnO<sub>2</sub> are also produced, and are used mainly for making 'dry' batteries and brick industry. KMnO<sub>4</sub> is an important oxidizing agent. Mn is biologically important and is necessary for photosynthesis. Manganese (*symbol* Mn) is the third most abundant transition metal in Earth's crust and the eighth most abundant crustal metal overall. In terms of abundance of transition metals manganese is considerable less abundant than iron. In periodic table this metal positioned in 4<sup>th</sup> period and 7<sup>th</sup> group having electronic configuration [Ar] 3d<sup>5</sup>4s<sup>2</sup>. It has only one naturally occurring isotope. Manganese is more

electropositive metal ion as compared to its neighbour in the periodic table. Oxidation states of manganese have been observed from -III to VII but on the basis of geochemical distribution of manganese in hydrosphere, lithosphere and atmosphere mainly Mn(II), Mn(III) and Mn(IV) were involved. Out of these metal oxidation state Mn(II) is most stable one. Spin pairing in manganese (II) complexes can be achieved using ligands such as cyanide.  $[\text{Mn}(\text{CN})_6]^{3-}$  is low-spin octahedral complex of manganese. Almost all Mn(III) complexes are high-spin and have octahedral geometry. Mn(IV) is found in photosystem II which is a water oxidising enzyme. Mn(VII) behaves as an extremely strong oxidising agent. These oxidation states behave as Lewis acids and exhibit a preferential coordination for the oxygen donors.<sup>31</sup>

#### **1.3.1.1. Biological role of manganese**

Manganese is found to be an essential element in living beings and plays key role in various important functions such as photosystem II and disposal of harmful radicals (such as superoxide dismutase). A healthy human adult contain 10–20 mg of manganese. In biological system manganese may have oxidation state II, III, IV and possibly V. In many proteins containing manganese, preferentially manganese is having II oxidation state with high-spin and no coordination geometry preference. Strength of complexes is weak as compared to other transition metal ions found in biological system excluding Ca(II) and Mg(II) ions. Due to the similar ionic radius Mn(II) can substitute Zn(II) and Fe(II) in protein. The one of the crucial role of manganese in nature is in photosynthesis (Fig. 1.1).<sup>32-</sup>

<sup>33</sup> Manganese is found in the active site of various enzymes and imparts crucial properties to achieve specific functions. Table 1.3 depicts the enzyme containing manganese in the active site and functions performed by them.

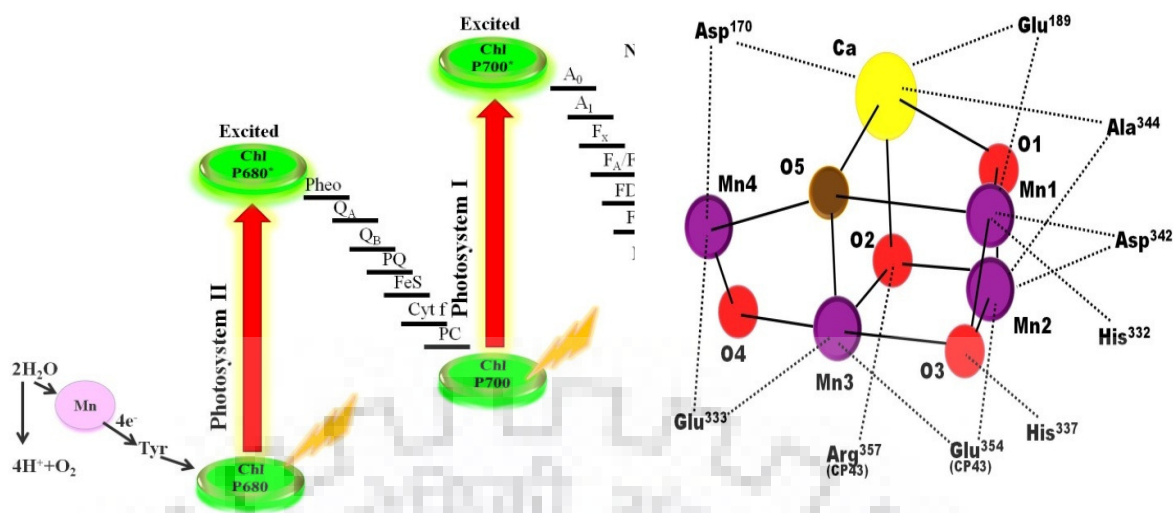


Fig. 1.1 Manganese in oxygen evolving complex in photosystem II<sup>34</sup>

Table 1.3 List of enzymes containing manganese in active site and their functions

Enzymes	Functions	Type
Manganese superoxide dismutase (Mn-SOD) <sup>35</sup>	Dismutation of superoxide radicals	Mononuclear
Manganese peroxidase (Mn-P) <sup>36</sup>	Convert peroxide to water using H <sup>+</sup>	Mononuclear
Manganese dioxygenase <sup>37</sup>	Incorporating two atoms of oxygen	Mononuclear
3-Deoxy-D-arabino-heptuloson ate-7-phosphate synthetase (DAHPS) <sup>38</sup>	Responsible for synthesis of aromatic compounds in microorganism and plants	Mononuclear
2-C-methyl-D-erythritol 2,4-cyclodiphosphate synthase (MECDP) <sup>39</sup>	Part of isoprenoid biosynthesis in many plants and bacteria	Mononuclear
Inorganic phosphatase <sup>40</sup>	Catalyze the hydrolysis of P <sub>2</sub> O <sub>7</sub> <sup>4-</sup> to phosphate	Mononuclear
Isopentenyl diphosphate isomerase <sup>41</sup>	Catalyze the isomerisation of isopentenyl diphosphate to dimethylallyl diphosphate	Mononuclear
Manganese lipoxygenase (Mn-LO) <sup>42</sup>	Catalyze dioxygenation of polyunsaturated fatty acids in lipids	Mononuclear

Oxalate oxidase <sup>43,44</sup>	Convert oxalate to CO <sub>2</sub> and H <sub>2</sub> O <sub>2</sub>	Mononuclear
Oxalate decarboxylase <sup>45</sup>	Convert oxalate to formate and CO <sub>2</sub>	Mononuclear
Manganese ribonucleotide reductase <sup>46</sup>	Catalyzes the formation of deoxyribo-nucleotides from ribonucleotides	Dinuclear
Arginases <sup>47</sup>	Catalyze the hydrolysis of L-arginine to L-ornithine and urea	Dinuclear
Manganese catalase <sup>48</sup>	Detoxification of hydrogen peroxide	Dinuclear
Amino peptidase <sup>49</sup>	Catalyze the hydrolysis of the amino end of polypeptides and protein	Dinuclear
Isomerases <sup>50</sup>	Catalyze the interconversion of D-glucose and D-fructose	Dinuclear
Transferases <sup>51</sup>	Catalyze the transfer of nucleotide sugar residue to a hydroxyl group on target protein, lipid or carbohydrate	Dinuclear
Glutamine synth <sup>52</sup>	Catalyze the conversion of L-glutamate, ATP and ammonia into L-glutamine, ADP and PO <sub>4</sub> <sup>3-</sup>	Dinuclear
Phosphoglycerate mutase <sup>53</sup>	Catalyze the inter-conversion of 3-phosphoglycerate and 2 phosphor-glycerate	Dinuclear
Oxygen evolving complex (OEC) or (PSII) <sup>54</sup>	Carry out the four electron oxidation of water to dioxygen	Tetranuclear

### 1.3.2 Iron: (*symbol: Fe; electronic configuration: [Ar] 3d<sup>6</sup>, 4s<sup>2</sup>*)

Iron is a distinctive metal present around and inside us having electron configuration [Ar] 3d<sup>6</sup>4s<sup>2</sup>. It is a member of 4<sup>th</sup> period and 8<sup>th</sup> group in the modern periodic table. This metal has been a part of man's material progress since prehistoric times. It is found to be the fourth most abundant element (after oxygen, silicon and aluminium) and the second most abundant metal in Earth's crust. Iron has four naturally occurring isotopes. Iron can have



oxidation state –II to VI, although two most stable oxidation states are II and III. Iron (III) complexes may be low or high–spin and generally have octahedral geometry.

One important aspect to be considered in the iron chemistry is the effect of ligand on oxidation and spin state of iron as shown in Fig. 1.2. Ligand strength and the environment around metal centre have a tendency to modulate the redox property of the iron. A complex will be labile if it is having a weak field ligand and will form preferentially high–spin complexes and *vice versa*. Presence of large, bulky ligands as in metalloproteins can cause a tetrahedral environment, in which iron prefers to form high–spin complexes in both the oxidation state.<sup>33</sup>

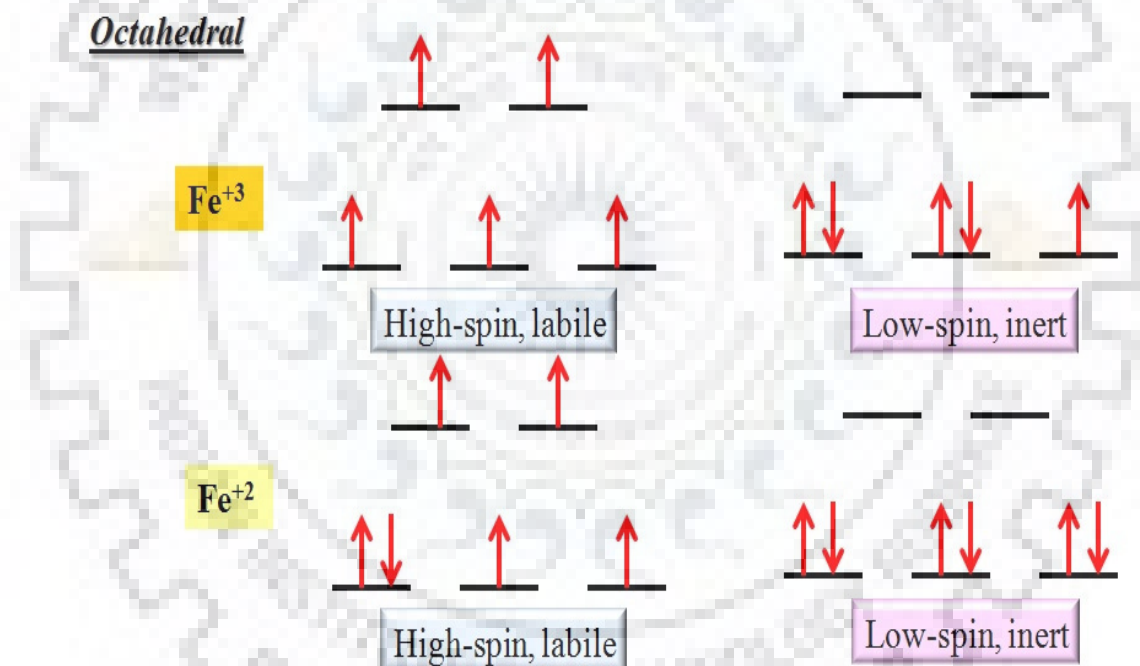


Fig. 1.2 Effect of ligand environment on the oxidation state and spin state of iron

Iron has been found an important metal in various catalytic processes due to its biological relevance and abundance in nature.<sup>55-57</sup>

### 1.3.2.1 Biological role of iron

Being vital to plant as well as animal, iron imparts valuable role in biology. The adult human body contains about 4 g of iron out of which only 1 g of iron per day is absorbed while about 3 g are in the form of haemoglobin.

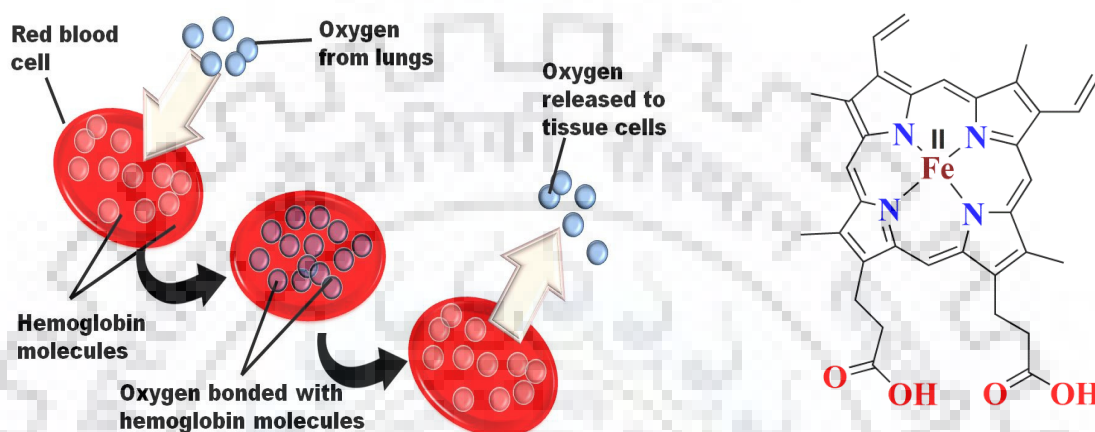


Fig. 1.3 Role of iron in oxygen transport

Iron is important in several aspects such as dioxygen transport and storage (Fig. 1.3), electron transfer, nitrogen fixation, superoxide dismutation.<sup>34,58</sup>

Iron is preferred over other transition metal due to some characteristic feature present in iron, less or not at all present in the other transition metals which are as followed:

- Abundant and ubiquitous in nature.
- Ease of swapping between the oxidation states II and III and can reach up to IV and V in some processes.
- Change of spin state in the presence of ligand environment and strength.
- Flexibility towards donor atom in a ligand, coordination and geometry.

Iron containing protein can be classified depending on its prosthetic group as depicted in Table 1.4.

**Table 1.4** Iron containing protein and their sites

Iron containing protein					
<b>Heme protein</b>	<b>Protein</b>	Hemoglobin	Myoglobin	Cytochrome oxidase	Cytochrome P450
	<b>Fe atom</b>	4	1	2	1
	<b>Site</b>	RBC	Muscle	Mitochondria	ER, Mitochondria
<b>Non-heme protein</b>	<b>Protein</b>	Aconitase	Transferrin	Lactoferrin	Ferritin
	<b>Fe atom</b>	2	2	2	4000
	<b>Site</b>	TCA cycle	Plasma	Milk	Tissue
<b>Iron-sulfur proteins</b>	<b>Protein</b>	Complex III FeS	Xanthine oxidase	Succinate DH	Adrenodoxin
	<b>Fe atom</b>	2	8	4	2
	<b>Site</b>	Mitochondria	Liver	Mitochondria	Mitochondria

One of the interesting enzymes containing iron is cytochromes which are the member of heme proteins (Table 1.5).<sup>59-62</sup> These are monooxygenase enzyme containing type b heme protein which catalyzes a variety of oxo transfer reactions such as hydroxylation, epoxidation, amine and sulphide oxidation.<sup>63-64</sup>

### 1.3.3 Cobalt (symbol: Co; electronic configuration: [Ar] 3d<sup>7</sup>, 4s<sup>2</sup>)

Cobalt generally occurs in nature in association with Ni or As. The most important minerals of cobalt are *smaltite* (CoAs<sub>2</sub>) and *cobaltite* (CoAsS). Cobalt can exhibit oxidation states from (-I) to (+V) though (I), (II) and (III) are the most common oxidation states. Among transition metal elements, the (+I) oxidation state is better represented by cobalt than any other element, except copper. Co(II) is the only d<sup>7</sup> ion of common occurrence and occurs in a wide range of coordination environments. The stereochemistry of Co(II) shows normal coordination numbers of 3, 4, 5 and 6 though few 8-coordinated complexes of Co(II) are also known. There are numerous simple or hydrated salts of cobalt(II), the latter being

mostly pink or red in color. The color change from blue to pink due to the conversion of anhydrous form to octahedral form of Co(II) is used as moisture indicator in silica gel drying agents. Co(II) may exist in both high-spin and low-spin states but examples of low-spin octahedral Co<sup>II</sup> complexes are very rare. Such complexes undergo strong Jahn-Teller distortion ( $t_{2g}^6 e_g^1$ ) and tend to lose ligands to form low-spin tetra- or penta-coordinated species. Co(II) gives rise to kinetically labile complexes while Co(III) complexes are kinetically inert in nature.<sup>65-67</sup> There are very less number of simple salts or binary compounds available for Co(III) since water reduces the uncomplexed Co(III) ions rapidly at room temperature. Co(III) can exhibit a coordination number of 4, 5 or 6 in its complexes. Most of the Co(III) complexes are octahedral though a few tetrahedral, planar and square antiprismatic complexes are also known. All known octahedral Co(III) complexes are diamagnetic in nature except  $[\text{Co}(\text{H}_2\text{O})_3\text{F}_3]$  and  $[\text{CoF}_6]^{3-}$  which are paramagnetic and have four unpaired electrons. Cobalt (III) shows a special affinity for nitrogen donors like ammonia, ethylenediamine, NO<sub>2</sub> groups and N-bonded SCN groups.

### **1.3.3.1 Role in biosystem**

Cobalt is present in vitamin B<sub>12</sub> (anti-pernicious anemia factor or cyanocobalamin) in the form of diamagnetic Co<sup>3+</sup> bound to a substituted corrin macrocycle. It is the only vitamin containing a metal and the nature's only organometallic compound.<sup>9</sup> An analogous compound 5'-deoxyadenosylcobalamin is known as coenzyme B<sub>12</sub> which is needed by several enzymes including methylmalonyl CoA mutase, glutamate mutase, α-methylene-glutarate mutase, dioldehydrase, glyceroldehydrase, ethanoldeaminase, L-β-lysine mutase, D-α-lysine mutase, methane synthetase, ribonucleotide reductase, methionine synthetase, methyl transferase and acetate synthetase to exhibit their activity.<sup>6</sup>

Numerous non-corrin cobalt containing enzymes are also known which are listed in Table 1.5.<sup>69</sup>

**Table 1.5** Cobalt-containing proteins and their functions<sup>30</sup>

<b>Protein</b>	<b>Source</b>	<b>Role of Cobalt</b>	<b>Cofactor content</b>
Methionine aminopeptidase	Yeast, bacteria, animals	Hydrolysis	2 Co per subunit
Nitrile hydratase	Actinomycetes, bacteria	H <sub>2</sub> O activation, CN-triple-bond hydration and protein folding	1 Co in each $\alpha$ -subunit
Glucose isomerase	Actinomycetes	Isomerization	1 Co per 4 subunit
Prolidase	Archae	Hydrolysis	1-2 Co per subunit
Cobalt transporter	Actinomycetes and yeast	Cobalt uptake	
Methylmalonyl-Co-A carboxytransferase	Bacteria	Carboxytransferation	1 Co, 1 Zn per subunit
Aldehyde decarbonylase	Algae	Decarbonylation for aldehyde	1 Co-porphyrin per $\alpha\beta$ subunit
Lysine-2,3-aminomutase*	Bacteria	Mutation	0.5-1 Co per subunit
Bromoperoxidase	Bacteria	Bromination	$\approx$ 0.35 Co per 2 subunit
Cobalt-porphyrin-containing protein	Bacteria	Electron carrier	1 Co-porphyrin per protein

\* Besides cobalt, iron sulphur clusters, zinc and PLP are also found as cofactors in lysine-2,3-aminomutase

### 1.3.3.2 Applications of cobalt

#### 1.3.3.2.1 Tracer and therapeutics

Radioactive cobalt (<sup>60</sup>Co) is widely used as a concentrated source of  $\gamma$ -radiations in cancer therapy, food sterilization and as radioactive tracer in wide range of processes since the natural isotope (<sup>59</sup>Co) is converted to non-radioactive nickel (<sup>60</sup>Ni) on the neutron bombardment leading to emission of  $\beta$ - and  $\gamma$ - radiations.<sup>69</sup>

### **1.3.3.2.2 Spectroscopic probes for metalloenzymes**

Due to the characteristic spectroscopic properties of cobalt correlated with its stereochemistry, it is frequently used as a spectroscopic probe for metalloenzymes.<sup>70</sup> Several “spectroscopically–silent” zinc containing enzymes have been successfully substituted with cobalt giving rise to functioning enzymes which can actively respond to optical namely absorption, magnetic circular dichroism spectral data and magnetic resonance spectroscopy (NMR, EPR and ENDOR).<sup>71</sup> Such substitution is helpful to elucidate the coordination environment of active centres in those proteins as well as the structural and stereochemical aspects responsible for the catalytic activity of these enzymes.<sup>69</sup> It is documented in literature that, in some cases, substitution with cobalt resulted the restoration of the enzymatic activity whereas in some enzymes the activity got enhanced due to substitution with cobalt ion.<sup>72</sup>

### **1.3.3.2.3 Oxygen carrier**

The metal catalysts which can activate dioxygen and promote oxygen atom transfer, possess remarkable biological importance and find potential industrial applications.<sup>73</sup> After the affinity of cobalt complexes towards dioxygen was realized, a number of cobalt complexes derived from dien, salen, porphyrin, pentacyano, trispyrazoleborato, tetraazamacrocyclic and various other ligands have been designed and synthesized. Such molecules found their applications as spectroscopic models to elucidate the oxygen binding chemistry of heme enzymes due to their potential for irreversible or reversible binding with dioxygen and their ability to work as oxygen carriers<sup>74</sup> and oxygen reservoir.<sup>75</sup> Simultaneously, a plethora of cobalt complexes has been developed to catalyze the oxidation of various organic substrates utilizing molecular oxygen where the affinity of cobalt towards oxygen is successfully exploited (vide infra).

#### **1.3.3.2.4 Nitric oxide sensor sensors**

Sensing of nitric oxide is of immense significance due to its diversified roles in physiological processes like anticancer activity, host immune system defense, neurotransmission, and vasodilation as well as pathological processes like cancer, ischemia, septic shock, inflammation and neurodegeneration.<sup>76-81</sup> Furthermore, higher doses of NO may induce inhibition of respiratory complexes, DNA damage and modification, gene mutation and cell apoptosis also.<sup>81,82</sup> A number of cobalt complexes including Co-DATI systems,<sup>83,84</sup> Co-dansyl systems<sup>85,86</sup> and Co-FATI systems<sup>87</sup> have been successfully employed for the fluorescent detection of nitric oxide.<sup>88</sup>

#### **1.3.3.2.5 Dye sensitized solar cells(DSSCs)**

Most of the DSSCs utilize an iodide/triiodide redox shuttle to regenerate the oxidized dye. However, several disadvantages including large energy loss, corrosiveness and competitive absorption of light by triiodide associated with the iodide/triiodide system limit its application.<sup>89</sup> A number of cobalt complexes<sup>90</sup> with special attention to cobalt polypyridyl complexes<sup>89-95</sup> have been synthesized in search of alternative redox shuttle and till today, the best alternative redox shuttle is composed of Co(II/III) polypyridyl complexes.<sup>90</sup>

#### **1.3.3.2.6 Catalysis**

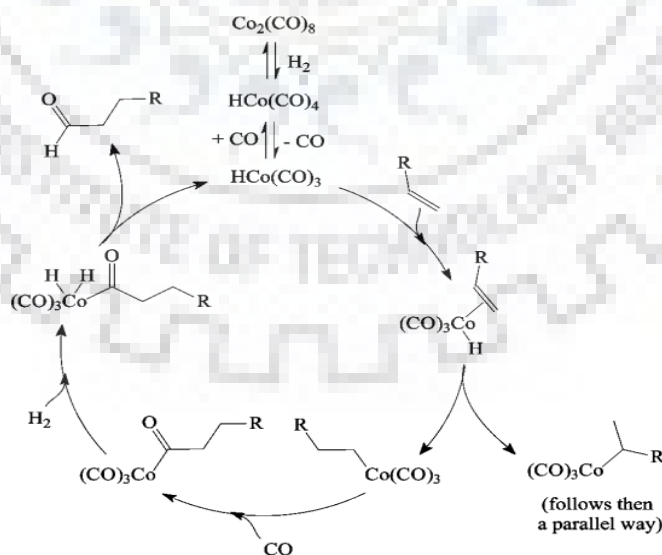
##### **1.3.3.2.6.1 Fischer-Tropsch process**

Fischer-Tropsch process is a widely used commercial method to synthesize hydrocarbon fuels from syngas derived from the natural gas and coal. Fischer and Tropsch proposed cobalt and iron as first catalysts for the syngas conversion<sup>96</sup> and commercial FT plants still utilize iron and cobalt catalysts for this purpose. Although ruthenium and nickel also show excellent catalytic properties for the hydrogenation of carbon monoxide, ruthenium is highly expensive and less abundant whereas nickel catalysts produce excessive methane which limits their commercial usage as catalysts for the FT process in large scale industries.<sup>96</sup>

Recently, a comparison between the efficiencies of cobalt and iron catalysts for the Fischer-Tropsch process was made by Davis<sup>97</sup> and it was found that cobalt was more efficient catalyst under low severity conditions whereas iron was more active under more severe conditions (higher space velocities and higher reactor pressures). Furthermore cobalt catalysts were accompanied with two major advantages over iron catalysts; (1) because of lack of the water gas shift (WGS) reaction, a process known to compete with the Fischer-Tropsch process, cobalt catalysts efficiently convert the oxygen in CO to water rather than CO<sub>2</sub> exhibiting higher activities than the iron catalysts; (2) cobalt catalysts can achieve the robustness if provided with a support which is a significant factor for the accomplishment of the process.<sup>97</sup>

### 1.3.3.2.6.2 Oxo process<sup>98</sup>

The cobalt catalyzed hydroformylation of alkenes which is also known as oxo process involves the conversion of alkenes into the corresponding aldehydes and receives considerable synthetic importance. The catalytic cycle involves [Co(H)(CO)<sub>4</sub>] as the oxo-cobalt catalyst.

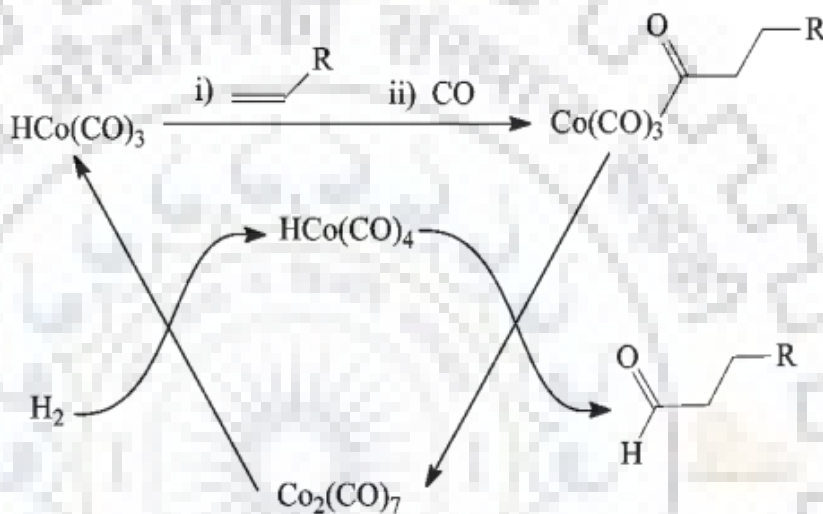


**Scheme 1.7** Cobalt catalysed hydroformylation mechanism of alkenes<sup>98</sup>



During the catalytic cycle, it loses a CO ligand giving rise to a  $16e^-$  species  $[\text{Co}(\text{H})(\text{CO})_3]$  which undergoes a number of steps including alkene coordination, hydride transfer, CO coordination and migratory CO insertion, oxidative addition of  $\text{H}_2$  and reductive elimination of aldehyde to regenerate the active species (Scheme 1.7).

An alternative pathway may also be operative when the reactions are carried out under stoichiometric conditions with high concentrations of cobalt (Scheme 1.8).



**Scheme 1.8** An alternate pathway of dinuclear mechanism of hydroformylation<sup>98</sup>

#### 1.3.3.2.6.3 Miscellaneous conversions

Cobalt can catalyze the oxidation of a variety of organic substrates in presence of molecular oxygen. A large number of cobalt catalysts have been developed which can promote the epoxidation of alkenes, oxidation of alkenes to alcohols and ketones, allylic oxidation, oxidative dehydrogenation of alkanes to alkenes, oxygenation of alkanes, benzylic oxidation and aromatic C-H oxidation.<sup>99</sup>

#### 1.3.3.2.6.4 Splitting of water

To meet the global energy demand on one hand, and simultaneously to avoid the release of green house gases on the other, hydrogen is emerging as an alternative clean fuel. In nature,

iron or nickel dependent hydrogenase enzymes generate H<sub>2</sub> from the aqueous media. However, this process can be also be accomplished artificially by utilizing some synthetic transition metal–based catalysts. A number of cobalt complexes have been designed and developed for this purpose.<sup>100</sup> Krishnan and Sutin reported the first photocatalytic system for the generation of hydrogen through photoreduction of water utilizing [Co(bpy)<sub>n</sub>]<sup>2+</sup> (n = undefined) complex as catalyst and [Ru(bpy)<sub>3</sub>]<sup>2+</sup> as photosensitizer.<sup>62</sup> Later on, the same system exhibited simultaneous reduction of CO<sub>2</sub> and water driven from the visible light.<sup>101</sup> Rigsby et al. synthesized a family of dinuclear Co<sup>III</sup>Co<sup>III</sup> peroxy complexes analogous to ruthenium based water oxidation catalysts. The electrochemical studies suggested that those complexes may be used as molecular electrocatalysts for oxidation of water in acidic media.<sup>102</sup> Chang and co-workers reported a molecular cobalt polypyridine catalyst derived from the ligand Py5Me2 which exhibited high stability and activity for the electrocatalytic generation of hydrogen from neutral water.<sup>103</sup> Gray and co-workers presented a cobalt complex derived from non-innocent bis(iminopyridine) ligand as a highly active electrocatalyst for water reduction in buffered aqueous media.<sup>104</sup> Leung et al. reported a cobalt(II) quaterpyridine complex [Co<sup>II</sup>(qpy)(OH<sub>2</sub>)<sub>2</sub>]<sup>2+</sup> (where qpy = 2,2':6',2'':6'',2''':6''',2''''-quaterpyridine) as an efficient visible light–driven catalyst for the photochemical oxygen evolution through water oxidation as well as photochemical hydrogen generation through water reduction.<sup>105</sup>

#### **1.3.3.2.6.5 Activation of small molecules**

Nitrogen, which is abundant in the atmosphere in the form of an extremely inert molecule known as dinitrogen, is an important constituent of biomolecules. Although dinitrogen continuously enters in our body, it does not participate in the metabolism owing to its extreme inertness.<sup>106</sup> Furthermore, it's activation through chemical processes (like

Frank–Caro cyanamide process and Haber–Bosch process) demands harsh conditions.<sup>106</sup>

However, cobalt can bind a variety of neutral molecules including  $N_2$ <sup>107-112</sup> and  $CO_2$ <sup>113</sup> and promote their activation. Such complexes may serve as benchmark to develop efficient catalysts for reactions having considerable economic, industrial and biological importance.

#### **1.3.4 Nickel (symbol: Ni; electronic configuration: [Ar] 3d<sup>8</sup>, 4s<sup>2</sup>)**

Nickel is mainly found in nature associated with arsenic, antimony and sulphur. The most important ore of nickel is *millerite* (NiS). It is also found in the form of *garnierite*, which is a magnesium–nickel silicate and the iron mineral *pyrrhotite* which contains 3 to 5% Ni. It can exhibit the oxidation states from -1 to +4 though +2 oxidation state is the most common.<sup>114</sup> Nickel(II) can form variety of complexes having the coordination numbers 3 to 6. Among penta–coordinated complexes of Ni(II), both trigonal bipyramidal geometry and square pyramidal geometry are common and high–spin as well as low–spin complexes of each geometry are known. There are few interesting phenomena associated with Ni(II) complexes. Ni(II) square planar complexes are known to undergo ligand association to form 5– and 6–coordinate metal complexes accompanied with the change in their spin state. In some cases the complexes undergo monomer–polymer equilibrium to expand their coordination number. Ni(II) complexes also show planar–tetrahedral equilibria where the same species exists in solution in an equilibrium distribution between the tetrahedral and square forms. Sometimes, it is possible to isolate the two forms of the species where it is termed as square–tetrahedral isomerism. Ni(II) complexes also exhibit thermochromism where temperature–dependent structural changes give rise to variations in *d–d* absorption bands. Ni(I) usually exhibits distorted octahedral or square–planar geometry whereas Ni(III) generally forms low–spin complexes with distorted–octahedral or trigonal bipyramidal geometry.<sup>115</sup>

### 1.3.4.1 Role in biosystem

Nickel is an essential trace element<sup>116</sup> supposed to be involved in protein structure and function.<sup>117</sup> In biology, nickel can catalyze a multitude of biochemical reactions including simple hydrolytic to multi-step redox reactions spanning over a wide range of redox potential of around 1.5 V. There are eight known nickel-containing enzymes till date, most of which catalyze the usage/production of gases relevant to the global carbon, nitrogen or oxygen cycles (Table 1.4).<sup>118</sup>

**Table 1.6** Nickel containing enzymes and their functions<sup>115</sup>

Enzymes	Ni center	Functions
Urease	High-spin Ni <sup>II</sup> dimer	$\text{Urea} + \text{H}_2\text{O} \rightarrow 2\text{NH}_3 + \text{H}_2\text{CO}_3$
Hydrogenase	NiFe center	$2\text{H}^+ + 2\text{e}^- \leftrightarrow \text{H}_2$
CO Dehydrogenase	NiFe <sub>4</sub> S <sub>4</sub> cluster or NiFe <sub>4</sub> S <sub>5</sub> cluster	$\text{CO} + \text{H}_2\text{O} \leftrightarrow 2\text{H}^+ + \text{CO}_2 + 2\text{e}^-$
Acetyl-CoA synthase	NiNiFe <sub>4</sub> S <sub>4</sub> cluster	$\text{CH}_3\text{-CFeSP} + \text{CoASH} + \text{CO} \rightarrow \text{CH}_3\text{-CO-SCoA} + \text{CFeSP}$
Methyl-CoM reductase	Ni tetrapyrrole (tetracorphin)	$\text{Methyl-SCoM} + \text{CoBSH} \rightarrow \text{CH}_4 + \text{CoBS-SCoM}$
Superoxide Dismutase	4-5 coordinate Ni site	$2\text{O}_2^- + 2\text{H}^+ \rightarrow \text{H}_2\text{O}_2 + \text{O}_2$
Glyoxalase I	6-coordinate Ni site	$\text{Methylglyoxal} + \text{glutathione} \leftrightarrow \text{GS-derivative}$
Aci-reductone Dioxygenase	6-coordinate Ni site	$\text{Aci-reductone} + \text{O}_2 \rightarrow \text{methylthiopropionate}$

### 1.3.4. 2 Application of nickel

#### 1.3.4.2.1 As tracer

Ni is a  $\beta$ -emitting radioactive isotope of nickel which has a half life of 100.1 years. Ni has been employed successfully as tracer for several biological studies.<sup>114</sup>

#### 1.3.4.2.2 In industries

Nickel and its complexes possess considerable significance in modern industries. Nickel is resistant to attack by air or water at ordinary temperatures hence it is used for electroplating.<sup>1</sup> It is also used for making Ni–Cd batteries, stainless steel and electronic equipments.<sup>114</sup> Nickel is used to produce a number of alloys: <sup>114</sup> inox steel for metallurgical and mechanic industry, cupro–nickel for manufacture of coins, chromium–nickel for cutlery, iron–nickel for magnets and copper–nickel–zinc (German silver) for ornamental and domestic objects.

#### 1.3.4.2.3 In catalysis

##### 1.3.4.2.3.1 Hydrogenation

Nickel–aluminium alloy when treated with aqueous sodium hydroxide under inert atmosphere leaches out aluminium giving rise to finely divided nickel particles known as Raney nickel. Raney nickel is widely used as hydrogenation catalyst on commercial scale in industries.<sup>1</sup> Finely divided nickel functions as a catalyst in the hydrogenation of vegetable oils.<sup>119</sup>

##### 1.3.4.2.3.2 Ethylene oligomerization

The discovery of the “*nickel effect*” on the nature of products in Al–R<sub>3</sub> catalyzed growth reaction of ethylene by Ziegler et al. set foundation for “Ziegler catalysis” which was further developed by Wilke and others over decades.<sup>120</sup> Numerous Ni(II) catalysts tend to favour chain termination over propagation and to yield internal olefins which makes them suitable

for various processes pertaining to dimerization of  $\alpha$ -olefins.<sup>120</sup> *Shell Higher Olefin Process (SHOP)* is one of the remarkable catalytic systems which utilizes nickel based catalysts for the oligomerization of ethylene with selective formation of linear  $\alpha$ -olefins.<sup>120</sup>

#### **1.3.4.2.3.3 Activation of small molecules**

Nickel also exhibits properties similar to cobalt for the coordination and activation of small molecules like  $N_2$ ,<sup>121-123</sup>  $CO_2$ ,<sup>124,126</sup> and  $H_2$ .<sup>122,123,126</sup> Hydrogen activation by catalysts derived from abundant and inexpensive metals like nickel may be significant for the development of future hydrogen-based energy storage and delivery systems. Nickel exhibits a remarkable property to occlude carbon monoxide also. It is estimated that hundred grams of nickel can absorb 500–800 mL of carbon monoxide ( $Ni(CO)_4$ ).<sup>114</sup> Nickel-catalyzed hydrogenation of carbon monoxide to methane is known for a long time which is used to remove carbon monoxide from a stream of hydrogen gas on an industrial scale e.g. in the production of ammonia. Interestingly, the reverse reaction i.e. cleavage of methane (steam reforming) also proceeds *via* nickel-based catalysts.<sup>127</sup> Reppe utilized the nickel-carbon monoxide affinity to develop a series of homogeneous catalytic reactions known as carbonylations.<sup>127</sup>

#### **1.3.4.2.3.4 Splitting of water**

A number of nickel complexes have been synthesized as artificial models of [NiFe] hydrogenase and nickel based functional complexes. However, no model complex of [NiFe] hydrogenase could produce hydrogen from water till date and all complexes exhibited electrocatalytic proton reduction from acids<sup>128</sup> however, few nickel-based functional models have shown the electrocatalytic production of hydrogen from water. McLaughlin et al. reported a nickel(II) based catalyst for visible light-driven hydrogen production from

water in presence of  $[\text{Ru}(\text{bpy})_3]^{2+}$  or Eosin Y (photosensitizer) and ascorbate.<sup>129</sup> **1.3.4.2.3.5**

### **Miscellaneous conversions**

In addition to aforementioned processes, several nickel based catalysts have been developed to catalyze a wide range of chemical conversions including epoxidation of alkenes, Baeyer-Villiger oxidation, sulphoxidation,<sup>99</sup> selective hydrogenolysis of aryl ethers,<sup>130</sup> Friedel-Crafts alkylation,<sup>131</sup> cyclo-addition reactions and cross-coupling reactions.<sup>132</sup> Furthermore, many reactions involving carbon-carbon bond formation can proceed with high selectivity if catalyzed by organo-nickel complexes.<sup>127</sup>

### **1.3.5 Copper (symbol: Cu; electronic configuration: $[\text{Ar}] 3d^{10}, 4s^1$ )**

Copper occurs in nature in the form of sulphides, arsenides, chlorides and carbonates. Its major ores are *chalcopyrite* ( $\text{CuFeS}_2$ ), *chalcocite* ( $\text{Cu}_2\text{S}$ ), *cuprite* ( $\text{Cu}_2\text{O}$ ) and *malachite* ( $\text{Cu}_2\text{CO}_3(\text{OH})_2$ ).<sup>133</sup> It shows the oxidation states from (I) to (III) though the (III) oxidation state is relatively uncommon. Copper(I) exhibits a wide range of coordination numbers including 2, 3, 4 and 5 having linear, planar, tetrahedral or distorted planar and square pyramidal geometries respectively. Copper(I) compounds are diamagnetic due to the  $d^{10}$  electronic configuration, and colorless except where the color arises from the anion or due to charge-transfer bands. Copper(II) affords a variety of complexes with the coordination numbers 3, 4, 5 and 6 with almost all possible geometries though a few hepta- or octa-coordinated complexes of Cu(II) are also known. Generally, copper(II) complexes are blue or green in color due to the presence of an unpaired electron, however, some complexes exhibit a charge-transfer band in the UV-vis spectrum which imparts them a reddish-brown color. Magnetic moments of mononuclear copper(II) complexes generally fall within the range 1.75–2.20 B.M. irrespective of their stereochemistry. Due to the  $d^9$  configuration of Cu(II), it undergoes severe Jahn-Teller distortion when having octahedral

or tetrahedral arrangement of donor atoms around it. The relative stability of  $\text{Cu}^{\text{I}}$  and  $\text{Cu}^{\text{II}}$  vary considerably with solvent and depend on the nature of anions when present in aqueous solutions. Most of the  $\text{Cu}(\text{I})$  compounds undergo disproportionation to  $\text{Cu}(0)$  and  $\text{Cu}(\text{II})$  in aqueous solutions and the only simple compounds of  $\text{Cu}(\text{I})$  which are stable to water are those which are insoluble in water like  $\text{CuCl}$  or  $\text{CuCN}$ . Acetonitrile solvates the  $\text{Cu}^{\text{I}}$  ion very effectively resulting in higher stability of  $\text{Cu}^{\text{I}}$  in acetonitrile than  $\text{Cu}^{\text{II}}$ . Unlike  $\text{Cu}^{\text{II}}$ ,  $\text{Cu}^{\text{I}}$  forms a large number of compounds with  $\text{Cu}-\text{C}$  bond which find their application in organic synthesis.

#### **1.3.5.1 Role in biosystem**

Copper is the third most abundant metallic element in the human body.<sup>1</sup> It is known to coordinate with several kinds of biological ligands including imidazole nitrogen, amine and amide nitrogen, carboxylate oxygen and cysteine and methionine sulphur donor atoms.<sup>134</sup> It occurs in a variety of metalloenzymes as cofactor due to its ability to switch between  $\text{Cu}^+$  and  $\text{Cu}^{2+}$  at biologically relevant redox potentials. On the basis of spectroscopic properties, three classical types of active sites have been recognized in copper proteins – (i) type I copper centers or “blue copper centers” (mononuclear), (ii) type II centres or “non-blue copper centers” (mononuclear) and (iii) type III copper centers (dinuclear). However, the active sites of some enzymes like laccase, ascorbate oxidase and ceruloplasmin do not strictly resemble to any of these classes and can be described as composed of trinuclear moiety having a combination of type II and type III centers. Cytochrome *c* oxidase also exhibits two another type of copper sites which may be regarded as  $\text{CuA}$  and  $\text{CuB}$  sites.<sup>135</sup> Few copper containing enzymes and their functions have been summarized in the Table 1.7



**Table 1.7** Copper containing enzymes and their functions<sup>136-13</sup>

Class	Protein	Function
<b>Type I</b>	Azurin	} Electron carriers
	Pseudoazurin	
	Stellacyanin	
	Plastocyanin	
	Amicyanin	
	Auracyanin	
<b>Type II</b>	Galactose oxidase	Conversion of primary alcohol to aldehyde
	Amine oxidases	Conversion of primary amine to aldehyde
	Superoxide dismutase	Superoxide scavenging
	Lysine oxidase	Connective tissue biosynthesis
	Dopamine- $\beta$ -monooxygenase	Catecholamine synthesis
<b>Type III</b>	Hemocyanin	Oxygen carrier
	Tyrosinase	Phenol oxidation, melanin synthesis
<b>Multiple types of copper</b>	Laccase	} $O_2 \rightarrow H_2O$
	Ascorbate oxidases	
	Ceruloplasmin	
	Cytochrome <i>c</i> oxidase	
	Nitrite reductase	Denitrification

### 1.3.5.2 Application of copper

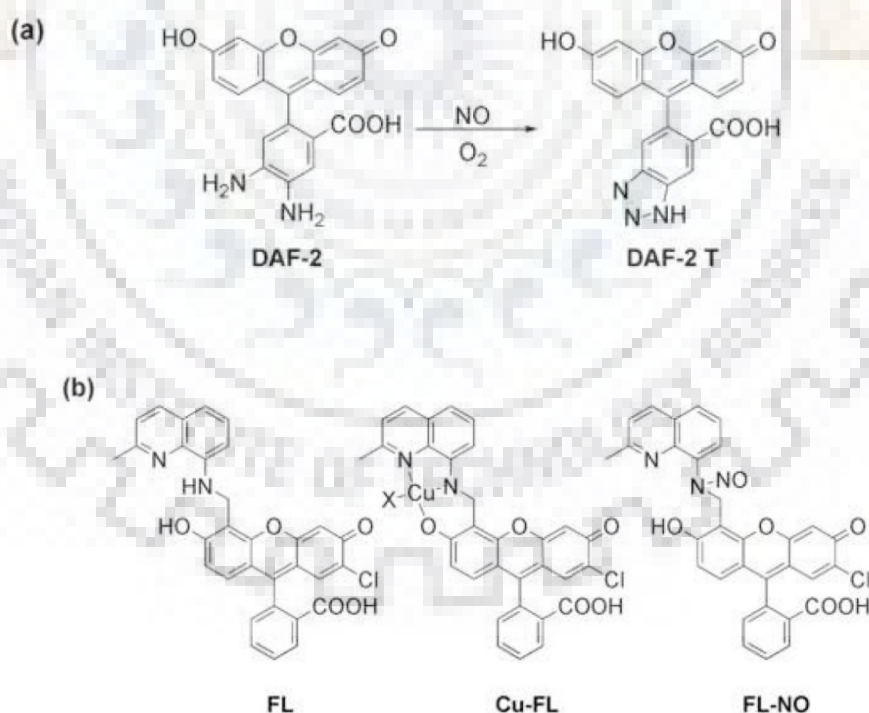
#### 1.3.5.2.1 Copper in radiopharmaceutics and imaging

Several positron emitting radionuclides of copper have been investigated for molecular imaging purposes.<sup>64</sup>Cu decays by  $\beta^-$  emission and electron capture resulting in Auger electron emission and can be used for therapeutic applications.<sup>139</sup> <sup>67</sup>Cu can emit  $\beta^-$  particles

and gamma photons which have been used for imaging.<sup>139</sup> Pyruvaldehyde–bis(4–methylthiosemicarbazonato)copper(II) ( $\text{Cu}^{\text{II}}(\text{ptsm})$ ) complexes radiolabelled with  $^{62}\text{Cu}$  and  $^{67}\text{Cu}$  have been recognized as ideal tracers for evaluation of cerebral and myocardial blood flow.<sup>139</sup>

### 1.3.5.2.2 Nitric oxide and nitroxl sensor

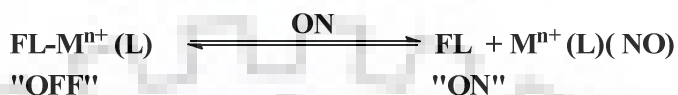
Among many approaches employed to devise fluorescence NO sensor, designing an organic molecule based on *o*-phenylenediamine scaffold has been one of the most trivial strategies. Such molecules oxidize to the corresponding aryl triazole in presence of air and NO (Scheme 1.9 (a)).<sup>140</sup> The large difference in the electronic nature of the diamine (*electron rich*) and the triazole (*electron poor*) provides an indirect means of NO detection. One major disadvantage to use such systems is the requirement of molecular oxygen limiting the direct and real–time detection of NO by such organic moieties.<sup>140</sup>



Scheme 1.9 Fluorescent probes used for NO detection<sup>140</sup>

In the past few years, enormous interest has emerged in developing transition metal complex based NO probes since such systems offer the promise of direct detection of NO. After reacting with NO, these complexes may undergo one of the following processes with concomitant retrieval or/and enhancement of the emission intensity:<sup>141</sup>

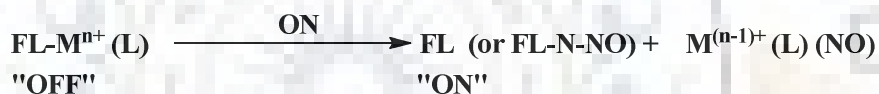
(a) Fluorophore displacement without metal reduction;



(b) Metal reduction without fluorophore displacement;



(c) Metal reduction accompanied with fluorophore displacement



Lippard and co-workers reported a metal based NO sensor using Cu(II)–fluorescein complex as an alternative approach for the direct detection of nitric oxide in living cells (Scheme 1.12 (b)).<sup>142</sup> The fluorescence of the derivatized fluorescein ligand FL quenched after coordinating with the paramagnetic Cu(II) ion. In presence of nitric oxide, Cu(II) of Cu–FL underwent NO mediated reduction to Cu(I) and subsequently leading to the generation of bright nitrosylated fluorophore FL–NO by dissociation of the Cu(I):FL–NO complex.<sup>142,143</sup> Detection of nitric oxide by similar type of mechanism has also been reported by Ford and co-workers using Cu(II) cyclam complex containing an anthracene fluorophore<sup>144</sup> and Zhang and co-workers using MNIP fluorophore–Cu(II) complexes (MNIP = 4-methoxy-2-(1H-naphtho[2,3-d]imidazol-2-yl)phenol).<sup>145</sup> On the other hand, several copper(II) fluorophore complexes have also been devised as probes for nitric oxide

which follow a different mechanism for NO detection. Although, coordination of copper(II) ion with fluorophore results the quenching of emission because of the paramagnetic nature of Cu(II), the recovery of emission properties of fluorophore is achieved here due to the reduction of Cu(II) to diamagnetic Cu(I) after reacting with NO thus enabling the direct imaging of nitric oxide.<sup>146</sup> Recently, Lippard and co-workers reported Cu(II) complexes bearing dansyl and anthracenyl fluorophore ligands as efficient probes for the detection of nitric oxide in organic and aqueous environment where the fluorescence was restored due to the reduction of Cu(II).<sup>141</sup> With similar approach, Yao and co-workers developed a coumarin based copper containing turn-on fluorescent probe for the detection of nitroxyl in living cells.<sup>147</sup>

### **1.3.5.2.3 Catalysis**

#### **1.3.5.2.3.1 Wacker process**

Wacker process is an industrial process widely used for large-scale catalytic production of acetaldehyde which involves the oxidation of ethylene by a mixed-metal PdCl<sub>2</sub>/CuCl<sub>2</sub> system in presence of O<sub>2</sub> and H<sub>2</sub>O. In the catalytic cycle, palladium presents the catalytically active metal centre and switches between Pd<sup>0</sup> and Pd<sup>II</sup> oxidation states. Cu<sup>II</sup> redox co-catalyst plays an important role of oxidizing Pd<sup>0</sup> back to Pd<sup>II</sup> with the help of dioxygen to complete the catalytic cycle.<sup>1,148</sup> Mixed palladium /copper systems have also been employed to catalyze a number of other processes including cyclization of allylphenols, acetylation of alkenes and oxidation of terminal alkenes in presence of air.<sup>149</sup>

#### **1.3.5.2.3.2 Miscellaneous conversions**

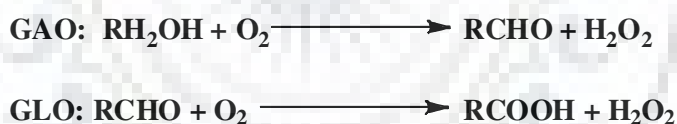
Several chemical reactions including oxygenation of alkanes, benzylic oxidation, aromatic C-H oxidation, Baeyer-Villiger oxidation,<sup>99</sup> cross-coupling reactions, allylic alkylation reactions, carbene transfer reactions<sup>132</sup> and asymmetric Friedel-Crafts alkylation

reactions<sup>150</sup> can also be catalyzed successfully by using copper based catalysts.

## 1.4 Metalloenzymes as a structural functional model for several activities

### 1.4.1 Galactose oxidase and glyoxal oxidase

Galactose oxidase (GAO) is a small (68 kDa), monomeric, type 2–copper–containing extracellular enzyme of fungal origin which incorporates a copper–coordinated tyrosyl radical at its active site. It catalyzes two–electron oxidation of D–galactose and a broad range of primary alcohols to aldehydes coupled with the conversion of O<sub>2</sub> to H<sub>2</sub>O<sub>2</sub> (Scheme 1.10).<sup>151-158</sup> A related enzyme, glyoxal oxidase (GLO), which catalyzes the oxidation of aldehydes to carboxylic acids with the concomitant reduction of O<sub>2</sub> to H<sub>2</sub>O<sub>2</sub> (Scheme 1.10), also possesses similar active site structure composed of a tyrosyl radical–copper catalytic motif.<sup>153,159</sup> The tyrosyl radical generated in the active site of galactose oxidase exhibits remarkable stability ( $t_{1/2} = 7.2$  d) which is necessary for its catalytic function, however, the tyrosyl radical generated in glyoxal oxidase is 40–fold less stable ( $t_{1/2} = 4$  h).<sup>160</sup>



#### Scheme 1.10 Catalytic activity of galactose oxidase (GAO) and glyoxal oxidase (GLO)

The active site in galactose oxidase comprises of a copper atom in a distorted square–pyramidal geometry where a tyrosine residue (Tyr 495) is occupying the axial position with a long Cu–O distance of 2.7 Å (Fig. 1.1).<sup>151</sup> Two histidine residues (His 496 and His 581), a tyrosine residue (Tyr 272) covalently cross–linked to a neighbouring cysteine residue (Cys 228) through a thioether bond resulting from the oxidative post–translational modification and an exogenous ligand (H<sub>2</sub>O or acetate) coordinate copper in equatorial positions.<sup>152,161-163</sup> This thioether linkage is presumably responsible for the lowering of tyrosyl/tyrosine redox potential<sup>152,160,162,164</sup> whereas the axial tyrosinate ligand

Tyr 495 functions as a general base during catalysis.<sup>165,166</sup> A tryptophan residue Trp 290 exhibits  $\pi$ -stacking interactions with redox active tyrosine residue (Tyr 272) and shields the Cys-Tyr cofactor from exposure to solvent by controlling the access to the active site.<sup>152,165</sup>

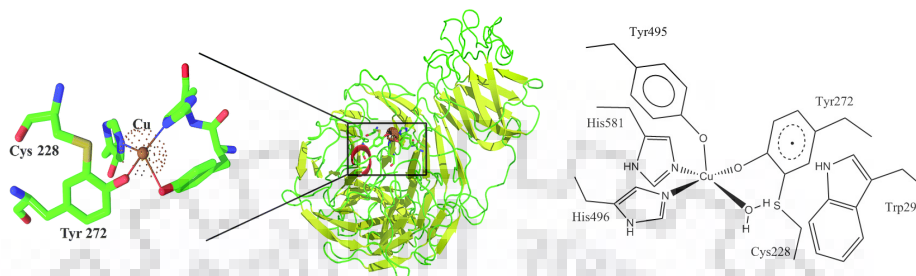
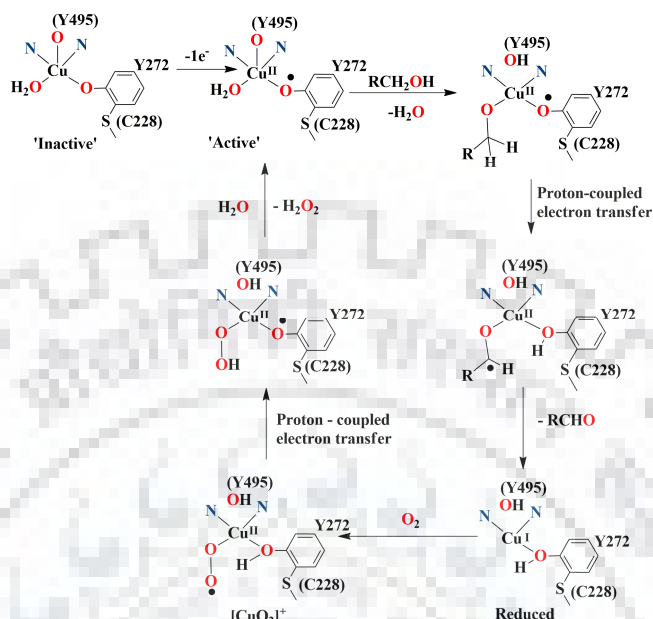


**Fig 1.4** Galactose oxidase enzyme and its active site

Copper participates in the catalytic cycle through single electron Cu(I)/Cu(II) redox shuttle and the second oxidizing equivalent necessary for catalytic oxidation of alcohol is achieved from Cys cross-linked tyrosyl radical.<sup>161</sup> The enzyme can exist in three distinct oxidation states which can be distinguished by their characteristic spectroscopic signatures: (a) Cu<sup>II</sup>-tyrosyl radical oxidized form (green, catalytically active), (b) intermediate Cu<sup>II</sup>-tyrosinate form (blue, catalytically inactive) and (c) reduced Cu<sup>I</sup>-tyrosine form (colorless, catalytically active).<sup>152,165</sup> The catalytic cycle of galactose oxidase completes in two half reactions: in the first half reaction, the alcohol substrate coordinates to the oxidized Cu<sup>II</sup>-radical active site with the concomitant reduction of both redox centres (tyrosyl radical and copper(II) ion) and release of the aldehyde product; in the second half reaction, the Cu<sup>I</sup>-tyrosine site binds dioxygen to regenerate the initial Cu<sup>II</sup>-tyrosyl radical state with the conversion of O<sub>2</sub> to H<sub>2</sub>O<sub>2</sub>.<sup>152</sup> The complete catalytic mechanism is shown in Scheme 1.11. Several metal-coordinated phenoxyl radicals have been characterized during the past years in order to mimic the active site of galactose oxidase which could lead to improved understanding of metal radical interactions (*vide infra*). Some of these complexes catalyzed

the oxidation of organic substrates also, predominantly the alcohols, thereby exhibiting the functional mimicking of the enzyme.<sup>154,155,167-187</sup>



Scheme 1.11 Reaction mechanism of galactose oxidase enzyme

### 1.5 Cytochrome P-450<sup>188</sup>

- Cytochrome P450 has a heme cofactor
- Oxidizes hydrocarbons to alcohols
- Selectively oxidizes the long aliphatic side chain of cholesterol, in the biosynthesis of the female hormone progesterone.

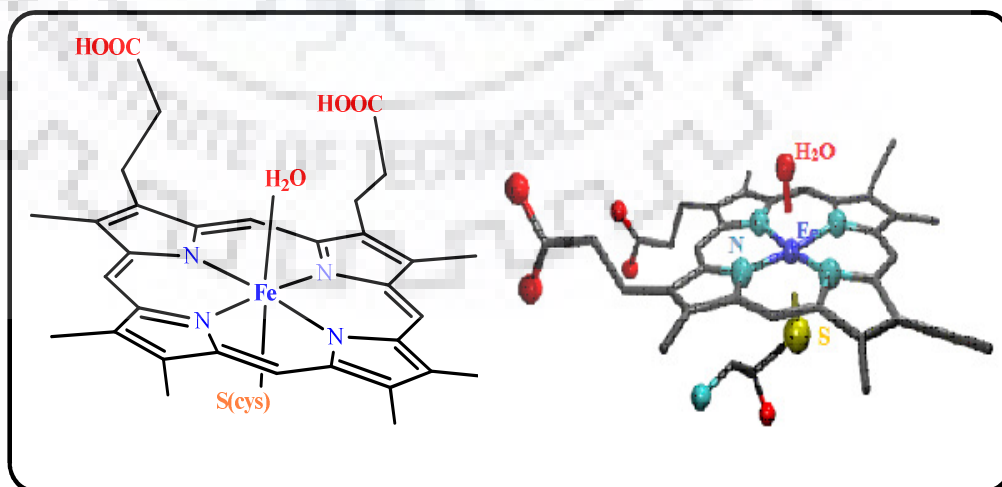


Fig. 1.5 Active site of cytochrome P450<sup>188</sup>

The active site of cytochrome P450 contains a hemeiron center. The iron is tethered to the protein via a cysteine thiolate ligand and water molecule (as shown in above Fig. 1.5)

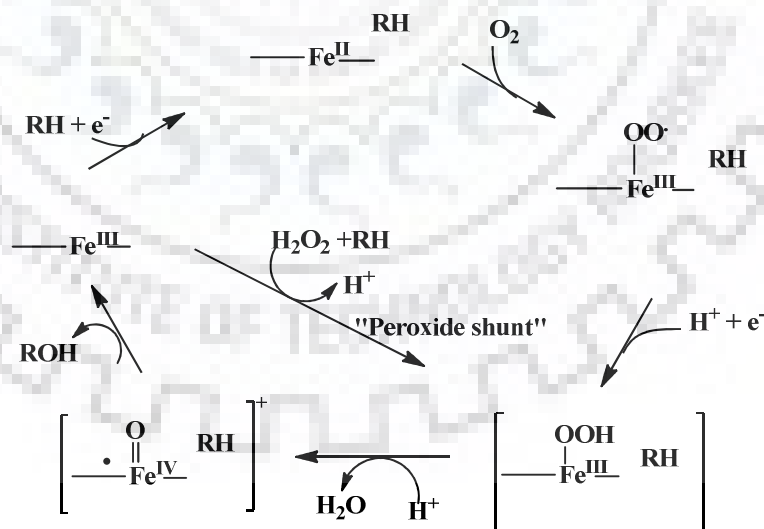
The defining reaction for P450 enzymes is the reductive activation of molecular oxygen. In this reaction, one of the oxygen atoms of molecular oxygen is inserted into the substrate and the other oxygen atom is reduced to a molecule of water. With one exception to date, the electrons required for this reduction of molecular oxygen derive from reduced pyridine nucleotides (NADH or NADPH).(Scheme 1.12)



**Scheme 1.12** Hydrocarbon oxidation by P450

Where R-H stands for a substrate with a hydroxyl table site. P450 enzymes therefore belong to the monooxygenase class of enzymes that only insert one of the oxygen atoms of molecular oxygen into their substrates.

### 1.5.1 Proposed mechanism for the oxidation of hydrocarbon by P450



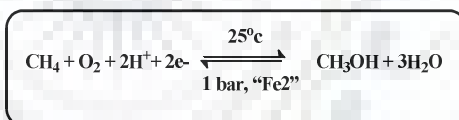
**Scheme 1.13** Mechanism proposed by cytochrome P-450 for alkane hydroxylation<sup>188</sup>



The first step is the binding of the substrate alkane to the active site which triggers the one electron reduction of the  $\text{Fe}^{\text{III}}$ . An adduct analogous to haemoglobin forms when  $\text{O}_2$  binds  $\text{Fe}^{\text{II}}$ . The transfer of one electron and a proton to the active site generates an  $\text{Fe}^{\text{III}}\text{-OOH}$  which was characterized by epr and density functional theory. decomposition of this intermediate takes place heterolytically and forms  $\text{Fe}^{\text{IV}}=\text{O}$  species which is responsible for substrate oxidation. In a better it can be described as  $[(\text{Por}^{\cdot})\text{Fe}^{\text{IV}}=\text{O}]^+$ . This high valent intermediate can also be generated with peroxides through a peroxide shunt or with single oxygen atom donors and it was concluded from the mechanism that substrate oxidation occurs due to transfer of terminal oxo atom<sup>188</sup>. (Scheme 1.13)

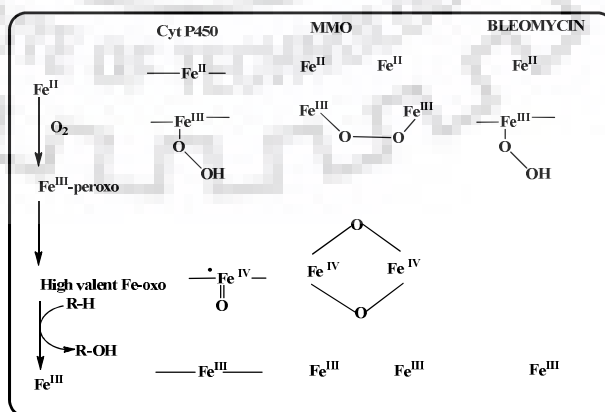
### 1.6 Methane monooxygenase

- It is an enzyme having non heme as a cofactor
- It has a carboxylate-bridged diiron site.
- catalyses the  $\text{O}_2$ -dependent conversion of methanol



Scheme 1.14 Oxidation of methane<sup>189</sup>

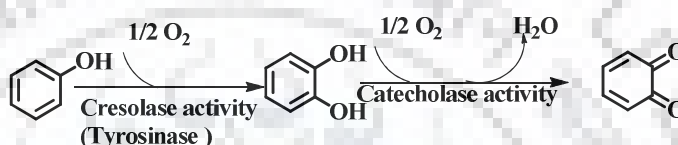
#### 1.6.1 Comparison of the reaction mechanisms of cytochrome P-450, MMO and bleomycin



Scheme 1.15 Comparison of mechanism of cytochrome P-450, MMO and bleomycin<sup>190</sup>

### 1.7 Catechol oxidase

Catechol oxidase, belongs to the type-3 class of dicopper proteins and resembles strongly to tyrosinase enzyme which is another member of this group. Tyrosinase exhibits two main catalytic activities: (a) hydroxylation of monophenols to *o*-diphenols, known as cresolase activity and (b) oxidation of *o*-diphenols to *o*-quinones, known as catecholase activity (Scheme 1.16). However the specificity of catechol oxidase is limited to the conversion of *o*-diphenols to *o*-quinones only.<sup>119,135,191</sup>



**Scheme 1.16** Reaction mechanism of tyrosinase as well as catecholase activity

This enzyme prepares a defense mechanism for plants where the quinone products autopolymerize to form brown polyphenolic catecholmelanins. This process helps the damaged plant to protect against pathogens and insects.

The crystal structure of *I. batatas* catechol oxidase showed that it is a monomeric 39 kDa protein with dicupric Cu(II) – Cu(II) active site in the center of the four-helix bundle motif where each copper site is coordinated with three histidine residues (H 88, H 109 and H 118 for CuA and H 240, H 244 and H 274 for CuB) (Fig. 1.6).<sup>191</sup> One interesting feature of the active site of catechol oxidase is an unusual thioether bridge between C 92 and H 109 which is believed to create geometrical restraints over the CuA site to permit fast binding of dioxygen substrate and for optimizing the electronic structure of metal atom for the catalytic function. The *met* form of the enzyme contains both copper sites in four-coordinate trigonal

pyramidal coordination environment where the fourth coordination site is occupied by a hydroxide ion bridging both copper atoms.<sup>135</sup>

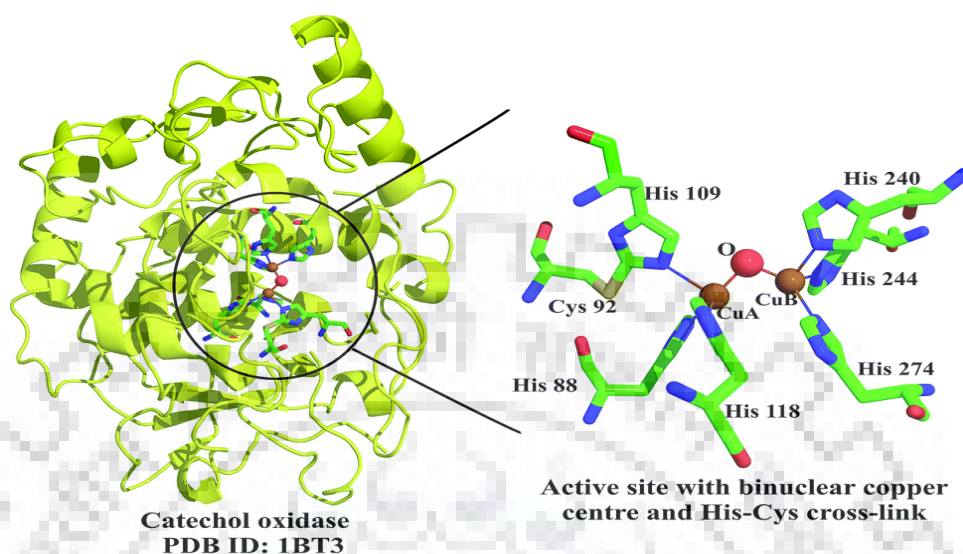
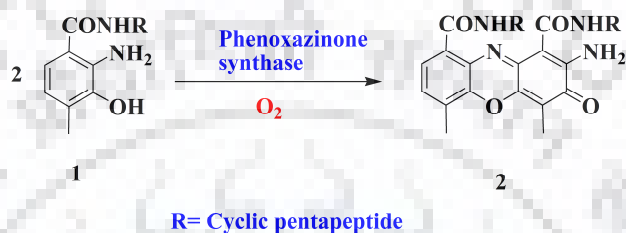


Fig. 1.6 Catechol oxidase enzyme active site

The metal–metal separation in the *met* state is about 2.9 Å. In the *deoxy* or reduced state of enzyme, this separation increases to 4.4 Å without causing any significant changes in the conformation of protein. The reduced enzyme contains CuA in trigonal pyramidal coordination environment where a coordinating water molecule completes the coordination sphere of CuA and CuB adopts a square planar geometry with one missing coordination site.<sup>135</sup> On the basis of the mode of coordination of the catechol substrate to the dicopper core, two different mechanisms have been proposed for the catalytic conversion of catechol to quinone.<sup>193,194</sup> Solomon and co-workers presented a mechanism involving the bidentate coordination of catechol to the dicopper centre as bridging ligand.<sup>195</sup> On the other hand, Krebs and co-workers suggested a monodentate asymmetric coordination of substrate to the dicopper active site<sup>191</sup>

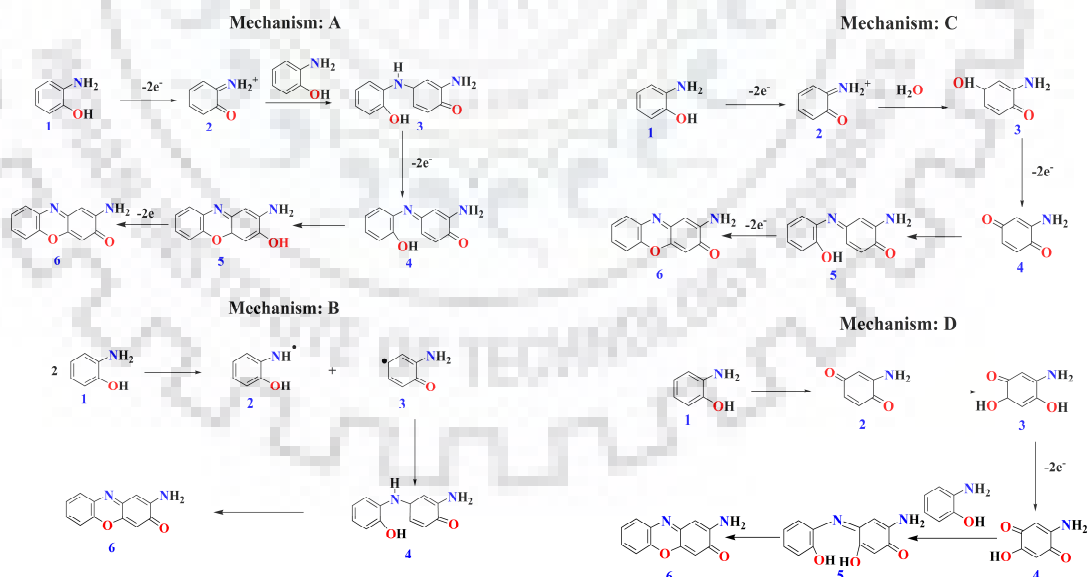
1.8 *o*-Aminophenol oxidase

The enzyme phenoxazinone synthase is naturally isolated from bacterium *Streptomyces antibioticus* and catalyzes the oxidative coupling of two molecules of a substituted *o*-aminophenol to phenoxazinone chromophore in the final step in the biosynthesis of the antineoplastic agent acinomycin D.<sup>167</sup> General reaction can be summarized as in Scheme 1.17.



**Scheme 1.17** Oxidation of *o*-aminophenol in presence of oxygen

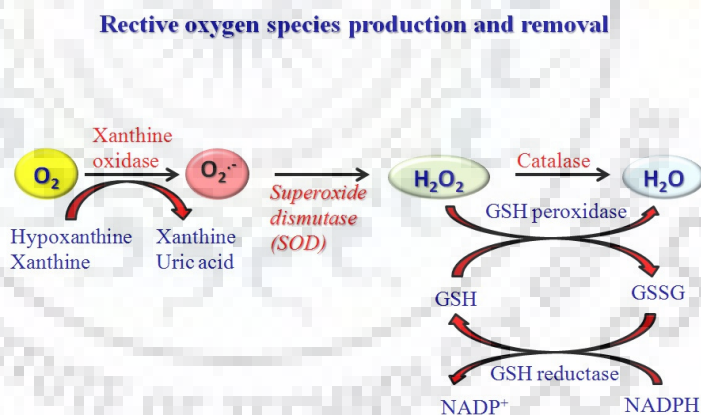
Later on, according to the extensive study on chemistry of the phenoxazinone chromophore, four pathways were proposed for the oxidation of *o*-aminophenol to 2-aminophenoxazinone for the enzymatic reaction (Scheme 1.18).<sup>168,169</sup>



**Scheme 1.18** Proposed mechanism for the formation of 2-aminophenoxazinone

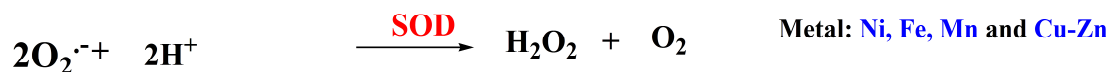
### 1.9 Superoxide dismutase enzymes

Superoxide radical is a reactive oxygen species (ROS) produced during cellular processes or some environmental conditions such as interaction of UV radiation with biomolecules, enzymatic activities in phagocytic cells (neutrophils and macrophages) or as a by-product of cellular respiration. Reactive oxygen species (ROS) such as hydrogen peroxide, hydroxyl radicals and peroxynitrites are also formed through superoxide ions.<sup>196</sup> These reactive oxygen species initiates damaging and uncontrollable reactions in cells leading damage to DNA and other cell component.<sup>197,198</sup> These uncontrolled production of ROS and damage caused by them is responsible for many diseases such as atherosclerosis, rheumatoid arthritis, autoimmune disease, Parkinson's disease, Huntington's disease and Alzheimer's disease.<sup>198,199</sup> Superoxide radicals can act as signalling agent, a safe intermediate which decomposes immediately or a toxic species. In body its level is regulated by two enzymes superoxide reductase(SOR) and superoxide dismutase(SOD) (Scheme 1.19).<sup>200</sup>



**Scheme 1.19** Superoxide dismutase: Production and dismutation of reactive oxygen species (plasma reduced glutathione (GSH), GSSG–oxidised glutathione or Glutathione disulfide)

Both the metalloenzymes are redox active and controls the concentration of superoxide radicals. The equations shown below represent the difference in the function of two enzymes.



Superoxide dismutase enzymes were first discovered by Irwin Fridovich and Joe McCord.<sup>201</sup> This enzyme is responsible for the regulation of antioxidant–oxidant balance in many organisms.<sup>200</sup> On the basis of metal ion present, this metalloenzyme has been categorized into four types: Ni–SOD,<sup>201</sup> Mn–SOD,<sup>1</sup> Fe–SOD,<sup>202</sup> and Cu/Zn–SOD.<sup>203</sup> Ni–SOD was found in cytosol of *streptomyces* and *cyanobacteria*,<sup>204</sup> as well as in a few green algae.<sup>205,206</sup> Mn–SOD was discovered in the cytosol of *archaea*,<sup>207,208</sup> bacteria<sup>209</sup> and eukaryotic cells typically contain Mn–SOD in the mitochondrial matrix. Fe–SOD is found in bacterial cytosol enzyme.<sup>209</sup> In eukaryotic cells, Cu/Zn–SOD is primarily found in cytosol but also found in the mitochondrial membrane space and nucleus.<sup>210</sup>

The Mn–SOD and Fe–SOD enzymes both have subunit of size about 22 kDa and have substantial sequence similarity.<sup>211</sup> Two residues are considered as distinguishing Mn–SOD from Fe–SODs which are residue 77 (*E. coli* numbering) is glycine in Mn–SODs and glutamine in Fe–SODs and residue 146 is alanine in all Fe–SODs, and either glutamine or histidine in Mn–SODs.

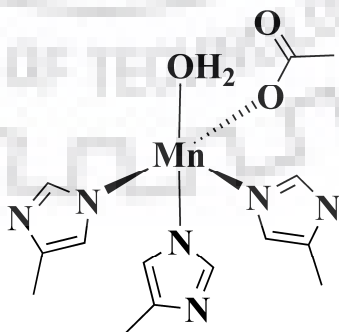
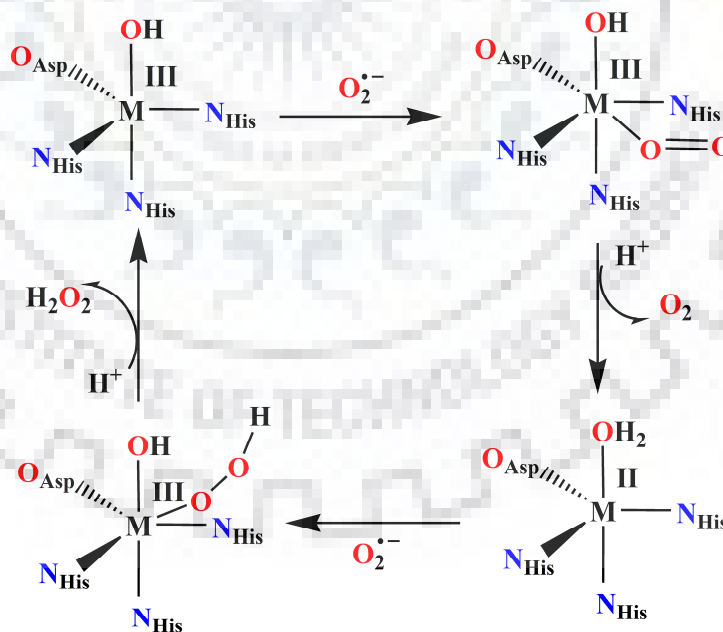


Fig. 1.7 Active site structure of human mitochondrial Mn–SOD

Metal ion is located deep within hydrophobic pocket in the protein formed by two subunits. Manganese coordination geometry is distorted trigonal bipyramidal with two histidine ligands and the aspartate donor in the equatorial plane and axial histidine and a water or OH<sup>-</sup> group in axial position (Fig. 1.7).

The catalytic mechanism is shown in Scheme 1.20 which involves change in oxidation state of metal ion between III and II.<sup>212</sup> In the beginning metal is found in oxidized state where axial ligand is hydroxide. On arrival of superoxide anion metal centre expands its coordination number (trigonal bipyramidal to octahedral) and metal itself got reduced to Mn(II) on protonation of the -OH group and finally release of a dioxygen molecule occurs. Another superoxide anion binds to this reduced Mn(II) centre, which oxidizes to transfer its proton with the production of hydroperoxo species. Finally, H<sub>2</sub>O<sub>2</sub> release subsequently upon protonation of the manganese (III)-hydroperoxo intermediate.



**Scheme 1.20** Schematic representation of mechanism of superoxide dismutase enzyme

### 1.9.1 Manganese and iron complexes as a SOD mimic

Manganese and iron both the metals are found in the active site of native enzyme<sup>211,213-215</sup> but these molecules as such cannot be utilized as pharmaceutical agents.<sup>216</sup> These metals have been used widely for structural, functional or structural–functional mimicking of these metal enzymes. In this regard complexes which are cheap, low molecular weight, less toxic and having good solubility in water are highly demanding.

Manganese complexes have been displayed SOD activity and used to cure oxidative stress. Several manganese complexes have been synthesized in this regard using ligands as shown in Fig. 1.8. Remarkable work in this area has been done by several groups. Ivanovic–Burmazovic and co–workers have synthesized seven–coordinated manganese complexes  $[\text{Mn}(\text{L})(\text{H}_2\text{O})_2]^{2+}$ , L represents an equatorial pentadentate macrocyclic ligand with five nitrogen donor atoms. SOD activities of these complexes were monitored and these complexes found to be a potent superoxide dismutase (SOD) mimetics. They have also indicated probable use of the synthesized complexes as potential human therapeutics for the treatment of diseases caused by the overproduction of superoxide.<sup>217</sup> In continuation of these works, Burmazovic and co–workers have utilized Stopped–flow measurements combined with time–resolved UV–visible spectroscopy for the spectral analysis of superoxide decay. This group have performed the comparative study of catalytic activity of putative manganese SOD (superoxide dismutase) mimics known in the literature.<sup>218</sup> Recently Kose and co–workers have synthesized manganese (II) complexes utilizing pentadentate ligand derived from Schiff's base which exhibited excellent SOD ( $\text{IC}_{50} \sim 1 \mu\text{M}$ ) activity.<sup>219</sup> Similarly Signorella and coworkers synthesized manganese(III) complex using unsymmetrical hexadentate ligand 1–[N–(2–pyridylmethyl),N–(2–hydroxybenzyl)amino]–3–[N'–(2–hydroxybenzyl),N'–(4–methylbenzyl)amino]propan–2–ol having  $\text{N}_3\text{O}_3$  donor which exhibited SOD activity having good  $\text{IC}_{50}$  value (1.26  $\mu\text{M}$ ). These complexes were found to



be efficient in disproportionation of  $H_2O_2$  and superoxide ion.<sup>220</sup> Scorpionand-like ligands are also an important class of ligands. Clares *et. al.* have utilized these macrocyclic ligands to prepare manganese(II) complexes and monitored *in vitro* and *in vivo* activities. *In vitro* activity was performed following the McCord–Fridovich method. Manganese complexes were subjected to monitor the antioxidant behaviour of these compounds on bacteria, yeast and fish embryos.<sup>221</sup>

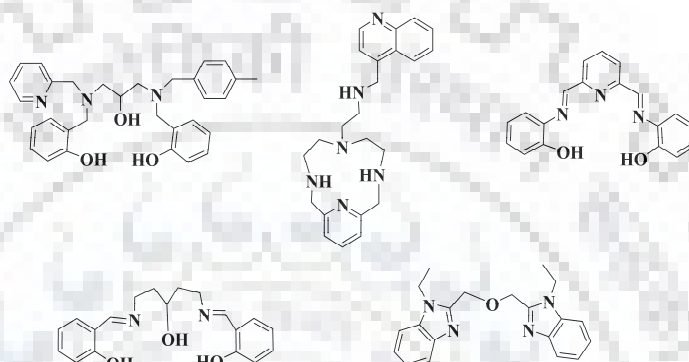


**Fig. 1.8** Ligands utilized for the synthesis of complexes as a SOD mimic

Studies on, SOD activities have been an interesting area to explore and a lot of work has been done in this regard.<sup>222–235</sup> Most of the SOD mimic molecules are manganese complexes as mentioned above and they have been found successful in *in vitro* as well as *in vivo* studies such as EUK–134. EUK–134 has been found a potent antioxidant in rat kidneys and limbic systems.<sup>236,237</sup> Investigation of the literature illustrated that manganese(II) as well as manganese(III) complexes could be used as superoxide scavenger molecules.

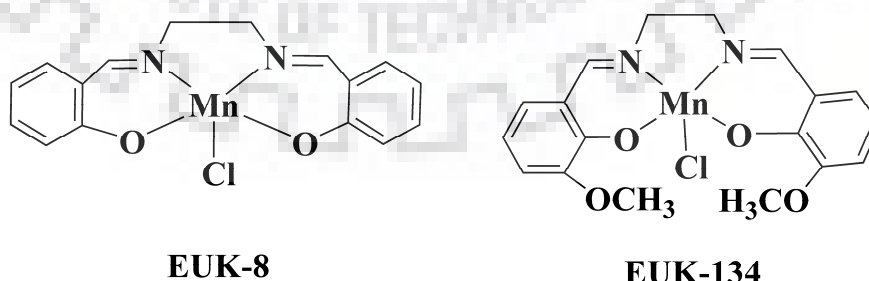


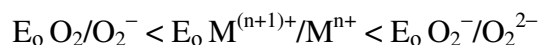
**Fig. 1.9** Manganese complexes as a potent SOD mimic

Iron complexes have also been studied as SOD mimic although they can produce hydroxyl radical on reacting with H<sub>2</sub>O<sub>2</sub> which could be fatal. The advantage of iron complex over manganese is that these complexes are kinetically and thermodynamically more stable.<sup>238</sup> Recently, Hitomi and co-workers reported iron complexes [Fe<sup>III</sup>(dpaq<sup>R</sup>)Cl]Cl having different electron donating and withdrawing substituent in ligand framework and these complexes served as a pure SOD mimic without any peroxidase activity. Iron complexes were found to be more effective SOD mimic as compare to iron salen complexes. Introduction of electron donating group in ligand frame showed enhancement in the SOD activity.<sup>239</sup> Pap and co-workers reported hexacoordinated iron(III) complexes utilizing isoindoline derived ligands. The SOD activities of complexes were evaluated using indirect method and NBT assay. Synthesized complex exhibited good correlation between the redox potential and SOD activity. SOD like activity exhibited that the rate determining step is the reduction of the metal center.<sup>240</sup> Ivanovic-Burmazovic and co-workers have synthesized seven-coordinated iron and manganese complexes [Fe<sup>III</sup>(dapsox)(H<sub>2</sub>O)<sub>2</sub>]ClO<sub>4</sub>·H<sub>2</sub>O, [Fe<sup>II</sup>(H<sub>2</sub>dapsox)(H<sub>2</sub>O)<sub>2</sub>](NO<sub>3</sub>)<sub>2</sub>·H<sub>2</sub>O and [Mn<sup>II</sup>(H<sub>2</sub>dapsox)(CH<sub>3</sub>OH)(H<sub>2</sub>O)](ClO<sub>4</sub>)<sub>2</sub>(H<sub>2</sub>O) using acyclic and rigid pentadentate H<sub>2</sub>dapsox ligand [H<sub>2</sub>dapsox=2,6-diacetylpyridinebis(semioxamide)]. Superoxide dismutase activities of these complexes were studied spectrophotometrically, electrochemically, and using a submillisecond mixing UV-visible stopped-flow techniques. The IC<sub>50</sub> values were found to be in the millimolar range and proved to be effective SOD mimic.<sup>241</sup> In this regard several iron complexes were synthesized and there SOD activities were optimized.<sup>239,241-248</sup>

### **1.9.2 Superoxide dismutase activity**

Dismutation of superoxide is a redox process hence electrochemical behaviour of all complexes was examined prior to investigate their SOD-like activity. For any model complex (M), the redox potential should fall in between one-electron reduction potential for

oxygen (-0.16 V vs. NHE, -0.40 V vs. SCE, pH 7.0) and one-electron reduction potential of superoxide radical (0.89 V vs. NHE, 0.65 V vs. SCE, pH 7.0) in order to exhibit the SOD activity<sup>226</sup> i.e.



McCord–Fridovich (McCF) method was employed to determine the SOD activity of complexes which involves the enzymatic generation of superoxide radicals by xanthine/xanthine oxidase system in presence of cytochrome C (cyt c) or nitro blue tetrazolium (NBT) indicators.<sup>331</sup> The assay is based on the competition between SOD/SOD mimic and the redox active indicator for superoxide radicals.<sup>226</sup> In the experiments, steady state low levels of superoxide ions were maintained in the reaction medium using xanthine/xanthine oxidase system. The experiments were carried out in presence of a fixed concentration of nitro blue tetrazolium (NBT) indicator which gets reduced by superoxide ions and produces a blue formazan dye after reduction. Reduction of NBT was followed spectrophotometrically by measuring its absorbance at 560 nm. The relative amounts of superoxide ions present in the reaction medium were estimated indirectly by measuring the concentration of reduced NBT produced by the reaction between superoxide ions and NBT. IC<sub>50</sub> value of a compound for SOD activity has been described as the concentration of that particular compound required for 50% inhibition of NBT–reduction by superoxide ions.

## **1.10 DNA binding and DNA cleavage**

### **1.10.1 Structure of DNA<sup>68</sup>**

The three-dimensional double helical structure of DNA molecule was discovered by Watson and Crick in 1953. DNA is composed of two polynucleotide strands organized in an antiparallel arrangement and wound round each other to form a double helix. The exterior of the helix is decorated alternatively with deoxyribose sugar units and phosphate groups

having two formal negative charge which are linked together by phosphodiester bonds (Fig. 1.4). The interior of helix is anchored with purine (adenine and guanine) and pyrimidine (cytosine and thymine) bases. The double helical structure of DNA is stabilized by the interstrand complementary base pairing through hydrogen bonding and  $\pi$ - $\pi$  stacking interactions among the adjacent base pairs along the helical column.

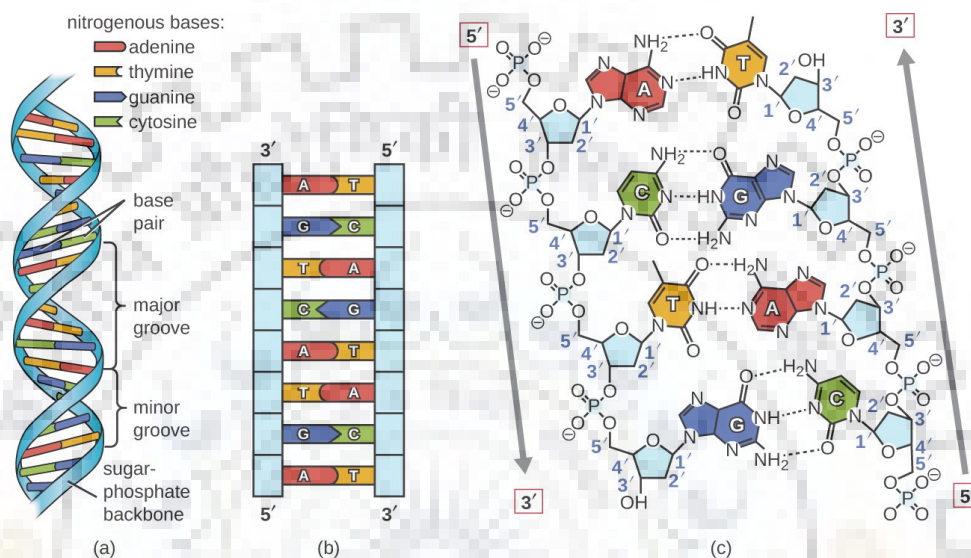


Fig. 1.10 Structure of DNA and its components

### 1.10.2 DNA binding

Small molecules which can bind to DNA offer significant promise as diagnostic probes, reactive agents and therapeutics. Metal complexes can interact with DNA either through coordination to phosphate oxygen atoms, sugar oxygen atoms, atoms of the nucleobases (N,C,O) or indirectly via their ligands. Both, strong covalent and weak non-covalent types of association of metal complexes with nucleic acids have been recognized.

#### 1.10.2.1 Covalent Binding

Covalent type of binding generally involves the coordination of soft metal ions to the nucleophilic positions of heterocyclic bases of DNA and RNA. The preferred sites for covalent binding of metal complexes are N7 on guanine, N1 and/or N7 on adenine, N3 on cytosine, O4 on thymine and deprotonated N3 position on thymine and uracil.<sup>68,249</sup> A

familiar example of such complexes is the anti-cancer drug *cis*-platin which interacts with polynucleotide strand through coordination of platinum center to the N7 positions of adjacent guanine bases of one strand (Fig. 1.11).<sup>250</sup> This results in intrastrand cross-linking between neighbouring guanine residues.

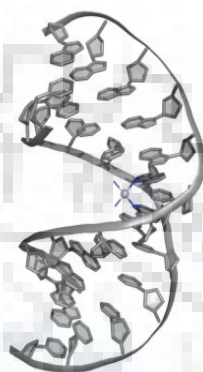


Fig. 1.11 Covalent DNA binding by *cis*-platin<sup>250</sup>

In addition, transition metal complexes with lesser degree of softness may exhibit some sort of covalent binding with oxygen atoms of phosphate groups also, where the ionic versus covalent character of interaction is mainly dictated by the metal ion involved.<sup>68</sup>

Covalent-coordinate type of interactions with the sugar moiety are rather less common but may exist with some heavy metal compounds like osmate esters.<sup>68</sup> Covalent binding occurs irreversibly and affords complete inhibition of DNA processes ultimately leading to cell death.

#### 1.10.2.2 Non-covalent binding

Non-covalent binding implies interaction of compound with DNA through hydrogen bonding, electrostatic forces, Van der Waal's forces, hydrophobic interactions or intercalation.<sup>68</sup> There are three fundamental modes of non-covalent DNA binding (i) external or electrostatic interaction, (ii) groove or surface interaction and (iii) intercalation.

**(i) External binding or electrostatic binding**

The electrostatic interaction between positive charge of metal ion and negatively charged phosphate backbone of DNA or electron donor groups of nucleobases is referred as external binding. The strength of the binding is predominantly governed by the charge of the molecule, the ligand hydrophobicity and the total size of the ion.<sup>251,252</sup> This type of DNA interaction gives rise to association of DNA duplexes to form aggregates or condensed structures.<sup>251</sup>

**(ii) Groove binding or surface binding**

Groove binding involves lodging of drug molecules into the grooves of the double, triple or G-quadruplex helices of DNA (Fig. 1.12).<sup>249</sup> Unlike intercalators which exhibit planarity and rigidity, groove binders should have flexible structures and distort the DNA backbone to a lesser extent than that caused by intercalators.<sup>249</sup> Groove binding is stabilized by a combined action of electrostatic, H-bonding and Van der Waal's interactions which brings about the drug-DNA complexes more stable than those resulted by intercalation only.<sup>249</sup>

Groove binding of molecules with DNA may occur in two distinct ways: (i) via major groove and (ii) via minor groove. It has been observed that DNA binding proteins or gene-targeted oligonucleotides interact via major groove whereas small and crescent shaped molecules bind through the minor groove of helix.<sup>251</sup> Major groove binders possess multiple interaction sites and exhibit comparatively stronger binding ability with guest molecules. In terms of size, flexibility, electrostatic potential and water bonding properties, minor grooves may serve as better receptors for small, flat and cationic DNA binding molecules.<sup>251</sup> As a general rule, minor groove binding molecules cause little or no perturbation in the structure of DNA which is reflected by little or no change in the DNA circular dichroism.<sup>251</sup> Distamycin, metallobleomycins and Sigman's bis(1,10-phenanthroline)copper(I) complex are excellent examples of such molecules which bind DNA through minor grooves.<sup>253</sup>

**(iii) Intercalation**

Intercalation was first reported by Lerman in 1961.<sup>254</sup> It may be defined as irreversible sandwiching of a molecule between the adjacent base pairs of the DNA base stack, stabilized by  $\pi$ - $\pi$  stacking interactions, dipole-dipole interactions and hydrogen bonding interactions with planar aromatic bases (Fig. 1.12). Slight unwinding of the helix at the intercalation site, stiffening of the helix, lengthening of DNA equal to the height of one base pair and enhanced DNA stability are main consequences of the DNA intercalation event.<sup>254</sup> However, no bending or kinking results after intercalation and the overall structure of DNA remains unperturbed.<sup>254</sup> Intercalating ligands and metal complexes should possess extended planar aromatic ring system of suitable size and chemical nature to slot between base pairs. Examples include planar organic moieties such as ethidium, daunomycin and metal complexes bearing planar aromatic ligands like phen (1,10-phenanthroline), phe (9,10-phenanthrenequinone diimine) or dppz (dipyrido[3,2-*a*:2',3'-*c*]phenazine).<sup>270</sup> Coordinative saturation, rigidity and inertness for substitution are important characteristics of metallointercalators which make them suitable for intercalation and hamper their coordination with DNA.<sup>254</sup>

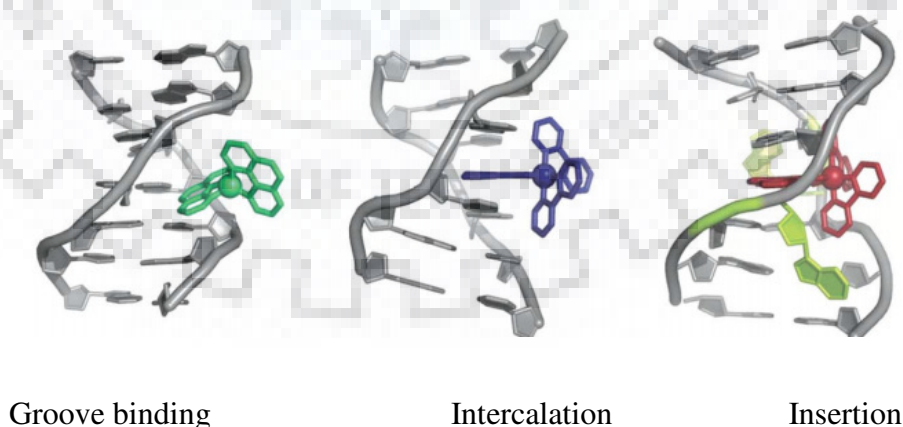


**Fig. 1.12** DNA and its binding modes with the metal complexes

In addition to these three fundamental modes, alternative modes for DNA interaction may also exist. Insertion is one of these alternative pathways which involves binding with DNA helix through separation and displacement of base pairs. Metalloinsertors contain a planar aromatic ligand which can act as a  $\pi$ -stacking replacement in the DNA base stack and eject the bases of a single base pair.<sup>253</sup> Very recently, Barton and co-workers posited the first example of molecules exhibiting this type of DNA binding.<sup>253</sup>

### **1.10.2.3 DNA interaction studies**

The mode of DNA interaction was investigated by absorption titration, fluorescence quenching and circular dichroism spectral studies. We performed DNA interaction studies in 0.1 M phosphate buffer (pH = 7.2) and sometimes dimethylformamide, methanol or acetonitrile was added for better solubility of complexes. Stability of the complexes was investigated in phosphate buffer (pH = 7.2) for 6 h to 3 days, prior to begin the DNA interaction experiment. The DNA binding experiments were carried out in 0.1 M phosphate buffer (pH 7.2) using a solution of calf thymus DNA (CT-DNA) which showed the ratio of UV-visible absorbance at 260 and 280 nm ( $A_{260}/A_{280}$ ) of *ca.* 1.8, indicating that the CT-DNA was sufficiently protein free.<sup>225</sup> The concentration of DNA solution was determined by measuring its absorbance at 260 nm and the extinction coefficient  $\epsilon_{260}$  was taken as 6600  $M^{-1}cm^{-1}$  as reported in the literature.<sup>225</sup>

DNA interaction studies were investigated by absorbance titration experiments where a fixed concentration of complex was titrated with varying CT-DNA concentration in 0.1 M phosphate buffer (pH 7.2). The binding constants ( $K_b$ ) were determined from a plot of  $[DNA]/(\epsilon_a - \epsilon_f)$  vs.  $[DNA]$  using the equation:<sup>225</sup>

$$[DNA]/(\epsilon_a - \epsilon_f) = [DNA]/(\epsilon_b - \epsilon_f) + [K_b(\epsilon_a - \epsilon_b)]^{-1} \quad (1.1)$$



where [DNA] represents the concentration of DNA in base pairs. The apparent absorption coefficients  $\epsilon_a$ ,  $\epsilon_f$  and  $\epsilon_b$  represent  $A_{\text{obs}}/[\text{Complex}]$ , the extinction coefficient of free complexes and the extinction coefficient of complexes in fully bound form, respectively. The binding mode of metal complexes with CT-DNA can be predicted by observing the changes in the absorption spectra as well as the order of binding constant ( $K_b$ ). Hypochromicity for charge transfer transition without bathochromic shift indicates interaction between the surface or groove of DNA and metal complexes.<sup>253,256-258</sup> Hypochromicity accompanied with bathochromic shift shows the intercalative mode of binding.<sup>259-261</sup> Hyperchromicity predicts electrostatic interaction of metal complexes with DNA.<sup>262,263</sup> The binding constants ( $K_b$ ) of various metal complexes follow the order – groove or surface binder < intercalator < metalloinsertor.<sup>264</sup> In order to get better insight into the DNA binding event, competitive binding of ethidium bromide vs test compounds with DNA was investigated using fluorescence spectroscopy. Ethidium bromide (EB) emits intense fluorescence in presence of DNA due to its strong intercalation between adjacent DNA–base pairs. Addition of complexes to the EB-DNA mixture may lead to the quenching of enhanced fluorescence of ethidium bromide indicating their competitive binding with DNA. Fluorescence quenching experiments were carried out by successive addition of complexes to the DNA (25  $\mu\text{M}$ ) solutions pretreated with 5–10  $\mu\text{M}$  ethidium bromide (EB) in 0.1 M phosphate buffer (pH 7.2). The samples were excited at 250 nm and emissions were recorded within the range of 400–700 nm. Stern–Volmer quenching constants were calculated using equation 1.2.<sup>255</sup>

$$I_0/I = 1 + K_{sv} [Q] \quad (1.2)$$

Where  $I_0$  and  $I$  represent the emission intensities in the absence and presence of complex respectively and  $[Q]$  is the concentration of quencher (metal complex).  $K_{sv}$  is the linear

Stern–Volmer constant which is given by the ratio of slope to intercept in the plot of  $I_0/I$  versus  $[Q]$ . The order of Stern–Volmer constant ( $K_{sv}$ ) can predict the mode of binding with DNA and it follows the order: groove or surface binder < intercalator < metalloinsertor.

Circular dichroism (CD) spectroscopic technique is a sensitive and significant tool to monitor the conformational changes of DNA in solution. The CD spectrum of CT–DNA in the range 225–300 nm exhibits one positive band at 278 nm due to base stacking and one negative band at 246 nm due to helicity.<sup>255</sup> To investigate the mode of DNA interaction by metal complexes, CD spectra of CT–DNA in absence and presence of complexes were recorded with a 0.1 cm path–length cuvette after 10 min incubation at 25 °C. The concentration of the complexes and CT–DNA were 50 and 200  $\mu\text{M}$  respectively. The mode of interaction of metal complexes with DNA can be elucidated on the basis of change in molar ellipticity values and shifting in the position of positive and negative bands. No shift in the wavelengths of positive and negative bands indicates that the conformation of DNA remains largely unaltered after binding with the metal complex.

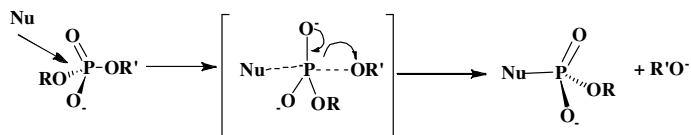
### **1.11 DNA cleavage or nuclease**

Nucleases are the enzymes which serve as excellent biological tools to destroy foreign nucleic acids and, to excise and repair the mutations in DNA in order to maintain the integrity of the genetic substances. However, nucleic acid strand scission may also arise from the exposure of cell to free radical species. In general, modification of nucleic acids may occur mainly by two major pathways: (i) nucleophilic pathway, and (ii) oxidative pathway.

#### **(i) Nucleophilic pathway**

The nucleophilic cleavage begins with the attack of a nucleophile on the phosphorus atom of phosphodiester moiety to form a trigonal bipyramidal transition state having the attacking

nucleophile and the departing alkoxide on apical positions which ultimately ends up with the cleavage of phosphodiester bond (Scheme 1.21).

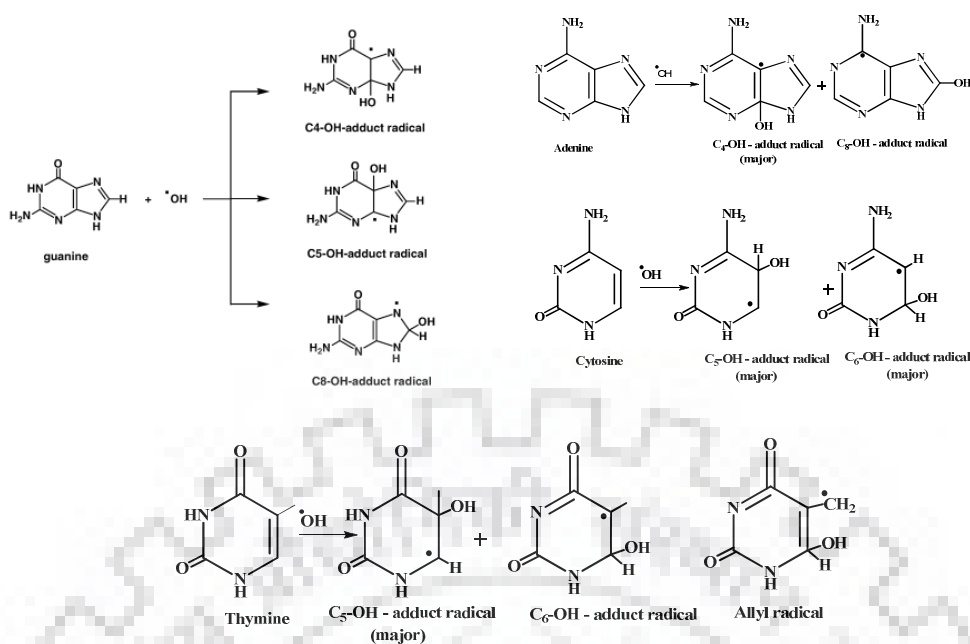


**Scheme 1.21** Nucleophilic cleavage path way of phosphodiester bond

This process is known as *nucleic acid hydrolysis* when water or hydroxide ion acts as nucleophile. On the other hand, when the nucleophile is an alcohol or alkoxide, the process is termed as *transesterification*.<sup>136</sup> The uncatalyzed hydrolysis of phosphate esters is exceedingly slow under physiological conditions. The remarkable stability of phosphodiester bonds renders the hydrolysis of nucleic acids quite challenging. The extreme kinetic inertness of DNA and RNA towards nucleophilic cleavage derives from strong repulsion between the potential nucleophiles and highly negatively charged backbones of nucleic acids.<sup>136</sup> Furthermore, formation of the requisite transition state for nucleophilic cleavage is also strongly unfavoured by base stacking interactions.<sup>265</sup> The active sites of most nucleases contains divalent cation like  $Mg^{2+}$ ,  $Ca^{2+}$ ,  $Mn^{2+}$  or  $Zn^{2+}$ . The presence of these cations greatly enhances the hydrolysis of phosphate ester by activating them towards nucleophilic attack via charge neutralization as well as by assisting the departure of the alkoxide leaving group through stabilizing interactions.<sup>265</sup>

### (ii) Oxidative pathway

In biology, oxidative cleavage generally involves oxidation of sugar moiety and/or the nucleobases by reactive intermediates of intracellular or extracellular origin which ultimately lead to the strand scission. However, redox-active transition metal complexes can also mediate DNA oxidation by generating such intermediates through redox-cycling in presence of oxidants/reductants or without any assisting agents.



**Scheme 1.22** Oxidation sites in nucleobase by reactive oxygen species

These reactive intermediates generally include reactive oxygen species (ROS) like hydroxyl radical ( $\text{HO}^\bullet$ ), superoxide anion ( $\text{O}_2^-$ ), hydrogen peroxide ( $\text{H}_2\text{O}_2$ ) and singlet oxygen ( $^1\text{O}_2$ ).<sup>266</sup> Hydroxy radical is an extremely strong oxidant which can abstract hydrogen from any carbon of the pentose sugar. It can add to the double bonds of DNA bases and abstract hydrogens from various positions of nucleobases as shown in Scheme 1.22.

The C-centered radicals of sugar moiety and C- or N- centered radicals of DNA bases generated this way, may then undergo further reactions resulting in a variety of final products.<sup>267</sup> Singlet oxygen can also cleave DNA oxidatively with energy transfer.<sup>266</sup> Furthermore, reactive metal-oxo species (RMOS) e.g. end-on and side-on peroxo/superoxo metal species ( $\text{M-OH/M-OOH}$ ) and metal oxo species ( $\text{M=O}$ ) may also cause DNA cleavage at specific sites through binding with DNA in selective ways.<sup>271</sup>

The oxidative modification of DNA can also be induced by photochemical methods where reactive intermediates responsible for the DNA cleavage are generated by photo-irradiation.<sup>268</sup> This type of cleavage is termed as *photo-induced DNA cleavage* which

is extensively used for clinical applications like photodynamic therapy.

### **1.11.1 Nuclease activity**

The cleavage of supercoiled (SC) plasmid DNA may give rise to nicked circular (NC) and linear circular (LC) forms which are separated on the basis of their sizes. However the relative migration rates of these three types also depend upon applied voltage, buffer concentration, agarose concentration and the amount of superhelical twists in DNA. The rate of migration is highest for the supercoiled form and lowest for the nicked form while the linear form runs in the middle. After electrophoresis, gel is stained with ethidium bromide and visualized using Gel-Doc system. The relative amounts of supercoiled, nicked and linear forms are determined by comparing the intensities of the individual bands. Cleavage of plasmid DNA was monitored by agarose gel electrophoresis in Tris-boric acid-EDTA (TBE) buffer (pH = 8.4). Supercoiled pBR322 DNA was incubated with test complexes in 0.1 M phosphate buffer (pH = 7.2) at 37 °C for varying time periods. The oxidative DNA cleavage by complexes was studied in presence of varying concentrations of H<sub>2</sub>O<sub>2</sub> (oxidizing agent) or 2-mercaptoethanol (BME) (reducing agent).

To investigate the mechanism of nuclease activity, DNA cleavage experiments were carried out in presence of variety of standard radical scavengers and reaction inhibitors like DMSO, D<sub>2</sub>O, ethanol, urea (20 mM), NaN<sub>3</sub> (20 mM), L-histidine (20 mM), catalase (10 U) and neocuproine (400 μM).<sup>259,269,270</sup> After incubation, the reaction was quenched by adding loading buffer (25% bromophenol blue and 30% glycerol) to each vial. Electrophoresis of the DNA cleavage products was performed in Tris-boric acid-EDTA (TBE) buffer at 60 V for 2 h over an agarose gel (0.8%) containing 0.4 μg/mL of ethidium bromide (EB). The fragments were identified by placing the stained gel under an illuminated UV lamp and photographed using Gel-documentation system.

### 1.12 Organic dyes degradation

Organic dyes are widely used in different industry such as textile, plastic, medicine and many other industries. The hazardous effects of these organic dyes in water have been major concern. From this type of industries, large quantity of high content color effluents is released; those are more toxic and resistant to destruction by conventional methods. When these dyes are accumulated in water the problem of eutrophication, reduces the reoxygenation capacity and makes severe damage to the aquatic organisms by hindering the infiltration of sunlight. Organic dyes are typically resistant to microbial attack therefore it is difficult to remove from the waste water. There are several conventional methods like ultrafiltration, adsorption, chemical and electrochemical methods to remove the organic dyes from the waste water<sup>271</sup>

### 1.13 Summary of present investigation

In **First chapter**, presents an introduction to coordination chemistry and several reactivity studies. The various chemical methods and spectroscopic techniques used were comprehensively summarized in this chapter.

In **chapter two**, we have described Complexes  $[\text{Cu}(\text{PyPhime-sali})\text{ClO}_4]$  (**1**) and  $[\text{Cu}(\text{PyPhime-}^t\text{Bu-sali}(\text{CH}_3\text{OH}))\text{NO}_3].2\text{CH}_3\text{OH}$  (**2**) ( $\text{L}^1\text{H}_2$  and  $\text{L}^2\text{H}_2$  (PyPhime-sali = 2,2'-((1E,1'E)(2,2'-(pyridine-2,6-diyl)bis(2-phenylhydrazin-2-yl)ylidene)) bis(methanylylidene)) diphenol, PyPhime-<sup>t</sup>Bu-sali = 6,6'-((1E,1'E)-(2,2'-(pyridine-2,6-diyl)bis(2-phenylhydrazin-2-yl)ylidene))bis(methanylylidene))bis(2,4-di-tert-butylphenol) and H is dissociable proton) were synthesized and characterized by different spectroscopic methods. Molecular structures of the complexes were determined by X-ray crystallography and redox properties were investigated. Complex **1** was found to be a phenolato complex whereas complex **2** was a phenoxyl radical complex.

In **chapter three**, describes hexacoordinated non-heme iron complexes  $[\text{Fe}^{\text{II}}(\text{Cl-pyhyd-Pycarbo})_2](\text{ClO}_4)_2$  (**3**) and  $[\text{Fe}^{\text{II}}(\text{Cl-pyhyd-methyl-Pycarbo})_2](\text{PF}_6)_2$  (**4**) have been synthesized using ligands  $[\text{Cl-pyhyd-Pycarbo} = (\text{E})\text{-2-chloro-6-(2-(pyridin-2-ylmethylene)hydrazinyl)pyridine}$  and  $\text{Cl-pyhyd-methyl-Pycarbo} = (\text{E})\text{-2-chloro-6-(2-(1-(pyridin-2-yl)ethylidene)hydrazinyl)pyridine}$ . These complexes are highly active non-heme iron catalysts to catalyse the  $\text{C}(\text{sp}^3)\text{-H}$  bonds of alkanes. These iron complexes have been characterized using ESI-MS analysis and molecular structures were determined by X-ray crystallography. ESI-MS analysis also helped to understand the generation of intermediate species like  $\text{Fe}^{\text{III}}\text{-OOH}$  and  $\text{Fe}^{\text{IV}}\text{=O}$ . These complexes have also been utilized in degradation of organic dyes. DFT and TD-DFT calculations revealed that the oxidation reactions were performed through high-valent iron centre and a probable reaction mechanism was proposed. These complexes were also utilized for the degradation of orange II and methylene blue dyes.

In **chapter four**, copper complex  $[\text{Cu}(\text{TETA}^{\text{TA}})(\text{Cl}_2)]$  (**5**) derived from tridentate ligand ( $\text{TETA}^{\text{TA}}$ ) ( $\text{L} = 2\text{-}((2\text{-}((2\text{-}(\text{aminoethyl})\text{amino})\text{ethyl})\text{- amino})\text{ethyl})\text{isoindoline-1,3-dione}$ ) having NNN donor, was synthesized, characterized and molecular structure was determined using X-ray crystallography. This was found a robust catalyst for the degradation the organic dyes such as Orange II dye, Rhodamine B and Methylene blue. This catalyst was also utilised for the oxidation of catechol and 2-aminophenol. The catecholase and phenoxazinone synthase activity were determine using UV-visible spectroscopic studies. Theoretical calculations were performed to understand the electronic properties of this molecule.

In **chapter five**, Bio-inspired  $[\text{Mn}(\text{PyPhime-Pycarbo})(\text{H}_2\text{O})(\text{CH}_3\text{OH})](\text{ClO}_4)_2$  (**6**) and  $[\text{Fe}(\text{PyPhime-Pycarbo})(\text{H}_2\text{O})(\text{ClO}_4)]\text{ClO}_4$  (**7**). Complexes with a pentadentate ligand ( $\text{PyPhime-Pycarbo} = 2,6\text{-bis}((\text{E})\text{-1-phenyl-2-(pyridin-2-ylmethylene)hydrazinyl)pyridine}$ )

framework containing N<sub>5</sub> binding motif displayed excellent superoxide dismutase activity (SOD), with high stability in physiological conditions.

In **chapter six**, Complexes [Mn(PyPhime-Cina)Cl<sub>2</sub>](**8**), [Fe(PyPhime-Cina)Cl<sub>2</sub>] (**9**) [Co(PyPhime-Cina)Cl<sub>2</sub>] (**10**), [Ni(PyPhime-Cina)Cl<sub>2</sub>] (**11**) [Cu(PyPhime-Cina)Cl<sub>2</sub>] (**12**) have been synthesized using ligand (PyPhime-Cina=2,6-bis((E)-1-phenyl-2-((E)-3-phenylallylidene)hydrazinyl)pyridine) with NNN type moiety. The complexes have been used to studies the DNA interaction studies.

In **chapter seven** presents the synthesis of complexes of [Cu(PyPhime-Ben)<sub>2</sub>](NO<sub>3</sub>)<sub>2</sub> (**13**) and [Cu(PyPhime-Ben)<sub>2</sub>](ClO<sub>4</sub>)<sub>2</sub> (**14**) using ligand PyPhime-Ben = 2,6-bis((E)-2-benzylidene-1-phenylhydrazinyl)pyridine, [Cu(PyPhime-p-methoxyBen)(PF)<sub>2</sub>] (**15**) and [Co(PyPhime-p-methoxyBen)Cl<sub>2</sub>] (**16**) complexes using ligand PyPhime-p-methoxyBen = 2,6-bis((E)-2-(4-methoxybenzylidene)-1-phenylhydrazinyl)pyridine. These complexes were utilized for DNA interaction studies. Using tetradentate we have synthesized eight coordinated [Mn(Gimpy)<sub>2</sub>](ClO<sub>4</sub>)<sub>2</sub>(**17**) and [Mn(Gimpy)(NO<sub>3</sub>)<sub>2</sub>] (**18**) complexes for magnetic resonance imaging (MRI) contrast agents. In this chapter we have also synthesized petadentate ligand L<sup>6</sup> and using this ligand cobalt [Co(PyPhime-Pycarbo)(H<sub>2</sub>O)(ClO<sub>4</sub>)](ClO<sub>4</sub>), (**19**) manganese [Mn(PyPhime-Pycarbo)(H<sub>2</sub>O)<sub>2</sub>](Fe(CN)<sub>5</sub>NO)(**20**) and nickel [Ni<sub>2</sub>(PyPhime-Pycarbo)<sub>2</sub>Cl<sub>2</sub>](ClO<sub>4</sub>)<sub>2</sub>,(**21**) complexes have been synthesized and their molecular structure characterized with single crystal X- ray diffraction analysis. These complexes utilised for the in- vitro inhibition of superoxide anion i.e superoxide dismutase activity (SOD) studies. We have also synthesized complexes [Fe<sub>2</sub>(PyPhime-sali)<sub>2</sub>](Fe(CN)<sub>5</sub>NO) (**22**) and [Fe<sub>2</sub>(PyPhime-sali)<sub>2</sub>](ClO<sub>4</sub>)<sub>2</sub> (**23**) using pentadentate ligand L<sup>1</sup> also checked in- vitro superoxide dismutase activity (SOD) studies.



## **1.14 Measurements**

Several physical and spectroscopic techniques have been utilized for the characterization of synthesized compounds and investigation of their properties which have been described in detail in the subsequent chapters. These are briefly described below.

### **(i) Elemental analyses**

The measurements of the C, H, N contents of the samples were carried out with the help of Elementar Vario EL III elemental analyser which utilizes thermal conductivity data for gas (CO<sub>2</sub>, H<sub>2</sub>O, N<sub>2</sub>) analysis.

### **(ii) Infrared spectroscopy**

IR spectra were recorded as KBr pellets with Thermo Nicolet Nexus FT-IR spectrometer, using 16 scans and reported in cm<sup>-1</sup>.

### **(iii) Mass spectrometry**

Electro-Spray Ionization (ESI) mass spectra of the complexes were recorded as acetonitrile solutions under positive or negative ion mode with the help of a Bruker MicroTOF-QII mass spectrometer.

### **(iv) NMR spectroscopy**

<sup>1</sup>H and <sup>13</sup>C NMR spectra were recorded on Bruker AVANCE, 500.13 MHz spectrometer. The chemical shifts for all NMR spectra were related to internal standard Me<sub>4</sub>Si for all residual protium in the deuterated solvents.

### **(v) EPR spectroscopy**

EPR measurements (CW X-band (9.4 GHz)) were carried out with a Bruker Elexsys E500 series using the Bruker ER4122 SHQE cavity. The spectra at 120 K were recorded with an Oxford ESR900 helium continuous flow cryostat. All spectra were recorded with 0.5 mT modulation amplitude and 2 mW powers.

**(vi) UV–visible spectrophotometer**

Electronic absorption spectra were recorded in phosphate buffer (pH = 7.2), acetonitrile and methanol as solvents with a SHIMADZU, UV–2450 UV–visible spectrophotometer. For better solubility, 5–10% DMF was used when spectra were recorded in phosphate buffer. A matched pair of quartz cell of path length 1 cm was used.

**(vii) Fluorescence spectrophotometer**

Emission spectra were recorded with SHIMADZU, RF–5301 PC spectrofluorophotometer. Solution preparations were same as those for electronic spectral experiments.

**(viii) Circular dichroism**

Circular dichroism spectra of DNA and BSA were obtained by using a Chirascan circular dichroism spectrometer operating at 25 °C. The regions 220–320 nm and 190–260 nm were scanned using a cuvette of 1 mm path length to obtain the spectra of DNA and BSA respectively. The complexes were incubated with CT DNA and BSA for 10 min in phosphate buffer (pH = 7.2). Due to the lesser solubility of some complexes in buffer, 5–10 % of methanol was used.

**(ix) Cyclic voltammetry**

Cyclic voltammetry measurements were performed in different solvents such as DMF, dichloromethane and acetonitrile using a CH–600C electroanalyzer with a conventional three–electrode arrangement consisting of Ag(s)/AgCl electrode as reference electrode, glassy carbon as working electrode and platinum wire as auxiliary electrode. Tetrabutylammonium perchlorate (TBAP) (0.1 M) was used as the supporting electrolyte and complex concentration of  $10^{-3}$  M was used for experiments. All experiments were performed at room temperature. Solutions were thoroughly degassed with nitrogen prior to begin the experiments, and nitrogen atmosphere was maintained during the measurements.

The  $E_{1/2}$  value for ferrocene/ferrocenium couple vs. Ag/AgCl was determined under the same experimental conditions.

**(x) X-Ray structure determination**

The X-ray data collection and processing for ligands and complexes were performed on Bruker Kappa Apex-II CCD diffractometer by using graphite monochromated Mo-K $\alpha$  radiation ( $\lambda = 0.71070 \text{ \AA}$ ). Crystal structures were solved by direct methods. Structure solution, refinement and data output were carried out with the SHELXTL program.<sup>350,351</sup> All non-hydrogen atoms were refined anisotropically. Hydrogen atoms were placed in geometrically calculated positions and refined using a riding model. Images were created with DIAMOND and MERCURY programs.<sup>352-353</sup>

$R1$ ,  $wR2$  and goodness-of-fit (GOF) are expressed by following equations respectively.

$$R1 = \frac{\sum ||F_o| - |F_c||}{\sum F_o} \quad (1.5)$$

$$wR2 = \left[ \frac{\sum [w(F_o^2 - F_c^2)^2]}{\sum [w(F_o^2)^2]} \right]^{1/2} \quad (1.6)$$

$$^a\text{GOF} = \left[ \frac{\sum [w(F_o^2 - F_c^2)^2]}{M-N} \right]^{1/2} \quad (1.7)$$

where,  $M$  = number of reflections,  $N$  = number of parameters refined

Specific details for each compound will be given in the concerned chapter.

**(xi) Gel documentation**

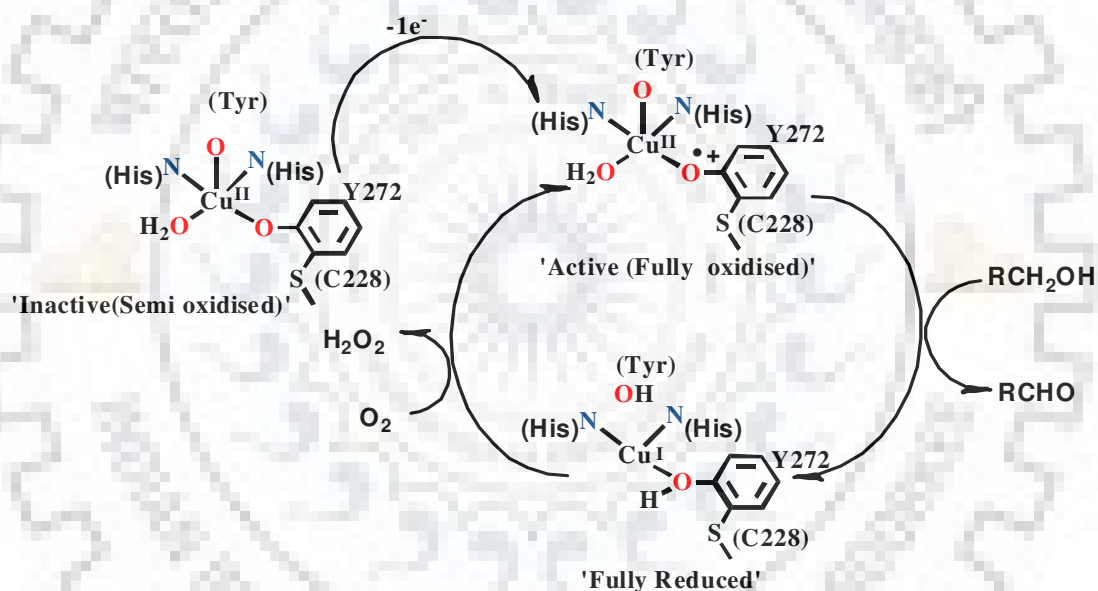
DNA fragments were identified by placing the gel under an illuminated UV lamp and photographed by using gel documentation system (BIO RAD).

**(xii) Chemical and solvents**

The chemicals and solvents used were analytical grade and most of them were used as obtained. The standard purification methods were followed wherever required.

## 2.1. Introduction

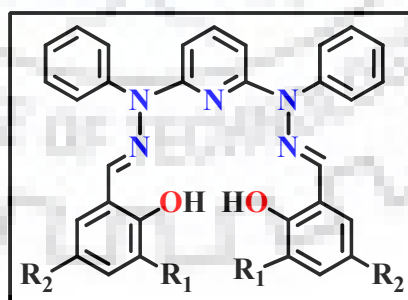
Galactose oxidase (GOase) is the simplest known copper-containing extracellular fungal enzyme. Crystallographic and spectroscopic studies on GOase have shown that the active site involves a free radical on tyrosine residue (Tyr-272), which was one of the ligands coordinated to the  $\text{Cu}^{2+}$  cofactor.<sup>272</sup> This enzyme is capable of catalyzing stereo-selective oxidation of primary alcohols, D-galactose etc. ranging from small molecules to polysaccharides.<sup>273</sup> GOase enzyme catalyses two-electron, two-proton oxidation of primary alcohols to the corresponding aldehydes and the concomitant reduction of dioxygen to hydrogen peroxide as shown in Scheme 2.1.



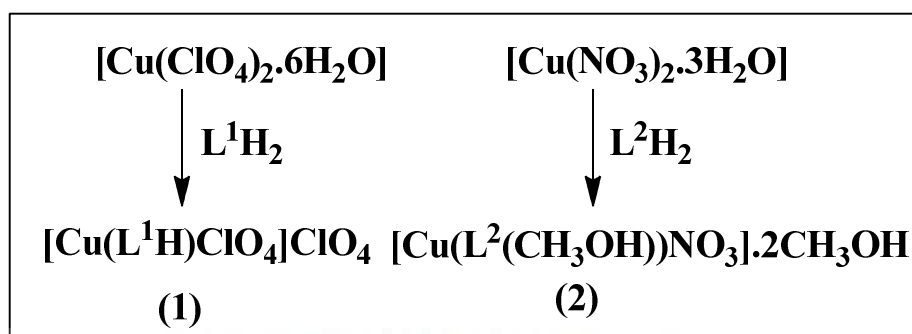
**Scheme 2.1** Inactive and active site of GOase during oxidation of primary alcohol to corresponding aldehyde

Ito *et al.* reported the crystal structure GOase enzyme<sup>274</sup> The flipping of copper oxidation states (Cu(II) and Cu(I)) as well as phenoxyl to phenolato function execute the two electron redox conversion of alcohol to aldehyde.<sup>27,151,152,161,275,276</sup> In the structural and functional modelling of metal site of galactose oxidase, there are several reports of phenoxyl radical complexes of copper.<sup>183,276-282</sup> Investigations of above reports clearly show that Stack and

co-workers,<sup>280</sup> Shimazaki and co-workers<sup>281</sup> and Thomas and co-workers<sup>183</sup> have reported X-Ray crystal structures of phenoxyl radical complexes of copper. Investigation on synthesis of phenoxyl radical complexes clearly showed that the phenolato complexes were prepared first and later on these complexes were oxidised by oxidising agent namely (AgSbF<sub>6</sub>, Ferroceniumhexafluoro phosphate, thianthrenyl (Th<sup>+</sup>) hexafluoroantimonate, (NH<sub>4</sub>)<sub>2</sub>[Ce<sup>IV</sup>(NO<sub>3</sub>)<sub>6</sub>](CAN). To the best of our knowledge there is no report of i) direct and one pot synthesis of phenoxyl radical complexes of copper and ii) crystal structures of copper phenoxyl radical complexes derived from ligand other than salen-type ligand system. Hence synthesis and structure determination of phenoxyl radical complexes of copper relevant to GOase enzyme active site remained a challenge to bioinorganic coordination chemists. Herein we report the design and synthesis of a new pentadentate ligand (shown in Scheme 2.2) and one pot single step synthesis of phenoxyl radical complexes of copper, [Cu(L<sup>2</sup>(CH<sub>3</sub>OH))NO<sub>3</sub>].2CH<sub>3</sub>OH (**2**). Corresponding phenolato complex [Cu(L<sup>1</sup>H)(ClO<sub>4</sub>)] (**1**) has been synthesized and will be discussed. Redox properties were examined. The oxidation of alcohol, catechol (catecholase activity) and o-amino phenol (phenoxazone synthase) have been investigated. The designed ligands were synthesized by reported procedure<sup>283</sup>



R <sub>1</sub>	R <sub>2</sub>	Ligand
H	H	L <sup>1</sup> H <sub>2</sub>
t-Bu	t-Bu	L <sup>2</sup> H <sub>2</sub>



**Scheme 2.2** Schematic drawing of ligands and synthesis of phenolato and phenoxyl radical complexes

## 2.2 Results and discussion

### 2.2.1 Synthesis and characterization

In dichloromethane-methanol (1:1) solution, reaction of  $\text{Cu}(\text{ClO}_4)_2 \cdot 6\text{H}_2\text{O}$  with ligand  $\text{L}^1\text{H}_2$  produced complex **1**; on the other hand, reaction of  $\text{Cu}(\text{NO}_3)_2 \cdot 3\text{H}_2\text{O}$  and  $\text{L}^2\text{H}_2$  afforded complex **2**. Schematic drawing of ligands and synthetic procedure are described in Scheme 2.2. The molecular structures of complexes **1** and **2** were determined by using X-ray crystallographic studies (Table 2.15) ORTEP diagrams of complex  $[\text{Cu}(\text{L}^1\text{H})\text{ClO}_4]$ (**1**) and  $[\text{Cu}(\text{L}^2(\text{CH}_3\text{OH}))\text{NO}_3] \cdot 2\text{CH}_3\text{OH}$  (**2**) are displayed in Fig. 2.1 and 2.2 respectively.

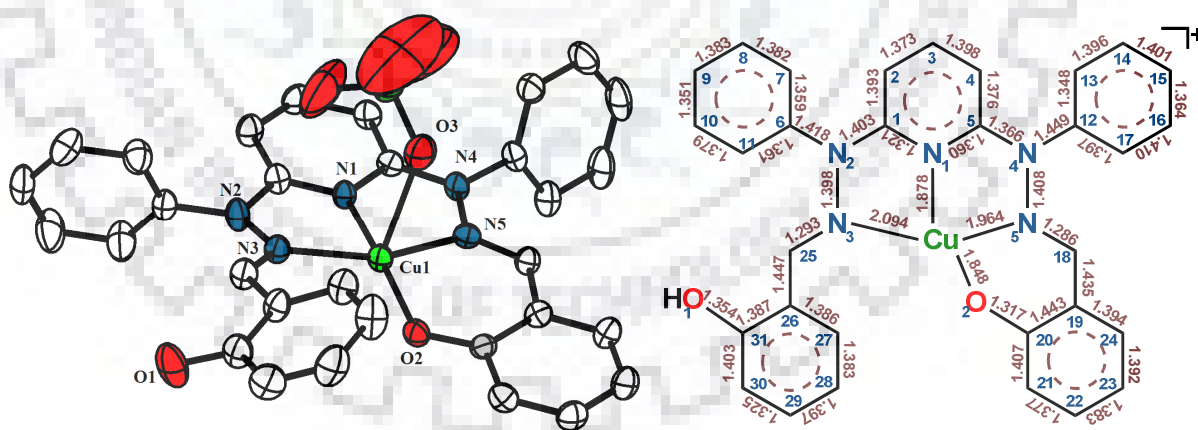


**Fig. 2.1** The ORTEP diagram and bond distances [Å] (30% probability level) of complex  $[\text{Cu}(\text{L}^1\text{H})\text{ClO}_4]$  (**1**). All hydrogen atoms and solvent molecules and extra anions are omitted for clarity.

All bond distances for both the complexes are depicted in Table 2.10 and 2.11. The bond angles for both the complexes are displayed in Table 2.12. All the characteristic properties of ligands  $L^1$  and  $L^2$  and corresponding metal complexes are displayed in Table 2.1.

In complex **1** copper centre was found to be pentacoordinated with a distorted square-pyramidal geometry. Pyridine nitrogen, two imine nitrogens and one phenolato function constitute the square plane and the oxygen atom from perchlorate anion occupied the apical position of the square pyramid. Hence the pentadentate ligand was found to be tetradentate with free (not coordinated to copper) phenolic -OH group. In the complex **2** copper centre has been found to be heptacoordinated with distorted pentagonal bipyramidal geometry. Pyridine nitrogen, two imine nitrogens and two oxygen atoms from phenolato function constitute the pentagonal coordination. One molecule of methanol and a nitrate oxo-anion were found to be coordinated in axial position. Here both the copper atoms were having the 0.5 occupancy. In complex **1** and **2** Cu-N<sub>py</sub> bond distances were found to be 1.878 Å and 1.891 Å respectively. These distances were found to be lower than the Cu-N<sub>py</sub> distances reported earlier.<sup>283</sup> However Cu-N<sub>py</sub> distances are also found to be lower than the terpy copper complexes reported in the literature.<sup>284</sup> Copper imine distances are constant with the literature value, these are close to 2 Å.<sup>283-284</sup> The difference between Cu-N<sub>im</sub> bond was found to be 0.13 Å in complex **1** however the same difference in complex **2** it was found to be 0.002 Å. The Cu-O<sub>ph</sub> distance (in complexes **1** and **2**) was found to be slightly lower than the value reported (1.866 Å).<sup>17b</sup> In complex **1**, Cu-O<sub>ph</sub> distance was found to be 1.848 Å (Fig. 2.1) but in complex **2** Cu-O<sub>ph</sub> bond distances were found to be 1.897 Å and 1.848 Å. (Fig. 2.2) With a difference of 0.049 Å between two Cu-O<sub>ph</sub> distances in complex **2**. Cu-O1 bond distance was found to be 1.897 Å and slightly tilted than the other one. These results clearly indicated the generation of phenoxyl radical.

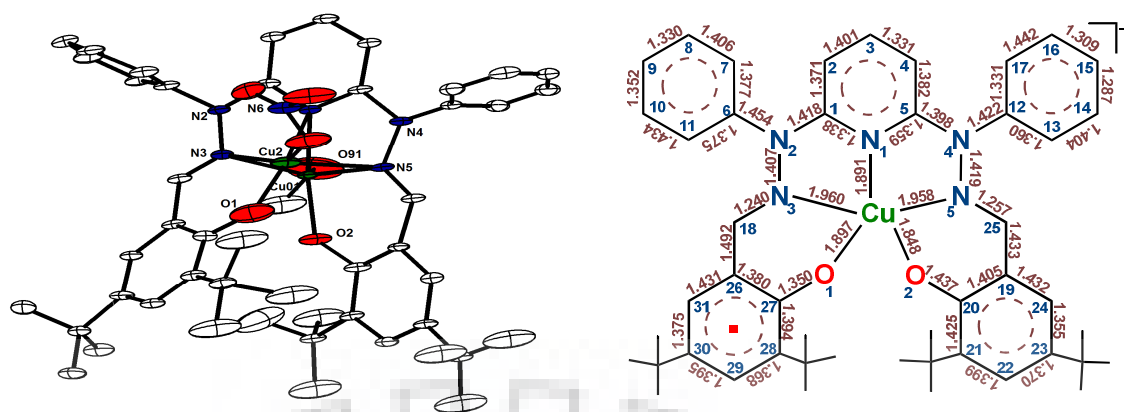


**Fig.2.2** The ORTEP diagram (30% probability level) of complex  $[\text{Cu}(\text{L}^2(\text{CH}_3\text{OH}))\text{NO}_3] \cdot 2\text{CH}_3\text{OH}$  (**2**). All hydrogen atoms and solvent molecules are omitted for clarity

Comparison of bond distances for both the complexes with respect to phenoxyl radical complex and without phenoxyl radical was done. It was found out that in complex **1** there were no tertiary butyl group attached to the phenolato ring that's why one phenol was coordinated to the copper centre and another was found to be free (uncoordinated). In the complex **2** there were two tertiary butyl group attached to the phenolate ring that help to stabilise the radical in the ring system. In complex **2** the ring without radical, the bond distances were compatible with the complex **1** where as the ring containing phenoxyl radical the bond distances alternatively increase and decrease due to the delocalization of a radical in the ring system.

**Table 2.1** Data for yield, elemental analysis, IR and UV-visible characterization

Complex	Yield %	Elemental analysis			IR data ( $\text{cm}^{-1}$ ) <sup>a</sup>			UV-visible data (nm) <sup>b</sup> ( $\epsilon/\text{M}^{-1}\text{cm}^{-1}$ )
		C	H	N	$\nu_{\text{C=N}}$	$\nu_{\text{NO}_3}$	$\nu_{\text{ClO}_4}$	
<b>L<sup>1</sup>H<sub>2</sub></b>	84	74.25	6.25	14.01	1588	.....	.....	239(20,900), 293(17,560), 349(25,900)
<b>L<sup>2</sup>H<sub>2</sub></b>	92	77.25	7.25	9.61	1589	.....	.....	243(22,680), 268(23,660), 358(36,020)
<b>Complex 1</b>	86	56.40	3.45	10.60	1590	.....	1090, 625	423(8,010), 361(23,360), 293(22,365)
<b>Complex 2</b>	85	63.70	7.20	8.79	1612	1384	.....	320(23,260), 730(470)

<sup>a</sup>KBr pellets, <sup>b</sup>Solvent: dichloromethane



The NIR-UV-visible spectra of both the complexes were recorded in dichloromethane (DCM) solution. as shown in Fig. 2.3.

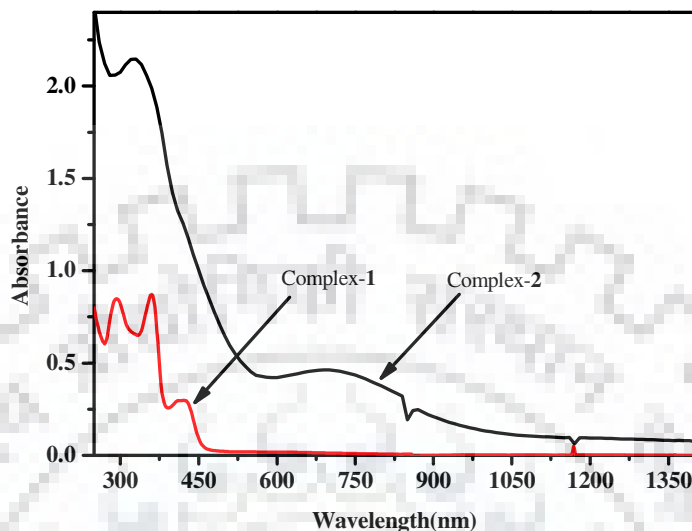


**Fig. 2.3** UV-Visible spectra of complexes  $[\text{Cu}(\text{L}^1\text{H})\text{ClO}_4](\mathbf{1})$  and  $[\text{Cu}(\text{L}^2)]\text{NO}_3 \cdot 2(\text{CH}_3\text{OH})_3$  ( $\mathbf{2}$ ) in NIR region

In complex  $\mathbf{2}$ , a broad band of low energy was observed around at 730nm for stable phenoxyl radical. In the native enzyme a similar band was found near 800nm<sup>285</sup>. On the other hand during mimicking of active site of GOase enzyme the model complexes afforded bands in the range of 700nm to 1000nm.<sup>183,280-281</sup>

IR spectra clearly showed perchlorate peaks at  $625\text{ cm}^{-1}$  and  $1090\text{ cm}^{-1}$  for complex  $\mathbf{1}$ . These data clearly indicated that charges for the metal ion was not satisfied although the ligand could provide two negatively charged phenolato donors. Hence one could speculate that only one of the phenolato donors was bound to copper. (Fig. 2.16). We have observed the presence of nitrate as counter anion ( $1384\text{ cm}^{-1}$ ) by analysing the IR spectra of complex  $\mathbf{2}$ . However the presence of nitrate ion also indicated the generation of phenoxyl radical complex (Fig. 2.19). These observation was authenticated by X-ray crystal structure and UV-visible spectra (*vide supra*).

### 2.2.2 Electrochemical investigation

The electrochemical investigation of complexes **1** and **2** in dichloromethane clearly indicated an irreversible response at  $-0.30\text{V}$  vs Ag/AgCl in cathodic region which was attributed to Cu(II)/Cu(I) couple.

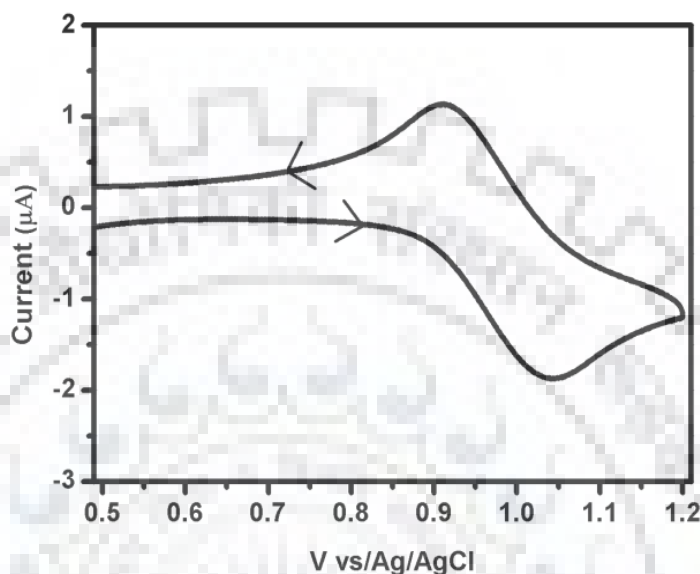


**Fig. 2.4** Cyclic voltammograms of a  $10^{-3}$  M solution of complex  $[\text{Cu}(\text{L}^1\text{H})\text{ClO}_4]$  (**1**) in dichloromethane in presence of 0.1 M tetrabutylammonium perchlorate (TBAP), using working electrode: glassy-carbon, reference electrode: Ag/AgCl; auxiliary electrode: platinum wire, scan rate  $0.1 \text{ V s}^{-1}$

An anodic peak near  $+0.67\text{V}$  was observed in complex **1** and  $+0.44\text{V}$  in complex **2** due to the oxidation of Cu(II)/Cu(III) metal center oxidation as shown in Fig. 2.21 and 2.22. Moreover, a quasireversible response was present near  $E_{1/2}$  value of  $+0.97\text{V}$  in case of complex **2** resulted due to the oxidation of coordinated phenol (or due to the formation of metal bounded phenoxyl radical cation). (Fig. 2.4) These data indicated that the stabilization of resultant phenoxyl radical cation in complex **2** due to the presence of substituted tert-butyl group in the ring containing phenolato function. The full spectrum of complex **2** was shown in Fig. 2.22. The electrochemical investigation data of both the complexes were depicted in Table 2.2.

**Table 2.2** Cyclic voltammetric data for complexes  $[\text{Cu}(\text{L}^1\text{H})\text{ClO}_4]$  (**1**) and  $[\text{Cu}(\text{L}^2(\text{CH}_3\text{OH}))\text{NO}_3].2\text{CH}_3\text{OH}$  (**2**) at 298 K. Conditions: solvent dichloromethane; supporting electrolyte TBAP(0.1 m); working electrode glassy carbon; reference electrode Ag/AgCl; scan rate  $0.1 \text{ Vs}^{-1}$ ; concentration  $10^{-3} \text{ m}$

Complexes	Cu(II)/Cu(I) $E_{pc}$	Cu(II)/Cu(III) $E_{pa}$	Phenoxyl radical $[\text{1}^{*\cdot}] (E_{1/2})$
<b>1</b>	-0.3137 V	+0.6726	-
<b>2</b>	-0.3093V	+0.4498	+0.9784

### 2.2.3 DPPH (2,2-diphenyl-1-picrylhydrazine) assay

The detection of phenoxyl radical has been done using DPPH (2,2-diphenyl-1-picrylhydrazine) assay.<sup>286</sup> DPPH radical has been used as free radical scavenger<sup>286(b)</sup> and it participates in homolytic additions with other radical species. The reactions of DPPH with different reactive oxygen species have been widely studied where violet colour of DPPH turns to light yellow colour and the antioxidant properties were quantified. We were interested to observe the disappearance of intense violet colour in presence of phenoxyl radical complex **2**. A methanolic solution of complex **2** ( $100 \mu \text{ M}$ ) was added in DPPH radical ( $3 \times 10^5 \text{ M}$ ) and we observed a decrease in absorbance of DPPH near 520 nm (shown in Fig. 2.23).

### 2.2.4 Oxidative analysis

The oxidation of benzyl alcohol to benzaldehyde using complex **2** has been reported in the Fig. 2.24. Catechol oxidation (catecholase activity) was done using both the complexes by monitoring UV-visible Spectra. For complex **1** the spectral changes were insignificant whereas the spectral changes clearly showed the oxidation of catechol (Fig. 2.25 and Fig. 2.27). We tried to investigate the oxidation of o-amino phenol to mimic the biological

activity of phenoxazinone synthase enzyme (Fig. 2.26 and Fig. 2.28). We would like to mention here that  $-NH_2$  and  $-OH$  functional groups are isoelectronic. The EPR spectra of both the complexes were recorded in solid state, in complex **2** a significant peak at  $g = 2.04$  indicated the formation of phenoxyl radical species as shown in Fig. 2.29. We have recently reported self-activated DNA cleavage and role of tert-butyl group in the ligand frame.<sup>283c</sup> Investigation of nuclease activity revealed that complex **2** exhibited self-activated DNA cleavage as shown in Fig. 2.30.

### **2.2.5 Theoretical investigation**

With respect to electronic structure of complexes **1** and **2** with redox active ligand, density functional theory (DFT) calculation offers valuable information, first, correct assignment of oxidation state of metal ion, second, the redox level of the coordinated ligands and third, the spectroscopic signature of complexes. DFT calculation with B3LYP level was done and geometry optimization of the complexes was done using coordinates obtained from X-ray crystal structure. Time dependent DFT (TD-DFT) calculations were also employed on the optimized geometries to evaluate the electronic transitions.

The frontier molecular orbital diagram for both the complexes from a spin unrestricted B3LYP calculation was depicted in Fig. 2.5 and 2.6. The HOMO and LUMO of complex **1** in alpha state were found to be mainly ligand centered (>97%) while in beta state HOMO was ligand centered (>98%) and LUMO was found to be metal centered (>54%) (HOMO corresponds to SOMO of complex **1**). In alpha and beta states of complex **2** HOMO and LUMO were found to be ligand centered (>96%). From the analysis it was found out that complex **2** involve the ligand centered orbital more than the complex **1**. Therefore it was expected to be a cation radical species. Density functional calculations on complexes **1** and **2** confirmed the asymmetry of the complexes.

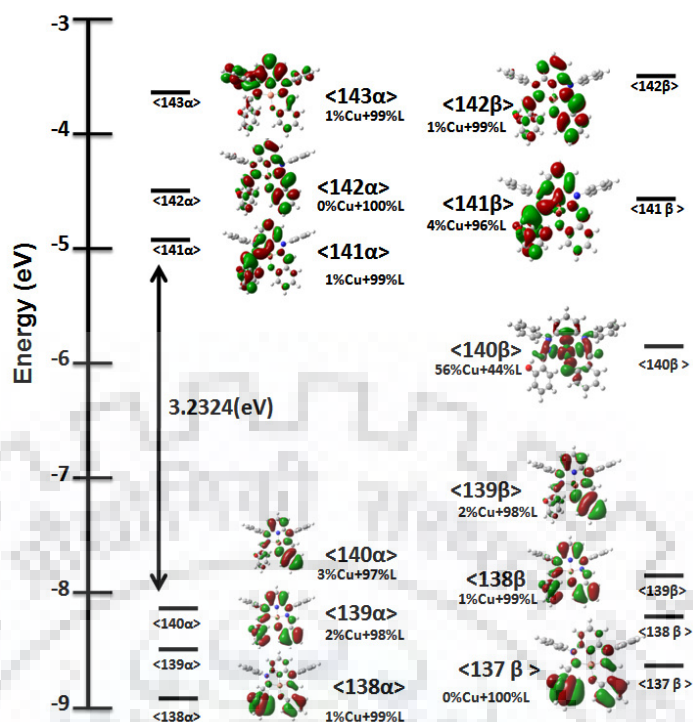


Fig. 2.5 Single occupied frontier molecular orbitals of complex [Cu(L<sup>1</sup>H)ClO<sub>4</sub>] (1), showing significant contribution of copper and ligand L<sup>1</sup>H<sub>2</sub> in SOMO

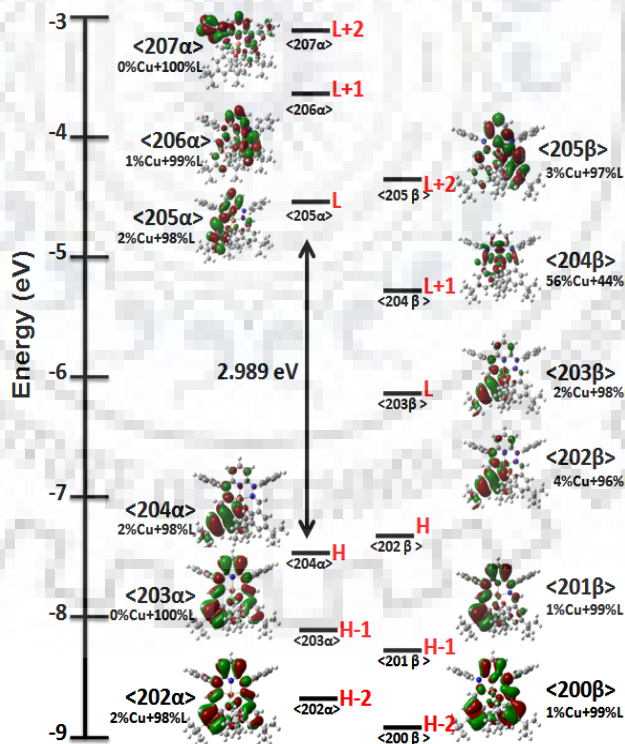
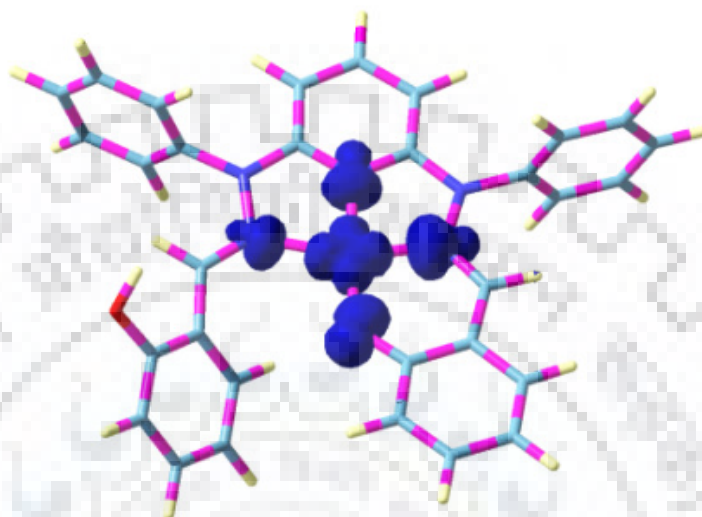
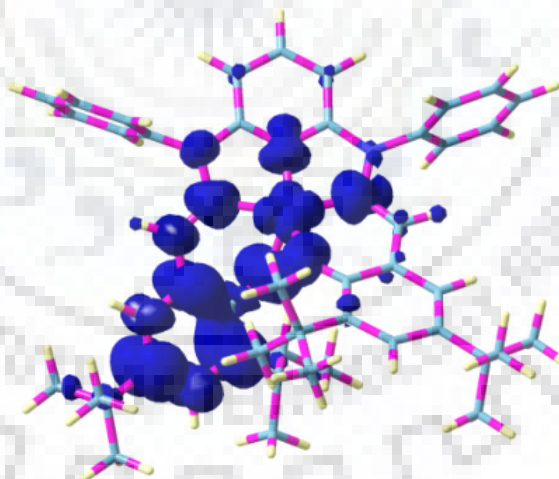


Fig. 2.6 Single occupied frontier molecular orbitals of complex [Cu(L<sup>2</sup>(CH<sub>3</sub>OH))NO<sub>3</sub>].2CH<sub>3</sub>OH (2), showing significant contribution of copper and ligand L<sup>2</sup>H<sub>2</sub> in SOMO

The Mulliken spin densities in complex **1** on Cu(0.55), N3(0.10), N5(0.13) and O2(0.13) and in complex **2** spin densities on Cu(0.58) N3(0.15) N5(0.12) O1(0.35) O2(0.12). ) (Shown in Fig. 2.7, 2.8 and Table 2.5, 2.8) It can be concluded that the ring containing phenoxyl radical having more Mulliken density over the phenoxyl ring system.



**Fig. 2.7** Mulliken spin density plot of complex  $[\text{Cu}(\text{L}^1\text{H})\text{ClO}_4]$  (**1**), using B3LYP level (iso value 0.02)



**Fig. 2.8** Mulliken spin density plot of complex  $[\text{Cu}(\text{L}^2(\text{CH}_3\text{OH}))\text{NO}_3] \cdot 2\text{CH}_3\text{OH}$  (**2**), using B3LYP level (iso value 0.02)

### 2.3 Conclusion

In conclusion pentadentate ligands were designed, synthesized and characterized using different spectroscopic techniques. The ligand without substituent in the phenyl ring

containing phenolato function gave rise to a square pyramidal copper complex and one phenolato function was found to be free (not coordinated) to copper centre but the distances and bond angle data from X-ray crystal structure clearly authenticated that complex **2** was a phenoxyl radical complex and UV-visible data gave rise to new peaks near 730 nm. Investigation of redox properties afforded an oxidation couple near 1 volt which was designated as ligand oxidation. Theoretical calculation validated total electron density in both the complexes were found in the ligand system, maximum metal contribution was three percent only. Complex **2** was found to be very much unstable and did not provide NMR spectra. Due to the instability, it was difficult to measure the variable temperature magnetic moment. However both the complexes responded to alcohol oxidation, catecholase, o-amino phenol oxidase activity and nuclease activity study.

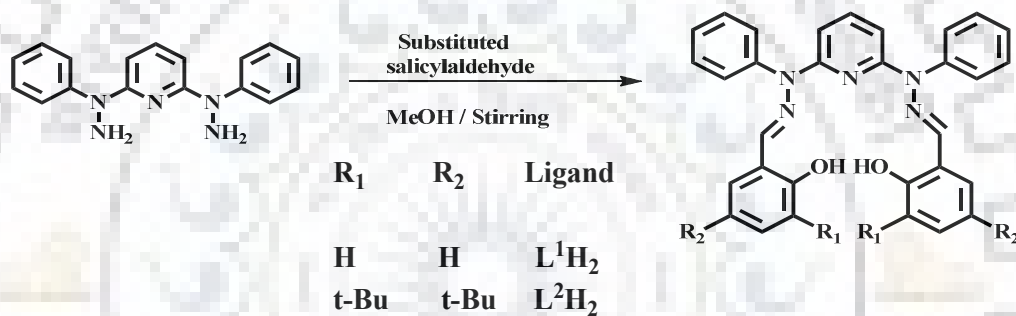
#### **2.4 Experimental Section**

All the chemicals were purchased from Sigma Aldrich, S.D. Fine and Fluka chemika. phenylhydrazine, (S.D. Fine, Mumbai, India), 2,6-diChloropyridine (Sigma Aldrich, China), salicylaldehyde (Fluka chemika Switzerland) was used as obtained. 3, 5-ditertiary butyl 2-hydroxy benzaldehyde was purchased from sigma aldrich. Solvent used for spectroscopic studies were HPLC grade and purified by standard procedure before use. Elemental analyses (carbon, hydrogen, and nitrogen) were performed using a Perkin-Elmer 240C analyzer. IR spectra ( $4000\text{--}400\text{ cm}^{-1}$ ) were performed at  $25^\circ\text{C}$  on a Thermo Nicolet Nexus FT-IR spectrometer using KBr as a medium. Electronic spectra ( $2000\text{--}200\text{ nm}$ ) were performed at  $25^\circ\text{C}$  using a Thermo Scientific UV-visible spectrophotometer, where HPLC grade acetonitrile was used as a medium as well as a reference. Cyclic voltammograms were performed in  $\text{CH}_2\text{Cl}_2$  solutions containing 0.1 M TBAP at  $25^\circ\text{C}$  using a three-electrode configuration (Glassy carbon working electrode, Pt counter electrode, Ag/AgCl reference) and a CH-600 electroanalyser. (ESI-MS) experiments were performed on a Brüker

microTOFTM-Q-II mass spectrometer. EPR of complex **1** and complex **2** were performed on 9.5 GHz JEOL spectrometer operated at X-band frequency.

### 2.4.1 Synthesis of the ligands

2,6-bis(1-phenylhydrazinyl)pyridine was prepared according to the method reported in the literature.<sup>22</sup> Both the ligands have been synthesized using different substituted aldehyde. Substituted aldehydes were used in 1:2 ratio with 2,6-bis(1-phenylhydrazinyl)pyridine in methanolic solution. As shown in Scheme 2.3. The reaction was stirred at room temperature for 1 hours and we obtained yellow precipitate while stirring, filter the reaction and washed with methanol.



**Scheme 2.3** Synthesis of ligands using different substituted aldehydes

Ligands L<sup>1</sup>H<sub>2</sub> and L<sup>2</sup>H<sub>2</sub> have been synthesized using different substituted aldehyde. Substituted salicylaldehyde was used in 1:2 ratio with 2,6-bis(1-phenylhydrazinyl)pyridine in methanolic solution. The reaction was stirred at room temperature for 1 hour, we got yellow precipitate during stirring, filter the reaction and washed with methanol.

#### 2.4.1.1 Synthesis of 2,2'-((1E,1'E)-(2,2'-(pyridine-2,6-diyl)bis(2-phenylhydrazin-2-yl-1-ylidene))bis(methanylylidene))diphenol [L<sup>1</sup>H<sub>2</sub>]

Salicylaldehyde (244.0 mg, 2.00 mmol) and 2,6-bis(1-phenylhydrazinyl)pyridine (291.0 mg, 1.00 mmol) were dissolved in 10 mL methanol. The reaction mixture was stirred at room temperature. A yellow precipitate began to separate out within 20 min and stirring was



continued for another one hours. Yellow precipitate was filtered, washed thoroughly with methanol, and then dried in vacuo. Yield 84%. Anal. Calcd for  $C_{31}H_{25}N_5O_2$  (499.56): C, 74.53; H, 6.04; N, 14.02. Found: C, 74.25; H, 6.25; N, 14.01. IR data (KBr,  $\nu_{\max}/\text{cm}^{-1}$ ): 3050,  $\nu_{\text{OH}}$ , 1588,  $\nu_{\text{C=Nimine}}$  and 1265,  $\nu_{\text{C-Ophenol}}$ . (Fig. 2.9) UV-visible [ $\text{CH}_2\text{Cl}_2$ ;  $\lambda_{\max}/\text{nm}$  ( $\epsilon/\text{M}^{-1}\text{cm}^{-1}$ )]: 349 (25,900), 293 (17,560), 239 (20,900), (Fig 2.10);  $^1\text{H}$  NMR ( $\text{CDCl}_3$ ,  $\delta/\text{ppm}$ ): 11.25 (s, 2H) 7.61-7.55 (t, 1H) 7.41- 7.36 (m, 8H) 7.21-7.17 (d, 2H) 7.08-7.07 (d,4H) 6.96-6.92 (t, 4H) 6.80-6.79 (t,2H) 6.68-6.66 (d,2H). ESI-MS data [ $\text{CH}_2\text{Cl}_2$ ] [ $\text{L}^1\text{H}_2+\text{Na}$ ] $^+$ = 522.1946.

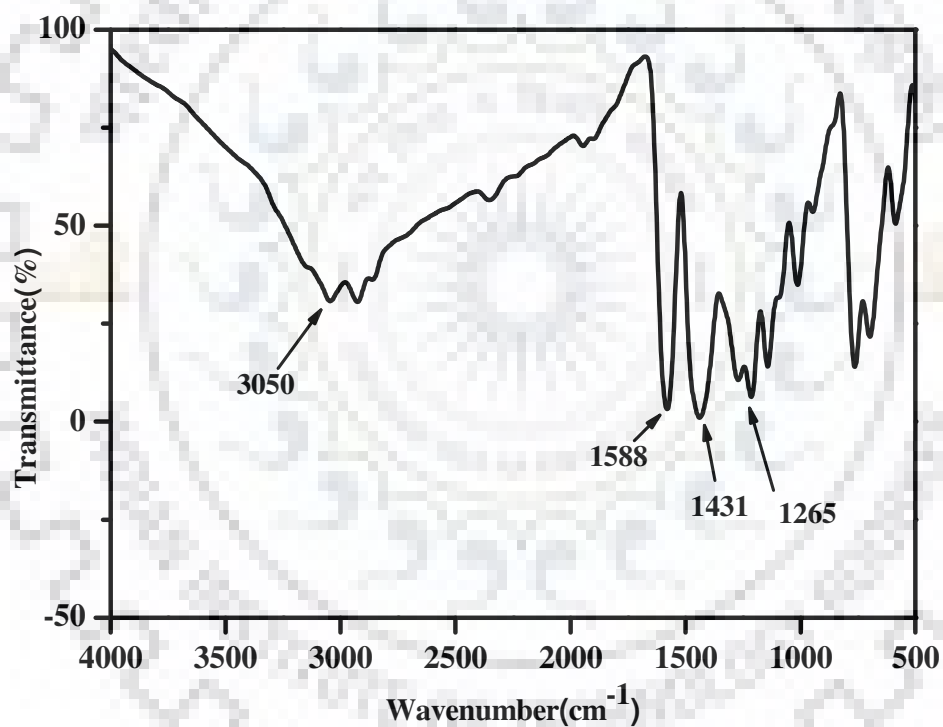


Fig. 2.9 IR spectrum of 2,2'-((1E,1'E)-(2,2'-(pyridine-2,6-diyl)bis(2-phenylhydrazin-2-yl-1-ylidene))bis(methanylylidene))diphenol. [ $\text{L}^1\text{H}_2$ ]

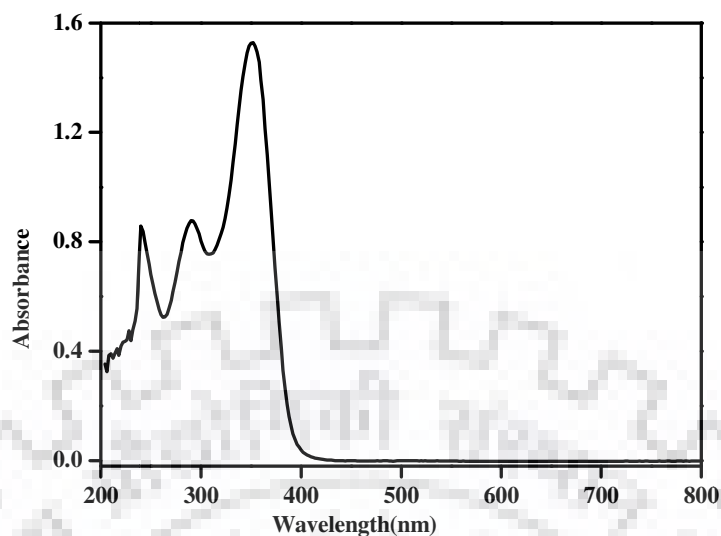


Fig. 2.10 UV-visible spectrum of 2,2'-((1E,1'E)-(2,2'-(pyridine-2,6-diyl)bis(2-phenylhydrazin-2-yl-1-ylidene))bis(methanylylidene))diphenol. [ $L^1H_2$ ]

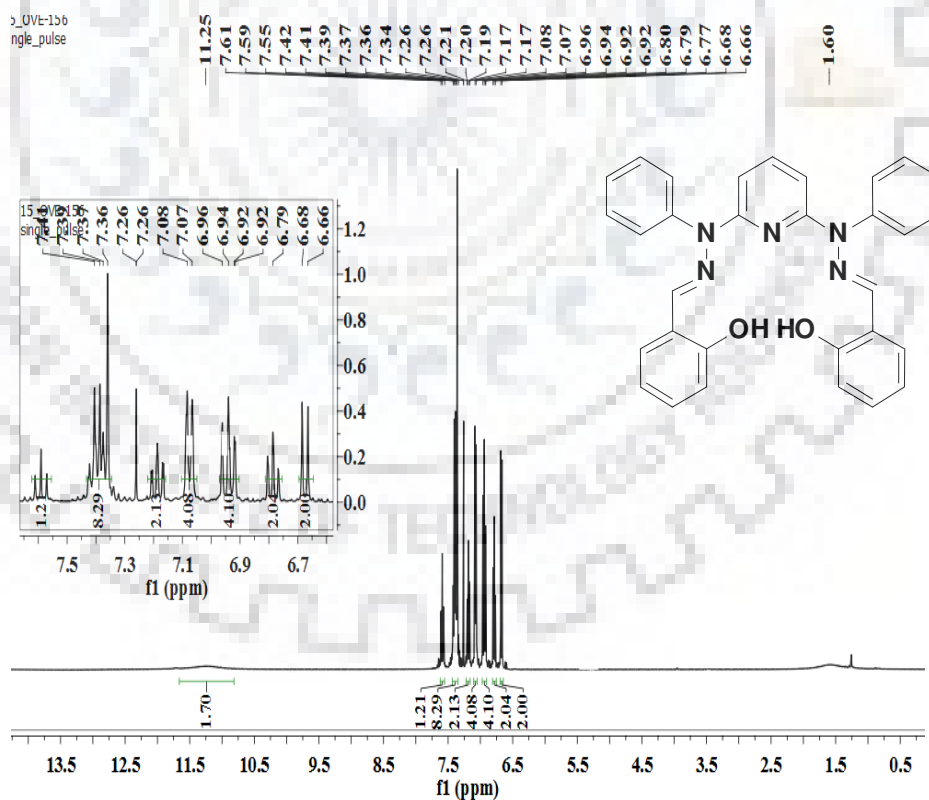
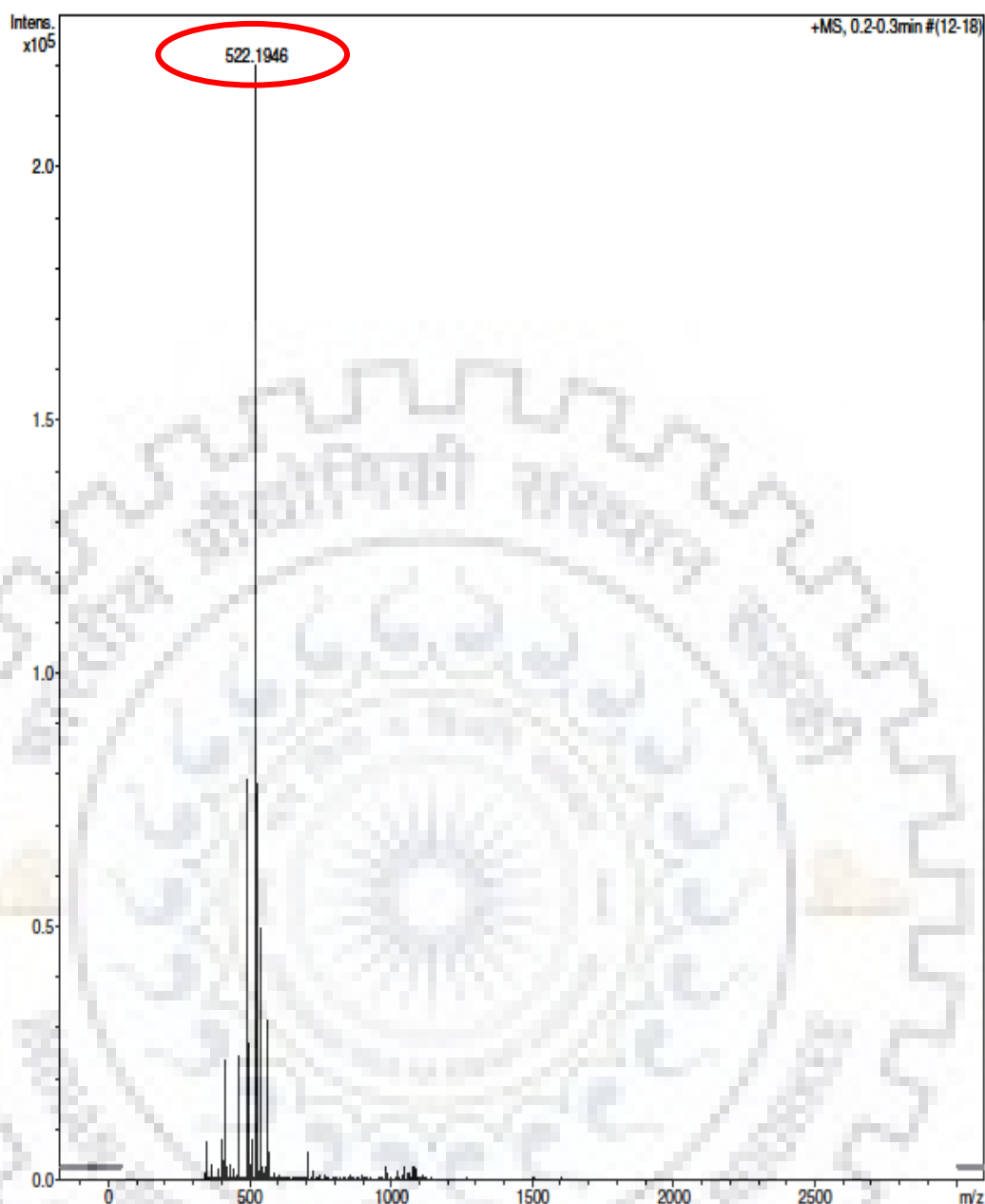


Fig. 2.11  $^1H$  NMR spectrum of 2,2'-((1E,1'E)-(2,2'-(pyridine-2,6-diyl)bis(2-phenylhydrazin-2-yl-1-ylidene))bis(methanylylidene))diphenol. [ $L^1H_2$ ]



**Fig. 2.12** HRMS of 2,2'-((1E,1'E)-(2,2'-(pyridine-2,6-diyl)bis(2-phenylhydrazin-2-yl-1-ylidene))bis(methanylylidene))diphenol.  $[L^1H_2+Na]^+$

#### 2.4.1.2 Synthesis of 6,6'-((1E,1'E)-(2,2'-(pyridine-2,6-diyl)bis(2-phenylhydrazin-2-yl-1-ylidene))bis(methanylylidene))bis(2,4-di-tert-butylphenol) $[L^2H_2]$

3,5-di-tert-butyl-2-hydroxybenzaldehyde (468.32 mg, 2.00 mmol) and 2,6-bis(1-phenylhydrazinyl)pyridine (291.35 mg, 1.00 mmol) were dissolved in 10 mL methanol. The reaction mixture was stirred at room temperature. A light yellow precipitate began to

separate out within 20 min and stirring was continued for another one hours. Precipitate was filtered out and washed with methanol, and then dried in vacuo. Yield 92%. Anal. Calcd for  $C_{47}H_{57}N_5O_2$  (723.98) : C, 77.97; H, 7.94; N, 9.67. Found: C, 77.25; H, 7.25; N, 9.61. IR data (KBr,  $\nu_{max}/cm^{-1}$ ): 1589,  $\nu_{C=Nimine}$  and 1239,  $\nu_{C-O}$  phenol. (Fig. 2.13); UV-visible [ $CH_2Cl_2$ ;  $\lambda_{max}/nm$  ( $\epsilon/M^{-1}cm^{-1}$  )]: 358 (36,020), 298 (23,660), 243 (22,680),  $^1H$  NMR ( $CDCl_3$ ,  $\delta/ppm$ ) 11.52 (s, 2H) 7.70-7.68(d,1H) 7.66-7.34 (m,10H) 7.05-7.03 (d,4H) 6.78-6.73 (t,4H) 1.48(s,18H) 1.22 (s, 18H). ESI-MS data [ $CH_2Cl_2$ ] [ $L^2H_2+Na$ ] $^+$ = 746.4471.

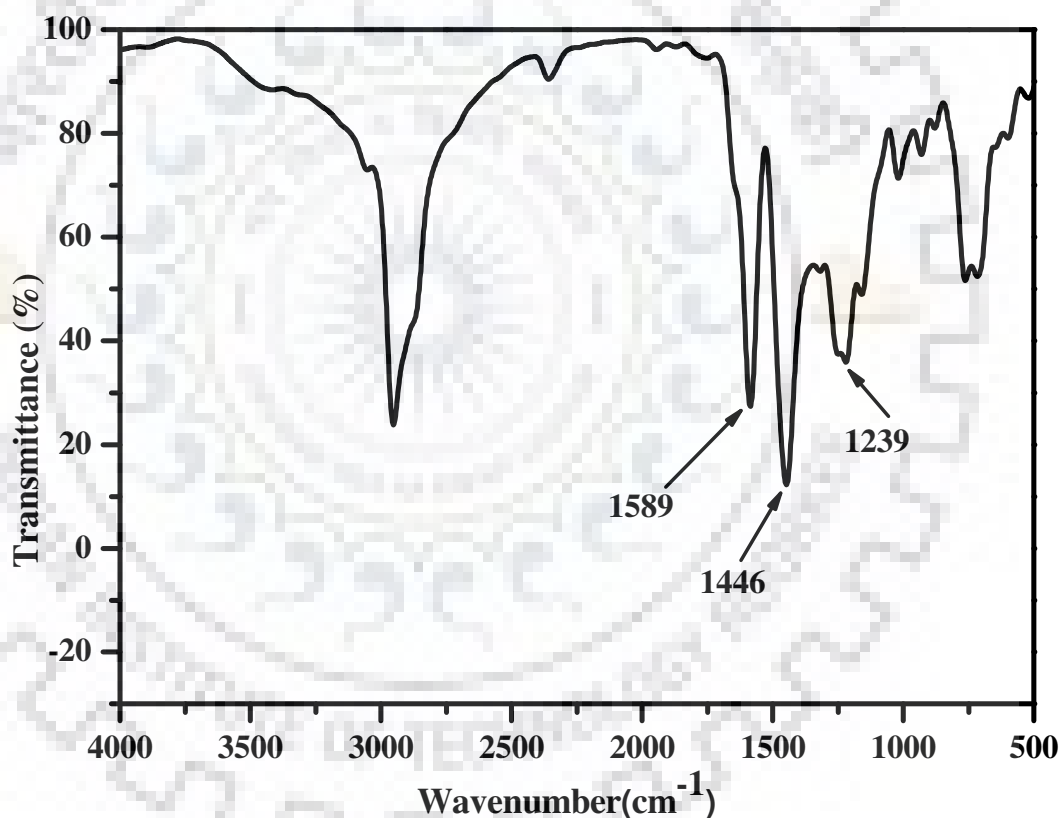


**Fig. 2.13** IR spectrum of 6,6'-((1E,1'E)-(2,2'-(pyridine-2,6-diyl)bis(2-phenylhydrazin-2-yl-1-ylidene))bis(methanylylidene))bis(2,4-di-tert-butylphenol) [ $L^2H_2$ ]

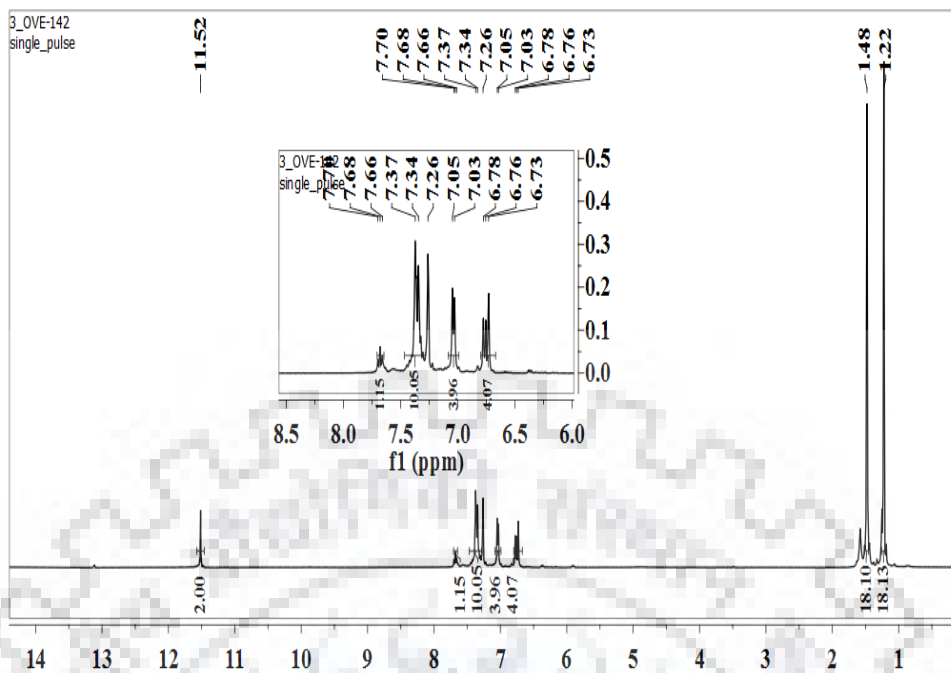


**Fig. 2.14** <sup>1</sup>H NMR spectrum of 6,6'-((1E,1'E)-(2,2'-(pyridine-2,6-diyl)bis(2-phenylhydrazin-2-yl-1-ylidene))bis(methanylylidene))bis(2,4-di-tert-butylphenol)) ([L<sup>2</sup>H<sub>2</sub>])

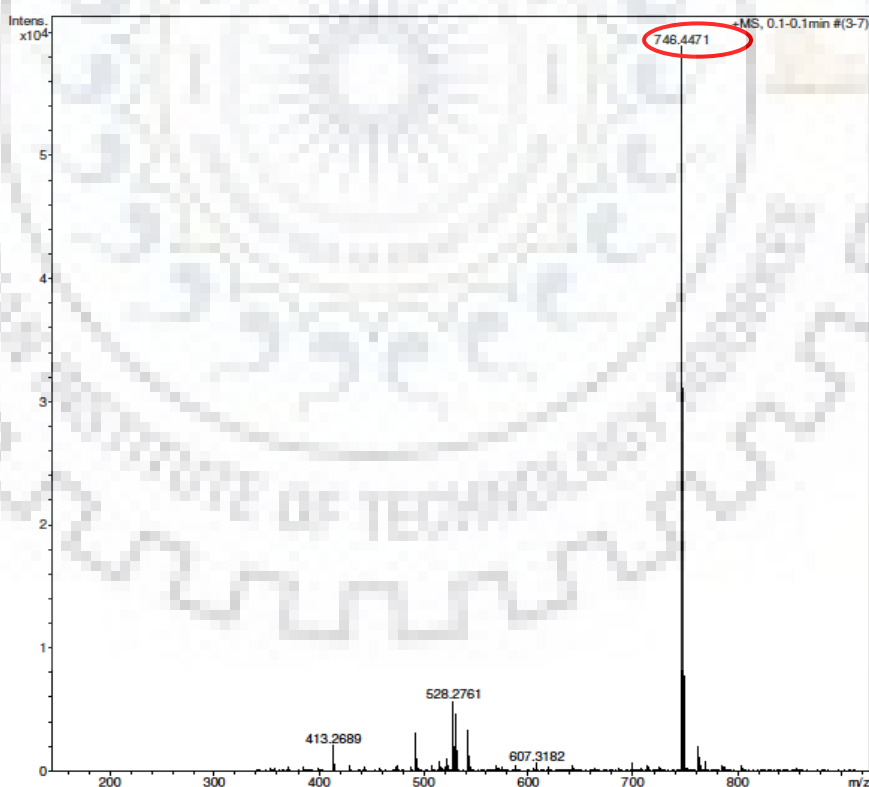


**Fig. 2.15** HRMS of 2,2'-((1E,1'E)-(2,2'-(pyridine-2,6-diyl)bis(2-phenylhydrazin-2-yl-1-ylidene))bis(methanylylidene))diphenol. [L<sup>2</sup>H<sub>2</sub>+Na]<sup>+</sup>

## 2.4.2 Synthesis of the metal complexes

### 2.4.2.1 Synthesis of $[\text{Cu}(\text{L}^1\text{H})\text{ClO}_4](1)$

Complex **1** was synthesized using (0.0998g, 0.2mmol) ligand  $\text{L}^1\text{H}_2$  in dichloromethane, and copper (II) perchlorate hexahydrate (0.0741g, 0.2mmol) in methanol.  $\text{Cu}(\text{ClO}_4)_2 \cdot 6\text{H}_2\text{O}$  was added dropwise into the ligand. After two hours green precipitate was separated out. The precipitate was washed with diethylether and dried in vacuum. Square shaped green crystals were obtained in dichloromethane and methanol mixture (1:1) by slow evaporation within two days. yield 86% Anal. Calcd for  $\text{C}_{31}\text{H}_{24}\text{ClCuN}_5\text{O}_6$  (661.55) C,56.28; H, 3.66; N, 10.59 Found: C,56.40; H, 3.45; N, 10.60. IR data (KBr,  $\nu_{\text{max}}/\text{cm}^{-1}$ ): 3380  $\nu_{\text{OH}}$ , 1590,  $\nu_{\text{C=Nimine}}$ , 1304,  $\nu_{\text{C-O(Phenol)}}$ , 1090, 625,  $\nu_{\text{ClO}_4^-}$ . (Fig. 2.16); UV-visible [DCM  $\lambda_{\text{max}}/\text{nm}$  ( $\epsilon/\text{M}^{-1}\text{cm}^{-1}$ ): 423 (8,010), 361 (23,260), 293 (22,365). (Fig. 2.17);  $m/z=561.1265$  due to  $[\text{1-ClO}_4]^+$  (Fig. 2.18).

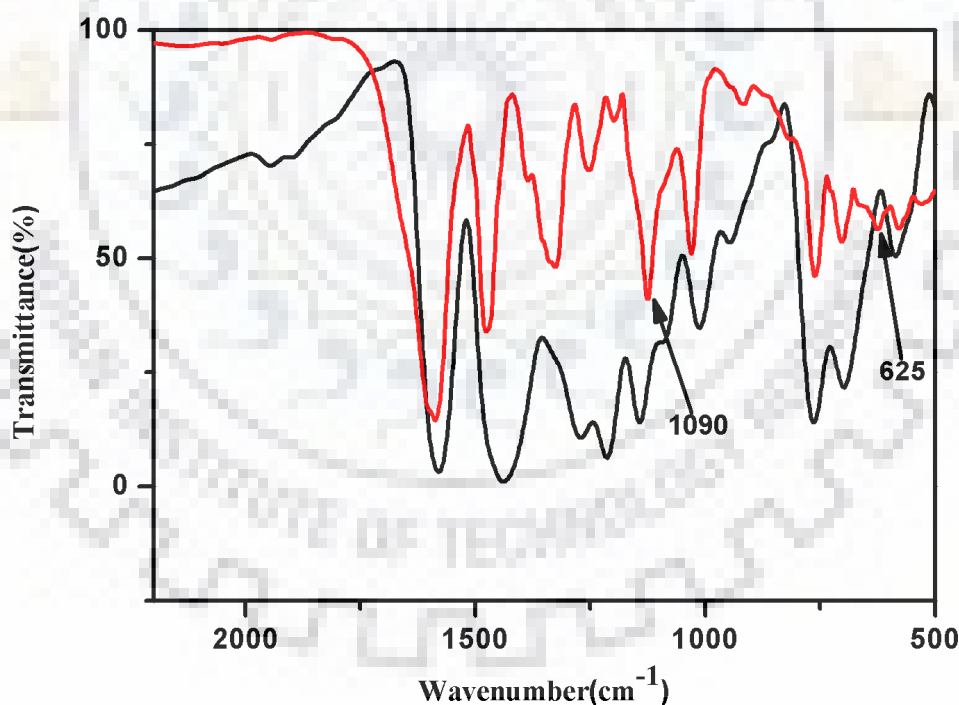


**Fig. 2.16** IR spectra of complex  $[\text{Cu}(\text{L}^1\text{H})\text{ClO}_4](1)$  (red) and corresponding ligand  $[\text{L}^1\text{H}_2]$  (Black)

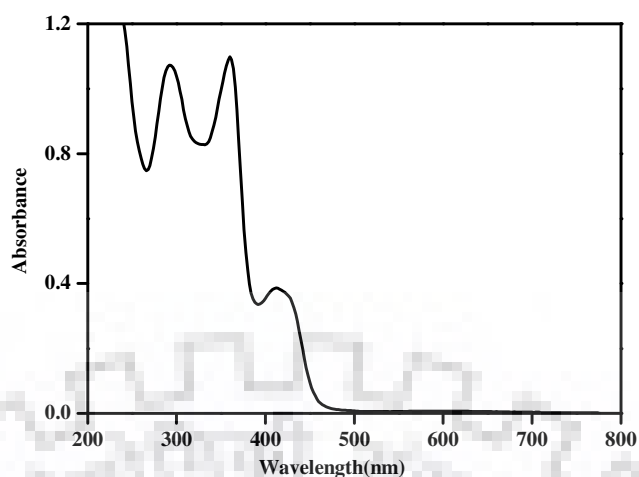


Fig. 2.17 UV-visible spectrum of of complex [Cu(L<sup>1</sup>H)ClO<sub>4</sub>](1)

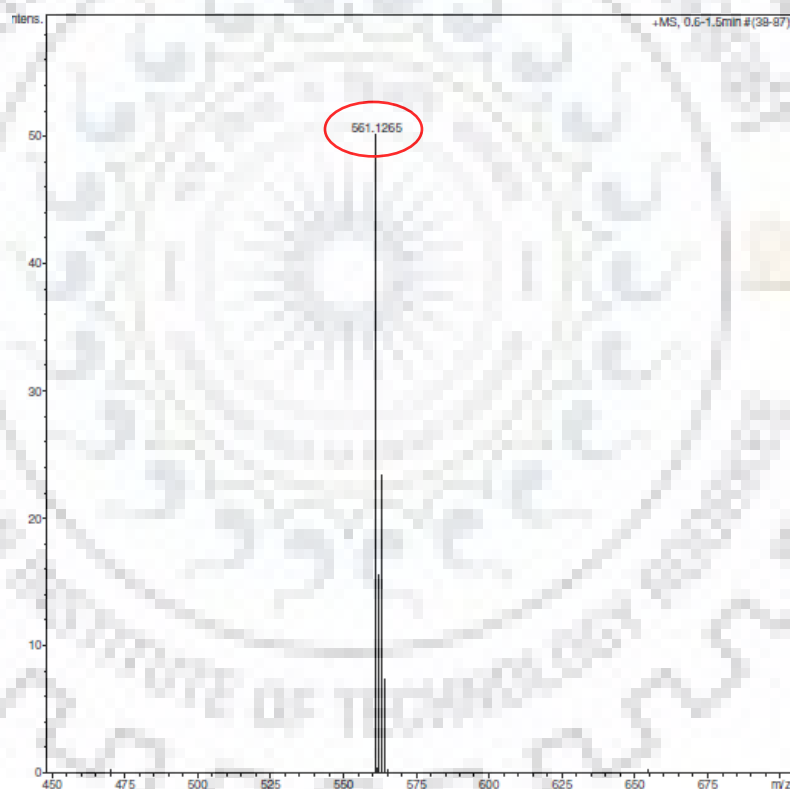


Fig. 2.18 ESI-MS of complex [1-ClO<sub>4</sub>]<sup>+</sup>

#### 2.4.2.2 Synthesis of [Cu(L<sup>2</sup>)]NO<sub>3</sub>·(CH<sub>3</sub>OH)<sub>3</sub> (2)

Complex **2** was synthesized using (0.1446g, 0.2mmol) ligand L<sup>2</sup>H<sub>2</sub> in dichloromethane, and copper (II) nitrate trihydrate (0.0482g, 0.2mmol) in methanol. Cu(NO<sub>3</sub>)<sub>2</sub>·3H<sub>2</sub>O was added

dropwise and on stirring a dark green coloured solid was obtained. The crystallization was done into DCM by layering of methanol and dark green coloured crystals were obtained. Yield 85%. Anal. Calcd for  $C_{50}H_{67}CuN_6O_8$  ( 943.65) C, 63.64; H, 7.16; N, 8.91; Found: C, 63.70; H, 7.20; N, 8.79. IR data (KBr,  $\nu_{max}/cm^{-1}$ ): 1612,  $\nu_{C=Nimine}$ , 1384,  $\nu_{NO_3}$ , (Fig. 2.19); UV-visible [ $CH_3CN \lambda_{max} /nm$  ( $\epsilon/M^{-1}cm^{-1}$ )]: 730 (470), 320 (23,260;  $m/z= 785.3825$  (Fig. 2.20).

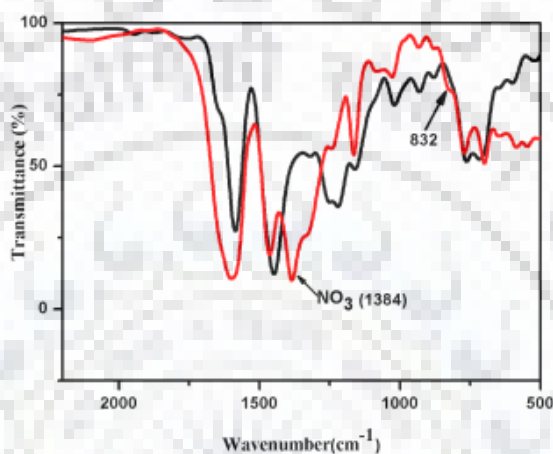


Fig. 2.19 IR spectra of complex 2.(red) and corresponding ligand  $[L^2H_2]$  (black)

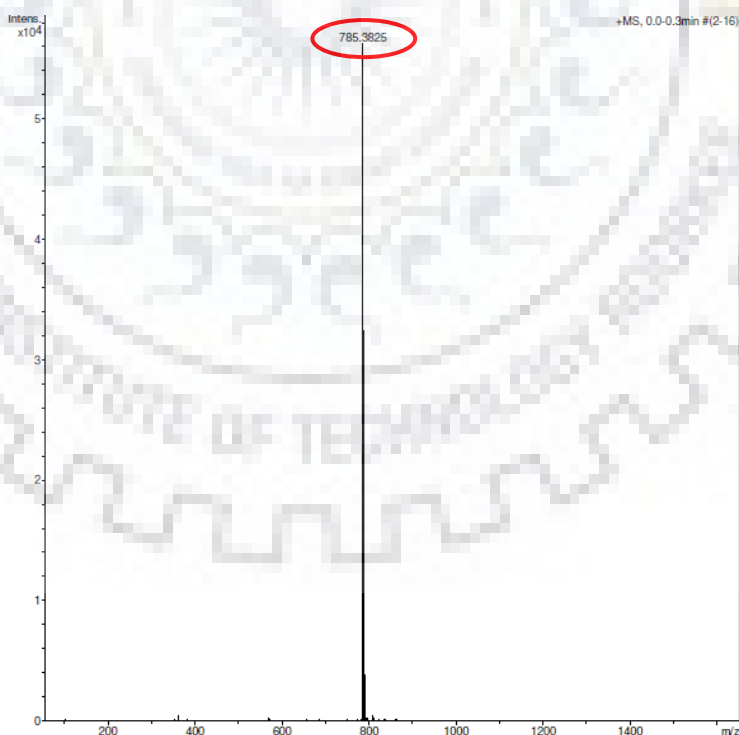
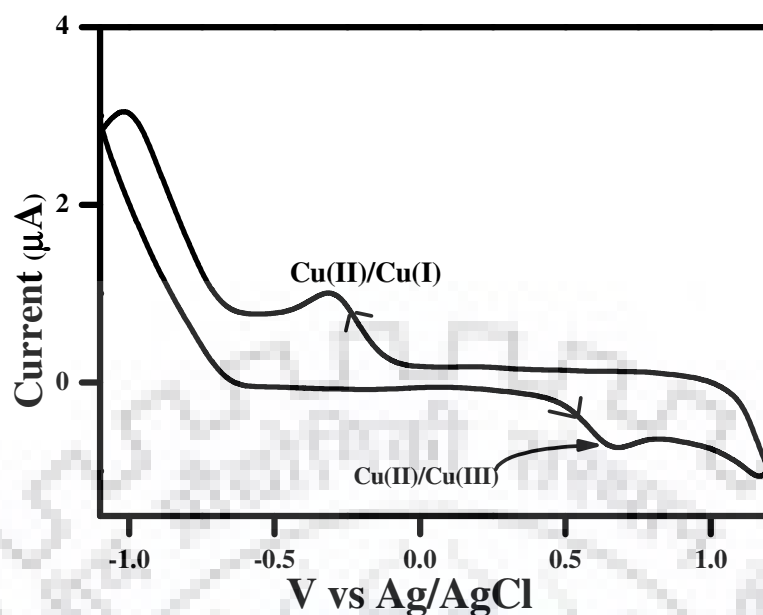
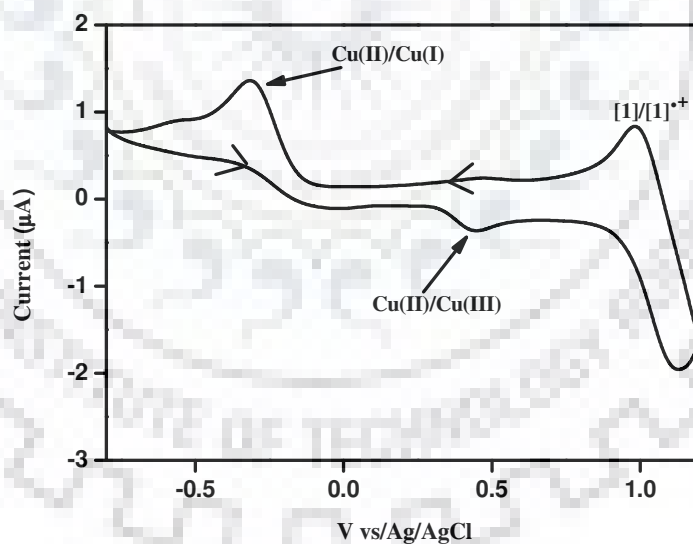


Fig. 2.20 ESI-MS of complex  $[2-NO_3]^+$





**Fig. 2.21** Cyclic voltammograms of a  $10^{-3}$  M solution of complex  $[\text{Cu}(\text{L}^1\text{H})\text{ClO}_4]$  (**1**) in dichloromethane in presence of 0.1 M tetrabutylammonium perchlorate (TBAP), using working electrode: glassy-carbon, reference electrode: Ag/AgCl; auxiliary electrode: platinum wire, scan rate  $0.1 \text{ Vs}^{-1}$



**Fig. 2.22** Cyclic voltammograms of a  $10^{-3}$  M solution of complex  $[\text{Cu}(\text{L}^2(\text{CH}_3\text{OH}))\text{NO}_3] \cdot 2\text{CH}_3\text{OH}$  (**2**) in dichloromethane in presence of 0.1 M tetrabutylammonium perchlorate (TBAP), using working electrode: glassy-carbon, reference electrode: Ag/AgCl; auxiliary electrode: platinum wire, scan rate  $0.1 \text{ Vs}^{-1}$

## 2.5 Reactivity Studies:

### 2.5.1 DPPH Assay

DPPH (2,2-diphenyl-1-picrylhydrazine) is a well-known radical and have been used to trap other radical species. In this radical a strong absorption band at about 520nm, for which violet color solution was observed. This can be detect visual monitoring of the reaction.

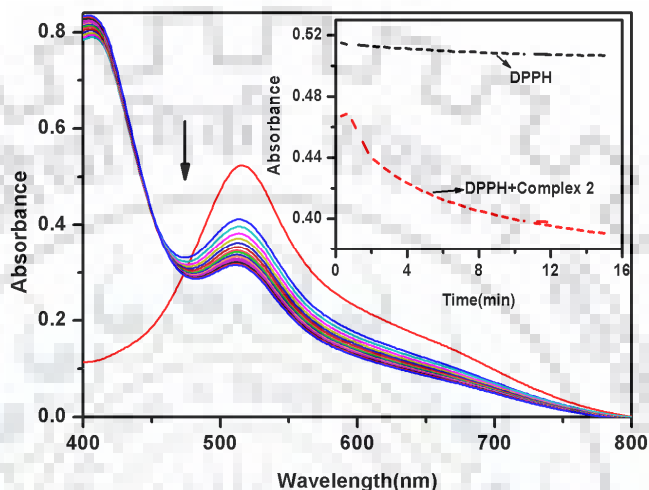


**Fig. 2.23** Reaction of phenoxyl radical from complex **2** (100 $\mu$ M) with DPPH radical ( $\sim 3 \times 10^{-5}$  M) MeOH solution

Experiment was performed in methanol solvent. The phenoxyl radical complex **2** (100 $\mu$ M) was taken with DPPH radical ( $\sim 3 \times 10^{-5}$  M) and a decrease in absorbance was observed at 520 nm (Fig. 2.23).

### 2.5.2 Oxidation of benzyl alcohol

The oxidation of benzyl alcohol to benzaldehyde in the presence of phenoxyl radical complexes was monitored using UV-visible spectroscopy. The complex **2** [0.1mM] was monitored on adding benzyl [0.57 M] alcohol, the disappearance of the 730nm peak continuously indicate the oxidation of benzyl alcohol.(Fig.2.24)

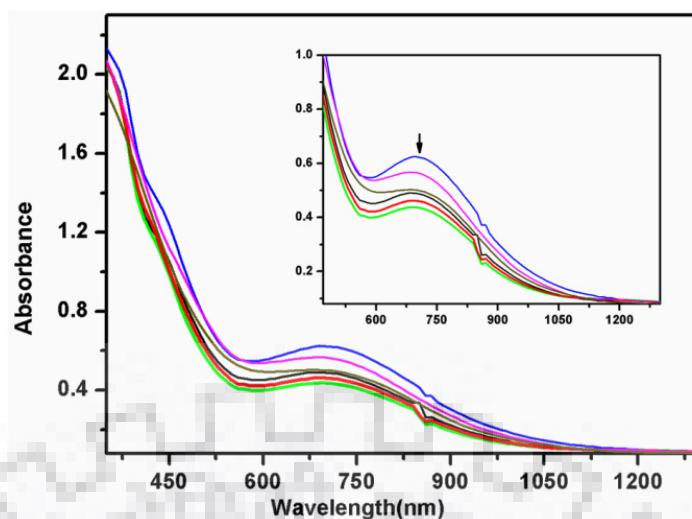


**Fig. 2.24** UV- visible spectrum Changes of  $[\text{Cu}(\text{L}^2(\text{CH}_3\text{OH}))\text{NO}_3] \cdot 2\text{CH}_3\text{OH}$  (2) during the reaction with benzyl alcohol. Solvent =  $\text{CH}_2\text{Cl}_2$ ,  $[\text{Benzyl alcohol}] = 0.57 \text{ M}$ ,  $[\text{Cu}(\text{L}^2(\text{CH}_3\text{OH}))\text{NO}_3] \cdot 2\text{CH}_3\text{OH}$  (2) =  $0.1 \text{ mM}$  Total measuring time: 90 min

The oxidation of benzyl alcohol was also monitored GC-mass spectrometer as shown in Table 2.3.

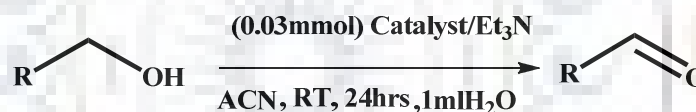


**Table 2.3** Oxidation of substituted benzyl alcohol<sup>a</sup>

Substrate (R)	Substrate (mmol)	Product	Complex- 1 % Conversion (24hrs)	Complex -1 TON	Complex- 2 % Conversion (24hrs)	Complex-2 TON
Benzyl alcohol	6.10	Benzaldehyde	40	81	84	170
p-Methoxy benzyl alcohol	6.10	p-Methoxy Benzaldehyde	36	73	76	155
p-Methyl benzyl alcohol	6.10	p-Methyl Benzaldehyde	46	94	88	178
p-Nitro benzyl alcohol	6.10	p-NitroBenzaldehyde	52	105	92	187

<sup>a</sup>All reactions carried out in acetonitrile:water mixture at room temperature. The yields were measured by GC 24 hours after the beginning of the reaction. Turn over number (TON) defined as  $[\text{TON} = \{(\% \text{ conversion}) \times (\text{mmol of substrate}) / (\text{mmol of catalyst}) \times 100\}]$ .

## 2.5.3 Catecholase and phenoxazinone synthase activity studies

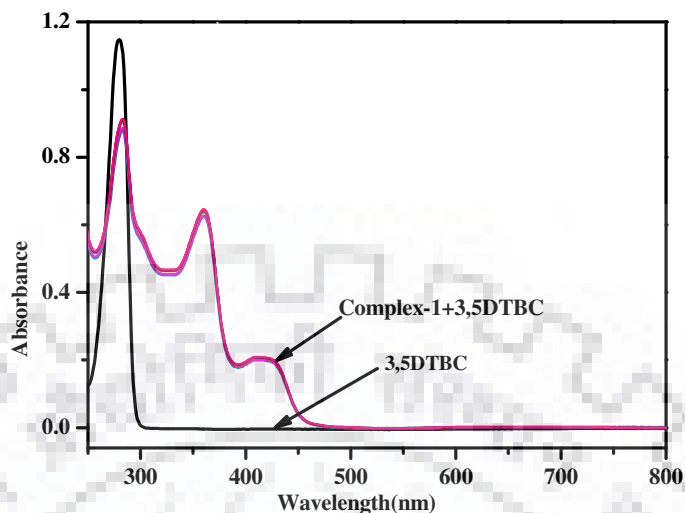


**Fig. 2.25** UV- visible spectra in range the (250-800 nm) showed no conversion was found from catechol to quinone in presence of complex **1**: Complex **1** concentration was (0.1mM) in acetonitrile; 3,5-DTBC concentration (0.01×mM) was added and spectra was recorded for 1 hours of reaction in dioxygen-saturated acetonitrile at 25 °C

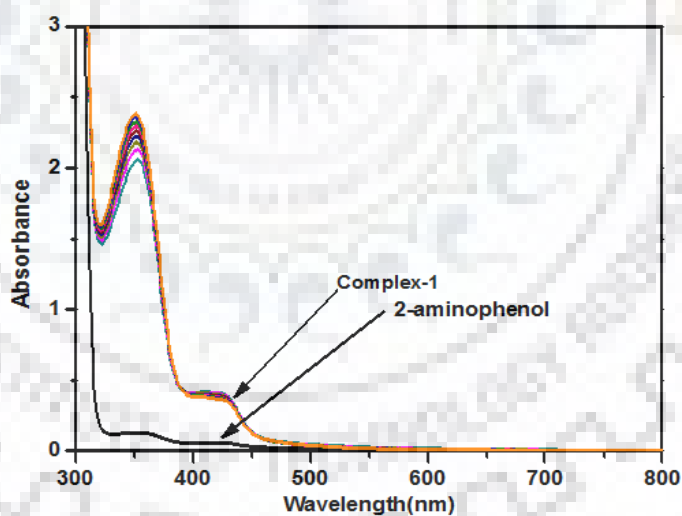


**Fig. 2.26** 2-amino phenol to 2-aminophenoxazine -3-one conversion was recorded in presence of complex [Cu(L<sup>1</sup>H)ClO<sub>4</sub>] (**1**). UV-visible spectral changes for the oxidation of *o*-aminophenol (0.01mM) catalyzed by the complex [Cu(L<sup>1</sup>H)ClO<sub>4</sub>] (**1**). (0.1mM) for up to 1 hours of reaction in dioxygen-saturated acetonitrile solvent system at 25 °C

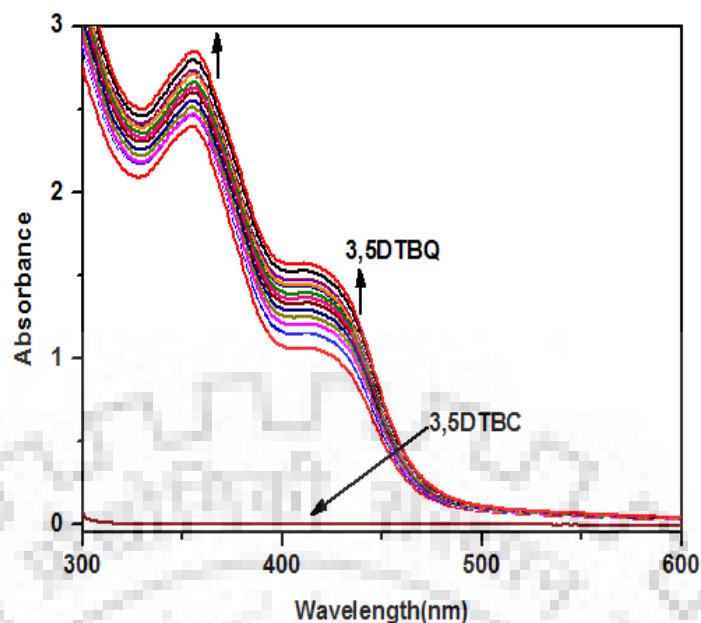


**Fig. 2.27** UV-visible spectra in range the (300-600 nm) showed the conversion of catechol to quinone in presence of  $[\text{Cu}(\text{L}^2(\text{CH}_3\text{OH}))\text{NO}_3] \cdot 2\text{CH}_3\text{OH}$  (**2**):  $[\text{Cu}(\text{L}^2(\text{CH}_3\text{OH}))\text{NO}_3] \cdot 2\text{CH}_3\text{OH}$  (**2**) concentration was (0.1mM) in acetonitrile; 3,5-DTBC concentration (0.01×mM) was added and spectra was recorded for 1 hours of reaction in dioxygen-saturated acetonitrile at 25 °C

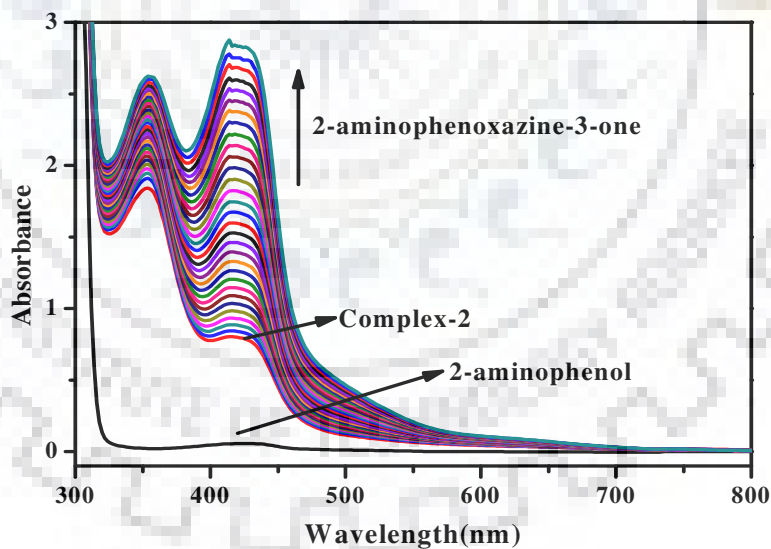


**Fig. 2.28** 2-amino phenol to 2-aminophenoxazine-3-one conversion was recorded in presence of complex  $[\text{Cu}(\text{L}^2(\text{CH}_3\text{OH}))\text{NO}_3] \cdot 2\text{CH}_3\text{OH}$  (**2**) . UV-visible spectral changes for the oxidation of *o*-aminophenol (0.01mM) catalyzed by the complex  $[\text{Cu}(\text{L}^2(\text{CH}_3\text{OH}))\text{NO}_3] \cdot 2\text{CH}_3\text{OH}$  (**2**). (0.1mM) for up to 1 hours of reaction in dioxygen-saturated acetonitrile solvent system at 25 °C

## 2.5.4 Electron paramagnetic resonance (EPR) studies

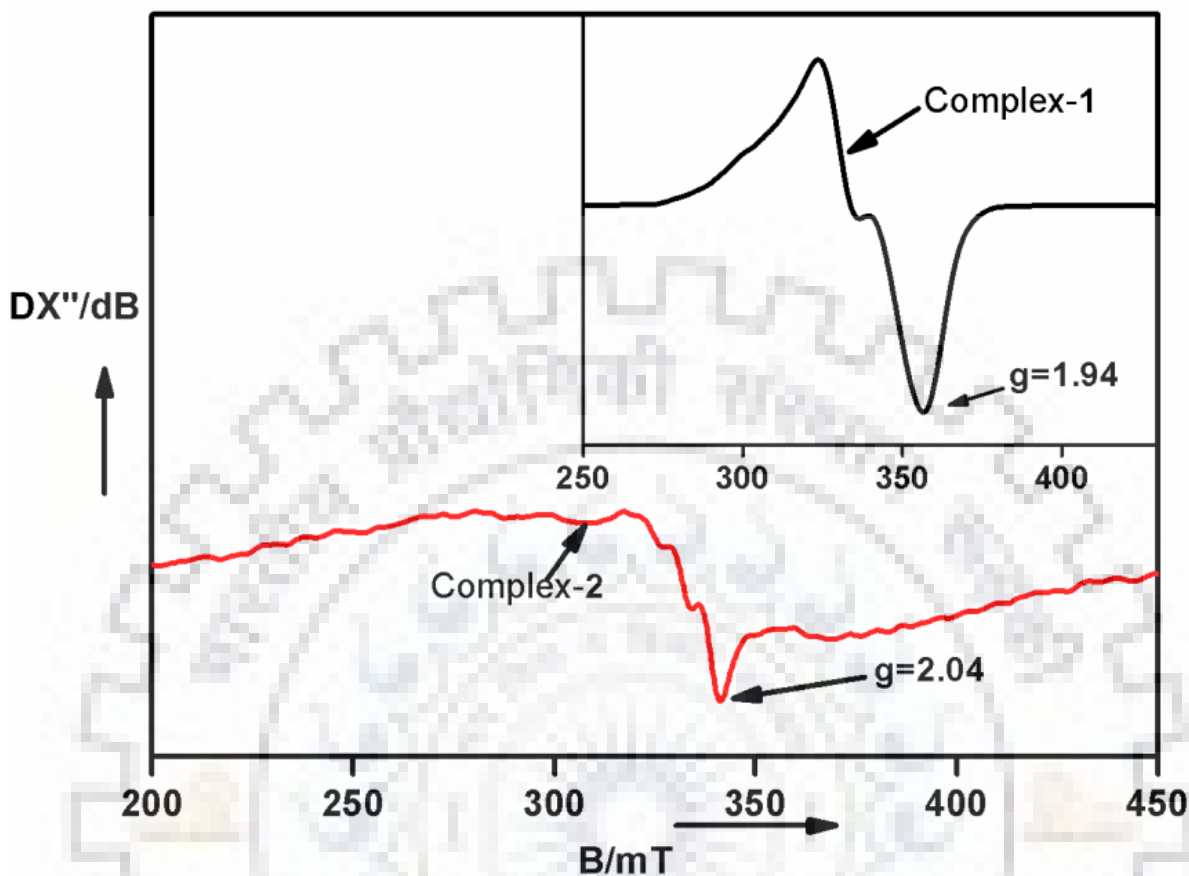


**Fig. 2.29** X-Band EPR spectra of complex  $[\text{Cu}(\text{L}^1\text{H})\text{ClO}_4]$  (1) and complex  $[\text{Cu}(\text{L}^2(\text{CH}_3\text{OH}))\text{NO}_3] \cdot 2\text{CH}_3\text{OH}$  (2), the concentration are 1mM  $\text{CH}_2\text{Cl}_2$  (+0.1 MTBAP). Microwave Frequency: 9.725 GHz, Power : 0.612mW, Mod. Frequency: 100 kHz, Mod. Amplitude: 6G,  $T = 14^\circ\text{C}$

## 2.5.5 Nuclease activity

An increase the concentration of both the complexes from  $50\mu\text{M}$  to  $150\mu\text{M}$  was afforded the disappearance of DNA in case of complex 2. The result indicated that the complex without phenoxyl radical does not showed effective cleavage of pBR322 DNA but in the presence of complex 2 we found a different type of nuclease activity where the disappearance of both bands (SC, LC and NC DNA) were observed. Investigation of nuclease activity revealed that complex 2 exhibited self- activated DNA cleavage as shown in Fig. 2.30.

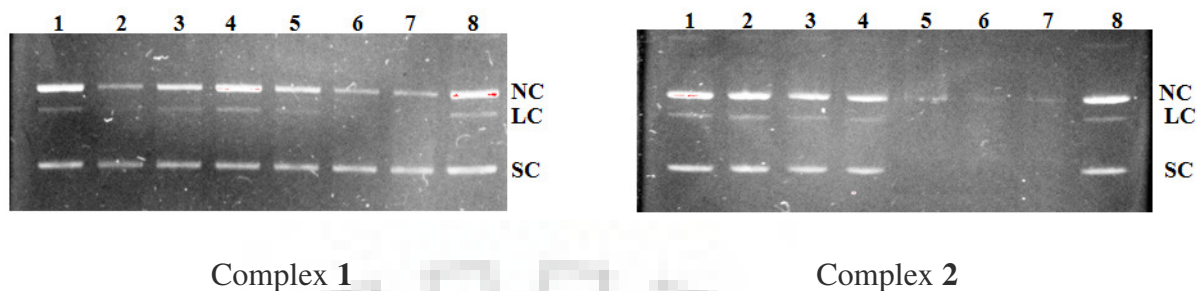


**Fig. 2.30** Gelelectrophoresis separations showing the oxidative cleavage of supercoiled pBR322 DNA (100ng) by complexes **1** and **2**, 5% DMF incubated at 37 °C for 1.5 h. (Lane 1); DNA Control, (Lane 2); [DNA + Cu(ClO<sub>4</sub>)<sub>2</sub>.6H<sub>2</sub>O (50μM) (Gel-1)], [DNA + Cu(NO<sub>3</sub>)<sub>2</sub>.3H<sub>2</sub>O (50μM) (Gel-2)], (Lane 3); DNA + L<sup>1</sup>H<sub>2</sub> and L<sup>2</sup>H<sub>2</sub> (50 μM), (Lane 4); DNA + Complexes **1** and **2** (50μM), (Lane 5); DNA + Complexes **1** and **2** (100μM), (Lane 6); DNA + Complexes **1** and **2** (150μM), (Lane 7); DNA + Complexes **1** and **2** (200μM), (Lane 8); DNA + DMF (2 μl)

### 2.5.6 DFT calculation

DFT calculations were performed for both the complexes. The structural and geometrical optimization for both complexes was done by DFT and time-dependent DFT(TDDFT) methods with the B3LYP exchange correlation function to the better insight of the electronic properties for both the complexes. As shown in Fig. 2.31 and 2.33. On the basis of the optimized geometry structures of the ligands, the absorption was calculated by the time-dependent density functional theory (TDDFT). As shown in Fig. 2.32 and 2.34. Due to the presence of electronic correlation in the TDDFT (B3LYP) method it can yield more accurate electronic excitation energies. The orbital contribution and significant transition and their contribution at a particular wavelength (theoretically and experimentally) for both the complexes was shown in Table 2.4, 2.6 for complex **1** and Table 2.7, 2.9 for complex **2**. The basis set LANL2DZ was used for the valence shell. Frontier molecular orbitals were prepared by using the GaussView 5.0 software. All the DFT calculations were performed with the help of Gaussian 09W software package.<sup>287</sup> The GaussSum 2.1<sup>288</sup> was used to calculate the molecular orbital contributions from groups or atoms.

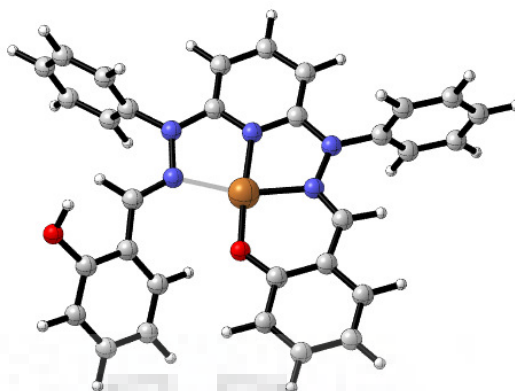


Fig. 2.31 Optimized geometry of complex  $[\text{Cu}(\text{L}^1\text{H})\text{ClO}_4]$  (1) using B3LYP/LANL2DZ

Table 2.4 Percentage contribution of complex  $[\text{Cu}(\text{L}^1\text{H})\text{ClO}_4]$  (1) in both alpha and beta orbitals

%Contribution of alpha orbitals							
Orbitals	Cu	Free phenalato	Bound phenalato	Imine bounds	Pyridine ring	Phenyl ring -1	Phenyl ring -2
LUMO+5	0	2	1	1	1	58	38
LUMO+4	0	0	0	6	2	26	65
LUMO+3	1	0	1	8	9	52	29
LUMO+2	0	3	5	17	46	22	7
LUMO+1	1	6	27	49	15	1	0
LUMO	3	22	5	48	21	1	0
HOMO	2	4	62	19	13	0	1
HOMO-1	1	19	38	21	20	1	0
HOMO-2	0	69	16	9	4	0	0
HOMO-3	2	43	25	22	5	2	1
HOMO-4	14	3	43	23	11	1	5
HOMO-5	1	32	26	15	21	2	4
%Contribution of beta orbitals							
LUMO+5	0	0	0	6	1	39	57
LUMO+4	1	1	1	8	10	78	14
LUMO+3	0	3	5	16	44	16	63
LUMO+2	1	7	27	48	16	7	24
LUMO+1	4	22	5	47	21	0	1
LUMO	56	1	13	18	10	0	1
HOMO	2	4	64	18	12	1	1
HOMO-1	1	19	36	22	20	1	0
HOMO-2	0	67	18	10	4	0	1
HOMO-3	1	47	22	22	5	0	0
HOMO-4	1	28	30	14	23	1	2
HOMO-5	0	0	2	1	1	3	2

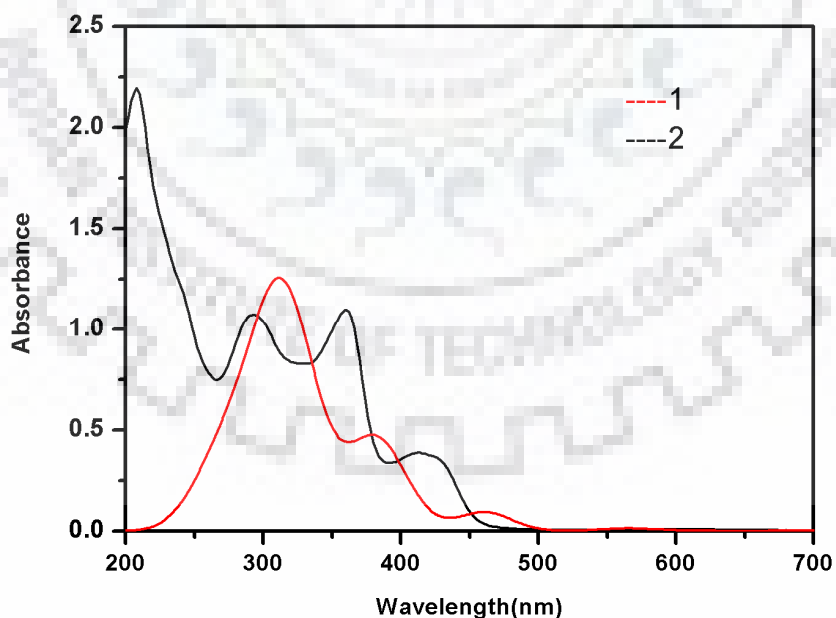


**Table 2.5** Mulliken spin density for a spin unrestricted B3LYP calculation for complex [Cu(L<sup>1</sup>H)ClO<sub>4</sub>] (1)

Atoms	Mulliken spin density	Atoms	Mulliken spin density	Atoms	Mulliken spin density	Atoms	Mulliken spin density
Cu <sub>1</sub>	<b>0.55</b>	C <sub>16</sub>	0.00	N <sub>46</sub>	0.00	C <sub>58</sub>	0.00
C <sub>2</sub>	-0.01	C <sub>22</sub>	0.00	N <sub>47</sub>	0.00	C <sub>62</sub>	0.00
C <sub>4</sub>	0.00	C <sub>28</sub>	0.00	C <sub>51</sub>	-0.01		
C <sub>5</sub>	-0.02	N <sub>42</sub>	0.13	C <sub>53</sub>	-0.00		
C <sub>8</sub>	0.00	N <sub>43</sub>	0.10	O <sub>55</sub>	0.00		
C <sub>9</sub>	0.00	N <sub>44</sub>	0.06	C <sub>56</sub>	0.00		
C <sub>14</sub>	0.01	O <sub>45</sub>	0.13	C <sub>57</sub>	0.00		

**Table 2.6** Significant transition and their contribution at a particular wavelength (theoretically and experimentally) of complex [Cu(L<sup>1</sup>H)ClO<sub>4</sub>] (1)

Theoretically $\lambda_{\max}/\text{nm}(f)$	Exp. $\lambda_{\max}$	Significant contribution
461 (0.0554)	420	HOMO( $\alpha$ ) $\rightarrow$ LUMO( $\alpha$ ) (78%) HOMO( $\beta$ ) $\rightarrow$ LUMO+1( $\beta$ ) (94%)
380 (0.2212)	360	HOMO-1( $\alpha$ ) $\rightarrow$ LUMO( $\alpha$ ) (36%) HOMO-1( $\beta$ ) $\rightarrow$ LUMO+1( $\beta$ ) (44%)
309 (0.2488)	293	HOMO-2( $\alpha$ ) $\rightarrow$ LUMO+1( $\alpha$ ) (42%)

**Fig. 2.32** UV- visible spectra of complex [Cu(L<sup>1</sup>H)ClO<sub>4</sub>] (1). Red colour for theoretical calculation and black one for experimental

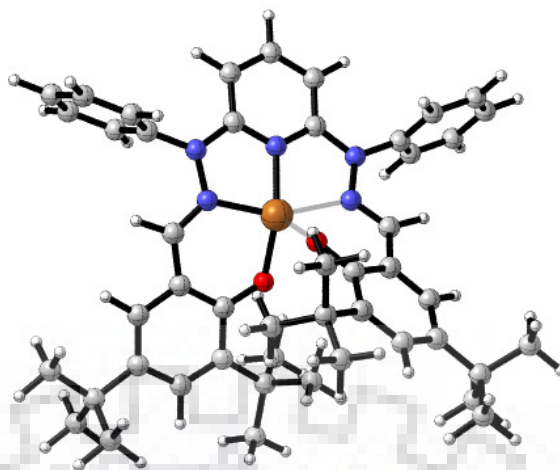


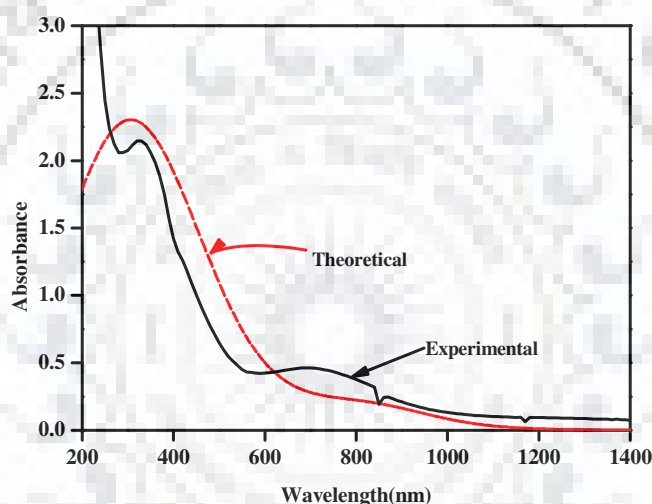
Fig. 2.33 Optimized geometry of complex  $[\text{Cu}(\text{L}^2(\text{CH}_3\text{OH}))\text{NO}_3].2\text{CH}_3\text{OH}$  (2) using B3LYP/LANL2DZ

Table 2.7 Percentage contribution of complex  $[\text{Cu}(\text{L}^2(\text{CH}_3\text{OH}))\text{NO}_3].2\text{CH}_3\text{OH}$  (2) in both alpha and beta orbitals

% Contribution of alpha orbitals							
Orbitals	Cu	Phenalato ring	Phenoxyl radical	Imine bonds	Pyridine	Phenyl ring -1	Phenyl ring-2
LUMO+5	0	7	0	1	7	8	77
LUMO+4	0	0	0	6	1	88	5
LUMO+3	0	2	4	13	28	12	41
LUMO+2	0	1	4	13	16	4	62
LUMO+1	1	6	26	42	23	0	2
LUMO	2	30	3	45	20	0	0
HOMO	2	1	84	10	4	0	0
HOMO-1	0	15	32	28	23	1	1
HOMO-2	2	59	23	13	2	0	0
HOMO-3	4	30	33	18	13	1	1
HOMO-4	7	6	55	19	10	2	1
HOMO-5	5	54	13	18	8	1	2
% Contribution of beta orbitals							
LUMO+5	0	3	5	18	30	14	30
LUMO+4	1	0	2	8	5	2	83
LUMO+3	1	9	24	44	20	0	2
LUMO+2	3	24	5	39	29	0	0
LUMO+1	56	1	15	16	9	1	1
LUMO	2	84	1	10	3	0	0
HOMO	4	1	80	10	4	0	0
HOMO-1	1	3	46	27	21	1	0
HOMO-2	1	27	25	29	16	0	2
HOMO-3	9	20	57	8	5	0	1
HOMO-4	5	46	37	6	5	0	0
HOMO-5	2	47	15	19	13	2	2

**Table 2.8** Mulliken spin density for a spin unrestricted B3LYP calculation for complex  $[\text{Cu}(\text{L}^2(\text{CH}_3\text{OH}))\text{NO}_3].2\text{CH}_3\text{OH}(\mathbf{2})$

Atoms	Mulliken spin density	Atoms	Mulliken spin density	Atoms	Mulliken spin density	Atoms	Mulliken spin density
Cu <sub>21</sub>	<b>0.58</b>	C <sub>39</sub>	-0.01	N <sub>22</sub>	0.03	C <sub>59</sub>	-0.16
C <sub>27</sub>	0.00	C <sub>34</sub>	0.02	C <sub>25</sub>	-0.01	C <sub>43</sub>	0.33
C <sub>25</sub>	0.01	C <sub>56</sub>	-0.01	C <sub>49</sub>	-0.10	C <sub>28</sub>	-0.09
C <sub>35</sub>	0.02	N <sub>24</sub>	<b>0.12</b>	C <sub>33</sub>	<b>0.21</b>		
C <sub>32</sub>	0.01	N <sub>26</sub>	0.00	O <sub>86</sub>	<b>0.35</b>		
C <sub>54</sub>	0.00	N <sub>31</sub>	0.10	C <sub>42</sub>	-0.04		
C <sub>57</sub>	0.01	O <sub>66</sub>	<b>0.14</b>	C <sub>41</sub>	<b>0.28</b>		



**Fig. 2.34** UV- visible spectra of complex  $[\text{Cu}(\text{L}^2(\text{CH}_3\text{OH}))\text{NO}_3].2\text{CH}_3\text{OH}(\mathbf{2})$  in NIR region. Red colour for theoretical calculation and black one for experimental

**Table 2.9** Significant transitions and their contribution at a particular wavelength (theoretically and experimentally) of complex  $[\text{Cu}(\text{L}^2(\text{CH}_3\text{OH}))\text{NO}_3].2\text{CH}_3\text{OH}(\mathbf{2})$

Theoretically $\lambda/\text{nm}(f)$	Exp. $\lambda$	Significant contribution
764.77(0.0249)	730	HOMO-2( $\beta$ ) $\rightarrow$ LUMO ( $\beta$ ) (81 %) HOMO-1( $\beta$ ) $\rightarrow$ LUMO( $\beta$ ) (7%) HOMO-3( $\beta$ ) $\rightarrow$ LUMO ( $\beta$ ) (17 %)
323.90(0.0222)	320	HOMO-2( $\alpha$ ) $\rightarrow$ LUMO+1( $\alpha$ ) (30 %) HOMO-4( $\beta$ ) $\rightarrow$ LUMO+2( $\beta$ ) (27%)

**Table 2.10** Selected bond distances (Å) at the copper centre for complex [Cu(L<sup>1</sup>H)ClO<sub>4</sub>] (1)

Bond type	Experimental	Theoretical
Cu-N1	1.878(8)	1.921
Cu-N3	2.094(12)	2.851
Cu-N5	1.964(11)	1.983
Cu- O2	1.848(8)	1.863
N2-N3	1.398(12)	1.429
N4- N5	1.408(8)	1.422

**Table 2.11** Selected bond distances (Å) at the copper centre for complex [Cu(L<sup>2</sup>(CH<sub>3</sub>OH))NO<sub>3</sub>].2CH<sub>3</sub>OH (2)

Bonds types	Experimental	Theoretical
Cu-N1	1.891(10)	1.953
Cu-N3	1.960(8)	1.977
Cu-N5	1.958(8)	2.140
Cu- O1	1.897(19)	1.913
Cu- O2	1.848(5)	2.284
N2-N3	1.407(13)	1.427
N4-N5	1.419(10)	1.405

**Table 2.12** Selected bond angles (°) at the copper centre for complex [Cu(L<sup>1</sup>H)ClO<sub>4</sub>] (1) and complex [Cu(L<sup>2</sup>(CH<sub>3</sub>OH))NO<sub>3</sub>].2CH<sub>3</sub>OH (2)

Complex-1		Complex-2	
O2—Cu1—N1	168.55(20)	O2—Cu01—N1	169.28(8)
O2—Cu1—N5	94.84(20)	O2—Cu01—N5	93.02(8)
N1—Cu1—N5	81.62(20)	N1—Cu01—N5	82.19(7)
O2—Cu1—N3	105.29(19)	N1—Cu01—N3	76.26(7)
N1—Cu1—N3	79.0(2)	N5—Cu01—N3	151.79(8)
N5—Cu1—N3	159.76(19)	C1—N1—Cu01	122.59(14)

### 2.5.7 Natural transition orbitals (NTO) analysis

Natural transition orbitals of complex **1** and **2** were analysed using TD-DFT/B3LYP LANL2DZ Level calculation the results are depicted in the Table 2.13 and 2.14. The electron densities of complex **1** and **2** in Fig 2.35 and 2.36 clearly indicated the formation of phenoxyl radical in complex **2**.

**Table 2.13** Main optical transition at the TD-DFT/B3LYP LANL2DZ Level for the complex [Cu(L<sup>1</sup>H)ClO<sub>4</sub>] (**1**) with composition in terms of molecular orbital contribution of the transition, Computed Vertical excitation energies, and oscillator strength in dichloromethane

Transition	Energy (eV)	Osc. Strength (f)	Wavelength (nm) (Theo./exp)	Transition	Contributions	Assignment
S <sub>0</sub> → S <sub>5</sub>	2.322	0.0076	534	π(phenolato + ph) → d(Cu) + π* (imine)	H-9(B) → LUMO(B) (29%) H-2(B) → LUMO(B) (13%)	MLCT
S <sub>0</sub> → S <sub>9</sub>	2.7765	0.1025	446	π(phenolato + imine) → d(Cu) + π* (imine + phenolato)	HOMO(A) → LUMO(A) (41%), HOMO(B) → L+1(B) (40%)	ILCT/MLCT
S <sub>0</sub> → S <sub>17</sub>	3.337	0.325	371	π(phenolato + py + imine) → π* (imine + py phenolato)	H-1(A) → LUMO(A) (33%), H-1(B) → L+1(B) (28%)	ILCT /LLCT
S <sub>0</sub> → S <sub>37</sub>	4.010	0.1677	306	π(phenolato + py + imine + ph) → d(Cu) + π* (imine + phenolato)	H-2(A) → L+1(A) (10%), H-10(B) → LUMO(B) (15%), H-9(B) → LUMO(B) (15%)	ILCT/MLCT/LLCT

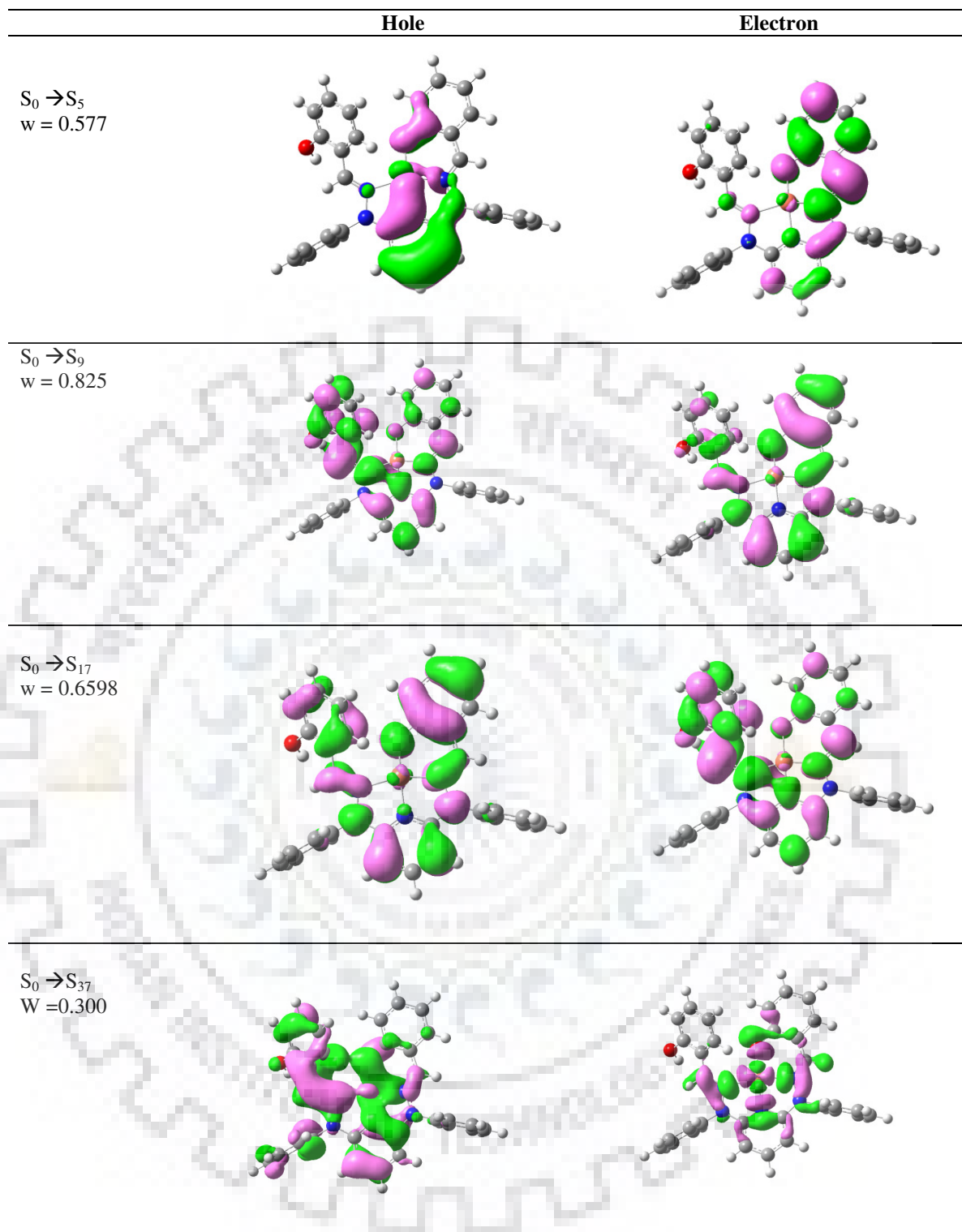


**Fig. 2.35** Natural transition orbitals (NTOs) for complex  $[\text{Cu}(\text{L}^1\text{H})\text{ClO}_4]$  (**1**) illustrating the nature of singlet excited states in the absorption bands in the range 300–600 nm. For each state, the respective number of the state, transition energy (eV), and the oscillator strength (in parentheses) are listed. Shown are only occupied (holes) and unoccupied (electrons) NTO pairs that contribute more than 25% to each excited state

**Table 2.14** Main optical transition at the TD-DFT/B3LYP LANL2DZ Level for the complex  $[\text{Cu}(\text{L}^2(\text{CH}_3\text{OH}))\text{NO}_3] \cdot 2\text{CH}_3\text{OH}$  (**2**) with composition in terms of molecular orbital contribution of the transition, Computed Vertical excitation energies, and oscillator strength in dichloromethane

Transition	Energy (eV)	Osc. Strength (f)	Wave length (nm) (Theo./exp)	Contributions	Assignment
$S_0 \rightarrow S_4$	7243.6 6	0.0622	1380.5	H4(B) $\rightarrow$ LUMO(B) (11%) H-2(B) $\rightarrow$ LUMO(B) (36%) H-1(B) $\rightarrow$ LUMO(B) (34%)	$\pi(\text{phenoxy}) \rightarrow \pi(\text{phenolato}) + d_{x^2-y^2}(\text{Cu})$ ILCT/LLCT
$S_0 \rightarrow S_6$	8800.3 1	0.0307	1136.3	H-4(B) $\rightarrow$ LUMO(B) (10%), H-4(B) $\rightarrow$ L+1(B) (26%), HOMO(B) $\rightarrow$ L+1(B) (19%)	$\pi(\text{phenoxy}) + d_{z^2}(\text{Cu}) \rightarrow \pi(\text{phenolato}) + d_{x^2-y^2}(\text{Cu})$ MLCT/ILCT
$S_0 \rightarrow S_{10}$	14593. 7	0.0298	685.	H-6(B) $\rightarrow$ LUMO(B) (81%)	$\pi(\text{phenoxy}) \rightarrow \pi(\text{phenolato}) + d_{x^2-y^2}(\text{Cu})$ ILCT/LMCT
$S_0 \rightarrow S_{13}$	16101. 2	0.037	621	H-5(B) $\rightarrow$ LUMO(B) (65%), H-3(B) $\rightarrow$ L+1(B) (18%)	$d_{z^2}(\text{Cu}) + \pi(\text{phenolato}) \rightarrow \pi(\text{phenoxy}) + d_{x^2-y^2}(\text{Cu})$ MLCT/ILCT
$S_0 \rightarrow S_{24}$	22299. 6168	0.0433	448	H-(A) $\rightarrow$ LUMO(A) (31%), HOMO(A) $\rightarrow$ L+1(A) (15%), HOMO(B) $\rightarrow$ L+2(B) (15%)	$\pi(\text{phenolato}) \rightarrow \pi(\text{phenoxy})$ ILCT
$S_0 \rightarrow S_{30}$	25572. 614	0.1161	391.	H-1(A) $\rightarrow$ LUMO(A) (23%), HOMO(A) $\rightarrow$ LUMO(A) (11%), HOMO(B) $\rightarrow$ L+2(B) (23%)	$d_{x^2-y^2}(\text{Cu}) + \pi(\text{phenolato}) \rightarrow \pi(\text{phenoxy}) + d_{x^2-y^2}(\text{Cu})$ ILCT/MLCT
$S_0 \rightarrow S_{68}$	33298. 59960 1	0.117	300.	H-5(A) $\rightarrow$ LUMO(A) (20%), H-26(B) $\rightarrow$ LUMO(B) (36%)	$\pi(\text{L}) \rightarrow \pi^*(\text{L})$

	Hole	Electron
$S_0 \rightarrow S_4$ $w = 0.007$ $\pi(\text{phenoxy}) \rightarrow$ $\pi(\text{phenolato}) + d_{x^2-y^2}(\text{Cu})$ ILCT/LLCT		
$S_0 \rightarrow S_6$ $w = 0.518$ $\pi(\text{phenoxy}) + d_{z^2}(\text{Cu}) \rightarrow$ $\pi(\text{phenolato}) + d_{x^2-y^2}(\text{Cu})$ MLCT/ILCT		
$S_0 \rightarrow S_{10}$ $w = 1.623$ $\pi(\text{phenoxy}) \rightarrow$ $\pi(\text{phenolato}) + d_{x^2-y^2}(\text{Cu})$ ILCT/LMCT		
$S_0 \rightarrow S_{13}$ $w = 1.292$ $d_{z^2}(\text{Cu}) + \pi(\text{phenolato}) \rightarrow$ $\pi(\text{phenoxy}) + d_{x^2-y^2}(\text{Cu})$ MLCT/ILCT		



$S_0 \rightarrow S_{24}$   
 $W = 0.624$   
 $\pi(\text{phenolato}) \rightarrow$   
 $\pi(\text{phenoxy})$   
 ILCT



$S_0 \rightarrow S_{30}$   
 $W = 0.459$   
 $d_{x^2-y^2}(\text{Cu})$   
 $+ \pi(\text{phenolato}) \rightarrow$   
 $\pi(\text{phenoxy}) + d_{x^2-y^2}(\text{Cu})$   
 ILCT/MLCT



$S_0 \rightarrow S_{68}$   
 $W = 0.727$   
 $\pi(L) \rightarrow \pi^*(L)$



**Fig. 2.36** Natural transition orbitals (NTOs) for complex  $[\text{Cu}(\text{L}_2(\text{CH}_3\text{OH}))\text{NO}_3] \cdot 2\text{CH}_3\text{OH}$  (2) illustrating the nature of singlet excited states in the absorption bands in the range 300–1400 nm. For each state, the respective number of the state, transition energy (eV), and the oscillator strength (in parentheses) are listed. Shown are only occupied (holes) and unoccupied (electrons) NTO pairs that contribute more than 25% to each excited state

### 2.5.8 X-ray structure determination

The X-ray data collection and processing of complex 1 and complex 2 performed on Bruker Kappa Apex-II CCD diffractometer by using graphite monochromated Mo-K $\alpha$  radiation ( $k = 0.71070 \text{ \AA}$ ) at 293 K. Crystal structures were solved by SIR-92 GUI control methods. Structure solution, refinement and data output were carried out with the SHELXTL

program. All non-hydrogen atoms were refined anisotropically. Hydrogen atoms were placed in geometrically calculated positions and refined using a riding model. Images were created with the DIAMOND program.

**Table 2.15** Crystallographic data for complex [Cu(L<sup>1</sup>H)ClO<sub>4</sub>](1) and [Cu(L<sup>2</sup>(CH<sub>3</sub>OH))NO<sub>3</sub>].2CH<sub>3</sub>OH (2)

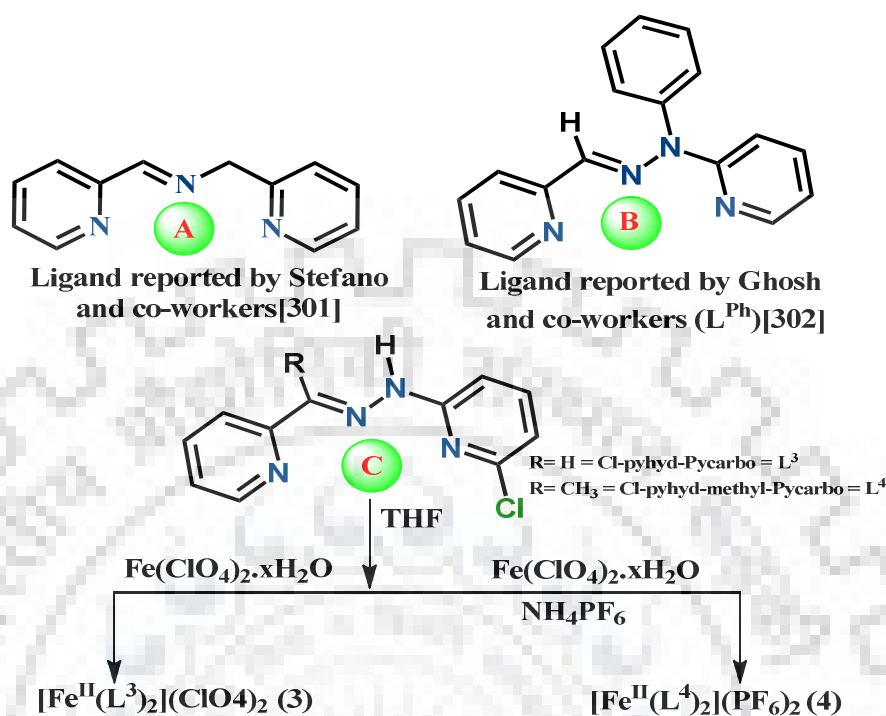
	[Cu(L <sup>1</sup> H)ClO <sub>4</sub> ](1)	[Cu(L <sup>2</sup> (CH <sub>3</sub> OH))NO <sub>3</sub> ].2CH <sub>3</sub> OH (2)		[Cu(L <sup>1</sup> H)ClO <sub>4</sub> ](1)	[Cu(L <sup>2</sup> (CH <sub>3</sub> OH))NO <sub>3</sub> ].2CH <sub>3</sub> OH (2)
<b>Empirical formula</b>	C <sub>31</sub> H <sub>24</sub> ClCuN <sub>5</sub> O <sub>6</sub>	C <sub>48</sub> H <sub>59</sub> CuN <sub>6</sub> O <sub>6</sub> .2(CH <sub>4</sub> O)	<b>Z</b>	4	1
<b>Color</b>	Green	Green	<b>ρ<sub>calc</sub>(gcm<sup>-3</sup>)</b>	1.450	1.238
<b>Formula weight</b>	661.55	943.65	<b>F(000)</b>	1356.0	1004.0
<b>Temperature (K)</b>	293(2)	293(2)	<b>Theta range for data collection</b>	1.74 - 28.40	0.85-28.36
<b>λ (Å) (Mo-Kα)</b>	0.71073	0.71073	<b>Index ranges</b>	-16<h<16,-19<k<20,-22<l<22	-14<h<11,-13<k<13,-14<l<32
<b>Crystal system</b>	Monoclinic	Triclinic	<b>Refinement method</b>	Full matrix least-squares on F <sup>2</sup>	Full matrix least-squares on F <sup>2</sup>
<b>Space group</b>	P21/c	P -1	<b>Data/restraints/parameters</b>	7490/0/397	12652/0/614
<b>a(Å)</b>	12.053(4)	10.584(2)	<b>GOF<sup>a</sup> on F<sup>2</sup></b>	1.002	1.216
<b>b(Å)</b>	15.087(5)	10.847(2)	<b>R<sub>1</sub><sup>b</sup> [I &gt; 2σ(I)]</b>	0.0799	0.1312
<b>c(Å)</b>	17.155(5)	24.324(5)	<b>R<sub>1</sub> (all data)</b>	0.1531	0.3245
<b>α(°)</b>	90.000(18)	96.709(12)	<b>wR<sub>2</sub><sup>c</sup> (I &gt; 2σ(I))</b>	0.2504	0.3958
<b>β(°)</b>	103.692(17)	96.312(13)	<b>wR<sub>2</sub> (all data)</b>	0.3060	0.3004
<b>γ(°)</b>	90.000(18)	112.177(12)			

GOF =  $[\sum[w(F_o^2 - F_c^2)^2]/(M-N)]^{1/2}$  (M = number of reflections, N = number of parameters refined).  $^bR_1 = \sum \|F_o\| - \|F_c\| / \sum \|F_o\|$ ,  $^c wR_2 = [\sum[w(F_o^2 - F_c^2)^2] / \sum[w(F_o^2)^2]]^{1/2}$

### 3.1 Introduction

The oxygenation of non-activated alkyl C-H bonds is a challenging area of research owing to their chemical inertness towards chemical oxidation. Consequently, highly reactive species, generated by suitable catalyst, are necessary to perform such chemistry.<sup>288</sup> In the chemical industries, such catalytic oxidation and during oxidation process, desired selectivity of the organic molecules produced, are extremely important.<sup>289</sup> It is well known that alkanes are thermodynamically stable and difficult to oxidise in a controlled and selective fashion. Chromate and permanganate have already been used as conventional oxidants however these oxidants are rather inefficient and barely selective,<sup>290</sup> thus enhancement in the efficiency and selectivity of the hydrocarbon oxidation became the goal of industrial as well as academic research. Nature has developed several metalloenzymes (heme as well as non-heme) which selectively catalyse the oxidation of hydrocarbon.<sup>291-294</sup> Iron containing metalloenzymes play important roles in these biological processes. For example, cytochrome P450 selectively oxidizes the aliphatic side chain of cholesterol, and the same metalloprotein is involved in biosynthesis of the female hormone progesterone.<sup>295</sup> Iron-dependent cytosolic protein, soluble methane monooxygenase (sMMO) activates C-H bond and converts methane to methanol.<sup>296</sup>  $\text{Fe}^{\text{III}}\text{-OOH}$  species has been observed and was implicated in the catalytic cycle of C-H bond oxidation. Anticancer drug bleomycin, naphthalene dioxygenase, and rieske oxygenase enzymes are also involved in such oxidation processes.<sup>297</sup> The first non-heme iron(IV)-oxo complex was characterized spectroscopically by Wieghardt and co-workers,<sup>298</sup> however, there has been considerable current interest<sup>299</sup>. The present study stems from our interest in such oxidation chemistry.<sup>300</sup> Stefano and co-workers recently reported oxidation of hydrocarbons by using mononuclear iron complexes derived from tridentate meridional ligands. In the mechanism of the reaction hexacoordinated iron was found to be pentacoordinated with the dissociation of one of the

Fe-N bonds during the reaction with hydrogen peroxide was reported and an intermediate iron complex having  $\text{Fe}^{\text{IV}}=\text{O}$  moiety was generated.<sup>301</sup>



**Scheme 3.1** Synthesis of complex 3 and complex 4 using different substituted ligands

We have recently reported iron complex derived from meridional tridentate ligand ( $L^{\text{Ph}}$ ) having NNN donors (shown in Scheme 3.1).<sup>302</sup> Addition of  $\text{H}_2\text{O}_2$  to this complex did not provide us the indication of generation of stable hydroperoxo and oxo species in solution. Investigation of literature revealed that Borovik and co-workers, Goldberg and co-workers, and Fout and co-workers reported the stabilization of  $\text{Fe}^{\text{IV}}=\text{O}$  through hydrogen bonding because the hydrogen atom present in the ligand system showed proximity with the  $\text{Fe}^{\text{IV}}=\text{O}$ .<sup>303</sup> We have performed theoretical (DFT and TD-DFT) calculations for the complex derived from  $L^{\text{Ph}}$  described in our previous report<sup>302</sup> (Shown in Fig. 3.45) and we designed new ligands ( $L^3$  and  $L^4$  as shown in Scheme 3.1) which possibly could stabilise hydroperoxo and oxo species through hydrogen bonding during catalytic activity. Costas and co-workers described that some iron complexes are capable of C-H bond oxidation reaction and selectively transform reactant(s) into the products.<sup>304</sup> On the other hand, formation of high-

valent iron hydroperoxo and oxo species could also be utilised for the degradation of organic dye pollutants.<sup>305-306</sup> Collins and co-workers synthesized the iron complex capable of generating high-valent hydroperoxo and oxo iron complexes and catalytic degradation of orange II dye was investigated.<sup>305</sup> Hitomi and co-workers used iron(III) tetradentate monoamido complex as a non-heme iron-based peroxidase mimetic for the catalytic oxidation of organic dye.<sup>307</sup>

With the view of above literature data, herein, we have designed, synthesized and characterized mononuclear iron(II) complexes  $[\text{Fe}^{\text{II}}(\text{L}^3)_2](\text{ClO}_4)_2$  (**3**) and  $[\text{Fe}^{\text{II}}(\text{L}^4)_2](\text{PF}_6)_2$  (**4**) derived from a tridentate ligands  $\text{L}^3$  and  $\text{L}^4$  (shown in Scheme 3.1). Molecular structures of  $[\text{Fe}^{\text{II}}(\text{L}^3)_2](\text{ClO}_4)_2$  (**3**) and  $[\text{Fe}^{\text{II}}(\text{L}^4)_2](\text{PF}_6)_2$  (**4**) were determined by X-ray crystallography. Efficient and selective oxidation of cyclohexane, benzyl alcohol, 1-phenyl ethanol and fluorene in presence of catalytic amount  $[\text{Fe}^{\text{II}}(\text{L}^3)_2](\text{ClO}_4)_2$  (**3**) and  $[\text{Fe}^{\text{II}}(\text{L}^4)_2](\text{PF}_6)_2$  (**4**) was investigated. Complexes **3** and **4** were utilised for oxidative degradation of orange II and methylene blue dyes. The intermediate species  $\text{Fe}^{\text{II}}\text{-OOH}$  and  $\text{Fe}^{\text{IV}}\text{=O}$  were characterised by UV-visible spectroscopy, ESI-MS and resonance Raman analysis. A reaction model for oxidation reaction and dye degradation will be scrutinized on the basis of our observations in reactivity studies.

## **3.2 Results and Discussions**

### **3.2.1 Synthesis and characterization**

New tridentate ligands, ( $\text{L}^3$ ) and ( $\text{L}^4$ ) having NNN type binding<sup>283,308</sup> have been synthesized by reacting 2-chloro-6-hydrazinylpyridine with 2-pyridinecarboxaldehyde and 2-acetylpyridine respectively. Ligand  $\text{L}^3$  reacted with  $\text{Fe}(\text{ClO}_4)_2 \cdot x\text{H}_2\text{O}$  in 2:1 equivalent (ligand and metal salt ratio) and yielded red solid of  $[\text{Fe}^{\text{II}}(\text{L}^3)_2](\text{ClO}_4)_2$  (**3**). For complex **4**, ligand  $\text{L}^4$  reacted with  $\text{Fe}(\text{ClO}_4)_2 \cdot x\text{H}_2\text{O}$  in similar fashion as complex **3**, after that  $\text{NH}_4\text{PF}_6$  was added to get the resultant product in good yield (Scheme 3.1). Complex **3** and **4** have

been characterized by various spectral and analytical techniques. Coordination of imine N to iron metal centre was indicated by the shifting of azomethine ( $\nu_{C=N}$ ) stretching frequency from  $1590\text{ cm}^{-1}$  in free ligand to  $1605\text{ cm}^{-1}$ . The characteristic peaks for perchlorate anion were observed near  $1090$  and  $625\text{ cm}^{-1}$  in IR spectral studies in complex **3** (shown in Fig. 3.35). However we observed the shifting of azomethine from  $1599\text{ cm}^{-1}$  in free ligand to  $1610\text{ cm}^{-1}$  in complex **4**. The presence of  $\text{PF}_6^-$  was expressed by the peak at  $836\text{ cm}^{-1}$ . (Shown in Fig. 3.39) The UV-visible spectra of complexes were recorded in acetonitrile solution. The absorption bands near  $328$  and  $240\text{ nm}$  were assigned as  $n \rightarrow \pi^*$  and  $\pi \rightarrow \pi^*$  transitions for ligand. Complex **3** showed two broad bands near  $460$  and  $503\text{ nm}$  due to ligand-to-metal charge transfer transitions (LMCT) (Shown in Fig. 3.37). In case of complex **4**, the peaks near  $240$ ,  $272$  and  $324\text{ nm}$  were assigned to intra-ligand  $n \rightarrow \pi^*$  and  $\pi \rightarrow \pi^*$  transitions. Complex **4** also showed a broad band near  $454$  and  $509\text{ nm}$  due to ligand-to-metal charge transfer transition (LMCT) (Fig. 3.39). Complexes **3** and **4** were found to be low spin and provided  $^1\text{H}$  NMR spectra in  $\text{DMSO-}d_6$ . As compare to the free ligands ( $\text{L}^3$  and  $\text{L}^4$ ), the NMR signals were shifted towards high field after complexation (Shown in Fig. 3.37 and 3.40 for complexes **3** and **4**). The ESI-mass spectral study was performed for both the complexes in acetonitrile solution. Complexes  $[\text{Fe}^{\text{II}}(\text{L}^3)_2](\text{ClO}_4)_2$  (**3**) and  $[\text{Fe}^{\text{II}}(\text{L}^4)_2](\text{ClO}_4)_2$  (**4**) provided a peak at  $m/z = 519.0317$  (for  $[\text{Fe}^{\text{II}}(\text{L}^3)_2]^{2+}$  ion) and  $m/z = 547.0655$  (for  $[\text{Fe}^{\text{II}}(\text{L}^4)_2]^{2+}$  ion) respectively (Fig. 3.36 and Fig. 3.42). The molecular structures of complex  $[\text{Fe}^{\text{II}}(\text{L}^3)_2](\text{ClO}_4)_2$  (**3**) and  $[\text{Fe}^{\text{II}}(\text{L}^4)_2](\text{PF}_6)_2$  (**4**) were determined by using X-ray crystallographic studies (Table 3.13) and their ORTEP diagrams are displayed in Fig. 3.1 and 3.2 respectively. The coordination environment around the metal centre is described as hexacoordinated distorted octahedral geometry. In complex  $[\text{Fe}^{\text{II}}(\text{L}^3)_2](\text{ClO}_4)_2$  (**3**) the tridentate ligand ( $\text{L}^3$ ) was coordinated to the Fe(II) centre in a meridional fashion via two imine nitrogen ( $\text{N}_{\text{im}}$ ) and four pyridine nitrogen ( $\text{N}_{\text{py}}$ ) donors. The Fe- $\text{N}_{\text{im}}$  bond

distances are 1.875 Å (Fe1—N3) and 1.912 Å Fe1—N7 and Fe—N<sub>py</sub> distances have been found to have slight differences 2.031 Å (Fe1—N8), 2.031 Å (Fe1—N5), 2.093 Å (Fe1—N4), 2.122 Å (Fe1—N1). A similar pattern was observed in case of complex **4** (minor differences in N<sub>py</sub> distances) N<sub>py</sub> distances were found consistent with the data reported in the literature<sup>302</sup>, However, the N<sub>im</sub> distances were shorter in our case as compare to the reported values. The bond parameters for complexes **3** and **4** were quite similar to the data obtained from theoretically optimized geometries of both the complexes (shown in Table 3.14). We have investigated the bond distances and bond angles reported in the literature<sup>309</sup> for similar type of complexes and observed that such type of co-ordination may lead to spin-state equilibrium and generation of complexes showing spin crossover (SCO). Hence we are trying to extend this work in that direction of SCO complexes and we will be published in elsewhere.

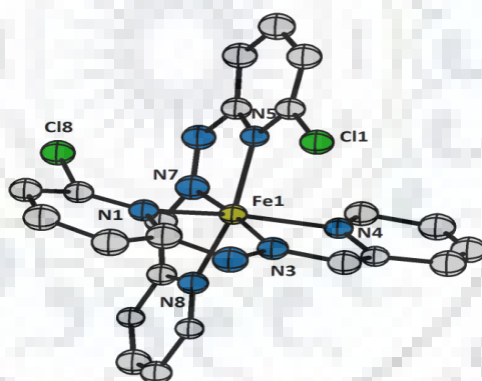


**Fig. 3.1** ORTEP diagram (50% probability level) of complex [Fe<sup>II</sup>(L<sup>3</sup>)<sub>2</sub>](ClO<sub>4</sub>)<sub>2</sub> (**3**), All hydrogen atoms and counter anions are omitted for clarity

The selected bonds angles in complex **3** are N3—Fe1—N7 = 173.27°, N8—Fe1—N5 = 160.92° and N4—Fe1—N1 = 160.99° and in complex **4** are N3—Fe1—N7 = 172.81°, N8—Fe1—N5 = 159.03° and N4—Fe1—N1 = 160.97°. These values clearly indicated a distorted octahedral geometry in complexes.

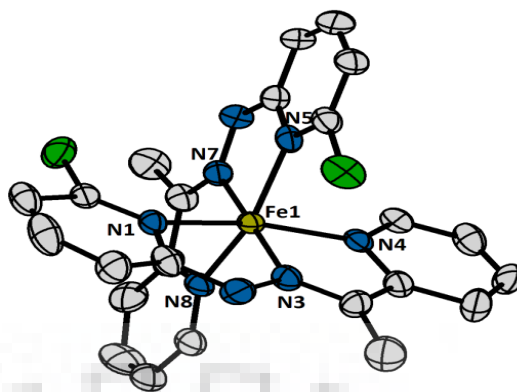


**Fig. 3.2** ORTEP diagram (50% probability level) of complex  $[\text{Fe}^{\text{II}}(\text{L}^4)_2](\text{PF}_6)_2(\mathbf{4})$  All hydrogen atoms and counter anions are omitted for clarity

The packing diagrams of complex **3** and **4** along the 'a' axis exhibited the interaction between the counter ions and complex cation (Fig. 3.43 and 3.44).

### 3.2.2 Electrochemical investigation

The electrochemical properties of both the complexes **3** and **4** were investigated in dimethylsulfoxide. The  $E_{1/2}$  values for complexes **3** and **4** were found to be 0.286V and 0.123 V respectively. As shown in Table 3.1.

Complexes	Fe(II) /Fe(III)			
	$E_{\text{pa}}/\text{V}$	$E_{\text{pc}}/\text{V}$	$E_{1/2}^{\text{b}}, \text{V} (\Delta E_{\text{p}}^{\text{c}}, \text{mV})$	$^{\text{d}}n = i_{\text{pa}}/i_{\text{pc}}$
<b>3</b>	0.380	0.193	0.286(187)	1.27
<b>4</b>	0.152	0.094	0.123(58)	0.09

<sup>[a]</sup>Electrochemical data measured in dimethylsulfoxide (DMSO) with 0.1m tetrabutylammonium perchlorate (TBAP). <sup>[b]</sup>Data from cyclic voltammetric measurements;  $E_{1/2}$  is calculated as average of anodic ( $E_{\text{pa}}$ ) and cathodic ( $E_{\text{pc}}$ ) peak potentials  $E_{1/2} = 0.5 (E_{\text{pa}} + E_{\text{pc}})$ ; and <sup>[c]</sup>  $\Delta E_{\text{p}} = E_{\text{pa}} - E_{\text{pc}}$  at scan rate 0.1  $\text{Vs}^{-1}$ , <sup>[d]</sup> Constant-potential coulometric data  $n = i_{\text{pa}}/i_{\text{pc}}$  calculated for  $1e^-$  transfer.



Complex **4** was oxidised at lower potential due to electron donating methyl group present at the azomethine bond that helps to oxidise the iron centre ( $\text{Fe}^{\text{II}}/\text{Fe}^{\text{III}}$ ) easily at lower potential. (As shown in Fig. 3.3).

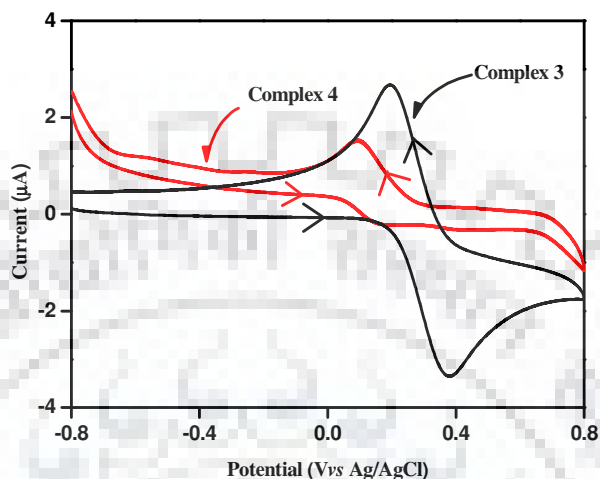


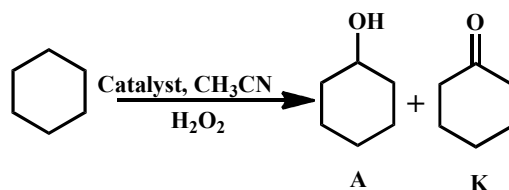
**Fig. 3.3** Cyclic voltammograms of a  $10^{-3}$  M solution of complexes (**3** and **4**) in dimethyl sulfoxide in presence of 0.1 M tetrabutylammonium perchlorate (TBAP), using working electrode: glassy-carbon, reference electrode: Ag/AgCl; auxiliary electrode: platinum wire, scan rate  $0.1 \text{ V s}^{-1}$

### 3.2.3 Catalytic oxidation of hydrocarbons

As a part of our ongoing research in the field of catalytic oxidation of hydrocarbons,<sup>300</sup> we have synthesized and characterized Fe(II) complexes which are capable to stabilise the  $\text{Fe}^{\text{IV}}=\text{O}$  species in the presence of  $\text{H}_2\text{O}_2$  and as a result oxidised the hydrocarbons to corresponding products.

#### 3.2.3.1 Oxidation of cyclohexane

Oxidation of cyclohexane was performed using complexes **3** and **4** as catalysts. (Scheme 3.2) The percentage conversion and TON has been shown in the Table 3.2. On the basis of A/K ratio, it was found that our complexes provided better catalytic activity as compared to the results reported by Stefano and coworkers<sup>303</sup> however, less efficient than the catalysts reported by Que and coworkers.<sup>310</sup> (As shown in Table 3.3)



**Scheme 3.2** Oxidation of cyclohexane to cyclohexanol (A) and cyclohexanone (K)

**Table 3.2** Oxidation of cyclohexane.<sup>a</sup> The amount of catalyst was taken 0.02 mmol for complex **3** and **4**, 1ml H<sub>2</sub>O<sub>2</sub>, temperature 80°C, time was taken 24 hours for all experiments

Complexes	Substrate	Substrate (mmol)	% Conversion	TON <sup>b</sup>	Product
<b>3</b>		1.42	72 and 20	51 (A), 14(K)	
<b>4</b>		1.42	57 and 36	40(A), 25(K)	

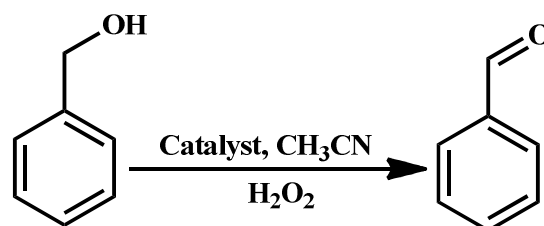
<sup>a</sup>All reactions carried out in acetonitrile at 80 °C. The yields were measured by GC 24 hours after the beginning of the reaction. <sup>b</sup>TON defined as [TON= {(% conversion) × (mmol of substrate)/ (mmol of catalyst) × 100}].

**Table 3.3** Comparative study with the literature for the oxidation of cyclohexane

S. No.	Catalyst	A	K	Total	A/K	Ref.
1	(L1) <sub>2</sub> Fe(OTf) <sub>2</sub>	14±1	10±1	24	1.40	303
2	(L2) <sub>2</sub> Fe(OTf) <sub>2</sub>	14±1	14±1	28	1.00	303
3	(L3) <sub>2</sub> Fe(OTf) <sub>2</sub>	9±0.5	14±1	23	0.64	303
4	(L4) <sub>2</sub> Fe(OTf) <sub>2</sub>	14±1	7.0±0.5	21	0.50	303
5	[(TPA)Fe(OTf) <sub>2</sub> ]	-	-	3.2	5.00	310
6	Complex <b>3</b>	51±1	14±1	65	3.64	This work
7	Complex <b>4</b>	40±1	25±1	65	1.60	This work

### 3.2.3.2 Oxidation of benzyl alcohol

Benzyl alcohol oxidation reaction was also performed with both the complexes and we got the benzaldehyde selectively with both the catalysts. (Scheme 3.3) The rate of conversion with methyl substituted complex was found more as compare to unsubstituted complex **3**. (Shown in Table 3.4)



Scheme 3.3 Oxidation of benzyl alcohol to benzaldehyde

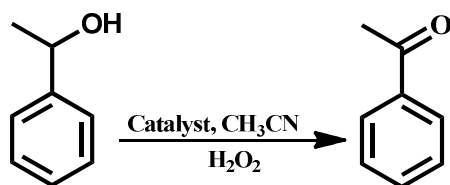
**Table 3.4** Oxidation of benzyl alcohol<sup>c</sup>. The amount of catalyst 0.02 m mol, and 1ml H<sub>2</sub>O<sub>2</sub>, temperature 80<sup>o</sup>C, time was taken 24 hours for all experiments

Complexes	Substrate	Substrate (mmol)	% Conversion	TON <sup>d</sup>	Selectivity (%)	Product
3.		1.10	87	48	100	
4.		1.10	90	50	100	

<sup>c</sup> Benzyl alcohol oxidation reaction was carried out in acetonitrile at 80 °C. <sup>d</sup>See the footnote of Table 3.2.

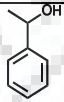
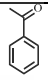
### 3.2.3.3 Oxidation of 1-phenyl ethanol

Secondary benzylic alcohol (1-phenyl ethanol) oxidation was also be carried out to its corresponding ketone is a major concern in the oxidation chemistry. We have performed the reaction with 1-phenyl ethanol oxidation using both the catalyst. Selectively we got acetophenone with a good conversion rate. (Shown in 3.4 and Table 3.5) McGaf and coworkers reported the oxidation of primary and secondary benzylic alcohols with hydrogen peroxide and tert-butyl hydroperoxide catalyzed with the good conversion rate but with the complex **3** and complex **4** the conversion rate was less.<sup>311</sup> (As shown in Table 3.6)



**Scheme 3.4** Oxidation of 1-phenyl ethanol to acetophenone

**Table 3.5** Oxidation of 1-phenyl ethanol and the amount of catalyst 0.02 mmol, 1ml H<sub>2</sub>O<sub>2</sub>, temperature 80<sup>o</sup>C, time was taken 8 hours for all experiments

Complexes	Substrate	Substrate (mmol)	% Conversion	TON <sup>e</sup>	Selectivity (%)	Product
<b>3</b>		0.60	36	11	100	
<b>4</b>		0.60	97	29	100	

<sup>e</sup>See the footnote of Table 3.2

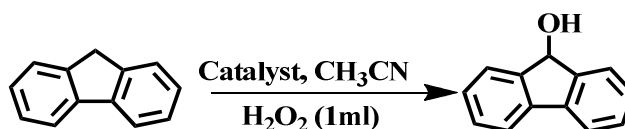
**Table 3.6** Comparative study with the literature for the oxidation of benzyl alcohol and 1-phenylethanol

S. No.	Catalyst	Substrate	Product	TON	Ref.
1	Fe <sup>+3</sup> L	Benzyl alcohol	Benzaldehyde	84	311
2	Complex <b>3</b>	Benzyl alcohol	Benzaldehyde	48	This work
3	Complex <b>4</b>	Benzyl alcohol	Benzaldehyde	50	This work
4	Fe <sup>+3</sup> L	1-phenyl ethanol	Acetophenone	230	311
5	Complex <b>3</b>	1-phenyl ethanol	Acetophenone	11	This work
6	Complex <b>4</b>	1-phenyl ethanol	Acetophenone	29	This work

### 3.2.3.4 Oxidation of Fluorene

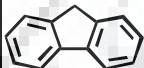
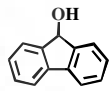
Fluorene oxidised to fluorenol selectively in the presence of both the catalysts. (Shown in Scheme 3.5). The reaction was done in acetonitrile solvent system and hydrogen peroxide,

selectively fluorenol was obtained. The product was analysed using GC-Mass spectrometry analysis. The results obtained are shown in Table 3.7.



**Scheme 3.5** Oxidation of fluorene to fluorenol

**Table 3.7** Oxidation of fluorene the amount of catalyst 0.02 mmol, and 1ml H<sub>2</sub>O<sub>2</sub>, temperature 80<sup>o</sup>C time was taken 8 hours for all experiments

Complexes	Substrate	Substrate (mmol)	(%) Conversion	TON <sup>f</sup>	Selectivity (%)	Product
<b>3.</b>		0.40	40	8	100	
<b>4.</b>		0.40	44	9	100	

<sup>f</sup>See the footnote of Table 3.2

### 3.3 Characterization of reactive intermediates

Generation of reactive species after addition of H<sub>2</sub>O<sub>2</sub> in the acetonitrile solution of complex **3** and complex **4** was authenticated by the generation of Fe<sup>III</sup>-OOH and concomitant production of Fe<sup>IV</sup>=O in solution. (shown in Scheme 3.6) The addition of hydrogen peroxide molecule generated the active [Fe<sup>III</sup>-OOH(L<sup>3</sup>)<sub>2</sub>]<sup>2+</sup> species which undergo homolytic cleavage and <sup>•</sup>OH radical species and complex having Fe<sup>IV</sup>=O moiety were produced. Generation of Fe<sup>IV</sup>=O intermediate can be further supported by UV-visible titration of [Fe<sup>II</sup>(L<sup>3</sup>)<sub>2</sub>](ClO<sub>4</sub>)<sub>2</sub> (**3**) and [Fe<sup>II</sup>(L<sup>4</sup>)<sub>2</sub>](PF<sub>6</sub>)<sub>2</sub>(**4**) with H<sub>2</sub>O<sub>2</sub> at low temperature. (Shown in Fig.3.4) For the complex **3** the band at around 540 nm ( $\epsilon = 1020 \text{ M}^{-1} \text{ cm}^{-1}$ ) in complex [Fe<sup>II</sup>(L<sup>3</sup>)<sub>2</sub>](ClO<sub>4</sub>)<sub>2</sub> (**3**) decrease after addition of H<sub>2</sub>O<sub>2</sub> (1.5 equivalent) and a band around 662 nm ( $\epsilon = 480 \text{ M}^{-1} \text{ cm}^{-1}$ ) appeared with a fast color change from red to green at 0 °C (As shown in Fig. 3.5 and 3.6). ESI-MS spectra of this complex was done with H<sub>2</sub>O<sub>2</sub> as an

oxidising agent we got  $[\text{Fe}^{\text{IV}}(\text{O})(\text{L}^3)_2]^{2+}$   $m/z=535.0219$  species in acetonitrile solvent. (As shown in the Figure 3.8)

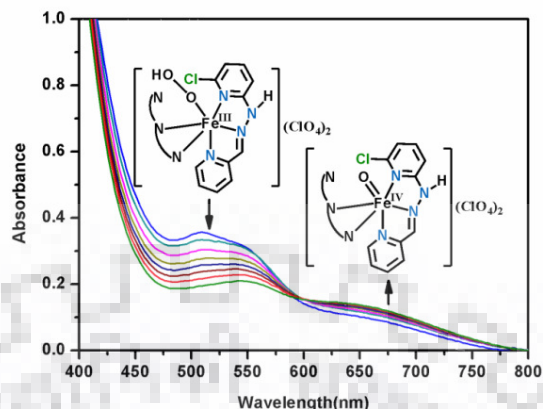


**Fig. 3.4** UV-visible spectral changes observed during the reaction  $[\text{Fe}^{\text{II}}(\text{L}^3)_2](\text{ClO}_4)_2$  (**3**) ( $1.25 \times 10^{-4}$  M) with 1.5 equiv. of  $\text{H}_2\text{O}_2$  in acetonitrile at  $0^\circ\text{C}$

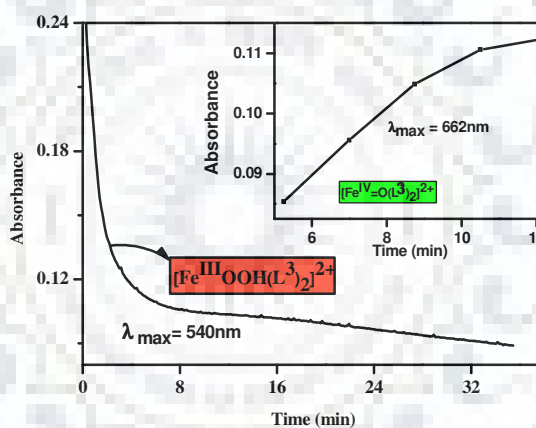


**Fig. 3.5** UV-visible spectral changes observed during the reaction, formation of  $[\text{Fe}^{\text{III}}\text{OOH}(\text{L}^3)_2](\text{ClO}_4)_2$  540nm to  $[\text{Fe}^{\text{IV}}(\text{O})(\text{L}^3)_2](\text{ClO}_4)_2$  662 nm

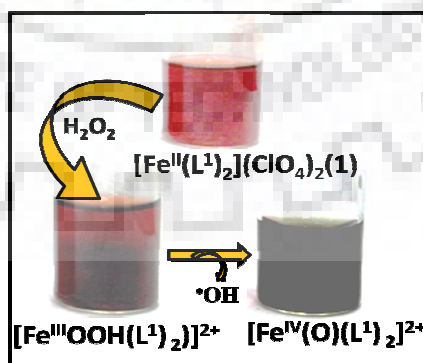
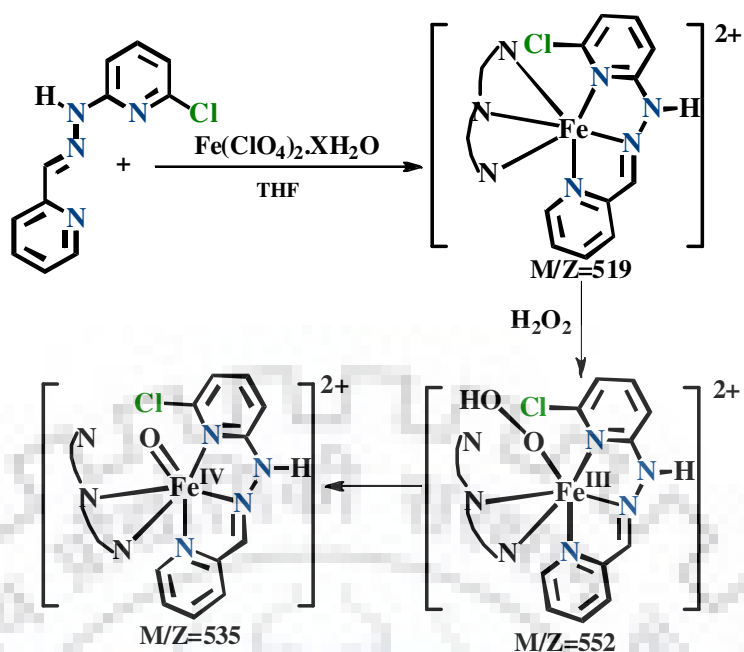


**Fig. 3.6** Visible changes in the colour of the complex  $[\text{Fe}^{\text{II}}(\text{L}^3)_2](\text{ClO}_4)_2$  (**3**) (red) upon addition  $\text{H}_2\text{O}_2$ , the formation of  $[\text{Fe}^{\text{III}}\text{OOH}(\text{L}^3)_2](\text{ClO}_4)_2$  light green and  $[\text{Fe}^{\text{IV}}(\text{O})(\text{L}^3)_2](\text{ClO}_4)_2$  dark green



**Scheme 3.6** Reaction pathway for the formation  $[\text{Fe}^{\text{IV}}(\text{O})(\text{L}^3)_2](\text{ClO}_4)_2$  species using  $\text{H}_2\text{O}_2$

The EPR spectrum of complex **3** with (1.5 equivalent  $\text{H}_2\text{O}_2$ ) was recorded in acetonitrile solvent and we got EPR signal at 2.01. The spectra  $g = 2.01$  clearly indicated that this spectra does not showed three line EPR signal reported by Que and co-workers<sup>312</sup> however this spectra may be due to the production of hydroxyl ( $\text{HO}^\bullet$ ) radical species generated in solution shown in Fig. 3.7

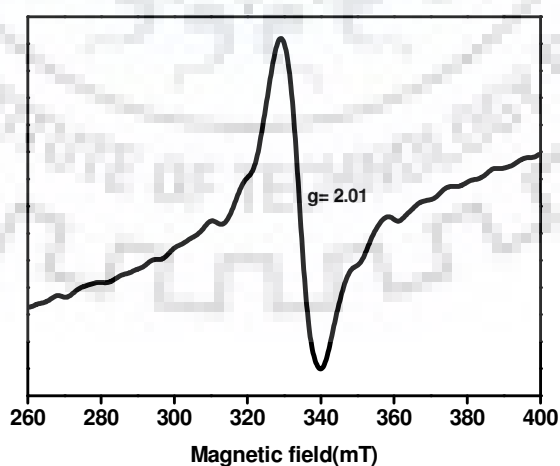


**Fig. 3.7** EPR spectrum of complex **3** in acetonitrile on adding  $\text{H}_2\text{O}_2$  recorded at room temperature. Generation of  $[\text{Fe}^{\text{III}}\text{OOH}(\text{L}^3)_2](\text{ClO}_4)_2$  species

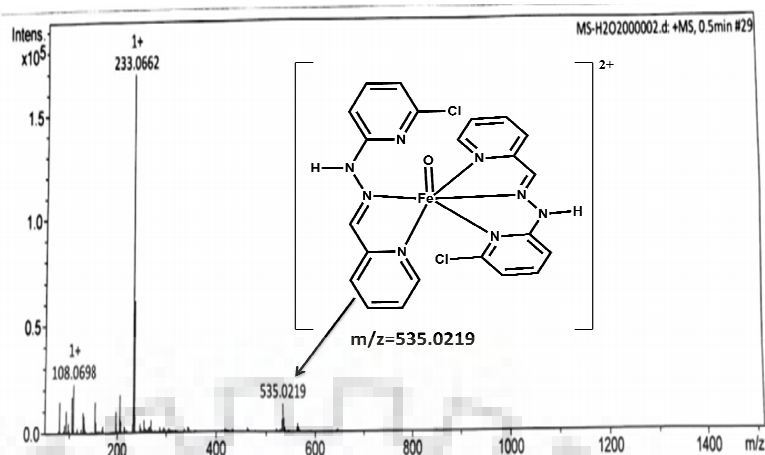


**Fig. 3.8** ESI-MS spectra of complex **3** on adding  $\text{H}_2\text{O}_2$ , recorded in acetonitrile for the formation of  $[\text{Fe}^{\text{IV}}(\text{O})(\text{L}^3)_2]^{2+}$   $m/z=535.0129$

The resonance Raman spectra of both the complexes were recorded to analyse the reactive intermediates on adding  $\text{H}_2\text{O}_2$  in both the complexes. The vibrational modes were generating from the stable iron oxo species due to the iron oxygen stretching mode. In complex **3** it was  $825\text{ cm}^{-1}$  and for complex **4**,  $831\text{ cm}^{-1}$ . (As shown in the Fig. 3.9 and Fig. 3.10) The data obtained from the UV-visible and resonance was conform the formation of stable  $\text{Fe}^{\text{IV}}=\text{O}$  species as compare with literature<sup>313</sup> and it was found quite similar. The comparison data shown in the Table 3.8.

**Table 3.8** Spectroscopic characterization data of  $\text{Fe}^{\text{IV}}=\text{O}$  intermediates

Complexes	$\lambda_{\text{max}}$ (nm), $\epsilon$ ( $\text{M}^{-1}\text{ cm}^{-1}$ )	$\nu_{\text{Fe}=\text{O}}$ ( $\text{cm}^{-1}$ )	References
$[\text{Fe}^{\text{IV}}(\text{O})(\text{TMC})(\text{NCMe})]^{2+}$	824 (400)	839	314
$\text{Fe}^{\text{IV}}(\text{O})(\text{TMC-Py})]^{2+}$	834 (260)	826	315
$[\text{Fe}^{\text{IV}}(\text{O})(\text{TMCSO}_2)]^+$	830 (170)	831	316
$[\text{Fe}^{\text{IV}}(\text{O})(15\text{cyclam})]^{2+}$	750 (500)	841	317
$[\text{Fe}^{\text{IV}}(\text{O})(\text{TPEN})]^{2+}$	730 (380)	818	318
$[\text{Fe}^{\text{IV}}(\text{O})(\text{L}^3)_2]^{2+}$	662(484)	825	This work
$[\text{Fe}^{\text{IV}}(\text{O})(\text{L}^4)_2]^{2+}$	725(670)	831	This work



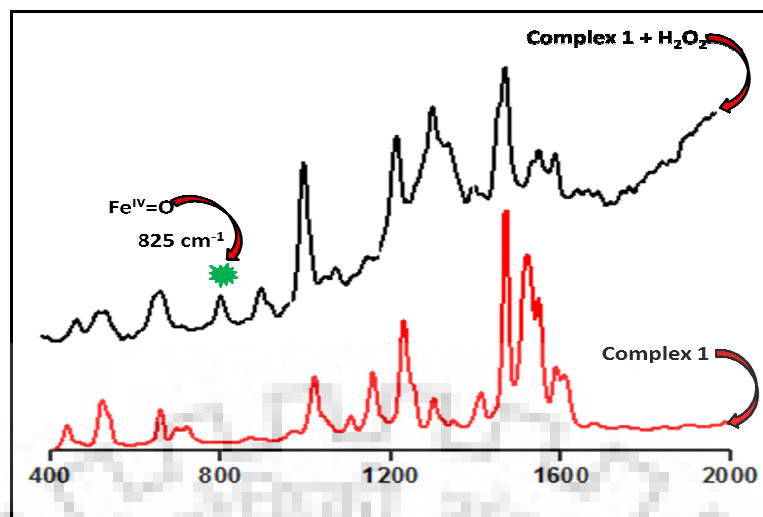


**Fig. 3.9** Resonance Raman spectra of complex  $[\text{Fe}^{\text{II}}(\text{L}^3)_2](\text{ClO}_4)_2$  (**3**) and on adding  $\text{H}_2\text{O}_2$  formation of  $\text{Fe}-\text{OOH}$  and  $\text{Fe}^{\text{IV}}=\text{O}$  intermediates

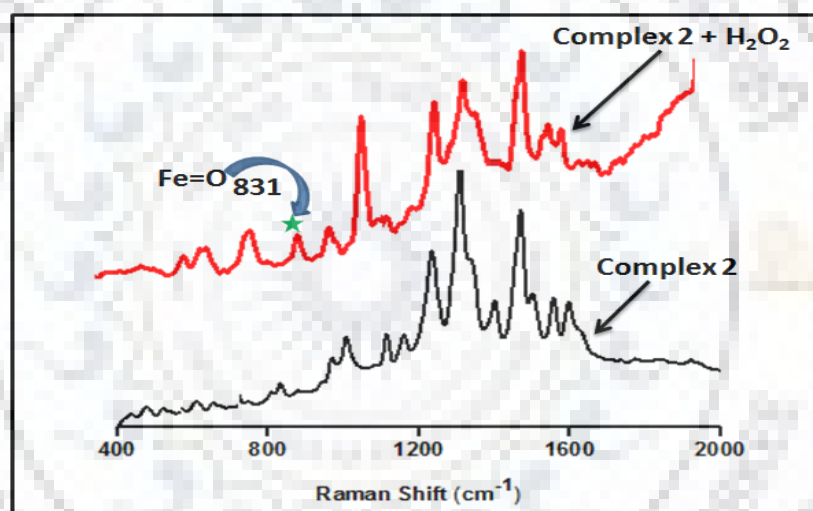


**Fig. 3.10** Resonance Raman spectra of complex  $[\text{Fe}^{\text{II}}(\text{L}^4)_2](\text{PF}_6)_2$  (**4**) and on adding  $\text{H}_2\text{O}_2$  formation of  $\text{Fe}^{\text{IV}}=\text{O}$  intermediates

DPPH (2, 2-diphenyl-1-picrylhydrazine) radical quenching assay was performed for the detection of reactive  $\cdot\text{OH}$  radical formation. Hydroxyl radical was formed during the homolytic cleavage of hydroperoxo species when  $\text{H}_2\text{O}_2$  was added in complex **3**. (As shown in scheme 3.6). The color of the DPPH solution was disappear when the complex **3** and  $\text{H}_2\text{O}_2$  were added simultaneously in the DPPH solution and electronic spectra of this radical was recorded by UV-visible spectroscopy.

In UV- visible, the band at 520 nm was responsible for this radical and it was gradually decrease when it reacted with  $\cdot\text{OH}$  radical. (As shown in the Fig. 3.11). Similar reaction was performed with the complex **4**. The concern spectrum was depicted in the Fig. 3.12.

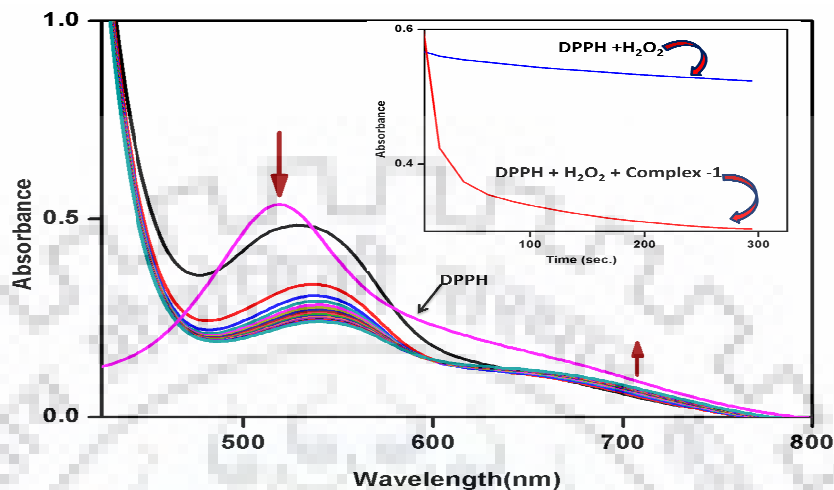


**Fig. 3.11** Reaction of complex **3** ( $1 \times 10^{-6} \text{M}$ ) with DPPH ( $1 \times 10^{-5} \text{M}$ ) in the presence of  $\text{H}_2\text{O}_2$  ( $20 \mu\text{M}$ )

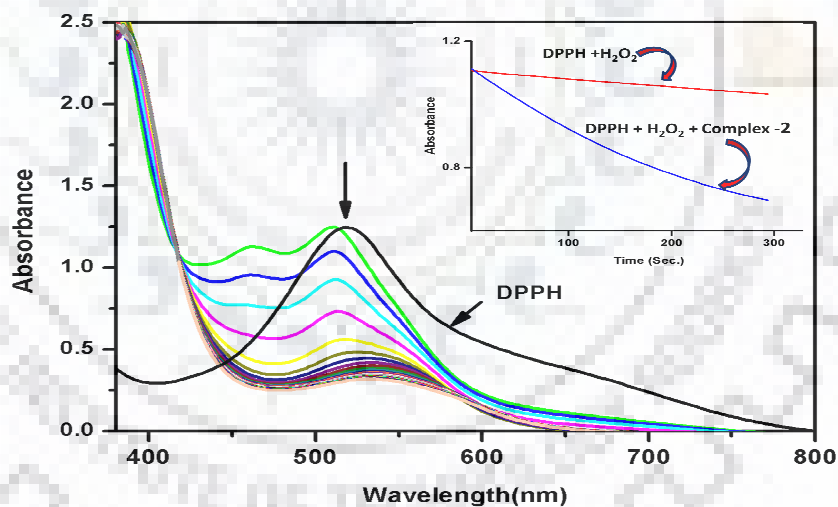


**Fig. 3.12** Reaction of complex **4** ( $2 \times 10^{-6} \text{M}$ ) with DPPH ( $2 \times 10^{-5} \text{M}$ ) in the presence of  $\text{H}_2\text{O}_2$  ( $20 \mu\text{M}$ )

### 3.4 Theoretical investigation

Theoretical calculations were employed to develop a deeper understanding for the  $\text{Fe}^{\text{IV}}=\text{O}$  stabilization. We have performed DFT calculation for the intermediate  $\text{Fe}^{\text{III}}-\text{OOH}$ ,  $\text{Fe}^{\text{IV}}=\text{O}$ , we have found out that  $\text{Fe}^{\text{IV}}=\text{O}$  was more stable because of  $(\text{Fe}^{\text{IV}}=\text{O} \cdots \text{H}-\text{N})$  hydrogen

bonding (shown in the Fig. 3.13 for complex **3** and Fig. 3.14 for complex **4**). The Gibbs free energy ( $\Delta G$ ) for the complex **3**, **4**,  $\text{Fe}^{\text{III}}\text{-OOH}$  and  $\text{Fe}^{\text{IV}}\text{=O}$  were calculated. The relative  $\Delta G$  value for  $\text{Fe}^{\text{IV}}\text{=O}$  species was found more negative, it indicated the stabilization  $\text{Fe}^{\text{IV}}\text{=O}$  reactive intermediate as compare to the other species. As shown in Fig. 3.15 and 3.16.

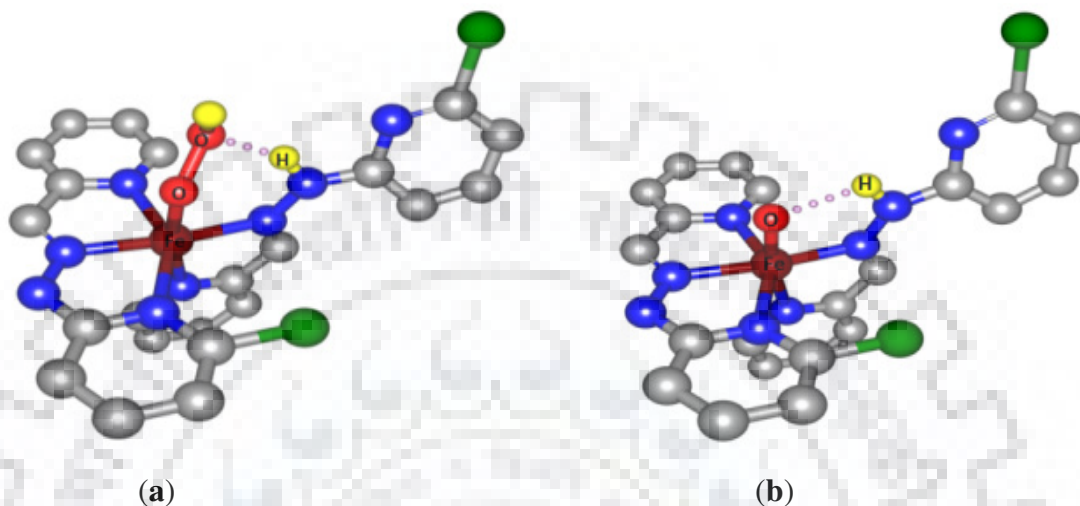


**Fig. 3.13** Geometry optimizations, of intermediates  $\text{Fe}^{\text{III}}\text{-OOH}$  and  $\text{Fe}^{\text{IV}}\text{=O}$  species. The dotted line represents the hydrogen bonding

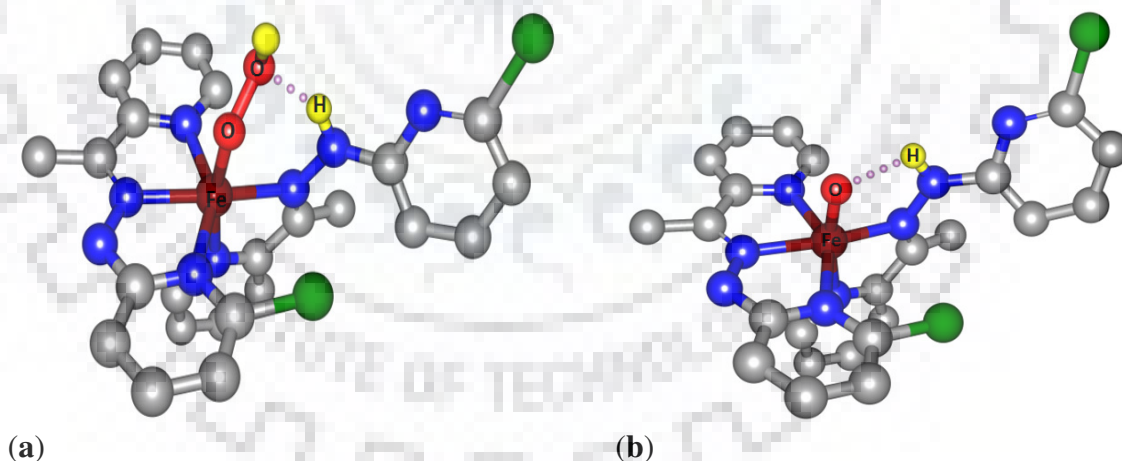


**Fig. 3.14** Geometry optimizations, relative free energies of complex **4** at room temperature. With the view of this indication of  $\Delta G$  value for  $\text{Fe}^{\text{IV}}\text{=O}$  stabilization helps in the oxidation of hydrocarbons (shown in the Fig. 3.15 for complex **3** and Fig. 3.16 for complex (**4**))

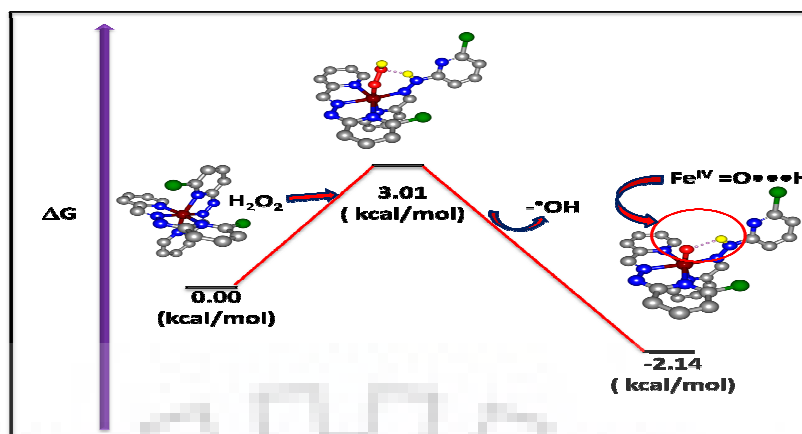


**Fig. 3.15** Profile of the calculated relative  $\Delta G$  for the reaction of hydrogen peroxide and complex **3**, the formation of hydroperoxo species and by removal of  $\cdot\text{OH}$  radical stabilization of  $\text{Fe}^{\text{IV}}=\text{O}$  intermediate. The relative Gibbs free energies are given in kcal mol<sup>-1</sup>

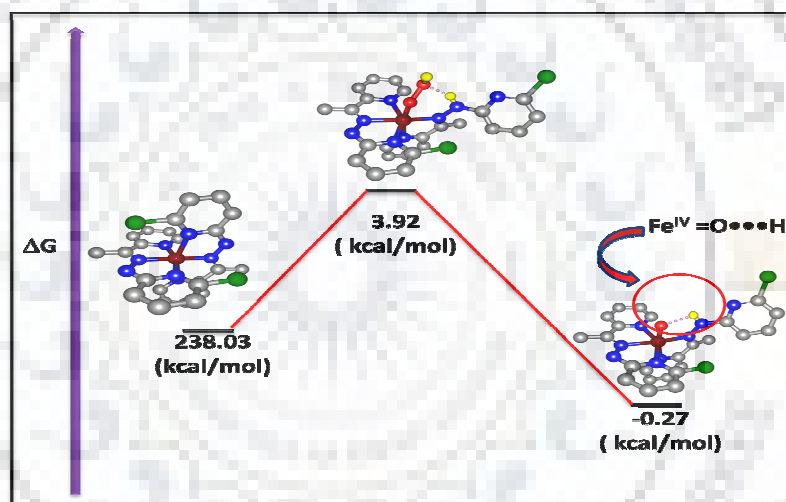


**Fig. 3.16** Profile of the calculated relative  $\Delta G$  for the reaction of hydrogen peroxide and complex **4**, the formation of hydroperoxo species and by removal of  $\cdot\text{OH}$  radical stabilization of  $\text{Fe}^{\text{IV}}=\text{O}$  intermediate. The relative Gibbs free energies are given in kcal mol<sup>-1</sup>

Mulliken spin density calculations were also done for the both intermediates. It was found out that maximum spin density over the metal centre, for that metal based oxidation reaction involved such type of complexes. The Mulliken spin density of both the intermediates shown in the Fig. 3.17 for complex **3** and Fig. 3.18 for complex **4**.

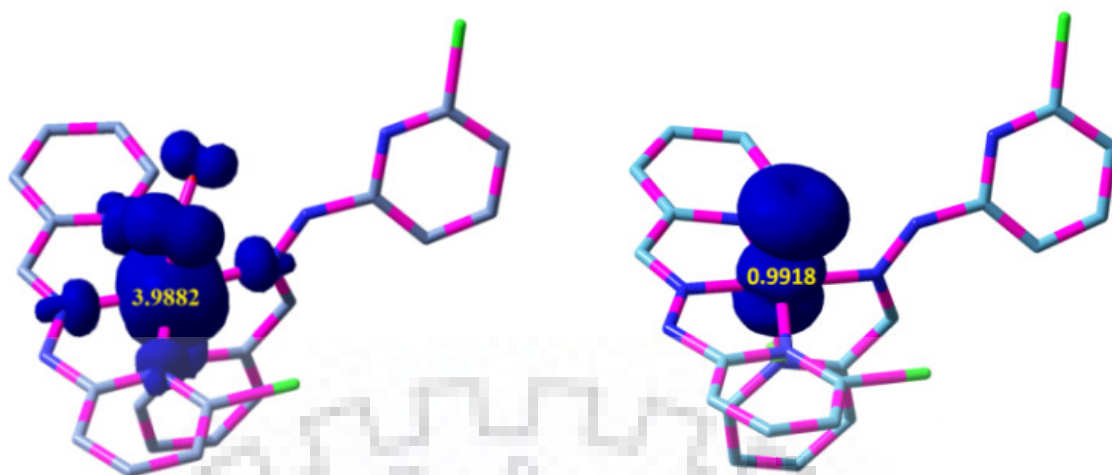


**Fig. 3.17** Spin density plots for  $\text{Fe}^{\text{III}}\text{-OOH}$  and  $\text{Fe}^{\text{IV}}\text{=O}$  intermediates from complex **3** (isosurface cutoff value = 0.002)

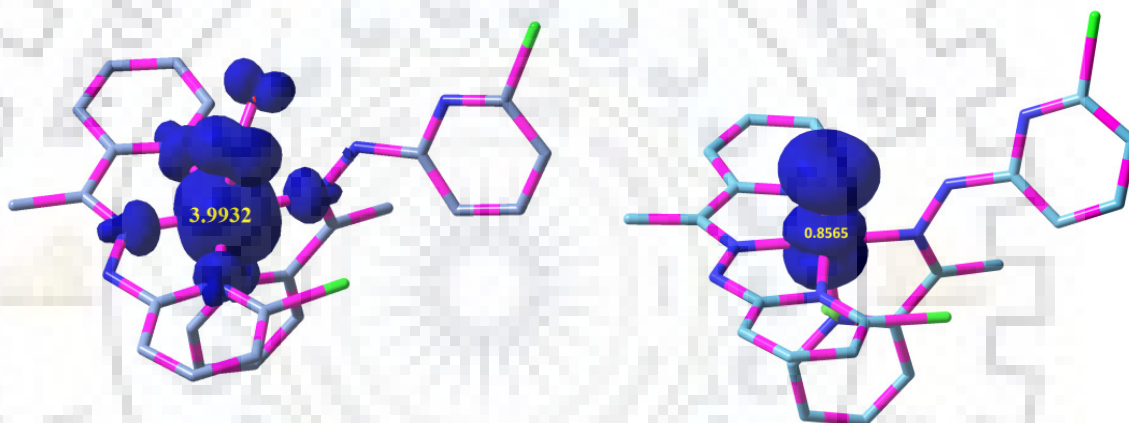


**Fig. 3.18** Spin density plot for  $\text{Fe}^{\text{III}}\text{-OOH}$  and  $\text{Fe}^{\text{IV}}\text{=O}$  intermediates from complex **4** (isosurface cutoff value= 0.002)

In complex **4** a band around 654 nm ( $\epsilon = 1650 \text{ M}^{-1}\text{cm}^{-1}$ ) appeared on adding (1.5equiv.)  $\text{H}_2\text{O}_2$  which decrease in short period time of and a new band around 725 nm ( $\epsilon = 670 \text{ M}^{-1}\text{cm}^{-1}$ ) appear with a fast color change of red to green at  $0^\circ\text{C}$ . As shown in Fig. 3.19 and Scheme 3.7.

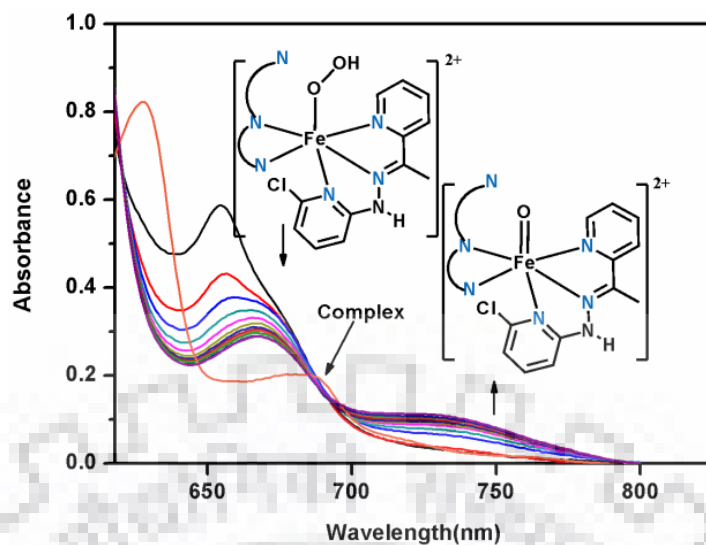
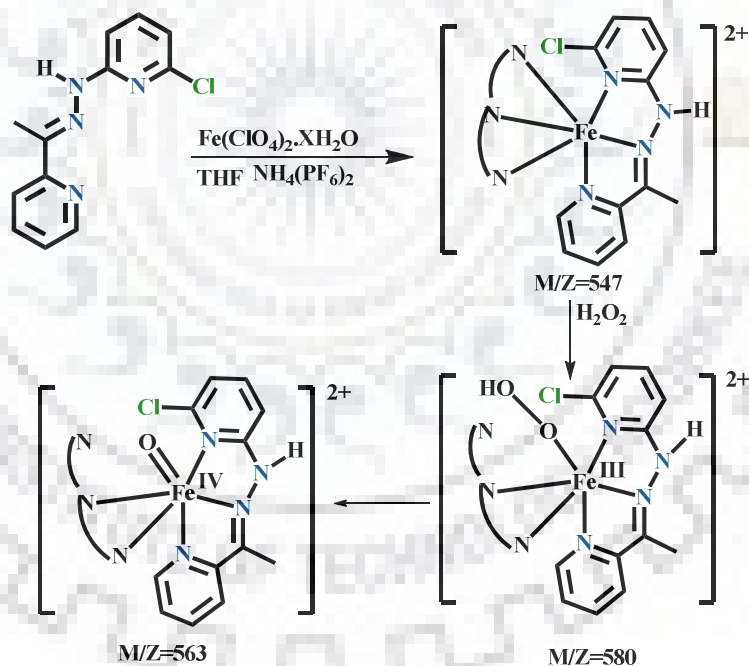


**Fig. 3.19** UV-visible spectral changes observed during the reaction of  $[\text{Fe}^{\text{II}}(\text{L}^4)_2]^{2+}(\text{PF}_6)_2(\mathbf{4})$  ( $1.25 \times 10^{-4} \text{ M}$ ) with 1.5 equiv. of  $\text{H}_2\text{O}_2$  in MeCN at  $-0^\circ\text{C}$ . The UV-visible spectral changes clearly indicate the reaction monitored at 654 nm and 725 nm due to the formation of  $[\text{Fe}^{\text{IV}}(\text{O})(\text{L}^4)_2]^{2+}$



**Scheme 3.7** Reaction pathway for the formation  $[\text{Fe}^{\text{IV}}(\text{O})(\text{L}^4)_2]^{2+}$  species using  $\text{H}_2\text{O}_2$

ESI-MS spectra of complex **4** was recorded in the presence of  $\text{H}_2\text{O}_2$ , the mass peak of  $[\text{Fe}^{\text{IV}}(\text{O})(\text{L}^4)_2]^{2+}$  ( $m/z = 563.0566$ ) species was observed in acetonitrile solvent

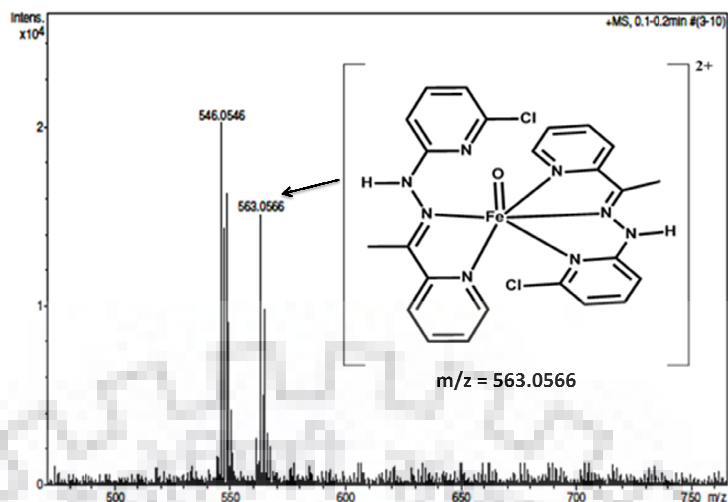
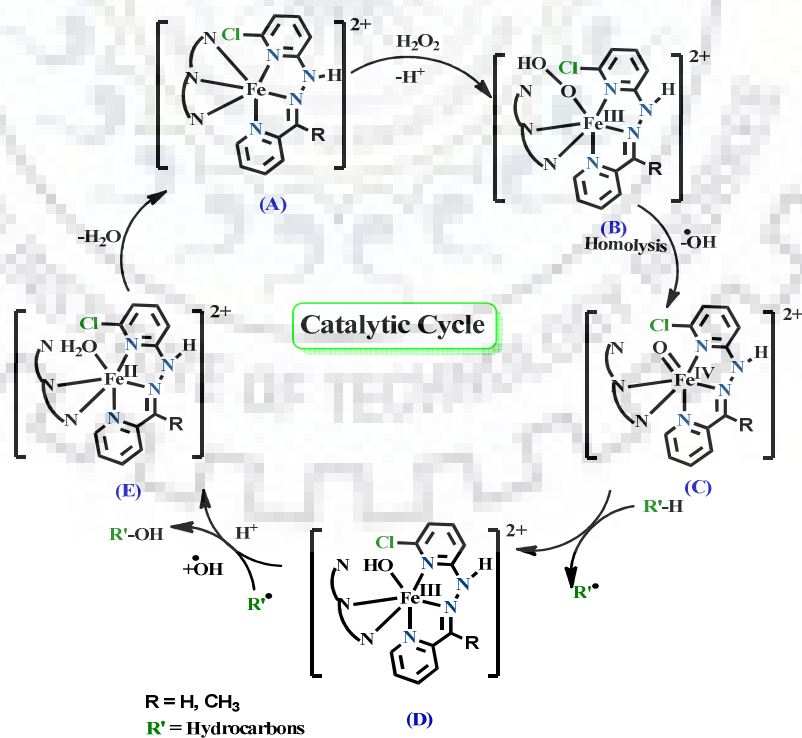


**Fig. 3.20** ESI-MS spectra of complex **4**, recorded in acetonitrile for the formation of  $[\text{Fe}^{\text{IV}}(\text{O})(\text{L}^4)_2]^{2+}$   $m/z=563.0566$

### 3.5 Proposed mechanism for oxidation

The probable mechanism for the oxidation of hydrocarbons using complex **3** and complex **4** have been shown in the Scheme 3.8. By the addition of hydrogen peroxide one nitrogen opened by removing the  $\text{H}^+$  and generates an active species  $[\text{Fe}(\text{L}^3)_2\text{OOH}]^{2+}$ .



**Scheme 3.8** Proposed reaction mechanism for oxidation of hydrocarbons

The hydroperoxo species of both the complexes upon homolysis generate  $\cdot\text{OH}$  radical and formed a  $\text{Fe}^{\text{IV}}=\text{O}$  intermediates, as shown in step "C". Generation of  $\text{Fe}^{\text{IV}}=\text{O}$  intermediates for the both complexes further supported by UV-visible titration (As shown in Fig. 3.4 and Fig. 3.19 ) and ESI-MS spectrum (As shown in Fig. 3.8 and 3.20). This  $\text{Fe}^{\text{IV}}=\text{O}$  species further upon addition of substrate molecule generate  $\text{R}\cdot$  species (step C). Further  $\cdot\text{OH}$  radical leads to alcohol formation in step "D" and water elimination happen in step "E" followed by  $[\text{Fe}(\text{L}^{\text{n}})_2]^{2+}$  ( $n=1, 2$ ) species formed. In this mechanism substrate oxidized in the presence of high-valent oxo-species.<sup>304, 319</sup>

Investigation of catalytic oxidation of cyclohexane, benzyl alcohol, 1- phenyl ethanol, and fluorene clearly indicated that both the complexes selectively converted benzyl alcohol, 1-phenyl ethanol, and fluorene to benzaldehyde, acetophenone, and fluorenone. Since  $\text{Fe}^{\text{IV}}=\text{O}$  was the key intermediate for the oxidation of alkane because it abstract the hydrogen from the alkane and same time reactive oxygen species ( $\cdot\text{OH}$ ) which was consumed in oxidation reaction. From the literature<sup>305</sup> it was clear that these reactive oxygen species utilise for the degradation of different organic dyes.

### **3.6 Dye degradation**

Organic dyes are chemically stable and not biodegradable in water, which makes them potentially harmful for the eco-environment.<sup>320-321</sup> Orange II, and methylene blue (MB) are the typical pollutants, highly toxic and difficult to degrade, have become one of the most serious global environmental issues today<sup>322-323</sup> Therefore, an effective and economical technique needs to be developed to reduce the concentration of these organic pollutants before releasing the wastewater into the aquatic environment. The degradation experiment was carried out in acetonitrile solvent and it was monitored using UV-visible absorbance at different wavelength and GC-MS spectrophotometer for corresponding dyes.



### 3.6.1 Degradation of orange II dye

This dye was degraded in the presence of both the complexes, and degraded products were determined on the bases of GC-MS analysis. Since the high-valent hydroperoxo and oxo species are more stable in both the complexes, so degradation mechanism was proposed on the bases of that intermediates. (As shown in the. 3.21 and scheme 3.9)

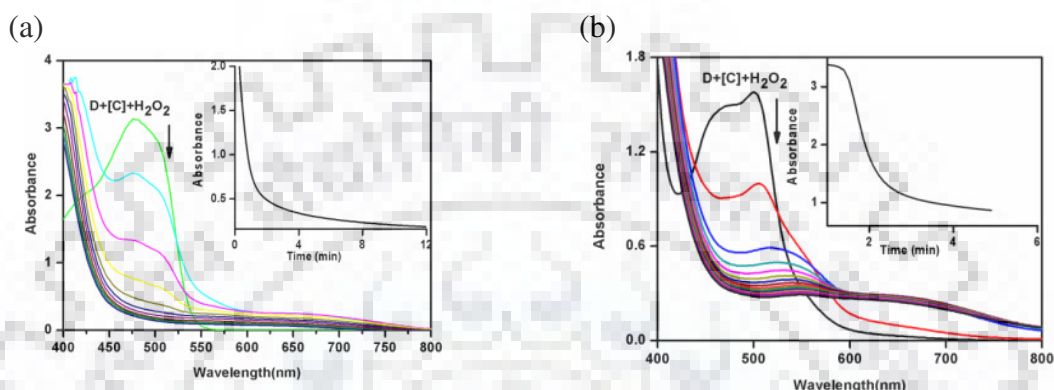
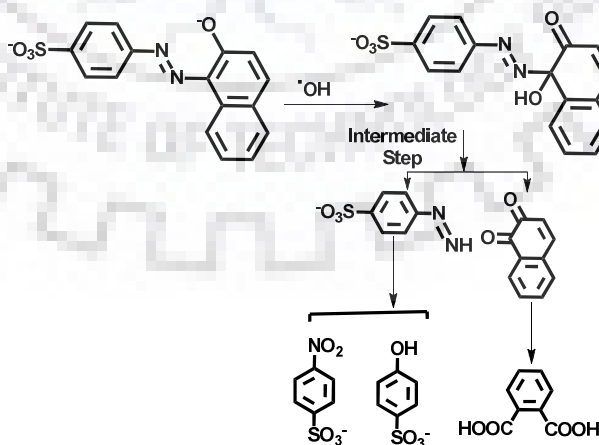


**Fig. 3.21** Oxidative degradation of orange II dye (D) ( $1 \times 10^{-3} \text{M}$ ). In the presence of complex  $[\text{Fe}^{\text{II}}(\text{L}^3)_2](\text{ClO}_4)_2$  (**3**) (a) and  $[\text{Fe}^{\text{II}}(\text{L}^4)_2](\text{PF}_6)_2$  (**4**) ( $1 \times 10^{-6} \text{M}$ ) with  $\text{H}_2\text{O}_2$  (20 equivalent) in acetonitrile

The degradation of orange II was found much faster with complex **4** as compare to complex **3**. This is probably due to methyl group present on the azomethine bonds which stabilise the metal centre at higher oxidation state which correspond to stabilise the intermediates such as hydroperoxo and oxo which increase the oxidation reaction.



**Scheme 3.9** Degraded products of orange II dye

### 3.6.2 Degradation of methylene blue

Oxidative degradation of methylene blue was also done in the presence of both the complexes. It was found out that the degradation in the presence of complex **4** was happened faster than complex **3**. Same condition of hydroperoxo and oxo were responsible for the faster degradation of methylene blue dye. The oxidative degraded products were analysed and determined with the help of UV-visible and GC-MS analysis. (As shown in the Fig. 3.22 and scheme 3.10)

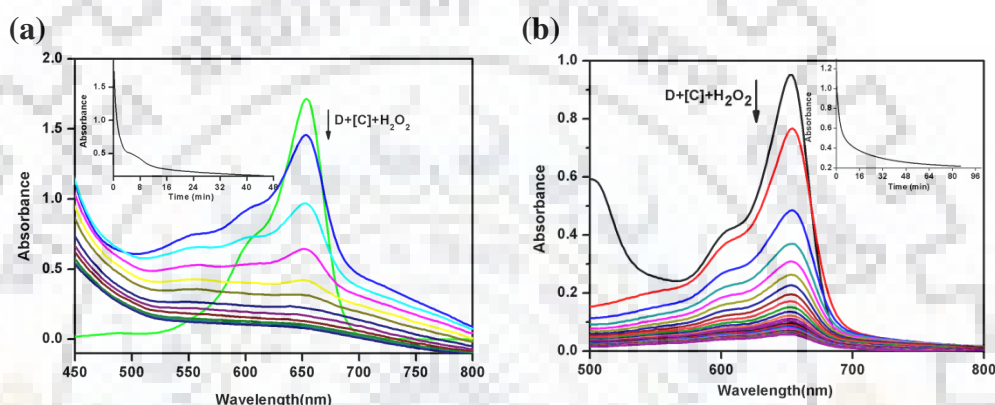
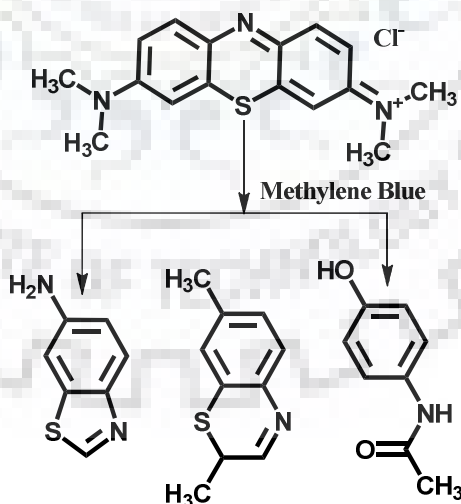


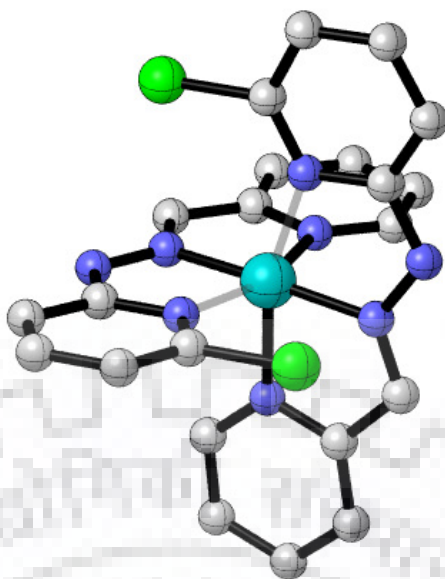
**Fig. 3.22** Degradation of methylene blue ( $1 \times 10^{-3} \text{M}$ ) in the presence of complex  $[\text{Fe}^{\text{II}}(\text{L}^3)_2](\text{ClO}_4)_2$  (**3**) (a) and  $[\text{Fe}^{\text{II}}(\text{L}^4)_2](\text{PF}_6)_2$  (**4**) ( $1 \times 10^{-6} \text{M}$ ) with  $\text{H}_2\text{O}_2$  (20 equivalent) in  $\text{CH}_3\text{CN}$



**Scheme 3.10** Degraded product of methylene blue dye

### 3.7 Theoretical calculations

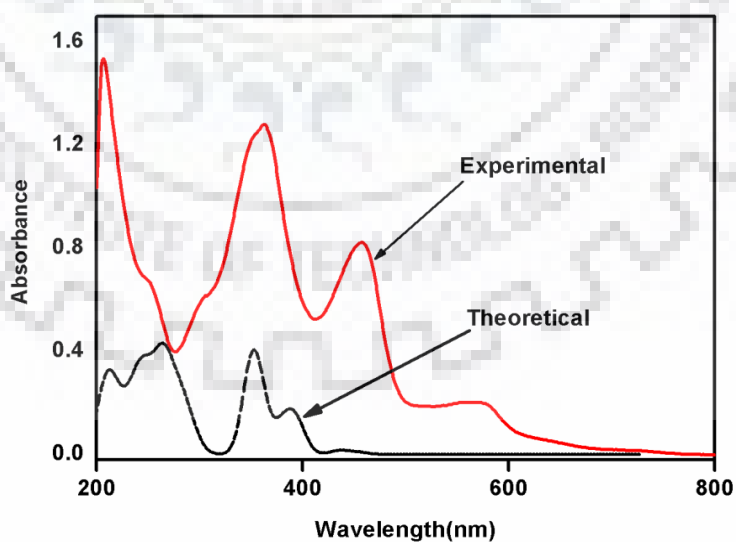
The geometry optimizations for both the complexes were performed at DFT level (Fig. 3.23 and 3.26).<sup>287</sup> Theoretical experiments for both the complexes have been carried out using the density functional theory (DFT) employing the LANL2DZ basis set. The molecular orbital diagram and significant contribution of iron and ligand in HOMOs and LUMOs have been shown in Fig. 3.45 and 3.46. The percentage contribution of particular atom in the complex also be calculated shown in Table 3.9 and 3.11. Total electron density plot over the molecule calculated using B3LYP level. (As shown in Fig. 3.25 and Fig. 3.27) A TD-DFT calculation was also performed for major transition along with their orbital contribution shown in Table 3.10 and 3.12. and Fig. 3.24 for the complex **3** the transition occur with the oscillator strength at different wavelength, at 240 nm the oscillator strength was found 0.0168 due to different transition like HOMO-8  $\rightarrow$  LUMO+1 (32%), HOMO-2  $\rightarrow$  LUMO+7 (8.5%) at 328 nm with oscillator strength(0.0018) the major transition was HOMO-2  $\rightarrow$  LUMO+9 (30%), at 457 nm with oscillator strength (0.0058) the major transition HOMO  $\rightarrow$  LUMO (64.6%) and 503nm with oscillator strength(0.0002) HOMO-3  $\rightarrow$  LUMO+6 (25%) was the major transition. For the complex **4** the transition along with oscillator strength was found to be H-5  $\rightarrow$  LUMO (70%) (0.007) at 270 nm, H-1  $\rightarrow$  L+2 (84%) (0.0107) at 307nm, HOMO  $\rightarrow$  LUMO (71%) (0.0048) at 449nm, H-3  $\rightarrow$  L+9 (23%) (0.0002) at 508nm. The energy gaps between HOMO and LUMO in both the complexes were found almost similar so both the complexes showed similar kind of activities only the rate performance of the complex **4** was found to be greater than the complex **3**. In HOMO the electron density existed over the metal center and in LUMO the major electron density was found over the ligand center so metal based oxidation reaction should be more favorable in these types of complexes.



**Fig. 3.23** Ground state optimized geometry of complex **3** using B3LYP/LANL2DZ

**Table 3.9** Percentage contribution of complex **3** in different orbitals

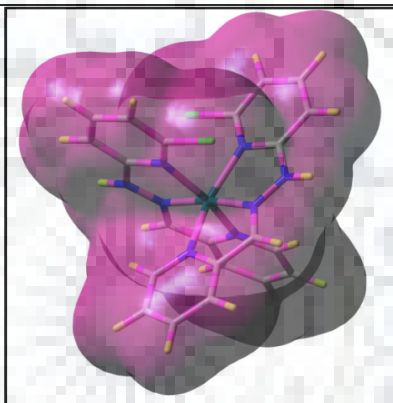
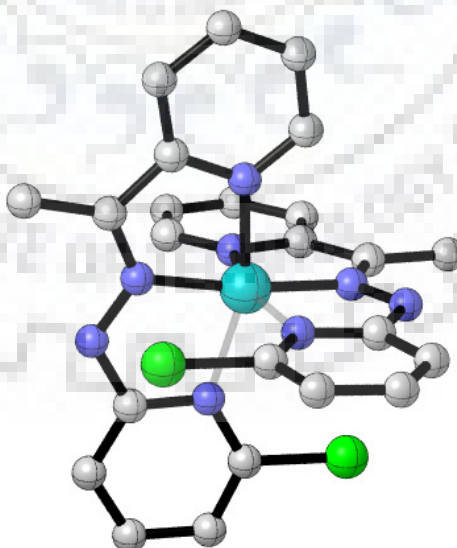
Orbitals	(Iron) Fe	Ligand L <sup>3</sup>	Ligand L <sup>3'</sup>	Main bond type
LUMO+2	75	12	13	3d (Fe)+ $\pi^*$ L <sup>3and 3'</sup>
LUMO+1	15	43	42	3d (Fe)+ $\pi^*$ L <sup>3and 3'</sup>
LUMO	14	43	43	3d (Fe)+ $\pi^*$ L <sup>3and 3'</sup>
HOMO	79	11	10	3d (Fe)+ $\pi$ L <sup>3and 3'</sup>
HOMO-1	74	13	13	3d (Fe)+ $\pi$ L <sup>3and 3'</sup>
HOMO-2	77	12	11	3d (Fe)+ $\pi$ L <sup>3and 3'</sup>



**Fig. 3.24** Experimental (red) and theoretical (black) absorption spectra of complex **3** ( $2 \times 10^{-5}$  M) recorded in acetonitrile

**Table 3.10** Major transition along with their orbital contribution in complex 3

$\lambda_{\max}$ (nm)	f	Transition and their contributions	Energy for transition
240	0.0168	HOMO-8 $\rightarrow$ LUMO+1 = 32% HOMO-2 $\rightarrow$ LUMO+7 = 8.5%	5.1566
328	0.0018	HOMO-4 $\rightarrow$ LUMO+9 = 4.9% HOMO-2 $\rightarrow$ LUMO+9 = 30% HOMO $\rightarrow$ LUMO+9 = 21%	3.5931
457	0.0058	HOMO-4 $\rightarrow$ LUMO = 5.9% HOMO-2 $\rightarrow$ LUMO = 20.5% HOMO-2 $\rightarrow$ LUMO+9 = 2.5% HOMO $\rightarrow$ LUMO = 64.6%	2.7243
503	0.0002	HOMO-5 $\rightarrow$ LUMO+6 = 2.7% HOMO-3 $\rightarrow$ LUMO+6 = 25% HOMO-2 $\rightarrow$ LUMO+9 = 11.9% HOMO-1 $\rightarrow$ LUMO+6 = 15%	2.4398

**Fig. 3.25** Total electron density plot over the molecule calculated using B3LYP level**Fig. 3.26** Ground state optimized geometry of complex 4 using B3LYP/LANL2DZ

**Table 3.11** Percentage contribution of complex **4** in different orbitals

Orbitals	(Iron) Fe	Ligand L <sup>4</sup>	Ligand L <sup>4'</sup>	Main bond type
LUMO+2	74	13	13	3d (Fe)+ $\pi^*$ L <sup>4and 4'</sup>
LUMO+1	13	43	44	3d (Fe)+ $\pi^*$ L <sup>4and 4'</sup>
LUMO	12	44	44	3d (Fe)+ $\pi^*$ L <sup>4and 4'</sup>
HOMO	78	11	11	3d (Fe)+ $\pi$ L <sup>4and 4'</sup>
HOMO-1	74	13	13	3d (Fe)+ $\pi$ L <sup>4and 4'</sup>
HOMO-2	77	12	11	3d (Fe)+ $\pi$ L <sup>4and 4'</sup>

**Table 3.12** Major transition along with their orbital contribution in complex **4**

$\lambda_{\max}$ (nm)	f	Transition and their contributions	Energy for transition
270	0.007	H-6 $\rightarrow$ L+1 (22%), H-5 $\rightarrow$ LUMO (70%)	4.5771
307	0.0107	H-1 $\rightarrow$ L+2 (84%) H-3 $\rightarrow$ L+2 (7%), HOMO $\rightarrow$ L+3 (3%)	4.0298
449	0.0048	H-2 $\rightarrow$ LUMO (13%), HOMO $\rightarrow$ LUMO (71%) H-4 $\rightarrow$ LUMO (7%), H-4 $\rightarrow$ L+9 (2%), H-2 $\rightarrow$ L+9 (3%)	2.7553
508	0.0002	H-4 $\rightarrow$ L+6 (14%), H-3 $\rightarrow$ L+9 (23%), H-2 $\rightarrow$ L+6 (17%), H-1 $\rightarrow$ L+9 (21%) H-5 $\rightarrow$ L+9 (2%), HOMO $\rightarrow$ L+1 (2%), HOMO $\rightarrow$ L+6 (4%)	2.4387

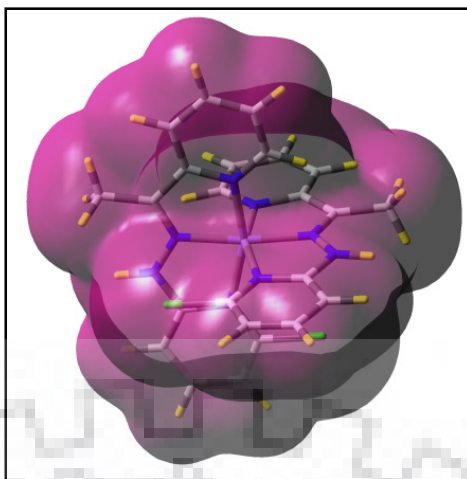


**Fig. 3.27** Complex 4 total electron density plot over the molecule calculated using B3LYP level

### 3.8 Conclusion

Following are the conclusions of the present study. First, inspired by the work of Stefano and co-workers as well as Costas and co-workers we have designed new ligands and synthesized iron complexes. Second, theoretical data clearly indicated the stabilization of hydroperoxo and oxo intermediates through hydrogen bonding. Third, complexes were characterized by different spectroscopic methods and redox properties were examined. Molecular structures of complexes **3** and **4** were determined by X-ray crystallography. Fourth, these complexes were found to be efficient as mild oxidising agents during catalytic activity. Complex **3** and complex **4** selectively converted benzyl alcohol to benzaldehyde, fluorene to fluorenol, 1-phenylethanol to acetophenone. Fifth, UV-vis. ESI-MS and resonance Raman data clearly authenticated the formation of hydroperoxo and oxo intermediates. Sixth, these complexes were found to be efficient in the degradation of orange II and methylene blue dyes through oxidation chemistry. Probable mechanism was also supported the formation of high-valent iron hydroperoxo and oxo intermediates. Details of these works and studies on extensive oxidation chemistry are under progress.

### 3.9 Experimental section

All the solvents used were reagent grade. 2-chloro-6-hydrazinylpyridine was prepared by reported procedure.<sup>324</sup> Pyridine 2-aldehyde was purchased from Acros organics, USA. Solvents used for spectroscopic studies were HPLC grade and purified by standard procedure before use.

#### 3.9.1 Physical measurements

Elemental analyses were carried micro analytically at Elemental Vario EL III. Infra red spectra were obtained as KBr pellets with Thermo Nicolet Nexus FT-IR spectrometer, using 16 scans and were reported in  $\text{cm}^{-1}$ . Electronic absorption spectra were recorded with an UV-visible spectrophotometer, Shimadzu (UV-2401). A PerkinElmer Clarus 680-ClarusSQ8T Gas chromatograph-Mass spectrometer was used to record the GC-MS spectra. Cyclic voltammetry measurements were carried out using a CH-600 electroanalyzer. A conventional three-electrode arrangement was using consisting a platinum wire as auxiliary electrode, glassy carbon as working electrode and the Ag(s)/AgCl as reference electrode. These measurements were performed in the presence of 0.1 M tetrabutylammonium perchlorate (TBAP) as the supporting electrolyte, using complex concentration  $10^{-3}$  M in acetonitrile. The ferrocene/ferrocenium couple was found at  $E_{1/2} = +0.40$  scan rate 0.1 V/s, with respect to Ag/AgCl under the same experimental conditions. Most of the experiments were performed at room temperature and solutions were thoroughly degassed with nitrogen prior to beginning the experiments. The X-ray data collection and processing for the complexes were performed on Bruker Kappa Apex-II CCD diffractometer by using graphite monochromated Mo-K $\alpha$  radiation ( $\lambda = 0.71070 \text{ \AA}$ ) at 296 K. Crystal structures were solved by direct methods. Structure solution, refinement and data output were carried out with the SHELXL program.<sup>325-326</sup> All non-hydrogen atoms were refined anisotropically. Hydrogen atoms were placed in geometrically calculated positions and refined using a riding model.





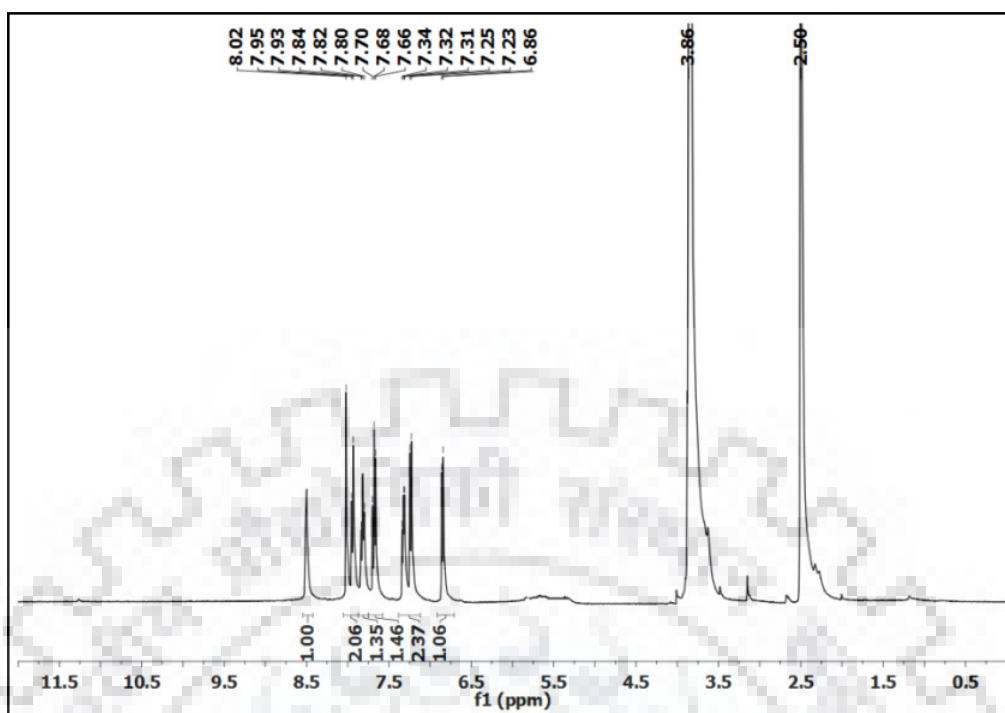


Fig. 3.29  $^1\text{H}$  NMR spectra of ligand  $\text{L}^3$  with  $\text{D}_2\text{O}$  in  $\text{DMSO-d}_6$

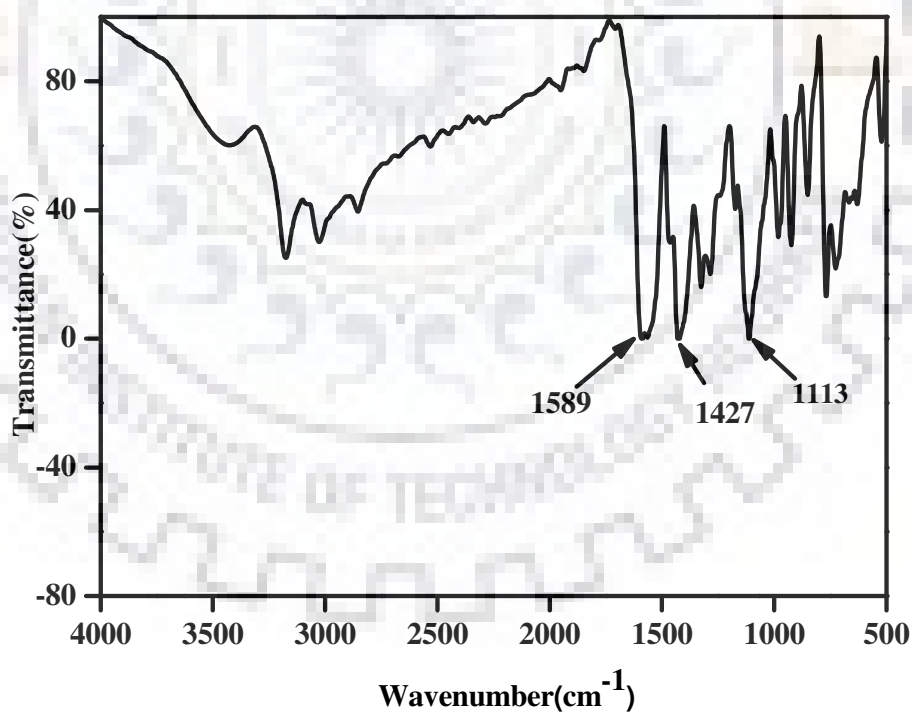


Fig. 3.30 IR spectrum of ligand  $\text{L}^3$

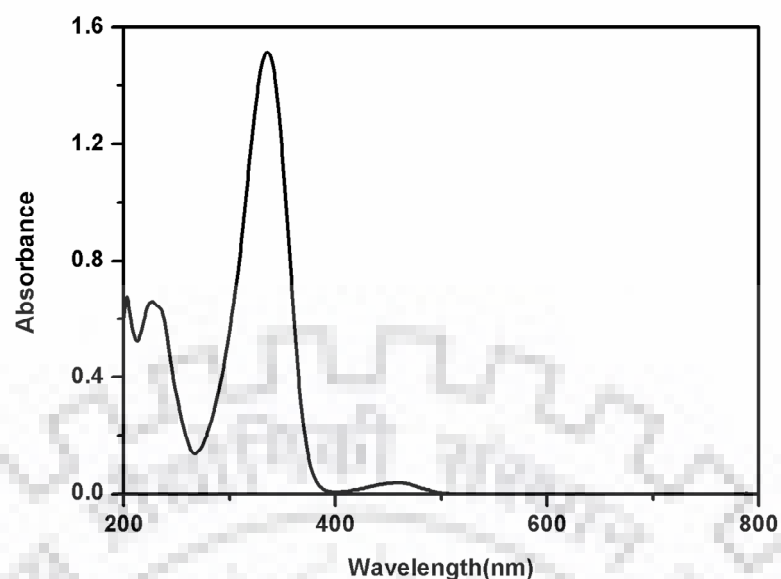


Fig. 3.31 UV-visible spectrum of ligand L<sup>3</sup>

### 3.9.2.2 Synthesis of Ligand [L<sup>4</sup>]

The ligand L<sup>4</sup> was synthesized using 2-chloro-6-hydrazinylpyridine (2mmol 0.286g) and (2 mmol 0.242g) 2-acetyl pyridine into 1:1 ratio by dissolving in 20 ml methanol. The reaction mixture was refluxed at 80°C for 2 hrs. After 2 hrs dil HCl was added into the reaction and the reaction was allowed for another 2 hours. After 4 hours of refluxed the reaction mixture was stirred until the yellow precipitate was obtained. The ligand was recrystallized in dichloromethane. Yield 82%. Anal. Calcd for C<sub>12</sub>H<sub>11</sub>ClN<sub>4</sub> (246.70) C, 58.42; H, 4.49; N, 22.71. Found: C, 58.01; H, 4.02; N, 23.01. <sup>1</sup>H NMR (400 MHz, DMSO-*d*<sub>6</sub>): 10.90 (s, 1H), 8.77-8.36 (d, 1H), 8.34-8.28 (m, 2H), 7.80-7.75 (m, 3H), 7.00-6.98 (d, 1H), 2.43(m, 3H) IR data (KBr,  $\nu_{\max}/\text{cm}^{-1}$ ): 1599,  $\nu_{\text{C=Nimine}}$ , 1429, 1348, 1120, 763. UV-visible [CH<sub>3</sub>CN  $\lambda_{\max}/\text{nm}$  ( $\epsilon/\text{M}^{-1}\text{cm}^{-1}$ ): 234(6700), 324(15,730), 473(740).

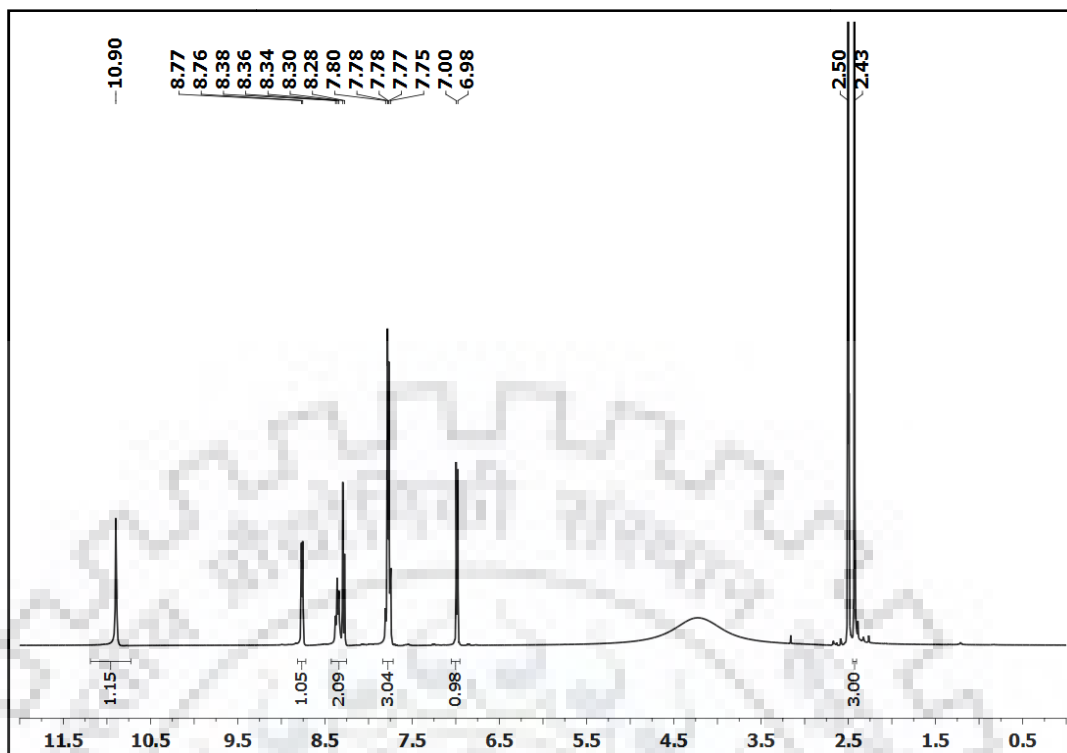


Fig. 3.32  $^1\text{H}$  NMR spectra of ligand  $\text{L}^4$  in  $\text{DMSO-d}_6$

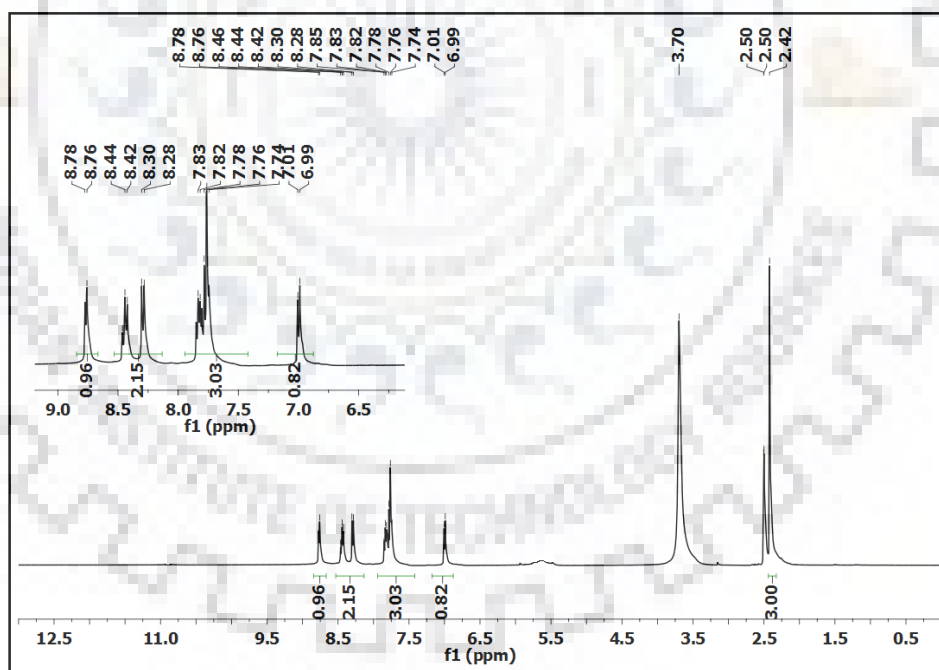


Fig. 3.33  $^1\text{H}$  NMR spectra of ligand  $\text{L}^4$  with  $\text{D}_2\text{O}$  in  $\text{DMSO-d}_6$

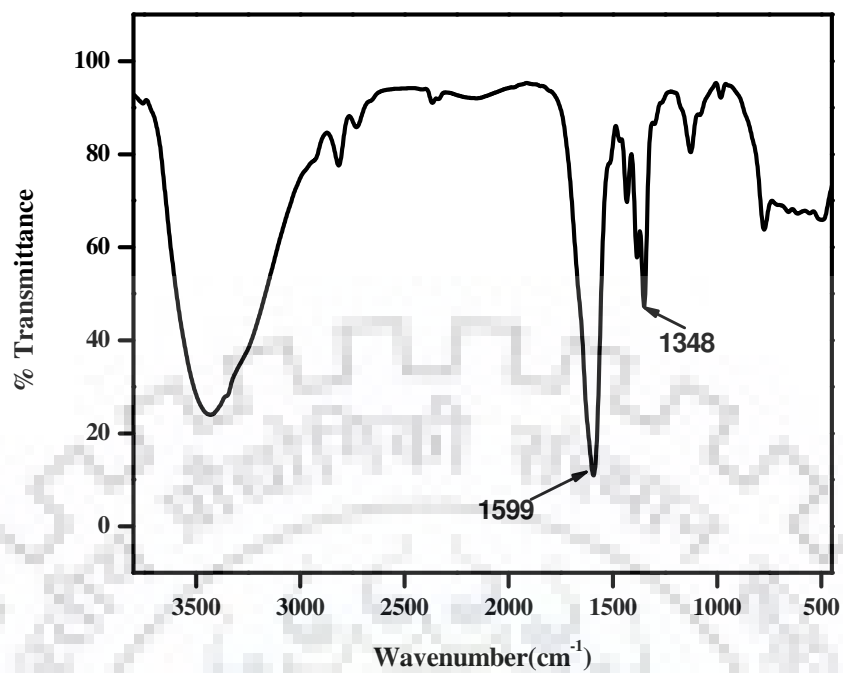


Fig. 3.34 IR spectrum of ligand L<sup>4</sup>

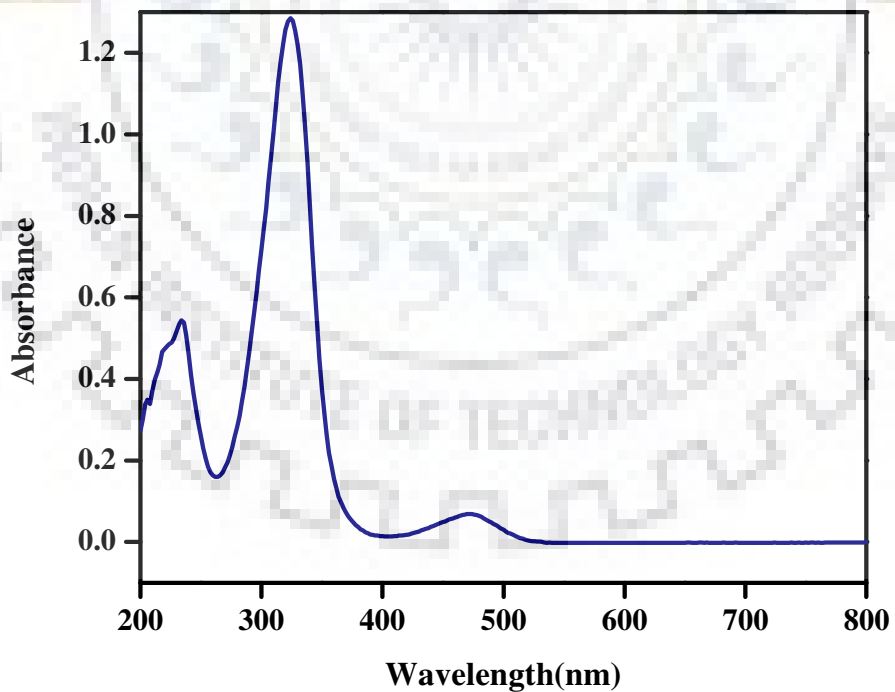


Fig. 3.35 UV-visible spectrum of ligand L<sup>4</sup>

### 3.9.3 Synthesis of metal complexes

#### 3.9.3.1 Synthesis of complex $[\text{Fe}^{\text{II}}(\text{L}^3)_2](\text{ClO}_4)_2$ (**3**)

A batch of ligand  $\text{L}^3$  (0.2 mM, 0.0464 g) was dissolved into 3 mL of tetrahydrofuran. A solution of  $\text{Fe}(\text{ClO}_4)_2 \cdot x\text{H}_2\text{O}$  (0.1 mM, 0.0254 g) with 2 mL of THF was added dropwise to the above solution. The resulting red solution was stirred for 15 minutes; a red colour precipitate was obtained. The solid was filtered out and washed with diethyl ether. The crystallization of the complex **3** was done by dissolving the complex **3** into dichloromethane in a vial and layered with methanol, red color crystals were obtained within two days. Yield 74%. Anal. Calcd for  $\text{C}_{22}\text{H}_{18}\text{Cl}_4\text{FeN}_8\text{O}_8$  (720.084): C, 36.70; H, 2.52; N, 15.56. Found: C, 36.50; H, 2.50; N, 15.47.  $^1\text{H}$  NMR (400 MHz,  $\text{DMSO}-d_6$ ): 11.45 (s, 2H), 8.47 (d, 2H), 7.96 (s, 2H), 7.91 (d, 2H), 7.89 (t, 2H), 7.76 (t, 2H), 7.26 (t, 2H), 7.18-7.17(d, 2H), 6.79-6.77 (d, 2H). IR data (KBr,  $\nu_{\text{max}}/\text{cm}^{-1}$ ): 1605,  $\nu_{\text{C=Nimine}}$ , 1090, 627,  $\nu_{\text{ClO}_4^-}$ , UV-visible [ $\text{CH}_3\text{CN}$   $\lambda_{\text{max}}/\text{nm}$  ( $\epsilon/\text{M}^{-1}\text{cm}^{-1}$ )]: 240 (24900), 328 (31030), 457(8260), 503 (5890). ESI-MS ( $\text{CH}_3\text{CN}$ ):  $m/z = 519.0317$  for  $[\text{Fe}(\text{L}^3)_2]^{2+}$ .

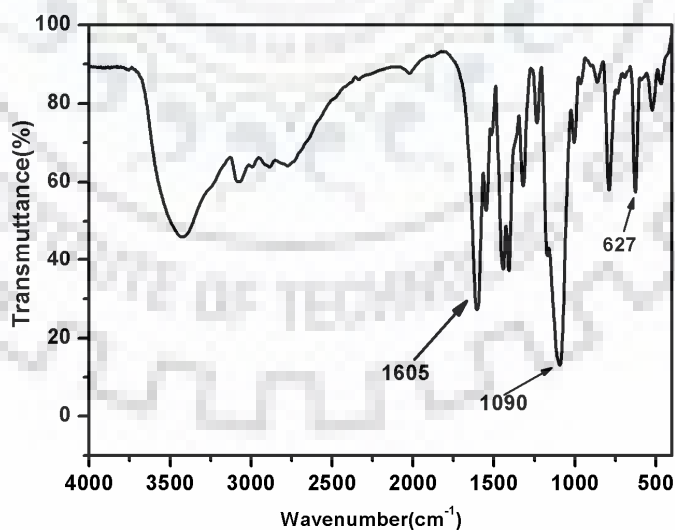


Fig. 3.36 IR spectrum of complex  $[\text{Fe}^{\text{II}}(\text{L}^3)_2](\text{ClO}_4)_2$  (**3**)

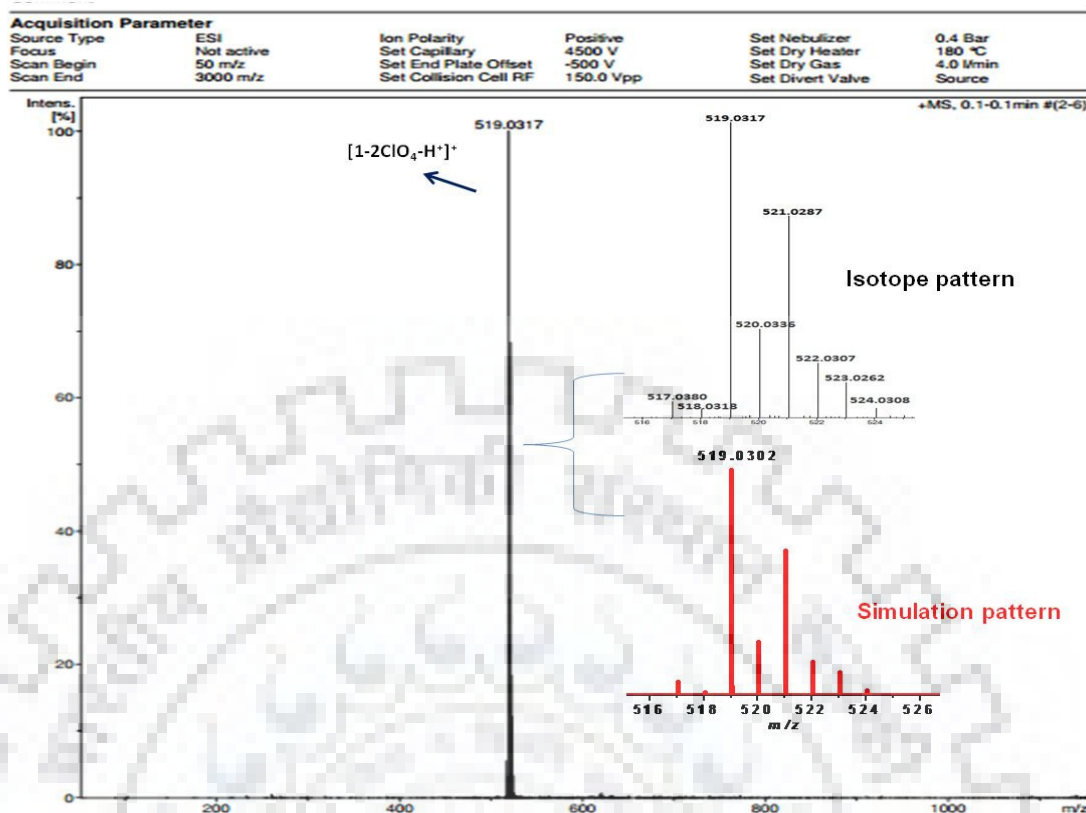


Fig. 3.37 ESI-MS spectrum of complex 3,  $[3-2\text{ClO}_4\text{-H}^+]^+$ ,  $m/z = 519.0317$

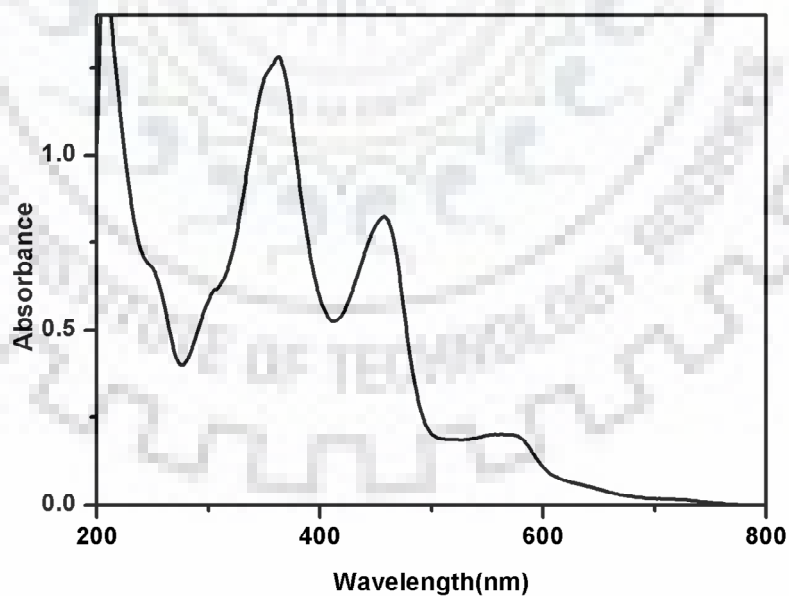


Fig. 3.38 UV-visible spectrum of complex  $[\text{Fe}^{\text{II}}(\text{L}^3)_2](\text{ClO}_4)_2(\mathbf{3})$

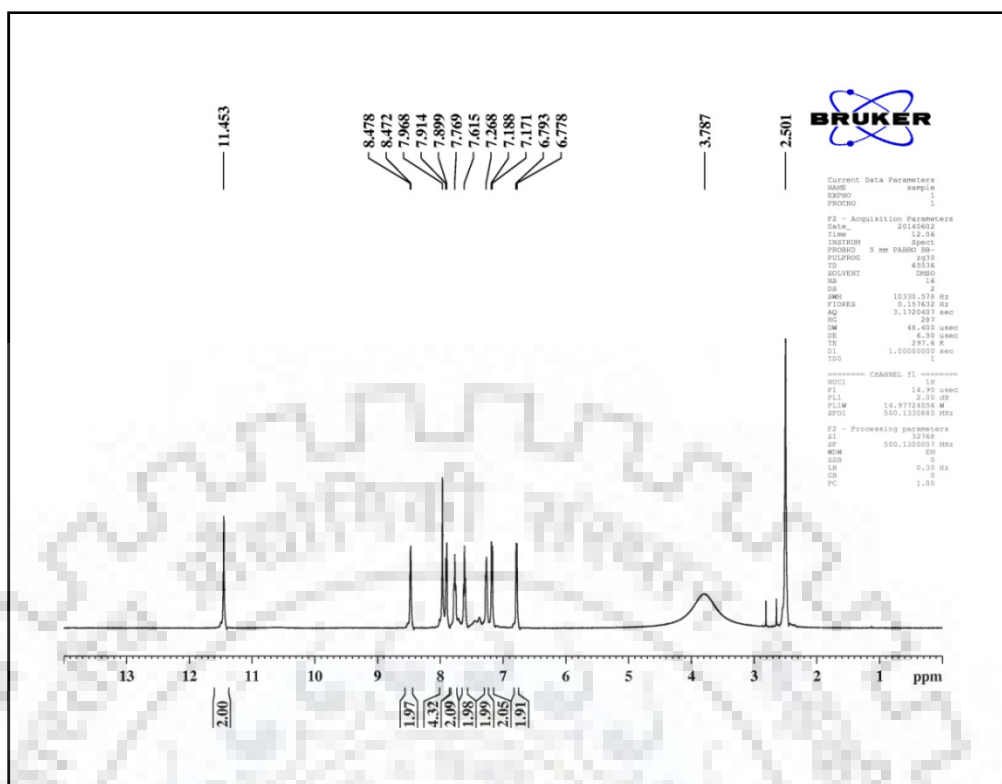


Fig. 3.39  $^1\text{H}$  NMR spectrum of complex  $[\text{Fe}^{\text{II}}(\text{L}^3)_2](\text{ClO}_4)_2(\mathbf{3})$

### 3.9.3.2 Synthesis of complex $[\text{Fe}^{\text{II}}(\text{L}^4)_2](\text{PF}_6)_2(\mathbf{4})$

The ligand ( $\text{L}^4$ ) (2 mM, 0.0492 g) was used to synthesize complex **4** following the same procedure as for complex **3** in THF. Moreover, a solution of  $\text{NH}_4\text{PF}_6$  (0.2 mM) with methanol was added to the reaction mixture in this case to replace the counter anion ( $\text{ClO}_4^-$ ). Single crystals of red color were grown by layering of methanol onto dichloromethane solution of complex **4**. Yield 82%. Anal. Calcd for  $\text{C}_{24}\text{H}_{22}\text{Cl}_2\text{F}_{12}\text{FeN}_8\text{P}_2$  (839.15) C, 34.35; H, 2.64; N, 13.35. Found: C, 34.03; H, 2.60; N, 13.03.  $^1\text{H}$  NMR (400 MHz,  $\text{DMSO}-d_6$ ): 10.40(s, 2H); 8.58-8.56(d, 3H); 8.15-8.13(d, 2H); 7.87-7.85(t, 3H); 7.73-7.70(t, 3H); 7.39-7.34(m, 4H); 6.90-6.88(d, 2H) 3.16(s, 6H). IR data (KBr,  $\nu_{\text{max}}/\text{cm}^{-1}$ ): 1610  $\nu_{\text{C=Nimine}}$ , 1455, 1298, 1122, 836  $\nu_{\text{PF}_6^-}$ , 538. UV-visible [ $\text{CH}_3\text{CN}$   $\lambda_{\text{max}}/\text{nm}$  ( $\epsilon/\text{M}^{-1}\text{cm}^{-1}$ )]: 240 (31,920), 272 (22,910), 324 (56,250), 455 (7,920), 509 (8,220). ESI-MS( $\text{CH}_3\text{CN}$ ):  $m/z = 547.0655$  for  $[\text{Fe}(\text{L}^4)_2]^{2+}$ .



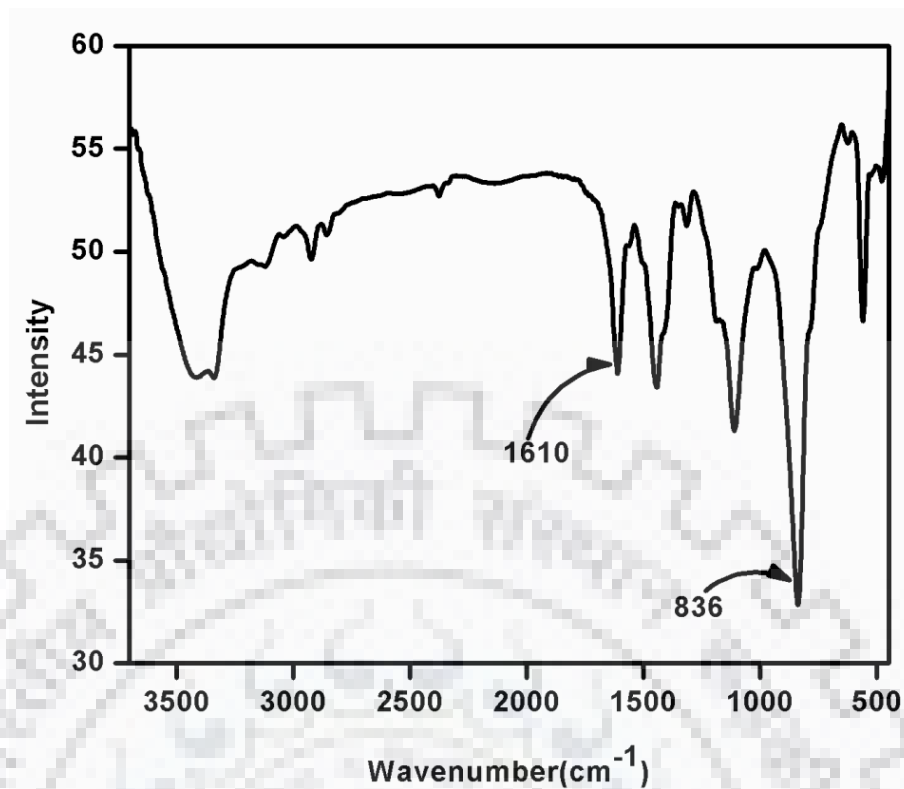


Fig. 3.40 IR spectrum of complex [Fe<sup>II</sup>(L<sup>4</sup>)<sub>2</sub>](PF<sub>6</sub>)<sub>2</sub> (4)

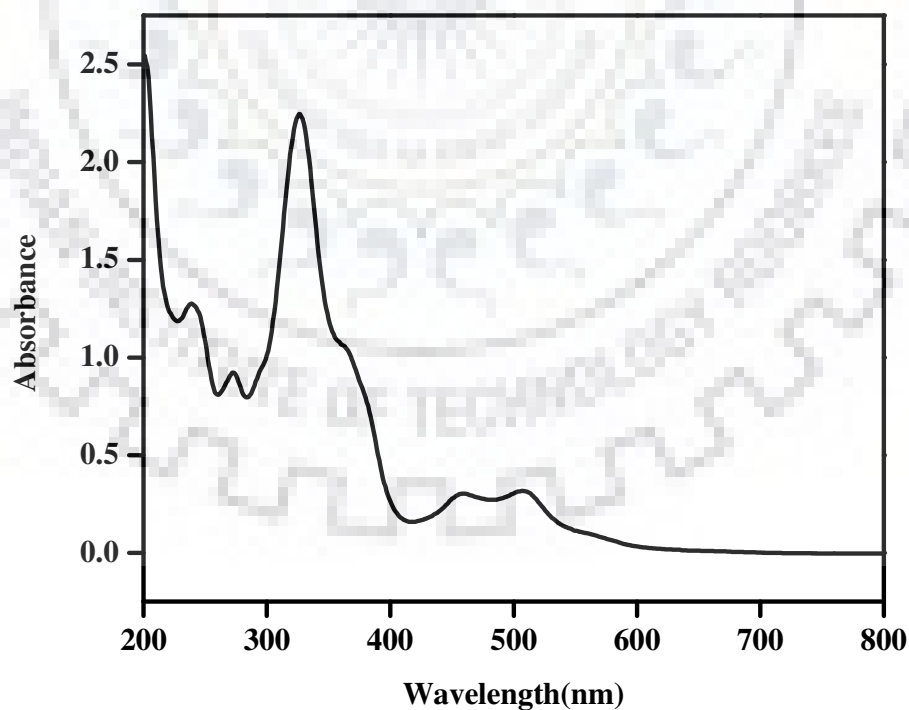


Fig. 3.41 UV-visible spectrum of complex [Fe<sup>II</sup>(L<sup>4</sup>)<sub>2</sub>](PF<sub>6</sub>)<sub>2</sub> (4)

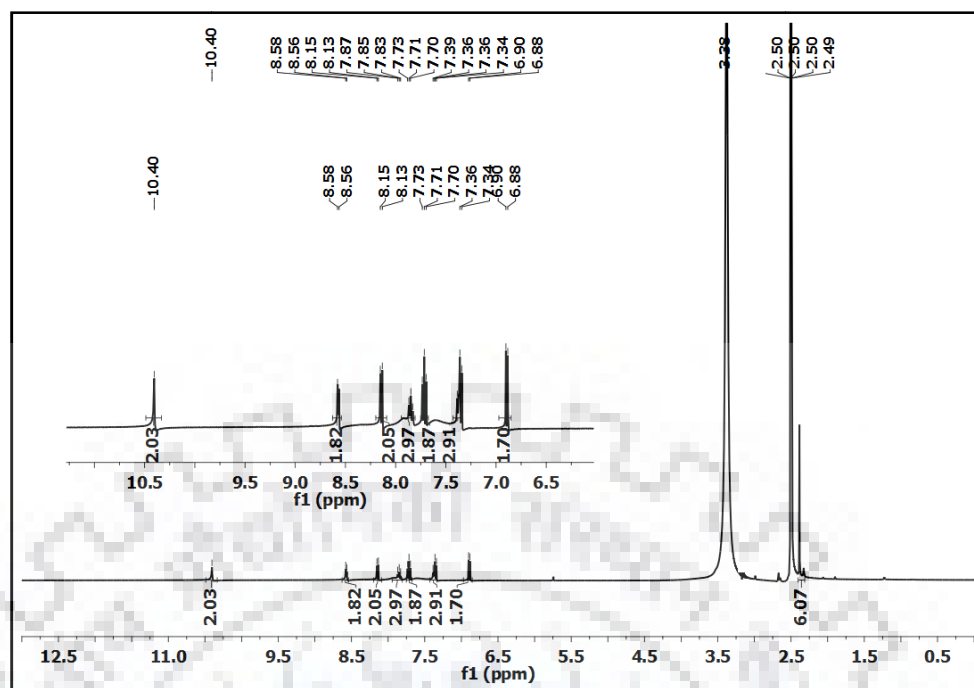


Fig. 3.42  $^1\text{H}$  NMR spectrum of complex  $[\text{Fe}^{\text{II}}(\text{L}^4)_2](\text{PF}_6)_2$  (**4**)

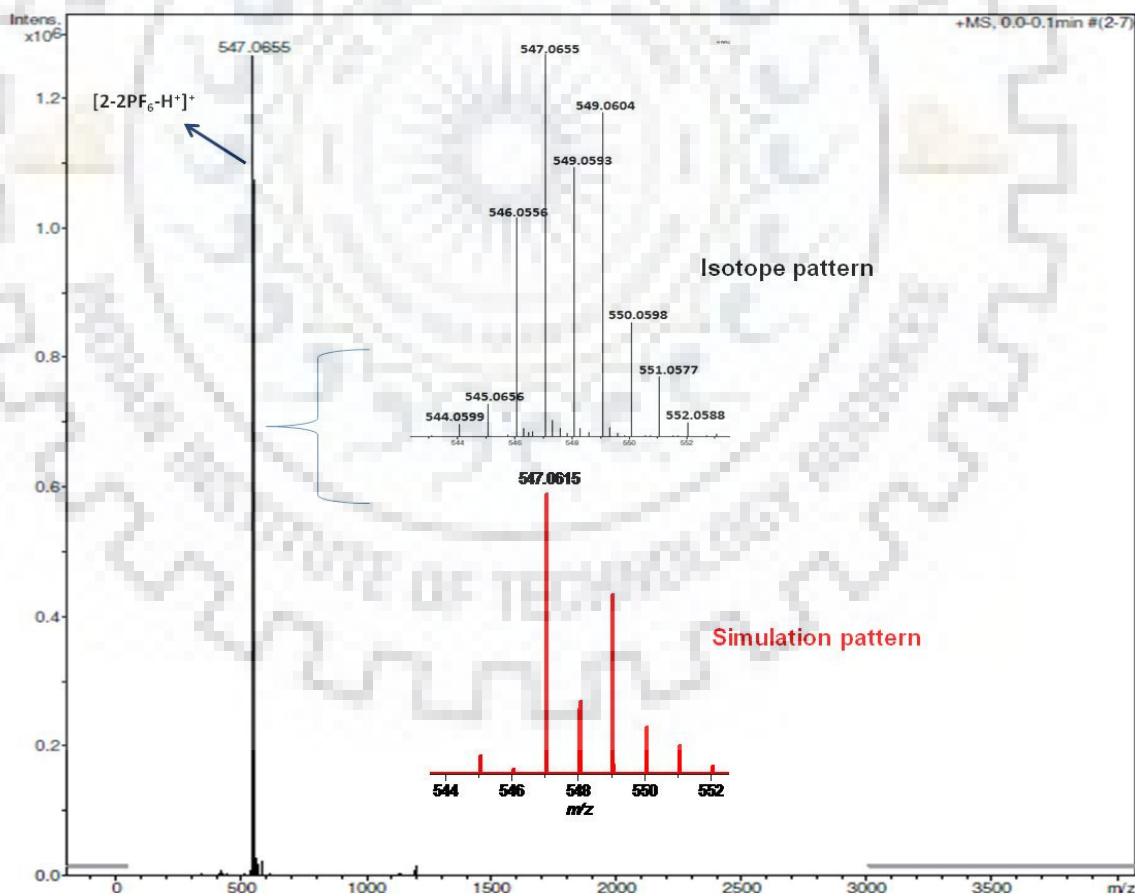


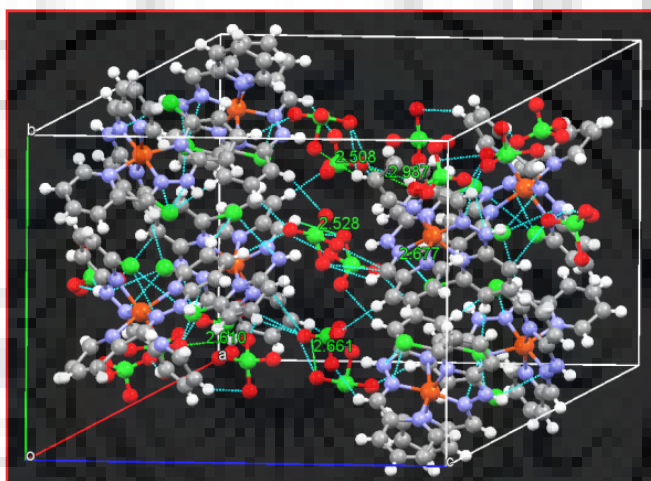
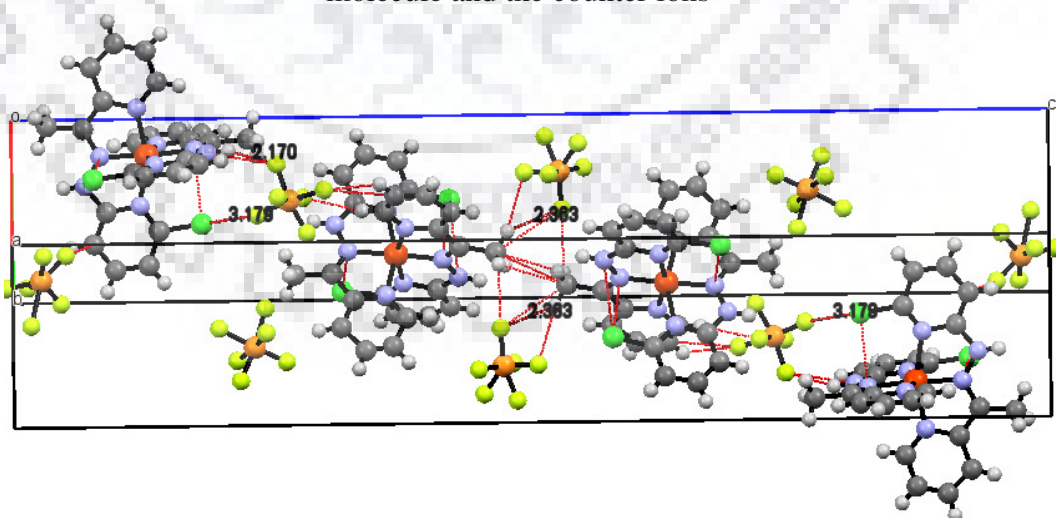
Fig. 3.43 ESI-MS spectrum of complex **4**  $[4-2\text{PF}_6-\text{H}^+]^+$ ,  $m/z=547.0655$

**Table 3.13** Crystal data and data collection parameters for the complex **3** and complex **4**

	<b>Complex 3</b>	<b>Complex 4</b>
<b>Empirical formula</b>	C <sub>22</sub> H <sub>18</sub> C <sub>14</sub> Fe N <sub>8</sub> O <sub>8</sub>	C <sub>24</sub> H <sub>22</sub> Cl <sub>2</sub> F <sub>12</sub> Fe N <sub>8</sub> P <sub>2</sub>
<b>Colour</b>	Red	Red
<b>Formula weight [g mol<sup>-1</sup>]</b>	720.09	839.19
<b>Temperature [K]</b>	296(2)	296(2)
<b>λ [Å] (Mo-Kα)</b>	0.71073	0.71073
<b>Crystal system</b>	Triclinic	Tetragonal
<b>Space group</b>	P-1	P21/n
<b>a [Å]</b>	17.094(2)	8.838(9)
<b>b [Å]</b>	17.098(3)	8.838
<b>c [Å]</b>	22.472(3)	41.586(6)
<b>α [°]</b>	82.511(10)	90.00
<b>β [°]</b>	78.233(8)	90.00
<b>γ [°]</b>	89.945(8)	90.00
<b>V [Å<sup>3</sup>]</b>	6372.9(16)	3248.2(6)
<b>Crystal size [mm]</b>	0.22 x 0.22 x 0.22	0.22 x 0.22 x 0.22
<b>Z</b>	8	4
<b>ρ<sub>calc</sub> [gcm<sup>-3</sup>]</b>	1.501	1.716
<b>F(000)</b>	2912.0	1680
<b>θ range for data Collection</b>	0.93-28.82	10.98-28.22
<b>Index ranges</b>	-23<h<23, -23<k<23, -30<l<30	-11<h<08, -11<k<11, -47<l<55
<b>Refinement method</b>	Full matrix least-squares on F <sup>2</sup>	Full matrix least-squares on F <sup>2</sup>
<b>Data/restraints/parameters</b>	6180 /0/689	8139/0/ 442
<b>GOF on F<sup>2</sup></b>	1.003	0.891
<b>R<sub>1</sub><sup>b</sup> [I&gt;2σ(I)]</b>	0.0710	0.1102
<b>R<sub>1</sub> [all data]</b>	0.1503	0.2142
<b>wR<sub>2</sub><sup>c</sup> [I&gt; 2σ(I)]</b>	0.2447	0.2880
<b>wR<sub>2</sub> [all data]</b>	0.3047	0.3443
<sup>a</sup> GOF = [Σ[w(F <sub>o</sub> <sup>2</sup> -F <sub>c</sub> <sup>2</sup> ) <sup>2</sup> ] /M-N] <sup>1/2</sup> (M = number of reflections, N = number of parameters refined). <sup>b</sup> R <sub>1</sub> = Σ   F <sub>o</sub>   -   F <sub>c</sub>    /Σ   F <sub>o</sub>   , <sup>c</sup> wR <sub>2</sub> = [Σ[w(F <sub>o</sub> <sup>2</sup> -F <sub>c</sub> <sup>2</sup> ) <sup>2</sup> ] /Σ [w(F <sub>o</sub> <sup>2</sup> ) <sup>2</sup> ] <sup>1/2</sup>		

**Table 3.14** Selected bond distances (Å) for complexes **3** and **4** with optimized DFT bond parameters in gas phase

Bond distances (Å)					
Complex 3			Complex 4		
Bonds type	Experimental	Theoretical	Bonds type	Experimental	Theoretical
Fe1—N3	1.875(21)	1.927	Fe1—N3	1.883(8)	1.923
Fe1—N7	1.912(23)	1.927	Fe1—N7	1.933(8)	1.923
Fe1—N8	2.031(22)	2.022	Fe1—N8	2.002(8)	2.010
Fe1—N5	2.031(21)	2.105	Fe1—N4	1.990(7)	2.103
Fe1—N4	2.093(22)	2.022	Fe1—N1	2.070(6)	2.012
Fe1—N1	2.122(23)	2.105	Fe1—N5	2.081(8)	2.054

**Fig. 3.44** Packing diagram for the complex **3**, showing the short interaction between molecule and the counter ions**Fig. 3.45** Packing diagram for the complex **4**, showing the short interaction between molecule and the counter ions

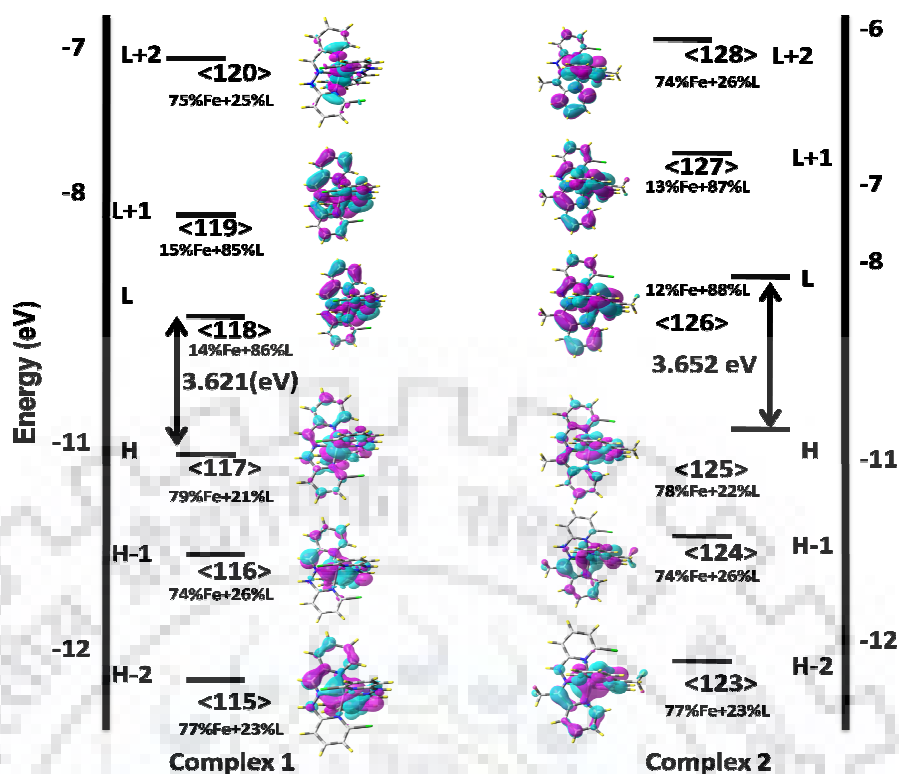


Fig. 3.46 Frontier molecular orbitals of complex 3 and complex 4 showing significant contribution of iron and ligand (L) in molecular orbitals

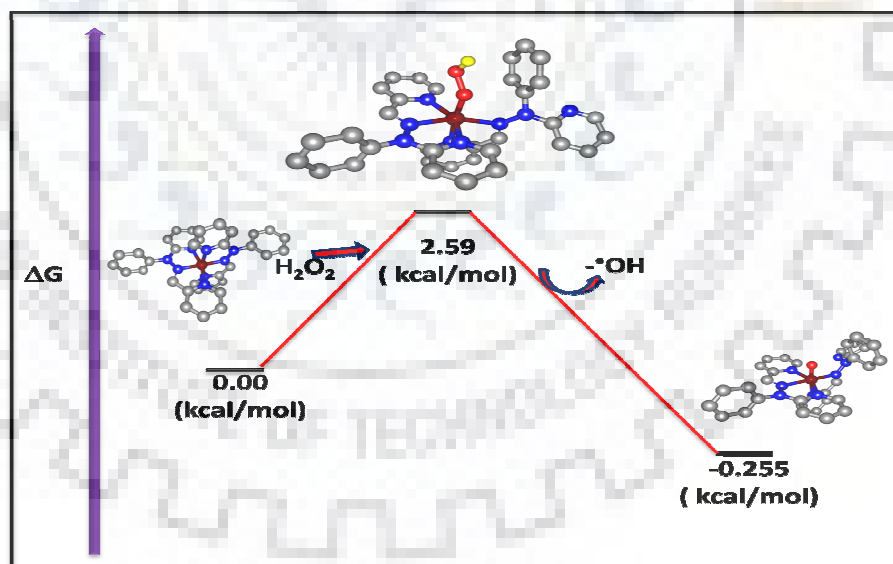
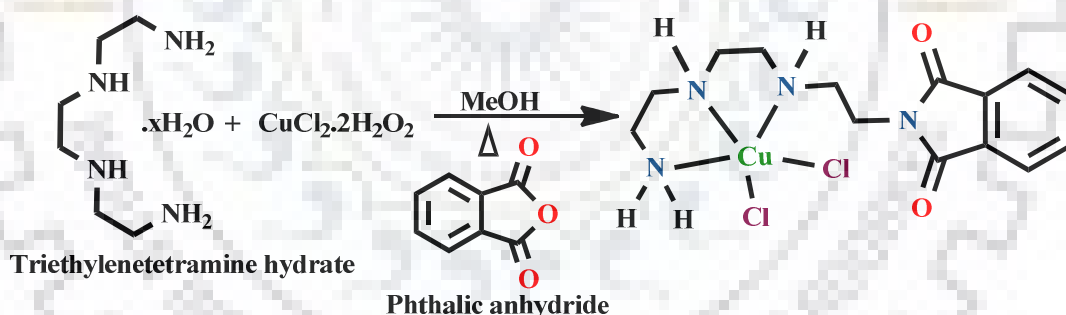


Fig. 3.47 Profile of the calculated relative  $\Delta G$  for the reaction of hydrogen peroxide and complex with  $L^{\text{ph}}$  ligand, the formation of hydroperoxo species and by removal of  $\cdot\text{OH}$  radical stabilization of  $\text{Fe}^{\text{IV}}=\text{O}$  intermediate. The relative Gibbs free energies are given in  $\text{kcal mol}^{-1}$ . In this calculation there is no stabilising hydrogen atom for reactive intermediates in the  $L^{\text{ph}}$  ligand system and from the profile also it clear that the reactive intermediates generated theoretically are not as much stable as in complex 3 and complex 4

## **4.1 Introduction**

Textile, leather, paints, printing inks, paper, rubber, art and craft, plastics, food, drugs and cosmetics industries utilize different types of synthetic dyes and pigments for coloring. These dyes and pigments are environmental pollutants and according to the World Bank report the textile industries are responsible for almost 17-20% of water pollution.<sup>328-329</sup> Hence textile wet processing industries bring forward significant environmental problems due to the effluents containing textile dyes.<sup>330</sup> The consumption of fibers and extensive use of the dyes all over the world continuously increase the discharges of dyes in water. The degradation of modern textile dyes are very difficult because of these dyes are stable and resistant to degradation by sun light, water, soap, bleach, and perspiration.<sup>331</sup> These dyes are also difficult to degrade under aerobic conditions that overcome in biological treatment plants.<sup>332,333</sup> The contamination of dyes in wastewater create aesthetic problems, reduce the efficacy of microbiological wastewater treatment because they may be toxic to the microorganism.<sup>334</sup> For the algae growth sunlight is necessary, due to contamination of these dyes the scattered light would be absorb by these dye and algae growth would be effected. The products produced by the degradation can be carcinogenic or mutagenic<sup>335</sup> and this may cause long -term health concerns.<sup>336</sup> More than 70% of all textile dye stuffs produced by azo dyes that incorporate the -N=N- moiety.<sup>331</sup> Different type of homogeneous as well as heterogeneous catalyst have been used for the degradation of different type of dyes.<sup>337</sup> People have been used long back Fenton's reagent to destroy the synthetic dyes.<sup>338</sup> It was developed in the 1890s by Fenton as an analytical reagent.<sup>339</sup> Collins and co-workers reported Fe<sup>III</sup>-TAML complex for the degradation of orange II dye by H<sub>2</sub>O<sub>2</sub> and organic peroxides.<sup>305-306,340</sup> B. Rodríguez-Cabo et al. reported the photo catalytic degradation of rhodamine B and also been used for the oxidative degradation of methylene blue.<sup>341-343</sup> Keeping in mind homogeneous as well as heterogeneous catalyst we have designed and

synthesized water soluble homogeneous copper complex  $[\text{Cu}(\text{TETA}^{\text{TA}})(\text{Cl}_2)](\mathbf{5})$  which is having pendant phthalic anhydride moiety. This phthalic anhydride moiety was utilized as a chromophore to make it heterogeneous later on where one terminal amino group would be utilized for anchoring to the solid surface. This homogeneous catalyst presently utilised for the oxidative degradation of orange II, rhodamine B as well as methylene blue in the presence of  $\text{H}_2\text{O}_2$ . Water solubility and oxidative degradation of dyes prompted us to investigate the functional mimicking of catecholase and phenoxazinone synthase enzymes which are two important enzymes in bioinorganic chemistry.<sup>344-346</sup> Interestingly the substrates of the two metalloenzymes are isoelectronic,<sup>347</sup> however fate of the substrates are completely different. Catechol was converted to quinone whereas 2-aminophenol was converted to 2-aminophenoxazine-3-one *via* oxidative coupling reaction. This catalyst (complex  $\mathbf{5}$ ) showed excellent catalytic promiscuity through oxidation of catechol and *o*-aminophenol to their corresponding products.



**Scheme 4.1** Synthesis of complex  $[\text{Cu}(\text{TETA}^{\text{TA}})(\text{Cl}_2)](\mathbf{5})$  using the ligand  $(\text{TETA}^{\text{TA}})$  ( $\text{L}=2$ - $(2-((2-((2\text{aminoethyl})\text{amino})\text{ethyl})\text{amino})\text{ethyl})\text{isoindoline-1,3-dione}$ )

## 4.2 Results and Discussions

### 4.2.1 Synthesis and characterization

The metal complex  $[\text{Cu}(\text{TETA}^{\text{TA}})(\text{Cl}_2)](\mathbf{5})$  have been synthesized *via* template synthesis utilizing  $\text{CuCl}_2 \cdot 2\text{H}_2\text{O}$ , 1,8-diamino-3,6-diazaoctane and phthalic anhydride in methanol (Shown in scheme 4.1). The molecular structure of complex  $[\text{Cu}(\text{TETA}^{\text{TA}})(\text{Cl}_2)](\mathbf{5})$  was determined by using X-ray crystallographic studies are displayed in Fig. 4.1 and

crystallographic data was depicted in Table 4.1. In a unit cell four molecules were identified in complex **5**, these molecules were interacting with phthalic anhydride moiety; the packing diagram was shown in Fig. 4.2. The coordination environment around the metal centre is described as distorted trigonal bipyramidal with two chloride ion at the apical site and three nitrogen atoms were found to be meridional site. The trigonality index,  $\tau$ , value is found to be 0.94 [ $\tau = (b - a)/60$ , where  $b = \text{N1—Cu1—N3} = 161.64(13)^\circ$  and  $a = \text{Cl2—Cu1—Cl1} = 105.38(4)^\circ$  (Fig. 4.3) (for perfect square pyramidal and trigonal bipyramidal geometries the  $\tau$  values are zero and unity, respectively)<sup>348</sup> The Cu-N<sub>trien</sub> distance was found to be 2.022–2.055 which was found to be consistent to the reported result by Zhou and co-workers.<sup>349</sup> In the unit cell the one molecule having Cu1-Cl1 and Cu1-Cl2 different bond distances. One Cu1-Cl1 distance was found to be 2.547 Å and another Cu1-Cl2 was found to be 2.305 Å. The another molecule was having Cu2-Cl3 2.297 and Cu2-Cl4 2.259 Å which is similar as reported by Bond and co-workers.<sup>350</sup> The bond distances and bond angles around the copper centre were reported in Table 4.2 and 4.9. The UV-visible spectrum of complex **5** (Fig. 4.28) was recorded in 0.1 M phosphate buffer pH 7.2, a broad band near 634 nm ( $\epsilon=320 \text{ M}^{-1} \text{ cm}^{-1}$ ) was observed.<sup>351</sup>  $\nu_{\text{C-N}}$  stretching frequency was found near  $1,400 \text{ cm}^{-1}$  in IR spectra and C=O stretching frequency was observed at  $1,603 \text{ cm}^{-1}$  which was found to be shifted compare to free phthalic anhydride moiety.<sup>352</sup>

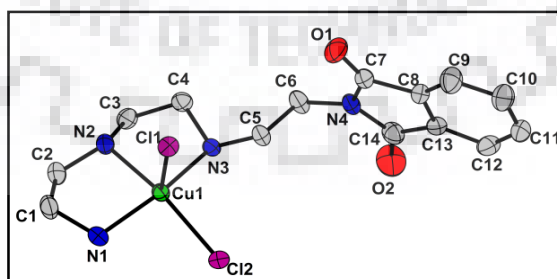


**Fig. 4.1** ORTEP diagram (50% probability level) of complex  $[\text{Cu}(\text{TETA}^{\text{TA}})(\text{Cl}_2)]$  (**5**), all hydrogen atoms are omitted for clarity



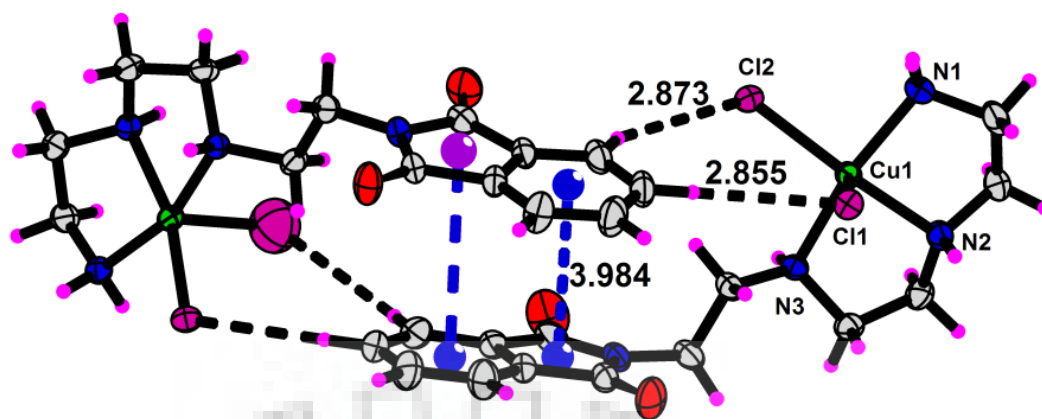


Fig. 4.2 Packing diagram of complex  $[\text{Cu}(\text{TETA}^{\text{TA}})(\text{Cl}_2)]$  (5)

Table 4.1 Summary of crystal data and data collection parameters for complex  $[\text{Cu}(\text{TETA}^{\text{TA}})(\text{Cl}_2)]$  (5)

Empirical formula	$\text{C}_{14}\text{H}_{20}\text{Cl}_2\text{CuN}_4\text{O}_2$	Z	4
Colour	green	$\rho_{\text{calc}}(\text{gcm}^{-3})$	1.415
Formula weight	410.79	F(000)	844
Temperature (K)	293(2)	$\theta$ range for data collection	0.731- 0.739
$\lambda$ (Å) (Mo-K $\alpha$ )	0.71073	Index ranges	-10<h<6, -19<k<18 -22 <l<18
Crystal system	triclinic	Refinement method	Full matrix least-squares on $F^2$
Space group	P-1	Data/restraints/parameters	1419/0/298
a(Å)	8.0599(2)	GOF <sup>a</sup> on $F^2$	1.102
b(Å)	14.5640(3)	$R_1^b$ [ $I > 2\sigma(I)$ ]	0.0571
c(Å)	16.9698(4)	$R_1$ (all data)	0.0758
$\alpha$ (°)	89.7100(10)	$wR_2^c$ ( $I > 2\sigma(I)$ )	0.1910
$\beta$ (°)	76.7930(10)	$wR_2$ (all data)	0.2043
$\gamma$ (°)	83.8450(10)		
<sup>a</sup> GOF = $[\sum[w(\text{Fo}^2 - \text{Fc}^2)^2]/M - N]^{1/2}$ (M = number of reflections, N = number of parameters refined). <sup>b</sup> $R_1 = \sum\ \text{Fol} - \text{Fc}\ /\sum\ \text{Fol}\ $ . <sup>c</sup> $wR_2 = [\sum[w(\text{Fo}^2 - \text{Fc}^2)^2] / \sum[(\text{Fo}^2)^2]]^{1/2}$ .			

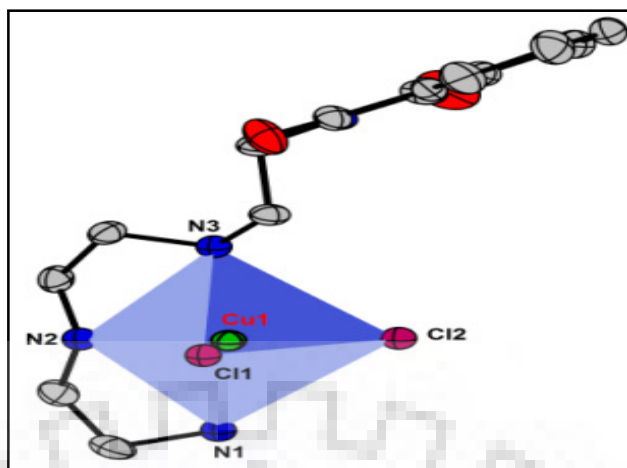


Fig. 4.3 Trigonal bipyramidal geometry around the copper center ( $\tau=0.94$ )

Table 4.2 Selected bond distances (Å) and bond angles (°) of  $[\text{Cu}(\text{TETA}^{\text{TA}})(\text{Cl}_2)]$  (5)

Bond distances		Bond angles	
Cu1—N1	2.022(4)	N1—Cu1—N2	84.27(13)
Cu1—N2	2.032(4)	N1—Cu1—N3	161.64(13)
Cu1—N3	2.055(3)	N2—Cu1—N3	83.44(13)
Cu1—Cl2	2.305(2)	N1—Cu1—Cl2	93.08(10)
Cu1—Cl1	2.547(2)	N2—Cu1—Cl2	160.29(10)
N1—C1	1.472(6)	N3—Cu1—Cl2	93.91(9)
C2—C1	1.504(9)	N1—Cu1—Cl1	96.3(1)
N2—C2	1.457(6)	N2—Cu1—Cl1	94.33(10)
N2—C3	1.452(7)	N3—Cu1—Cl1	98.18(9)
C4—C3	1.517(7)	Cl2—Cu1—Cl1	105.38(4)
N3—C4	1.466(6)		

#### 4.2.2 Electrochemical investigation

The electrochemical investigation of complex  $[\text{Cu}(\text{TETA}^{\text{TA}})(\text{Cl}_2)]$  (5) in 0.1 M phosphate buffer pH 7.2 clearly indicated an irreversible response at -0.46V vs. Ag/AgCl in cathodic

region which was attributed to Cu(II)/Cu(I) couple and another peak in anodic region at -0.06V vs. Ag/AgCl due to Cu(II)/Cu(0) (Fig. 4.4) due to stripping potential. The confirmation of this stripping potential was done by sweeping the segment in the range of 0 to -0.3 V vs Ag/AgCl<sup>353</sup> (As shown in Fig. 4.5)

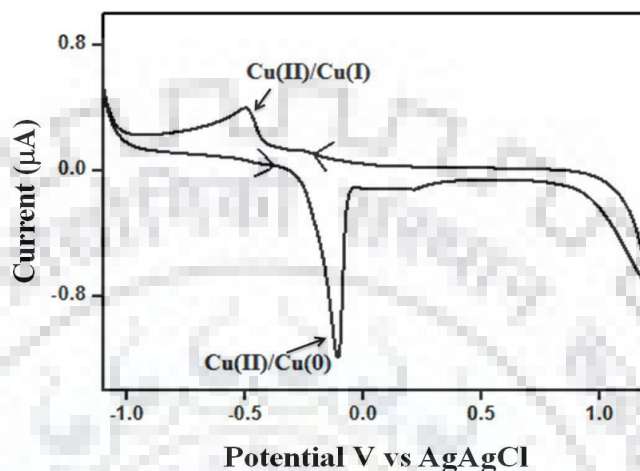


**Fig. 4.4** Cyclic voltammograms of a  $1 \times 10^{-3}$  M solution of complex  $[\text{Cu}(\text{TETA}^{\text{TA}})(\text{Cl}_2)]$  (5) in 0.1 M phosphate buffer pH 7.2) in presence of 0.4 M KCl, using working electrode: glassy-carbon, reference electrode: Ag/AgCl; auxiliary electrode: platinum wire, scan rate  $0.1 \text{ Vs}^{-1}$

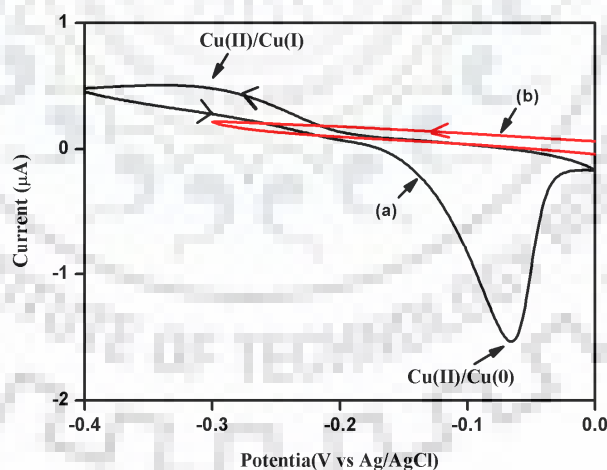


**Fig. 4.5** Cyclic voltammograms of a  $1 \times 10^{-3}$  M solution of complex  $[\text{Cu}(\text{TETA}^{\text{TA}})(\text{Cl}_2)]$  (5) in 0.1 M phosphate buffer pH 7.2) in presence of 0.4 M KCl, using working electrode: glassy-carbon, reference electrode: Ag/AgCl; auxiliary electrode: platinum wire, scan rate  $0.1 \text{ Vs}^{-1}$ . (Black colour represent the sweep segment in the range of 0 to -0.4 V vs Ag/AgCl and red colour 0 to -0.3 V and back to zero vs Ag/AgCl)

### 4.2.3 Organic dyes degradation

For the present study, we have taken orange II, rhodamine B and methylene blue dyes for our investigation<sup>305,306,339-343</sup> The complex was found to be stable in phosphate buffer pH 7.2 and this was ensured by UV-Visible. spectral studies.

#### 4.2.3.1 Degradation of Orange II

Orange II and complex  $[\text{Cu}(\text{TETA}^{\text{TA}})(\text{Cl}_2)]$  (**5**) was dissolved in phosphate buffer pH 7.2 at room temperature and later on  $\text{H}_2\text{O}_2$  was added to the reaction mixture. The reaction was monitored visibly (Fig.4.6) and by following the absorption band at 485nm which was characteristic of this dye. The collapse of 485 nm band was due to the loss of conjugation in dye leading to colourless oxidized products.

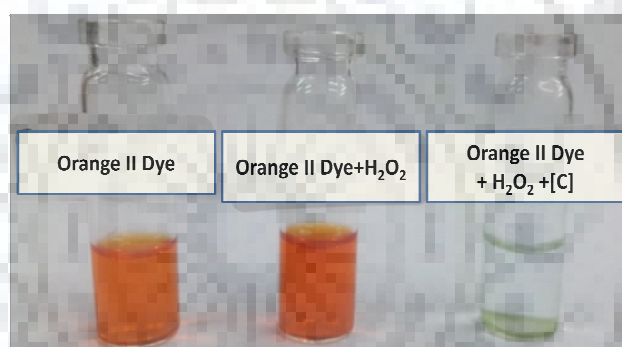
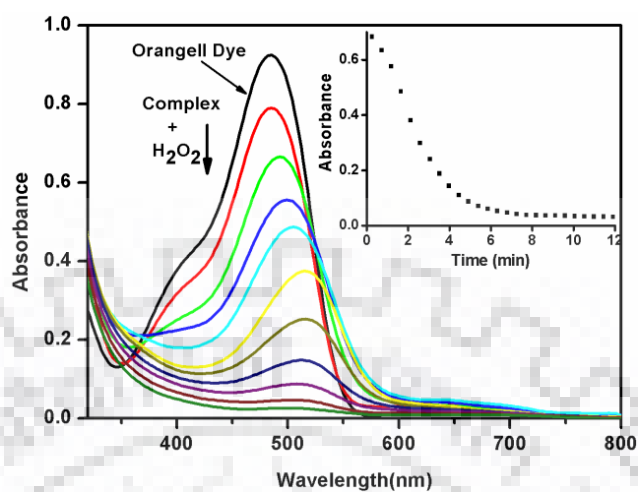


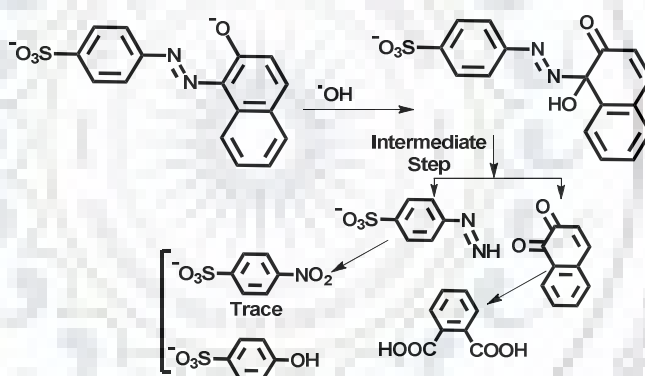
Fig. 4.6 Visible changes during the degradation of orange II dye

The catalytic degradation reaction was completed within 10-12 minutes (As shown in Fig. 4.7) which was comparatively good as reported in the literature.<sup>339</sup> From the investigation it was also be found out that the rate of degradation of orange II dye was very fast, within few minutes the colour of the solution become transparent. The reaction goes through a  $\cdot\text{OH}$  radical path way and the oxidation reaction path of orange II. (Shown in the Scheme 4.2) Control experiments with complex  $[\text{Cu}(\text{TETATA})(\text{Cl}_2)]$ (**5**) in the absence of  $\text{H}_2\text{O}_2$ , or with  $\text{H}_2\text{O}_2$  only in the absence of the catalyst indicated no degradation of orange II under these experimental conditions. Hence, catalyst and  $\text{H}_2\text{O}_2$  were needed for the degradation of

orange II, if its concentration is associated exclusively with the absorbance at 485 nm. Note this is only the color removing stoichiometry, not the complete oxidative degradation.



**Fig. 4.7** UV-visible spectral changes of Orange II in 0.1 M phosphate buffer pH 7.2. Concentrations: Orange II,  $3 \times 10^{-5}$  M; Complex,  $2.5 \times 10^{-6}$  M and  $\text{H}_2\text{O}_2$ ,  $4.4 \times 10^{-4}$  M



**Scheme 4.2** Degraded product of orange II

The degraded products were analysed time to time using GC-MS spectrophotometer. (Shown in Fig. 4.30 to 4.34) On the basis of the degraded products indicated by GC-MS studies a probable flow-chart describing degradation products were depicted in Scheme 4.2. The products finally formed, after the degradation is not much toxic and harmful for the environment.<sup>306,340</sup> The Fenton reagent work efficiently at the pH 3<sup>354</sup> and the activity of this reagent decrease significantly in neutral or alkaline condition due to flocculation. The complex **5** also significantly play an important role to degrade the all three dyes at different

pH (range 5.8 to 8.2). The orange II dye degradation in the pH range 7.0 to 7.8 would be more and it was found out that in more acidic or more alkaline solution the activity was less. As shown in the Fig.4.8.

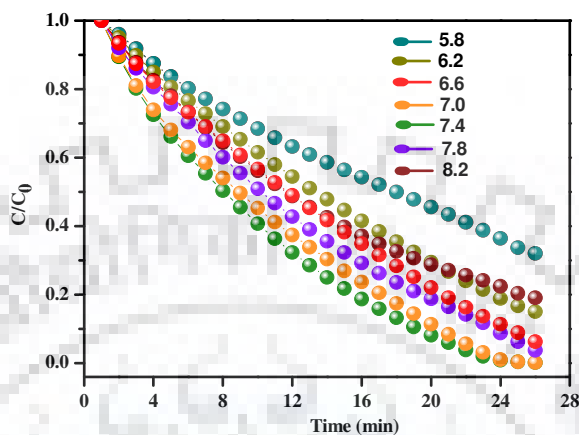


**Fig. 4.8** Effect of the pH on the catalytic oxidation of orange II dye in 0.1 M phosphate buffer pH 5.8 to 8.2

#### 4.2.3.2 Degradation of Rhodamine B (RhB)

Degradation of Rhodamine B (RhB) in the presence of complex  $[\text{Cu}(\text{TETA}^{\text{TA}})(\text{Cl}_2)]$  (**5**) on adding  $\text{H}_2\text{O}_2$  was monitored in phosphate buffer pH 7.2 at room temperature. The degradation of this dye was investigated visibly (Fig.4.9) and by absorption band at 550 nm which was characteristic for RhB. The band at 550 nm gradually decrease and it also represented the continuously degradation of RhB.

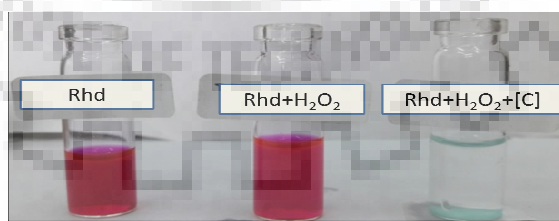


**Fig. 4.9** Visible changes during the degradation of Rhodamine B dye

The oxidation reaction of RhB also carried out in a similar fashion as we have done for the orange II dye. In comparison of orange II the degradation of RhB was found to be fast, as shown in the inset of the Fig. 4.10. The oxidation of the RhB in the presence of only catalyst

or only H<sub>2</sub>O<sub>2</sub> was found negligible but in the presence of both the RhB degrade fast. The analysis of the degraded product was done using GC-MS spectrophotometer. (As shown in Fig. 4.35 -4.40) The degraded products form RhB indicated by GC-MS studies, a probable flow-chart describing degradation products were depicted in Scheme 4.3.

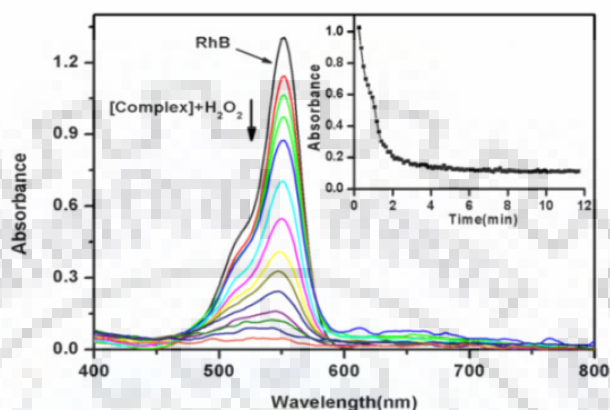
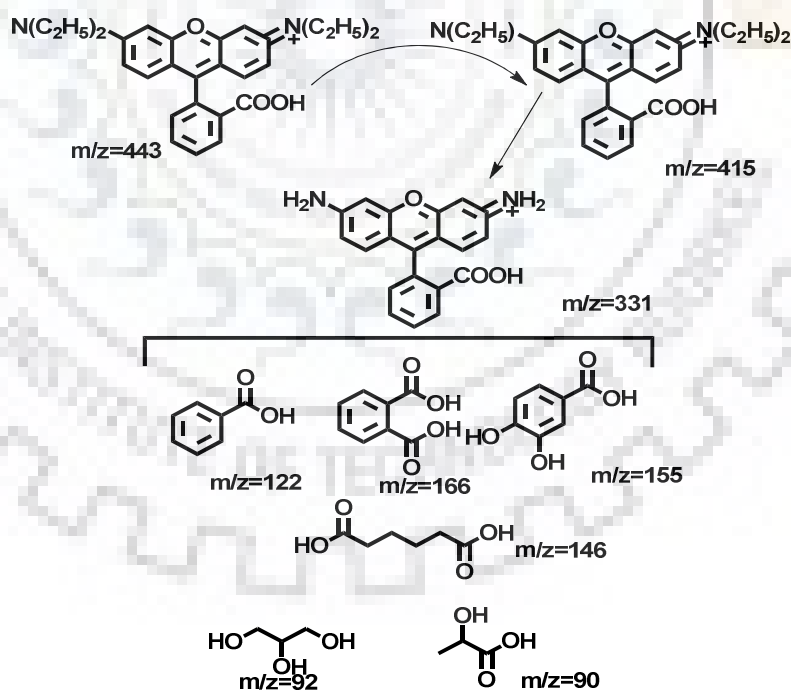


**Fig. 4.10** UV-visible spectral changes of rhodamine B in 0.1 M phosphate buffer pH 7.2. Concentrations: rhodamine B,  $5 \times 10^{-5}$  M ; Complex,  $2.5 \times 10^{-6}$  M and H<sub>2</sub>O<sub>2</sub>,  $4.4 \times 10^{-4}$  M



**Scheme 4.3** Degraded products of rhodamine B

The oxidative degradation of rhodamine B at different pH performed using UV-visible spectroscopy. For this dye the degradation in the pH range 7.0 to 7.8 was found more as compare to orange II dye. As shown in the Fig. 4.11.

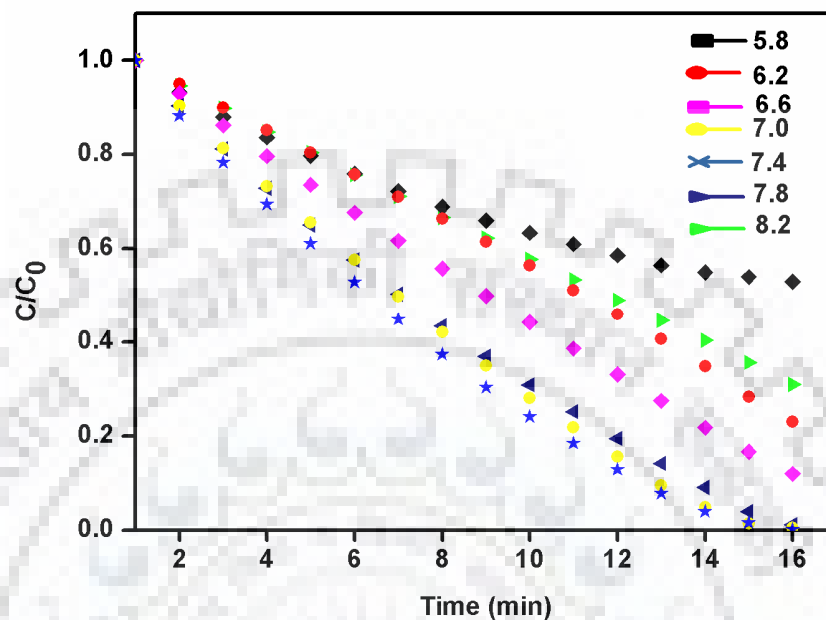


**Fig.4.11** Effect of the pH on the catalytic oxidation of Rhodamine B dye in 0.1 M phosphate buffer pH 5.8 to 8.2

#### 4.2.3.3 Degradation of Methylene blue [MB] dye

In textile dyes industries MB utilise as a commercial colorants. It was found major concern to cause the environmental pollution. Thus it was highly desirable to build up more efficient and environmental friendly catalyst to degrade residual MB. Methylene blue dye and complex  $[\text{Cu}(\text{TETA}^{\text{TA}})(\text{Cl}_2)](\mathbf{5})$  were also dissolved in similar way in phosphate buffer pH 7.2 at room temperature then hydrogen peroxide was added to the reaction mixture. The reaction was monitored visibly (Fig. 4.12) and absorption band at 665 nm. This band was also be found gradually decrease due to the degradation of methylene blue. It can be observed that the whole conjugated chromospheres structure of MB ( $\text{C}=\text{N}$  and  $\text{C}=\text{S}^+-\text{C}$ ) was destroyed, same experiments was done with dye also but there is no change but catalyst and  $\text{H}_2\text{O}_2$  effectively demolish the MB. (As shown in Fig. 4.13) The analysis of the degraded



product was done using GC-MS spectrophotometer. (As shown in Fig. 4.41- 4.43). On the basis GC-MS of degraded products the probable products depicted in scheme 4.4

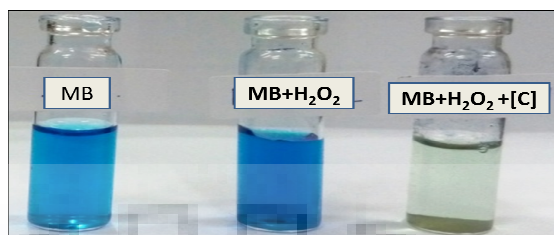


Fig.4.12 Visible changes during the degradation methylene blue dye

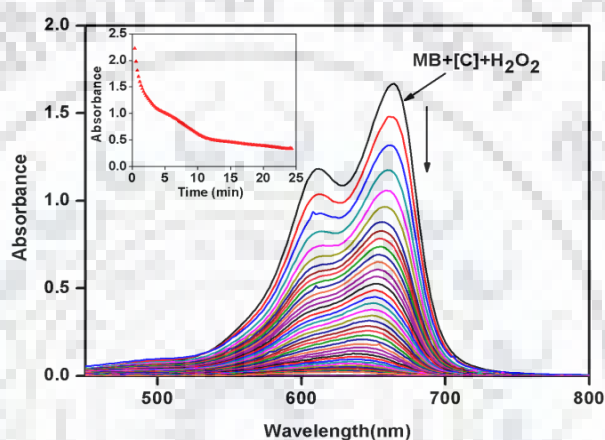
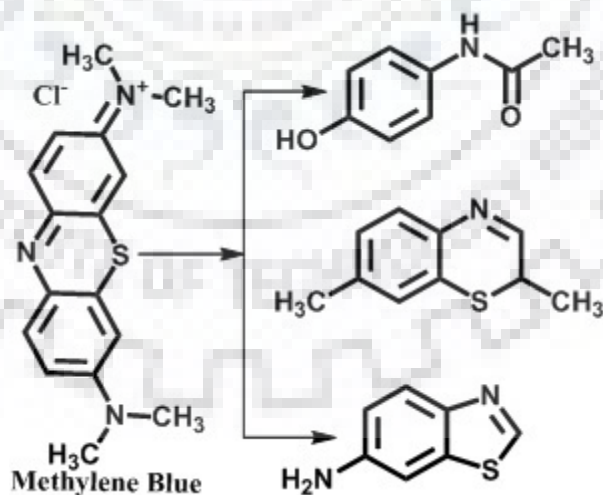


Fig. 4.13 UV-visible spectral changes of methylene blue in 0.1 M phosphate buffer pH 7.2. Concentrations: methylene blue,  $5 \times 10^{-5}$  M; Complex 1,  $2.5 \times 10^{-6}$  M and  $H_2O_2$   $4.4 \times 10^{-4}$  M



Scheme 4.4 Degraded products of methylene blue

The effect of the pH variation from 5.8 to 8.2 on this dye degradation was also be shown, for this dye also catalyst work effectively in the pH range 7 to 7.8 As shown in information 4.14.

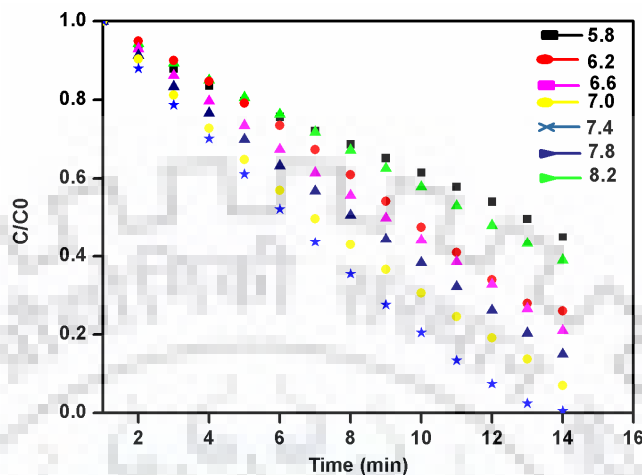


Fig. 4.14 Effect of the pH on the catalytic oxidation of methylene blue dye in 0.1 M phosphate buffer pH 5.8 to 8.2

#### 4.2.4 Kinetics of organic dye degradation

The visual trace of the dye degradation is shown in the inset of corresponding UV–visible spectra (Fig. 4.7, 4.10 and 4.13). Orange II, Rhodamine B, and Methylene blue (Fig. 4.8, 4.11 and 4.14) showed the variation in the concentrations ( $C/C_0$ ) on adding complex **5** and  $H_2O_2$ . Where  $C_0$  is the initial concentration for all dyes and  $C_t$  is the concentration of all dyes at t time. The catalytic degradation efficiency (D) was calculated using the formula.

$$D = \frac{A_0 - A_t}{A_0} = \frac{C_0 - C_t}{C_0}$$

where  $A_0$  and  $C_0$  are the corresponding initial absorbance and concentration before adding complex **5** and  $H_2O_2$  while  $A_t$  and  $C_t$  are the absorbance and concentration at time t. The kinetics of Orange II, Rhodamine B, and Methylene blue degradation with complex **5** and hydrogen peroxide was explored to present a numerical difference among the degradation

rates by catalyst. The general Langmuir–Hinshelwood model depicting apparent first-order kinetics is as follows.<sup>355</sup>

$$r = - \frac{dC}{dt} = \frac{kKC}{1+kC}$$

where  $r$  is the degradation rate of dye (mg/L min),  $C$  the concentration of dye (mg/L),  $t$  the degradation time,  $K$  is the coefficient of dye (L/mg), and  $k$  the reaction rate constant (mg/L min). If  $C$  is very small, then the above equation is simplified to

$$\ln \frac{C_0}{C} = kKt = k_{app}t$$

A plot of  $\ln(C_0/C)$  vs time resulting in a straight line for all dyes, and the slope is equal to the apparent first-order rate constant  $k_{app}$  which are 0.346, 0.277, and 0.102  $\text{min}^{-1}$  for Orange II, Rhodamine B, Methylene blue, respectively. (Shown in Fig. 4.15)

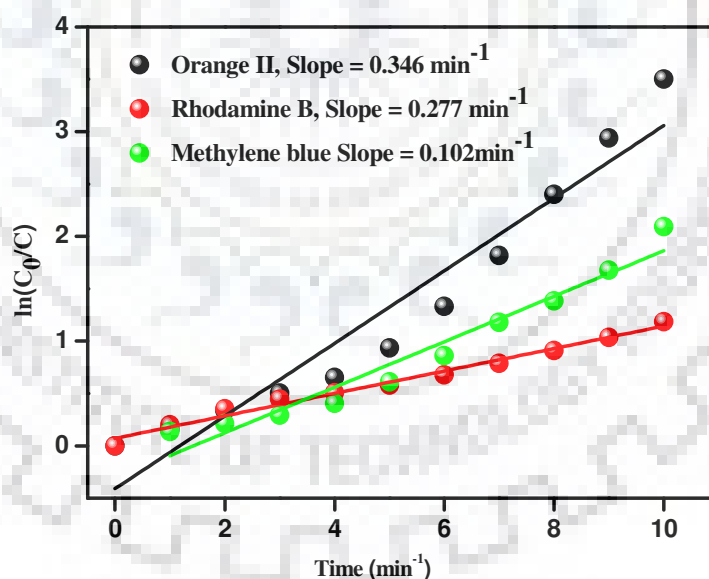


**Fig. 4.15** Kinetics of all three dyes degradation for first-order linear fitted plot  $\ln(C_0/C)$  vs  $t$ . The corresponding slope values for Orange II, Rhodamine B, Methylene blue are 0.346, 0.277, and 0.102  $\text{min}^{-1}$

Since this catalyst was found effective for the degradation of above three dyes and also be well-suited for oxidation of catechol and o-aminophenol oxidation.

### 4.3 Catecholase activity study

In this experiment the complex **5** ( $3.34 \times 10^{-4} \text{M}$ ) was dissolved in methanol and performing absorbance (UV-vis) titrations with 3,5-Di-*tert*-butylcatechol (3,5-DTBC) ( $8.25 \times 10^{-3} \text{M}$ ) in methanol and spectra was recorded for 30min at 25 °C. As shown in Fig. 4.16.

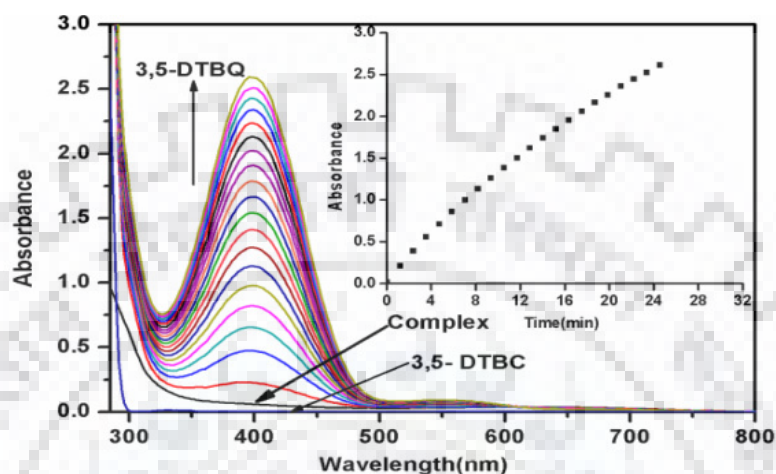


**Fig. 4.16** UV-visible spectral changes in the range (300-800 nm) showed the conversion of catechol to quinone in presence complex **5**

#### 4.3.1 Kinetics study

The oxidation kinetics of 3,5-DTBC was monitored by the initial rate method by monitoring the increase of the product DTBQ at 392nm. The concentration of the substrate should be 10

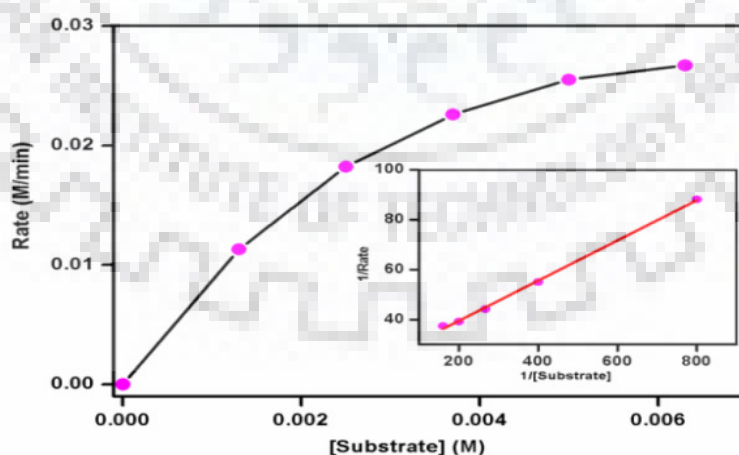


**Fig. 4.17** Plot of rate vs. [substrate] (3,5-DTBC) in presence of complex  $[\text{Cu}(\text{TETA}^{\text{TA}})(\text{Cl}_2)]$  (**5**) in MeOH inset: Lineweaver–Burk plot

times more as compare to the complex concentration. We have used the concentration of the 3,5-DTBC in the range of  $1.67 \times 10^{-3}$  M to  $8.25 \times 10^{-3}$  M and the complex **5** concentration was used  $3.34 \times 10^{-4}$  M.

The absorbance spectra were repeatedly monitored. The initial rate determined using slope of the tangent to the absorbance vs time curve at  $t=0$ . The Fig. 4.17 showed the dependence of the initial rate on the concentration of the catechol for the complex **5**. The *GraFit32* program for enzyme kinetics,  $K_M$  and  $V_{max}$  are calculated from the graph and the inset shows the Lineweaver -Burk plot. On increasing the concentration of 3,5-DTBC, a first order dependence was observed at low 3,5-DTBC concentration. However, copper complex **5** showed a saturation kinetic at higher concentration of 3,5-DTBC. A treatment on the basis of Michaelis- Menten model was seemed to be appropriate. From Lineweaver- Burk plots different complex parameter, such as maximum velocity ( $V_{max}$ ), rate constant for the dissociation of complex- substrate intermediate (turnover number,  $K_{cat}$ ), and Michaelis binding constant( $K_m$ ) were evaluated and data shown in Table 4.3. It was observed that during conversion of catechol to quinone the absorption spectra increase at 392nm continually, within half an hour's maximum catechol was converted into quinone. The kinetic data clearly indicate that  $K_{cat}$  was better than the data reported in the literature.<sup>356</sup> (Shown in Table 4.4) For this complex  $K_{cat}$  data was found to be better than the data reported by Anbu et. al<sup>356c</sup>, Bouwman and co-workers<sup>356d</sup>, and Thio et. al<sup>356e</sup> however the value of  $K_{cat}$  was found to be lower than the reported by Das and co-workers<sup>356a</sup>, and Wegner et. al<sup>356b</sup>. The product was also analysed with GC-MS spectroscopic technique.

**Table 4.3** Kinetic data for the oxidation of 3,5-DTBC catalyzed by the complex [Cu(TETA<sup>TA</sup>)(Cl<sub>2</sub>)] (**5**)

Solvent	$V_{\max}$ (M min <sup>-1</sup> )	Std. error	$K_M$ (M)	Std. error	$K_{\text{cat}}$ (h <sup>-1</sup> )
MeOH	0.0428	0.0002	0.0034	0.0001	7.68 x10 <sup>3</sup>

**Table 4.4** Kinetic data for the oxidation of 3,5-DTBC catalyzed by different complexes

Complex formula	Solvent	$k_{\text{cat}}$ (h <sup>-1</sup> )	$K_M$ (M)	$V_{\max}$ (M s <sup>-1</sup> )	Ref.
[Cu <sub>2</sub> (H <sub>2</sub> L(CH <sub>3</sub> ) <sub>11</sub> )(OH)(H <sub>2</sub> O)(NO <sub>3</sub> ) <sup>3+</sup> ]	CH <sub>3</sub> OH	3.24×10 <sup>4</sup>	2.3 × 10 <sup>-3</sup>	9.0 × 10 <sup>-4</sup>	344 <sup>a</sup>
[Cu <sub>2</sub> L19(N <sub>3</sub> ) <sub>2</sub> .2H <sub>2</sub> O]	CH <sub>3</sub> CN	2.16×10 <sup>4</sup>	3.7 × 10 <sup>-3</sup>	6.0 × 10 <sup>-4</sup>	356 <sup>a</sup>
[Cu(L134)] <sub>2</sub>	CH <sub>3</sub> CN	0.95×10 <sup>4</sup>	5.9 × 10 <sup>-3</sup>	-	356 <sup>b</sup>
[Cu <sub>2</sub> (L151)(CH <sub>3</sub> O)(NO <sub>3</sub> ) <sub>2</sub> (CH <sub>3</sub> O) <sub>2</sub> ] pH 8.2	HEPES buffer	1.13×10 <sup>3</sup>	8.14 × 10 <sup>-5</sup>	5.02 × 10 <sup>-5</sup>	365
[Cu(TETA <sup>TA</sup> )Cl <sub>2</sub> ]( <b>5</b> )	CH <sub>3</sub> OH	7.68×10 <sup>3</sup>	3.4 × 10 <sup>-3</sup>	7.13 × 10 <sup>-4</sup>	This Work
[Cu <sub>2</sub> (L155)](BF <sub>4</sub> ) <sub>4</sub> with 50 equiv. NEt <sub>3</sub>	CH <sub>3</sub> CN	6900	1.2 × 10 <sup>-3</sup>	3.80 × 10 <sup>-4</sup>	356 <sup>d</sup>
[Cu <sub>2</sub> (L116) <sub>2</sub> (H <sub>2</sub> O)]	CH <sub>3</sub> OH : DMSO	2760	20 × 10 <sup>-3</sup>	7.67 × 10 <sup>-5</sup>	356 <sup>e</sup>

The reactive intermediates have been characterised using GC-MS and EPR spectroscopic techniques. The EPR spectra of complex **5** was displayed in Fig. 4.19. The EPR spectrum indicated axial EPR with  $g_{\perp}$  value ~ 2.01 and  $g_{\parallel}$  ~ 2.13 so  $g_{\parallel}$  is greater than  $g_{\perp}$  which indicate that in solution the coordination geometry around the metal centre was probably squar pyriamidal.<sup>357</sup> Addition of 3,5-di-tert- butyl catechol to the solution of complex **5**, we

got an extra peak in EPR spectrum (near  $g \sim 2$ ) which was due to the formation of ligand centred radical generation.<sup>356f</sup> (Shown in Fig. 4.20 )

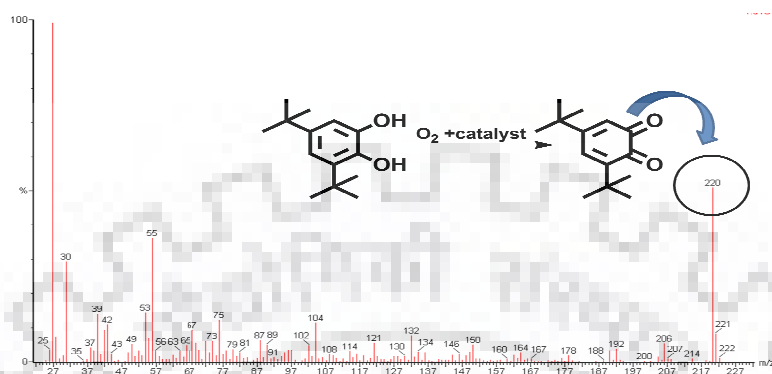


**Fig. 4.18** Mass spectra of 3,5 di tert butyl catechol to 3,5-Di-tert-butyl-o-benzoquinone

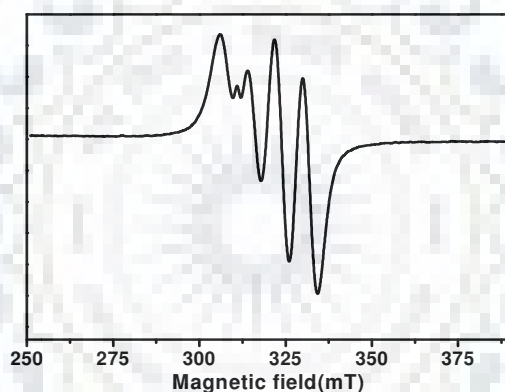


**Fig. 4.19** X-Band EPR spectra of complex 5 [(1mM) in methanol]. Microwave Frequency: 9.725 GHz, Power: 0.612mW, Mod. Frequency: 100 kHz, Mod. Amplitude: 6G, T=1 4°C

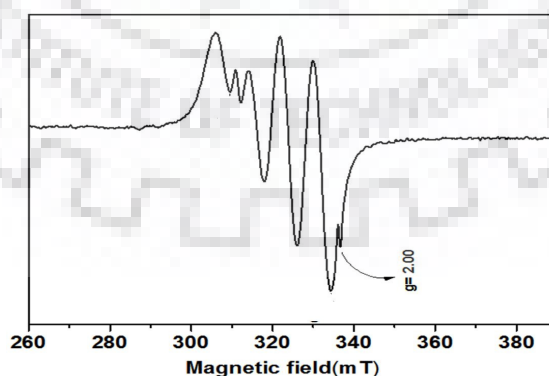
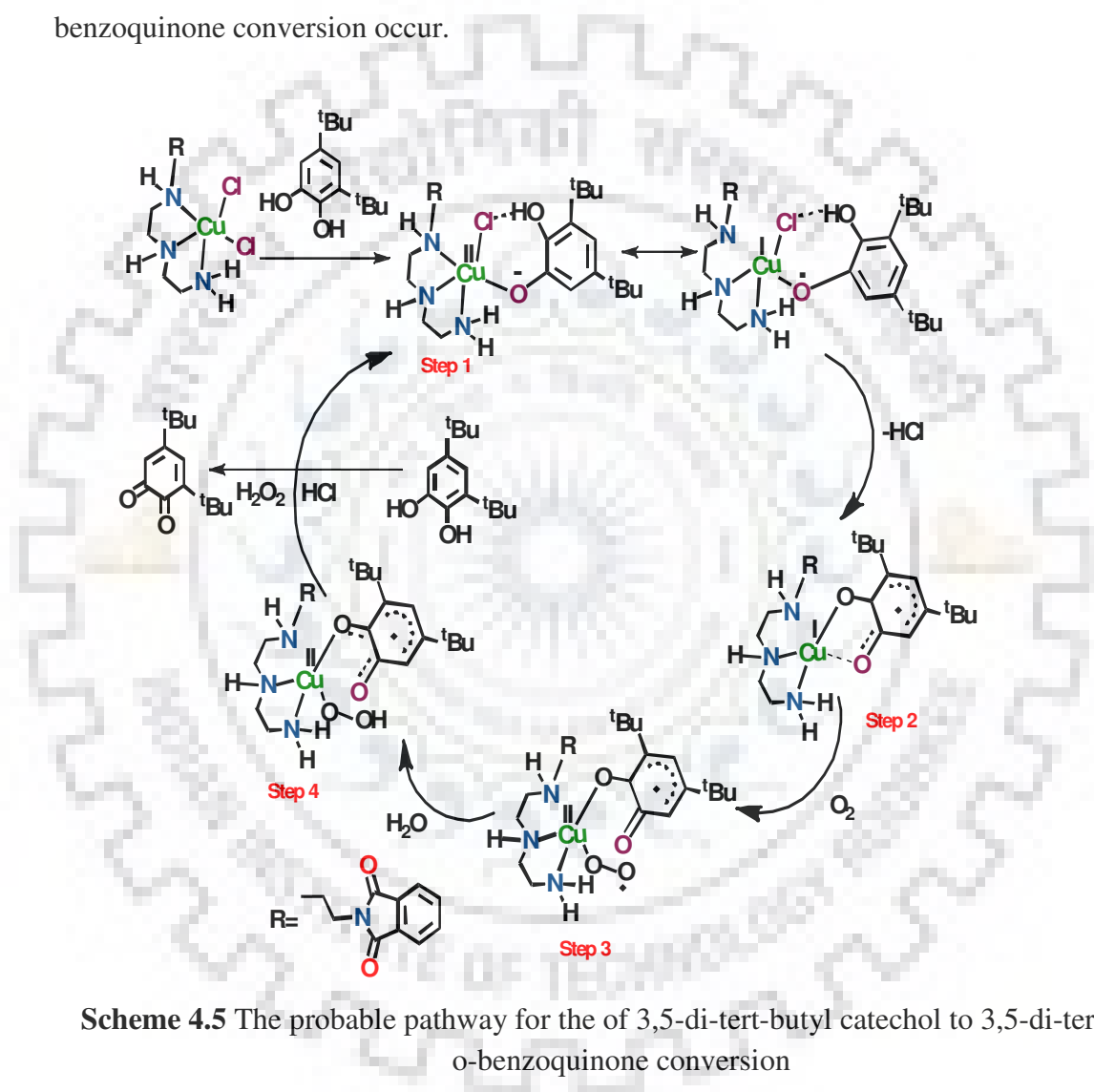


**Fig. 4.20** X-Band EPR spectra of 1:1 solution of complex 5 [(1mM) in methanol] with DTBC (1mM). Microwave Frequency: 9.725 GHz, Power: 0.612mW, Mod. Frequency: 100 kHz, Mod. Amplitude: 6G, T =14°C

### 4.3.2 Proposed Mechanism

The proposed mechanism was shown in scheme 4.5 in the first step the 3,5 di tert butyl catechol bound to the complex **5** and in the second step removal of HCl happen after that binding of O<sub>2</sub> to the copper (I) centre that abstract the hydrogen atom from the H<sub>2</sub>O molecule in step 4 simultaneously 3,5 di-tertbutylcatechol to 3,5 di-tert-butyl-o-benzoquinone conversion occur.



### 4.4 Phenoxazenone synthase activity study

The study of 2-aminophenol oxidation was done in methanol using the complex [Cu(TETA<sup>TA</sup>)(Cl<sub>2</sub>)] (**5**). The oxidation of 2-aminophenol to 2-aminophenoxazine-3-one in the presence of catalyst happens very fast. The kinetic data of aerobic oxidation of 2-



aminophenol catalysed by  $[\text{Cu}(\text{TETA}^{\text{TA}})(\text{Cl}_2)]$  (**5**) was investigated with the growth of the absorbance at 435nm which is characteristic of 2-aminophenoxazine-3-one in the oxygen saturated methanol. (As shown in Fig. 4.21) The rate of a reaction was determined by linear regression from the slope of absorbance *vs* time plot and averaged over three independent measurements. (Shown in the Fig. 4.22 and Table 4.5)

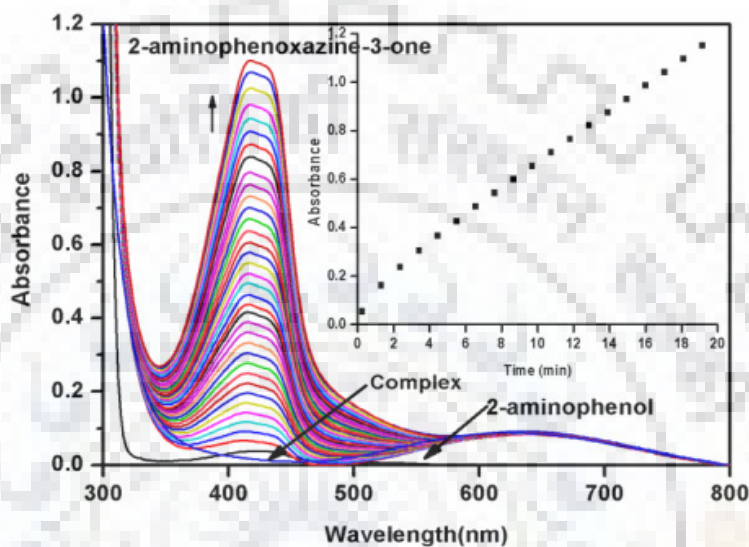


**Fig. 4.21** UV-visible spectral changes for 2-aminophenol to 2-aminophenoxazine -3-one conversion was recorded in presence of  $[\text{Cu}(\text{TETA}^{\text{TA}})(\text{Cl}_2)]$  (**5**)

#### 4.4.1 Kinetics study

UV-vis spectral changes for the oxidation of 2-aminophenol was investigated using variable concentration of substrate from  $1 \times 10^{-3}$  M to  $8 \times 10^{-3}$  M catalyzed by the complex **5** ( $3.346 \times 10^{-4}$  M) for up to 20 minutes of reaction in methanol solvent 25 °C. The 2-aminophenol to 2-aminophenoxazine-3-one conversion was monitored with time at a wavelength 435 nm. The rate *versus* substrate concentration data was analyzed on the basis of Michaelis-Menten parameter for enzyme kinetics to get the Lineweaver-Burk plot and different kinetic parameter such as  $V_{\text{max}}$ ,  $K_{\text{M}}$  and  $K_{\text{cat}}$ . The observed rate *vs* substrate concentration plot and Lineweaver -Burk plot was given in Fig. 4.22. The kinetic data listed in the Table 4.5.

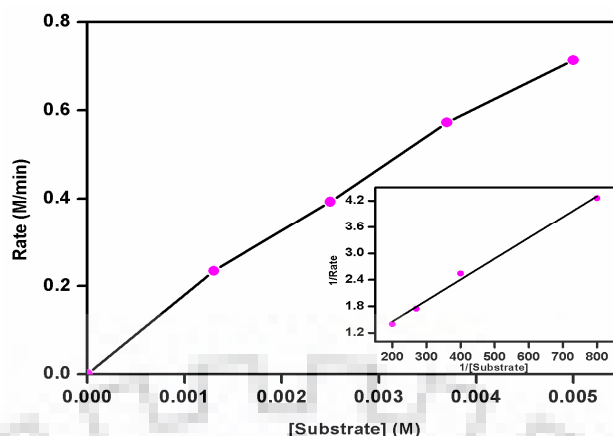


**Fig. 4.22** Plot of rate vs [substrate] (2-aminophenol) in presence of complex  $[\text{Cu}(\text{TETA}^{\text{TA}})(\text{Cl}_2)]$  (5) in MeOH inset: Lineweaver–Burk plot

**Table 4.5** Kinetic data for the oxidation of 2-aminophenol catalyzed by the complex  $[\text{Cu}(\text{TETA}^{\text{TA}})(\text{Cl}_2)]$  (5)

Solvent	$V_{\text{max}}$ ( $\text{M min}^{-1}$ )	Std. error	$K_{\text{M}}$ (M)	Std. error	$K_{\text{cat}}$ ( $\text{h}^{-1}$ )
MeOH	1.9746	0.0010	0.0094	0.0002	$3.54 \times 10^5$

The  $K_{\text{cat}}$  was found to be quite well again as reported in the literature<sup>358</sup> for copper complexes. The comparative data of  $K_{\text{cat}}$  for this complex showed better catalytic conversion of 2-aminophenol to 2-aminophenoxazine-3-one. (As shown in Table 4.6)

**Table 4.6** Kinetic data for the oxidation of 2-aminophenol catalyzed by different complexes

Complexes	Solvent	$k_{\text{cat}}$ ( $\text{h}^{-1}$ )	$K_{\text{M}}$ (M)	$V_{\text{max}}$ ( $\text{M s}^{-1}$ )	Ref.
PS- $[\text{Cu}(\text{hebmz})_2]$	DMF	132	-	-	358a
$[\text{CuII}_4(\text{L})_4]$	MeOH	$1.21 \times 10^5$	-	-	358b
$[\text{Cu}_4(\text{L})_4]$	DMSO	1029	$4.16 \times 10^{-3}$	-	358c
$[\text{Cu}(\text{TETA}^{\text{TA}})\text{Cl}_2]$ (5)	MeOH	$3.54 \times 10^5$	0.0094	1.9746	This Work

The product of 2-aminophenol to 2-aminophenoxazine-3-one formation was also analysed using ESI-MS spectrometry. The formation of 2-aminophenoxazine-3-one (Shown in the Fig. 4.23)

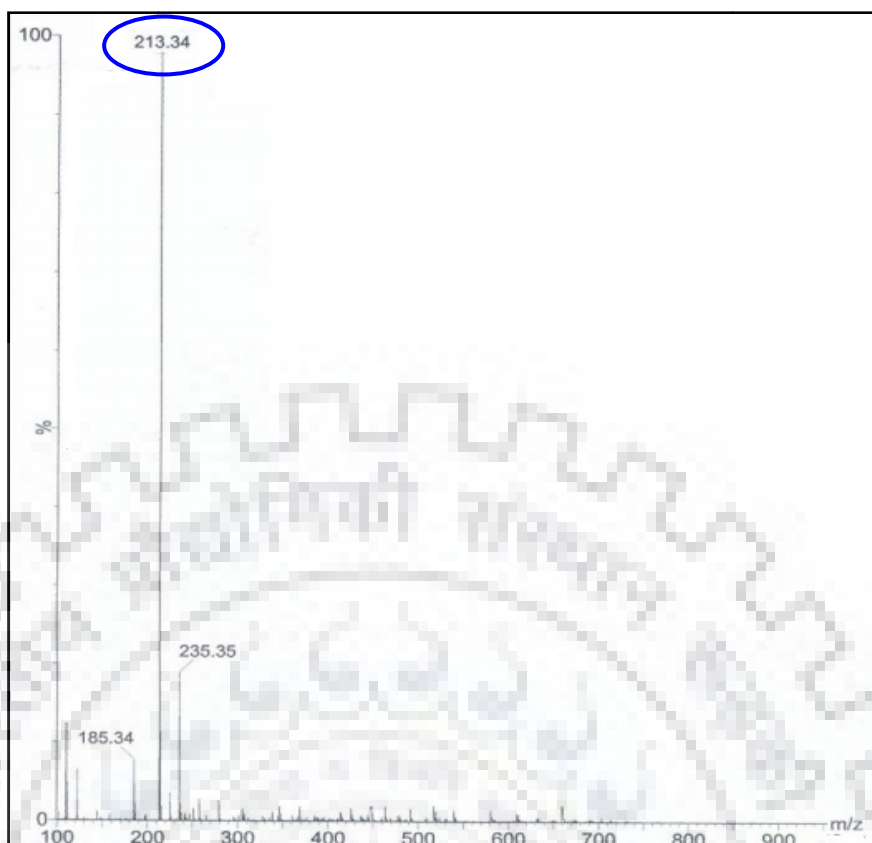
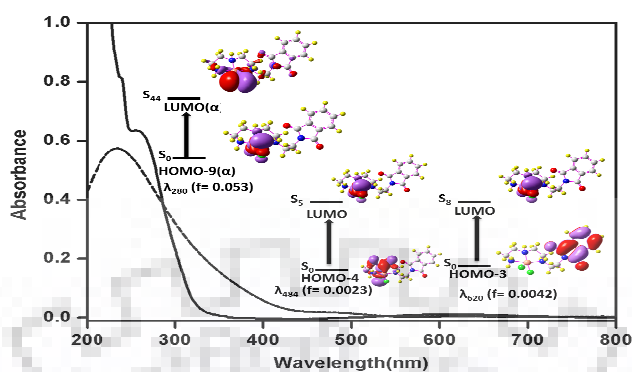


Fig. 4.23 ESI-MS spectrum of 2-aminophenol to 2-aminophenoxazine-3-one formation

#### 4.5 Computational studies

Geometry optimization for complex has been carried using density functional theory (DFT). The geometrical parameters as bond lengths in gas phase (Fig. 4.27) were calculated using Gaussian 09 package.<sup>287</sup> In order to describe the electronic properties of the transition involved in the absorption process of complex  $[\text{Cu}(\text{TETA}^{\text{TA}})(\text{Cl}_2)]$  (**5**), we optimized the geometry of complex **5**, (Fig. 4.29). Followed by the analysis with the aid of TD-DFT using B3LYP/LANL2DZ.<sup>359-360</sup> The percentage contribution of complex in both alpha and beta state have been determined as shown in Fig 4.7. The transitions with the oscillator strength ( $f=0.0042$ ) at around 620nm is correspond to H-3  $\rightarrow$  LUMO transition. This transition arises due to  $\pi$  (PA) to  $d_{x^2-y^2}$  (Cu) which corresponds to LMCT. Transition at 484 nm the oscillator strength ( $f=0.0023$ ) the main transition H-4  $\rightarrow$  LUMO transition. This transition also arises

due to  $\pi$  (PA) to  $d_{x^2-y^2}$  (Cu) which corresponds to LMCT. The transition at 280nm, oscillator strength ( $f=0.053$ ) arises due to transition  $H-9(\alpha) \rightarrow L(\alpha)$ . (Fig. 4.24)



**Fig. 4.24** UV-visible spectra of the complex **5** in gas phase and experimentally determined. The energy gap between HOMO and LUMO in both  $\alpha$  and  $\beta$  state was found to be 3.213eV and 3.128eV (Fig. 4.25)

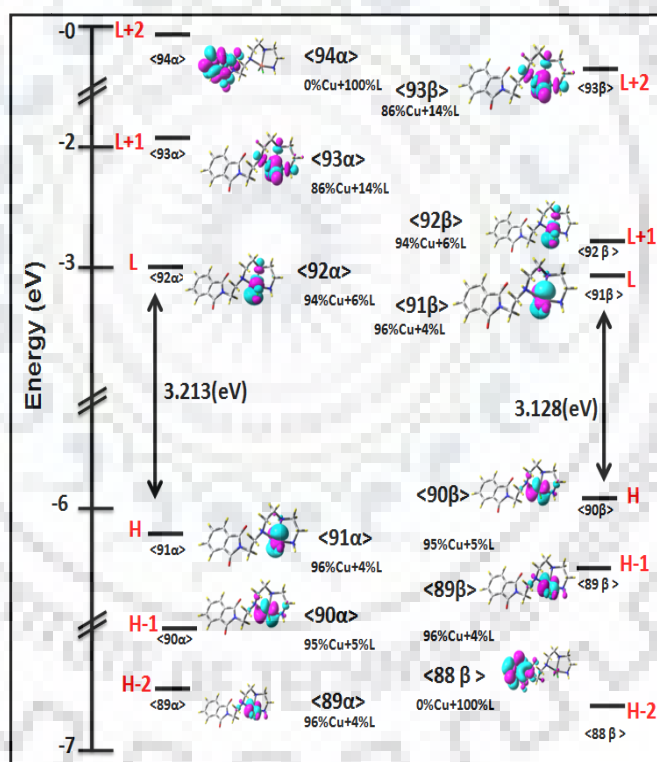


**Fig. 4.25** Single occupied frontier molecular orbitals of complex  $[Cu(TETA^{TA})(Cl_2)]$  (**5**). Showing significant contribution of copper and ligand (L) in SOMO

Energy gap of the energy orbitals (isovalue = 0.02). In the complex **5** electron density of HOMO mainly reside to  $d_{z^2}$  (Cu) metal centre in both  $\alpha$  and  $\beta$  state. In LUMO also the electron density mainly exists in  $d_{z^2}$  (Cu) metal centre in both  $\alpha$  and  $\beta$  state. The sum of the

total Mulliken atomic spin densities in the complex **5** was 1.00 and out of this on copper centre 0.52, both chlorine atoms having 0.23 and rest 0.25 on the ligand system. It was justify the oxidation state of copper in the complex. (Shown in Fig. 4.26 and Table 4.8).

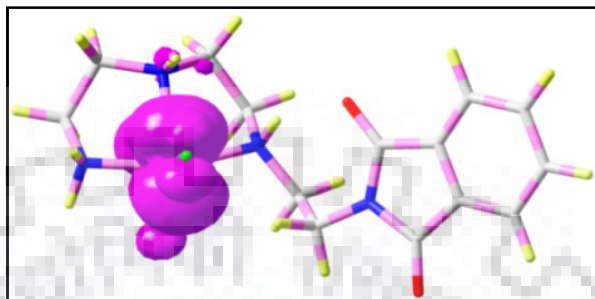


**Fig. 4.26** Mulliken spin density plot of complex [Cu(TETA<sup>TA</sup>)(Cl<sub>2</sub>)] (**5**) using B3LYP level

#### **4.6 Conclusions**

In the present study a water soluble copper complex derived from NNN type tridentate ligand having pendant phthalic anhydride moiety have been synthesized and characterized by different spectral studies. The molecular structure of the complex **5** has been determined using X-ray crystallography. The complex **5** was soluble and stable in buffer and this complex was found to be efficient in degradation of Orange II, Rhodamine B and Methylene blue via oxidation chemistry. This complex acted as functional models for catechol oxidase and phenoxazinone synthase and exhibited oxidation of catechol (catecholase activity) as well as oxidative coupling of o-aminophenol (phenoxazinone synthase activity). Design and synthesis of heterogeneous catalyst based on these results and knowledge gained by this study are under progress.

#### **4.7 Experimental Section**

##### **4.7.1 Physical measurements**

Elemental analyses were carried micro analytically at Elemenlar Vario EL III. Infra red spectra were obtained as KBr pellets with Thermo Nicolet Nexus FT-IR spectrometer, using 16 scans and were reported in cm<sup>-1</sup>. Electronic absorption spectra were recorded with an

UV/Visible spectrophotometer, Shimadzu(UV-2450). Cyclic voltammetry measurements were carried out using a CH-600 electroanalyzer. A conventional three-electrode arrangement was using consisting a platinum wire as auxiliary electrode, glassy carbon as working electrode and the Ag(s)/AgCl as reference electrode. These measurements were performed in the presence of 0.4 M KNO<sub>3</sub> as the supporting electrolyte, using complex concentration 10<sup>-3</sup> M in acetonitrile. The ferrocene/ferrocenium couple occurs at E<sub>1/2</sub> = +0.42 scan rate 0.1 V/s, Ag/AgCl under the same experimental conditions. All experiments were performed at room temperature and solutions were thoroughly degassed with nitrogen prior to beginning the experiments. (ESI-MS) experiments were performed on a Brüker micrOTOFMS-Q-II mass spectrometer.

#### **4.7.2 Reagents and material**

Copper chloride dihydrate was purchased from Alfa Aesar, India, Orange II, Rhodamine B, and Methylene blue (MB), were purchased from Rankem Chemicals, India. 3,5-Di-tert-butylcatechol and 2-aminophenol were purchased from Sigma Aldrich. Phosphate buffer were prepared in deionised water. Solvent used for spectroscopic studies were HPLC grade and purified by standard procedures before use.

#### **4.7.3 Synthesis complex [Cu(TETA<sup>TA</sup>)(Cl<sub>2</sub>)](5)**

Methanolic solution of CuCl<sub>2</sub> 2H<sub>2</sub>O (1.7 g, 10 mmol) was added drop wise into 1,8-diamino-3,6 diazaoctane (1.5ml, 10mmol) in 1:1 molar ratio. The colour of resulting solution was deep blue. This reaction mixture was stirred for 30 minute and subsequently phthalic anhydride (1.45 g, 10 mmol) dissolved in 20 ml methanol was added drop wise. The reaction mixture was refluxed for 2 hours and a green colour solid product was obtained. The product was filtered, washed with methanol and dried in vacuo. The crystallization was done into water methanol mixture; the colour of crystals was green and obtained in 20 days with slow evaporation. Yield 85%, Anal. Calc. for

$C_{14}H_{20}Cl_2CuN_4O_2$ (410.78): C, 42.82; H, 7.19; N,19.02 Found: C,42.74; H,7.05; N,19.10; IR data (KBr,  $\nu_{max}/cm^{-1}$ ): 1,603  $\nu_{C=O}$ , 1,398  $\nu_{C-N}$ , 2,809, 3,435, 772. UV-visible [Phosphate buffer  $P^H=7.2$ ;  $\lambda_{max}/nm$  ( $\epsilon/M^{-1}Cm^{-1}$  )]: 246(23,000), 270 (2,450), 634 (320).

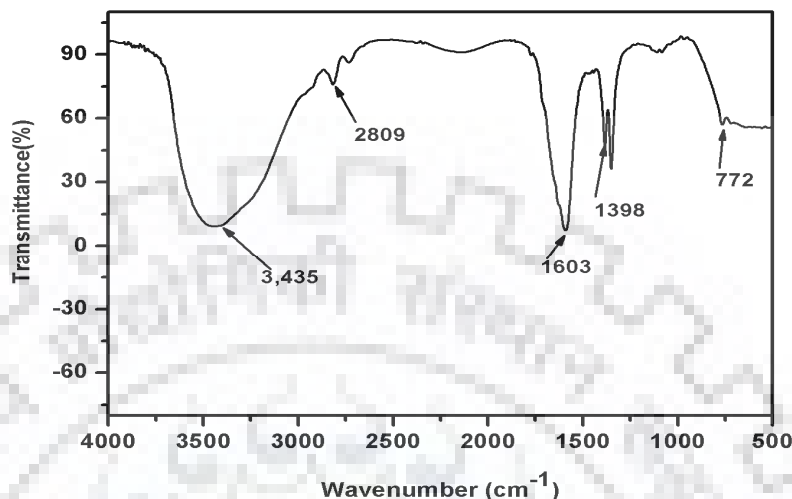


Fig. 4.27 Infrared spectrum of complex  $[Cu(TETA^{TA})(Cl_2)](5)$

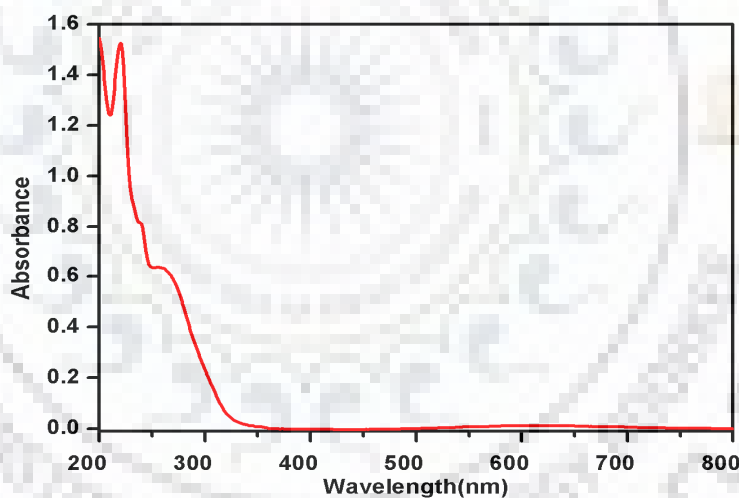


Fig. 4.28 UV-visible spectrum of complex  $[Cu(TETA^{TA})(Cl_2)](5)$  in 0.1 M phosphate buffer pH 7.2

#### 4.8 X - ray crystallography

The data collection and processing for the complex **5** were performed on Bruker Kappa Apex-II CCD diffractometer by using graphite monochromated Mo- $K\alpha$  radiation ( $\lambda = 0.71070 \text{ \AA}$ ) at 293K. Crystal structure was solved by direct methods. Structure solution, refinement and data output were carried out with the SHELXTL program.<sup>325,326,360</sup> All non-

hydrogen atoms were refined anisotropically. Hydrogen atoms were placed in geometrically calculated positions and refined using a riding model. Images were created with the DIAMOND program.<sup>327</sup>

#### 4.9 Organic Dye degradation

The degradation experiment was carried out in 0.1 phosphate buffer pH 7.2 and it was monitored using UV-visible absorbance at different wavelength for corresponding dyes. The complex concentration for the degradation was  $2.5 \times 10^{-6}$  M. The concentration orange II dye in phosphate buffer was  $3 \times 10^{-5}$  M, RhB concentration  $5 \times 10^{-5}$  M, and MB(  $5 \times 10^{-5}$  M). The hydrogen peroxide concentration for all the dye was taken ( $4.4 \times 10^{-4}$  M).

#### 4.10 Theoretical calculation

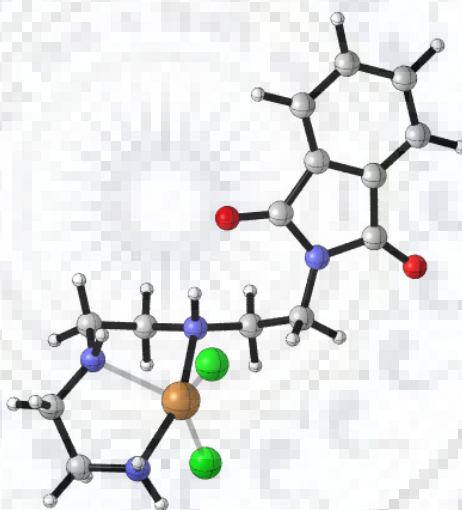


**Fig. 4.29** Ground state optimized geometry of complex  $[\text{Cu}(\text{TETA}^{\text{TA}})(\text{Cl}_2)]$  (5) using B3LYP/LANL2DZ

**Table 4.7** Percentage contribution of complex  $[\text{Cu}(\text{TETA}^{\text{TA}})(\text{Cl}_2)]$  (5) in both alpha and beta orbitals

Molecular orbitals	Orbital Contribution(alpha)						Main bond type
	N middle ( $N_m$ )	Cu	N residual ( $N_r$ )	N terminal ( $N_t$ )	Cl	Phthalic anhydride (PA)	
L+5	18	60	5	15	0	2	$d_{x^2-y^2}(\text{Cu}) + \pi^*(N_m) + \pi^*(N_t)$



L+4	6	13	4	6	0	71	$\pi^*$ (L)
L+3	15	43	2	23	0	16	$d_{z^2}$ (Cu) + $\pi^*$ (L)
L+2	0	0	0	0	0	100	$\pi^*$ (PA)
L+1	2	86	3	4	5	0	$d_{z^2}$ (Cu) + $\pi^*$ (L)
<b>LUMO</b>	3	94	0	0	3	0	$d_{z^2}$ (Cu)
<b>HOMO</b>	1	96	0	0	2	0	$d_{z^2}$ (Cu)
H-1	1	95	1	2	1	0	$d_{x^2-y^2}$ (Cu)
H-2	0	96	1	1	1	0	$d_{x^2-y^2}$ (Cu)
H-3	0	0	1	0	0	99	$\pi$ (PA)
H-4	0	0	0	0	0	100	$\pi$ (PA)
H-5	0	0	7	0	7	85	$\pi$ (N <sub>t</sub> ) + $\pi$ (Cl) $\pi$ (PA)

Molecular orbital	Orbital Contribution(beta)						Main bond type
	N middle (N <sub>m</sub> )	Cu	Nresidula (N <sub>r</sub> )	N terminal (N <sub>t</sub> )	Cl	Phthalic anhydride (PA)	
L+5	6	13	4	6	0	71	$\pi^*$ (L)
L+4	15	43	2	23	0	16	$d_{z^2}$ (Cu) + $\pi^*$ (L)
L+3	0	0	0	0	0	100	$\pi^*$ (PA)
L+2	2	86	3	4	5	0	$d_{z^2}$ (Cu) + $\pi^*$ (L)
L+1	3	94	0	0	3	0	$d_{z^2}$ (Cu)
<b>LUMO</b>	<b>1</b>	<b>96</b>	<b>0</b>	<b>0</b>	<b>2</b>	<b>0</b>	$d_{x^2-y^2}$ (Cu)
<b>HOMO</b>	<b>1</b>	<b>95</b>	<b>1</b>	<b>2</b>	<b>1</b>	<b>0</b>	$d_{x^2-y^2}$ (Cu)
H-1	0	96	1	1	1	0	$d_{x^2-y^2}$ (Cu)
H-2	0	0	1	0	0	99	$\pi$ (PA)
H-3	0	0	0	0	0	100	$\pi$ (PA)
H-4	0	0	7	0	7	85	$\pi$ (PA)
H-5	37	4	6	7	42	4	$\pi$ (N <sub>m</sub> ) + $\pi$ (Cl)

 Table 4.8 Mulliken atomic spin densities for complex [Cu(TETA<sup>TA</sup>)(Cl<sub>2</sub>)] (5)

Atoms	Mulliken atomic spin densities
Cu	0.5289
Cl1	0.0988
Cl2	0.1391
Rest ligand	0.2530

**Table 4.9** Selected bond distances (Å) and bond angles (°) of complex [Cu(TETA<sup>TA</sup>)(Cl<sub>2</sub>)] (5), theoretical as well as experimental

Bond distances			Bond angles		
Experimental		Theoretical	Experimental		Theoretical
Cu1—N1	2.022(4)	2.03405	N1—Cu1—N2	84.27(13)	82.244
Cu1—N2	2.032(4)	2.25863	N1—Cu1—N3	161.64(13)	160.005
Cu1—N3	2.055(3)	2.04638	N2—Cu1—N3	83.44(13)	79.746
Cu1—Cl2	2.305(2)	2.39630	N1—Cu1—Cl2	93.08(10)	92.662
Cu1—Cl1	2.547(2)	2.39811	N2—Cu1—Cl2	160.10(10)	150.786
N1—C1	1.472(6)	1.49572	N3—Cu1—Cl2	93.91(9)	97.458
C2—C1	1.504(9)	1.55018	N1—Cu1—Cl1	96.3(1)	87.181
N2—C2	1.457(6)	1.48444	N2—Cu1—Cl1	94.33(10)	94.942
N2—C3	1.452(7)	1.48805	N3—Cu1—Cl1	98.18(9)	97.458
C4—C3	1.517(7)	1.55571	Cl2—Cu1—Cl1	105.38(4)	110.820
N3—C4	1.466(6)	1.49929			

### 4.11 Degradation of orange II dye products

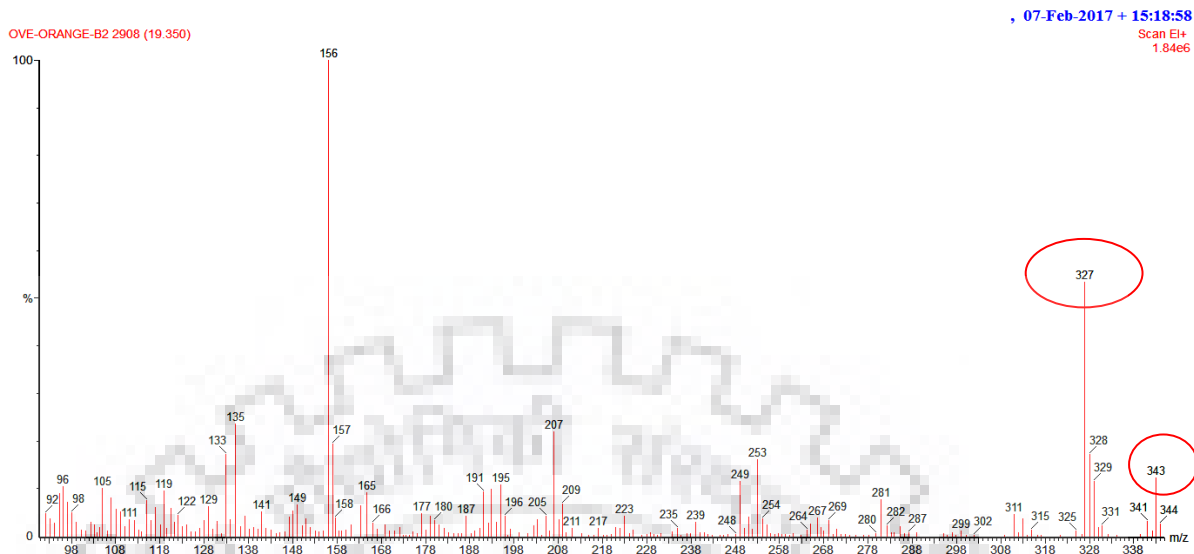


Fig. 4.30 Degradation product m/z monitored by GC-MS

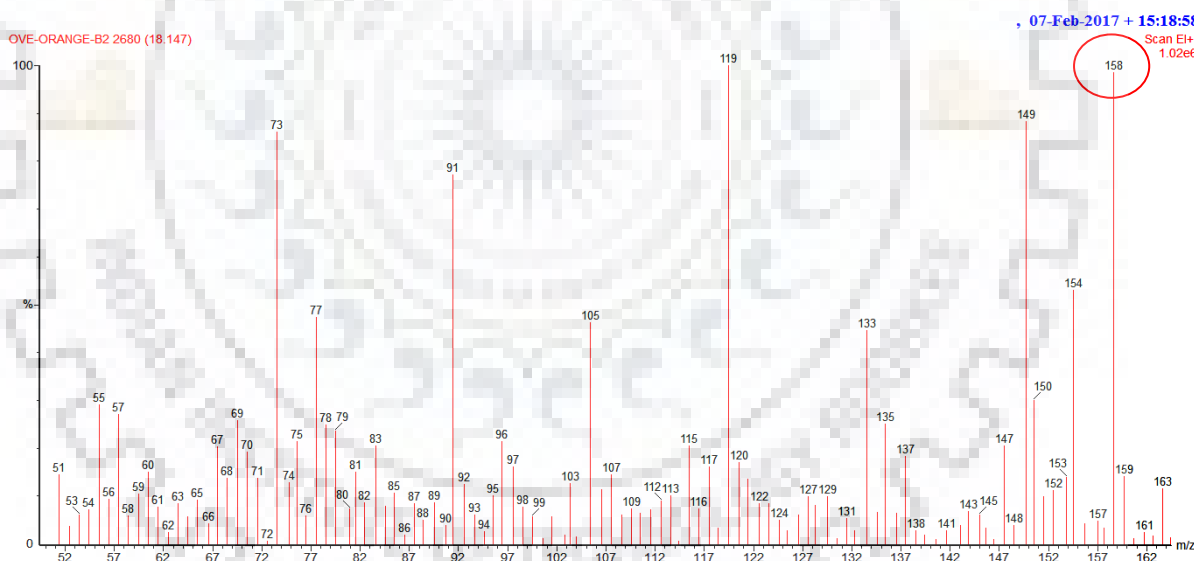


Fig. 4.31 Degradation product m/z monitored by GC-MS

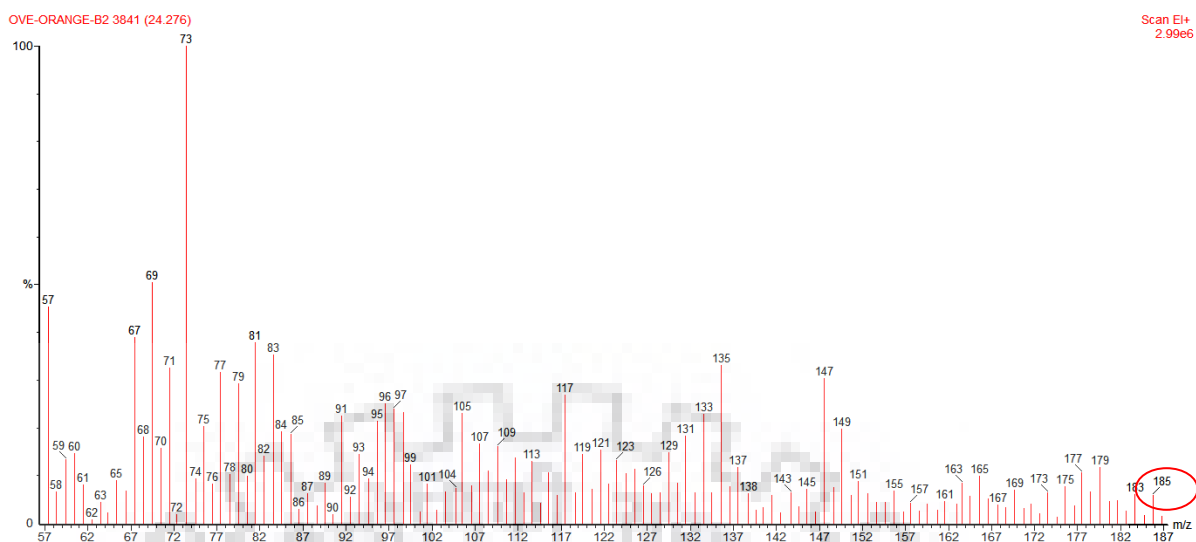


Fig. 4.32 Degradation product m/z monitored by GC-MS

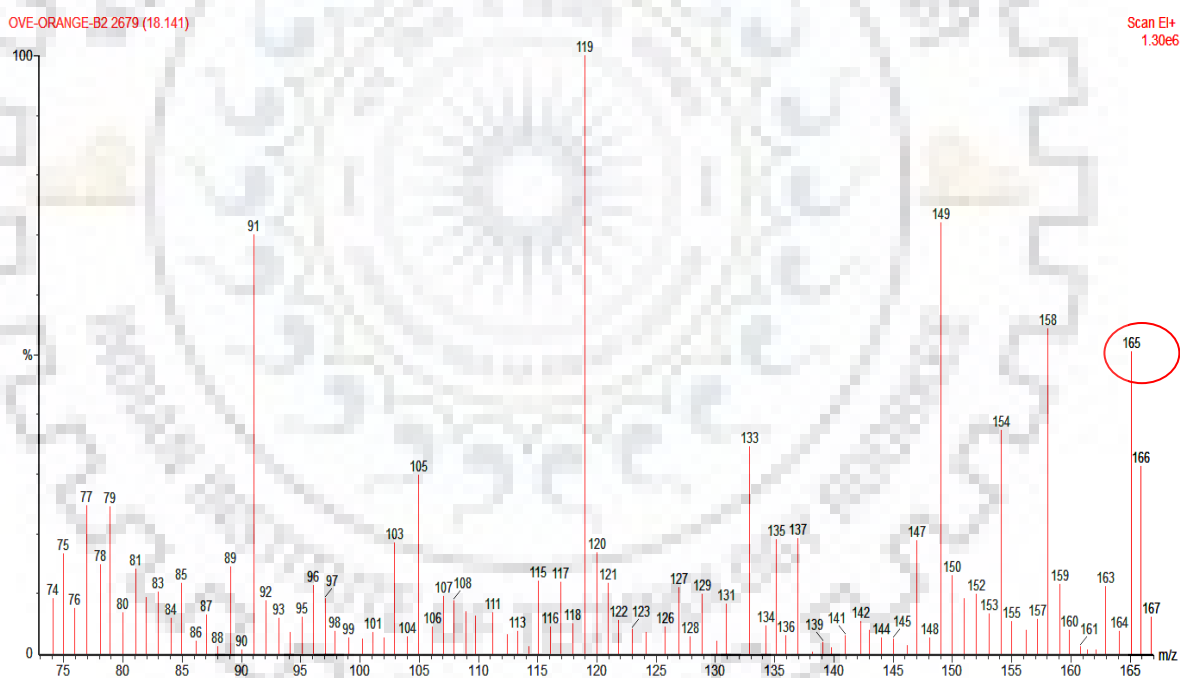


Fig. 4.33 Degradation product m/z monitored by GC-MS

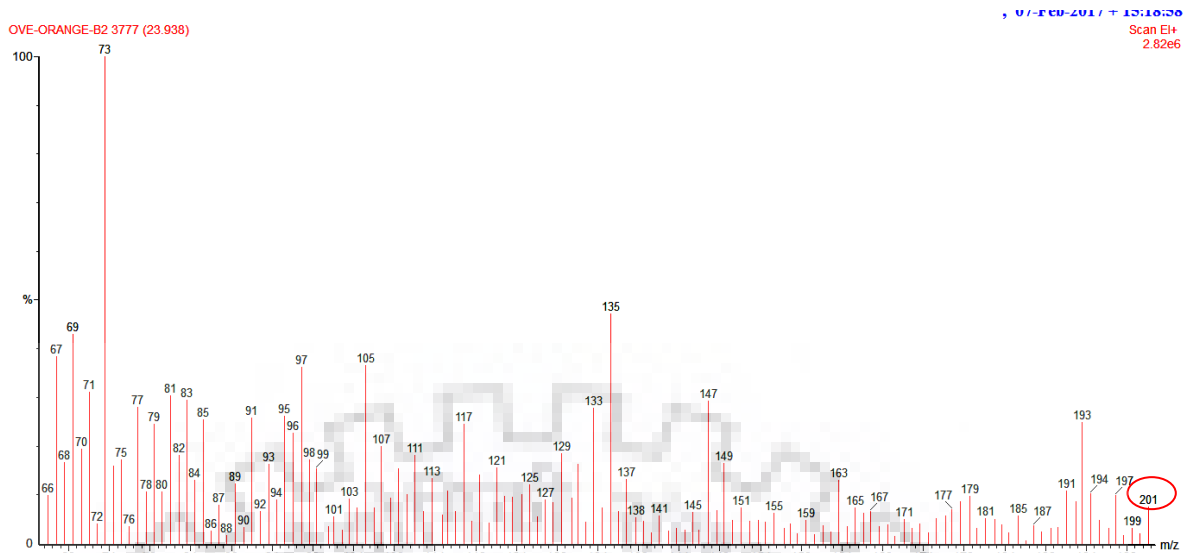


Fig. 4.34 Degradation product m/z monitored by GC-MS

#### 4.12 Degradation of rhodamine B (RhB) dye products

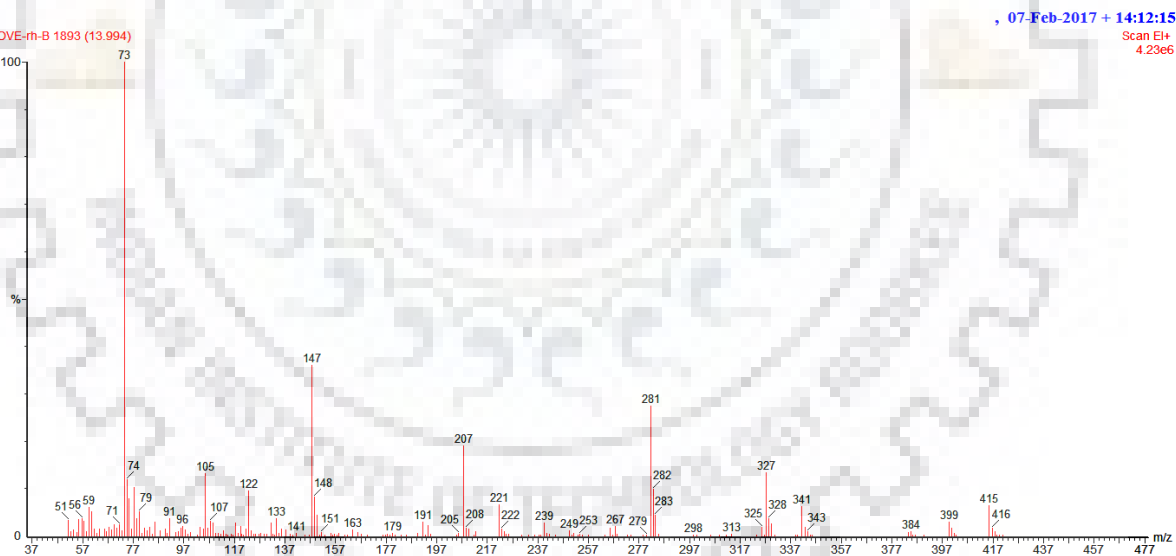


Fig. 4.35 Degradation product m/z monitored by GC-MS

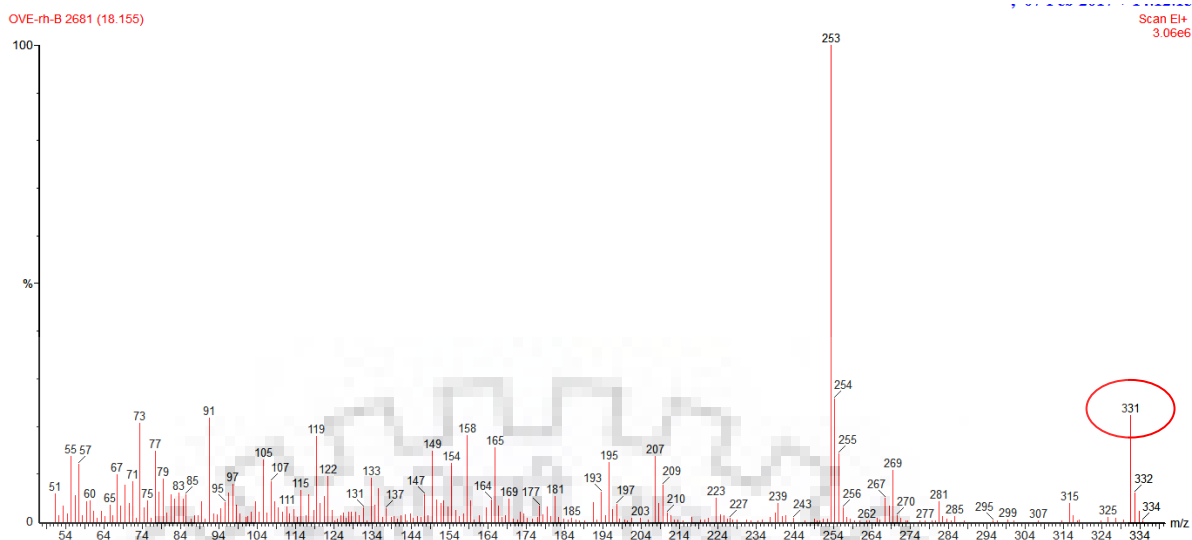


Fig. 4.36 Degradation product m/z monitored by GC-MS

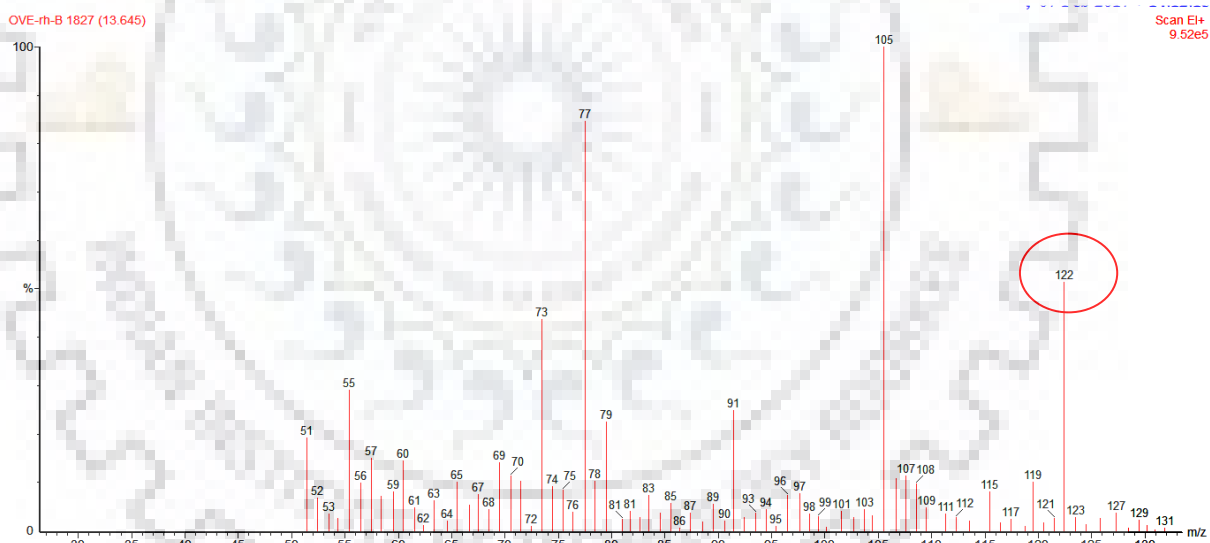


Fig. 4.37 Degradation product m/z monitored by GC-MS

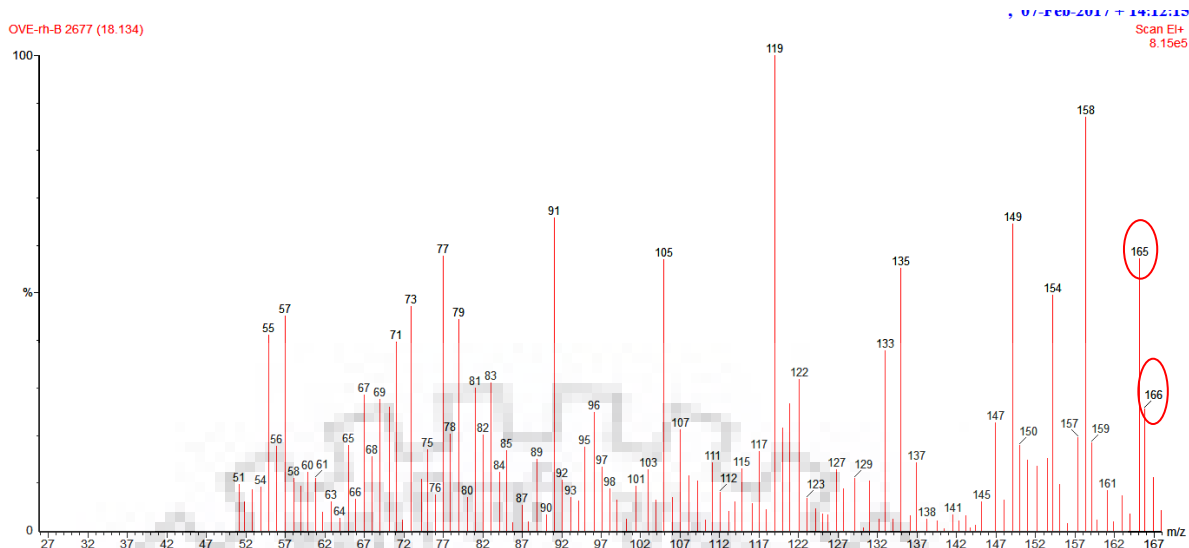


Fig. 4.38 Degradation product m/z monitored by GC-MS

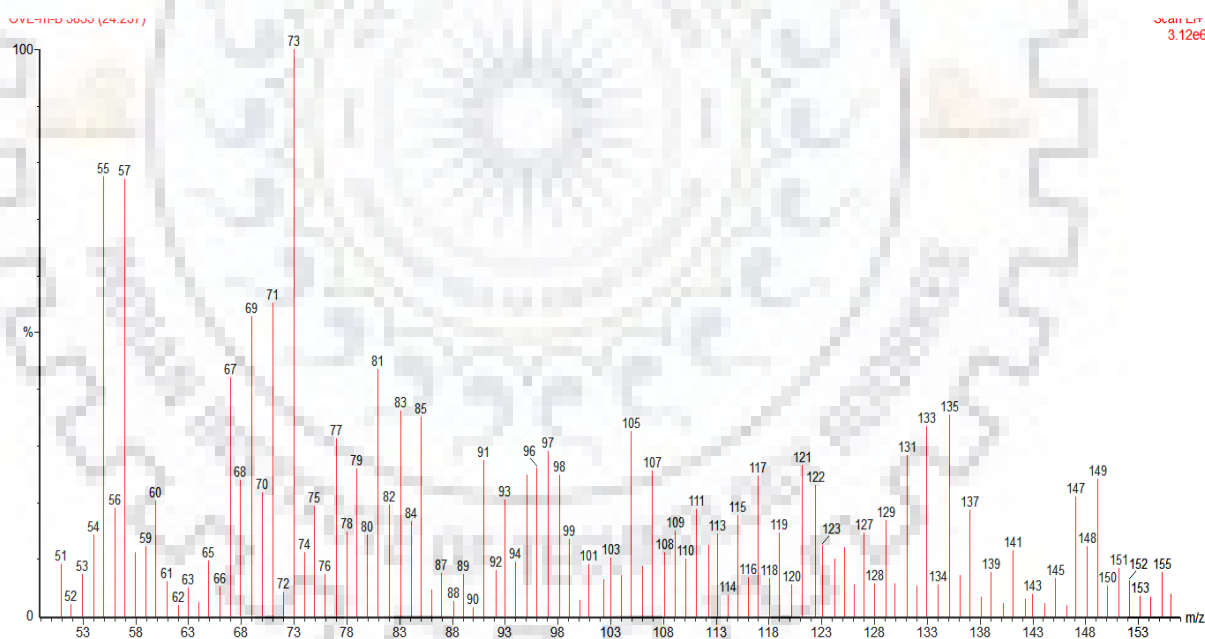


Fig. 4.39 Degradation product m/z monitored by GC-MS

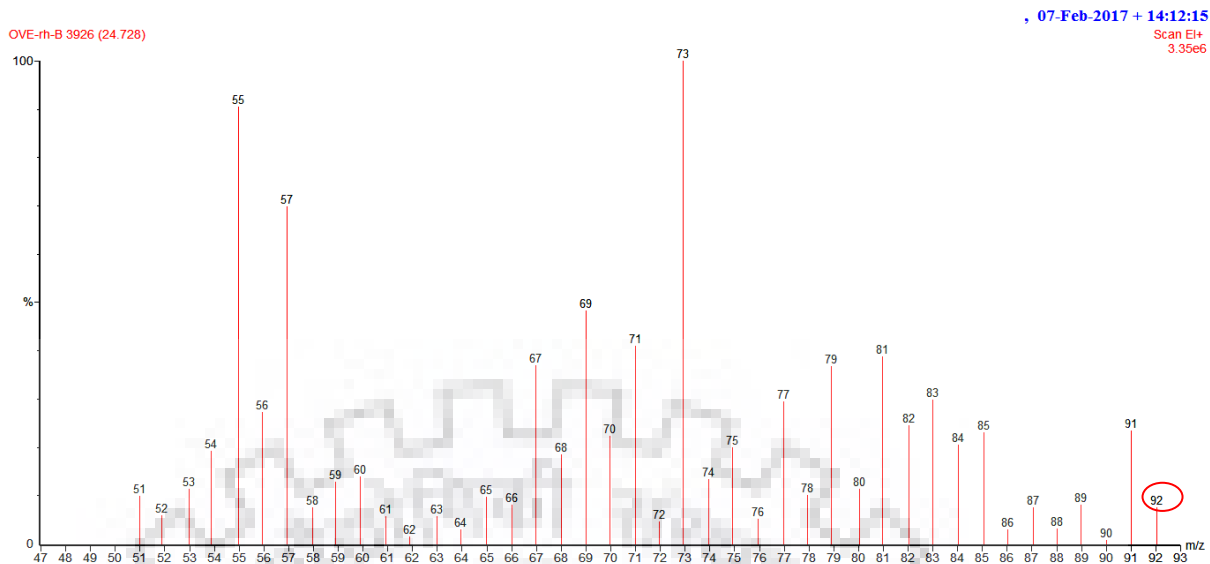


Fig. 4.40 Degradation product m/z monitored by GC-MS

### 4.13 Degradation of methylene blue dye products

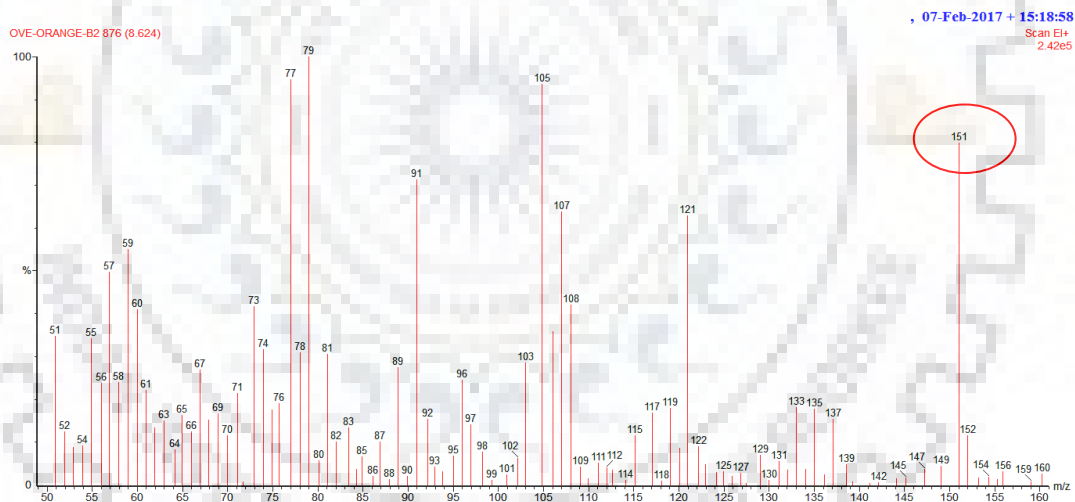


Fig. 4.41 Degradation product m/z monitored by GC-MS



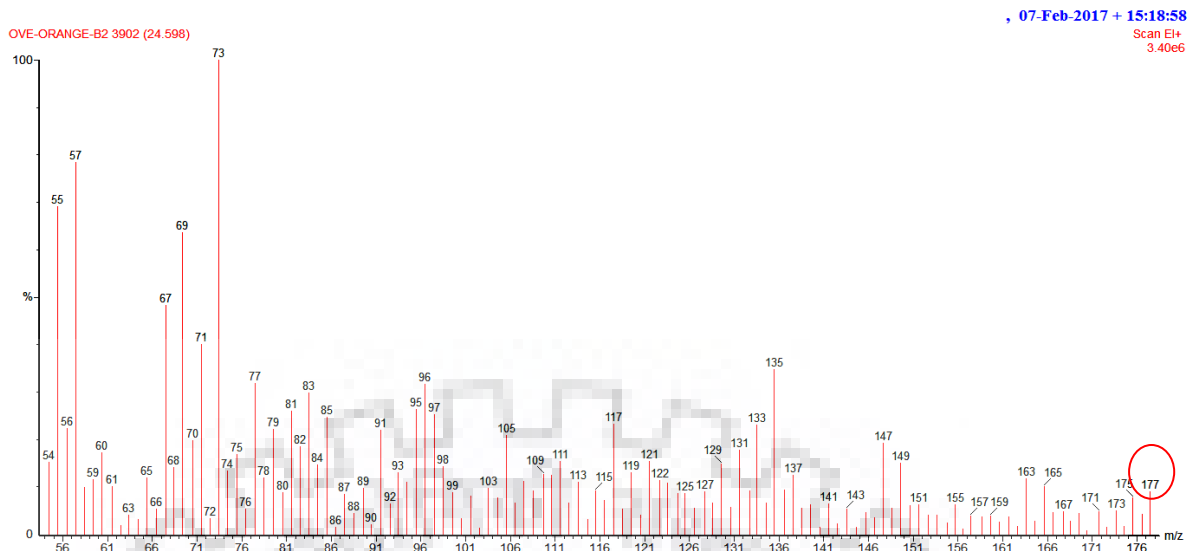


Fig. 4.42 Degradation product m/z monitored by GC-MS

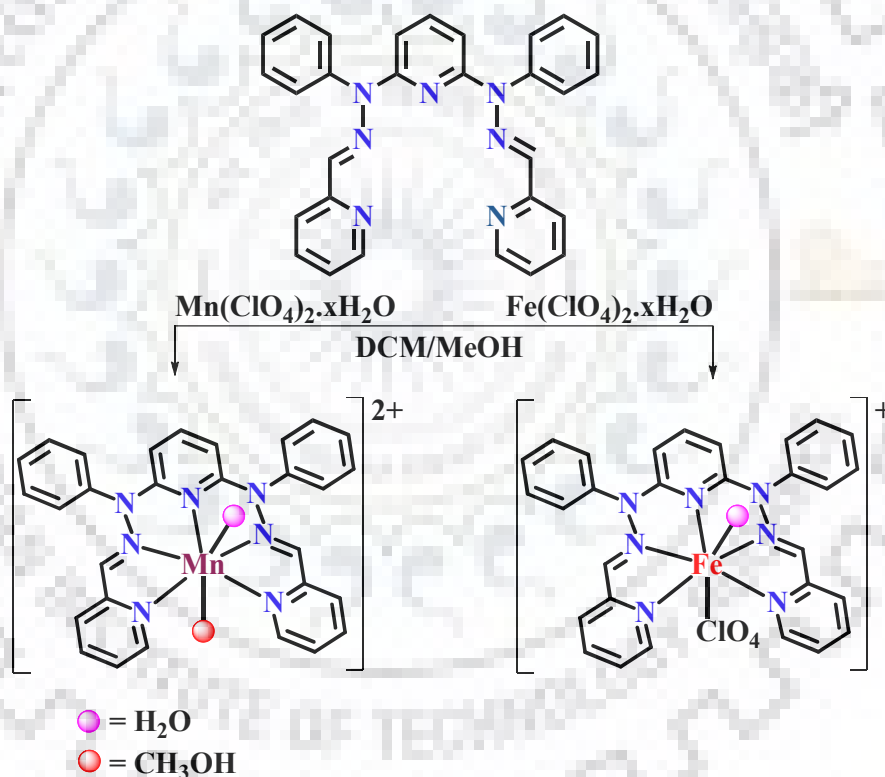


Fig. 4.43 Degradation product m/z monitored by GC-MS

## 5.1 Introduction

Reactive oxygen species (ROS) are produced due to cellular metabolic process superoxide ( $O_2^{\bullet-}$ ) ion is a by-product of aerobic metabolism and integral part of ROS.<sup>361,362</sup> Superoxide are destroyed by a class of metalloenzymes which are called SOD enzymes. The dismutation/disproportion of superoxide happens through the conversion of ( $O_2^{\bullet-}$ ) to either oxygen or hydrogenperoxide ( $H_2O_2$ ) catalysed by SOD enzymes.<sup>187,363</sup> It is well known in the literature this detrimental superoxide ion could mediate several diseases like Parkinson's disease, neuronal apoptosis, cancer and AIDS. Hence, there are considerable endeavour for the design and synthesis of small molecules superoxide dismutase mimetics because these small molecules would be important for therapeutic applications and such molecules are important in metallopharmaceutical research.<sup>364</sup> Iron and manganese SOD are two closely related enzyme having sequence similarity and overall fold. The coordination and conformation of the ligands with the metals have been found to assists the high SOD activity.<sup>365</sup> Investigation of literature revealed that few research groups reported small molecule mimic for SOD enzyme by rational design of manganese and iron complexes with proper shape and ligand donor sets. These complexes should be stable under physiological condition and metal ion should be tightly bound to perform catalytic activity.<sup>366</sup> Superoxide dismutase mimetics in seven-coordinate macrocyclic Mn(II) complexes of pentaaza crowns which have been considered as clinical candidates for a variety of inflammatory conditions.<sup>238</sup> Burmazović and co-workers reported the seven coordinated manganese complexes which showed excellent superoxide dismutase activity.<sup>217, 241,367-369</sup> Burmazović also reported macrocyclic porphyrin complexes as small molecule iron containing SOD mimetics.<sup>370</sup> Bonchio and co-workers recently reported porphyrin manganese complexes for the dismutation/disproportion of superoxide into oxygen and hydrogen peroxide.<sup>371</sup> Britovsek and co-workers showed the manganese complexes with series of seven-

coordinated linear pentadentate ligands which are capable showing superoxide dismutase activity.<sup>372</sup> Ueyama and co-workers reported novel seven-coordinated Mn(II) complexes showing superoxide dismutase activity.<sup>373</sup> Salen complexes of manganese, iron and their derivatives were extensively used for the mimicking of SOD activity.<sup>374,375</sup> From the literature survey it is clear that they have been utilized macrocyclic ligands because the ligand provided better thermodynamic and kinetic stability in vivo.<sup>365</sup> Herein, we report the systematic design and synthesis of novel pentadentate ligand, manganese and iron complexes and their superoxide dismutase like activity studies



**Scheme 5.1** Synthetic procedure for complex  $[\text{Mn}(\text{L}^6)(\text{H}_2\text{O})(\text{CH}_3\text{OH})](\text{ClO}_4)_2$  (6) and Complex  $[\text{Fe}(\text{L}^6)(\text{H}_2\text{O})(\text{ClO}_4)]\text{ClO}_4$  (7)

## 5.2 Results and discussions

### 5.2.1 Synthesis and characterization

Complex  $[\text{Mn}(\text{L}^6)(\text{H}_2\text{O})(\text{CH}_3\text{OH})](\text{ClO}_4)_2$  (**6**) and  $[\text{Fe}(\text{L}^6)(\text{H}_2\text{O})(\text{ClO}_4)]\text{ClO}_4$  (**7**) were characterized by different spectroscopic methods; furthermore molecular structures of both the complexes were determined by X-ray crystallography. Ligand  $\{\text{PyPhime-pycarbo}=(\text{L}^6)\}$  was synthesized on stirring 2,6-bis(1-phenylhydrazinyl)pyridine and pyridine-2-carboxaldehyde in 1:2 ratio at room temperature in methanol solvent a yellow precipitate was obtained within 30 min and characterized by using different spectroscopic techniques. Complex  $[\text{Mn}(\text{L}^6)(\text{H}_2\text{O})(\text{CH}_3\text{OH})](\text{ClO}_4)_2$  (**6**) and  $[\text{Fe}(\text{L}^6)(\text{H}_2\text{O})(\text{ClO}_4)]\text{ClO}_4$  (**7**) were synthesized by the reaction of  $\text{L}^6$  and manganese  $[\text{Mn}(\text{ClO}_4)_2 \cdot 6\text{H}_2\text{O}]$  or iron  $[\text{Fe}(\text{ClO}_4)_2 \cdot 6\text{H}_2\text{O}]$  metal salts respectively in dichloromethane-methanol (1:1) solution. The synthetic procedure of the complex  $[\text{Mn}(\text{L}^6)(\text{H}_2\text{O})(\text{CH}_3\text{OH})](\text{ClO}_4)_2$  (**6**) and  $[\text{Fe}(\text{L}^6)(\text{H}_2\text{O})(\text{ClO}_4)]\text{ClO}_4$  (**7**) were described in Scheme 5.1. Both the complexes were characterized by various spectral and analytical techniques. In complex  $[\text{Mn}(\text{L}^6)(\text{H}_2\text{O})(\text{CH}_3\text{OH})](\text{ClO}_4)_2$  (**6**) the coordination of the imine N with the metal centre was verified with IR spectroscopic peak shift from  $1572 \text{ cm}^{-1}$  ( $\nu_{\text{C}=\text{N}}$  for ligand) to  $1600 \text{ cm}^{-1}$  ( $\nu_{\text{C}=\text{N}}$  for complex  $[\text{Mn}(\text{L}^6)(\text{H}_2\text{O})(\text{CH}_3\text{OH})](\text{ClO}_4)_2$  (**6**) and  $1589 \text{ cm}^{-1}$  ( $\nu_{\text{C}=\text{N}}$  for complex  $[\text{Fe}(\text{L}^6)(\text{H}_2\text{O})(\text{ClO}_4)]\text{ClO}_4$  (**7**)). The IR spectra of both the complex  $[\text{Mn}(\text{L}^6)(\text{H}_2\text{O})(\text{CH}_3\text{OH})](\text{ClO}_4)_2$  (**6**) and  $[\text{Fe}(\text{L}^6)(\text{H}_2\text{O})(\text{ClO}_4)]\text{ClO}_4$  (**7**), were dominated by vibrations of the pyridyl moiety as verified by the absorptions observed around  $1474$  and  $1590 \text{ cm}^{-1}$ .<sup>308,376,377</sup> Characteristic peaks for counter anion, perchlorate, were observed near  $1090$  and  $625 \text{ cm}^{-1}$  for both the complex  $[\text{Mn}(\text{L}^6)(\text{H}_2\text{O})(\text{CH}_3\text{OH})](\text{ClO}_4)_2$  (**6**) and  $[\text{Fe}(\text{L}^6)(\text{H}_2\text{O})(\text{ClO}_4)]\text{ClO}_4$  (**7**). (Spectra are shown in Fig. 5.10, 5.13).<sup>308,376,377</sup> The UV-visible spectrum of complex  $[\text{Mn}(\text{L}^6)(\text{H}_2\text{O})(\text{CH}_3\text{OH})](\text{ClO}_4)_2$  (**6**) and  $[\text{Fe}(\text{L}^6)(\text{H}_2\text{O})(\text{ClO}_4)]\text{ClO}_4$  (**7**) were recorded in methanolic solution and the broad band near

410 nm was obtained probably due to ligand-to-metal charge transfer transition (LMCT) (Fig. 5.11 and 5.14).<sup>378</sup> The molecular structures of the complexes  $[\text{Mn}(\text{L}^6)(\text{H}_2\text{O})(\text{CH}_3\text{OH})](\text{ClO}_4)_2$  (**6**) and  $[\text{Fe}(\text{L}^6)(\text{H}_2\text{O})(\text{ClO}_4)]\text{ClO}_4$  (**7**) were determined by using X-ray crystallographic studies and their ORTEP plots are displayed in Fig. 5.1. The packing diagrams were displayed in Fig. 5.16 and 5.17. The crystallographic parameters for both the complex  $[\text{Mn}(\text{L}^6)(\text{H}_2\text{O})(\text{CH}_3\text{OH})](\text{ClO}_4)_2$  (**6**) and  $[\text{Fe}(\text{L}^6)(\text{H}_2\text{O})(\text{ClO}_4)]\text{ClO}_4$  (**7**) are shown in (Table 5.3). In both the complexes  $[\text{Mn}(\text{L}^6)(\text{H}_2\text{O})(\text{CH}_3\text{OH})](\text{ClO}_4)_2$  (**6**) and  $[\text{Fe}(\text{L}^6)(\text{H}_2\text{O})(\text{ClO}_4)]\text{ClO}_4$  (**7**) pentadentate ligand ( $\text{L}^6$ ) coordinated to metal centres in distorted pentagonal bipyramidal geometry. Coordinating sites of both the complexes showed three pyridine ( $\text{N}_{\text{py}}$ ), two imine ( $\text{N}_{\text{im}}$ ) nitrogens which were coordinated in a plane whereas the apical sites were occupied by a water, methanol (in case of complex  $[\text{Mn}(\text{L}^6)(\text{H}_2\text{O})(\text{CH}_3\text{OH})](\text{ClO}_4)_2$  (**6**) and water, perchlorate anion (in case of complex  $[\text{Fe}(\text{L}^6)(\text{H}_2\text{O})(\text{ClO}_4)]\text{ClO}_4$  (**7**)). Selected bond angles of both the complexes were depicted in Table 5.4 and selected bond distances were in Table 5.5 and 5.6. In complex  $[\text{Mn}(\text{L}^6)(\text{H}_2\text{O})(\text{CH}_3\text{OH})](\text{ClO}_4)_2$  (**6**) the Mn- $\text{N}_{\text{py}}$  bond distances (Å) were found to be 2.311 (Mn-N4), 2.394 (Mn-N1), 2.341 (Mn-N7), and Mn- $\text{N}_{\text{im}}$  2.321 (Mn-N2), 2.356 (Mn-N6), which are consistent to the reported literature.<sup>367,371</sup> The Mn-O1 bond distance was 2.154 (Å) for coordinated water molecule and Mn-O2 distance was 2.220 (Å) for the methanol bond to the manganese metal ion. However, in complex  $[\text{Fe}(\text{L}^6)(\text{H}_2\text{O})(\text{ClO}_4)]\text{ClO}_4$  (**7**), Fe- $\text{N}_{\text{py}}$  bond distances (Å) were found to be 2.222 (Fe1-N6), 2.286 (Fe1-N4), 2.306 (Fe1-N3); Fe- $\text{N}_{\text{im}}$   $\text{N}_{\text{py}}$  bond distances (Å) were found to be 2.231 (Fe1-N7), 2.218 (Fe1-N5). The Fe1-O10 bond distance was 2.137 (Å) for coordinating water molecule and Fe1-O4 distance was 2.276 (Å) for the coordinating perchlorate ion. Bond distances in complex  $[\text{Mn}(\text{L}^6)(\text{H}_2\text{O})(\text{CH}_3\text{OH})](\text{ClO}_4)_2$  (**6**) and  $[\text{Fe}(\text{L}^6)(\text{H}_2\text{O})(\text{ClO}_4)]\text{ClO}_4$  (**7**) clearly express the presence of high-spin manganese and iron centres, respectively.

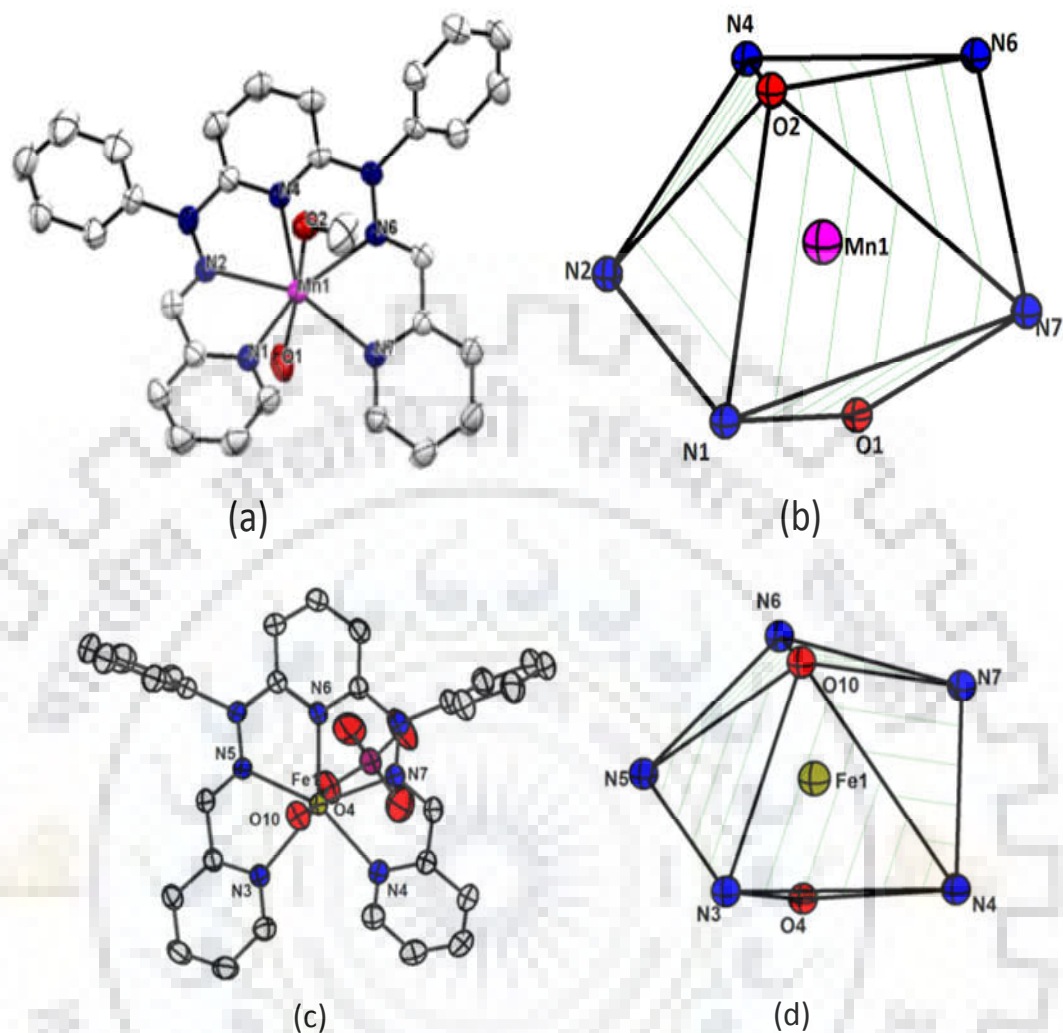


**Fig.5.1** (a)ORTEP diagram (50% probability level) of complex  $[\text{Mn}(\text{L}^6)(\text{H}_2\text{O})(\text{CH}_3\text{OH})](\text{ClO}_4)_2$  (6); (b) Distorted pentagonal bipyramidal geometry around the metal centre; (c) ORTEP diagram (50% probability level) of complex  $[\text{Fe}(\text{L}^6)(\text{H}_2\text{O})(\text{ClO}_4)]\text{ClO}_4$  (7); (d) Distorted pentagonal bipyramidal geometry of the molecule around the metal centre. (All hydrogen atoms and anions are omitted for clarity)

### 5.2.2 Electrochemical investigation

The electrochemical properties of both the complex  $[\text{Mn}(\text{L}^6)(\text{H}_2\text{O})(\text{CH}_3\text{OH})](\text{ClO}_4)_2$  (6) and complex  $[\text{Fe}(\text{L}^6)(\text{H}_2\text{O})(\text{ClO}_4)]\text{ClO}_4$  (7) were investigated by cyclic voltammetric studies. An irreversible voltammogram ( $\text{Mn}^{\text{II}}/\text{Mn}^{\text{III}}$ ) at 1.14 V vs Ag/AgCl was recorded for complex  $[\text{Mn}(\text{L}^6)(\text{H}_2\text{O})(\text{CH}_3\text{OH})](\text{ClO}_4)_2$  (6) that is quite similar as reported by Britovsek and co-workers<sup>372</sup> whereas, complex  $[\text{Fe}(\text{L}^6)(\text{H}_2\text{O})(\text{ClO}_4)]\text{ClO}_4$  (7) provided quasi-reversible

(Fe<sup>II</sup>/Fe<sup>III</sup>) redox couple with  $E_{1/2}$  value of 0.96V vs Ag/AgCl (voltammograms are shown in Fig. 5.12 and 5.15). The data obtained was depicted in Table 5.1.

**Table 5.1.** Electrochemical data for M<sup>II</sup>/M<sup>III</sup> redox couple 298 K<sup>a</sup> vs Ag/ AgCl. (M = Mn and Fe)

Complexes	M <sup>II</sup> /M <sup>III</sup>			
	$E_{pa}/V$	$E_{pc}/V$	$E_{1/2}^b, V (\Delta E_p^c, mV)$	$n = i_{pa}/i_{pc}$
<b>6</b>	1.14	.....	.....	.....
<b>7</b>	1.01	0.92	0.96(90)	2.068

<sup>[a]</sup> Electrochemical data measured in DMSO with 0.1m tetrabutylammonium perchlorate (TBAP). <sup>[b]</sup>Data from cyclic voltammetric measurements;  $E_{1/2}$  is calculated as average of anodic ( $E_{pa}$ ) and cathodic ( $E_{pc}$ ) peak potentials  $E_{1/2}=1/2(E_{pa}+E_{pc})$ ; and <sup>[c]</sup>  $\Delta E_p = E_{pa} - E_{pc}$  at scan rate 0.1 Vs<sup>-1</sup>, <sup>[d]</sup> Constant-potential coulometric data  $n=i_{pa}/i_{pc}$  calculated for 1e<sup>-</sup> transfer.

### 5.2.3 Superoxide dismutase (SOD) activity study

The Fe/Mn-N<sub>5</sub> binding motif were known to displayed excellent SOD activity, we have also check the effectiveness of the complex [Mn(L<sup>6</sup>)(H<sub>2</sub>O)(CH<sub>3</sub>OH)](ClO<sub>4</sub>)<sub>2</sub> (**6**) and [Fe(L<sup>6</sup>)(H<sub>2</sub>O)(ClO<sub>4</sub>)]ClO<sub>4</sub> (**7**) towards antioxidant activity using nitroblue tetrazolium (NBT) assay.<sup>378</sup> We have also performed the stability of complex [Mn(L<sup>6</sup>)(H<sub>2</sub>O)(CH<sub>3</sub>OH)](ClO<sub>4</sub>)<sub>2</sub> (**6**) and [Fe(L<sup>6</sup>)(H<sub>2</sub>O)(ClO<sub>4</sub>)]ClO<sub>4</sub> (**7**) in physiological condition and it was found that complex [Mn(L<sup>6</sup>)(H<sub>2</sub>O)(CH<sub>3</sub>OH)](ClO<sub>4</sub>)<sub>2</sub> (**6**) and [Fe(L<sup>6</sup>)(H<sub>2</sub>O)(ClO<sub>4</sub>)]ClO<sub>4</sub> (**7**) found stable in wide range of pH 6.8-7.8. The effectiveness of the SOD was determined with the IC<sub>50</sub> values, lower the IC<sub>50</sub> more effective will be the complexes to inhibit the superoxide generated in the reaction media (shown in Table 5.2 and chart 5.1). In NBT method, superoxide anions were generated *in situ* enzymatically by xanthine/xanthine oxidase and dismutation of superoxide anions by the complexes were detected spectrophotometrically by reduction of NBT and monitored by the inhibition curve. Additionally, this inhibition of superoxide radical was further supported by cyclic voltammetric studies (*vide-infra*). From the inhibition curve, complex [Mn(L<sup>6</sup>)(H<sub>2</sub>O)(CH<sub>3</sub>OH)](ClO<sub>4</sub>)<sub>2</sub> (**6**) exhibited good SOD activity with IC<sub>50</sub> value of 1.53±0.42 μM. Whereas, complex [Fe(L<sup>6</sup>)(H<sub>2</sub>O)(ClO<sub>4</sub>)]ClO<sub>4</sub> (**7**)

exhibited  $IC_{50}$  value of  $2.09 \pm 0.33 \mu\text{M}$ . Complex  $[\text{Mn}(\text{L}^6)(\text{H}_2\text{O})(\text{CH}_3\text{OH})](\text{ClO}_4)_2$  (**6**) exhibited excellent SOD activity as compare to complex  $[\text{Fe}(\text{L}^6)(\text{H}_2\text{O})(\text{ClO}_4)]\text{ClO}_4$  (**7**) (Fig.5.2) which was comparable to the same reported for seven-coordinated manganese and iron complexes by Ivanovic-Burmazovic<sup>217,241,367-369</sup> and Ueyama.<sup>373</sup>

**Table 5.2**  $IC_{50}$  value and kinetic catalytic constant ( $k_{\text{McCF}}$ ) of complex  $[\text{Mn}(\text{L}^6)(\text{H}_2\text{O})(\text{CH}_3\text{OH})](\text{ClO}_4)_2$  (**6**) and complex  $[\text{Fe}(\text{L}^6)(\text{H}_2\text{O})(\text{ClO}_4)]\text{ClO}_4$  (**7**) using NBT assay

Complexes	$IC_{50}(\mu\text{M})$	$k_{\text{McCF}} (\text{M}^{-1} \text{s}^{-1})^{\text{a}}$	Reference
Complex <b>6</b>	$1.53^* \pm 0.42$	$1.16 \times 10^7$	This work
Complex <b>7</b>	$2.09^* \pm 0.33$	$0.85 \times 10^7$	This Work
$[\text{MnII}(\text{H}_2\text{dapsox})(\text{CH}_3\text{OH})(\text{H}_2\text{O})](\text{ClO}_4)_2(\text{H}_2\text{O})$	0.013	$1.2 \times 10^7$	241
$[\text{MnII}(\text{Me}_2[15]\text{pyridinaneN}_5)(\text{H}_2\text{O})_2]\text{Cl}_2, \text{H}_2\text{O}$	0.024	$5.3 \times 10^6$	241
$[\text{Mn}(1)(\text{Cl})_2]$	2.57	$2 \times 10^6$	372
$[\text{Mn}(2'\text{or}3')(\text{OTf})_2]$	0.75-1.41	..	372
Mn Salen complexes	0.004–0.75	...	374
Fe Salen complexes	$1.32-8.86 \pm 0.66$	...	375

\*values are average of three experiments performed under identical experimental conditions.

<sup>a</sup>Calculated kinetic catalytic constant<sup>378</sup>



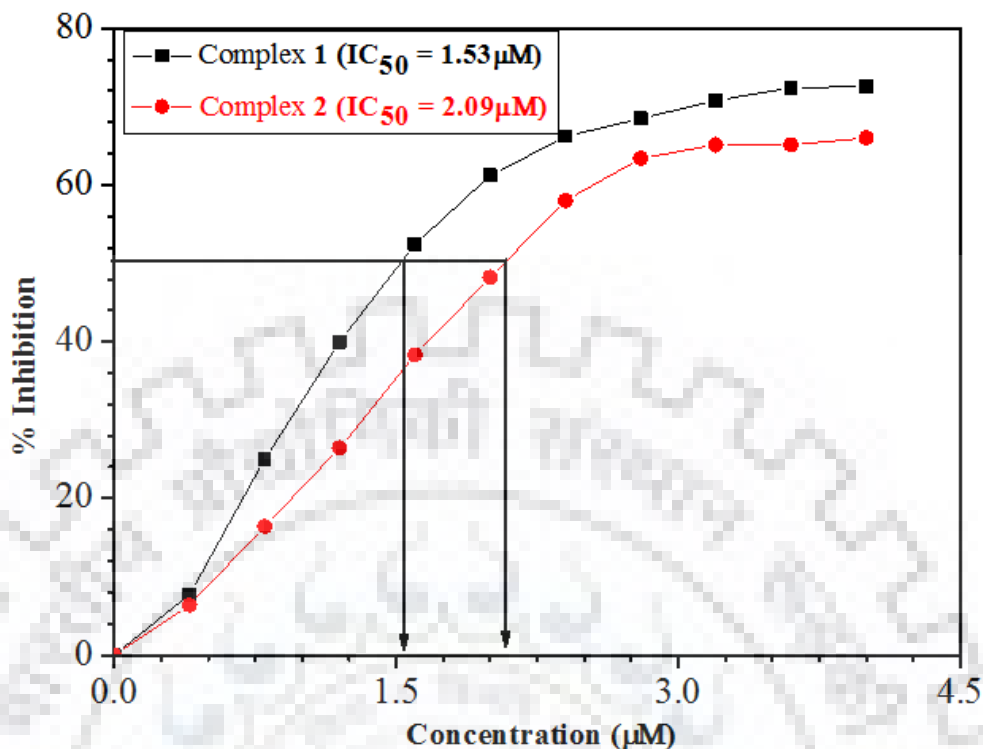


**Fig. 5.2** Superoxide dismutase activity of complex  $[\text{Mn}(\text{L}^6)(\text{H}_2\text{O})(\text{CH}_3\text{OH})](\text{ClO}_4)_2$  (**6**) and  $[\text{Fe}(\text{L}^6)(\text{H}_2\text{O})(\text{ClO}_4)]\text{ClO}_4$  (**7**) with xanthine oxidase–nitro blue tetrazolium assay (NBT assay)

In order to further support the inhibition of superoxide radical, we have performed the cyclic voltammetric measurements in oxygen saturated DMSO in the range of 0 to -1.2 V vs Ag/AgCl.<sup>367</sup> Nitrogen saturated DMSO didn't provide any reduction peak whereas in presence of oxygen a quasi-reversible peak was obtained which clearly indicates the reduction of oxygen<sup>367</sup>, and generation of superoxide ion. (Fig.5.3)

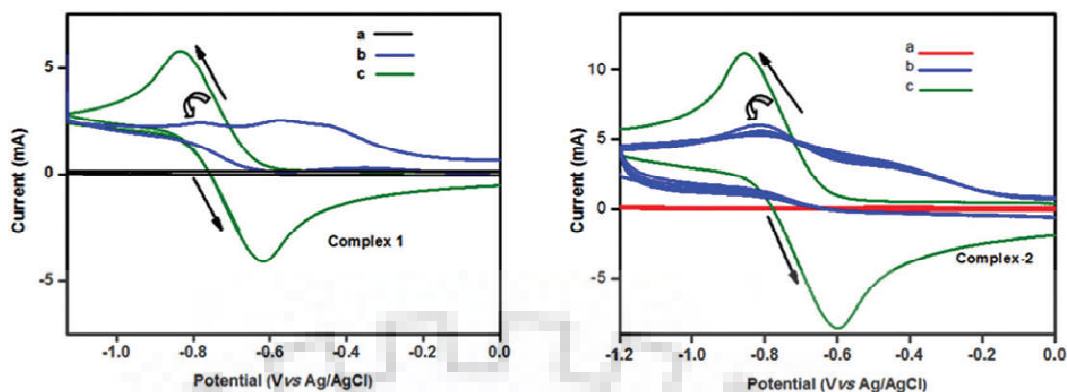
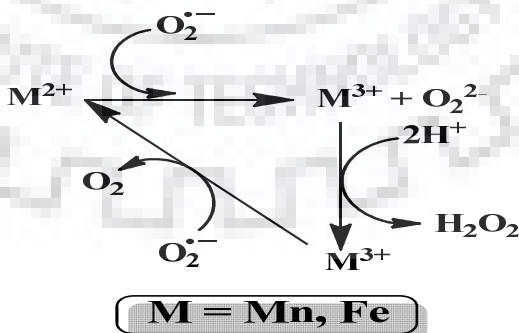


**Fig. 5.3** Cyclic voltammograms of a  $10^{-3}$  M solution of complex  $[\text{Mn}(\text{L}^6)(\text{H}_2\text{O})(\text{CH}_3\text{OH})](\text{ClO}_4)_2$  (**6**) and complex  $[\text{Fe}(\text{L}^6)(\text{H}_2\text{O})(\text{ClO}_4)]\text{ClO}_4$  (**7**) in DMSO in presence of 0.1 M tetrabutylammonium perchlorate (TBAP), using working electrode: glassy-carbon, reference electrode: Ag/AgCl; auxiliary electrode: platinum wire, scan rate  $0.1 \text{ Vs}^{-1}$ . (a) Complexes purged with nitrogen (b) Complexes purged with oxygen (c) Pure DMSO purged with oxygen

Disappearance of this quasi-reversible peak in presence of complex  $[\text{Mn}(\text{L}^6)(\text{H}_2\text{O})(\text{CH}_3\text{OH})](\text{ClO}_4)_2$  (**6**) and complex  $[\text{Fe}(\text{L}^6)(\text{H}_2\text{O})(\text{ClO}_4)]\text{ClO}_4$  (**7**) clearly expressed superoxide dismutation as shown in the Fig. 5.3. Same experiments were also performed with the ligand as a control experiment but we did not get similar type of result.

A probable reaction model for such activity was proposed in Scheme 5.2. Oxidation of the metal complex followed by generation of  $\text{H}_2\text{O}_2$  and finally oxidation of superoxide ions are involved in the mechanism. A similar mechanism was also proposed by Burmazovic and co-workers.<sup>241</sup>



**Scheme 5.2** Proposed reaction mechanism for SOD activity<sup>10</sup>

### 5.2.4 Theoretical calculation

Theoretical calculation was performed using (B3LYP/ LANL2DZ) it provide more electronic structural description for both the complexes.<sup>287</sup> The geometry optimizations for both the complexes were performed at DFT level as shown in Fig. 5.18 and 5.21. In both the complexes alpha and beta states were generated during calculation and it was found out that in the alpha state of manganese, HOMO was mainly metal centered and in beta state HOMO was found ligand centered.(Fig. 5.20 and 5.23) The percentage contribution of different atoms in particular orbitals in both the complexes have been calculated and are listed in (Table 5.7 and 5.10). From Mulliken atomic spin densities calculation of complex  $[\text{Mn}(\text{L}^6)(\text{H}_2\text{O})(\text{CH}_3\text{OH})](\text{ClO}_4)_2$  (**6**), it was clear that the total Mulliken atomic spin densities was five and out of this 4.58 was found on manganese (Shown in Fig. 5.4).

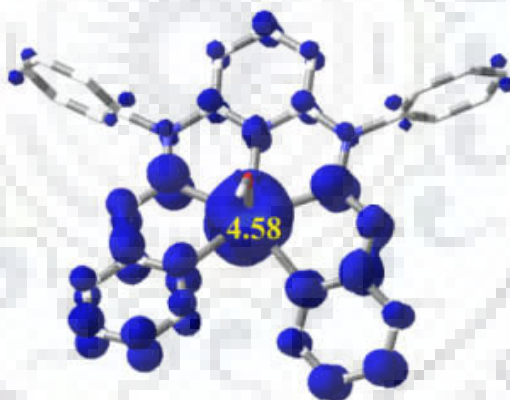


**Fig. 5.4** Mulliken atomic spin densities over the complex  $[\text{Mn}(\text{L}^6)(\text{H}_2\text{O})(\text{CH}_3\text{OH})](\text{ClO}_4)_2$  (**6**) (isovalue = 0.02)

The UV-visible spectra of complexes  $[\text{Mn}(\text{L}^6)(\text{H}_2\text{O})(\text{CH}_3\text{OH})](\text{ClO}_4)_2$  (**6**) and  $[\text{Fe}(\text{L}^6)(\text{H}_2\text{O})(\text{ClO}_4)]\text{ClO}_4$  (**7**) were analysed on the basis of TD-DFT calculations. Experimental and theoretical spectra were displayed in Fig. 5.19 and Fig. 5.22 respectively. The oscillator strengths of three bands at 291 nm, 351 nm and 441 nm were found to be 0.0011, 0.0041 and 0.1134 respectively for complex  $[\text{Mn}(\text{L}^6)(\text{H}_2\text{O})(\text{CH}_3\text{OH})](\text{ClO}_4)_2$  (**6**) On

the other hand, complex  $[\text{Fe}(\text{L}^6)(\text{H}_2\text{O})(\text{ClO}_4)]\text{ClO}_4$  (**7**) exhibited bands near 293 nm, 347 nm and 407 nm with oscillator strengths 0.0534, 0.1799 and 0.0663 respectively. The molecular orbitals involved and their contributions for these transitions are described in Table 5.8 and Table 5.9. These transitions were probably due to n-  $\pi$  and  $\pi$ -  $\pi^*$  electronic transitions. Mulliken atomic spin density calculations for complex  $[\text{Fe}(\text{L}^6)(\text{H}_2\text{O})(\text{ClO}_4)]\text{ClO}_4$  (**7**) gave rise to a value of 4 and out of this, 3.75 was found to be on the iron (Fig. 5.5).

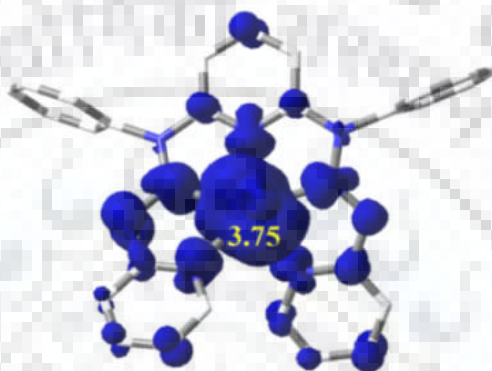


**Fig. 5.5** Mulliken atomic spin densities over the complex  $[\text{Fe}(\text{L}^6)(\text{H}_2\text{O})(\text{ClO}_4)]\text{ClO}_4$  (**7**) (isovalue = 0.02)

### 5.3 Conclusions

We have designed and synthesized new pentadentate ligand which provided seven-coordinated manganese(II) and iron(II) complexes. Molecular structures were determined using single-crystal X-ray diffraction. Utilizing NBT-tetrazolium assay, we determined the superoxide dismutase (SOD) activity using these complexes. It has been found out that both complexes are efficient for SOD activity. The activity was also authenticated by cyclic voltammetry. Theoretical calculations were performed to understand the electronic nature of both the complexes. Seven coordinated iron and manganese complexes with flexible ligands represent the better SOD activity than the rigid complexes.<sup>241</sup> Modification of ligand, synthesis of manganese and iron complexes and biological applications of these complexes are under progress.

## 5.4 Experimental section

### 5.4.1 Materials

All the solvents used were reagent grade. 2,6-bis(1-phenylhydrazinyl)pyridine was prepared by reported procedure<sup>21</sup> Pyridine 2-aldehyde (Acros organics, USA) Solvent used for spectroscopic studies were HPLC grade and purified by standard procedure before use, Mn(ClO<sub>4</sub>)<sub>2</sub>.xH<sub>2</sub>O and Fe(ClO<sub>4</sub>)<sub>2</sub>.xH<sub>2</sub>O, Sigma Aldrich, Steinheim, Germany.

### 5.4.2 Physical measurements

Elemental analyses were carried micro analytically at Elemenlar Vario EL III. Infra red spectra were obtained as KBr pellets with Thermo Nicolet Nexus FT-IR spectrometer, using 16 scans and were reported in cm<sup>-1</sup>. Electronic absorption spectra were recorded with an UV/Vis spectrophotometer, Shimadzu (UV-2401). Cyclic voltammetry measurements were carried out using a CH-600 electroanalyzer. A conventional three-electrode arrangement was using consisting a platinum wire as auxiliary electrode, glassy carbon as working electrode and the Ag(s)/AgCl as reference electrode. These measurements were performed in the presence of 0.1 M tetrabutylammonium perchlorate (TBAP) as the supporting electrolyte, using complex concentration 10<sup>-3</sup> M in acetonitrile. The ferrocene/ferrocenium couple occurs at E<sub>1/2</sub>=+0.40 scan rate 0.1 vs Ag/AgCl under the same experimental conditions. All experiments were performed at room temperature and solutions were thoroughly degassed with nitrogen prior to beginning the experiments. The X-ray data collection and processing for both the complexes were performed on Bruker Kappa Apex-II CCD diffractometer by using graphite monochromated Mo-K $\alpha$  radiation ( $\lambda = 0.71070 \text{ \AA}$ ) at 293 K and 296 K respectively. Crystal structures were solved by SIR-92 method. Structure solution, refinement and data output were carried out with the SHELXTL program.<sup>325,326</sup> All non-hydrogen atoms were refined anisotropically. Hydrogen atoms were placed in geometrically calculated positions and refined using a riding model. Images were created

with the DIAMOND program.<sup>327</sup> (ESI-MS) experiments were performed on a Brüker micrOTOFM-Q-II mass spectrometer.

### 5.4.3 Synthesis of ligand

#### 5.4.3.1 Synthesis of Ligand (L<sup>6</sup>)

2,6-bis(1-phenylhydrazinyl)pyridine was prepared according to the method reported in the literature.<sup>21</sup> Ligand (L<sup>6</sup>) was synthesized by reacting 2,6-bis(1-phenylhydrazinyl)pyridine (291.35mg, 1.00 mmol) and pyridine-2-carboxaldehyde (214.22mg, 2mmol) (1:2 ratio) respectively in methanol. The reaction mixture was stirred at room temperature for 30 min and got light yellow solid. The solid was washed with methanol and dried under vacuum. Yield: 75%. Anal. Calcd for C<sub>29</sub>H<sub>23</sub>N<sub>5</sub> (269.53) C, 74.18; H, 4.94; N, 20.88; Found: C, 73.99; H, 5.01; N, 20.79; IR data (KBr,  $\nu_{\max}/\text{cm}^{-1}$ ): 1572,  $\nu_{\text{C=Nimine}}$ , 1435, 1200, 1137, 1001, 910, 773, 692, 574 ; UV-visible[CH<sub>2</sub>Cl<sub>2</sub>  $\lambda_{\max}/\text{nm}$  ( $\epsilon/\text{M}^{-1}\text{cm}^{-1}$ ): 230 (19,567), 292 (20,810), 312 (21594), 348 (42,054); <sup>1</sup>H NMR (500 MHz, CDCl<sub>3</sub>): 8.374-8.365 (d 2H), 7.932-7.916 (d 2H), 7.593-7.571(m 3H), 7.199-7.154 (m 7H), 7.140-7.111 (m 3H), 7.095-7.045 (m 2H), 6.885-6.869 (m 4H).; ESI-MS (CH<sub>2</sub>Cl<sub>2</sub>) m/z +Na = 492.

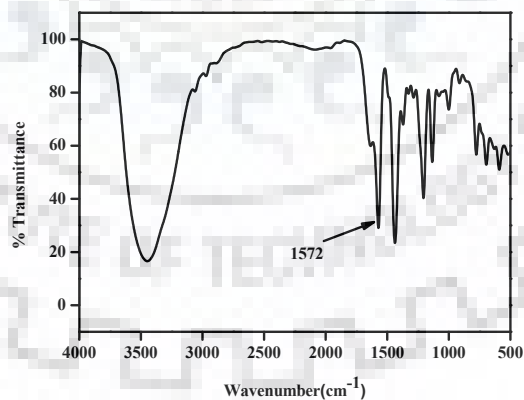


Fig. 5.6 IR spectrum of ligand L<sup>6</sup>

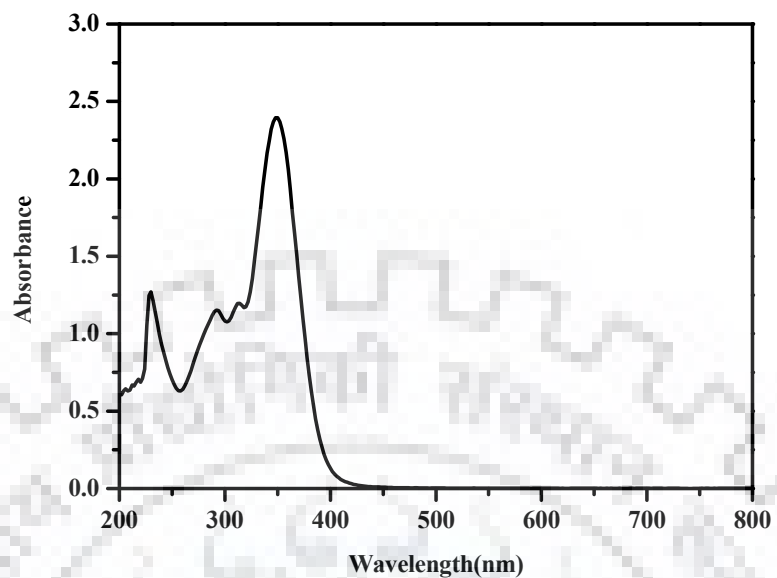


Fig. 5.7 UV-visible spectrum of ligand L<sup>6</sup> in CH<sub>2</sub>Cl<sub>2</sub> solvent

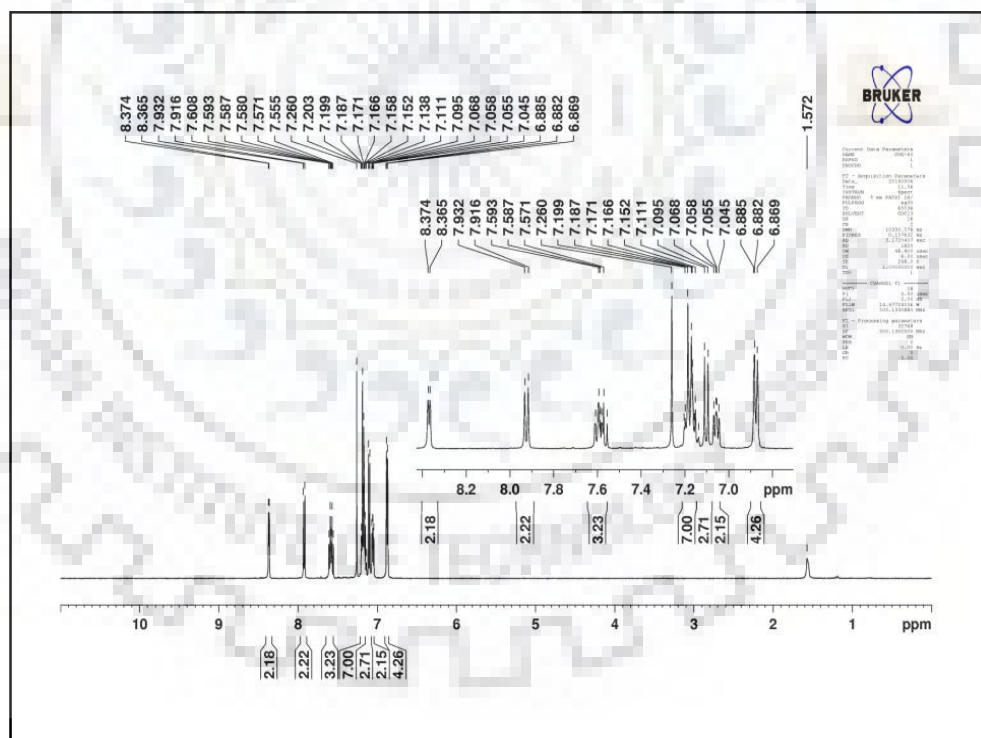
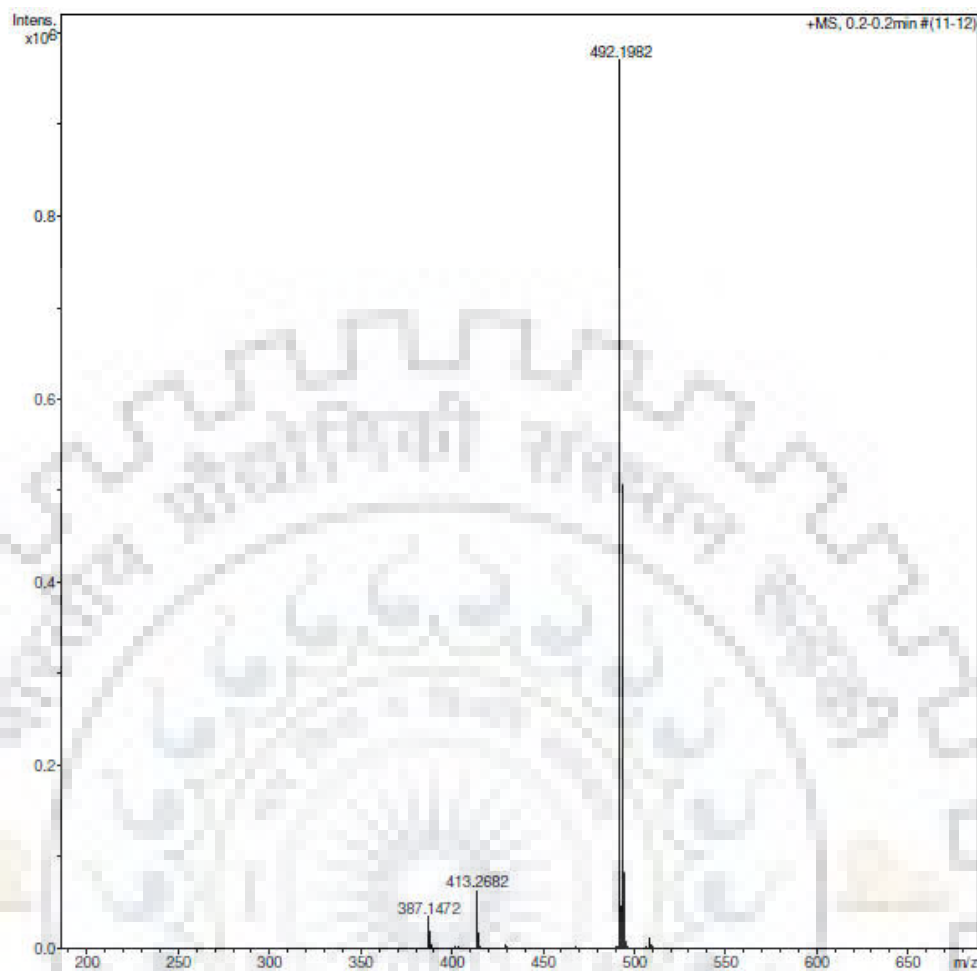


Fig. 5.8 <sup>1</sup>H NMR spectra of ligand L<sup>6</sup> in CDCl<sub>3</sub>



**Fig. 5.9** ESI-MS of ligand L<sup>6</sup> in acetonitrile [L<sup>6</sup>+Na]<sup>+</sup>

#### 5.4.4 Synthesis of complexes

##### 5.4.4.1 Synthesis of [Mn(L<sup>6</sup>)(H<sub>2</sub>O)(CH<sub>3</sub>OH)](ClO<sub>4</sub>)<sub>2</sub> (6)

A batch of ligand L<sup>6</sup> (93.8mg, 0.2 mmol) was stirred in dichloromethane solution at room temperature after that a batch of Mn(ClO<sub>4</sub>)<sub>2</sub>.xH<sub>2</sub>O (50.6mg, 0.2 mmol) was dissolved in methanol and added dropwise into the stirred ligand. The colour of the solution change yellow to orange, after 3 hours stirring orange colour solid was obtained. The solid was filtered out and dried under vacuo. Crystallization of the complex was done by dissolving the compound in dichloromethane and layered on it with methanol, with slow diffusion the orange colour crystals were obtained within 24 hours. Yield 80% Anal. Calcd for



$C_{30}H_{29}Cl_2MnN_7O_{10}$  (772.43): C, 46.59; H, 3.78; N, 12.68; Found: C, 47.01; H, 4.01; N, 12.90. IR data (KBr,  $\nu_{max}/cm^{-1}$ ): 1600,  $\nu_{C=Nimine}$ , 1446, 1383, 1264, 1090, 623,  $\nu_{ClO_4^-}$ , 901, 784, 721, 584 UV-visible [MeOH  $\lambda_{max}$  /nm ( $\epsilon/M^{-1}cm^{-1}$ ): 290 (19,100), 352 (29,910), 410 (11,440).

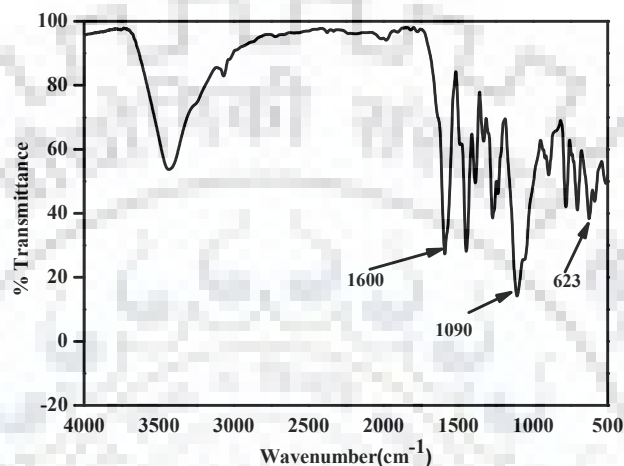


**Fig. 5.10** IR spectrum of complex  $[Mn(L^6)(H_2O)(CH_3OH)](ClO_4)_2$  (**6**)

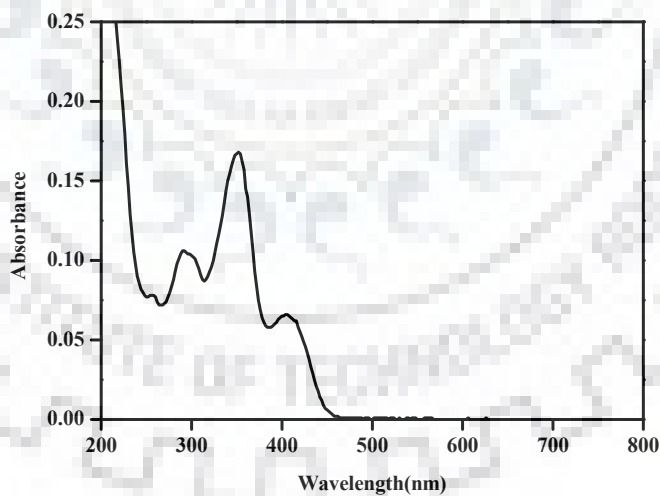


**Fig. 5.11** UV-visible spectrum of complex  $[Mn(L^6)(H_2O)(CH_3OH)](ClO_4)_2$  (**6**) was recorded ( $1 \times 10^{-3}$  M) in methanol solvent

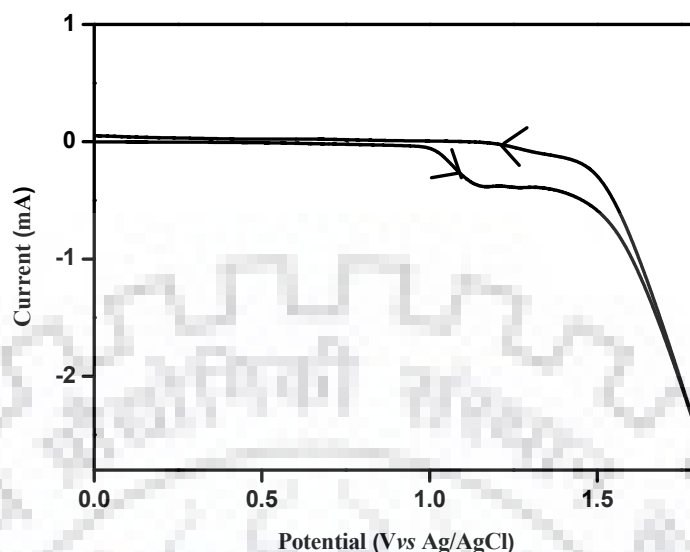


**Fig. 5.12** Cyclic voltammograms of a  $10^{-3}$  M solution of complex  $[\text{Mn}(\text{L}^6)(\text{H}_2\text{O})(\text{CH}_3\text{OH})](\text{ClO}_4)_2$  (**6**) in DMSO in presence of 0.1 M tetrabutylammonium perchlorate (TBAP), using working electrode: glassy-carbon, reference electrode: Ag/AgCl; auxiliary electrode: platinum wire, scan rate  $0.1 \text{ Vs}^{-1}$

#### 5.4.4.2 Synthesis of $[\text{Fe}(\text{L}^6)(\text{H}_2\text{O})(\text{ClO}_4)]\text{ClO}_4$ (**7**)

A batch of ligand  $\text{L}^6$  (93.8mg, 0.2 mmol) was stirred in dichloromethane solution at room temperature after that a batch of  $\text{Fe}(\text{ClO}_4)_2 \cdot x\text{H}_2\text{O}$  (50.8mg, 0.2 mmol) was dissolved in methanol and added dropwise into the stirred ligand. The colour of the solution change yellow to dark red, after 4 to 5 hours red colour solid was obtained. The reaction was filtered off and dried under vacuo. The crystallization of this complex was done in tetrahydrofuran with slow evaporation in a glass vials. The crystals were obtained within 24 hours. Yield 85%. Anal. Calcd for  $\text{C}_{29}\text{H}_{25}\text{Cl}_2\text{FeN}_7\text{O}_9$  (742.30); C, 46.92; H, 3.39; N, 13.21; Found: C, 47.01; H, 3.49; N, 13.30. IR data (KBr,  $\nu_{\text{max}}/\text{cm}^{-1}$ ): 1589  $\nu_{\text{C=Nimine}}$ , 1446, 1400, 1264, 1090, 626  $\nu_{\text{ClO}_4^-}$ , 911, 784, 711, UV-visible[MeOH  $\lambda_{\text{max}}/\text{nm}$  ( $\epsilon/\text{M}^{-1}\text{cm}^{-1}$ ): 298 (15,530), 338 (26,140), 411 (7,780).

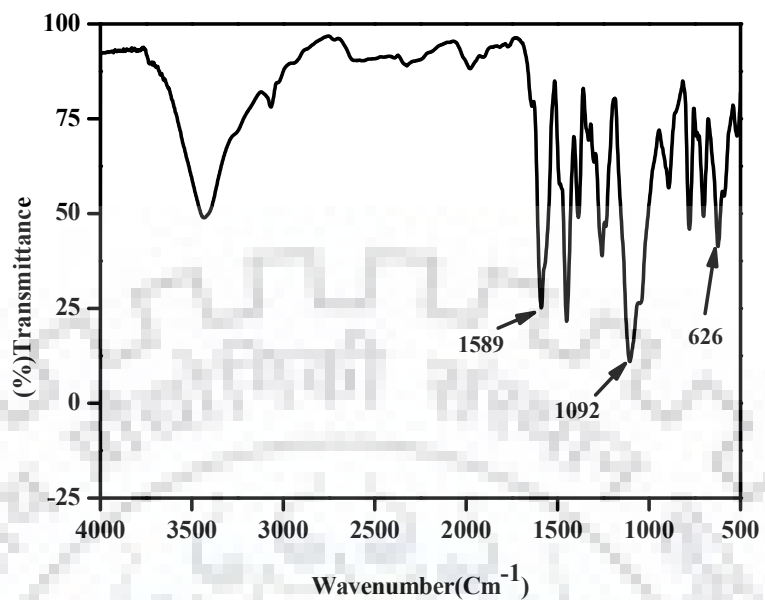


Fig. 5.13 IR spectrum of complex [Fe(L<sup>6</sup>)(H<sub>2</sub>O)(ClO<sub>4</sub>)]ClO<sub>4</sub> (7)

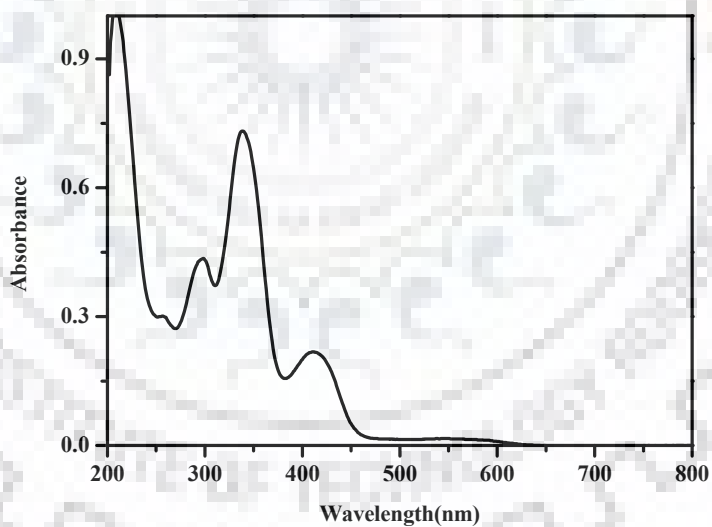
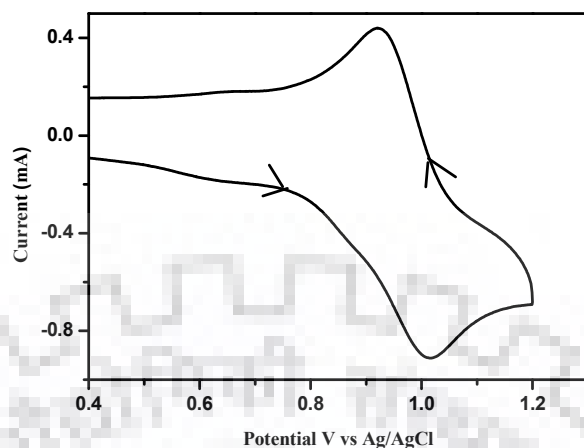


Fig. 5.14 UV-visible spectrum of complex, [Fe(L<sup>6</sup>)(H<sub>2</sub>O)(ClO<sub>4</sub>)]ClO<sub>4</sub> (7) was recorded 1x10<sup>-3</sup> M in methanol solvent



**Fig. 5.15** Cyclic voltammograms of a  $10^{-3}$  M solution of complex  $[\text{Fe}(\text{L}^6)(\text{H}_2\text{O})(\text{ClO}_4)]\text{ClO}_4$  (7) in DMSO in presence of 0.1 M tetrabutylammonium perchlorate (TBAP), using working electrode: glassy-carbon, reference electrode: Ag/AgCl; auxiliary electrode: platinum wire, scan rate  $0.1 \text{ V s}^{-1}$

#### 5.4.5 Superoxide dismutase (SOD) Activity

The superoxide dismutase activity for both the complexes was tested with indirect method using xanthine–xanthine oxidase–nitro blue tetrazolium assay.<sup>379</sup> The assays for SOD was performed separately at duplicate in 50 mM potassium phosphate buffer at pH 7.2. All the experiments with these complexes were carried out in buffer pH 7.2 utilizing 0.6 mM xanthine, 0.3 mM NBT, 0.07 U/mL xanthine oxidase and catalase 1000 U/mL (final volume = 750  $\mu\text{L}$ ). The reaction was started after adding 0.07 U/mL xanthine oxidase and the measurement time interval for each.

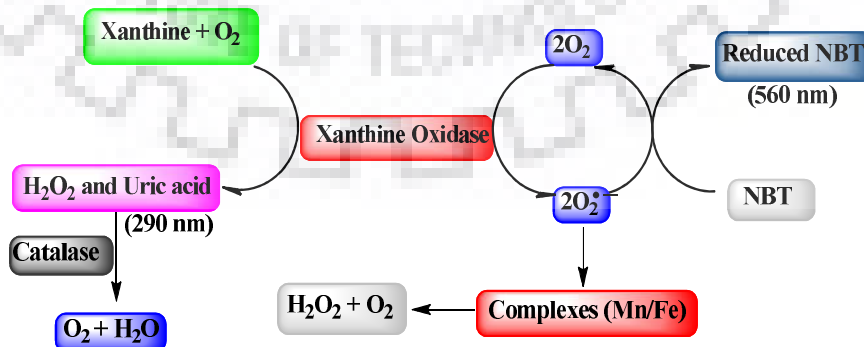


**Chart 5.1** Schematic diagram of superoxide dismutase activity

## 5.4.6 X-ray Analysis

**Table 5.3** Crystallographic parameters of complex  $[\text{Mn}(\text{L}^6)(\text{H}_2\text{O})(\text{CH}_3\text{OH})](\text{ClO}_4)_2$  (**6**) and complex  $[\text{Fe}(\text{L}^6)(\text{H}_2\text{O})(\text{ClO}_4)]\text{ClO}_4$  (**7**)

	<b>Complex 6</b>	<b>Complex 7</b>
<b>Colour</b>	Orange	Red
<b>Empirical formula</b>	$\text{C}_{30}\text{H}_{29}\text{MnN}_7\text{O}_2, 2(\text{ClO}_4)$	$\text{C}_{29}\text{H}_{25}\text{ClFeN}_7\text{O}_5, (\text{ClO}_4)$
<b>Formula weight [g mol<sup>-1</sup>]</b>	773.44	742.31
<b>Temperature [K]</b>	90(2)	296(2)
<b><math>\lambda</math> [Å] (Mo-K<math>\alpha</math>)</b>	0.71073	0.71073
<b>Crystal system</b>	triclinic	Monoclinic
<b>Space group</b>	<i>P</i> -1	<i>P</i> 21/ <i>n</i>
<b>a [Å]</b>	9.3017(5)	16.2831(10)
<b>b [Å]</b>	14.0136(7)	8.1985(5)
<b>c [Å]</b>	14.6344(8)	24.4790(14)
<b><math>\alpha</math> [°]</b>	111.6887(7)	90.00
<b><math>\beta</math> [°]</b>	103.5835(7)	101.909(3)
<b><math>\gamma</math> [°]</b>	100.6113(7)	90.00
<b>V [Å<sup>3</sup>]</b>	1643.62(15)	3197.5(3)
<b>Crystal size[mm]</b>	0.440x 0.200x 0.120	0.22x 0.22x 0.22
<b>Z</b>	2	4
<b><math>\rho_{\text{calc}}</math> [gcm<sup>-3</sup>]</b>	1.563	1.542
<b>F(000)</b>	794	1520
<b><math>\theta</math> range for data Collection</b>	2.361-31.501	1.38- 27.89
<b>Index ranges</b>	-13<h<13, -20<k<21, -21<l<21	-21<h<21, -10<k<10, -32<l<32
<b>Refinement method</b>	Full matrix least-squares on F <sup>2</sup>	Full matrix least-squares on F <sup>2</sup>
<b>Data/restraints/parametes</b>	10848/4/ 511	7637/0/ 441
<b>GOF on F<sup>2</sup></b>	1.057	1.094
<b>R<sub>1</sub><sup>b</sup>[I&gt;2<math>\sigma</math>(I)]</b>	0.0326	0.0431
<b>R<sub>1</sub>[all data]</b>	0.0344	0.0710
<b>wR<sub>2</sub><sup>c</sup>[I&gt; 2<math>\sigma</math>(I)]</b>	0.0872	0.1239
<b>wR<sub>2</sub> [all data]</b>	0.0857	0.1490
<sup>a</sup> GOF = $[\sum[w(\text{F}_o^2 - \text{F}_c^2)^2] / \text{M-N}]^{1/2}$ (M = number of reflections, N = number of parameters refined). <sup>b</sup> R <sub>1</sub> = $\sum   \text{F}_o  -  \text{F}_c   / \sum  \text{F}_o $ , <sup>c</sup> wR <sub>2</sub> = $[\sum[w(\text{F}_o^2 - \text{F}_c^2)^2] / \sum [w(\text{F}_o^2)^2]]^{1/2}$		

**Table 5.4** Selected bond angles(°)

Complex 6			Complex 7	
<b>1</b>	O1—Mn1—O2	173.03(13)	O10—Fe1—N6	88.95(10)
<b>2</b>	O1—Mn1—N4	97.68(13)	O10—Fe1—N5	94.21(10)
<b>3</b>	O2—Mn1—N4	87.68(10)	N6—Fe1—N5	69.50(9)
<b>4</b>	O1—Mn1—N2	84.58(14)	O10—Fe1—N7	86.22(10)
<b>5</b>	O2—Mn1—N2	93.42(10)	N6—Fe1—N7	69.33(8)
<b>6</b>	N4—Mn1—N2	67.68(9)	N5—Fe1—N7	138.81(9)
<b>7</b>	O1—Mn1—N7	83.79(13)	O10—Fe1—O4	171.92(9)
<b>8</b>	O2—Mn1—N7	95.7(1)	N6—Fe1—O4	88.12(9)
<b>9</b>	N4—Mn1—N7	134.00(9)	N5—Fe1—O4	77.71(9)
<b>10</b>	N2—Mn1—N7	156.7(1)	N7—Fe1—O4	99.76(9)
<b>11</b>	O1—Mn1—N6	105.33(14)	O10—Fe1—N4	104.67(10)
<b>12</b>	O2—Mn1—N6	80.84(11)	N6—Fe1—N4	136.99(9)
<b>13</b>	N4—Mn1—N6	66.78(10)	N5—Fe1—N4	146.39(9)
<b>14</b>	N2—Mn1—N6	134.26(11)	N7—Fe1—N4	71.10(9)
<b>15</b>	N7—Mn1—N6	68.55(10)	O4—Fe1—N4	82.53(9)
<b>16</b>	O1—Mn1—N1	90.79(13)	O10—Fe1—N3	80.69(10)
<b>17</b>	O2—Mn1—N1	82.25(10)	N6—Fe1—N3	138.43(8)
<b>18</b>	N4—Mn1—N1	135.35(10)	N5—Fe1—N3	71.27(8)
<b>19</b>	N2—Mn1—N1	69.66(10)	N7—Fe1—N3	148.33(9)
<b>20</b>	N7—Mn1—N1	90.38(10)	O4—Fe1—N3	96.58(9)
<b>21</b>	N6—Mn1—N1	151.34(10)	N4—Fe1—N3	84.46(9)

**Table 5.5** Selected bond distances (Å) of complex [Mn(L<sup>6</sup>)(H<sub>2</sub>O)(CH<sub>3</sub>OH)](ClO<sub>4</sub>)<sub>2</sub> (6)

Bond type	Experimental	Theoretical
Mn1-O1	2.154(4)	2.244
Mn1-O2	2.220(5)	2.250
Mn1-N4	2.311(4)	2.328
Mn1-N2	2.321(3)	2.336
Mn1-N7	2.341(4)	2.395
Mn1-N6	2.356(4)	2.359
Mn1-N1	2.394(2)	2.378

**Table 5.6** Selected bond distances (Å) of complex [Fe(L<sup>6</sup>)(H<sub>2</sub>O)(ClO<sub>4</sub>)]ClO<sub>4</sub> (7)

Bond type	Experimental	Theoretical
Fe1-O10	2.137 (3)	2.137
Fe1-N5	2.218 (4)	2.230
Fe1-N6	2.222 (4)	2.221
Fe1-N7	2.231 (4)	2.218
Fe1-O4	2.276 (3)	2.275
Fe1-N4	2.286 (3)	2.306
Fe1-N3	2.306(3)	2.285

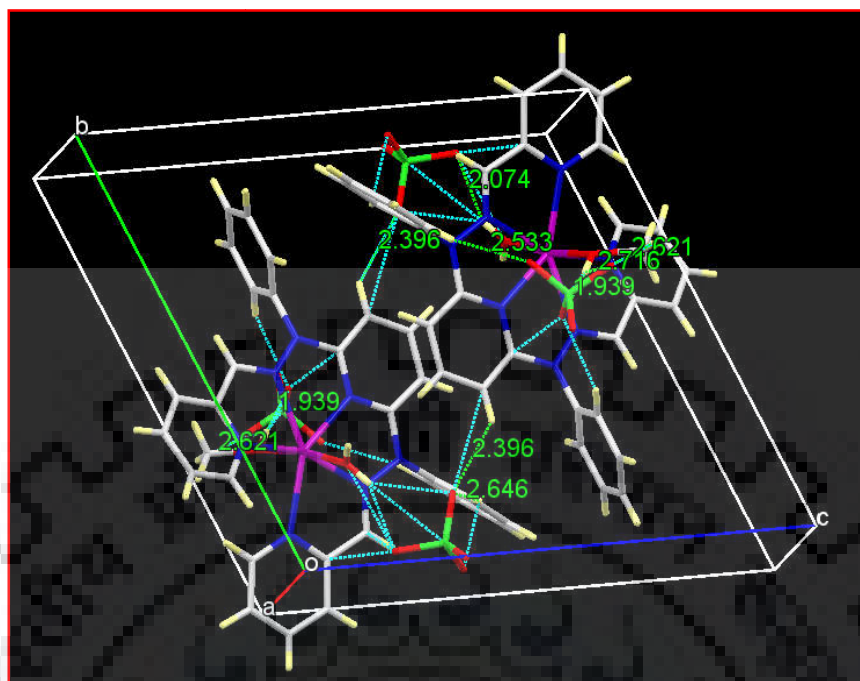


**Fig. 5.16** Packing diagram of complex  $[\text{Mn}(\text{L}^6)(\text{H}_2\text{O})(\text{CH}_3\text{OH})](\text{ClO}_4)_2$  (6) showing the short interaction and hydrogen bonding with the neighbor atoms

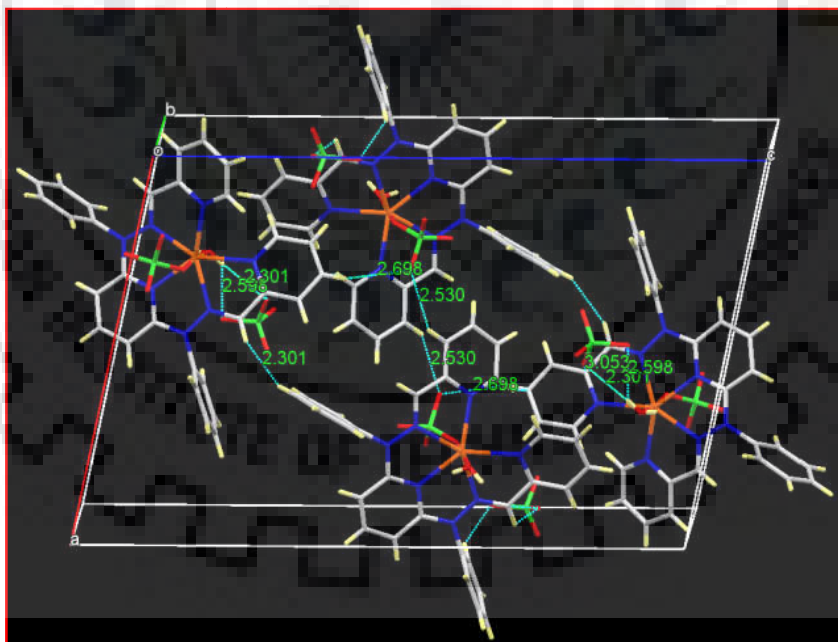


**Fig. 5.17** Packing diagram of Complex  $[\text{Fe}(\text{L}^6)(\text{H}_2\text{O})(\text{ClO}_4)]\text{ClO}_4$  (7) showing the short interaction and hydrogen bonding with the neighbor atoms



## 5.5 Theoretical investigation

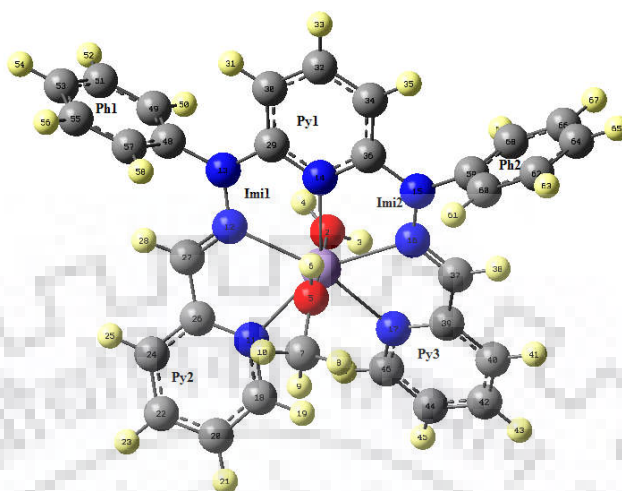


**Fig. 5.18** Ground state optimized geometry of complex  $[\text{Mn}(\text{L}^6)(\text{H}_2\text{O})(\text{CH}_3\text{OH})](\text{ClO}_4)_2$  (6) using B3LYP/LANL2DZ

**Table 5.7** Percentage contribution of complex  $[\text{Mn}(\text{L}^6)(\text{H}_2\text{O})(\text{CH}_3\text{OH})](\text{ClO}_4)_2$  (6) in different orbitals

Alpha molecular orbital percentage contribution											
Orbitals	MeOH	Fe	Imi1	Ph1	Py1	Py2	Py3	Ph1	H <sub>2</sub> O	Imi2	Main bond Type
LUMO+2	0	19	2	33	6	3	5	30	0	1	3d (Fe) + $\pi^*$ L
LUMO+1	0	56	2	10	3	16	2	10	0	21	3d (Fe) + $\pi^*$ L
<b>LUMO</b>	<b>0</b>	<b>16</b>	<b>1</b>	<b>2</b>	<b>1</b>	<b>31</b>	<b>40</b>	<b>6</b>	<b>0</b>	<b>2</b>	<b>3d (Fe) + <math>\pi^*</math> L</b>
<b>HOMO</b>	<b>0</b>	<b>52</b>	<b>5</b>	<b>1</b>	<b>7</b>	<b>13</b>	<b>15</b>	<b>2</b>	<b>0</b>	<b>5</b>	<b>3d (Fe) + <math>\pi</math> L</b>
HOMO-1	0	62	4	6	5	6	7	5	0	5	3d (Fe) + $\pi$ L
HOMO-2	0	55	5	0	2	17	16	0	0	4	3d (Fe) + $\pi$ L
Beta molecular orbital percentage contribution											
LUMO+2	0	55	5	0	2	17	16	0	0	4	3d (Fe) + $\pi^*$ L
LUMO+1	0	32	11	0	19	11	14	0	0	13	3d (Fe) + $\pi^*$ L
<b>LUMO</b>	<b>1</b>	<b>47</b>	<b>10</b>	<b>0</b>	<b>4</b>	<b>15</b>	<b>14</b>	<b>0</b>	<b>0</b>	<b>8</b>	<b>3d (Fe) + <math>\pi^*</math> L</b>
<b>HOMO</b>	<b>0</b>	<b>0</b>	<b>24</b>	<b>1</b>	<b>35</b>	<b>7</b>	<b>7</b>	<b>1</b>	<b>0</b>	<b>25</b>	<b><math>\pi</math> L</b>
HOMO-1	0	1	31	2	14	10	10	2	0	31	3d (Fe) + $\pi$ L
HOMO-2	0	0	7	2	31	24	25	2	0	7	$\pi$ L

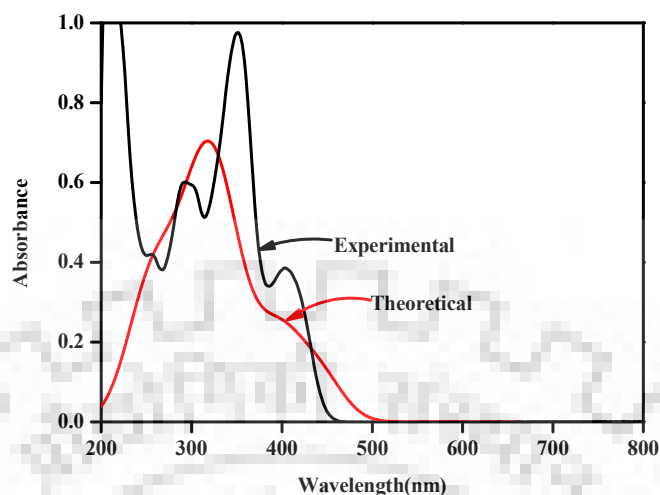


**Fig. 5.19** UV-visible spectra of complex  $[\text{Mn}(\text{L}^6)(\text{H}_2\text{O})(\text{CH}_3\text{OH})](\text{ClO}_4)_2$  (**6**) experimental as well as theoretical calculation

**Table 5.8** Major transition along with their orbital contribution in complex  $[\text{Mn}(\text{L}^6)(\text{H}_2\text{O})(\text{CH}_3\text{OH})](\text{ClO}_4)_2$  (**6**)

$\lambda_{\text{max}}$ (nm)	f (Osc. Strength)	Transition and their contributions
291	0.0011	H-8(A) $\rightarrow$ L+1(A) (34%), H-7(A) $\rightarrow$ L+1(A) (32%), H-2(A) $\rightarrow$ L+1(A) (15%) H-6(A) $\rightarrow$ LUMO(A) (6%), H-6(A) $\rightarrow$ L+1(A) (2%)
351	0.0041	H-6(A) $\rightarrow$ L+1(A) (17%), H-3(A) $\rightarrow$ L+1(A) (37%), H-2(A) $\rightarrow$ LUMO(A) (20%) H-8(A) $\rightarrow$ LUMO(A) (6%), H-4(A) $\rightarrow$ L+1(A) (4%), H-2(A) $\rightarrow$ L+1(A) (2%), H-1(A) $\rightarrow$ LUMO(A) (2%), H-1(A) $\rightarrow$ L+1(A) (6%)
441	0.1134	HOMO(A) $\rightarrow$ LUMO(A) (50%), HOMO(B) $\rightarrow$ LUMO(B) (50%)

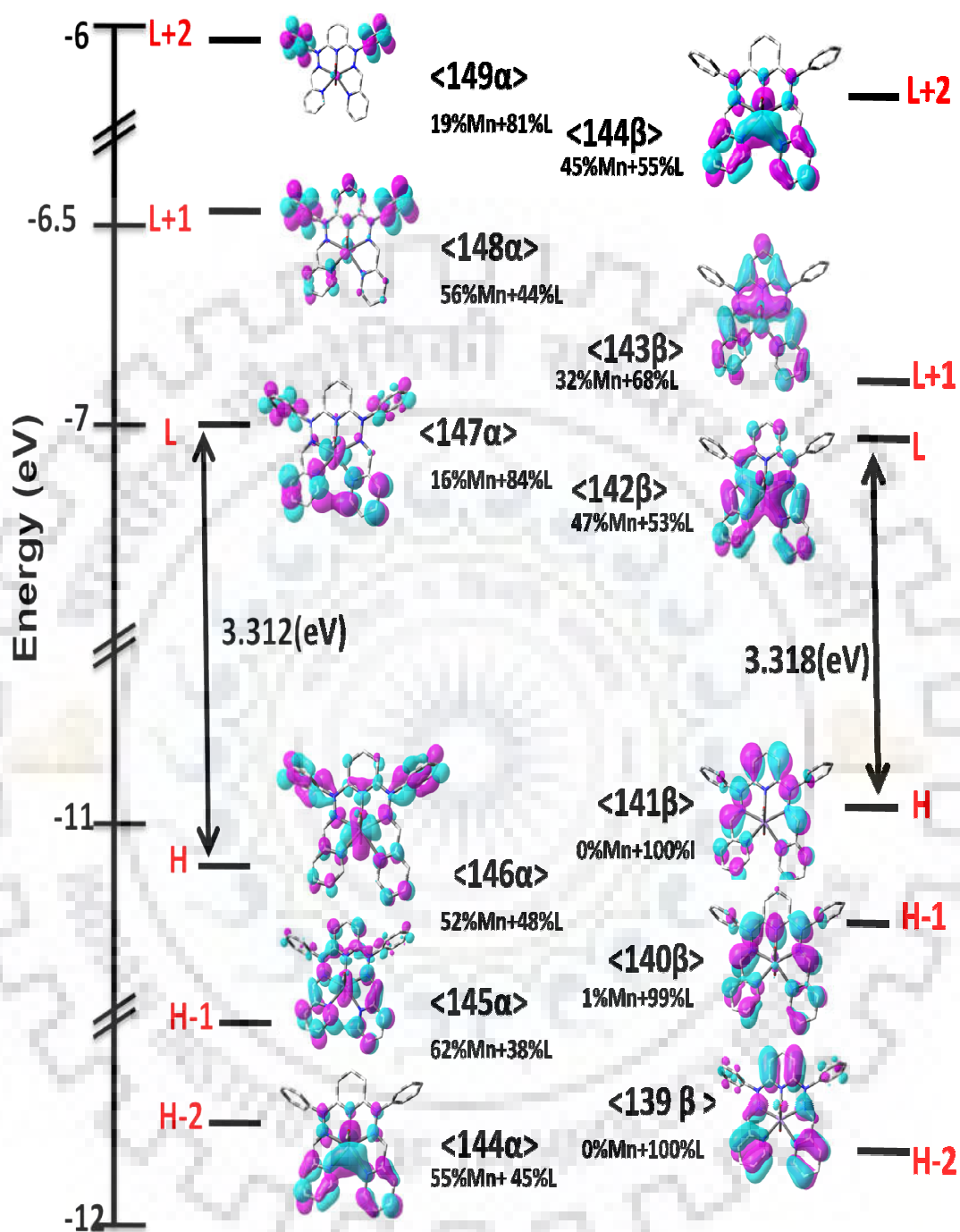
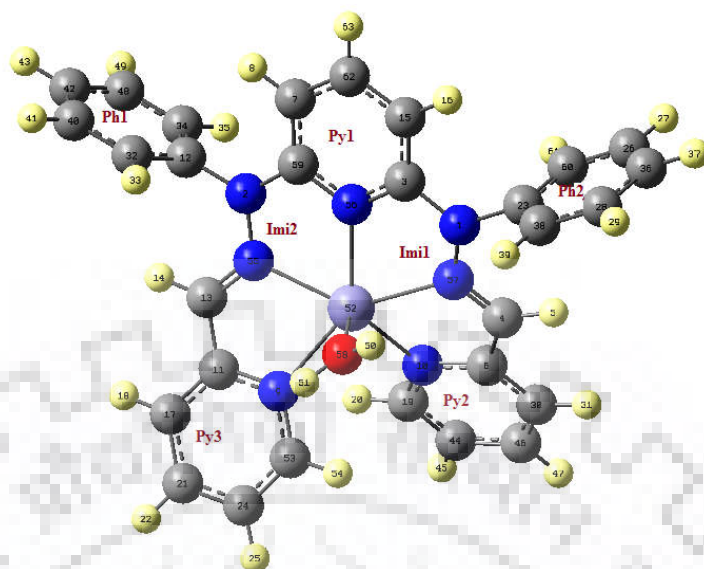
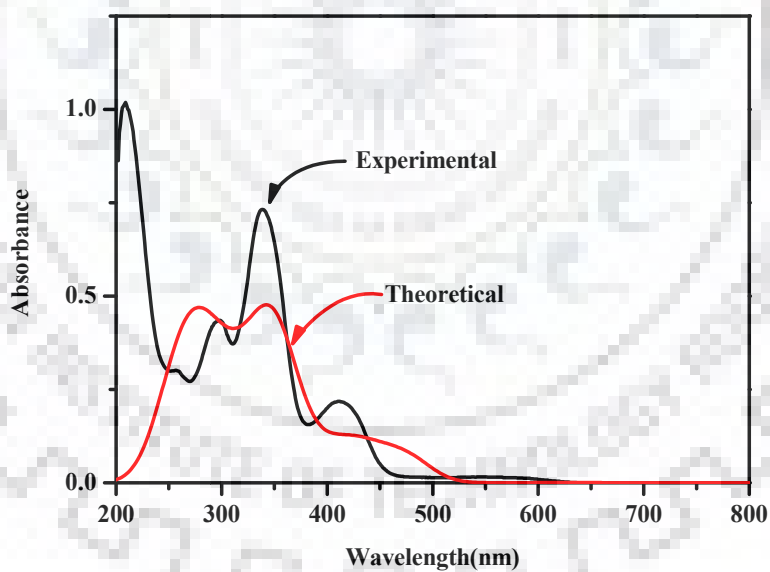


Fig. 5.20 Frontier molecular orbitals of complex  $[\text{Mn}(\text{L}^6)(\text{H}_2\text{O})(\text{CH}_3\text{OH})](\text{ClO}_4)_2$  (**6**) showing significant contribution of manganese and ligand ( $\text{L}^6$ ) in molecular orbitals



**Fig. 5.21** Ground state optimized geometry of complex [Fe(L<sup>6</sup>)(H<sub>2</sub>O)(ClO<sub>4</sub>)]ClO<sub>4</sub> (7) using B3LYP/LANL2DZ



**Fig. 5.22** UV-visible spectra of complex [Fe(L<sup>6</sup>)(H<sub>2</sub>O)(ClO<sub>4</sub>)]ClO<sub>4</sub> (7) experimental as well as theoretical calculation

**Table 5.9** Major transition along with their orbital contribution in complex [Fe(L<sup>6</sup>)(H<sub>2</sub>O)(ClO<sub>4</sub>)]ClO<sub>4</sub> (7)

$\lambda_{\max}$ (nm)	f (Osc. Strength)	Transition and their contributions
293	0.0534	HOMO(A) $\rightarrow$ L+3(A) (31%), HOMO(B) $\rightarrow$ L+6(B) (51%) H-11(A) $\rightarrow$ LUMO(A) (2%), H-10(A) $\rightarrow$ L+1(A) (2%)
347	0.1799	H-5(A) $\rightarrow$ LUMO(A) (22%), H-4(A) $\rightarrow$ LUMO(A) (12%) H-3(A) $\rightarrow$ L+1(A) (2%), H-2(A) $\rightarrow$ L+1(A) (5%), HOMO(A) $\rightarrow$ L+1(A) (2%), HOMO(A) $\rightarrow$ L+2(A) (2%), H-8(B) $\rightarrow$ LUMO(B) (2%), H-6(B) $\rightarrow$ LUMO(B) (9%), H-6(B) $\rightarrow$ L+1(B) (2%), H-5(B) $\rightarrow$ LUMO(B) (9%), H-5(B) $\rightarrow$ L+1(B) (2%), H-3(B) $\rightarrow$ L+1(B) (9%), HOMO(B) $\rightarrow$ L+2(B) (3%)
407	0.0663	H-1(A) $\rightarrow$ LUMO(A) (12%), HOMO(A) $\rightarrow$ L+1(A) (45%) H-5(A) $\rightarrow$ LUMO(A) (4%), H-4(A) $\rightarrow$ LUMO(A) (6%), H-2(A) $\rightarrow$ LUMO(A) (2%), HOMO(A) $\rightarrow$ LUMO(A) (2%), H-6(B) $\rightarrow$ LUMO(B) (3%), H-5(B) $\rightarrow$ LUMO(B) (4%), H-2(B) $\rightarrow$ LUMO(B) (5%), HOMO(B) $\rightarrow$ L+1(B) (3%), HOMO(B) $\rightarrow$ L+2(B) (5%)

**Table 5.10** Percentage contribution of complex  $[\text{Fe}(\text{L}^6)(\text{H}_2\text{O})(\text{ClO}_4)]\text{ClO}_4$  (7) in different orbitals

Alpha molecular orbital percentage contribution										
Orbitals	Py2	Py3	Py1	H2O	Ph2	Imi2	Fe	Imi1	Ph1	Main bond type
LUMO+2	49	41	2	0	0	3	2	3	0	3d (Fe) + $\pi^*$ L
LUMO+1	28	20	9	0	0	12	15	16	0	3d (Fe) + $\pi^*$ L
<b>LUMO</b>	<b>14</b>	<b>23</b>	<b>10</b>	<b>1</b>	<b>0</b>	<b>14</b>	<b>26</b>	<b>12</b>	<b>0</b>	<b>3d (Fe) + <math>\pi^*</math> L</b>
<b>HOMO</b>	<b>3</b>	<b>1</b>	<b>4</b>	<b>0</b>	<b>1</b>	<b>2</b>	<b>82</b>	<b>6</b>	<b>1</b>	<b>3d (Fe) + <math>\pi</math> L</b>
HOMO-1	1	6	4	1	0	3	84	1	0	3d (Fe) + $\pi$ L
HOMO-2	8	5	4	1	0	7	71	4	0	3d (Fe) + $\pi$ L
Beta molecular orbital percentage contribution										
LUMO+2	1	6	4	1	0	3	84	1	0	3d (Fe) + $\pi^*$ L
LUMO+1	9	5	4	1	0	7	71	4	0	3d (Fe) + $\pi^*$ L
<b>LUMO</b>	<b>3</b>	<b>2</b>	<b>2</b>	<b>1</b>	<b>0</b>	<b>3</b>	<b>88</b>	<b>1</b>	<b>0</b>	<b>3d (Fe) + <math>\pi^*</math> L</b>
<b>HOMO</b>	<b>4</b>	<b>4</b>	<b>2</b>	<b>0</b>	<b>0</b>	<b>3</b>	<b>84</b>	<b>4</b>	<b>0</b>	<b>3d (Fe) + <math>\pi</math> L</b>
HOMO-1	7	7	38	0	1	24	0	22	1	$\pi$ L
HOMO-2	11	10	13	0	2	29	2	31	2	3d (Fe) + $\pi$ L

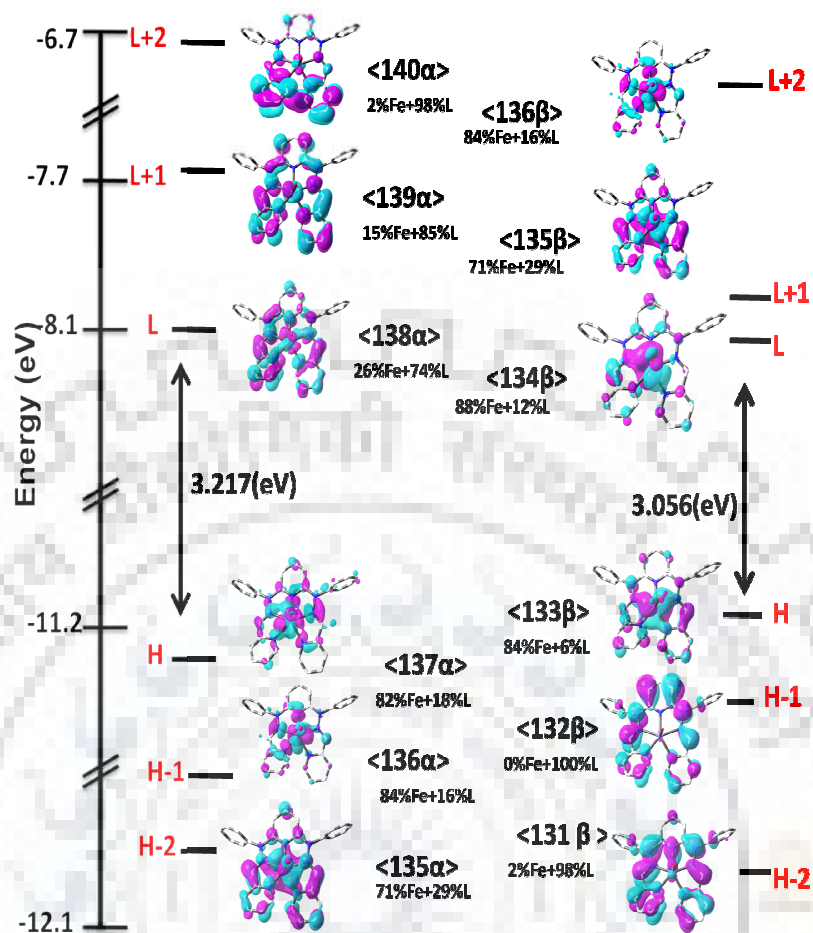


Fig.5.23 Frontier molecular orbitals of complex  $[\text{Fe}(\text{L}^6)(\text{H}_2\text{O})(\text{ClO}_4)]\text{ClO}_4$  (7) showing significant contribution of iron and ligand ( $\text{L}^6$ ) in molecular orbitals

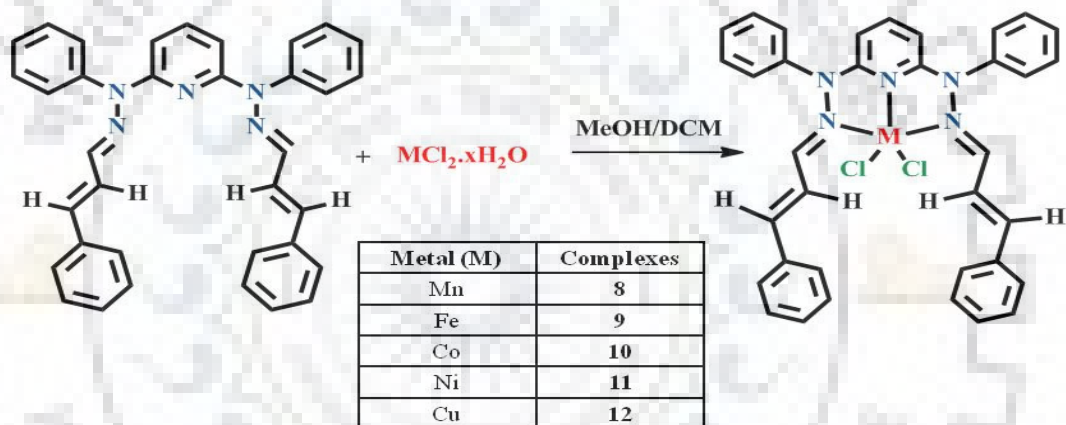
## 6.1 Introduction

Pincer ligands are tridentate ligands which will bind to the metal in a  $\eta^3$ -*mer* fashion and there will be at least one M–C  $\sigma$  bond. However, there are several reports on tridentate meridional ligands which have NNN donor site. These ligands coordinate with the metal centre in a  $\eta^3$ -*mer* fashion. They are named as “pincer” owing to their specific binding mode. These may be represented by the general formula  $[2,6-(\text{ECH}_2)_2\text{C}_6\text{H}_3]^-$  or (ECE) where E denotes a neutral two electron donor like  $\text{NR}_2$ ,  $\text{PR}_2$ ,  $\text{AsR}_2$ , OR or SR and C is the anionic aryl carbon atom of the 2,6-disubstituted phenyl ring. These ligands coordinate to metals affording the complexes of general formula  $[\text{MX}_n(\text{ECE})\text{L}_m]$  which generally exhibit exceptional thermal stability along with high reactivity.<sup>11</sup> In these systems, the steric and electronic properties of the complexes can be efficiently tailored without any significant changes in their coordination pattern. Interaction of transition metal complexes with DNA received considerable current interest because of their potential applications in gene regulation, mapping of the protein, probing of DNA specific structure and anticancer treatment.<sup>265, 266</sup> *cis*-Diamminedichloroplatinum(II) (*cis*-platin) is one of the most effective chemotherapeutic agents used to cure various types of cancers like testicular cancer, ovarian cancer, oropharyngeal carcinoma, cervical carcinoma, lymphoma, osteosarcoma, bladder carcinoma, neuroblastoma and melanoma.<sup>361</sup> In spite of its efficiency in the treatment of cancers, *cis*-platin also exhibits some serious side effects such as nephrotoxicity, neurotoxicity, bone marrow suppression and emetogenesis.<sup>361</sup> It is interesting to explore the manganese, iron, cobalt, nickel, copper chemistry because these are biologically relevant metal ions.<sup>362-367</sup> Manganese is present in the active site of several enzymes such as oxygen evolving complex (OEC),<sup>368,369</sup> manganese lipoxygenase,<sup>370-373</sup> manganese dioxygenase,<sup>37</sup> manganese catalase,<sup>374</sup> superoxide dismutase,<sup>375-378</sup> arginase,<sup>47</sup> ribonucleotide reductases<sup>379</sup>



etc. In this regard, designing and synthesis of manganese complexes derived from nitrogen donor is gaining interest in DNA interaction studies.<sup>381-383</sup> Mononuclear iron complexes having tridentate N<sub>3</sub> donors are of extreme current interest in several areas of chemical research such as structural and functional modelling of mononuclear iron enzymes.<sup>365,384</sup> Chemistry of iron with the nitrogen donor ligands has been interesting area to explore.<sup>385-387</sup> Cobalt is one of the promising metals to develop artificial metallonucleases due to its biological relevance and its natural occurrence in the nucleolytic enzymes.<sup>67,72,388,390</sup> Cobalt also exhibit considerable potential to catalyze hydrolytic reactions<sup>391,392</sup>. A large number of cobalt complexes have been synthesized and investigated for their DNA binding and DNA cleavage ability. There are several reports for cobalt complex-mediated photolytic cleavage of DNA.<sup>268,393-397</sup> There are very few reports regarding nickel(II) complexes exhibiting DNA binding activity.<sup>398</sup> Kong and co-workers reported a family of Schiff's base tetraazamacrocyclic oxamido Ni(II) complexes which could bind with DNA by partial intercalative and groove binding modes.<sup>366</sup> Mariappan and co-workers synthesized a nickel(II) complex [Ni(daasal)] derived from a salen-functionalized ligand H<sub>2</sub>daasal (H<sub>2</sub>daasal = *N,N'*-Bis(salicylidene)-9-(3,4-diaminophenyl)acridine).<sup>399</sup> These complexes exhibited intercalative interaction with CT DNA and promoted the cleavage of pBR322 DNA upon irradiation under terminal oxidant oxone.<sup>399</sup> Palaniandavar and co-workers utilized several ligands with varying donor sets to synthesize mixed ligand copper(II) complexes<sup>400-403</sup> and explored the influence of diimine co-ligands on their DNA binding and cleavage properties. Currently, they have reported a series of copper(II) complexes having NNO and NNN donor ligands which exhibited covalent mode of binding with DNA through the replacement of easily removable chloride ions by DNA nucleobases.<sup>400</sup>

Hence in this chapter we have synthesized and characterized a series of manganese, iron, cobalt, nickel and copper complexes with meridional tridentate pincer ligand. The ligand  $L^7$  is having NNN donors ( $L^7 =$  PyPhime-Cina, 2,6-bis((E)-1-phenyl-2-((E)-3-phenylallylidene)hydrazinyl)pyridine). Molecular structures of the ligand as well as all the metal complexes were determined by X-ray crystallography. Redox properties of the complexes were determined by cyclic voltammetric experiments. The DNA binding properties of all the complexes were investigated using UV-visible, fluorescence, circular dichroism spectral studies and Hersfield surface analysis of metal complexes was also investigated.



**Scheme 6.1** Synthesis of pincer type complexes of (Mn, Fe, Co, Ni, and Cu) using ligand 2,6-bis((E)-1-phenyl-2-((E)-3-phenylallylidene)hydrazinyl)pyridine

## 6.2 Results and discussions

### 6.2.1 Synthesis and characterization of ligand

The ligand ( $L^7$ ) was synthesized by the reaction between a 1:2 mixture of 2,6-bis(1-phenylhydrazinyl)pyridine and cinnamaldehyde. The molecular structure was determined by X-ray crystallography and the data obtained were depicted in Fig. 6.1, Table.6.8 and ESI-MS analysis was also done to get the exact mass of the ligand shown in Fig.6.26. In this ligand (PyPhime-Cina) = ( $L^7$ ) two imine nitrogen (soft donor atom) along with one pyridine nitrogen donor atom are available for coordination.

### 6.2.2 Synthesis and characterization of metal complexes with different metal ions (Mn, Fe, Co, Ni and copper)

Complexes  $[\text{Mn}(\text{L}^7)\text{Cl}_2]$  (**8**)  $[\text{Fe}(\text{L}^7)\text{Cl}_2]$  (**9**)  $[\text{Co}(\text{L}^7)\text{Cl}_2]$  (**10**),  $[\text{Ni}(\text{L}^7)\text{Cl}_2]$  (**11**) and  $[\text{Cu}(\text{L}^7)\text{Cl}_2]$  (**12**) have been synthesized by the reaction of metal salts  $[\text{FeCl}_2, \text{MnCl}_2 \cdot 4\text{H}_2\text{O}, \text{CoCl}_2 \cdot 6\text{H}_2\text{O}, \text{NiCl}_2 \cdot 6\text{H}_2\text{O}, \text{and } \text{CuCl}_2 \cdot 2\text{H}_2\text{O}]$  and ligand (PyPhime-Cina=2,6-bis((E)-1-phenyl-2-((E)-3-phenylallylidene)hydrazinyl)pyridine) = ( $\text{L}^7$ ) with NNN type moiety in 1:1 molar ratio respectively. (As shown in Scheme 6.1) All the complexes have been characterized by various spectral and analytical techniques as shown in Table 6.1

**Table 6.1** Data for yield, elemental analysis, IR, UV-visible

Complex	Yield %	Elemental analysis			Selected IR data ( $\text{cm}^{-1}$ ) <sup>a</sup>	Selected UV-visible data (nm) <sup>b</sup>
		C	H	N		
<b>8</b>	82	65.01	4.50	10.91	1566, 1446, 1386, 1253, 1165, 1078, 969, 757, 698	413(16,160); 347(37,650); 241(10,140)
<b>9</b>	88	65.02	4.41	10.80	1599,1570,1488,1449,1388, 1258, 1163, 1066, 967, 752, 703, 525	435(18,810); 410 (18,370); 350(60,370); 240(20.110)
<b>10</b>	55	64.72	4.57	10.70	1568, 1453, 1391, 1259, 1165, 1063, 970, 753, 697,524	411(15,160); 348(47,1520); 249(16,490)
<b>11</b>	78	64.80	4.60	10.75	1567, 1454, 1386, 1296, 12,57, 1160, 1069, 962, 757, 695, 520	393(19,660); 351(38,940); 241(17,340)
<b>12</b>	87	64.02	4.01	10.41	1586, 1456, 1390, 1301, 1261, 1162, 1064, 968, 753, 698,523	408(21,960); 356(59,960); 300(25,470)

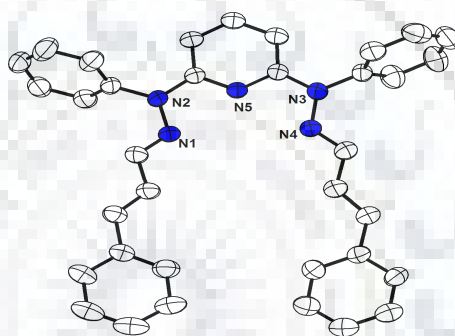
<sup>a</sup>KBr pellets, <sup>b</sup>Solvent  $\text{CH}_3\text{CN}$

The molecular structures of all the complexes were determined by X-ray crystallographic studies (Table.6.8) and their ORTEP diagrams were displayed in Fig.6.2 respectively. The coordination environments around the metals centre were found to be pentacoordinated distorted trigonal bipyramidal geometry. The selected bond distances and bond angles

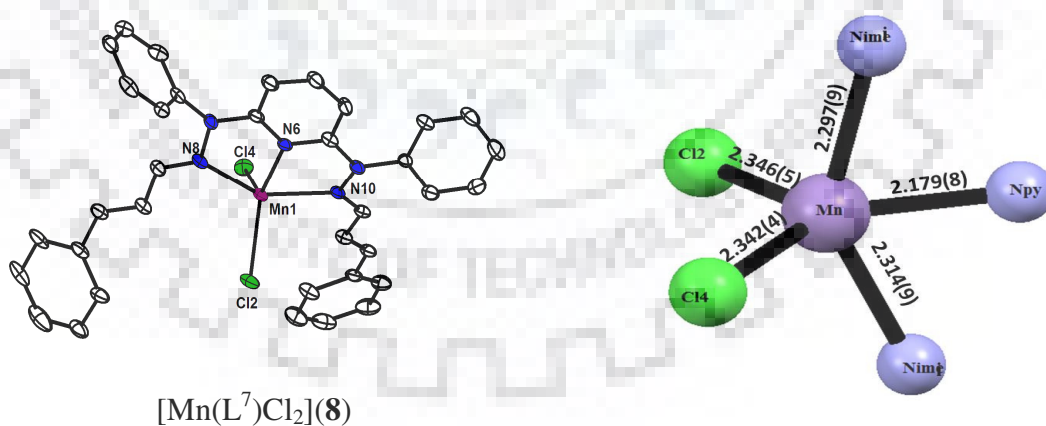
coordinated to the metal centre are displayed in Table 6.3 and 6.4. The geometry of all the complexes were determined with the help of trigonality index  $\tau$ ,<sup>348</sup> As shown in Table 6.2.

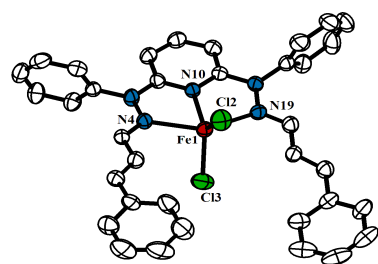
**Table 6.2** Trigonality indexes to determine the geometry of all the complexes

Complexes	a	b	Trigonality index ( $\tau$ )	Geometry
8	142.58(31)	129.62(19)	0.216	Distorted trigonal bipyramidal geometry
9	147.52(9)	120.80(7)	0.445	
10	152.98(15)	123.73(4)	0.487	
11	154.43(9)	127.93(4)	0.441	
12	155.60(12)	126.97(10)	0.477	

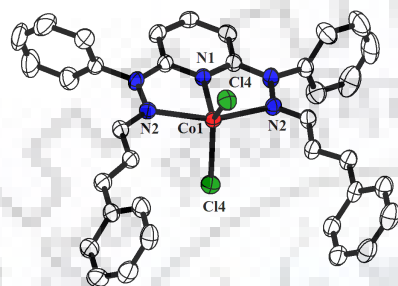
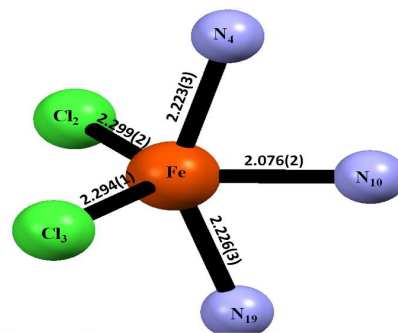


**Fig.6.1** ORTEP diagram (50% probability level) of ligand (PyPhime-Cina)

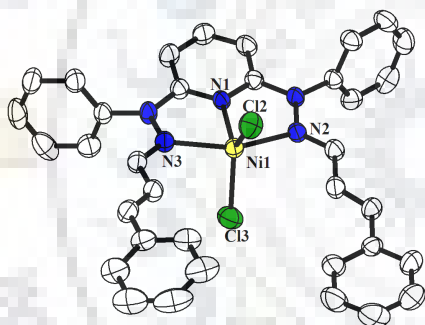
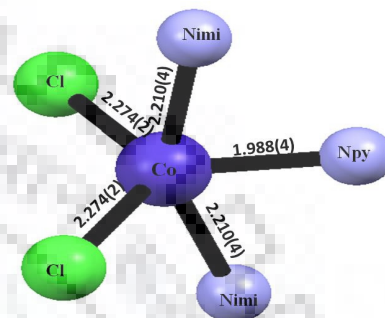




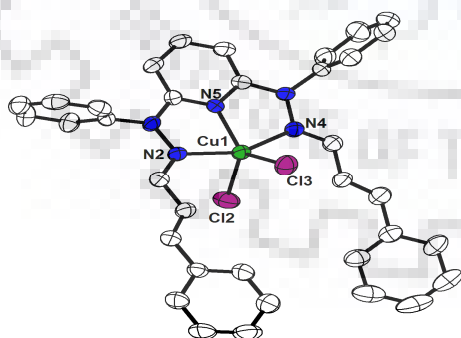
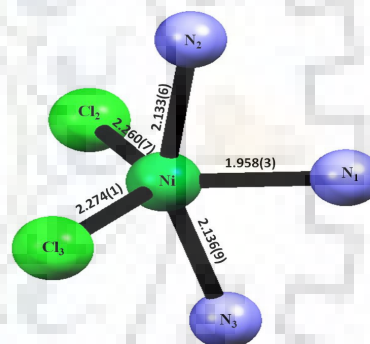
[Fe(L<sup>7</sup>)Cl<sub>2</sub>] (9)



[Co(L<sup>7</sup>)Cl<sub>2</sub>] (10)



[Ni(L<sup>7</sup>)Cl<sub>2</sub>] (11)



[Cu(L<sup>7</sup>)Cl<sub>2</sub>] (12)

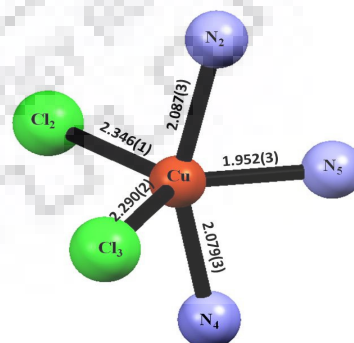


Fig. 6.2 ORTEP diagrams (50% probability level) of complexes (8-12). All hydrogen atoms are omitted for clarity

**Table 6.3** Selected bond distances (Å) for all the complexes (8-12)

Distances(Å) → ↓ Complexes	M- N <sub>py</sub>	M-N <sub>im</sub>	M-N <sub>im</sub>	M-Cl	M-Cl
Complex 8	2.177(4)	2.295(5)	2.311(5)	2.343(5)	2.340(2)
Complex 9	2.076(2)	2.223(3)	2.226(3)	2.299(2)	2.294(1)
Complex 10	1.988(4)	2.210(4)	2.274(2)	2.273(2)	2.274(2)
Complex 11	1.958(3)	2.136(9)	2.133(6)	2.274(1)	2.260(7)
Complex 12	1.952(3)	2.079(3)	2.087(3)	2.346(1)	2.290(2)

**Table 6.4** Selected bond angles (°) for all the complexes (8-12)

[Mn(L <sup>7</sup> )Cl <sub>2</sub> ](8)	[Fe(L <sup>7</sup> )Cl <sub>2</sub> ](9)	[Co(L <sup>7</sup> )Cl <sub>2</sub> ](10)	[Ni(L <sup>7</sup> )Cl <sub>2</sub> ](11)	[Cu(L <sup>7</sup> )Cl <sub>2</sub> ](12)
N6-Mn1-N8 = 71.52(31)	N10-Fe1-N19 = 74.12(8)	N1-Co1-N2 = 76.49(7)	N1-Ni1-N3 = 77.52(9)	N5-Cu1-N4 = 78.06(12)
N6-Mn1-N10 = 71.12(25)	N10-Fe1-N4 = 73.58(8)	N1-Co1-N2 <sup>i</sup> = 76.49(7)	N1-Ni1-N2 = 76.95(9)	N1-Cu1-N2 = 77.57(13)
N8-Mn1-N10 = 142.59(31)	N19-Fe1-N4 = 147.52(9)	N2-Co1-N2 <sup>i</sup> = 152.98(15)	N3-Ni1-N2 = 154.43(9)	N4-Cu1-N2 = 155.60(12)
N6-Mn1-Cl4 = 120.92 (26)	N10-Fe1-Cl3 = 119.19(6)	N1-Co1-Cl4 = 118.13(3)	N1-Ni1-Cl3 = 117.74(7)	N5-Cu1-Cl3 = 126.97(10)
N8-Mn1-Cl4 = 97.86 (24)	N19-Fe1-Cl3 = 101.10(6)	N2-Co1-Cl4 = 96.02(9)	N3-Ni1-Cl3 = 93.13(7)	N4-Cu1-Cl3 = 94.28(9)
N10-Mn1-Cl4 = 99.47(25)	N4-Fe1-Cl3 = 97.48(7)	Cl4-Co1-Cl4 <sup>i</sup> = 123.73(4)	N2-Ni1-Cl3 = 97.50(7)	N2-Cu1-Cl3 = 99.20(10)
N6-Mn1-Cl2 = 129.62(19)	N10-Fe1-Cl2 = 120.80(7)	N2 <sup>i</sup> -Co1-Cl4 <sup>i</sup> = 96.63(9)	N1-Ni1-Cl2 = 114.33(7)	N5-Cu1-Cl2 = 118.09(9)
N8-Mn1-Cl2 = 105.78 (20)	N19-Fe1-Cl2 = 94.03(6)	N1-Co1-Cl4 = 118.13(3)	N3-Ni1-Cl2 = 97.43(7)	N4-Cu1-Cl2 = 98.06(9)
N10-Mn1-Cl2 = 99.29 (18)	N4-Fe1-Cl2 = 99.47(7)	N2-Co1-Cl4 = 96.63(9)	N2-Ni1-Cl2 = 94.24(7)	N2-Cu1-Cl2 = 94.55(9)
Cl4-Mn1-Cl2 = 109.37(12)	Cl3-Fe1-Cl2 = 120.00(1)	N2 <sup>i</sup> -Co1-Cl4 = 96.02(9)	Cl3-Ni1-Cl2 = 127.93(4)	Cl3-Cu1-Cl2 = 114.93(4)

The packing diagrams of the complexes in a unit cell clearly indicated the C-H...Cl as well as C-H...π bond interaction. Except complex [Mn(L<sup>7</sup>)Cl<sub>2</sub>] (8) and [Co(L<sup>7</sup>)Cl<sub>2</sub>] (10) all molecule showed strong C-H...π bond interaction. The packing diagram of all the complexes were depicted in Fig. 6.3- 6.7

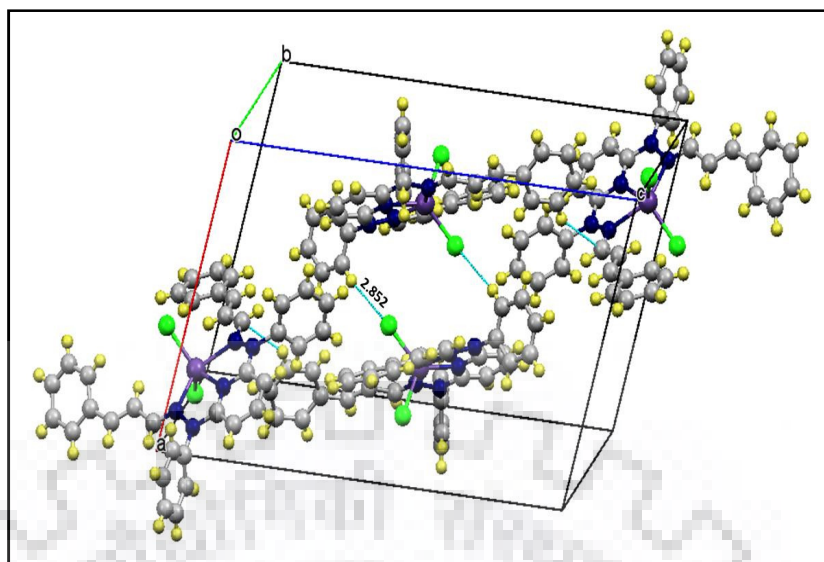


**Fig. 6.3** Packing diagram of complex  $[\text{Mn}(\text{L}^7)\text{Cl}_2]$  (**8**) (projection at  $b$ -axis )

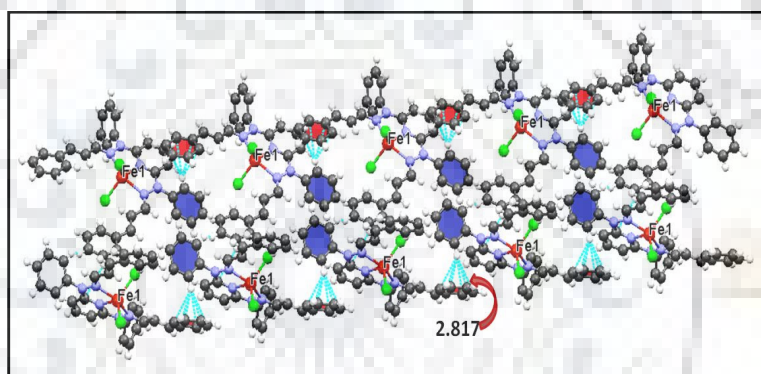


**Fig. 6.4** Packing diagram of complex  $[\text{Fe}(\text{L}^7)\text{Cl}_2]$  (**9**) (projection at  $c$ -axis )

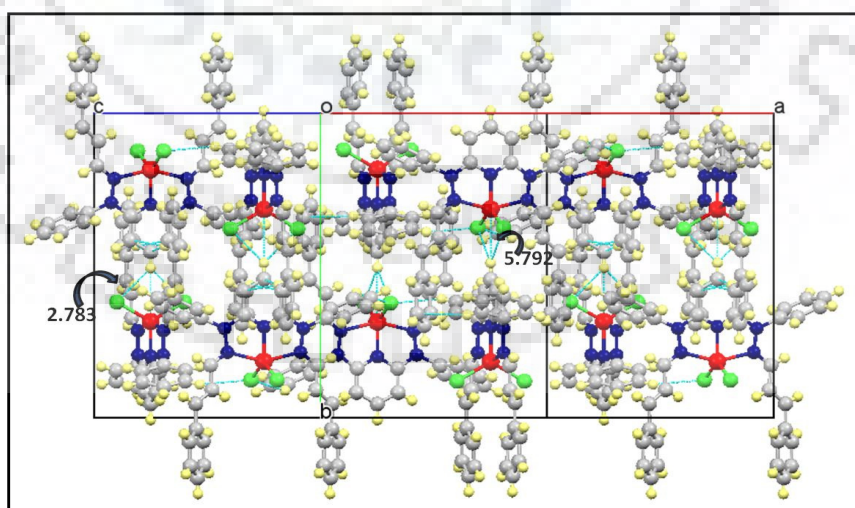


**Fig.6.5** Packing diagram of complex  $[\text{Co}(\text{L}^7)\text{Cl}_2]$  (**10**) (projection at  $c^*$ -axis )

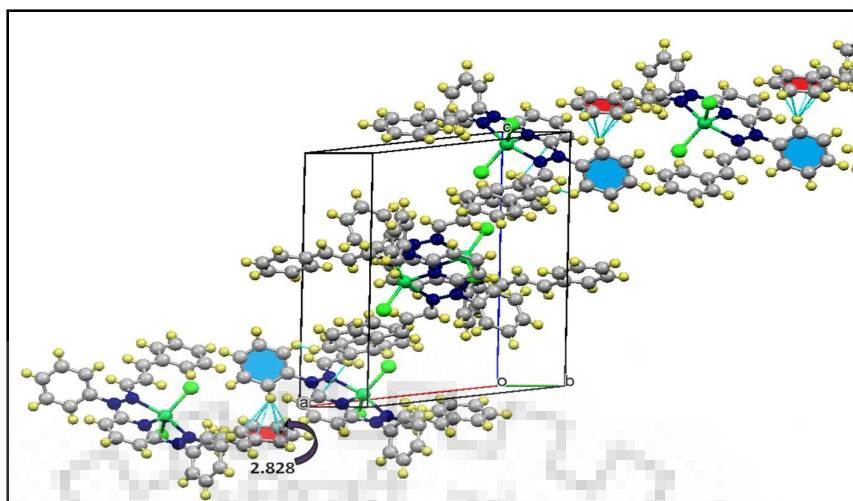


**Fig. 6.6** Packing diagram of complex  $[\text{Ni}(\text{L}^7)\text{Cl}_2]$  (**11**) (projection at  $b$ -axis )

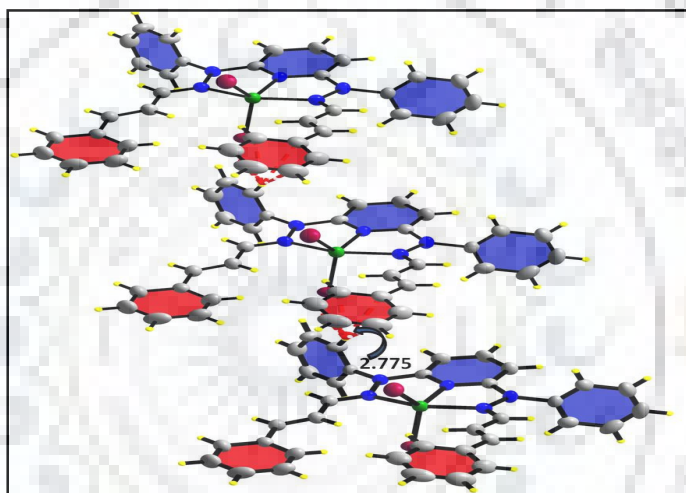
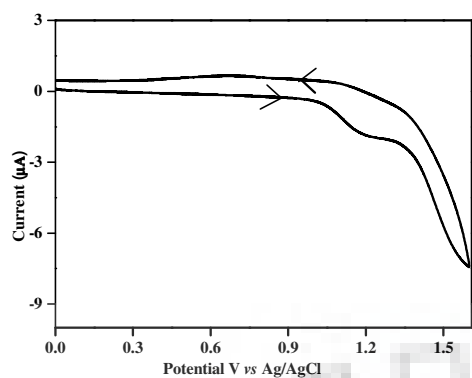


**Fig. 6.7** Packing diagram of complex  $[\text{Cu}(\text{L}^7)\text{Cl}_2]$  (**12**) (projection at  $b$ -axis )

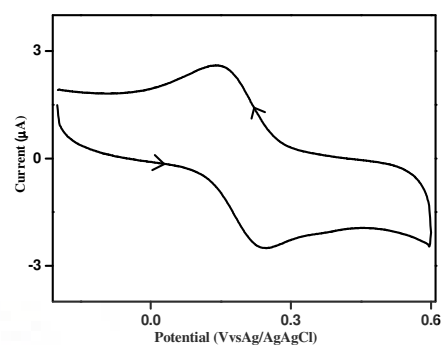
### 6.2.3 Electrochemical investigation

The electrochemical properties of all the complexes (**8-12**) were investigated by cyclic voltammetric studies. In complex  $[\text{Mn}(\text{L}^7)\text{Cl}_2]$  (**8**) an irreversible response was obtained due to Mn(II)/Mn(III) at 1.185 V vs Ag/AgCl while in complex  $[\text{Fe}(\text{L}^7)\text{Cl}_2]$  (**9**) Fe(II)/Fe(III) we got a quasireversible response with  $E_{1/2}$  0.193 V vs Ag/AgCl. In complex  $[\text{Co}(\text{L}^7)\text{Cl}_2]$  (**10**) and  $[\text{Ni}(\text{L}^7)\text{Cl}_2]$  (**11**) irreversible responses were obtained. In complex  $[\text{Cu}(\text{L}^7)\text{Cl}_2]$  (**12**) two irreversible responses were investigated at 0.458V and 0.099V vs Ag/AgCl were investigated. As shown in Fig.6.8 and Table 6.5.

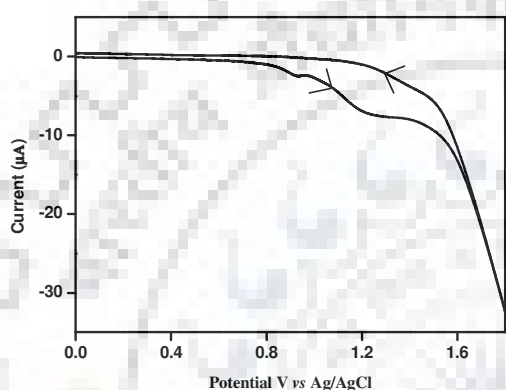




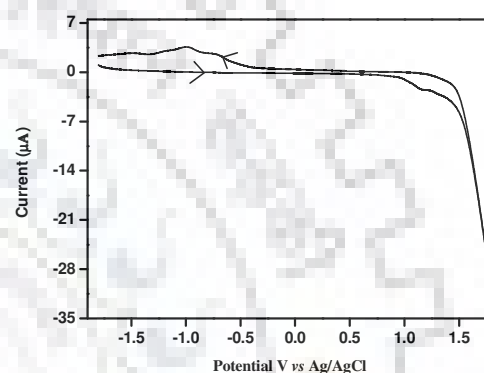
Complex  $[\text{Mn}(\text{L}^7)\text{Cl}_2]$  (8)



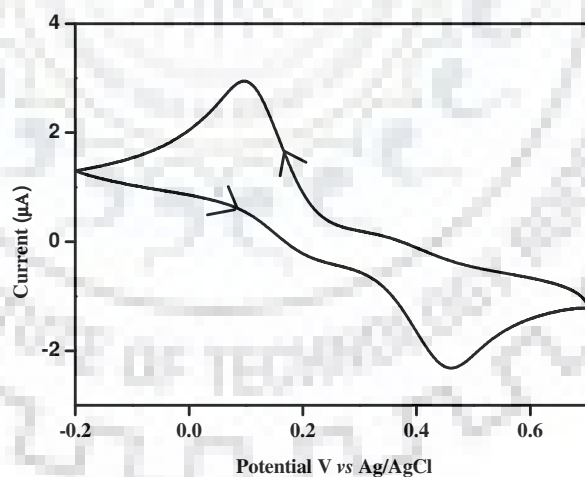
Complex  $[\text{Fe}(\text{L}^7)\text{Cl}_2]$  (9)



Complex  $[\text{Co}(\text{L}^7)\text{Cl}_2]$  (10)



Complex  $[\text{Ni}(\text{L}^7)\text{Cl}_2]$  (11)



Complex  $[\text{Cu}(\text{L}^7)\text{Cl}_2]$  (12)

**Fig.6.8** Cyclic voltammograms of a  $1 \times 10^{-3}$  M solution of complex **8-12** in DMSO in presence of 0.1 M tetrabutylammonium perchlorate (TBAP), using working electrode: glassy-carbon, reference electrode: Ag/AgCl; auxiliary electrode: platinum wire, scan rate  $0.1 \text{ V s}^{-1}$

**Table 6.5 Electrochemical data for redox properties 298 K<sup>a</sup> vs Ag/ AgCl.**

Complex	E <sub>pa</sub> /V	E <sub>pc</sub> /V	E <sub>1/2</sub> <sup>b</sup> , V (ΔE <sub>p</sub> <sup>c</sup> , mV)	<sup>d</sup> n = i <sub>pa</sub> /i <sub>pc</sub>
<b>8</b>	1.185	.....	.....	.....
<b>9</b>	0.244	0.142	0.193(102)	0.972
<b>10</b>	1.232	.....	.....	.....
<b>11</b>	1.148	-0.992	.....	.....
<b>12</b>	0.458	0.099	.....	.....

<sup>[a]</sup> Electrochemical data measured in DMSO with 0.1M tetrabutylammonium perchlorate

(TBAP). <sup>[b]</sup> Data from cyclic voltammetric measurements; E<sub>1/2</sub> is calculated as average of anodic (E<sub>pa</sub>) and cathodic (E<sub>pc</sub>) peak potentials E<sub>1/2</sub>=1/2(E<sub>pa</sub>+E<sub>pc</sub>); and <sup>[c]</sup> ΔE<sub>p</sub> = E<sub>pa</sub> -E<sub>pc</sub> at scan rate 0.1 Vs<sup>-1</sup>, <sup>[d]</sup> Constant-potential coulometric data n=i<sub>pa</sub>/ i<sub>pc</sub> calculated for 1e<sup>-</sup> transfer.

#### 6.2.4 DNA interaction studies

UV-visible spectroscopy has been used to investigate the DNA binding behaviour of metal complexes. To achieve this, a fixed concentration of metal complexes was titrated with increasing concentration of CT-DNA at physiological pH (7.2) and the spectral changes were monitored. The absorption spectra of all complexes in absence and presence of different concentrations of CT-DNA are shown in Fig. 6.9- 6.13. When the concentration of DNA was increased, the absorption spectra of all complexes gave rise some spectral changes (a) significant red shifts (b) hyperchromism in the charge transfer band

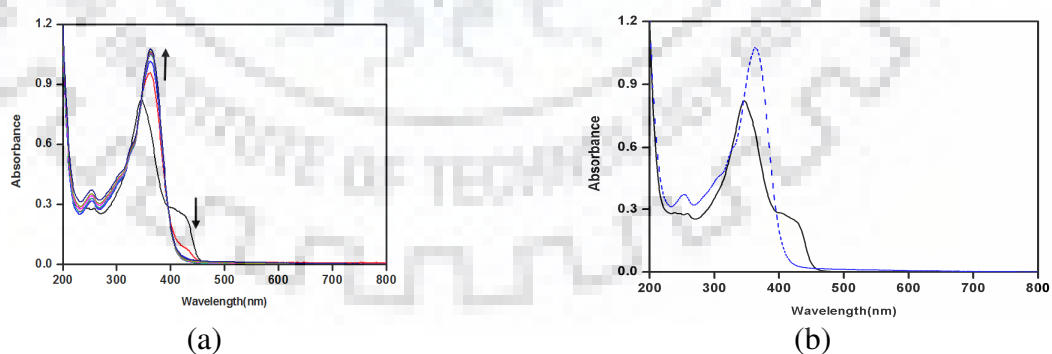


**Fig. 6.9** Absorption spectral changes of complex [Mn(L<sup>7</sup>)Cl<sub>2</sub>] (**8**) (100μM) (a) in 0.1M phosphate buffer (pH 7.2) in the presence of increasing the amount of DNA (0- 385μM). (b)hyperchromic shift with DNA between the initial and final spectra. Solid line represent the spectrum in the absence of DNA

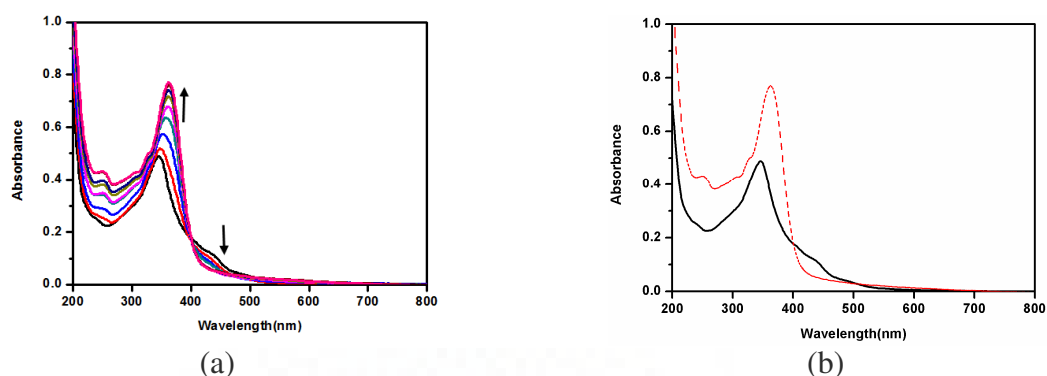


**Fig. 6.10** Absorption spectral changes of complex  $[\text{Fe}(\text{L}^7)\text{Cl}_2]$  (**9**) ( $80\mu\text{M}$ ) (a) in  $0.1\text{M}$  phosphate buffer ( $\text{pH } 7.2$ ) in the presence of increasing the amount of DNA ( $0- 550\mu\text{M}$ ). (b) hyperchromic shift with DNA between the initial and final spectra. Solid line represent the spectrum in the absence of DNA

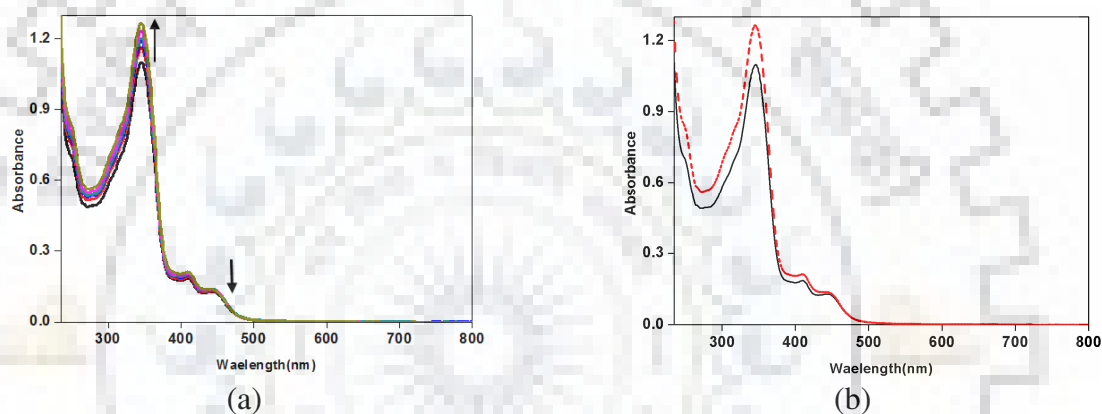


**Fig. 6.11** Absorption spectral changes of complex  $[\text{Co}(\text{L}^7)\text{Cl}_2]$  (**10**) ( $100\mu\text{M}$ ) (a) in  $0.1\text{M}$  phosphate buffer ( $\text{pH } 7.2$ ) in the presence of increasing the amount of DNA ( $0- 430\mu\text{M}$ ). (b) hyperchromic shift with DNA between the initial and final spectra. Solid line represent the spectrum in the absence of DNA

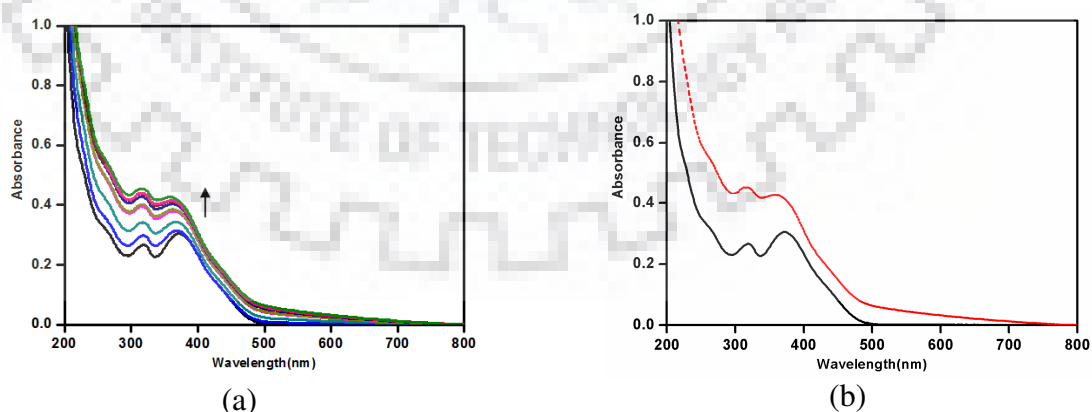


**Fig. 6.12** Absorption spectral changes of complex  $[\text{Ni}(\text{L}^7)\text{Cl}_2]$  (**11**) ( $100\mu\text{M}$ ) (a) in  $0.1\text{M}$  phosphate buffer ( $\text{pH } 7.2$ ) in the presence of increasing the amount of DNA ( $0- 460\mu\text{M}$ ). (b) hyperchromic shift with DNA between the initial and final spectra. Solid line represent the spectrum in the absence of DNA

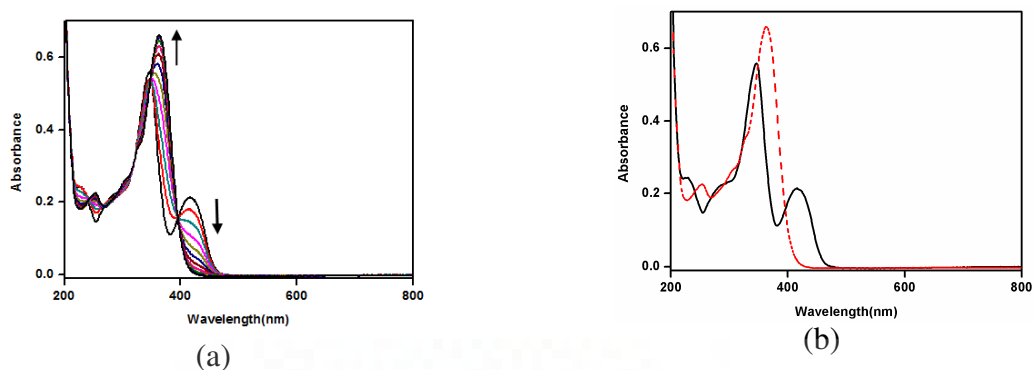


**Fig. 6.13** Absorption spectral changes of complex  $[\text{Cu}(\text{L}^7)\text{Cl}_2]$  (**12**) ( $100\mu\text{M}$ ) (a) in  $0.1\text{M}$  phosphate buffer ( $\text{pH } 7.2$ ) in the presence of increasing the amount of DNA ( $0-430\mu\text{M}$ ). (b) hyperchromic shift with DNA between the initial and final spectra. Solid line represent the spectrum in the absence of DNA

It can be noticed that all mono complex exhibited larger spectral shifts during DNA binding event. Manganese complexes afforded highest shifts among the family probably due to the lowest CFSE values indicating that CFSE may be one of the important factors determining the DNA binding affinity of complexes.<sup>349</sup> The binding constants for all complexes are listed in Table 6.6

**Table 6.6** Binding constants and Stern-Volmer constant for DNA interaction studies

Complexes	$K_b(\text{M}^{-1})$	$K_{sv}(\text{M}^{-1})$
$[\text{Mn}(\text{L}^7)\text{Cl}_2]$ ( <b>8</b> )	$5.341 \times 10^4$	$2.70 \times 10^5$
$[\text{Fe}(\text{L}^7)\text{Cl}_2]$ ( <b>9</b> )	$2.39 \times 10^4$	$3.00 \times 10^5$
$[\text{Co}(\text{L}^7)\text{Cl}_2]$ ( <b>10</b> )	$4.05 \times 10^4$	$3.84 \times 10^5$
$[\text{Ni}(\text{L}^7)\text{Cl}_2]$ ( <b>11</b> )	$1.48 \times 10^4$	$6.13 \times 10^5$
$[\text{Cu}(\text{L}^7)\text{Cl}_2]$ ( <b>12</b> )	$2.08 \times 10^4$	$4.61 \times 10^5$

A number of complexes are known which can intercalate between the base pairs of DNA giving rise to the shifts in the absorption bands of complexes. However the intercalative mode of interaction between the present series of metal complexes and DNA was unlikely since intercalation is evident when hyperchromism is accompanied by red shift in the

absorption spectrum without any change in the spectrum profile.<sup>259-261</sup> Furthermore, the binding constants calculated for the complexes [ $\sim 10^3$ – $10^4$ ] were much lower than those of classical intercalators and metallointercalators [ $\sim 10^6$ – $10^7$ ] indicating their non–intercalative mode of interaction.<sup>404</sup> Fluorescence quenching experiments were carried out by the successive addition of the metal complexes to the DNA (35  $\mu\text{M}$ ) solutions containing 5  $\mu\text{M}$  ethidium bromide (EB) in 0.1 M phosphate buffer (pH 7.2) and the reaction mixture was incubated for 2 min after each successive addition of the quencher molecules. These samples were excited at 250 nm and emissions were observed between 500 and 700 nm. (As shown in Fig. 6.14-6.19) The Stern–Volmer quenching constants ( $K_{\text{SV}}$ ) for all the complexes were calculated using linear Stern–Volmer equation (*Chapter 1*) and are listed in Table 6.6.

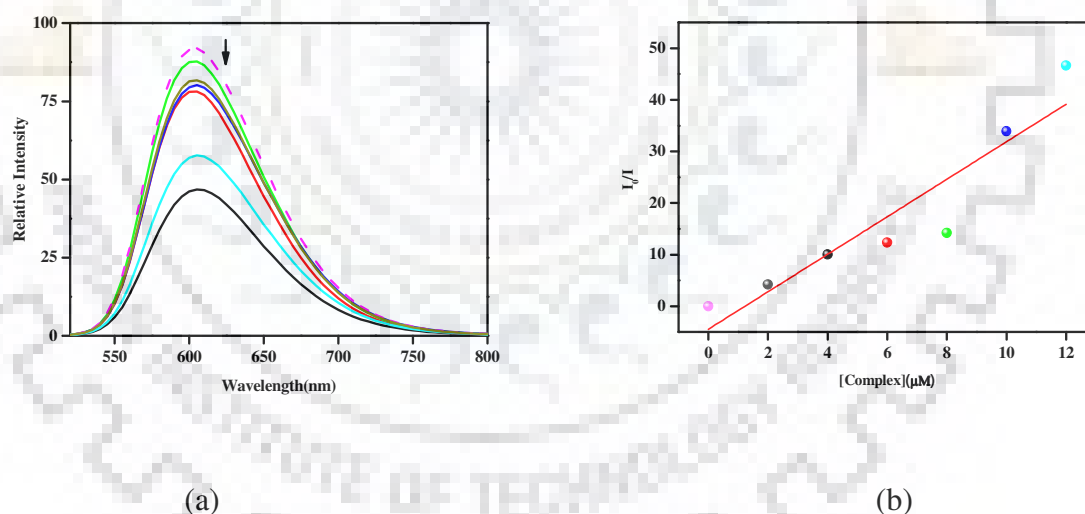


**Fig. 6.14** (a) Fluorescence emission spectra of CT-DNA in the presence of complex  $[\text{Mn}(\text{L}^7)\text{Cl}_2]$  (**8**) in 0.1M phosphate buffer (pH 7.2) containing 2% DMF.  $[\text{DNA}] = 35 \mu\text{M}$ ,  $[\text{complex } [\text{Mn}(\text{L}^7)\text{Cl}_2] (\mathbf{8})] = 0 - 12.01 \mu\text{M}$ ,  $\lambda_{\text{ex}} = 250\text{nm}$  and  $\lambda_{\text{em}} = 600\text{nm}$ . Dotted line represents the spectrum in the absence of complex  $[\text{Mn}(\text{L}^7)\text{Cl}_2]$  (**8**) (b) Stern-Volmer plot for complex  $[\text{Mn}(\text{L}^7)\text{Cl}_2]$  (**8**)

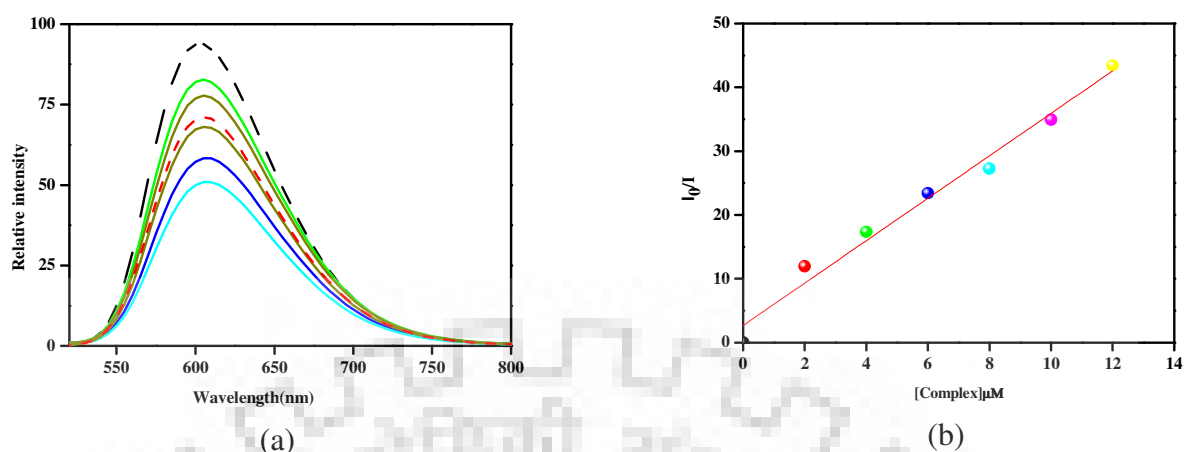


**Fig. 6.15** (a) Fluorescence emission spectra of CT-DNA in the presence of complex  $[\text{Fe}(\text{L}^7)\text{Cl}_2]$  (**9**) in 0.1M phosphate buffer (pH 7.2) containing 2% DMF.  $[\text{DNA}] = 35 \mu\text{M}$ ,  $[\text{complex } [\text{Fe}(\text{L}^7)\text{Cl}_2] (\mathbf{9})] = 0 - 12.01 \mu\text{M}$ ,  $\lambda_{\text{ex}} = 250\text{nm}$  and  $\lambda_{\text{em}} = 600\text{nm}$ . Dotted line represents the spectrum in the absence of complex  $[\text{Fe}(\text{L}^7)\text{Cl}_2]$  (**9**) (b) Stern-Volmer plot for complex  $[\text{Fe}(\text{L}^7)\text{Cl}_2]$  (**9**)

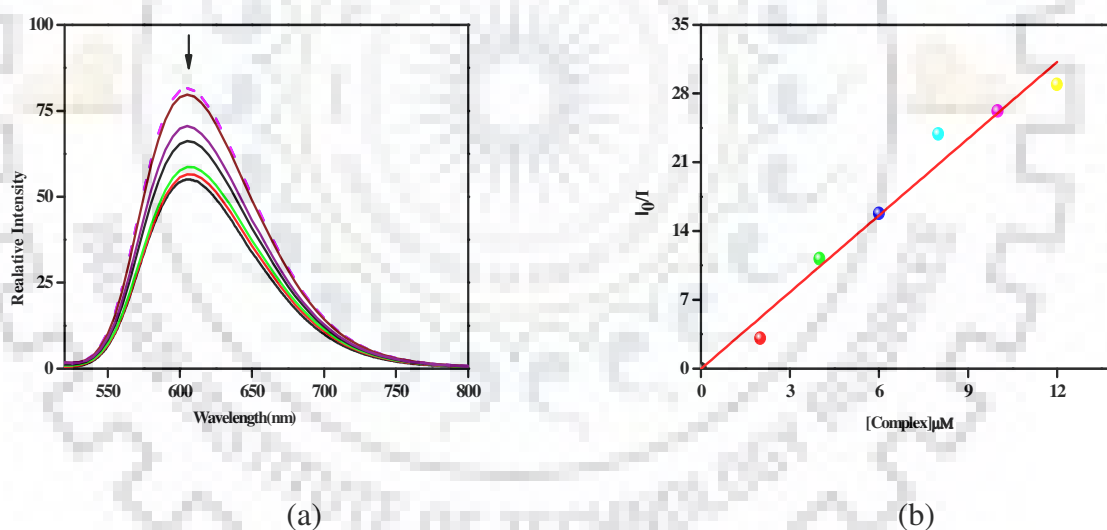


**Fig. 6.16** (a) Fluorescence emission spectra of CT-DNA in the presence of complex  $[\text{Co}(\text{L}^7)\text{Cl}_2]$  (**10**) in 0.1M phosphate buffer (pH 7.2) containing 2% DMF.  $[\text{DNA}] = 35\mu\text{M}$ ,  $[\text{complex } [\text{Co}(\text{L}^7)\text{Cl}_2] (\mathbf{10})] = 0 - 12.01 \mu\text{M}$ ,  $\lambda_{\text{ex}} = 250\text{nm}$  and  $\lambda_{\text{em}} = 600\text{nm}$ . Dotted line represents the spectrum in the absence of complex  $[\text{Co}(\text{L}^7)\text{Cl}_2]$  (**10**) (b) Stern-Volmer plot for complex  $[\text{Co}(\text{L}^7)\text{Cl}_2]$  (**10**)

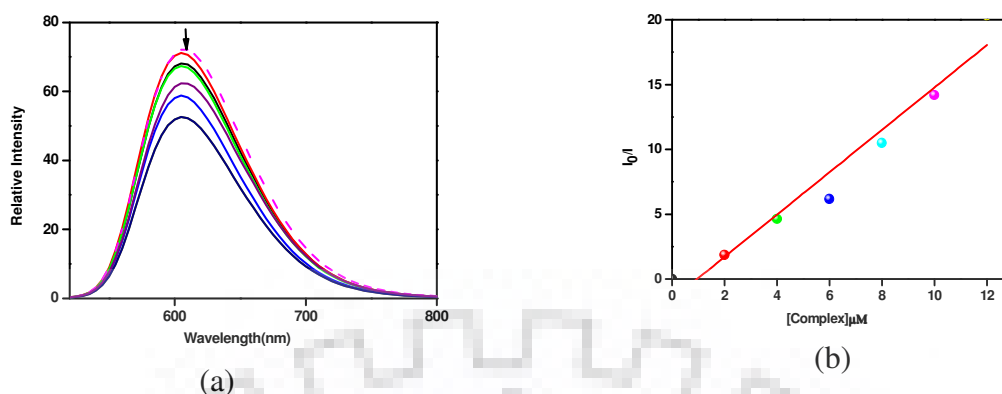


**Fig.6.17** (a) Fluorescence emission spectra of CT-DNA in the presence of complex  $[\text{Ni}(\text{L}^7)\text{Cl}_2]$  (**11**) in 0.1M phosphate buffer (pH 7.2) containing 2% DMF.  $[\text{DNA}] = 35 \mu\text{M}$ ,  $[\text{complex } [\text{Ni}(\text{L}^7)\text{Cl}_2] (\text{11})] = 0 - 12.01 \mu\text{M}$ ,  $\lambda_{\text{ex}} = 250\text{nm}$  and  $\lambda_{\text{em}} = 600\text{nm}$ . Dotted line represents the spectrum in the absence of complex  $[\text{Ni}(\text{L}^7)\text{Cl}_2]$  (**11**) (b) Stern-Volmer plot for complex  $[\text{Ni}(\text{L}^7)\text{Cl}_2]$  (**11**)

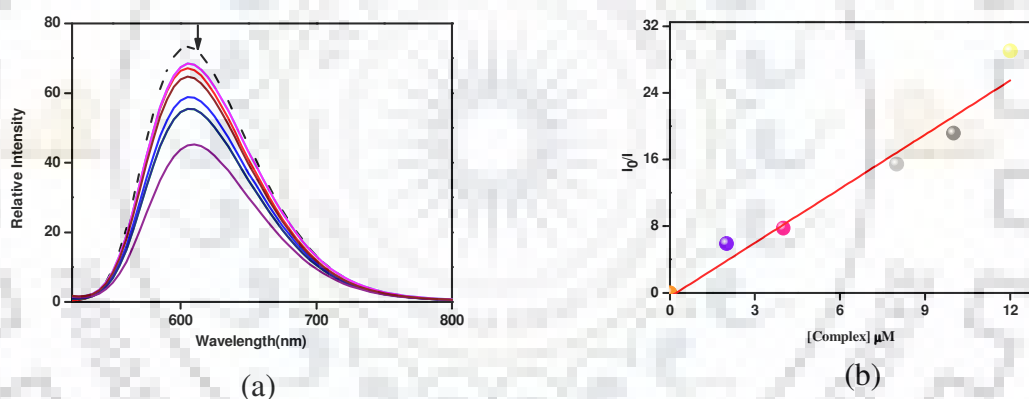


**Fig. 6.18** (a) Fluorescence emission spectra of CT-DNA in the presence of complex  $[\text{Cu}(\text{L}^7)\text{Cl}_2]$  (**12**) in 0.1M phosphate buffer (pH 7.2) containing 2% DMF.  $[\text{DNA}] = 35\mu\text{M}$ ,  $[\text{complex } [\text{Cu}(\text{L}^7)\text{Cl}_2] (\text{12})] = 0 - 12.00 \mu\text{M}$ ,  $\lambda_{\text{ex}} = 250\text{nm}$  and  $\lambda_{\text{em}} = 600\text{nm}$ . Dotted line represent the spectrum in the absence of complex  $[\text{Cu}(\text{L}^7)\text{Cl}_2]$  (**12**) (b) Stern-Volmer plot for complex  $[\text{Cu}(\text{L}^7)\text{Cl}_2]$  (**12**)

Circular Dichroism (CD) is a sensitive as well as important technique for probing the conformational changes in DNA induced by foreign DNA binding agents. The CD spectrum of CT-DNA exhibits one positive band near 275 nm due to base stacking and one negative band near 248 nm due to helicity. These are characteristic of the right handed

B-conformation of DNA. The CD-spectral changes of DNA in presence of all complexes are illustrated in the Fig. 6.19.

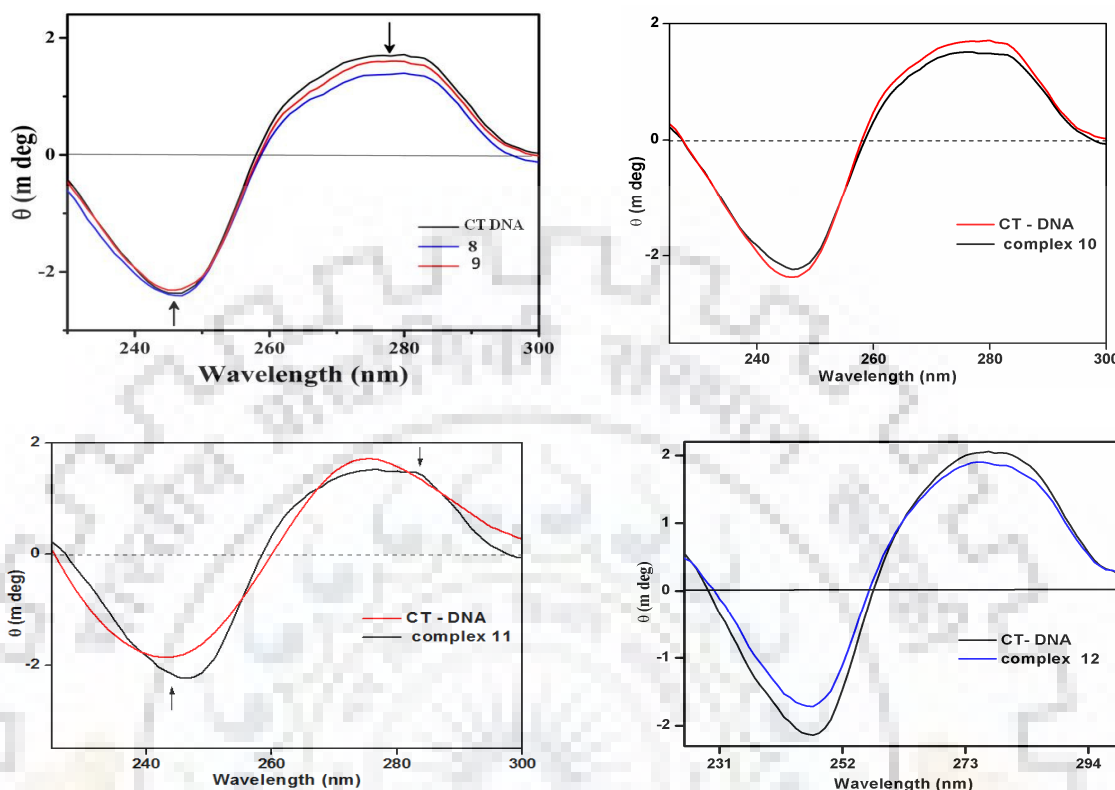


**Fig. 6.19** Circular dichroism spectra in 0.1 M phosphate buffer (pH 7.2) after 10 min incubation at 25 °C with CT-DNA and its interaction with complexes (8-12) spectra recorded in 2% dimethylformamide

The intensity of the negative band in complexes  $[\text{Mn}(\text{L}^7)\text{Cl}_2]$  (8) and  $[\text{Fe}(\text{L}^7)\text{Cl}_2]$  (9) was almost unaffected by incubation of DNA with metal complexes, however, little change in the intensity of positive band was observed without any considerable shift in the wavelength while in complexes  $[\text{Co}(\text{L}^7)\text{Cl}_2]$  (10),  $[\text{Ni}(\text{L}^7)\text{Cl}_2]$  (11) and  $[\text{Cu}(\text{L}^7)\text{Cl}_2]$  (12) there will be little change in negative as well as positive band with respect to CT-DNA. Occurrence of no significant red or blue shift predicted that the conformation of secondary structure of DNA remained largely unaltered after the DNA binding event<sup>405</sup>, however little enhancement in the stacking interactions could not be ruled out. It is well established that classical intercalators cause significant changes in intensities of both, positive and negative



bands due to enhancement of base stacking and stabilization of helicity whereas small molecules exhibiting groove binding or electrostatic interactions with DNA cause no perturbations.<sup>406,407</sup> Hence circular dichroism spectroscopic experiments supported a non-intercalative mode of interaction with DNA for the present series of complexes. These data were consistent with the results inferred from the absorption spectral titrations and competitive binding experiments.

### 6.2.5 Hirshfeld surface analysis

To visualize different types of interactions (for eg. H···H, C···H, N···H, Cl···H, halogen bonding, and  $\pi$ -based interactions) within a crystal structure, we have investigated Hirshfeld surface analysis.<sup>408</sup>

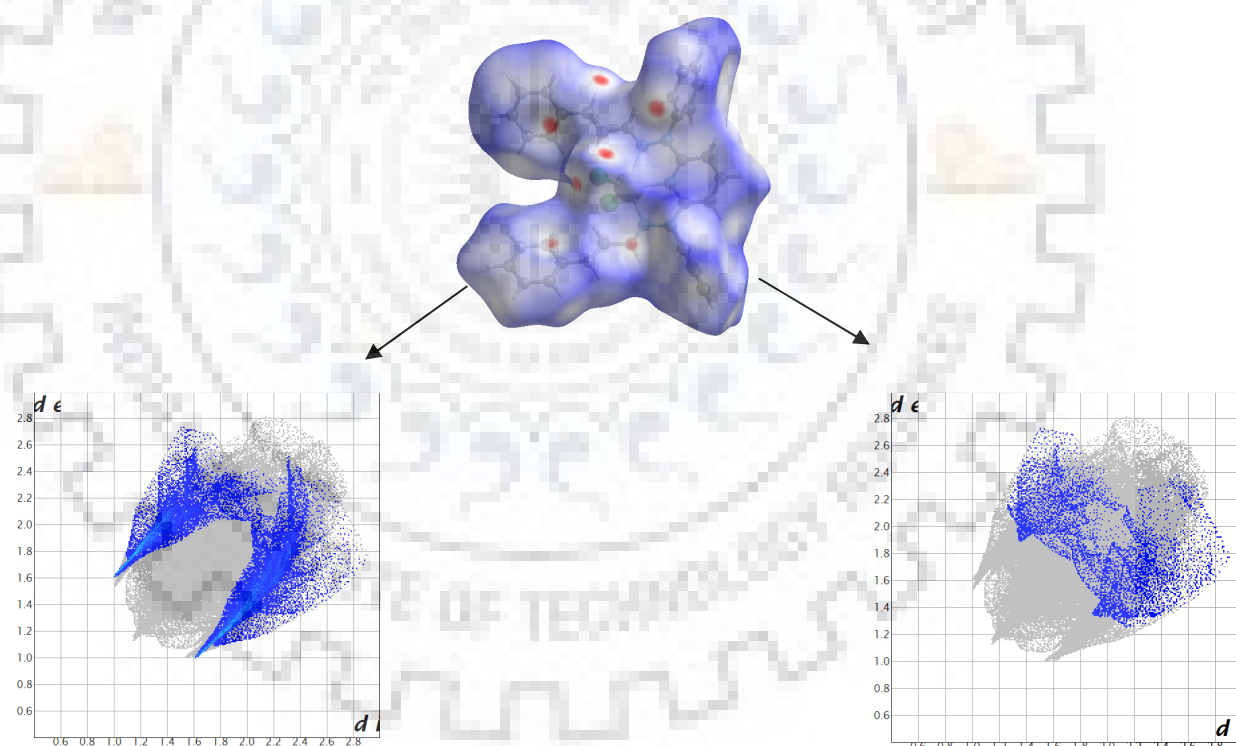


**Fig. 6.20**  $d_{\text{norm}}$  surface for the complex  $[\text{Mn}(\text{L}^7)\text{Cl}_2]$  (**8**) red spots indicates contacts shorter than van der Waals distance) B) 2D Fingerprint plots with  $d_i$  and  $d_e$  ranging from 0.6 to 2.8 Å, all the type of interaction C) finger print plot for Cl···H and D) N···H interactions

Hirshfeld surfaces were used to distinguish intermolecular interactions in the solid state. The function  $d_{\text{norm}}$  is a ratio surrounding the distances of any surface point to the nearest interior ( $d_i$ ) and exterior ( $d_e$ ) atom and the van der Waals radii of the atoms. The negative  $d_{\text{norm}}$  value indicates the sum of  $d_i$  and  $d_e$  is shorter than the sum of the van der Waals radii, and visualized as red colour in Hirshfeld surfaces. The white colour describes intermolecular distances close to van der Waals contacts ( $d_{\text{norm}}=0$ ), whereas contacts longer than the sum of van der Waals radii with positive  $d_{\text{norm}}$  values are coloured with blue. A plot of  $d_i$  vs  $d_e$  is a 2D fingerprint plot shows the existence of different types of intermolecular interactions (Fig. 6.20 - 6.24). The Hirshfeld surface analysis of all the complexes showed the presence of weak interactions which were displayed in Table 6.7.

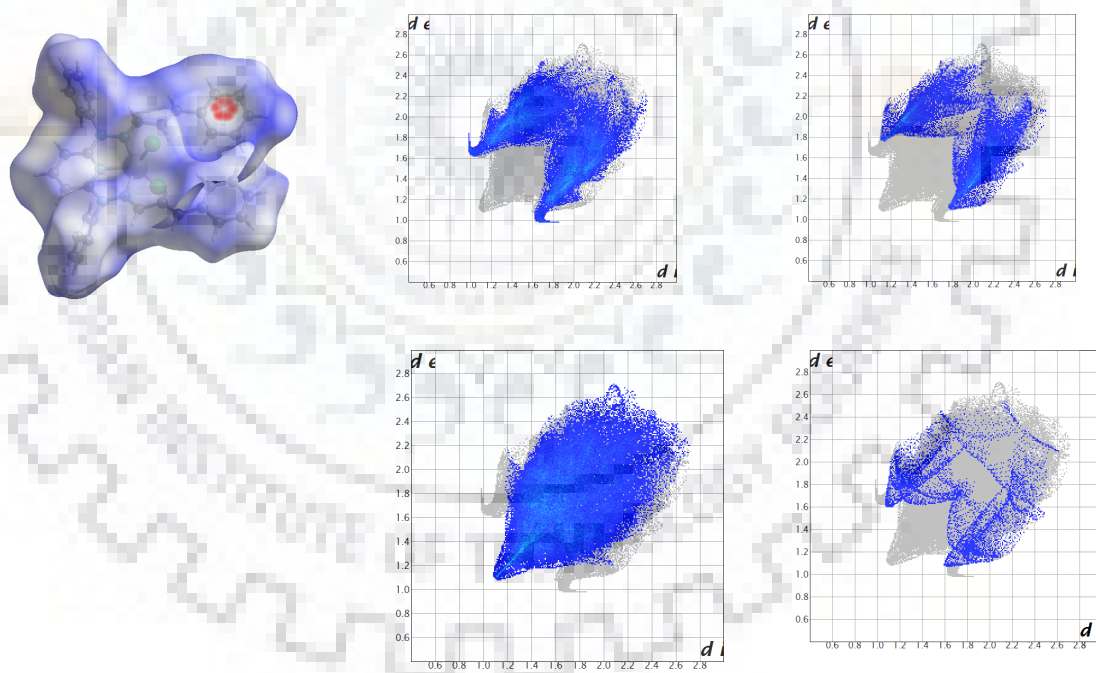


**Fig. 6.21**  $d_{\text{norm}}$  surface for the complex  $[\text{Fe}(\text{L}^7)\text{Cl}_2]$  (**9**) (red spots indicates contacts shorter than van der Waals distance) B) 2D Fingerprint plots with  $d_i$  and  $d_e$  ranging from 0.6 to 2.8 Å, all the type of interaction C) finger print plot for C...H, Cl...H, H...H and N...H interactions

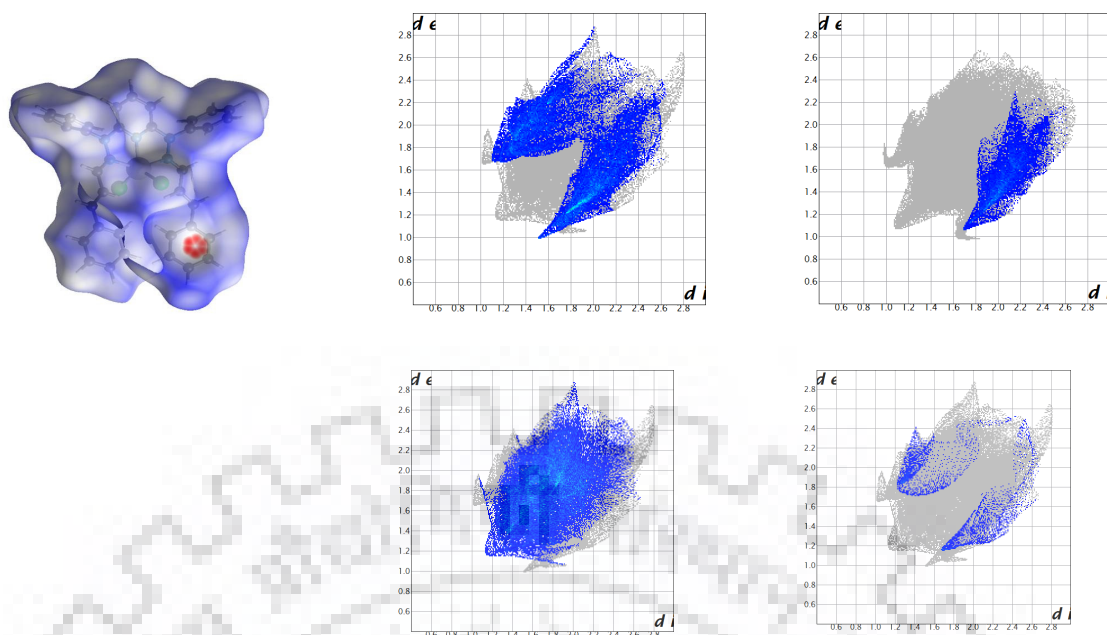


**Fig. 6.22**  $d_{\text{norm}}$  surface for the complex  $[\text{Co}(\text{L}^7)\text{Cl}_2]$  (10) (red spots indicates contacts shorter than van der Waals distance) B) 2D Fingerprint plots with  $d_i$  and  $d_e$  ranging from 0.6 to 2.8 Å, all the type of interaction C) finger print plot for  $\text{C}\cdots\text{H}$ ,  $\text{Cl}\cdots\text{H}$ ,  $\text{H}\cdots\text{H}$  and  $\text{N}\cdots\text{H}$  interactions

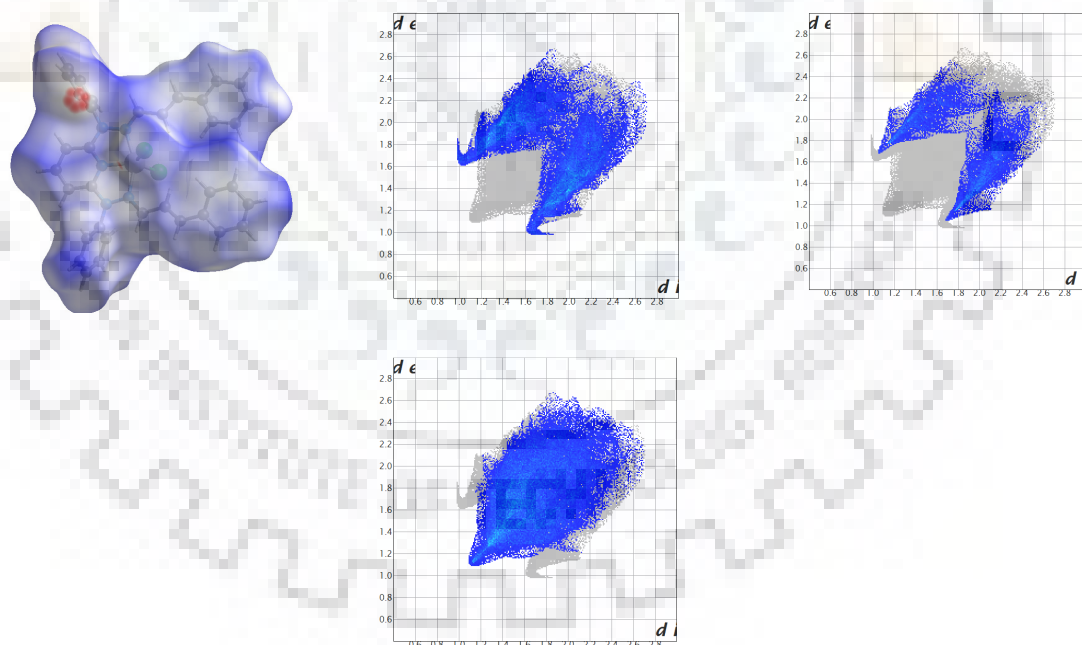


**Fig. 6.23**  $d_{\text{norm}}$  surface for the complex  $[\text{Ni}(\text{L}^7)\text{Cl}_2]$  (11) (red spots indicates contacts shorter than van der Waals distance) B) 2D Fingerprint plots with  $d_i$  and  $d_e$  ranging from 0.6 to 2.8 Å, all the type of interaction C) finger print plot for  $\text{C}\cdots\text{H}$ ,  $\text{Cl}\cdots\text{H}$  and  $\text{H}\cdots\text{H}$  interactions

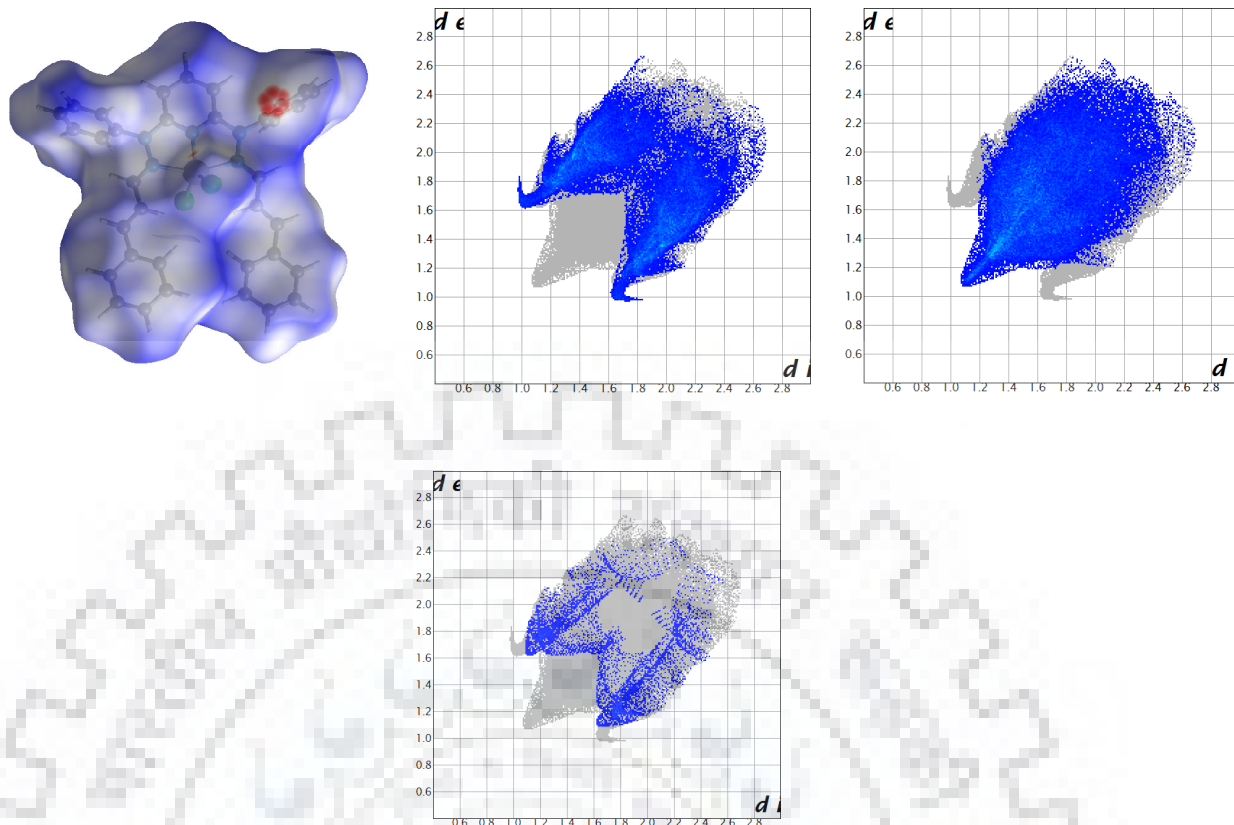


**Fig. 6.24**  $d_{\text{norm}}$  surface for the complex  $[\text{Cu}(\text{L}^7)\text{Cl}_2]$  (**12**) (red spots indicates contacts shorter than van der Waals distance) B) 2D Fingerprint plots with  $d_i$  and  $d_e$  ranging from 0.6 to 2.8 Å, all the type of interaction C) finger print plot for  $\text{C}\cdots\text{H}$ ,  $\text{H}\cdots\text{H}$  and  $\text{N}\cdots\text{H}$  interactions

**Table.6.7** The Hirshfeld surface analysis of all the complexes showed the presence of weak interactions

Complexes	Weak interactions (%)			
	$\text{C}\cdots\text{H}$	$\text{Cl}\cdots\text{H}$	$\text{H}\cdots\text{H}$	$\text{N}\cdots\text{H}$
<b>8</b>	.....	14.3	.....	3.7
<b>9</b>	32.7	14	45.9	4.1
<b>10</b>	30.2	8.2	49.2	3.4
<b>11</b>	32.7	14.1	46.3	....
<b>12</b>	32.8	.....	45.8	4

### 6.2.6 Theoretical investigation

Theoretical calculation was performed using (B3LYP/ LANL2DZ) to understand electronic structural description for all the complexes.<sup>287</sup> The geometry optimizations for all the complexes (**8-12**) were performed at DFT level as shown in Fig. 6.32. The energy gap between HOMO and LUMO of all the complexes were depicted in Fig.6.33- 6.37. The percentage contribution in each orbital's and main bond types were displayed in Table (6.9- 6.13). With the help of the TD-DFT calculations the electronic transitions happened in all the molecules were considered in the gas phase the theoretical data almost matches the experimental data as shown in Fig.6.37. Electronic transitions at particular wavelength and their percentage contribution were displayed in Table 6.14- 6.18.

### 6.3 Conclusion

A novel tridentate pincer type ligand (PyPhime-Cina) ( $L^7$ ) 2,6-bis((E)-1-phenyl-2-((E)-3-phenylallylidene)hydrazinyl) pyridine was synthesized and characterised. Using this ligand we have synthesized and characterised  $[Mn(L^7)Cl_2]$  (**8**),  $[Fe(L^7)Cl_2]$  (**9**),  $[Co(L^7)Cl_2]$  (**10**),  $[Ni(L^7)Cl_2]$  (**11**) and  $[Cu(L^7)Cl_2]$  (**12**) complexes. Molecular structures of the ligand ( $L^7$ ) and complexes  $[Mn(L^7)Cl_2]$  (**8**),  $[Fe(L^7)Cl_2]$  (**9**),  $[Co(L^7)Cl_2]$  (**10**),  $[Ni(L^7)Cl_2]$  (**11**) and  $[Cu(L^7)Cl_2]$  (**12**) were determined by X-ray crystallography. All the complexes were characterized by different spectroscopic methods. DNA interaction studies were evaluated by UV-visible absorption, fluorescence and circular dichroism spectral studies. Non covalent binding of all the complexes with CT-DNA was speculated. Hirshfeld surface analysis of all the complexes (**8-12**) was performed. Theoretical calculations were performed to understand the electronic properties of the molecules. The investigation of orbital contribution clearly indicated that HOMO of complexes  $[Mn(L^7)Cl_2]$  (**8**),  $[Fe(L^7)Cl_2]$  (**9**),  $[Co(L^7)Cl_2]$  (**10**),  $[Cu(L^7)Cl_2]$  (**12**) were having mostly ligand character excluding complex  $[Ni(L^7)Cl_2]$  (**11**). However, other reactivity studies are under progress.

## 6.4 Experimental section

**Materials** All the solvents used were reagent grade cinnamaldehyde was purchased from Acros organics, USA. Solvents used for spectroscopic studies were HPLC grade and purified by standard procedure before use.

### 6.4.1 Synthesis of ligand

#### 6.4.1.1 ligand (2,6-bis((E)-1-phenyl-2-((E)-3-phenylallylidene)hydrazinyl)pyridine) ( $L^7$ )

Ligand ( $L^7$ ) have been synthesized using cinnamaldehyde. Cinnamaldehyde was used in 2:1 ratio with 2,6-bis(1-phenylhydrazinyl)pyridine in methanolic solution. 2,6-bis(1-phenylhydrazinyl)pyridine was prepared according to the method reported in the literature.<sup>255</sup> The reaction was stirred at room temperature for 20 minutes, we got yellow precipitate during stirring, filter the reaction and washed with methanol and dried under vacuum. Yield 94%. Anal. Calcd for  $C_{35}H_{29}N_5$  (519.638) C, 80.90, H, 5.63, N, 13.48. Found: C, 79.90, H, 6.01, N, 12.98. UV-visible [ $CH_2Cl_2$ ;  $\lambda_{max}$  /nm ( $\epsilon/M^{-1}cm^{-1}$ )] 368(53,762); 257(18,036). IR data (KBr,  $\nu_{max}/cm^{-1}$ ) 1570,  $\nu_{C=Nimine}$ ; 1444, 1210, 1124, 975, 747, 691, 517.

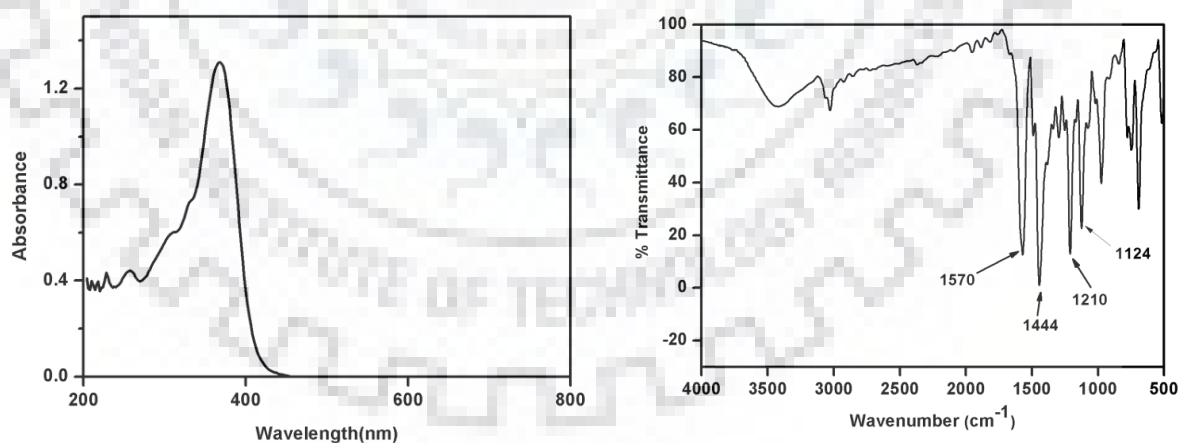


**Fig. 6.25** UV-Visible and IR spectrums of ligand ( $L^7$ )

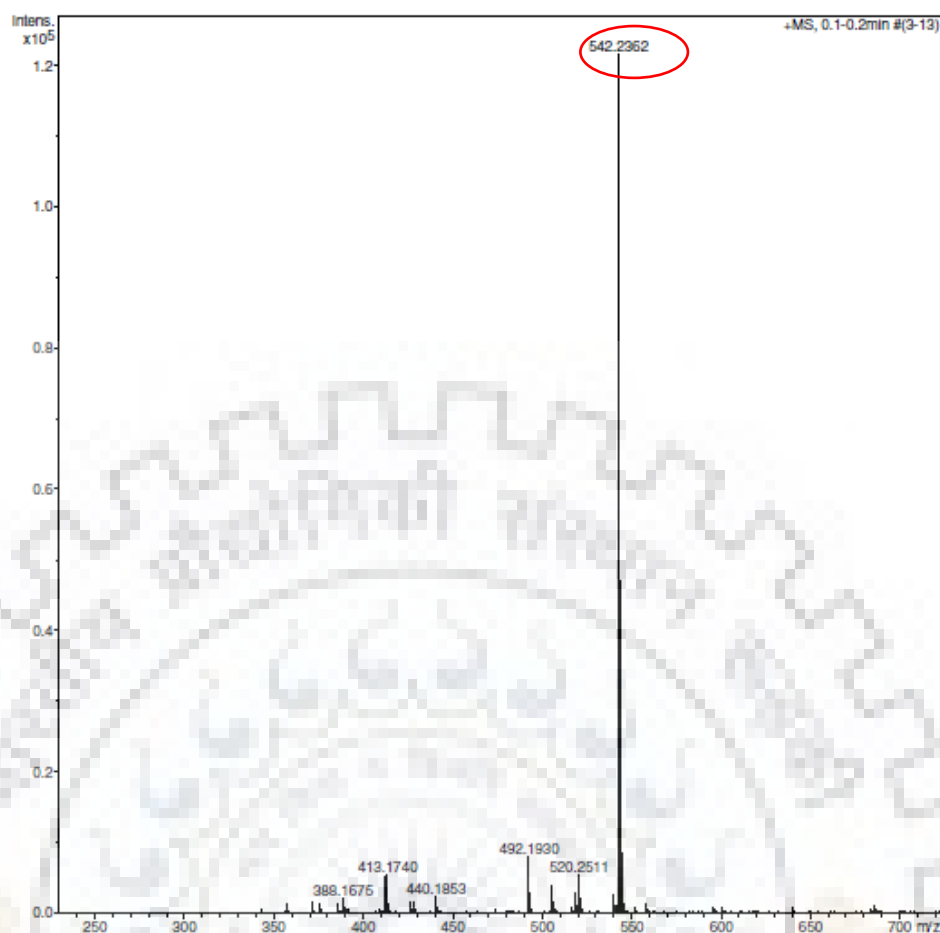


Fig. 6.26 ESI-MS of ligand  $L^7$  in acetonitrile  $[L^7+Na]^+$

## 6.4.2 Synthesis of Metal Complexes

### 6.4.2.1 Synthesis of complex $[Mn(L^7)Cl_2]$ (8)

A batch of ligand  $L^7$  (0.2mM 0.1039g) was dissolved into 3 mL of dichloromethane. A solution of  $MnCl_2 \cdot 4H_2O$  (0.2 mM, 0.038g) with 2 mL of methanol was added dropwise to the above solution. The resulting brown solution was stirred for 30 minutes; a brown colour precipitate was obtained. The solid was filtered out and washed with diethyl ether. The crystallization of the complex was done by dissolving the complex into dichloromethane in a vial and layered with methanol, brown color crystals were obtained within 24 hours. Yield 80%. Anal. Calcd for  $C_{35}H_{29}Cl_2MnN_5$  (645.48): C, 65.13; H, 4.53; N, 10.98. Found: C, 65.10; H, 4.50; N, 10.91. IR data (KBr,  $\nu_{max}/cm^{-1}$ ): 1566,  $\nu_{C=Nimine}$ , 1446, 1386, 1253, 1165,

1078, 969, 757, 698, 524. UV-visible [ $\text{CH}_3\text{CN}$   $\lambda_{\text{max}}$  /nm ( $\epsilon/\text{M}^{-1}\text{cm}^{-1}$ ): 413(16,170); 347(37,650); 241(10,140).

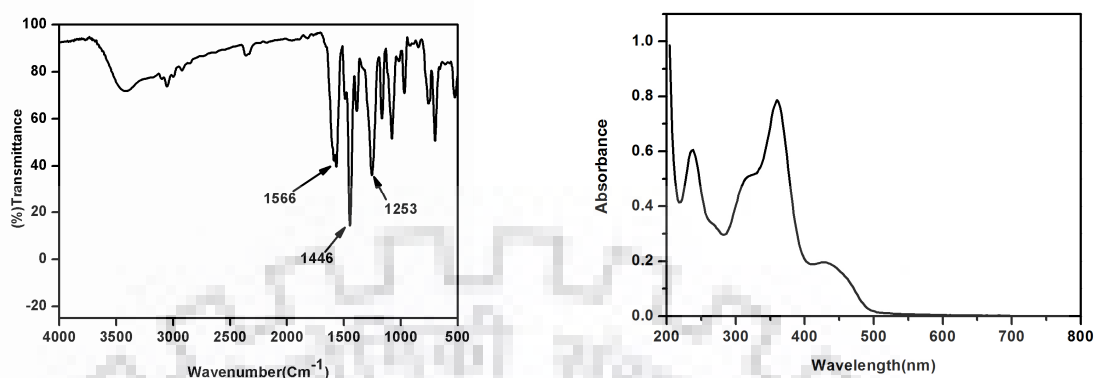
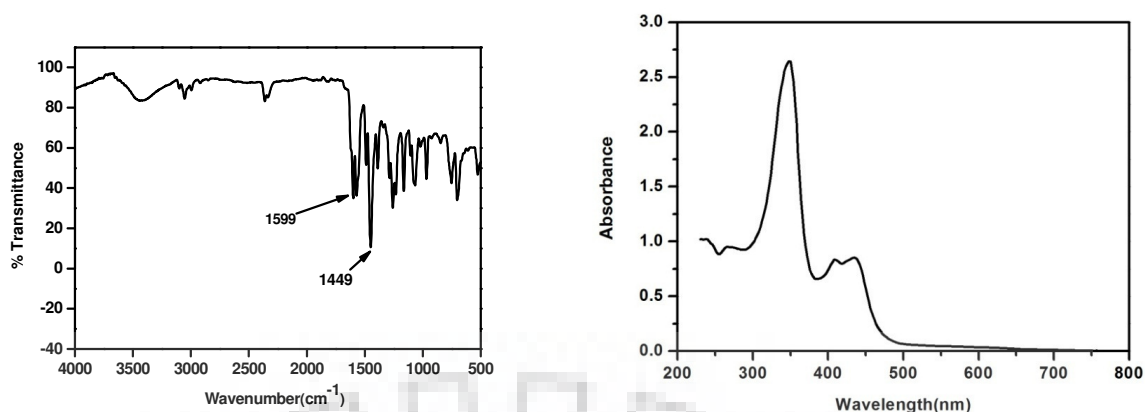


Fig. 6.27 IR and UV-visible spectrums of complex  $[\text{Mn}(\text{L}^7)\text{Cl}_2]$  (**8**)

#### 6.4.2.2 Synthesis of complex $[\text{Fe}(\text{L}^7)\text{Cl}_2]$ (**9**)

The complex  $[\text{Fe}(\text{L}^7)\text{Cl}_2]$  (**9**) was synthesized using the ligand  $\text{L}^7$  and  $\text{FeCl}_2$  into 1:1 ratio by dissolving the ligand in dichloromethane(DCM) and metal salt in methanolic solution. The ligand 0.2mM (0.1038g) of was dissolved into the dichloromethane on stirring at room temperature after that 0.2mM (0.025g) of  $\text{FeCl}_2$  was dissolved into methanol and added into the ligand dropwise the brown colour solid was obtained on stirring at room temperature. The solid was filtered off and dried under vacuum. The crystallization was done by dissolving the compound in dichloromethane solvent in a crystallization tube and layering of methanol on it. The crystallization of this complex was obtained in 24hrs and the brown colour shine crystal was obtained on the wall of the crystallization tube. Yield 90%. Anal. Calcd for  $\text{C}_{35}\text{H}_{29}\text{N}_5\text{FeCl}_2$  (646.39) C, 65.03, H, 4.52, N, 10.83. Found: C, 65.02, H, 4.41, N, 10.80. IR data (KBr,  $\nu_{\text{max}}/\text{cm}^{-1}$ ) 1599,  $\nu_{\text{C}=\text{N}}(\text{imine})$ ; 1570, 1488, 1449, 1388, 1258, 1163, 1066, 967, 752, 703, 525. UV-visible [ $\text{CH}_2\text{Cl}_2$ ;  $\lambda_{\text{max}}$  /nm ( $\epsilon/\text{M}^{-1}\text{cm}^{-1}$ )] 435(18,820); 410(18,370); 350(60,380); 240(20,110).





**Fig. 6.28** IR and UV-visible spectrum of complex  $[\text{Fe}(\text{L}^7)\text{Cl}_2]$  (**9**)

#### 6.4.2.3 Synthesis of complex $[\text{Co}(\text{L}^7)\text{Cl}_2]$ (**10**)

The complex  $[\text{Co}(\text{L}^7)\text{Cl}_2]$  (**10**) was synthesized using the ligand ( $\text{L}^7$ ) and  $\text{CoCl}_2 \cdot 6\text{H}_2\text{O}$  into 1:1 ratio by dissolving the ligand in dichloromethane (DCM) and metal salt in methanolic solution. 0.2 mM (0.1039g) of ligand was dissolved into the dichloromethane on stirring at room temperature after that 0.2 mM (0.047g) of  $\text{CoCl}_2 \cdot 6\text{H}_2\text{O}$  was dissolved into methanol and added into the ligand dropwise the red colour solid was obtained in 2 hours. The solid was filtered off and dried under vacuum. The crystallization was done by dissolving the compound in DCM solvent in a crystallization tube and layering of methanol on it. red colour shine crystal was obtained within two days. Yield 90%. Anal. Calcd for  $\text{C}_{35}\text{H}_{29}\text{N}_5\text{CoCl}_2$  (649.46) C, 64.73, H, 4.50, N, 10.78. Found: C, 64.72, H, 4.51, N, 10.70. IR data (KBr,  $\nu_{\text{max}}/\text{cm}^{-1}$ ) 1568,  $\nu_{\text{C}=\text{Nimine}}$ ; 1453, 1391, 1259, 1165, 1063, 970, 753, 697, 524. UV-visible [ $\text{CH}_2\text{Cl}_2$ ;  $\lambda_{\text{max}}/\text{nm}$  ( $\epsilon/\text{M}^{-1}\text{cm}^{-1}$ )] 446(11,390); 411(15,165); 348(47,152); 249(16,490).

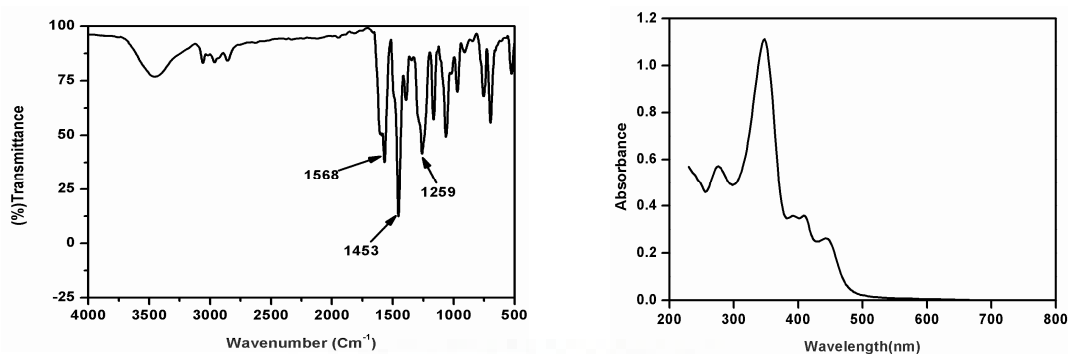


**Fig. 6.29** IR and UV-visible spectrum of complex  $[\text{Co}(\text{L}^7)\text{Cl}_2]$  (10)

#### 6.4.2.4 Synthesis of complex $[\text{Ni}(\text{L}^7)\text{Cl}_2]$ (11)

A batch of ligand ( $\text{L}^7$ ) (0.2mM 0.1039g) was dissolved into 3 mL of dichloromethane. A solution of  $\text{NiCl}_2 \cdot 6\text{H}_2\text{O}$  (0.2 mM, 0.095g) with 2 mL of methanol was added dropwise to the above solution. The resulting reddish brown solution was stirred for 30 minutes; a reddish brown colour precipitate was obtained. The solid was filtered out and washed with diethyl ether. The crystallization of the complex was done by dissolving the complex into dichloromethane in a vial and layered with methanol, red color crystals were obtained within 24 hours. Yield 80%. Anal. Calcd for  $\text{C}_{35}\text{H}_{29}\text{Cl}_2\text{NiN}_5$  (649.237): C, 64.75; H, 4.50; N, 10.79. Found: C, 64.80; H, 4.60; N, 10.75. IR data (KBr,  $\nu_{\text{max}}/\text{cm}^{-1}$ ): 1567,  $\nu_{\text{C=Nimine}}$ , 1454, 1386, 1296, 1257, 1160, 1069, 962, 751, 695, 520. UV-visible [ $\text{CH}_3\text{CN}$   $\lambda_{\text{max}}/\text{nm}$  ( $\epsilon/\text{M}^{-1}\text{cm}^{-1}$ )]: 393(19,663); 351(38,939); 241(17,340).

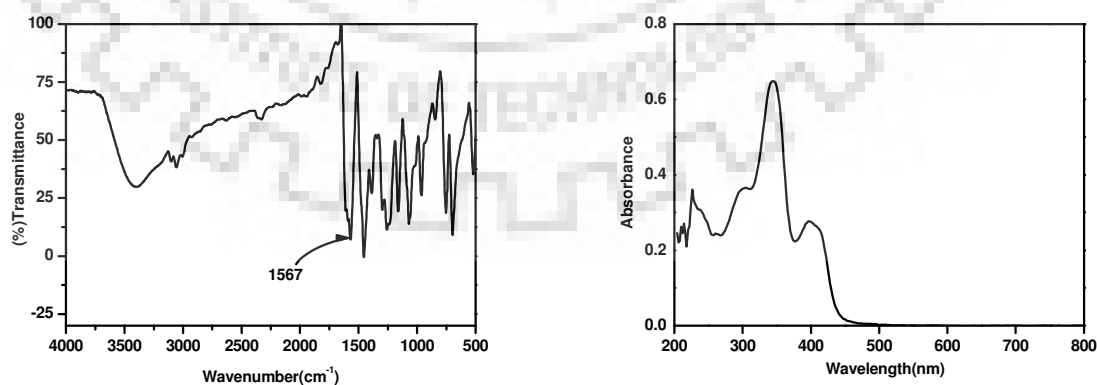


**Fig. 6.30** IR and UV-visible spectrums of complex  $[\text{Ni}(\text{L}^7)\text{Cl}_2]$ (11)

#### 6.4.2.5 Synthesis of complex $[\text{Cu}(\text{L}^7)\text{Cl}_2]$ (12)

The complex  $[\text{Cu}(\text{L}^7)\text{Cl}_2]$  was synthesized using the ligand ( $\text{L}^7$ ) and  $\text{CuCl}_2 \cdot 2\text{H}_2\text{O}$  into 1:1 ratio by dissolving the ligand in dichloromethane (DCM) and metal salt in methanolic solution. 0.2 mM (0.1039g) of ligand was dissolved into the dichloromethane on stirring at room temperature after that 0.2 mM (0.034g) of  $\text{CuCl}_2 \cdot 2\text{H}_2\text{O}$  was dissolved into methanol and added into the ligand dropwise the green colour solid was obtained in 2 hours. The solid was filtered off and dried under vacuum. The crystallization was done by dissolving the compound in DCM solvent in a crystallization tube and layering of methanol on it. Green colour shine crystal was obtained within two days. Yield 90%. Anal. Calcd for  $\text{C}_{35}\text{H}_{29}\text{N}_5\text{CuCl}_2$  (652.11) C, 64.27, H, 4.47, N, 10.71. Found: C, 64.02, H, 4.01, N, 10.40. IR data (KBr,  $\nu_{\text{max}}/\text{cm}^{-1}$ ) 1586,  $\nu_{\text{C=Nimine}}$ ; 1456, 1390, 1301, 1261, 1162, 1064, 968, 753, 698, 523. UV-visible [ $\text{CH}_3\text{CN}$ ;  $\lambda_{\text{max}}/\text{nm}$  ( $\epsilon/\text{M}^{-1}\text{cm}^{-1}$ )] 408(21,967); 350(59,961); 300(25,476).

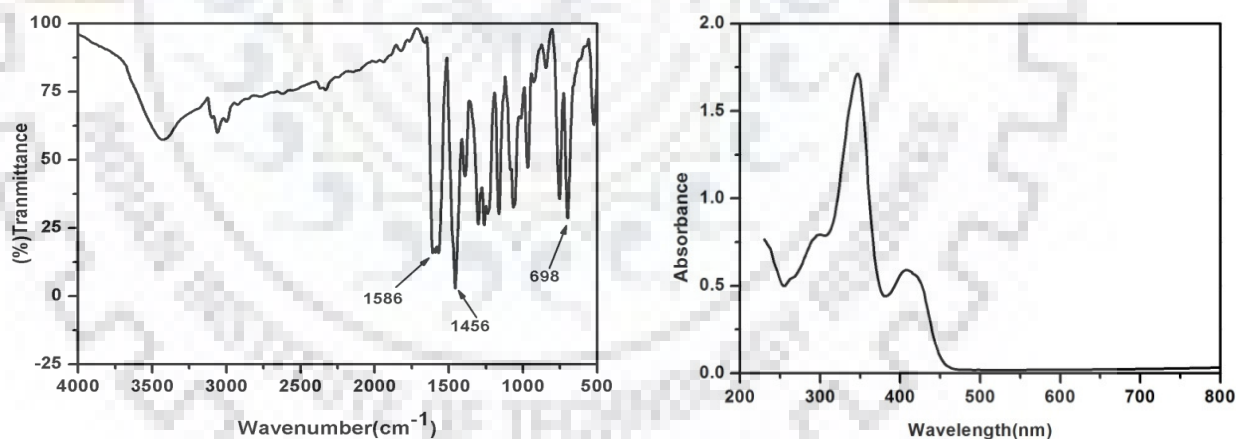


Fig. 6.31 IR and UV-Visible spectrums of complex  $[\text{Cu}(\text{L}^7)\text{Cl}_2]$  (12)

**Table 6.8** Crystal data and data collection parameters for the ligand and metal complexes (8-12)

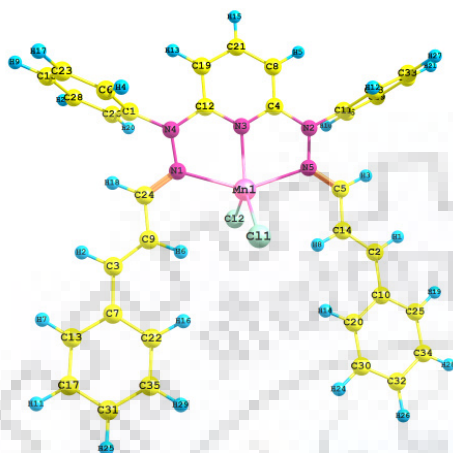
	Ligand	Complexes				
	(PyPhime-Cina)	[Mn(PyPhime - Cina)Cl <sub>2</sub> ] (8)	[Fe(PyPhime - Cina)Cl <sub>2</sub> ] (9)	[Co(PyPhime-Cina)Cl <sub>2</sub> ] (10)	[Ni(PyPhime - Cina)Cl <sub>2</sub> ] (11)	[Cu(PyPhime - Cina)Cl <sub>2</sub> ] (12)
Colour	White	Orange	Red	Red	Brown	Green
Empirical formula	C35 H29 N5	C35 H29 Cl2 Mn N5	C35 H29 Cl2 Fe N5	C35 H29 Cl2 Co N5	C35 H29 Cl2 N5 Ni	C35 H29 Cl2 Cu N5
Formula weight [g mol <sup>-1</sup> ]	519.63	645.47	646.38	649.46	649.22	654.08
Temperature [K]	296(2)	296(2)	296(2)	296(2)	296(2)	296(2)
λ [Å] (Mo-Kα)	0.71073	0.71073	0.71073	0.71073	0.71073	0.71073
Crystal system	triclinic	triclinic	monoclinic	monoclinic	monoclinic	monoclinic
Space group	<i>P</i> -1	<i>P</i> -1	<i>P</i> 21/ <i>n</i>	<i>C</i> 2/ <i>c</i>	<i>P</i> 21/ <i>n</i>	<i>P</i> 21/ <i>n</i>
a [Å]	9.7460(8)	11.1773(13)	11.0961(3)	24.911(11)	10.9814(15)	11.0179(2)
b [Å]	10.2553(8)	14.1413(15)	18.0403(5)	17.448(7)	18.066(3)	17.9960(3)
c [Å]	16.7345(14)	21.268(2)	15.8507(5)	19.505(9)	15.957(2)	15.7848(3)
α [°]	101.314(4)	76.714(3)	90.00	90.00	90.00	90.00
β [°]	104.637(4)	90.00	98.181(2)	129.69	98.111(8)	98.7510(10)
γ [°]	96.643(4)	90.00	90.00	90.00	90.00	90.00
V [Å <sup>3</sup> ]	1562.6(2)	3271.7(6)	3140.66(16)	6524(5)	3134.1(8)	3093.35(10)
Crystal size [mm]	0.22x 0.22x 0.22	0.24x0.24x0.24	0.22x 0.22x 0.22	0.18x 0.18x 0.18	0.22x 0.22x 0.22	0.18x0.18x0.18
Z	2	4	4	8	4	4
ρ <sub>calc</sub> [gcm <sup>-3</sup> ]	1.104	1.310	1.367	1.322	1.376	1.405
F(000)	548	1332	1336	2680	1344	1348
θ range for data collection	1.29-28.32	1.48-28.67	1.72 - 28.78	1.58-28.37	1.71-26.25	1.73-28.64
Index ranges	-13<h<13, -13<k<13, -22<l<22	-15<h<15, -19<k<19, -28<l<28	-15<h<15, -24<k<24, -21<l<21	-31<h<33, -23<k<22, -26<l<26	-11<h<11, -19<k<19, -16<l<16	-11<h<11, -18<k<18, -16<l<16
Refinement method	Full matrix least-squares on F <sup>2</sup>	Full matrix least-squares on F <sup>2</sup>	Full matrix least-squares on F <sup>2</sup>	Full matrix least-squares on F <sup>2</sup>	Full matrix least-squares on F <sup>2</sup>	Full matrix least-squares on F <sup>2</sup>
Data/restraints/parameters	7789/0/ 361	16862/0/ 775	3745/0/ 388	7196/0/391	3970/0/388	3624/0/388
GOF on F <sup>2</sup>	1.003	0.993	0.891	0.713	0.912	0.914
R <sub>1</sub> <sup>b</sup> [I>2σ(I)]	0.0967	0.0765	0.0312	0.0469	0.0300	0.0353
R <sub>1</sub> [all data]	0.1361	0.3060	0.0411	0.1304	0.0444	0.0533
wR <sub>2</sub> <sup>c</sup> [I>2σ(I)]	0.2420	0.1478	0.1169	0.1155	0.0986	0.1051
wR <sub>2</sub> [all data]	0.2339	0.2400	0.1002	0.1629	0.1195	0.1270

<sup>a</sup>GOF = [Σ[w(F<sub>o</sub><sup>2</sup>-F<sub>c</sub><sup>2</sup>)<sup>2</sup>]/(M-N)]<sup>1/2</sup> (M = number of reflections, N = number of parameters refined). <sup>b</sup>R<sub>1</sub> = Σ||F<sub>o</sub> - F<sub>c</sub>||/Σ |F<sub>o</sub>|. <sup>c</sup>wR<sub>2</sub> = [Σ[w(F<sub>o</sub><sup>2</sup>-F<sub>c</sub><sup>2</sup>)<sup>2</sup>]/Σ [w(F<sub>o</sub><sup>2</sup>)]<sup>1/2</sup>

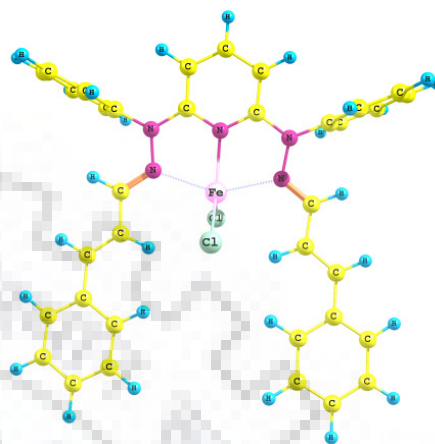
## 6.5 Theoretical calculation

### 6.5.1 DFT calculations

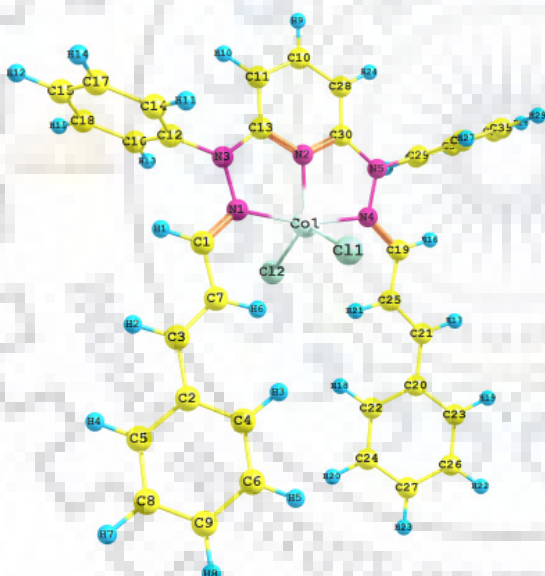
DFT calculations were performed using (B3LYP/ LANL2DZ).



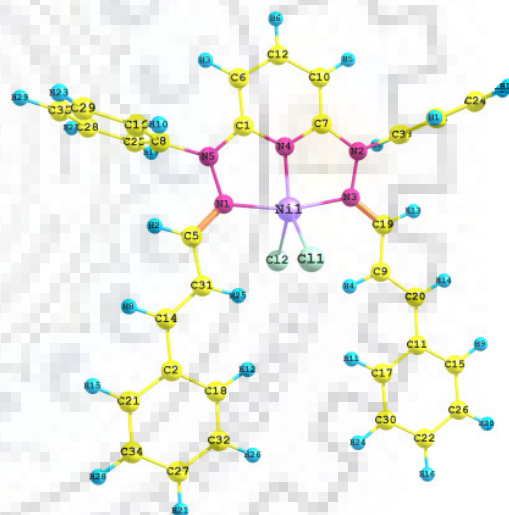
Complex  $[\text{Mn}(\text{L}^7)\text{Cl}_2]$  (8)



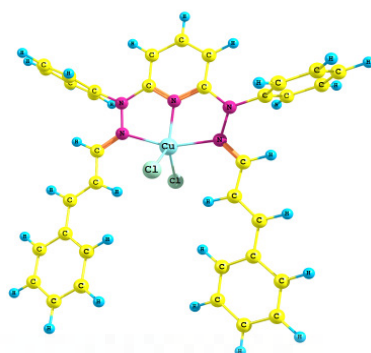
Complex  $[\text{Fe}(\text{L}^7)\text{Cl}_2]$  (9)



Complex  $[\text{Co}(\text{L}^7)\text{Cl}_2]$  (10)



Complex  $[\text{Ni}(\text{L}^7)\text{Cl}_2]$  (11)



Complex  $[\text{Cu}(\text{L}^7)\text{Cl}_2]$  (12)

Fig. 6.32 Ground state optimized geometry of complexes 8 -12 using B3LYP/LANL2DZ

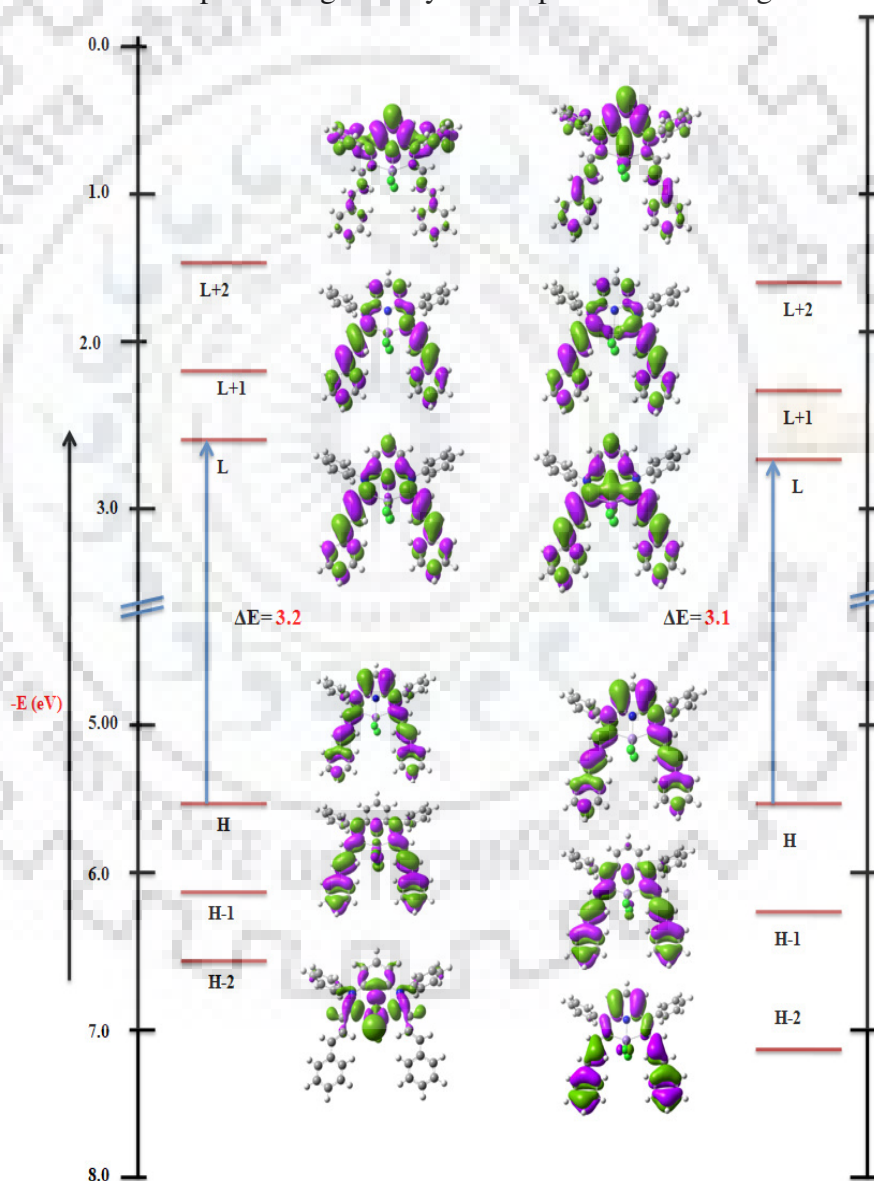
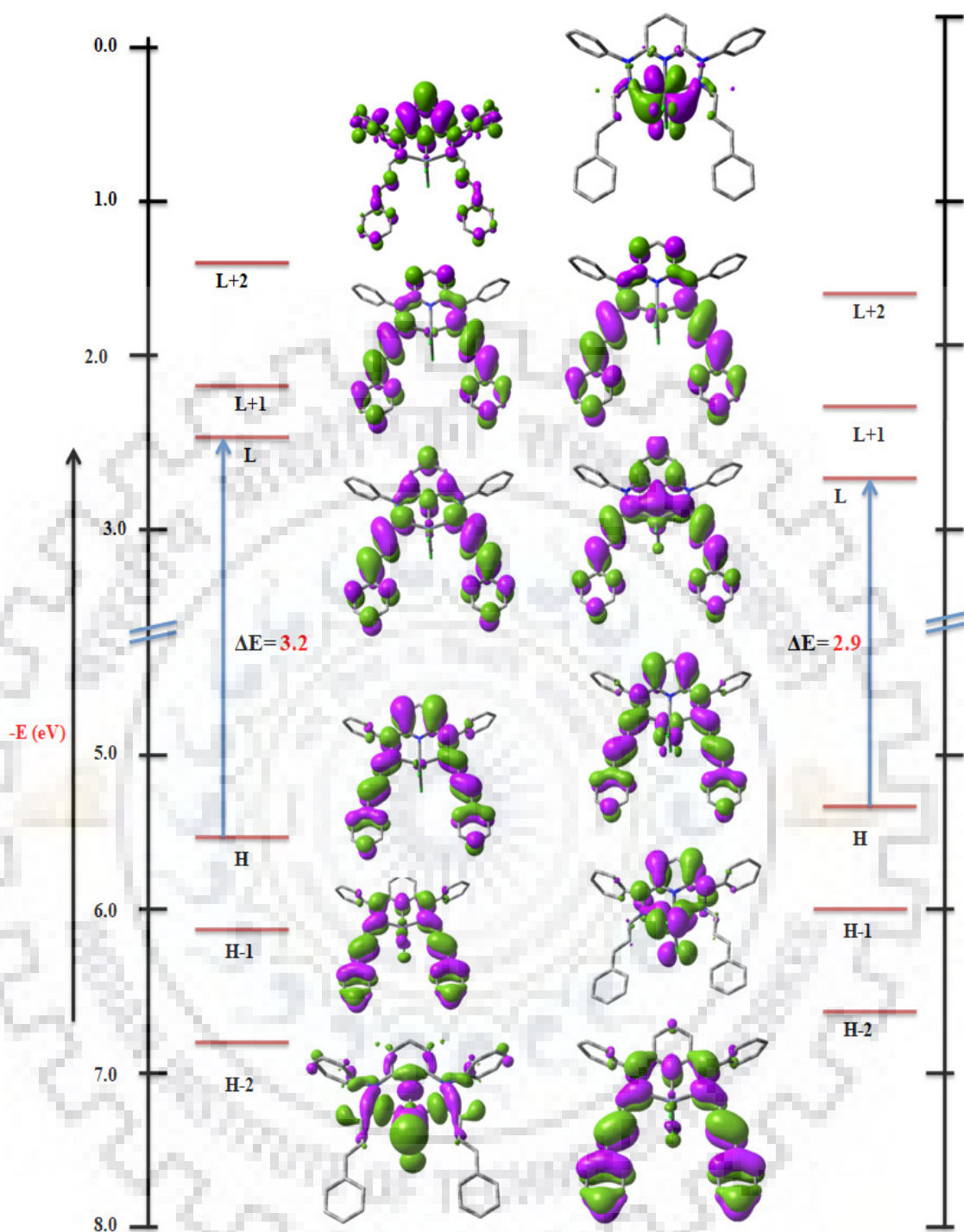
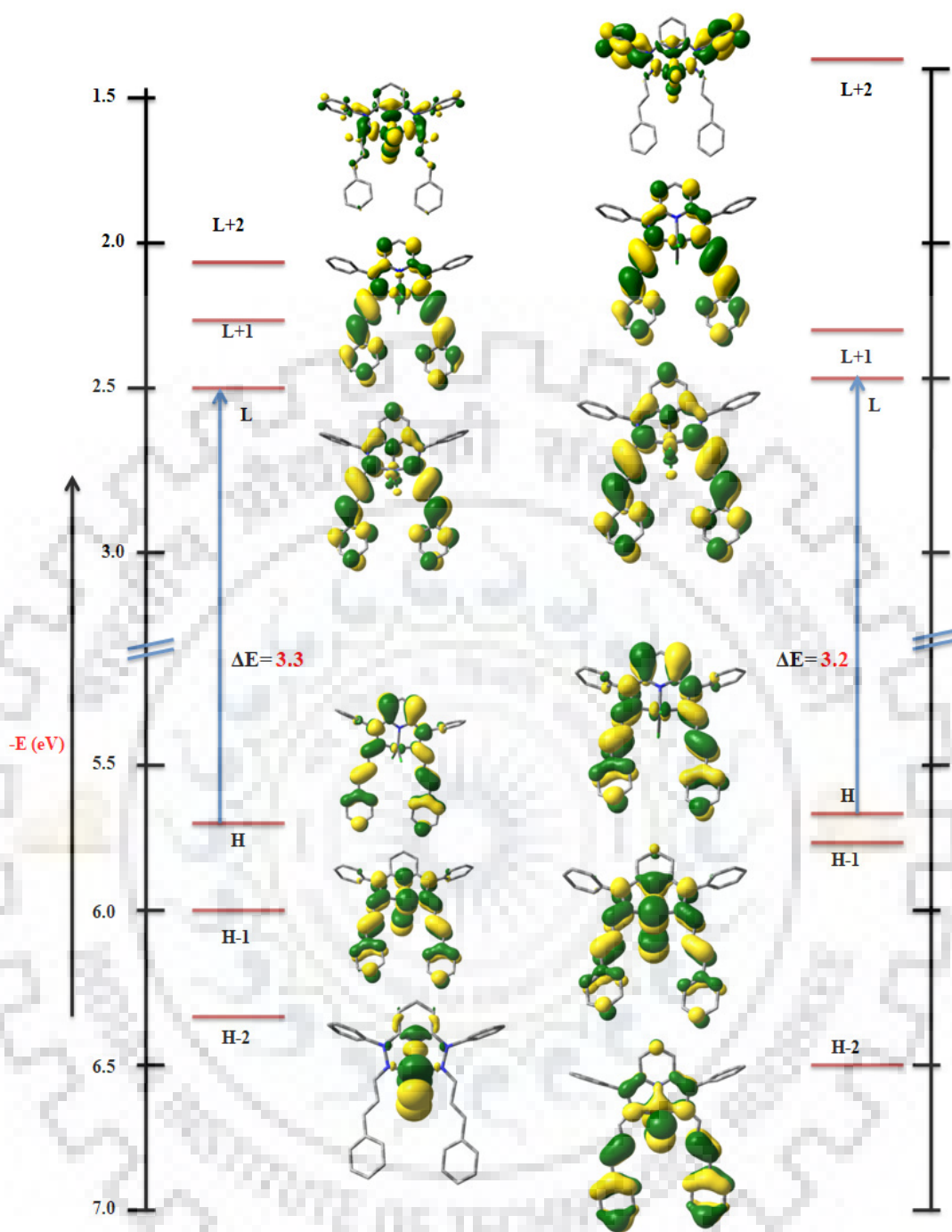


Fig.6.33 Frontier molecular orbitals of complex  $[\text{Mn}(\text{L}^7)\text{Cl}_2]$  (8) showing the HOMO LUMO energy gap



**Fig.6.34** Frontier molecular orbitals of complex  $[\text{Fe}(\text{L}^7)\text{Cl}_2]$  (9), showing the HOMO LUMO energy gap



**Fig.6.35** Frontier molecular orbitals of complex  $[Co(L^7)Cl_2]$  (**10**), showing the HOMO-LUMO energy gap



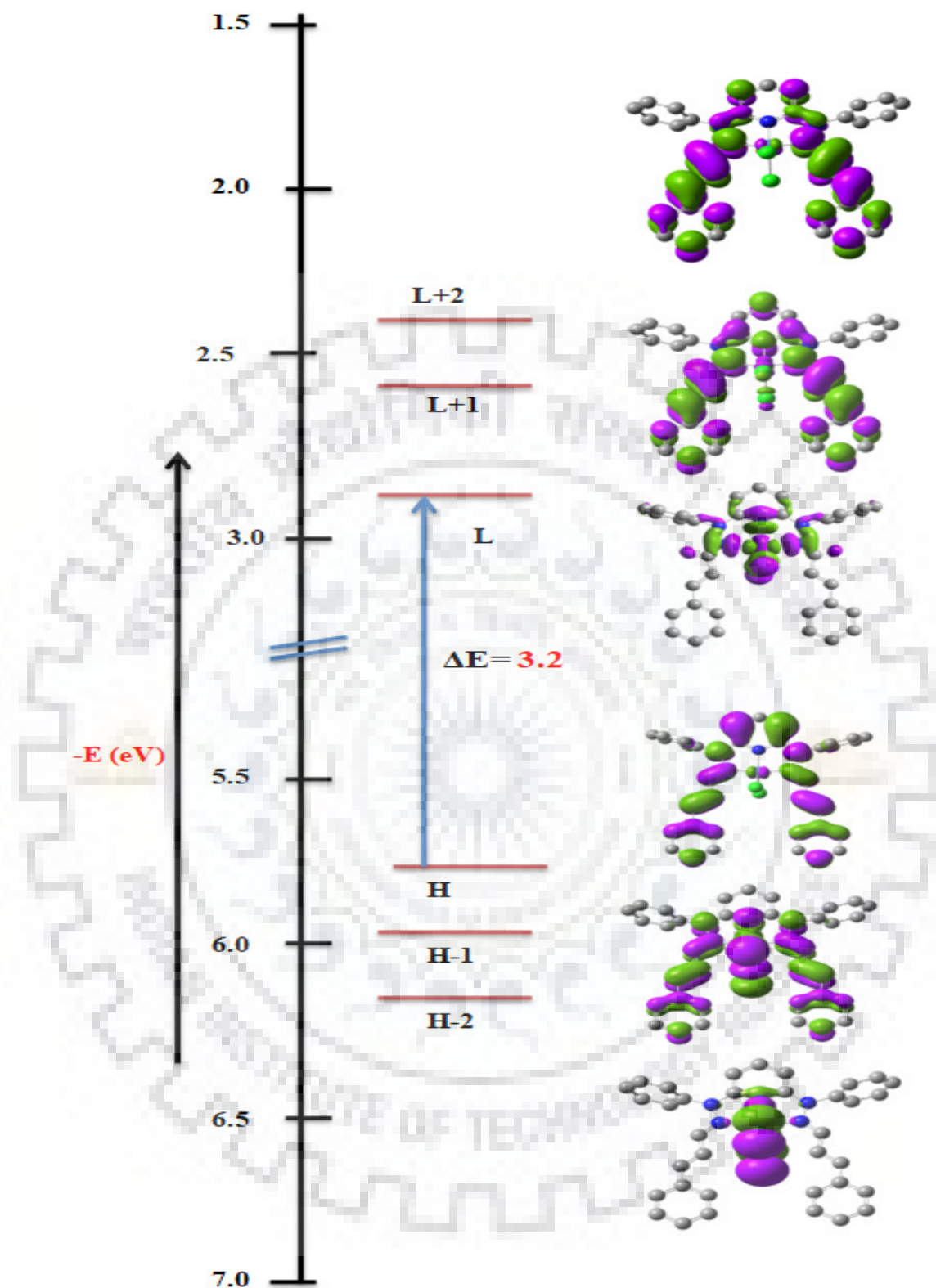


**Fig.6.36** Frontier molecular orbitals of complex  $[\text{Ni}(\text{L}^7)\text{Cl}_2]$  (**11**), showing the HOMO LUMO energy gap

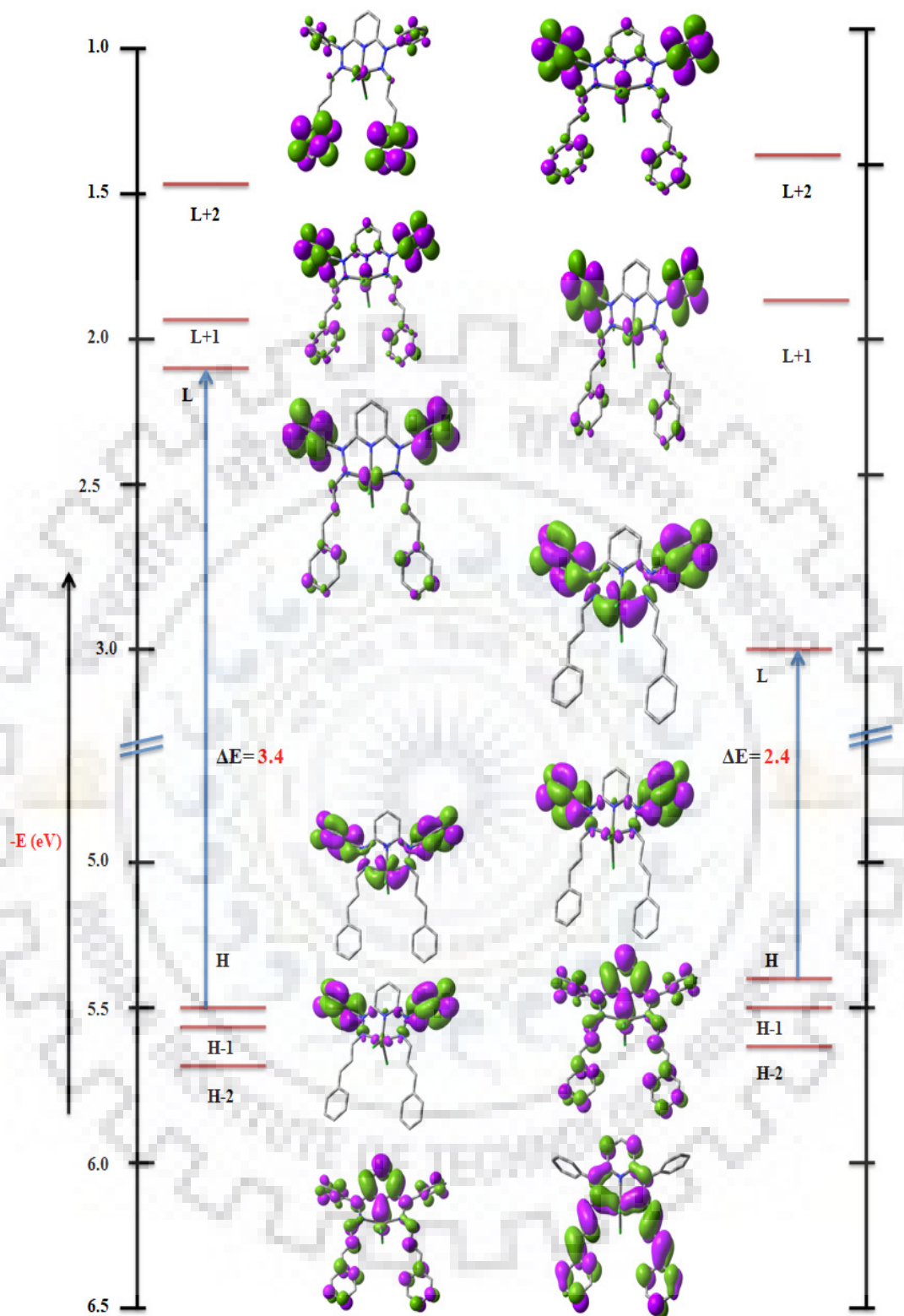


**Fig.6.37** Frontier molecular orbitals of complex  $[\text{Cu}(\text{L}^7)\text{Cl}_2]$  (12), showing the HOMO LUMO energy gap

**Table 6.9** Percentage contribution of complex  $[\text{Mn}(\text{L}^7)\text{Cl}_2]$  (**8**) in different orbitals

Orbital Alpha	Energy	%Contribution			Main Orbital contribution
		Mn	L	Cl	
L+2	-1.18	1	99	0	$\pi^*(\text{L})$
L+2	-2.3	0	100	0	$\pi^*(\text{L})$
L	-2.47	0	98	2	$\pi^*(\text{L})$
H	-5.67	0	100	0	$\pi(\text{L})$
H-1	-6.09	3	94	3	$\pi(\text{L})$
H-2	-6.53	40	43	16	$\pi(\text{L})+ 3d(\text{Mn})$
Orbital Beta	Energy	%Contribution			Main Orbital contribution
		Mn	L	Cl	
L+2	-1.27	3	97	0	$\pi^*(\text{L})$
L+2	-2.38	10	90	0	$\pi^*(\text{L})$
L	-2.55	4	96	0	$\pi^*(\text{L})$
H	-5.67	5	95	0	$\pi(\text{L})$
H-1	-6.15	0	100	0	$\pi(\text{L})$
H-2	-6.92	0	98	2	$\pi(\text{L})$

**Table 6.10** Percentage contribution of complex  $[\text{Fe}(\text{L}^7)\text{Cl}_2]$  (**9**) in different orbitals

Orbital Alpha	Energy	%Contribution			Main Orbital contribution
		Fe	L	Cl	
L+2	-1.22	1	99	0	$\pi^*(\text{L})$
L+2	-2.24	1	99	0	$\pi^*(\text{L})$
L	-2.44	1	98	1	$\pi^*(\text{L})$
H	-5.66	0	99	0	$\pi(\text{L})$
H-1	-6.07	1	95	3	$\pi(\text{L})$
H-2	-6.71	29	37	34	$\pi(\text{L})+ 3d(\text{Fe})+3d(\text{Cl})$
Orbital Beta	Energy	%Contribution			Main Orbital contribution
		Fe	L	Cl	
L+2	-1.56	91	7	2	3d(Fe)
L+2	-2.21	2	98	0	$\pi^*(\text{L})$
L	-2.62	3	86	1	$\pi^*(\text{L})$
H	-5.53	28	67	5	3d(Fe)+ $\pi(\text{L})$
H-1	-5.9	48	37	15	3d(Fe)+ $\pi(\text{L})$
H-2	-6.12	1	97	2	$\pi(\text{L})$

**Table 6.11** Percentage contribution of complex  $[\text{Co}(\text{L}^7)\text{Cl}_2]$  (10) in different orbitals

Orbital Alpha	Energy	%Contribution			Main Orbital contribution
		Co	L	Cl	
L+2	-2.11	61	33	6	$\pi^*(\text{L}) + 3d(\text{Co})$
L+2	-2.36	5	94	1	$\pi^*(\text{L})$
L	-2.51	2	97	1	$\pi^*(\text{L})$
H	5.77	2	98	0	$\pi(\text{L})$
H-1	-5.95	57	24	19	$3p(\text{Cl}) + 3d(\text{Co}) + \pi(\text{L})$
H-2	-6.37	36	10	54	$3p(\text{Cl}) + 3d(\text{Co})$
Orbital Beta	Energy	%Contribution			Main Orbital contribution
		Co	L	Cl	
L+2	-1.4	41	56	3	$3d(\text{Co}) + \pi^*(\text{L})$
L+2	-2.34	2	98	0	$\pi^*(\text{L})$
L	-2.51	2	97	1	$\pi^*(\text{L})$
H	-5.75	4	96	0	$\pi(\text{L})$
H-1	-5.81	37	41	21	$3p(\text{Cl}) + 3d(\text{Co}) + \pi(\text{L})$
H-2	-6.4	15	59	27	$\pi(\text{L}) + 3p(\text{Cl})$

**Table 6.12** Percentage contribution of complex  $[\text{Ni}(\text{L}^7)\text{Cl}_2]$  (11) in different orbitals

Orbital	Energy	%Contribution			Main Orbital contribution
		Ni	L	Cl	
L+2	-1.95	1	98	0	$\pi^*(\text{L})$
L+2	-2.12	58	33	9	$\pi^*(\text{L}) + 3d(\text{Ni})$
L	-2.17	2	95	2	$\pi^*(\text{L})$
H	-4.92	26	12	62	$3p(\text{Cl}) + 3d(\text{Ni})$
H-1	-5.03	28	5	68	$3p(\text{Cl}) + 3d(\text{Ni})$
H-2	-5.26	4	12	85	$3p(\text{Cl})$

**Table 6.13** Percentage contribution of complex  $[\text{Cu}(\text{L}^7)\text{Cl}_2]$  (12) in different orbitals

Orbital Alpha	Energy	%Contribution			Main Orbital contribution
		Cu	L	Cl	
L+2	-1.24	1	99	0	$\pi^*(\text{L})$
L+2	-2.39	0	100	0	$\pi^*(\text{L})$
L	-2.55	1	98	1	$\pi^*(\text{L})$
H	-5.79	1	100	1	$\pi(\text{L})$
H-1	-6.19	1	94	5	$\pi(\text{L})$
H-2	-6.83	1	57	42	$\pi(\text{L}) + 3d(\text{Cl})$
Orbital Beta	Energy	%Contribution			Main Orbital contribution
		Cu	L	Cl	
L+2	-2.36	0	99	0	$\pi^*(\text{L})$
L+2	-2.53	1	98	1	$\pi^*(\text{L})$
L	-3.82	62	30	8	$3d(\text{Cu}) + \pi^*(\text{L})$
H	-5.78	0	100	0	$\pi(\text{L})$
H-1	-6.15	1	93	6	$\pi(\text{L})$
H-2	-6.81	2	53	45	$\pi(\text{L}) + 3d(\text{Cl})$

## 6.5.2 TD-DFT calculations

Time dependent theoretical calculations were performed to understand the electronic absorption properties in the gaseous form.

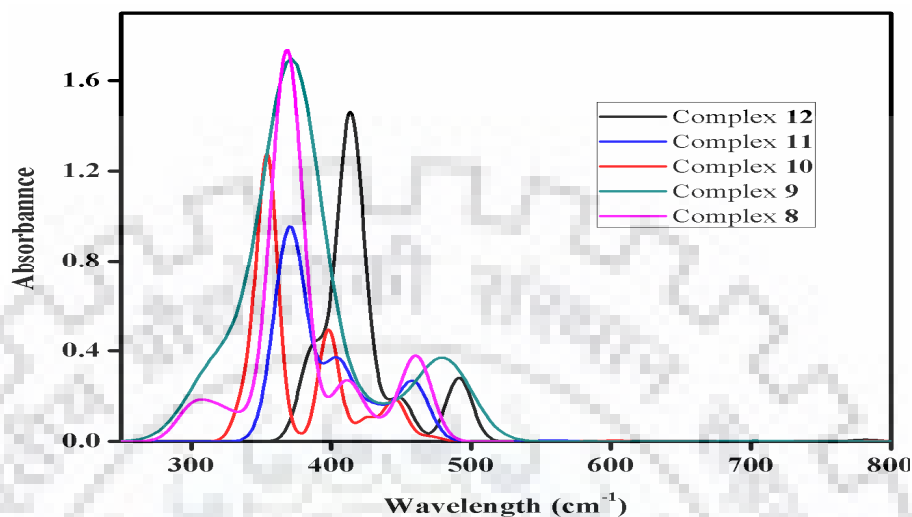


Fig. 6.37 Electronic absorption spectra of the complexes 8-12 in gaseous state

Table 6.14 Electronic transitions at particular wavelength and their percentage contribution in complex  $[\text{Mn}(\text{L}^7)\text{Cl}_2]$  (8)

Transitions	E (eV)	Osc. Strength (f)	Wavelength (nm) (Theo./exp)	Contributions Assignment
$S_0 \rightarrow S_6$	3.01	0.2629	411.1	HOMO(A) $\rightarrow$ L+1(A) (53%), HOMO(B) $\rightarrow$ L+1(B) (28%)
$S_0 \rightarrow S_{10}$	3.36	1.505	368.4	H-1(A) $\rightarrow$ LUMO(A) (38%), H-1(B) $\rightarrow$ LUMO(B) (41%)

Table 6.15 Electronic transitions at particular wavelength and their percentage contribution in complex  $[\text{Fe}(\text{L}^7)\text{Cl}_2]$  (9)

Transitions	E (eV)	Osc. Strength (f)	Wavelength (nm) (Theo./exp)	Contributions
$S_0 \rightarrow S_7$	2.57	0.3566	480.7	HOMO(A) $\rightarrow$ LUMO(A) (27%), HOMO(B) $\rightarrow$ LUMO(B) (49%)
$S_0 \rightarrow S_{13}$	3.25	0.5227	380.6	H-2(B) $\rightarrow$ LUMO(B) (22%)
$S_0 \rightarrow S_{15}$	3.35	1.0224	369.4	H-1(A) $\rightarrow$ LUMO(A) (33%), HOMO(B) $\rightarrow$ L+1(B) (11%)
$S_0 \rightarrow S_{19}$	3.47	0.148	356.9	H-1(A) $\rightarrow$ L+1(A) (25%), H-2(B) $\rightarrow$ L+1(B) (56%)

**Table 6.16** Electronic transitions at particular wavelength and their percentage contribution in complex  $[\text{Co}(\text{L}^7)\text{Cl}_2]$  (10)

Transition s	E (eV)	Osc. Strength (f)	Wavelength (nm) (Theo./exp)	Contributions
$S_0 \rightarrow S_{15}$	2.79	0.1478	443.6	HOMO(A) $\rightarrow$ LUMO(A) (59%), H-1(B) $\rightarrow$ L+1(B) (15%)
$S_0 \rightarrow S_{22}$	3.11	0.4844	397.4	HOMO(A) $\rightarrow$ L+1(A) (34%), HOMO(B) $\rightarrow$ L+1(B) (37%)
$S_0 \rightarrow S_{28}$	3.500	1.0412	354.2	H-3(A) $\rightarrow$ LUMO(A) (41%), H-2(B) $\rightarrow$ LUMO(B) (26%)

**Table 6.17** Electronic transitions at particular wavelength and their percentage contribution in complex  $[\text{Ni}(\text{L}^7)\text{Cl}_2]$  (11)

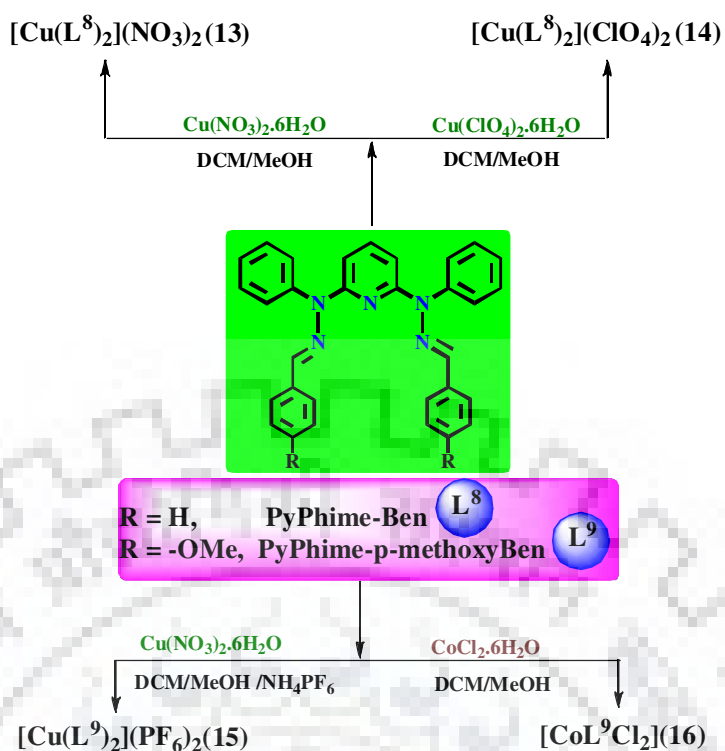
Transition	E (eV)	Osc. Strength (f)	Wavelength (nm) (Theo./exp)	Contributions
$S_0 \rightarrow S_{16}$	2.70	0.2351	458.7	HOMO(A) $\rightarrow$ L+1(A) (48%), HOMO(B) $\rightarrow$ L+1(B) (48%)
$S_0 \rightarrow S_{21}$	2.88	0.1367	430.3	H-1(A) $\rightarrow$ L+2(A) (46%), H-1(B) $\rightarrow$ L+2(B) (46%)
$S_0 \rightarrow S_{29}$	3.06	0.349	404.0	H-3(A) $\rightarrow$ L+1(A) (11%), HOMO(A) $\rightarrow$ L+2(A) (39%), H-3(B) $\rightarrow$ L+1(B) (11%), HOMO(B) $\rightarrow$ L+2(B) (39%)
$S_0 \rightarrow S_{39}$	3.34	0.9199	370.2	H-3(A) $\rightarrow$ L+1(A) (32%), H-3(B) $\rightarrow$ L+1(B) (32%)

**Table 6.18** Electronic transitions at particular wavelength and their percentage contribution in complex  $[\text{Cu}(\text{L}^7)\text{Cl}_2]$  (12)

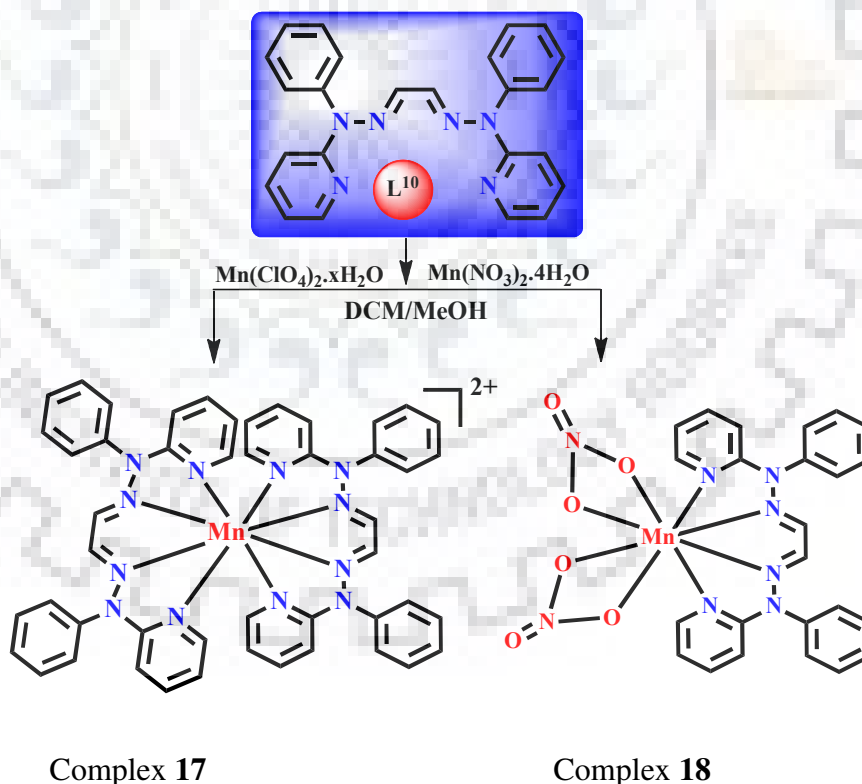
Transitions	E (eV)	Osc. Strength (f)	Wavelength (nm) (Theo./exp)	Contributions
$S_0 \rightarrow S_{14}$	2.77	0.2813	446.4	HOMO(A) $\rightarrow$ LUMO(A) (51%), HOMO(B) $\rightarrow$ L+1(B) (48%)
$S_0 \rightarrow S_{20}$	3.06	0.1835	404.2	HOMO(A) $\rightarrow$ L+1(A) (36%), HOMO(B) $\rightarrow$ L+2(B) (39%)
$S_0 \rightarrow S_{24}$	3.27	0.1266	378.2	H-13(B) $\rightarrow$ LUMO(B) (29%), H-1(B) $\rightarrow$ L+1(B) (11%)
$S_0 \rightarrow S_{28}$	3.36	1.088	367.9	H-1(A) $\rightarrow$ LUMO(A) (33%), H-1(B) $\rightarrow$ L+1(B) (23%)
$S_0 \rightarrow S_{31}$	3.62	0.3828	342.2	H-19(B) $\rightarrow$ LUMO(B) (25%), H-15(B) $\rightarrow$ LUMO(B)

## 7.1 Introduction

The Stability of particular oxidation state in the coordination chemistry depends on the ligand environment surrounding the metal centre.<sup>1</sup> By the literature it is well known that polydentate ligands having soft pyridine and imine nitrogen donor(s) stabilize the lower oxidation state whereas, ligand having hard carboxamido nitrogen donor(s) stabilize higher oxidation states.<sup>2,3</sup> It is important to note down that the ligand system play an important role with metal centre in biological activity.<sup>68</sup> In the past decade, substantial interest has aroused in the design and development of novel tri, tetra or multi-nuclear first row transition metal complexes due to their significant biological relevance.<sup>256</sup> Metal complexes which could hydrolyze DNA with high sequential and structural selectivity can be utilized as therapeutic agents and as indispensable tool for gene manipulation also.<sup>67</sup> Among them considerable attention has been paid to the structural and functional modelling of mononuclear manganese enzymes such as peroxidase,<sup>7,8</sup> dioxygenase,<sup>9</sup> superoxide dismutase.<sup>229, 412-418</sup> Superoxide dismutase are enzymes which catalyze the conversion of superoxide radical( $O_2^-$ ) to oxygen ( $O_2$ ) and hydrogen peroxide ( $H_2O_2$ ).<sup>209</sup> These impart significant role in protecting biological systems against the damage mediated by reactive oxygen species (ROS). These are defense enzymes in cells which are exhibiting important role in several pathological and disease states arising due to oxidative damage.<sup>224</sup> Due to lower toxicity, manganese complexes (II,III) have been utilized as potent SOD mimic.<sup>420-421</sup> It has been reported that native SOD enzymes interact with DNA and could exhibit nuclease activity.<sup>422,423</sup> So in this regard we have synthesized and characterized tridentate, tetradentate as well as pentadentate ligands and their corresponding manganese, iron, cobalt, nickel and copper complexes to check their DNA binding as well as their superoxide dismutase activity studies.

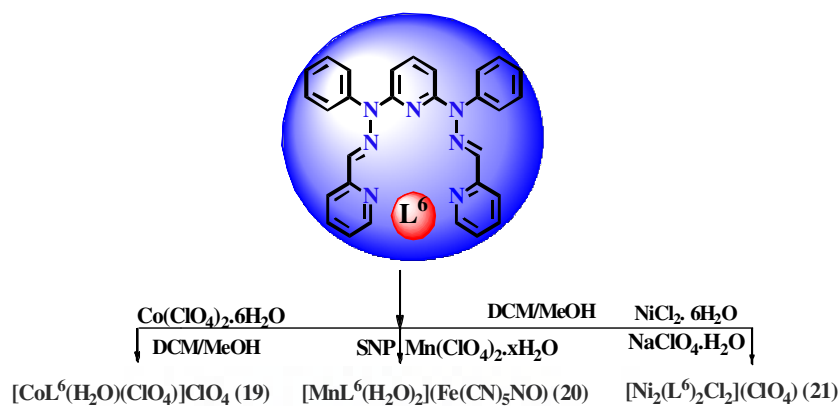


Scheme 7.1 Synthesis of pincer type complexes using tridentate ligands

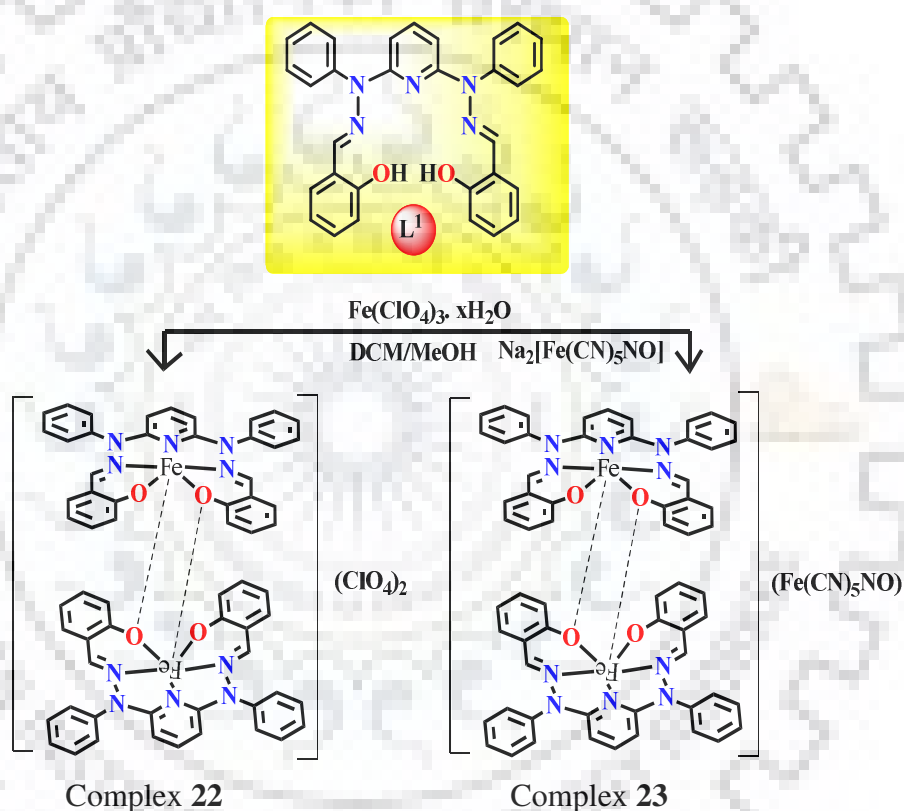


Scheme 7.2 Synthesis of manganese complexes using tetradentate ligand





Scheme 7.3 Synthesis of cobalt manganese and nickel complexes using pentadentate ligand



Scheme 7.4 Synthesis of iron complexes using pentadentate ligand

## 7.2 Results and discussions

### 7.2.1 Synthesis and characterization of complexes using tridentate ligands

The ligand  $L^8$  and  $L^9$  were synthesized using 2,6-bis(1-phenylhydrazinyl)pyridine and benzaldehyde and p-methoxybenzaldehyde in 1:2 molar ratio, on stirring at room temperature. The characterizations of the ligands  $L^8$  and  $L^9$  was done with different

spectroscopic techniques. The molecular structures of the ligands were determined by single crystal X-ray crystallographic studies. ORTEP diagrams of both the ligands were shown Fig. 7.1 and 7.3. Crystal data and structural refinement parameters were shown in Table 7.3. Complex **13** and **14** were synthesized using ligand  $L^8$  in dichloromethane-methanol (1:2) solution, reaction of  $Cu(NO_3)_2 \cdot 6H_2O$  and  $Cu(ClO_4)_2 \cdot 6H_2O$ . The molecular structures of complexes **13** and **14** were determined by using X-ray crystallographic studies and ORTEP diagrams are shown in Fig. 7.2 and structural refinement parameters were shown in Table 7.4. Using  $L^9$  we have synthesized bis as well as mono complexes of copper (**15**) and cobalt (**16**), for the synthesis of copper complex 1:2 molar ratio of  $Cu(NO_3)_2 \cdot 6H_2O$  and ligand in dichloromethane-methanol was stirred at room temperature, the green colour compound was obtained. For cobalt complex 1:1 molar ratio of  $CoCl_2 \cdot 6H_2O$  and ligand  $L^9$  was stirred in dichloromethane-methanol solvent at room temperature, a red colour complex was obtained within half an hour. The characterization of both the complexes was done with different spectroscopic technique. The molecular structure of the ligand  $L^9$  was analysed by X-ray crystallographic studies. The ORTEP diagram was displayed in Fig. 7.3. Both the complexes were also analysed by different spectroscopic methods and molecular structures were analysed single crystal X-ray crystallographic studies. The ORTEP diagrams were as shown in Fig. 7.4 and structural refinement parameters were displayed in Table 7.5.

### **7.2.2 Synthesis and characterization of complexes using tetradentate ligands**

The ligand  $L^{10}$  was synthesized using glyoxal and 2-(1-phenylhydrazinyl)pyridine 1:2 molar ratio, on stirring at room temperature. The characterization of the ligand ( $L^{10}$ ) was done with different spectroscopic technique. We have synthesized eight coordinated manganese complexes **17** and **18** using this ligand. The complex **17** was synthesized on stirring the ligand in dichloromethane and metal salt of  $Mn(ClO_4)_2 \cdot xH_2O$  was dissolved in methanol and added dropwise in the molar ratio 2:1. The yellow colour solid was obtained with in 30min.

The complex **18** was also obtained in the similar way but the metal salt  $\text{Mn}(\text{NO}_3)_2 \cdot x\text{H}_2\text{O}$  was added in the molar ratio of 1:1 with the ligand. The molecular structure of the ligand ( $\text{L}^{10}$ ) and both the complexes were determined by single crystal X-ray crystallographic studies. The ORTEP diagram of ligand as well as complex **17** and **18** were displayed in Fig. 7.5 and structural refinement parameters were shown in Table 7.6.

### **7.2.3 Synthesis and characterization of complexes using pentadentate ligands**

The ligand  $\text{L}^1$  and  $\text{L}^6$  were reported in *chapter 2* and *5*. We have synthesized seven coordinated cobalt (**19**), manganese (**20**) and nickel (**21**) complexes using ligand  $\text{L}^6$ . The complex **19** was synthesized in dichloromethane-methanol (1:1) solution, of metal salt  $\text{Co}(\text{ClO}_4)_2 \cdot 6\text{H}_2\text{O}$  and ligand ( $\text{L}^6$ ) on stirring at room temperature and complex **20** was synthesized in same solvent using  $\text{Mn}(\text{ClO}_4)_2 \cdot x\text{H}_2\text{O}$  and  $\text{L}^6$ , sodium nitroprusside was added by dissolving in methanol to get the final complex **20**. For the nickel complex, ligand ( $\text{L}^6$ ) was dissolved in dichloromethane and  $\text{NiCl}_2 \cdot 6\text{H}_2\text{O}$  by dissolving in methanol was added dropwise in 2:2 molar ratio and stirred for half an hour and 2 mmol  $\text{NaClO}_4$  was added in the reaction to get the original complex **21**. The molecular structures of all the complexes were determined single crystal X-ray crystallographic studies. The ORTEP diagrams of complexes **19** - **21** shown in Fig. 7.6. The crystal data and structural refinement parameters were shown in Table 7.7.

We have also synthesized seven coordinated phenolato bridge iron complexes using ligand  $\text{L}^1$ . The complex **22** was synthesized in dichloromethane-methanol (1:1) solution, of metal salt  $\text{Fe}(\text{ClO}_4)_3 \cdot x\text{H}_2\text{O}$  and ligand ( $\text{L}^1$ ) on stirring at room temperature and complex **23** was synthesized in same solvent using complex **22** in methanol and sodium nitroprusside was added by dissolving in methanol to get the final complex **23**. The molecular structures of complex **22** and **23** were determined single crystal X-ray crystallographic studies. The

ORTEP diagrams of both the complexes were depicted in Fig. 7.7. The crystal data and structural refinement parameters were shown in Table 7.8.

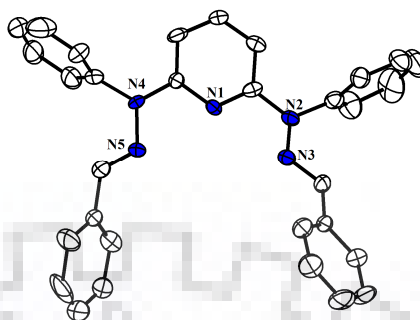


**Fig. 7.1** The ORTEP diagram of Ligand ( $L^8$ ) (2,6-bis((E)-2-benzylidene-1-phenylhydrazinyl)pyridine) (40% probability level) all hydrogen atoms are omitted for clarity

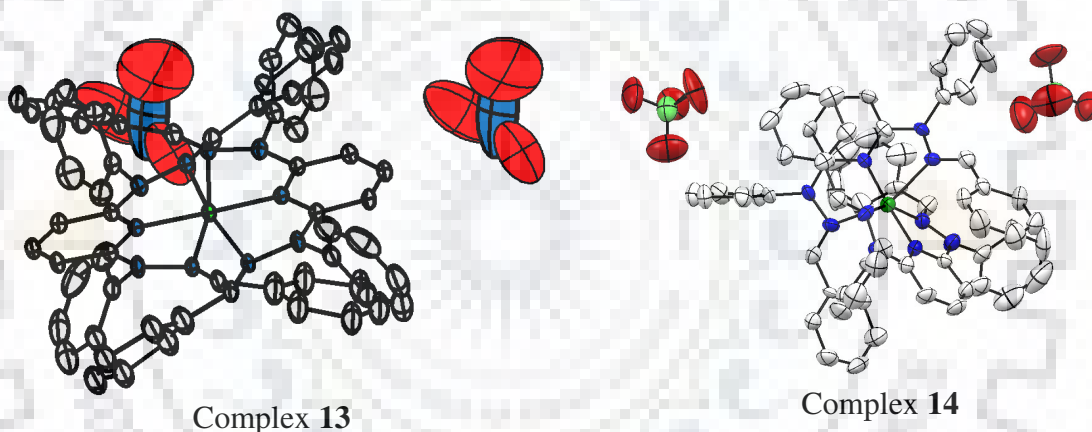


**Fig. 7.2** The ORTEP diagrams of complexes **13** and **14** (50% probability level) all hydrogen atoms are omitted for clarity

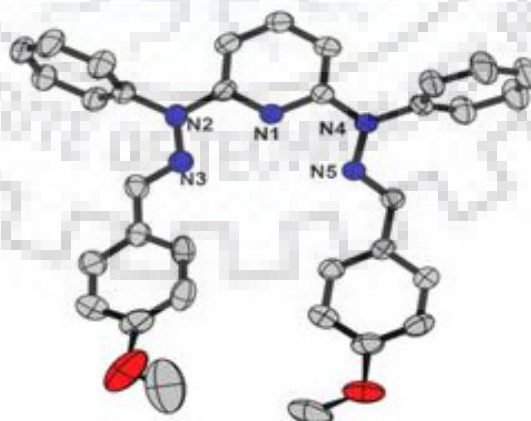


**Fig. 7.3** The ORTEP diagram of ligand  $L^9$ , (50% probability level) all hydrogen atoms are omitted for clarity

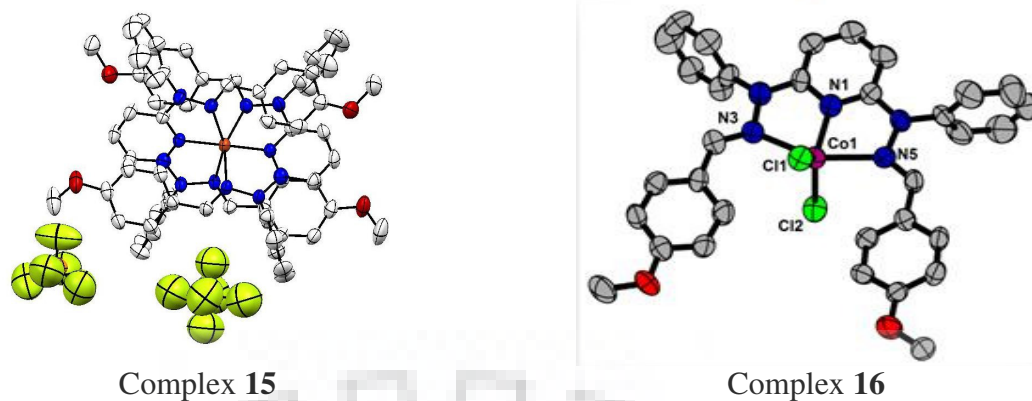


**Fig. 7.4** The ORTEP diagram of, complexes 15 and 16 (50% probability level) all hydrogen atoms and solvent molecules are omitted for clarity

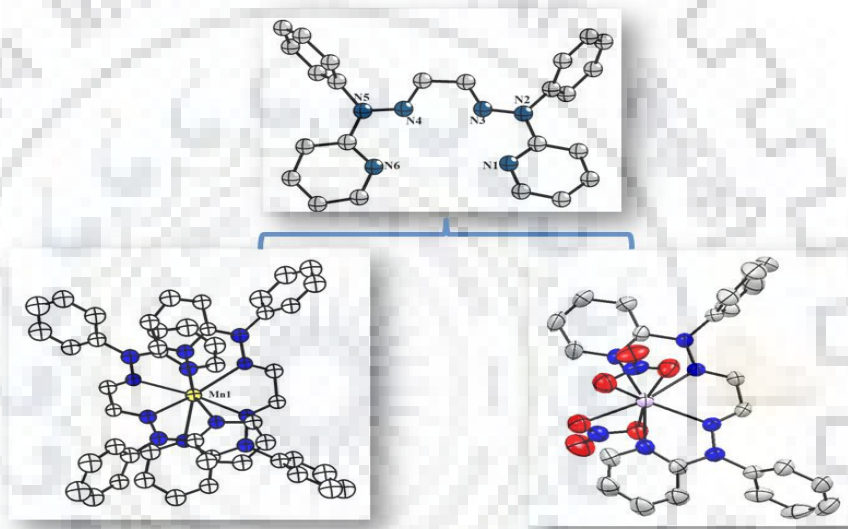


**Fig. 7.5** The ORTEP diagram (50% probability level) of ligand ( $L^{10}$ ) and complex 17 and 18 all hydrogen atoms and solvent molecules and extra anions are omitted for clarity

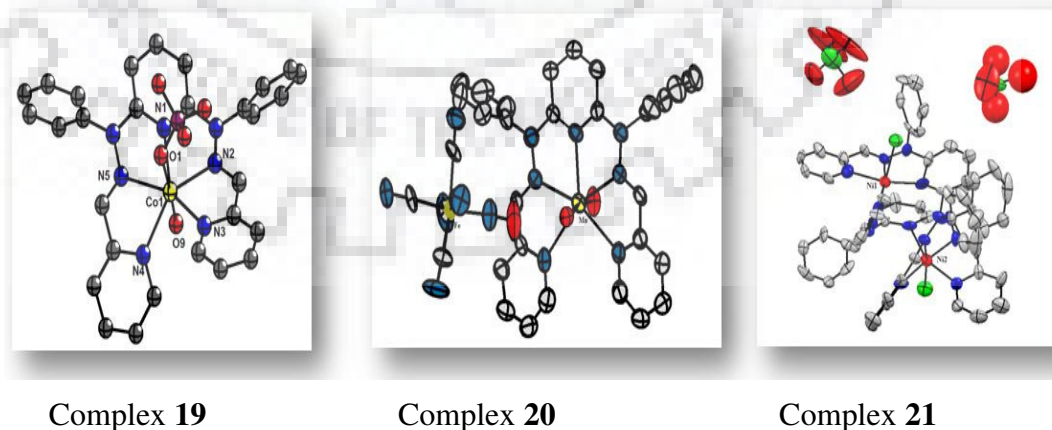
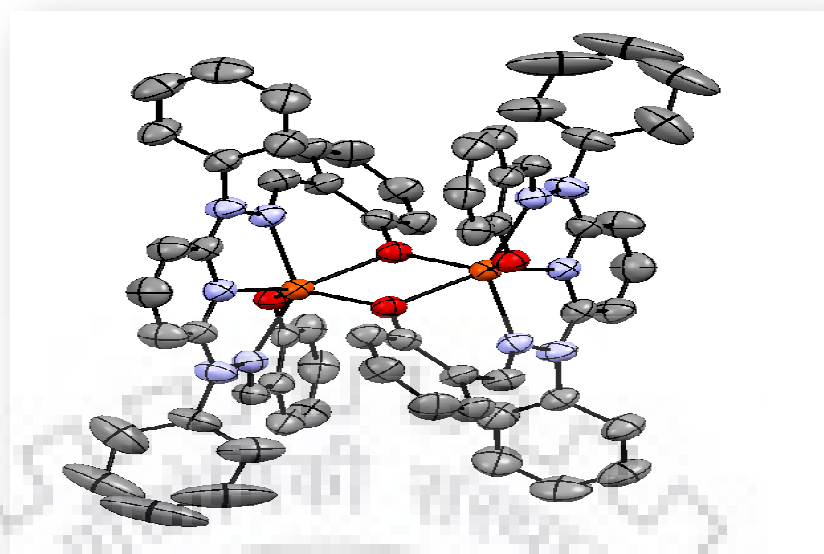
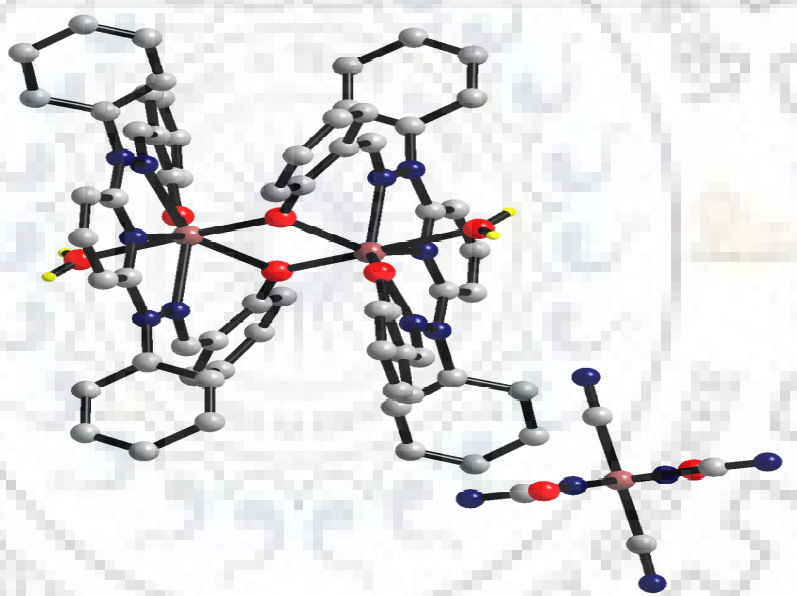


**Fig. 7.6** The ORTEP diagram (50% probability level) of complexes 19, 20 and 21. all hydrogen atoms and solvent molecules and extra anions are omitted for clarity



Complex 22



Complex 23

**Fig. 7.7** The ORTEP diagram (50% probability level) of complexes **22** and **23**. all hydrogen atoms and solvent molecules and extara anions are omitted for clarity

#### 7.2.4 DNA interaction studies

UV-visible spectroscopy, fluorescence quenching and circular dichroism (CD) have been used to investigate the DNA binding behaviour of metal complexes. For this, a fixed concentration of metal complexes was titrated with increasing concentration of CT-DNA at

physiological pH (7.2) and the spectral changes were monitored. The absorption spectra of all complexes (**13-16**) in absence and presence of different concentrations of CT-DNA were shown in Fig. 7.8-7.11. When the concentration of DNA increases, the absorption spectra of all complexes undergo some spectral changes. In complexes **13-16** showed hypochromicity and red shift in the UV-visible spectra.

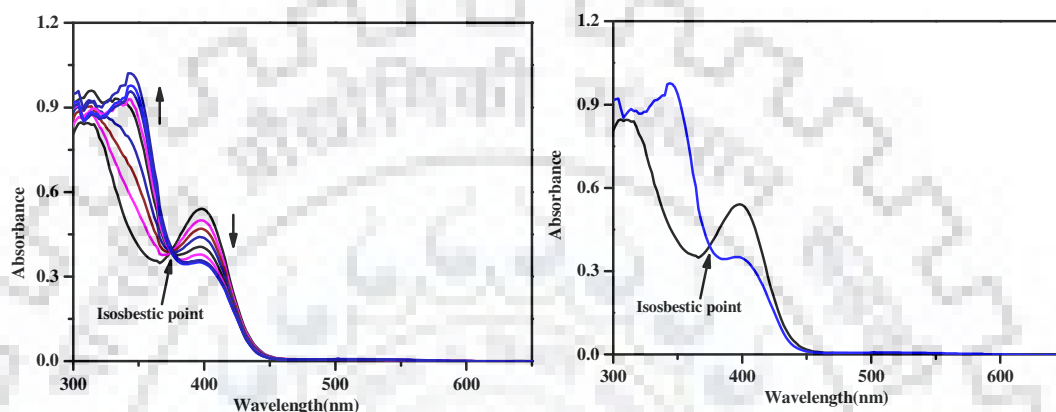


**Fig. 7.8** Absorption spectral changes of complex **13** (100 $\mu$ M) (a) in 0.1M phosphate buffer (pH 7.2) in the presence of increasing the amount of DNA (0-25 $\mu$ M). (b) hyperchromic shift with DNA between the initial and final spectra. Solid line represent the spectrum in the absence of DNA

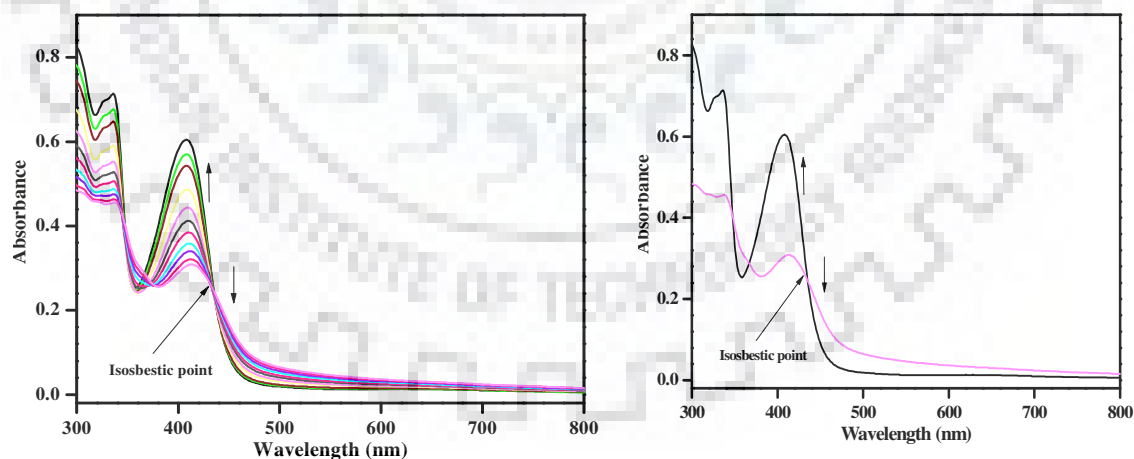


**Fig. 7.9** Absorption spectral changes of complex **14** (100 $\mu$ M) (a) in 0.1M phosphate buffer (pH 7.2) in the presence of increasing the amount of DNA (0-25 $\mu$ M). (b) hyperchromic shift with DNA between the initial and final spectra. Solid line represent the spectrum in the absence of DNA

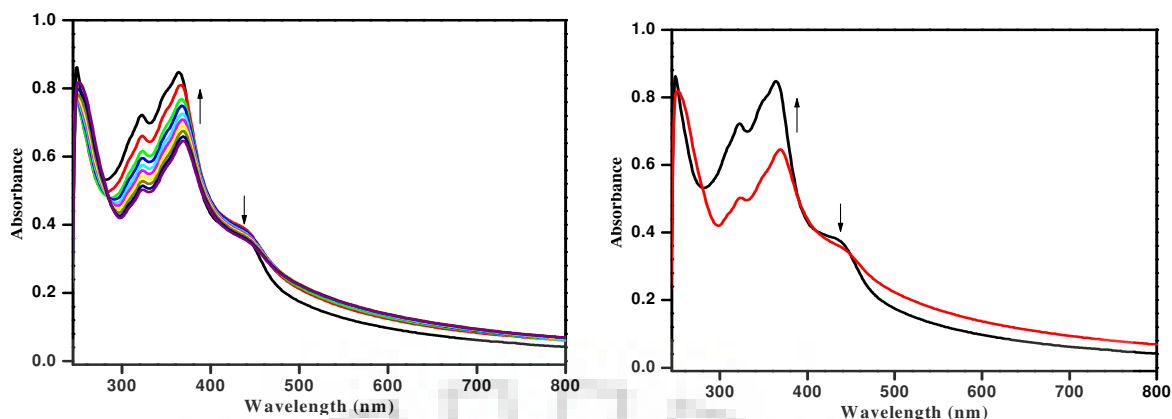


**Fig. 7.10** Absorption spectral changes of complex **15** ( $100\mu\text{M}$ ) (a) in  $0.1\text{M}$  phosphate buffer ( $\text{pH } 7.2$ ) in the presence of increasing the amount of DNA ( $0\text{--}25\mu\text{M}$ ). (b) hyperchromic shift with DNA between the initial and final spectra. Solid line represent the spectrum in the absence of DNA

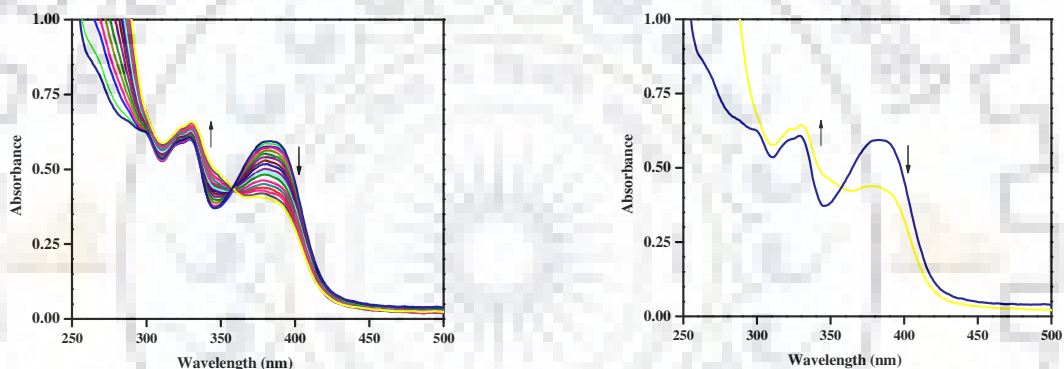


**Fig. 7.11** Absorption spectral changes of complex **16** ( $100\mu\text{M}$ ) (a) in  $0.1\text{M}$  phosphate buffer ( $\text{pH } 7.2$ ) in the presence of increasing the amount of DNA ( $0\text{--}25\mu\text{M}$ ). (b) hyperchromic shift with DNA between the initial and final spectra. Solid line represent the spectrum in the absence of DNA

Fluorescence quenching experiments were carried out by the successive addition of the metal complexes to the DNA ( $\sim 60\mu\text{M}$ ) solutions containing  $5\mu\text{M}$  ethidium bromide (EB) in  $0.1\text{M}$  phosphate buffer ( $\text{pH } 7.2$ ) and the reaction mixture was incubated for  $5\text{ min}$  after each successive addition of the quencher molecules. These samples were excited at  $250\text{ nm}$  and emissions were observed between  $500$  and  $700\text{ nm}$ . (Shown in Fig. 7.12-7.14) The Stern–Volmer quenching constants ( $K_{\text{SV}}$ ) for all the complexes were calculated using linear Stern–Volmer equation (*Chapter 1*) and listed in Table 7.1.



**Table 7.1** Binding constants and Stern-Volmer constant for DNA interaction studies

Complex	$K_b$	$K_{sv}$
<b>13</b>	$4.2 \times 10^4$	$3.12 \times 10^4$
<b>14</b>	$8.2 \times 10^4$	$7.21 \times 10^4$
<b>15</b>	$4.0 \times 10^4$	$2.95 \times 10^4$
<b>16</b>	$3.8 \times 10^4$	$2.85 \times 10^4$

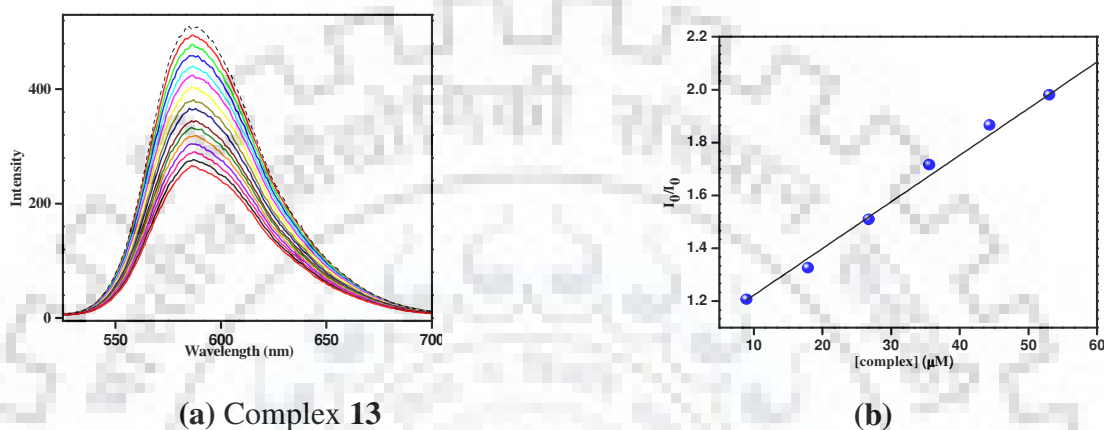


**Fig. 7.12** (a) Fluorescence emission spectra of CT-DNA in the presence of complex **13** in 0.1M phosphate buffer (pH 7.2) containing 2% DMF. [DNA] = 25 $\mu$ M, [complex **13**] = 0 - 60  $\mu$ M,  $\lambda_{ex}$  = 250nm and  $\lambda_{em}$  = 600nm. Dotted line represents the spectrum in the absence of complex **13** (b) Stern-Volmer plot for complex **13**

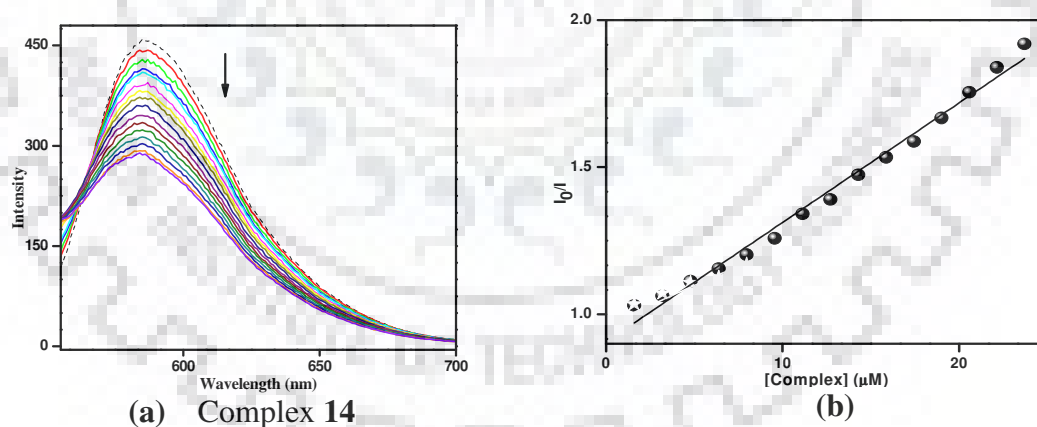


**Fig. 7.13** (a) Fluorescence emission spectra of CT-DNA in the presence of complex **14** in 0.1M phosphate buffer (pH 7.2) containing 2% DMF. [DNA] = 25 $\mu$ M, [complex **14**] = 0 - 30  $\mu$ M,  $\lambda_{ex}$  = 250nm and  $\lambda_{em}$  = 600nm. Dotted line represents the spectrum in the absence of complex **14** (b) Stern-Volmer plot for complex **14**

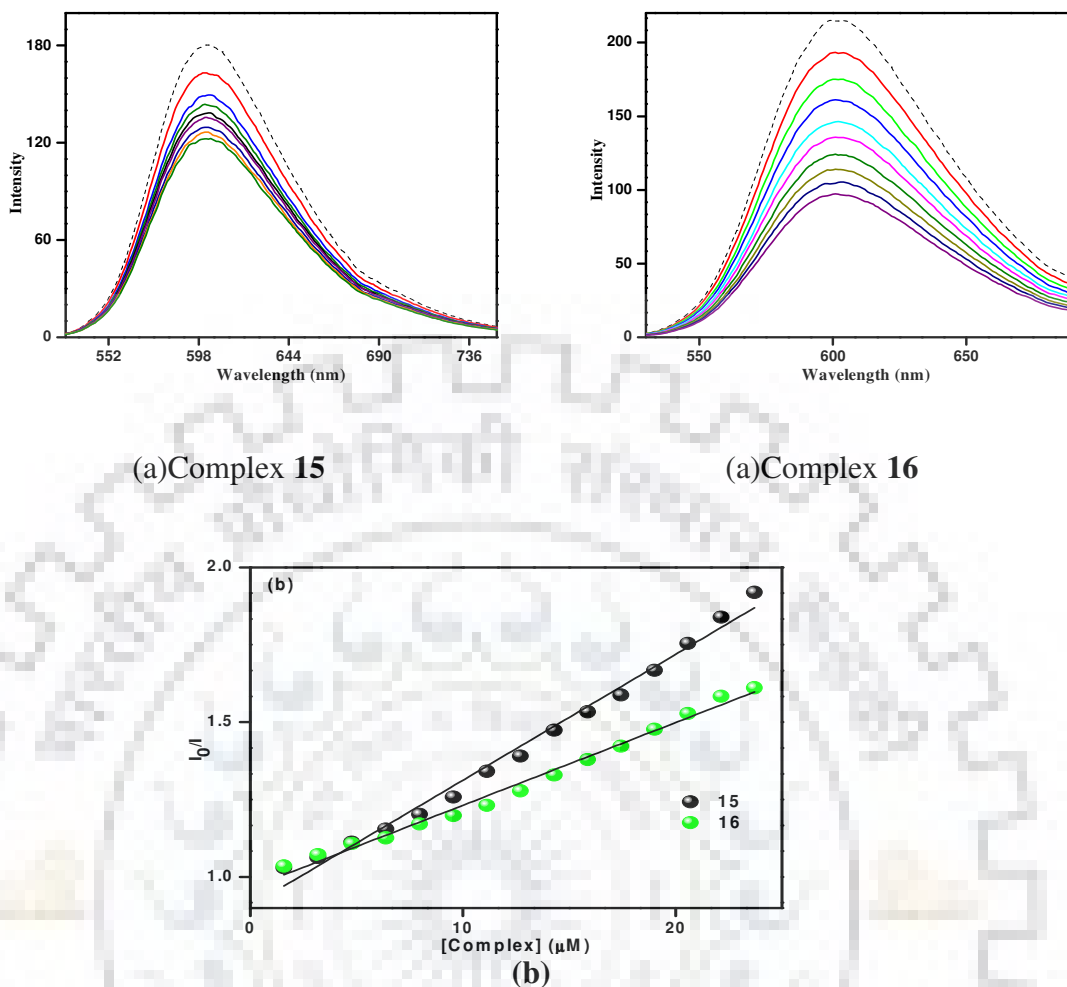


**Fig. 7.14** (a) Fluorescence emission spectra of CT-DNA in the presence of complex **15** and **16** in 0.1M phosphate buffer (pH 7.2) containing 2% DMF. [DNA] = 25 $\mu\text{M}$ , [complex **15** and **16**] = 0 - 30  $\mu\text{M}$ ,  $\lambda_{\text{ex}}$  = 250nm and  $\lambda_{\text{em}}$  = 600nm. Dotted line represents the spectrum in the absence of complex **15** and **16** (b) Stern-Volmer plot for complex **15** and **16**

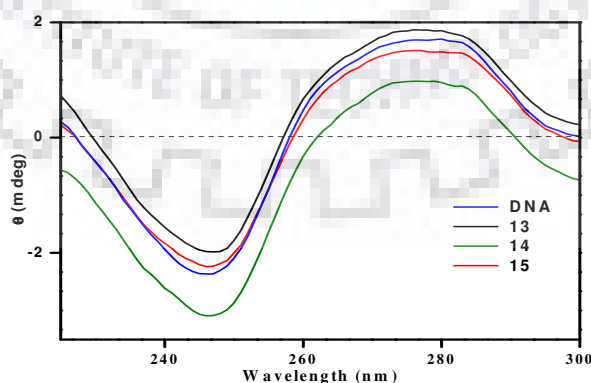


**Fig. 7.15** Circular dichroism spectra in 0.1 M phosphate buffer (pH 7.2) after 10 min incubation at 25 °C with CT-DNA and its interaction with complexes (**13-15**) spectra recorded in 2% dimethylformamide

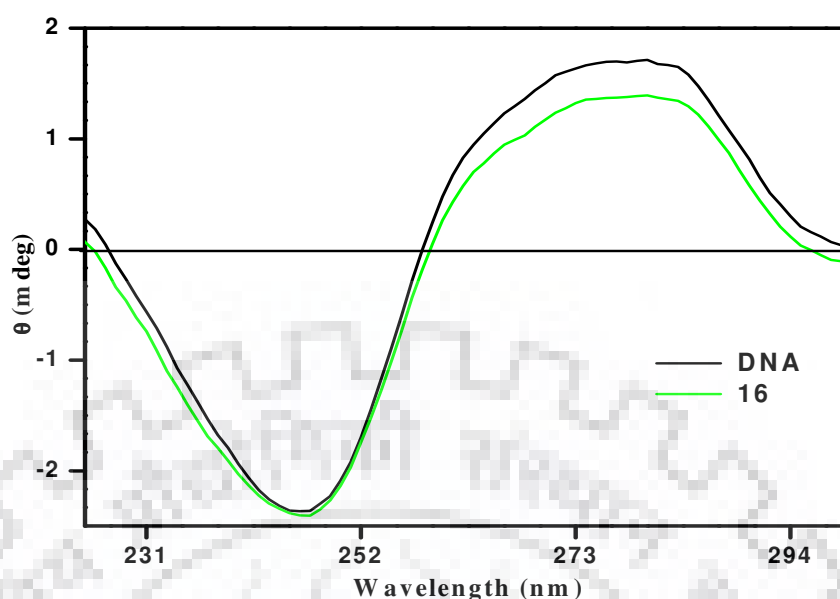


**Fig. 7.16** Circular dichroism spectra in 0.1 M phosphate buffer (pH 7.2) after 10 min incubation at 25 °C with CT-DNA and its interaction with complex **16** spectra was recorded in 2% dimethylformamide

### 7.2.5 Superoxide dismutase (SOD) activity study

The Mn/Fe/Co/Ni -N<sub>5</sub> binding motif were known to displayed excellent SOD activity, we have also check the effectiveness of the complexes **19-23** towards antioxidant activity using nitroblue tetrazolium (NBT) assay.<sup>218</sup> We have also performed the stability of complexes **19-23** in physiological condition and it was found that complexes **19-23** found stable in wide range of pH 6.8-7.8. The effectiveness of the SOD was determined with the IC<sub>50</sub> values, lower the IC<sub>50</sub> more effective will be the complexes to inhibit the superoxide generated in the reaction media. The details procedure to performed SOD activity was shown in (*Chapter 5*).

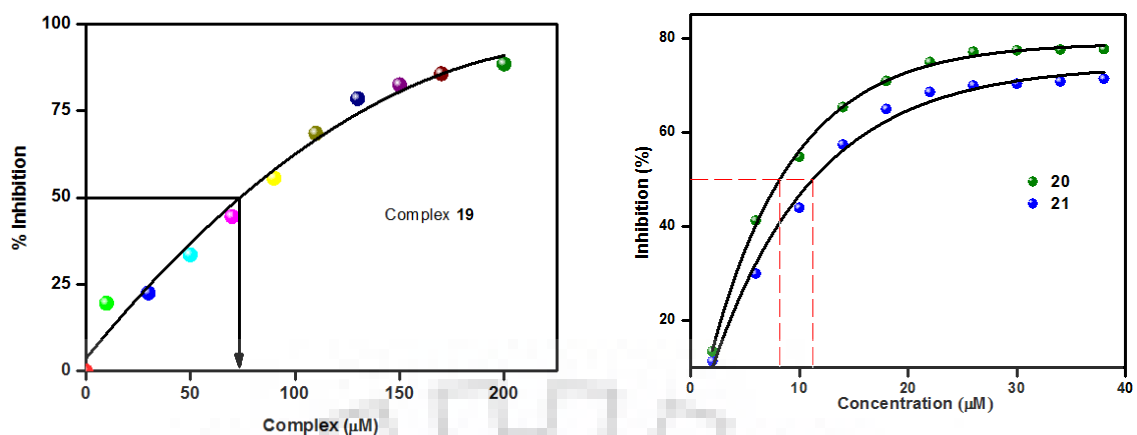


**Fig. 7.17** Superoxide dismutase activity of complexes **19**, **20** and **21** with xanthine oxidase–nitro blue tetrazolium assay (NBT assay)

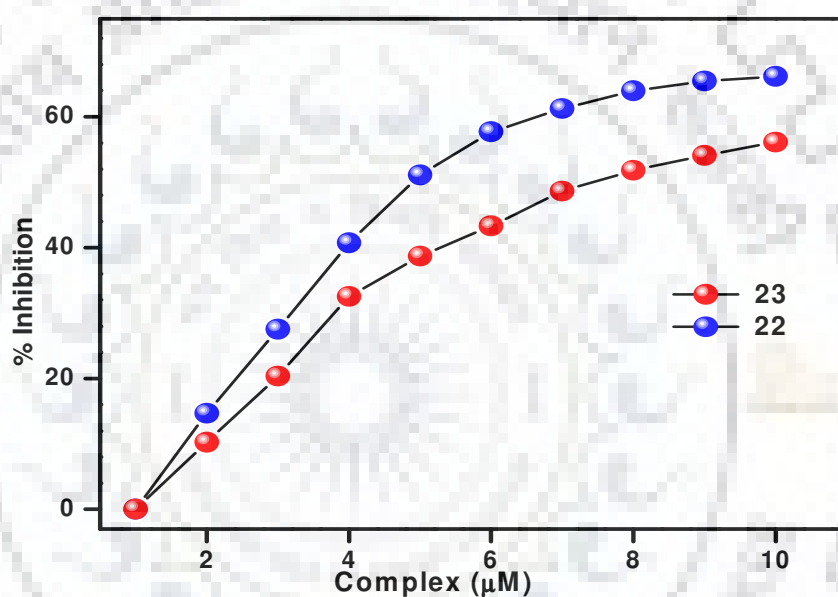


**Fig. 7.18** Superoxide dismutase activity of complexes **22** and **23** with xanthine oxidase–nitro blue tetrazolium assay (NBT assay)

**Table 7.2** IC<sub>50</sub> value of complexes **19 - 23** using NBT assay

Complexes	IC <sub>50</sub> (μM)
<b>19</b>	74.30
<b>20</b>	8.80
<b>21</b>	10.50
<b>22</b>	5.10
<b>23</b>	7.58

### 7.3 Conclusions

We have designed and synthesized new tridentate, tetradentate and pentadentate ligands systems the characterizations of all these ligands were done with different spectroscopic methods and their molecular structures were determined by single-crystal X-ray diffraction studies. Using these ligands we have synthesized complexes **13 - 23** respectively and their molecular structures were determined by single-crystal X-ray diffraction studies. Complexes **13-16** were utilised to study the DNA interaction studies and with complexes **19-23** SOD activities studies.

### 7.4 Experimental Section

#### 7.4.1 Synthesis of tridentate ligands L<sup>8</sup> and L<sup>9</sup>

The ligand L<sup>8</sup> have been synthesized using 2,6-bis(1-phenylhydrazinyl)pyridine (2mmol 0.582g) in 10mL methanol and (4mmol 0.424g) benzaldehyde was added dropwise into the reaction mixture. A off white colour solid was obtained within half an hour. The solid was washed with excess methanol and dried under vacuum. Yield 80%. Anal. Calcd for C<sub>31</sub>H<sub>25</sub>N<sub>5</sub> (467.21) C, 79.63; H, 5.39; N, 14.98. Found: C, 79.60; H, 5.60; N, 14.80. IR data (KBr,  $\nu_{\max}/\text{cm}^{-1}$ ): 1581,  $\nu_{\text{C=Nimine}}$  1453, 1285, 1087, 758, 700, UV-visible [CH<sub>2</sub>Cl<sub>2</sub>;  $\lambda_{\max}/\text{nm}$  ( $\epsilon/\text{M}^{-1}\text{cm}^{-1}$ ): 347 (24,780), 295 (16,430), 228 (19,860); <sup>1</sup>H NMR (500 MHz, CDCl<sub>3</sub>): 7.62(s,2H) 7.61-7.60 (s,4H) 7.59-7.58(s,4H) 7.55-7.480(t,2H) 7.35-7.33(s,4H) 7.23-7.23(s, 2H) 7.21(s, 2H)7.18(s,2H) 6.79-6.77(d, 2H), ESI-MS(DMSO)[L<sup>8</sup>+Na] m/z= 490.20.

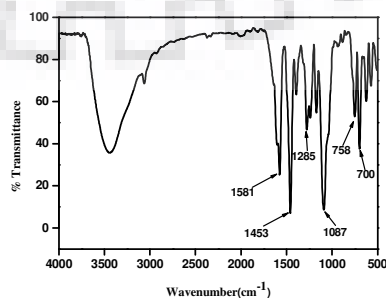


**Fig. 7.19** IR spectrum of 2,6-bis((E)-2-benzylidene-1-phenylhydrazinyl)pyridine

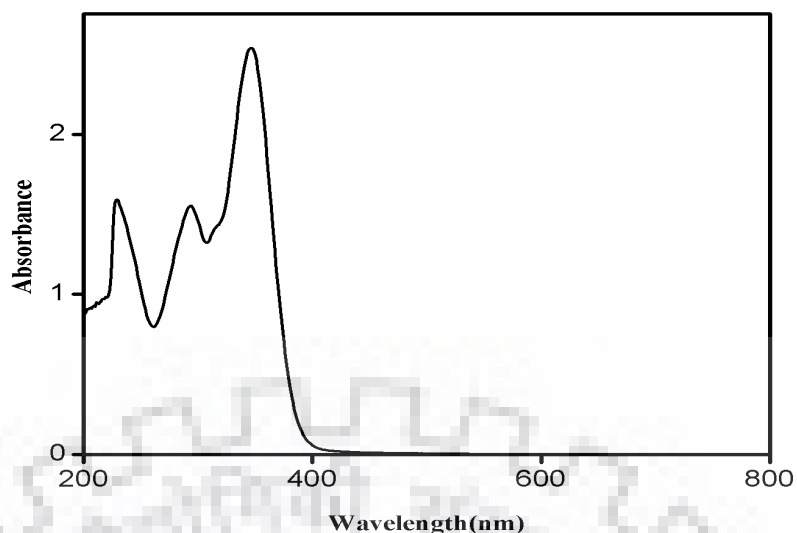


Fig. 7.20 UV-visible spectrum of 2,6-bis((E)-2-benzylidene-1-phenylhydrazinyl)pyridine in  $\text{CH}_2\text{Cl}_2$

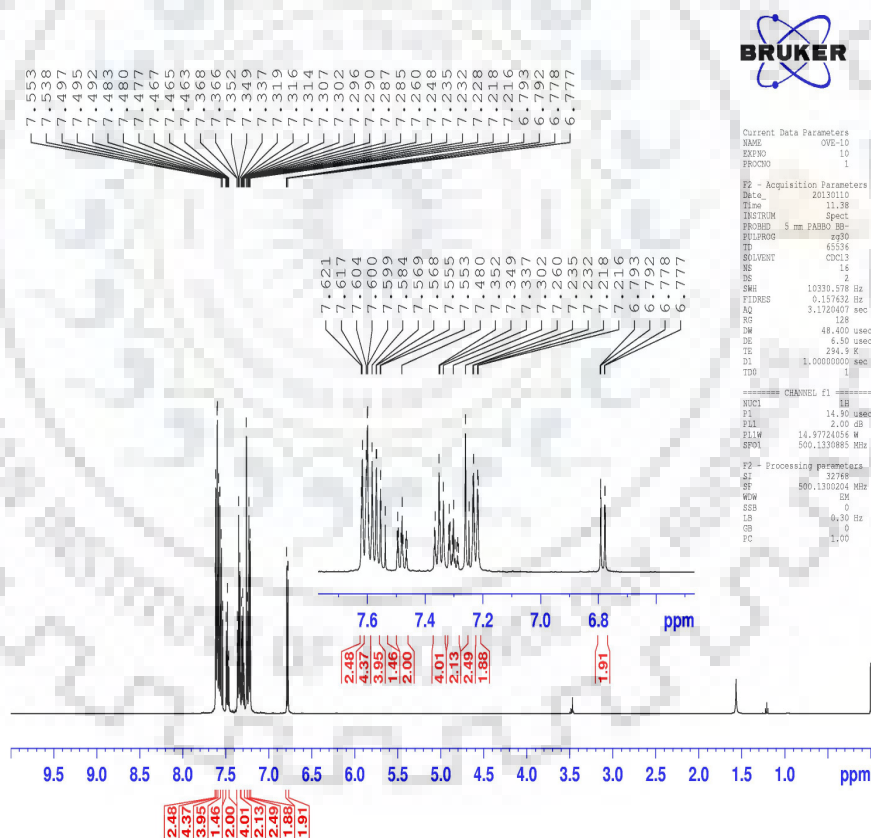
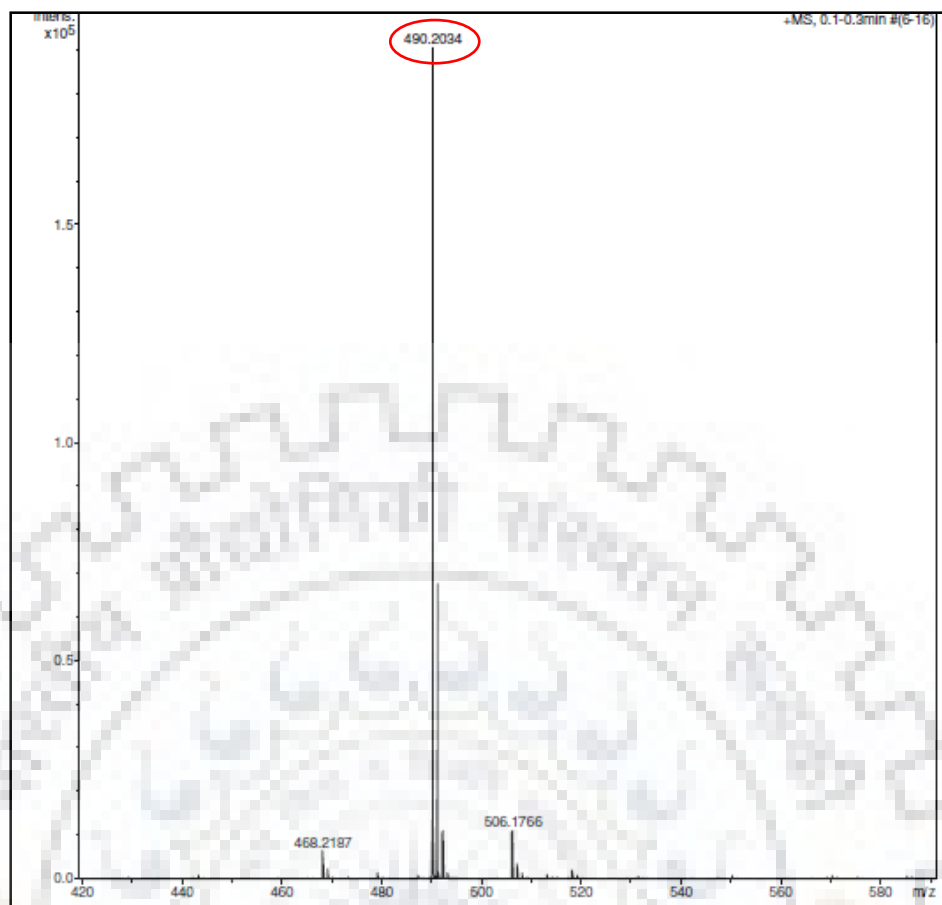


Fig. 7.21  $^1\text{H}$  NMR spectrum of 2,6-bis((E)-2-benzylidene-1-phenylhydrazinyl)pyridine



**Fig. 7.22** HRMS of 2,6-bis((E)-2-benzylidene-1-phenylhydrazinyl)pyridine (in DMSO)  $[L^8+Na]^+$

The ligand  $L^9$  have been synthesized using 2,6-bis(1-phenylhydrazinyl)pyridine (2mmol 0.582g) in 10mL methanol and (4mmol 0.544g) p-methoxybenzaldehyde was added dropwise into the reaction mixture. A off white colour solid was obtained within half an hour. The solid was washed with excess methanol and dried under vacuum. Yield 85%. Anal. Calcd for  $C_{33}H_{29}N_5O_2$  (527.61) C, 75.12; H, 5.54; N, 13.27. Found: C, 75.12; H, 5.60; N, 13.20. IR data (KBr,  $\nu_{max}/cm^{-1}$ ): 1579,  $\nu_{C=Nimine}$ , 1447, 1247. UV-visible [ $CH_2Cl_2$ ;  $\lambda_{max}/nm$  ( $\epsilon/M^{-1}cm^{-1}$ )]: 337 (26,680), 285 (17,430), 230 (18,760).  $^1H$  NMR (500 MHz,  $CDCl_3$ ): 7.60-7.51(m,8H) 7.24-7.28(m,7H) 7.15-6.95(m,4H) 6.87-6.85(m,4H) 3.81(s,6H). ESI-MS (DMSO)  $[L^9+Na]$ ;  $m/z = 550.2262$ .

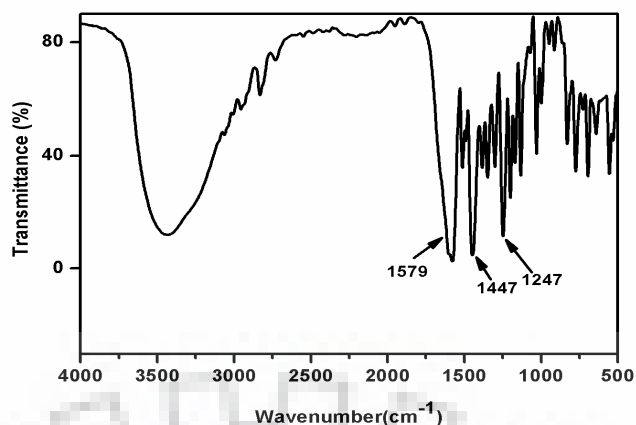


Fig. 7.23 IR spectrum 2,6-bis((E)-2-(4-methoxybenzylidene)-1-phenylhydrazinyl)pyridine

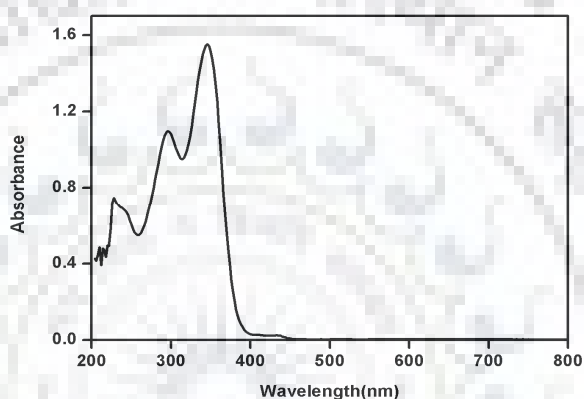


Fig. 7.24 UV-visible spectrum of 2,6-bis((E)-2-(4-methoxybenzylidene)-1-phenylhydrazinyl)pyridine.

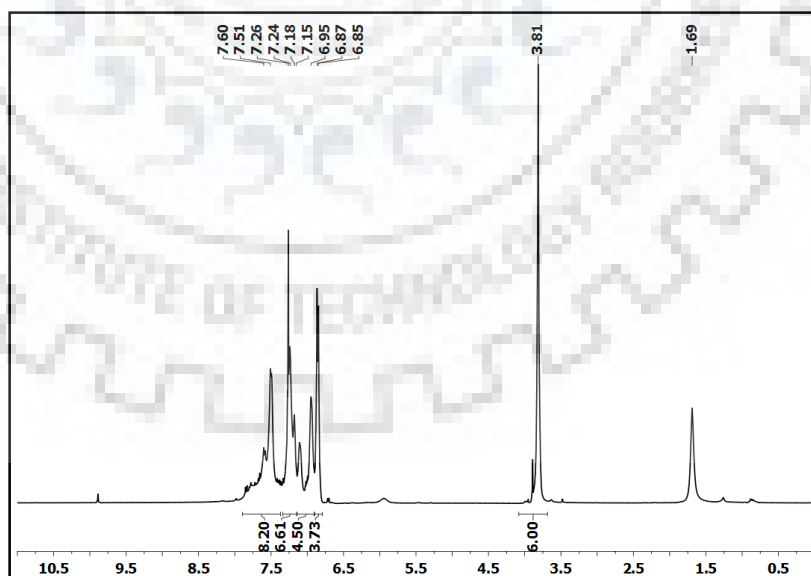
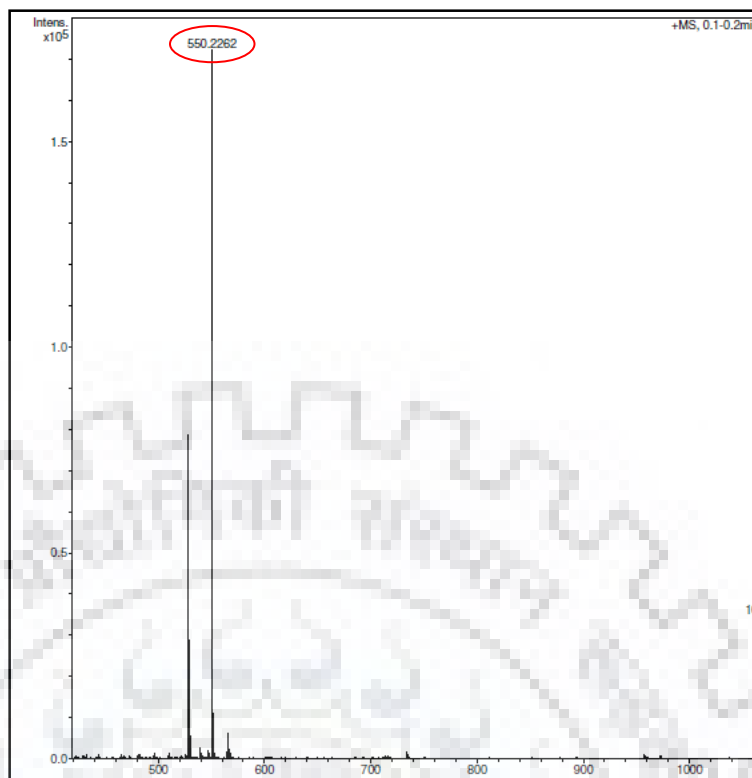


Fig. 7.25 <sup>1</sup>H NMR spectrum 2,6-bis((E)-2-(4-methoxybenzylidene)-1-phenylhydrazinyl)pyridine.





**Fig. 7.26** HRMS of 2,6-bis((E)-2-(4-methoxybenzylidene)-1-phenylhydrazinyl)pyridine. $[L^9+Na]^+$

#### 7.4.2 Synthesis of complex **13** using ligand **L<sup>8</sup>**

Complexes **13** was synthesized by mixing the (0.1mmol, 0.0467g) ligand **L<sup>8</sup>** in dichloromethane and (0.05mmol, 0.014g)  $Cu(NO_3)_2 \cdot 6H_2O$  in methanol. Metal salt was added dropwise into the reaction mixture and the reaction was stirred for 1 hour a green colour solid was obtained. The crystallization was done by dissolving the compound in dichloromethane and layered with methanol in a glass vial. The green colour crystals were crystallise on the wall of vial. Yield 72% Anal. Calcd for  $(C_{62}H_{52}CuN_{12}O_6)(1122.68)$  C, 66.33; H, 4.49; N, 14.97 Found: C, 65.98; H, 4.51; N, 14.72 IR data (KBr,  $\nu_{max}/cm^{-1}$ ): 1574,  $\nu_{C=Nimine}$ , 1455, 1381, 1275, 1168, 1040, 753, 698, 570, 506 UV-visible [ $CH_2Cl_2$ ;  $\lambda_{max}/nm$  ( $\epsilon/M^{-1}cm^{-1}$  )]: 400 (8,010), 311 (22,259), 237 (20,360).

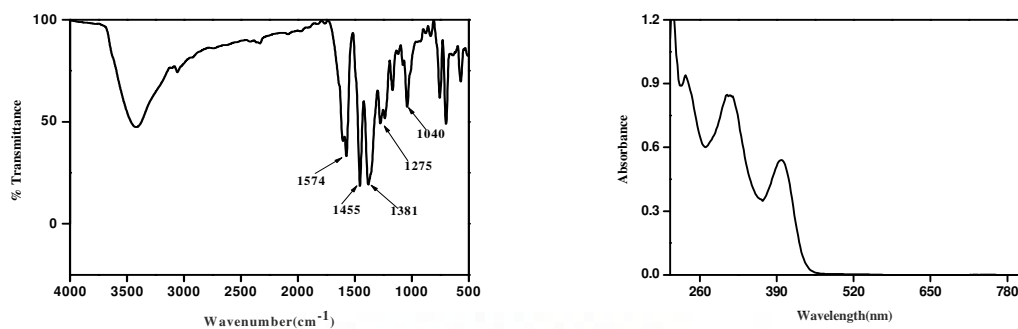


**Fig. 7.27** IR and UV-visible spectrums of complex **13**

### 7.4.3 Synthesis of complex **14** using ligand **L<sup>8</sup>**

Complexes **14** was also synthesized by mixing the (0.1mmol, 0.0467g) ligand **L<sup>8</sup>** in dichloromethane and (0.05mmol, 0.018g)  $\text{Cu}(\text{ClO}_4)_2 \cdot 6\text{H}_2\text{O}$  in methanol. Metal salt was added dropwise into the reaction mixture and the reaction was stirred until the green colour precipitate was obtained. The crystallization was done by dissolving the compound in dichloromethane and layered with methanol in a glass vial. The green colour crystals were crystallise in vial. Yield 72% Anal. Calcd for  $(\text{C}_{62}\text{H}_{52}\text{CuN}_{12}\text{O}_6)$  (1122.68) C, 66.33; H, 4.49; N, 14.97 Found: C, 65.98; H, 4.51; N, 14.72 IR data (KBr,  $\nu_{\text{max}}/\text{cm}^{-1}$ ): 1575,  $\nu_{\text{C=Nimine}}$ , 1457, 1393, 1278, 1172, 1090, 751, 698, 625, 572, 504 UV-visible [ $\text{CH}_2\text{Cl}_2$ ;  $\lambda_{\text{max}}/\text{nm}$  ( $\epsilon/\text{M}^{-1}\text{cm}^{-1}$ )]: 400 (8,810), 309 (23,260), 237 (28,460).

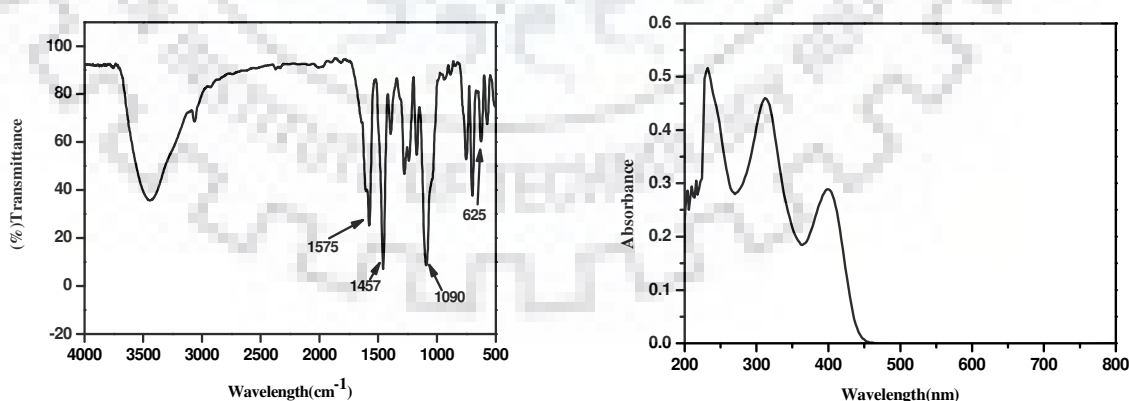


**Fig. 7.28** IR and UV-visible spectrums of complex **14**

#### 7.4.4 Synthesis of complex 15 using ligand L<sup>9</sup>

Complexes **15** was synthesized by adding the (0.1mmol, 0.0527g) ligand L<sup>9</sup> in dichloromethane and (0.05mmol, 0.018g) Cu(ClO<sub>4</sub>)<sub>2</sub>.6H<sub>2</sub>O in methanol. Metal salt was added dropwise into the reaction mixture and the reaction was stirred until the green colour solution was stirred for one hour after that (0.2mmol) NH<sub>4</sub>PF<sub>6</sub> was added to precipitate out the compound. The crystallization was done by dissolving the compound in dichloromethane and methanol (1:1) mixture in a glass vial. The green colour crystals were grow in vial. Yield 68% Anal. Calcd for (C<sub>66</sub>H<sub>58</sub>CuF<sub>6</sub>N<sub>10</sub>O<sub>4</sub>P) (1263.74) C, 62.73; H, 4.63; N, 11.08 Found: C, 62.88; H, 4.51; N, 11.22 IR data (KBr,  $\nu_{\max}/\text{cm}^{-1}$ ): IR data (KBr,  $\nu_{\max}/\text{cm}^{-1}$ ): 1610  $\nu_{\text{C=Nimine}}$ , 1455, 1298, 1122, 836  $\nu_{\text{PF}_6^-}$ , 538. UV-visible [CH<sub>2</sub>Cl<sub>2</sub>;  $\lambda_{\max}/\text{nm}$  ( $\epsilon/\text{M}^{-1}\text{cm}^{-1}$ )]: 390 (8,610), 315 (21,260), 240 (26,660).

#### 7.4.5 Synthesis of complex 16 using ligand L<sup>9</sup>

Complexes **16** was synthesized by adding the (0.1mmol, 0.0527g) ligand L<sup>9</sup> in dichloromethane and (0.05mmol, 0.011g) CoCl<sub>2</sub>.6H<sub>2</sub>O in methanol. Metal salt was added dropwise into the reaction mixture and the reaction was stirred until the red colour solid was precipitate out. The crystallization was done by dissolving the compound in dichloromethane and layered with methanol in a glass vial. The red colour crystals were grow in the bottom vial. Yield 70% Anal. Calcd for (C<sub>33</sub>H<sub>29</sub>CoCl<sub>2</sub>N<sub>5</sub>O<sub>2</sub>) (657.45) C, 60.29; H, 4.45; N, 10.65 Found: C, 60.28; H, 4.41; N, 10.22 IR data (KBr,  $\nu_{\max}/\text{cm}^{-1}$ ): IR data (KBr,  $\nu_{\max}/\text{cm}^{-1}$ ): 1584  $\nu_{\text{C=Nimine}}$ , 1453, 1240, 1021. UV-visible [CH<sub>2</sub>Cl<sub>2</sub>;  $\lambda_{\max}/\text{nm}$  ( $\epsilon/\text{M}^{-1}\text{cm}^{-1}$ )]: 415 (2,600), 392 (2,760), 330 (10,000), 270(3.30).

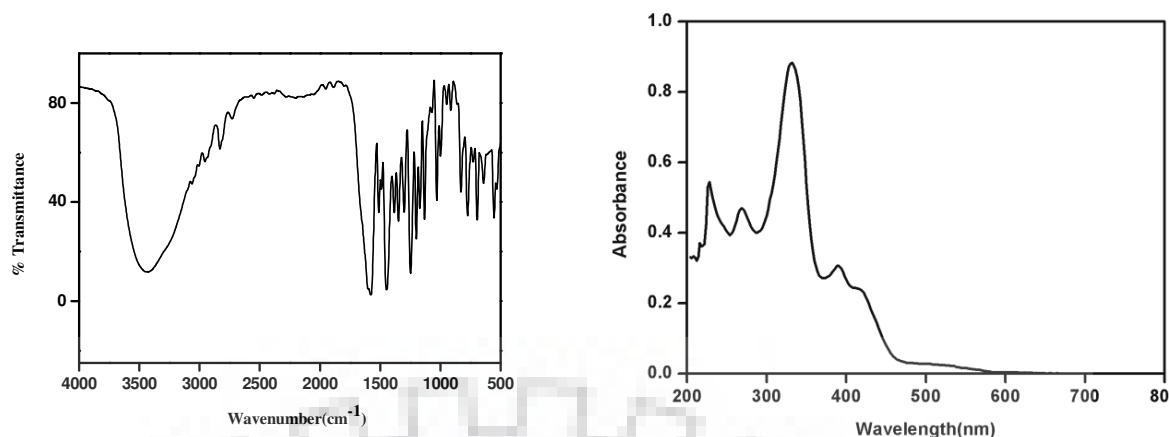


Fig. 7.29 IR and UV-visible spectrums of complex 16

#### 7.4.6 Synthesis of tetradentate ligand ( $L^{10}$ ) ((1z,2z)-1,2-bis(2-phenyl-2-(pyridine-2-yl)hydrazono)ethane)

The Schiff base tetradentate ligand, was synthesized according to the procedure reported earlier by our group.<sup>424</sup> A batch of 0.58 g (10 mmol) of glyoxal in 5 mL methanol was added to 2.22 g (12 mmol) of 2-(1-phenylhydrazinyl)pyridine in 10 mL methanol with continuous stirring at room temperature. After 1 h of stirring the reaction mixture gave the yellow precipitate. The yellow product was filtered off, washed with methanol and diethyl ether to remove the unreactive 2-(1-phenylhydrazinyl) pyridine. Yield: 86%. Anal. Calcd for  $C_{24}H_{20}N_6$ : C, 73.45; H, 5.14; N, 21.41. Found: C, 73.48; H, 5.19; N, 21.43. IR (KBr,  $\nu_{max}/cm^{-1}$ ): 1587(m) 1558(m), 1468(s), 1434(m), 1203(s). UV-visible [ $CH_2Cl_2$ ;  $\lambda_{max}$  /nm ( $\epsilon/M^{-1}cm^{-1}$ )]: 288(10760), 362 (51160).  $^1H$  NMR ( $CDCl_3$ ,  $\delta/ppm$ ): 6.76-6.78 (ddd,  $J = 7.0$  Hz, 4.8 Hz, 0.9 Hz, 2H), 7.15-7.18 (dt,  $J = 8.5$  Hz, 0.7 Hz, 2H), 7.18- 7.20 (dt,  $J = 8.1$  Hz, 1.3 Hz, 4H), 7.24 (s, 2H), 7.48-7.50 (dt,  $J = 7.5$  Hz, 1.2 Hz, 2H), 7.50-7.52 (dt,  $J = 9.0$  Hz, 1.5 Hz, 2H), 7.58-7.62 (tt,  $J = 7.5$  Hz, Hz, 4H), 8.16-8.18 (ddd,  $J = 5.0$  Hz, 1.9 Hz, 0.7 Hz, 2H).  $^{13}C$  NMR ( $CDCl_3$ ,  $\delta/ppm$ ): 109.78, 116.29, 128.95, 129.68, 130.68, 137.47, 138.25, 138.53, 147.85, 157.45.

#### 7.4.7 Synthesis of complex 17 using tetradentate ligand L<sup>10</sup>

The complex **17** was synthesized using a batch of 0.039g (0.1mmol) L<sup>10</sup> in dichloromethane and Mn(ClO<sub>4</sub>)<sub>2</sub>.xH<sub>2</sub>O 0.012g (0.05mmol) in 2mL methanol, was added dropwise with continuous stirring at room temperature. The light orange colour solid was obtained in 2 hours. The solid was washed with diethylether and dried under vacuum. The crystallization was done by dissolving the compound in 1:1 mixture of dichloromethane and methanol in a vial. Yield 62% Anal. Calcd for C<sub>48</sub>H<sub>40</sub>Cl<sub>2</sub>MnN<sub>12</sub>O<sub>8</sub> (1038.75): C, 55.50 H, 3.88 N, 16.18 Found: C, 55.40 H, 3.90 N, 16.20. IR (KBr,  $\nu_{max}/\text{cm}^{-1}$ ): 1592 1575, 1440, 1240. UV-visible [Methanol;  $\lambda_{max}/\text{nm}$  ( $\epsilon/\text{M}^{-1}\text{cm}^{-1}$ )]: 240(31,760); 340 (29,160); 390(10,380).

#### 7.4.8 Synthesis of complex 18 using tetradentate ligand L<sup>10</sup>

The complex **18** was synthesized using a batch of 0.039g (0.1mmol) L<sup>10</sup> in dichloromethane and Mn(NO<sub>3</sub>)<sub>2</sub>.xH<sub>2</sub>O 0.017g (0.1mmol) in 2mL methanol, was added dropwise with continuous stirring at room temperature. The light orange colour solid was obtained. The solid was washed with diethylether and dried under vacuum. The crystallization was done by dissolving the compound in 1:1 mixture of dichloromethane and methanol in a vial. Yield 70% Anal. Calcd for C<sub>24</sub>H<sub>20</sub>MnN<sub>6</sub>O<sub>6</sub> (571.40): C, 50.45 H, 3.53 N, 19.61 Found: C, 51.00 H, 3.45 N, 19.40. IR (KBr,  $\nu_{max}/\text{cm}^{-1}$ ): 1592 1575, 1440, 1440, 1384, 1240. 980, 720, 530; UV-visible [Methanol;  $\lambda_{max}/\text{nm}$  ( $\epsilon/\text{M}^{-1}\text{cm}^{-1}$ )]: 245(29,760); 345 (30,160); 380(8,380).

#### 7.4.9 Synthesis of complex 19 using pentadentate ligand L<sup>6</sup>

Complexes **19** was synthesized by adding the (0.2mmol, 0.0938g) ligand L<sup>6</sup> in dichloromethane and (0.2 mmol, 0.073g) Co(ClO<sub>4</sub>)<sub>2</sub>.6H<sub>2</sub>O in methanol and added dropwise into the stirred ligand. The colour of the compound was changed yellow to red, after 4 hours stirring red colour solid was obtained. The crystallization was done by dissolving the compound in dichloromethane and layered with methanol in a glass vial. The red colour crystals were found at the wall of the glass vial. Yield 60% Anal. Calcd for

( $C_{29}H_{25}CoCl_2N_7O_9$ ) (745.38) C, 46.73; H, 3.38; N, 13.15 Found: C, 46.78; H, 3.41; N, 13.22  
 IR data (KBr,  $\nu_{max}/cm^{-1}$ ): IR data (KBr,  $\nu_{max}/cm^{-1}$ ): 1590  $\nu_{C=Nimine}$ , 1090, 625  $\nu_{ClO_4^-}$ , UV-visible [ $CH_2Cl_2$ ;  $\lambda_{max}/nm$  ( $\epsilon/M^{-1}cm^{-1}$ )]: 280 (20,200), 350 (29,760), 415 (9,100).

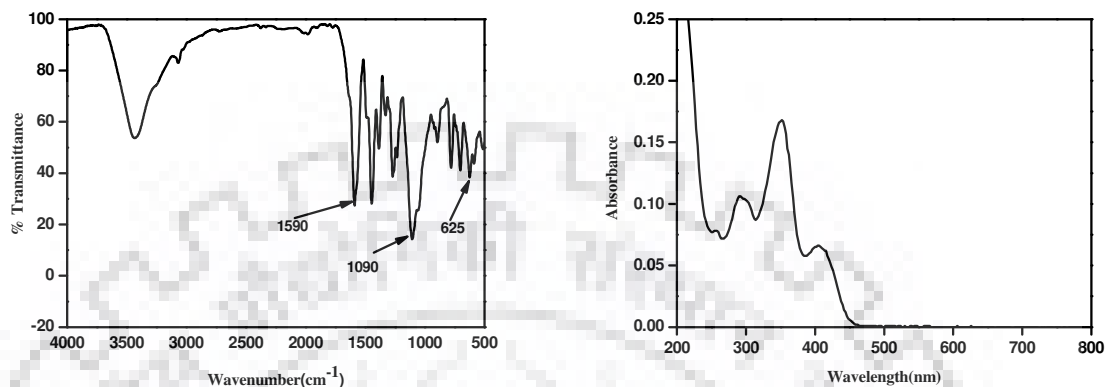


Fig. 7.30 IR and UV-visible spectrums of complex 19

#### 7.4.10 Synthesis of complex 20 using pentadentate ligand L<sup>6</sup>

A batch of ligand L<sup>6</sup> (0.047g, 0.1 mmol) was stirred in dichloromethane solution at room temperature after that a batch of  $Mn(ClO_4)_2 \cdot xH_2O$  (0.025g, 0.1 mmol) was dissolved in methanol and added dropwise into the stirred ligand. The colour of the solution change yellow to orange, after half an hour (0.1mmol, 0.026g)  $Na_2[Fe(CN)_5NO] \cdot 2H_2O$  was dissolved in 5mL methanol and added dropwise in the reaction mixture. A dark orange colour solid was obtained in 2hours. The solid was filtered out and dried under vacuo. Yield 60% Anal. Calcd for  $C_{34}H_{27}FeMnN_{13}O_3$  (776.44) C, 52.59; H, 3.50; N, 13.45; Found: C, 52.55; H, 3.45; N, 13.50; IR data (KBr,  $\nu_{max}/cm^{-1}$ ): 2169  $\nu_{C \equiv N}$ , 1935  $\nu_{N=O}$ , 1649  $\nu_{C=Nimine}$ , 1438, 1205, 1131, 1014, 773; UV-visible [ $CH_2Cl_2$ ;  $\lambda_{max}/nm$  ( $\epsilon/M^{-1}cm^{-1}$ ) ] 392 (6,232); 327 (19,270); 292 (27,900).

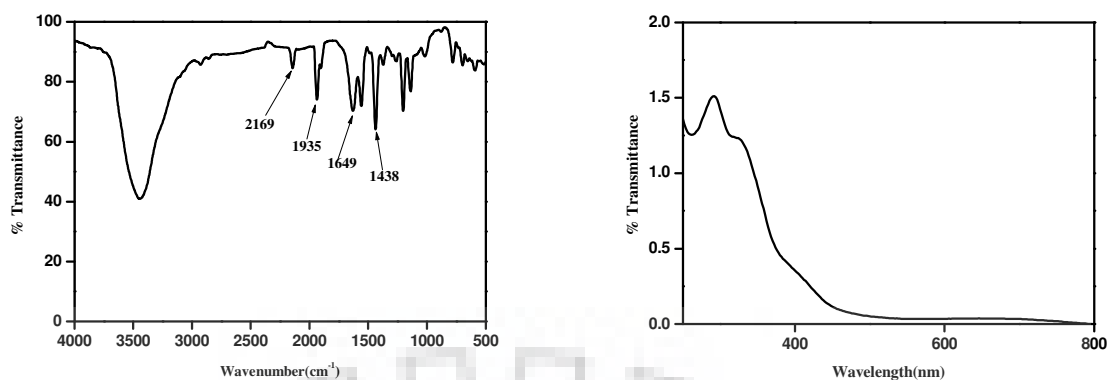


Fig.7.31 IR and UV-visible spectrums of complex 20

#### 7.4.11 Synthesis of complex 21 using pentadentate ligand L<sup>6</sup>

Complexes 21 was synthesized by dissolving the (0.2mmol, 0.0938g) ligand L<sup>6</sup> in dichloromethane and (0.2 mmol, 0.047g) NiCl<sub>2</sub>.6H<sub>2</sub>O in 5mL methanol was added dropwise into the stirred ligand. The colour of the compound was changed yellow to reddish yellow , after 1 hour stirring 2mmol of Na(ClO<sub>4</sub>)<sub>2</sub> was added in stirred solution, the dark yellow colour solid was obtained. The crystallization was done by dissolving the compound in dichloromethane and methanol(1:1) mixture in a glass vial. The reddish yellow colour crystals were obtained in the glass vial. Yield 65% Anal. Calcd for (C<sub>58</sub>H<sub>46</sub>Cl<sub>4</sub>N<sub>14</sub>Ni<sub>2</sub>O<sub>8</sub>) (1326.27); C, 52.52; H, 3.35; N, 14.79; Found: C, 51.98; H, 3.40; N, 14.60; IR data (KBr,  $\nu_{\max}/\text{cm}^{-1}$ ): 1595  $\nu_{\text{C=Nimine}}$  1492, 1090, 624  $\nu_{\text{ClO}_4^-}$ , UV-visible [CH<sub>2</sub>Cl<sub>2</sub>;  $\lambda_{\max}/\text{nm}$  ( $\epsilon/\text{M}^{-1}\text{cm}^{-1}$ ) 419(8,340),362(22,630), 261(32,320).

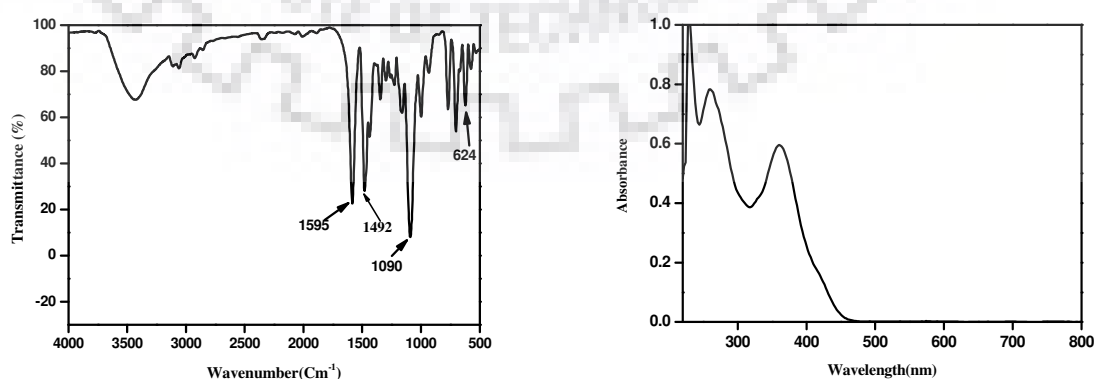


Fig.7.32 IR and UV-visible spectrums of complex 21

### 7.4.12 Synthesis of complex **22** using pentadentate ligand **L<sup>1</sup>**

A batch of ligand (**L<sup>1</sup>**) (0.2mmol; 0.099g) was dissolved in dichloromethane and metal salt (0.2mmol; 0.070g)  $\text{Fe}(\text{ClO}_4)_3 \cdot x\text{H}_2\text{O}$  was dissolved in methanol and added dropwise in the stirring reaction. A green colour solid was obtained in 3 hours. The solid was washed with diethyl ether and dried under vacuum. The crystallization was done in the crystallization tube by dissolving the compound in 1mL dichloromethane and layered with toluene. The green colour crystals were obtained on the wall of the crystallization tube. Yield 70%, Anal. Calcd for  $\text{C}_{62}\text{H}_{46}\text{Cl}_2\text{Fe}_2\text{N}_{10}\text{O}_{12}$  (1305.69) C, 57.03; H, 3.55; N, 10.73 Found: C, 56.98; H, 3.60; N, 10.69; IR data (KBr,  $\nu_{\text{max}}/\text{cm}^{-1}$ ): 1588  $\nu_{\text{C=Nimine}}$ , 1476, 1090, 625  $\nu_{\text{ClO}_4^-}$ , UV-visible [ $\text{CH}_2\text{Cl}_2$ ;  $\lambda_{\text{max}}/\text{nm}$  ( $\epsilon/\text{M}^{-1}\text{cm}^{-1}$ ) 420(6,410), 328(20,440), 293(29,800).

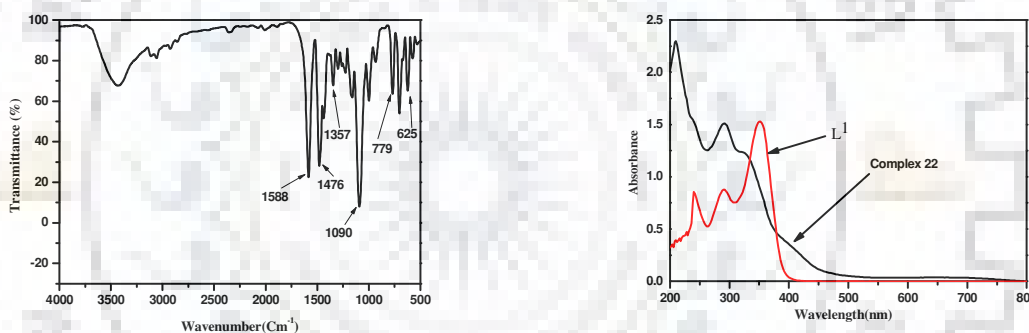


Fig. 7.33 IR and UV-visible spectrums of complex **22**

### 7.4.13 Synthesis of complex **23** using pentadentate ligand **L<sup>1</sup>**

This complex, **23** has been synthesized utilising complex **22**. The (0.1mmol, 0.1305g) complex **22** was dissolved in 5ml dichloromethane and 0.1mmol sodium nitroprusside was added by dissolving in 5 mL distilled water. The reaction mixture was stirred for 2 hours. The compound in dichloromethane was separated out and dried under vacuum. The re-crystallization was done in dichloromethane and methanol (1:1) mixture red colour was obtained within two days. Yield 70%, Anal. Calcd for  $\text{C}_{66}\text{H}_{50}\text{Fe}_3\text{N}_{16}\text{O}_8$  (1362.77) C, 59.22; H, 3.71; N, 16.49. IR data (KBr,  $\nu_{\text{max}}/\text{cm}^{-1}$ ): 2124  $\nu_{\text{C=N}}$ , 1891  $\nu_{\text{N=O}}$ , 1577



$\nu_{C=N}$ imine, 1460, 1286, 1088, 752; UV-visible [ $CH_2Cl_2$ ;  $\lambda_{max}$  /nm ( $\epsilon/M^{-1}cm^{-1}$ ) 434(18,830), 345(28,540).

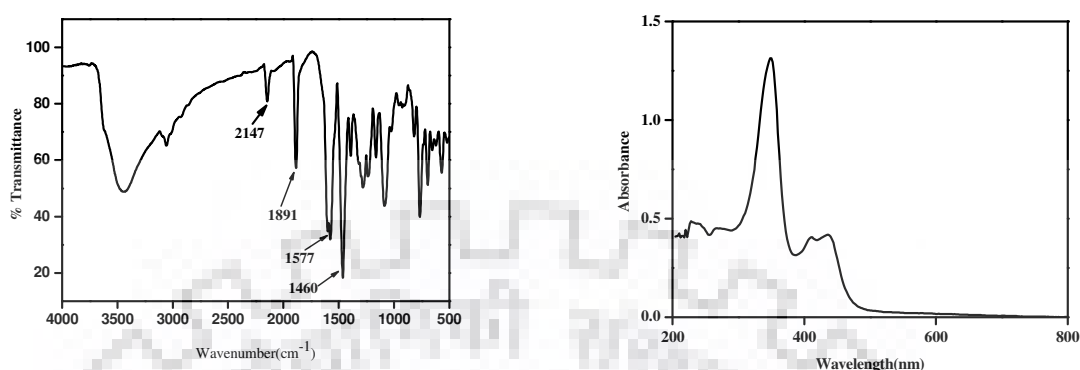


Fig. 7.34 IR and UV-visible spectrums of complex 23

Table 7.3 Crystal data and structural refinement parameters for ligand 8 and 9

	ligand 8	ligand 9		ligand 8	ligand 9
<b>Empirical formula</b>	$C_{31}H_{25}N_5$	$C_{33}H_{29}N_5O_2$	<b>Z</b>	4	4
<b>Colour</b>	white	white	$\rho_{calc}(gcm^{-3})$	0.980	0.556
<b>Formula weight</b>	467.56	527.61	<b>F(000)</b>	984.0	1112.0
<b>Temperature (K)</b>	293(2)	296(2)	<b><math>\theta</math> range for data collection</b>	1.80- 26.60	0.93 - 28.42
<b><math>\lambda</math> (Å) (Mo-K<math>\alpha</math>)</b>	0.71073	0.71073	<b>Index ranges</b>	-12<h<12, -30<k<30, -16 <l<16	-29 <h< -29, - 20 <k< 20 , - 25 <l< 25
<b>Crystal system</b>	monoclinic	monoclinic	<b>Refinement method</b>	Full matrix least-squares on $F^2$	Full matrix least-squares on $F^2$
<b>Space group</b>	P21/n	P21/c	<b>Data/restraint/parameters</b>	6622/0/325	15857 /0/ 361
<b>a(Å)</b>	10.2564(8)	21.976(2)	<b>GOF<sup>a</sup> on <math>F^2</math></b>	1.084	1.178
<b>b(Å)</b>	24.1934(18)	15.3145(17)	<b><math>R_1^b</math> [<math>I &gt; 2\sigma(I)</math>]</b>	0.0447	0.1912
<b>c(Å)</b>	12.8035(10)	18.738(2)	<b><math>R_1</math> (all data)</b>	0.0790	0.1945
<b><math>\alpha</math>(°)</b>	90.00	90.00	<b><math>wR_2^c</math> (<math>I &gt; 2\sigma(I)</math>)</b>	0.1219	1036
<b><math>\beta</math>(°)</b>	94.005(4)	92.419(7)	<b><math>wR_2</math> (all data)</b>	0.1402	0.1983
<b><math>\gamma</math>(°)</b>	90.00	90.00			

<sup>a</sup>GOF =  $[\sum(w(F_o^2 - F_c^2)^2) / (M - N)]^{1/2}$  (M = number of reflections, N = number of parameters refined). <sup>b</sup> $R_1 = \sum ||F_o| - |F_c|| / \sum |F_o|$ . <sup>c</sup> $wR_2 = [\sum[w(F_o^2 - F_c^2)^2] / \sum[(F_o^2)^2]]^{1/2}$ .

**Table 7.4** Crystal data and structural refinement parameters for complex **13** and **14**

	Complex <b>13</b>	Complex <b>14</b>		Complex <b>13</b>	Complex <b>14</b>
<b>Empirical formula</b>	C <sub>62</sub> H <sub>50</sub> Cu N <sub>12</sub> O <sub>6</sub>	C <sub>62</sub> H <sub>50</sub> Cl <sub>2</sub> Cu N <sub>10</sub> O <sub>8</sub>	<b>Z</b>	4	8
<b>Color</b>	green	green	$\rho_{\text{calc}}(\text{gcm}^{-3})$	1.221	1.445
<b>Formula weight</b>	1122.69	1197.57	<b>F(000)</b>	2332.0	4952.0
<b>Temperature (K)</b>	293(2)	296(2)	<b><math>\theta</math> range for data collection</b>	2.23- 25.00	1.03- 28.32
$\lambda$ (Å) (Mo-K $\alpha$ )	0.71073	0.71073	<b>Index ranges</b>	-30<h<30, -21<k<21, -17 <l<17	-18<h<13, -23<k<23, -55 <l<56
<b>Crystal system</b>	triclinic	triclinic	<b>Refinement method</b>	Full matrix least-squares on F <sup>2</sup>	Full matrix least-squares on F <sup>2</sup>
<b>Space group</b>	C2/c	P21/c	<b>Data/restraint/parameters</b>	5343 / 7/336	24764/0/1495
<b>a(Å)</b>	25.302(6)	15.658 (12)	<b>GOF<sup>a</sup> on F<sup>2</sup></b>	1.261	0.905
<b>b(Å)</b>	18.271(4)	17.820 (16)	<b>R<sub>1</sub><sup>b</sup> [I &gt; 2<math>\sigma</math>(I)]</b>	0.0843	0.0968
<b>c(Å)</b>	14.960(5)	42.41(4)	<b>R<sub>1</sub> (all data)</b>	0.1141	0.3541
<b><math>\alpha</math>(°)</b>	90.00	90.00	<b>wR<sub>2</sub><sup>c</sup> (I &gt; 2<math>\sigma</math>(I))</b>	0.2383	0.2812
<b><math>\beta</math>(°)</b>	117.988(5)	111.47(2)	<b>wR<sub>2</sub> (all data)</b>	0.2539	0.1774
<b><math>\gamma</math>(°)</b>	90.00	90.00			
<sup>a</sup> GOF = $[\sum[w(\text{Fo}^2 - \text{Fc}^2)^2]/(M - N)]^{1/2}$ (M = number of reflections, N = number of parameters refined). <sup>b</sup> R <sub>1</sub> = $\sum  \text{Fol} - \text{Fc}  /\sum \text{Fol} $ . <sup>c</sup> wR <sub>2</sub> = $[\sum[w(\text{Fo}^2 - \text{Fc}^2)^2]/\sum[(\text{Fo}^2)^2]]^{1/2}$ .					

**Table 7.5** Crystal data and structural refinement parameters for complex **15** and **16**

	Complex <b>15</b>	Complex <b>16</b>		Complex <b>15</b>	Complex <b>16</b>
<b>Empirical formula</b>	C <sub>64</sub> H <sub>58</sub> Cu F <sub>11</sub> N <sub>12</sub> O <sub>4</sub> P <sub>2</sub>	C <sub>33</sub> H <sub>29</sub> Cl <sub>2</sub> Co N <sub>5</sub> O <sub>2</sub>	<b>Z</b>	2	4
<b>Color</b>	green	red	<b><math>\rho_{\text{calc}}(\text{gcm}^{-3})</math></b>	1.470	1.162
<b>Formula weight</b>	1393.71	657.44	<b>F(000)</b>	1432.0	1356
<b>Temperature (K)</b>	293(2)	293(2)	<b><math>\theta</math> range for data collection</b>	2.46 - 28.310	2.46- 28.300
<b><math>\lambda</math> (Å) (Mo-K<math>\alpha</math>)</b>	0.71073	0.71073	<b>Index ranges</b>	-17 <h<17, -16<k<16, -25 <l<24	-17<h<17, -22<k<20, -24 <l<24
<b>Crystal system</b>	triclinic	monoclinic	<b>Refinement method</b>	Full matrix least-squares on F <sup>2</sup>	Full matrix least-squares on F <sup>2</sup>
<b>Space group</b>	P2/c	P21/c	<b>Data/restraint/parameters</b>	7825 / 0/ 427	9138/0/ 388
<b>a(Å)</b>	13.4656(11)	12.8312 (7)	<b>GOF<sup>a</sup> on F<sup>2</sup></b>	1.086	1.306
<b>b(Å)</b>	12.6292(9)	16.7835 (9)	<b>R<sub>1</sub><sup>b</sup> [I &gt; 2<math>\sigma</math>(I)]</b>	0.0704	0.1378
<b>c(Å)</b>	19.2371(15)	18.3109 (10)	<b>R<sub>1</sub> (all data)</b>	0.0924	0.2586
<b><math>\alpha</math>(°)</b>	90.00	90.00	<b>wR<sub>2</sub><sup>c</sup> (I &gt; 2<math>\sigma</math>(I))</b>	0.2361	0.3783
<b><math>\beta</math>(°)</b>	105.808(4)	107.583 (3)	<b>wR<sub>2</sub> (all data)</b>	0.2681	0.3783
<b><math>\gamma</math>(°)</b>	90.00	90.00			
<sup>a</sup> GOF = $[\sum[w(\text{Fo}^2 - \text{Fc}^2)^2]/M - N]^{1/2}$ (M = number of reflections, N = number of parameters refined). <sup>b</sup> R <sub>1</sub> = $\sum\ \text{Fol} - \text{Fcl}\ /\sum\ \text{Fol}\ $ . <sup>c</sup> wR <sub>2</sub> = $[\sum[w(\text{Fo}^2 - \text{Fc}^2)^2] / \sum[(\text{Fo}^2)^2]]^{1/2}$ .					

**Table 7.6** Crystal data and structural refinement parameters for complex **17** and **18**

	Complex <b>17</b>	Complex <b>18</b>		Complex <b>17</b>	Complex <b>18</b>
<b>Empirical formula</b>	C <sub>48</sub> H <sub>40</sub> C <sub>12</sub> Mn N <sub>12</sub> O <sub>8</sub>	C <sub>24</sub> H <sub>20</sub> Mn N <sub>8</sub> O <sub>6</sub>	<b>Z</b>	4	8
<b>Color</b>	orange	orange	<b><math>\rho_{\text{calc}}(\text{gcm}^{-3})</math></b>	1.162	1.438
<b>Formula weight</b>	1038.76	571.42	<b>F(000)</b>	2140.0	2344.0
<b>Temperature (K)</b>	296(2)	293(2)	<b><math>\theta</math> range for data collection</b>	2.23 - 28.520	1.11-26.970
<b><math>\lambda</math> (Å) (Mo-K<math>\alpha</math>)</b>	0.71073	0.71073	<b>Index ranges</b>	-21 <h<22, -23<k<24 -28 <l<28	-46<h<39, -10<k<10 -21 <l<21
<b>Crystal system</b>	triclinic	triclinic	<b>Refinement method</b>	Full matrix least-squares on F <sup>2</sup>	Full matrix least-squares on F <sup>2</sup>
<b>Space group</b>	P-1	C2/c	<b>Data/restraint/parameters</b>	28728/0/ 1279	5642 /1/ 352
<b>a(Å)</b>	17.042(3)	36.725(4)	<b>GOF<sup>a</sup> on F<sup>2</sup></b>	0.922	1.437
<b>b(Å)</b>	18.204(5)	8.5755(9)	<b>R<sub>1</sub><sup>b</sup> [I &gt; 2<math>\sigma</math>(I)]</b>	0.2029	0.0915
<b>c(Å)</b>	21.645(5)	16.7615 (19)	<b>R<sub>1</sub> (all data)</b>	0.4567	0.1090
<b><math>\alpha</math>(°)</b>	90.00	90.00	<b>wR<sub>2</sub><sup>c</sup> (I &gt; 2<math>\sigma</math>(I))</b>	0.5282	0.3295
<b><math>\beta</math>(°)</b>	90.00	91.143(3)	<b>wR<sub>2</sub> (all data)</b>	0.4111	0.3040
<b><math>\gamma</math>(°)</b>	62.183(8)	90.00			
<sup>a</sup> GOF = $[\sum[w(\text{Fo}^2 - \text{Fc}^2)^2]/M - N]^{1/2}$ (M = number of reflections, N = number of parameters refined). <sup>b</sup> R <sub>1</sub> = $\sum  \text{Fo}  - \text{Fc}  /\sum \text{Fo} $ . <sup>c</sup> wR <sub>2</sub> = $[\sum[w(\text{Fo}^2 - \text{Fc}^2)^2]/\sum[(\text{Fo}^2)^2]]^{1/2}$ .					

Table 7.7 Crystal data and structural refinement parameters for complex 19, 20, 21

	Complex 19	Complex 20	Complex 21		Complex 19	Complex 20	Complex 21
<b>Empirical formula</b>	C <sub>29</sub> H <sub>25</sub> Cl <sub>2</sub> Co N <sub>7</sub> O <sub>9</sub>	C <sub>34</sub> H <sub>27</sub> Fe Mn N <sub>13</sub> O <sub>3</sub>	C <sub>58</sub> H <sub>46</sub> Cl <sub>4</sub> N <sub>14</sub> Ni <sub>2</sub> O <sub>8</sub>	<b>Z</b>	2	4	4
<b>Color</b>	red	orange	yellow	<b><math>\rho_{\text{calc}}(\text{gcm}^{-3})</math></b>	1.555	1.419	1.400
<b>Formula weight</b>	745.39	776.48	1326.27	<b>F(000)</b>	990	1588.0	3886
<b>Temperature (K)</b>	296(2)	293(2)	293(2)	<b><math>\theta</math> range for data collection</b>	2.23 - 26.580	1.81-21.27	1.70-28.34
<b><math>\lambda</math> (Å) (Mo-K<math>\alpha</math>)</b>	0.71073	0.71073	0.71073	<b>Index ranges</b>	-9 <h<8, -17 <k<17 -20 <l<20	-18 <h<19, -14 <k<14, -13 <l<11	-37 <h<37, -19 <k<19 -22 <l<26
<b>Crystal system</b>	triclinic	triclinic	triclinic	<b>Refinement method</b>	Full matrix least-squares on F <sup>2</sup>	Full matrix least-squares on F <sup>2</sup>	Full matrix least-squares on F <sup>2</sup>
<b>Space group</b>	P-1	P21/c	Cc	<b>Data/restraint t/ parameters</b>	6611 /0/ 441	3918/148/ 464	14378/2/ 760
<b>a(Å)</b>	7.9434(2)	18.823(7)	28.0717(14)	<b>GOF<sup>a</sup> on F<sup>2</sup></b>	1.021	1.088	1.200
<b>b(Å)</b>	13.9006(4)	14.143(5)	14.2924(7)	<b>R<sub>1</sub><sup>b</sup> [I &gt; 2<math>\sigma</math>(I)]</b>	0.0447	0.1213	0.1025
<b>c(Å)</b>	15.9811(5)	13.767(5)	19.9288(18)	<b>R<sub>1</sub> (all data)</b>	0.0628	0.1437	0.1992
<b><math>\alpha</math>(°)</b>	68.1350(10)	90.00	90.00	<b>wR<sub>2</sub><sup>c</sup> (I &gt; 2<math>\sigma</math>(I))</b>	0.1453	0.3465	0.2794
<b><math>\beta</math>(°)</b>	76.714(2)	97.48(2)	128.113(2)	<b>wR<sub>2</sub> (all data)</b>	0.1697	0.3568	0.3378
<b><math>\gamma</math>(°)</b>	82.575(2)	90.00	90.00				

<sup>a</sup>GOF =  $[\sum[w(\text{Fo}^2 - \text{Fc}^2)^2]/(M - N)]^{1/2}$  (M = number of reflections, N = number of parameters refined). <sup>b</sup>R<sub>1</sub> =  $\sum\|\text{Fo} - \text{Fc}\|/\sum|\text{Fo}|$ . <sup>c</sup>wR<sub>2</sub> =  $[\sum[w(\text{Fo}^2 - \text{Fc}^2)^2]/\sum[(\text{Fo}^2)^2]]^{1/2}$ .

**Table 7.8** Crystal data and structural refinement parameters for complex **22** and **23**

	Complex <b>22</b>	Complex <b>23</b>		Complex <b>22</b>	Complex <b>23</b>
<b>Empirical formula</b>	C <sub>62</sub> H <sub>46</sub> C <sub>12</sub> Fe <sub>2</sub> N <sub>10</sub> O <sub>12</sub>	C <sub>66</sub> H <sub>50</sub> Fe <sub>3</sub> N <sub>16</sub> O <sub>8</sub>	<b>Z</b>	4	2
<b>Color</b>	green	red	<b><math>\rho_{\text{calc}}</math>(gcm<sup>-3</sup>)</b>	1.413	1.440
<b>Formula weight</b>	1305.69	1362.77	<b>F(000)</b>	3712	1440
<b>Temperature (K)</b>	293(2)		<b><math>\theta</math> range for data collection</b>	1.55-28.33	1.69-28.35
<b><math>\lambda</math> (Å) (Mo-K<math>\alpha</math>)</b>	0.71073		<b>Index ranges</b>	-34<h<33, -10<k<12, -37<l<36	-14<h<13, -24<k<24, -20<l<20
<b>Crystal system</b>	triclinic	triclinic	<b>Refinement method</b>	Full matrix least-squares on F <sup>2</sup>	Full matrix least-squares on F <sup>2</sup>
<b>Space group</b>	C2/c	P21/c	<b>Data/restraint/parameters</b>	7608/0/397	7583/0/186
<b>a(Å)</b>	25.7332 (13)	10.9959 (8)	<b>GOF<sup>a</sup> on F<sup>2</sup></b>	0.904	1.137
<b>b(Å)</b>	9.1036(4)	18.4953 (12)	<b>R<sub>1</sub><sup>b</sup> [I &gt; 2<math>\sigma</math>(I)]</b>	0.0773	0.1595
<b>c(Å)</b>	28.0589 (14)	16.0665 (12)	<b>R<sub>1</sub> (all data)</b>	0.1762	0.3207
<b><math>\alpha</math>(°)</b>	90.00	90.00	<b>wR<sub>2</sub><sup>c</sup> (I &gt; 2<math>\sigma</math>(I))</b>	0.2308	0.4125
<b><math>\beta</math>(°)</b>	110.991 (3)	98.356(5)	<b>wR<sub>2</sub> (all data)</b>	0.3008	0.4876
<b><math>\gamma</math>(°)</b>	90.00	90.00			

<sup>a</sup>GOF =  $[\sum[w(\text{Fo}^2 - \text{Fc}^2)^2]/M - N]^{1/2}$  (M = number of reflections, N = number of parameters refined). <sup>b</sup>R<sub>1</sub> =  $\sum||\text{Fol} - \text{Fc}||/\sum|\text{Fol}$ .  
<sup>c</sup>wR<sub>2</sub> =  $[\sum[w(\text{Fo}^2 - \text{Fc}^2)^2]/\sum[(\text{Fo}^2)^2]]^{1/2}$ .

**Table 7.9** Bond distances (Å) for L<sup>8</sup> and L<sup>9</sup>

L <sup>8</sup>		L <sup>9</sup>	
Bond type	Bond length(Å)	Bond type	Bond length(Å)
N4-N5	1.362(3)	N2-N3	1.513(2)
N2-N3	1.371(3)	N2-N5	1.357(3)

**Table 7.10** Bond distances (Å) and angles(°) of complex **13**

Bond type	Bond length(Å)	Bond type	Bond length(Å)
Cu1-N1	1.927(8)	Cu1-N2'	2.267(5)
Cu1-N1'	1.927(8)	Cu1-N3	2.307(5)
Cu1-N2	2.267(5)	Cu1-N3'	2.307(5)
Bond angles(°)			
N1'—Cu1—N1	178.45(17)	N1'—Cu1—N3'	76.37(15)
N1'—Cu1—N2'	77.53(15)	O2—Cu01—N5	93.02(8)
N1—Cu1—N2'	103.44(15)	N1—Cu1—N3'	102.62(14)
N1'—Cu1—N2	103.44(15)	N2'—Cu1—N3'	153.84(14)
N1—Cu1—N2	79.0(2)	N2—Cu1—N3'	82.96(14)
N2'—Cu1—N2	104.83(14)	N1'—Cu1—N3	102.62(14)
N1—Cu1—N3	76.37(15)	N2'—Cu1—N3	82.96(14)
N2—Cu1—N3	153.84(14)	N3'—Cu1—N3	101.11(14)

**Table 7.11** Bond distances (Å) and angles (°) of complex **14**

Bond type	Bond length(Å)	Bond type	Bond length(Å)
Cu1—N6	1.923(8)	Cu1—N5	2.256(30)
Cu1—N2	1.933(8)	Cu1—N10	2.280(9)
Cu1—N9	2.253(7)	Cu1—N4	2.308(14)
Bond angles(°)			
N6—Cu1—N2	175.01(29)	N2—Cu1—N10	107.30(27)
N6—Cu1—N9	76.65(28)	N9—Cu1—N10	153.51(27)
N2—Cu1—N9	99.14(28)	N5—Cu1—N10	82.84(26)
N6—Cu1—N5	106.72(26)	N6—Cu1—N4	99.92(27)
N2—Cu1—N5	76.60(27)	N2—Cu1—N4	76.89(30)
N9—Cu1—N5	102.05(26)	N9—Cu1—N4	84.94(25)
N6—Cu1—N10	77.02(27)	N5—Cu1—N4	153.33(27)
N10—Cu1—N4	102.41(25)		

**Table 7.12** Bond distances (Å) and angles of complex **15**

Bond type	Bond length(Å)	Bond type	Bond length(Å)
Cu1—N1	1.938(3)	Cu1—N3	2.269(3)
Cu1—N1'	1.938(3)	Cu1—N4	2.281(3)
Cu1—N3'	2.269(3)	Cu1—N4'	2.281(3)
Bond angles(°)			
N1—Cu1—N1'	179.4(1)	N3'—Cu1—N4	154.49(9)
N1—Cu1—N3'	102.20(9)	N3—Cu1—N4	100.20(9)
N1 <sup>1</sup> —Cu1—N3'	77.35(9)	N1—Cu1—N4'	77.15(9)



N1—Cu1—N3	77.35(9)	N1 <sup>1</sup> —Cu1—N4'	103.30(9)
N1'—Cu1—N3	102.20(9)	N3 <sup>1</sup> —Cu1—N4'	100.20(9)
N3'—Cu1—N3	84.72(8)	N3—Cu1—N4'	154.49(9)
N1—Cu1—N4	103.30(9)	N4—Cu1—N4'	86.14(9)
N1'—Cu1—N4	77.15(9)		

Table 7.13 Bond distances (Å) and angles (°) of complex 16

Bond type	Bond length(Å)	Bond type	Bond length(Å)
Co1—N1	1.958(8)	Co1—Cl1	2.271(3)
Co1—N5	2.233(7)	Co1—Cl2	2.269(5)
Co1—N3	2.258(7)		
Bond angles (°)			
N1—Co1—N5	76.96(27)	N3—Co1—Cl2	95.22(19)
N1—Co1—N3	77.35(27)	Cl1—Co1—Cl2	130.14(10)
N5—Co1—N3	154.27(25)	N3—Co1—Cl1	95.79(19)
N1—Co1—Cl1	116.78(21)	N1—Co1—Cl2	113.08(22)
N5—Co1—Cl1	96.93(19)	N5—Co1—Cl2	93.53(19)

**Table 7.14** Bond distances (Å) and angles (°) of complex **17**

<b>Bond type</b>	<b>Bond length(Å)</b>	<b>Bond type</b>	<b>Bond length(Å)</b>
Mn1—N10	2.364(11)	Mn1—N6	2.425(17)
Mn1—N9	2.361(10)	Mn1—N12	2.415(15)
Mn1—N4	2.381(10)	Mn1—N1	2.431(17)
Mn1—N3	2.401(10)	Mn1—N7	2.451(17)
<b>Bond angles(°)</b>			
N10—Mn1—N9	66.82(31)	N4—Mn1—N3	66.75(30)
N10—Mn1—N4	130.12(33)	N10—Mn1—N6	79.16(34)
N9—Mn1—N4	143.25(32)	N9—Mn1—N6	90.45(35)
N10—Mn1—N3	141.93(31)	N4—Mn1—N6	66.37(37)
N9—Mn1—N3	123.34(31)	N3—Mn1—N6	132.17(35)
N10—Mn1—N12	65.50(39)	N9—Mn1—N12	131.51(37)
N4—Mn1—N12	78.53(37)	N3—Mn1—N12	90.67(37)
N6—Mn1—N12	89.03(41)	N10—Mn1—N1	85.36(36)
N9—Mn1—N1	77.56(35)	N4—Mn1—N1	129.74(37)
N3—Mn1—N1	64.54(35)	N6—Mn1—N1	163.28(42)
N12—Mn1—N1	90.29(41)	N10—Mn1—N7	130.90(37)
N9—Mn1—N7	65.47(35)	N9—Mn1—N7	85.63(36)
N3—Mn1—N7	77.34(34)	N6—Mn1—N7	90.22(41)
N12—Mn1—N7	163.01(43)	N1—Mn1—N7	95.21(43)

**Table 7.15** Bond distances (Å) and angles (°) of complex **18**

Bond type	Bond length(Å)	Bond type	Bond length(Å)
Mn1—N6	2.277(4)	Mn1—N3	2.339(5)
Mn1—O6	2.289(4)	Mn1—N4	2.343(3)
Mn1—N1	2.290(4)	Mn1—O2	2.377(5)
Mn1—O1	2.300(5)	Mn1—O4	2.454(5)
<b>Bond angles (°)</b>			
N6—Mn1—O6	93.28(13)	N3—Mn1—N4	67.74(12)
N6—Mn1—N1	156.15(15)	N6—Mn1—O2	82.01(15)
O6—Mn1—N1	88.67(13)	O6—Mn1—O2	140.45(15)
N6—Mn1—O1	87.43(15)	N1—Mn1—O2	81.42(14)
O6—Mn1—O1	165.59(13)	O1—Mn1—O2	53.90(15)
N1—Mn1—O1	96.49(15)	N3—Mn1—O2	126.77(15)
N6—Mn1—N3	135.93(14)	N4—Mn1—O2	123.70(14)
O6—Mn1—N3	82.84(13)	N6—Mn1—O4	80.60(14)
N1—Mn1—N3	67.90(14)	O6—Mn1—O4	53.33(14)
O1—Mn1—N3	86.65(13)	N1—Mn1—O4	81.58(13)
N6—Mn1—N4	68.36(13)	O1—Mn1—O4	140.69(14)
O6—Mn1—N4	89.62(12)	N3—Mn1—O4	127.10(14)
N1—Mn1—N4	135.47(13)	N4—Mn1—O4	130.18(14)
O1—Mn1—N4	77.25(13)	O2—Mn1—O4	87.26(16)

**Table 7.16** bond distances (Å) and angles (°) of complex **19**

<b>Bond type</b>	<b>Bond length(Å)</b>	<b>Bond type</b>	<b>Bond length(Å)</b>
Co1—N1	2.149(3)	Co1—N7	2.206(4)
Co1—O5	2.157(3)	Co1—N4	2.253(3)
Co1—N6	2.173(3)	Co1—O4	2.332(3)
Co1—N3	2.193(3)		
<b>Bond angles(°)</b>			
N1—Co1—O5	92.56(10)	O5—Co1—N4	78.64(10)
N1—Co1—N6	71.33(9)	N6—Co1—N4	145.40(9)
O5—Co1—N6	83.44(10)	N3—Co1—N4	71.03(9)
N1—Co1—N3	71.11(9)	N7—Co1—N4	83.07(9)
O5—Co1—N3	101.75(10)	N1—Co1—O4	85.12(9)
N6—Co1—N3	142.26(9)	O5—Co1—O4	176.46(10)
N1—Co1—N7	138.35(9)	N6—Co1—O4	98.32(10)
O5—Co1—N7	103.04(10)	N3—Co1—O4	74.97(10)
N6—Co1—N7	72.43(10)	N7—Co1—O4	80.45(9)
N3—Co1—N7	139.48(10)	N4—Co1—O4	101.33(9)
N1—Co1—N4	138.29(9)		

**Table 7.17** Bond distances (Å) and angles (°) of complex **20**

Bond type	Bond length(Å)	Bond type	Bond length(Å)
Mn1—O2	2.128(12)	Mn1—N4	2.356(18)
Mn1—O1	2.131(11)	Mn1—N6	2.376(16)
Mn1—N1	2.335(12)	Mn1—N8	2.535(23)
<b>Bond angles(°)</b>			
O2—Mn1—O1	169.14(43)	O1—Mn1—N6	94.63(44)
O2—Mn1—N1	96.27(40)	N1—Mn1—N6	67.35(40)
O1—Mn1—N1	94.25(47)	N4—Mn1—N6	136.02(45)
O2—Mn1—N4	97.01(43)	O2—Mn1—N8	89.57(41)
O1—Mn1—N4	89.32(45)	O1—Mn1—N8	81.27(44)
N1—Mn1—N4	68.67(43)	N1—Mn1—N8	132.97(42)
O2—Mn1—N6	86.96(42)	N4—Mn1—N8	156.68(45)
N6—Mn1—N8	66.43(42)		

**Table 7.18** Bond distances (Å) and angles (°) of complex **21**

Bond type	Bond length(Å)	Bond type	Bond length(Å)
Ni01—N7	1.994(13)	Ni2—N3	1.995(13)
Ni01—N10	2.020(14)	Ni2—N12	2.072(13)
Ni01—N13	2.145(11)	Ni2—N4	2.116(13)
Ni01—N6	2.215(22)	Ni2—N1	2.122(11)
Ni01—N8	2.232(12)	Ni2—N14	2.225(18)
Ni01—Cl2	2.400(8)	Ni2—Cl1	2.360(8)
<b>Bond angles(°)</b>			
N7—Ni01—N10	172.83(57)	N3—Ni2—N12	169.03(54)

N7—Ni01—N13	93.75(55)	N3—Ni2—N4	76.16(67)
N10—Ni01—N13	79.39(52)	N12—Ni2—N4	93.41(60)
N7—Ni01—N6	77.19(58)	N3—Ni2—N1	78.08(51)
N10—Ni01—N6	99.92(56)	N12—Ni2—N1	112.08(48)
N13—Ni01—N6	84.64(62)	N4—Ni2—N1	154.04(56)
N7—Ni01—N8	111.28(49)	N3—Ni2—N14	97.12(63)
N10—Ni01—N8	75.54(49)	N12—Ni2—N14	77.94(55)
N13—Ni01—N8	154.93(50)	N4—Ni2—N14	82.83(68)
N6—Ni01—N8	99.18(57)	N1—Ni2—N14	97.25(53)
N7—Ni01—Cl2	93.17(54)	N3—Ni2—Cl1	89.84(62)
N10—Ni01—Cl2	89.44(49)	N12—Ni2—Cl1	94.64(50)
N13—Ni01—Cl2	94.21(50)	N4—Ni2—Cl1	95.70(61)
N6—Ni01—Cl2	170.17(52)	N1—Ni2—Cl1	87.38(45)
N8—Ni01—Cl2	85.99(49)	N14—Ni2—Cl1	172.30(45)

**Table 7.19** Bond distances (Å) and angles (°) of complex **22**

Bond type	Bond length(Å)	Bond type	Bond length(Å)
Fe1—O2	1.871(4)	O1—Fe1'	1.969(4)
Fe1—O1'	1.969(4)	Fe1—N3	2.134(6)
Fe1—N1	2.087(6)	Fe1—N5	2.181(5)
Fe1—O1	2.126(5)		
Bond angles(°)			
O2—Fe1—O1'	131.88(16)	N1—Fe1—N3	73.44(17)
O2—Fe1—N1	125.70(17)	O1—Fe1—N3	78.80(16)

O1'—Fe1—N1	96.00(16)	O2—Fe1—N5	81.58(17)
O2—Fe1—O1	83.02(15)	O1'—Fe1—N5	91.65(16)
O1'—Fe1—O1	72.27(14)	N1—Fe1—N5	71.69(18)
N1—Fe1—O1	144.18(16)	O1—Fe1—N5	140.20(16)
O2—Fe1—N3	105.18(17)	N3—Fe1—N5	140.77(19)
O1'—Fe1—N3	109.42(16)		

**Table 7.20** Bond distances (Å) and angles (°) of complex **23**

Bond type	Bond length(Å)	Bond type	Bond length(Å)
Fe1—O1	1.859(11)	Fe1—N4	2.207(8)
Fe1—O2'	2.002(9)	Fe1—N5	2.214(9)
Fe1—N1	2.116(8)	Fe1—O8	2.246(12)
Fe1—O2	2.141(8)	O2—Fe1'	2.002(9)
Bond angles(°)			
O1—Fe1—O2'	115.86(41)	O2—Fe1—N5	74.98(29)
O1—Fe1—N1	143.06(41)	N4—Fe1—N5	143.23(29)
O2'—Fe1—N1	90.09(31)	O1—Fe1—O8	71.56(45)
O1—Fe1—O2	78.26(40)	O2'—Fe1—O8	172.50(37)
O2'—Fe1—O2	71.0(3)	N1—Fe1—O8	82.79(36)
N1—Fe1—O2	137.52(30)	O2—Fe1—O8	112.92(36)
O1—Fe1—N4	81.12(40)	N4—Fe1—O8	90.56(35)
O2'—Fe1—N4	89.6(3)	N5—Fe1—O8	72.92(37)
N1—Fe1—N4	72.82(29)	O2'—Fe1—N5	102.73(33)
O2—Fe1—N4	141.39(29)	N1—Fe1—N5	72.66(30)
O1—Fe1—N5	121.66(41)		